In the footsteps of Antoni van Leeuwenhoek
&
EuroMEMBRANE
Advanced Practical Course

Zooming in on Plasmamembrane Dynamics with Advanced Light Microscopy

11- 15 June 2012
van Leeuwenhoek Centre for Advanced Microscopy
Amsterdam, The Netherlands

Zooming in on plasmamembrane dynamics with advanced light microscopy

Advanced practical course

van Leeuwenhoek Centre for Advanced Microscopy (LCAM)
11-15 June 2012
Amsterdam, the Netherlands

Content:

Section 1: General information

Section 1: General information

Objective of the course:

The aim of the EUROCORES Programme on EuroMEMBRANE is to answer long-standing questions in membrane biology using cutting-edge technologies. These will address functional problems in a quantitative manner bringing together experimental tools with theoretical approaches. There is a special emphasis on lipid-lipid and lipid-protein interactions in the plane of the membrane.

Recent technical developments have sparked a new wave of interest in this field. Microscopic techniques can be used to elucidate membrane composition, organization and dynamics, as this reflects the functions of cells and their organelles, transport of membranes, transport across membranes and signaling. Because of the recent technological revolution in advanced light microscopy (super-resolution imaging, functional imaging of molecules) it is now possible to directly monitor the dynamics of (single) molecules in biomembranes in living cells. Several new microscopy techniques are ideally suited for studying biomembrane dynamics but their application remains limited because most biologists have never been introduced to this technology. This practical advanced course is organized to provide participants the theoretical background and give hands-on experience of state-of-the-art (membrane) microscopy techniques.

Content:

During this 5-day course techniques like confocal and TIRF microscopy, Image correlation spectroscopy, Fluorescence recovery after photobleaching, Förster resonance energy transfer, Fluorescent protein and sensor development & Fluorescence lifetime and Super-resolution microscopy will be discussed during lectures, showing the theoretical background and applications, and practical sessions at the microscopes.

Organisers:

van Leeuwenhoek Centre for Advanced Microscopy (LCAM)

LCAM is a formal collaboration between three innovative microscopy centres at the Faculty of Science (FNWI) of the University of Amsterdam, the Academic Medical Centre (AMC) and the Netherlands Cancer Institute (NKI), all located in the Amsterdam region.

The formalized collaboration capitalizes on a large degree of synergy between the principle investigators in developing, adapting and applying advanced microscopy for use in cell biology. Besides delivering access to the diverse advanced microscopy instruments, LCAM has developed as a leading centre in functional live cell imaging (FRET, FLIM, FCCS, FCS, FRAP and spectral imaging). For more info check out www.lcam.nl

LCAM is named after one of the founders of microscopy, Antoni van Leeuwenhoek (1632-1723)

European Science Foundation (ESF)

The European Science Foundation (ESF) was established in 1974 to provide a common platform for its Member Organisations to advance European research collaboration and explore new directions for research.

It is an independent organisation, owned by 72 Member Organisations, which are research funding organisations, research performing organisations and academies from 30 countries. ESF promotes collaboration in research itself, in funding of research and in science policy activities at the European level. For more info visit www.esf.org

Safety:

The participant acknowledges that he/she is aware about the health and safety hazards that have to be followed during the practical sessions, notably laser safety, handling of chemicals & electrical apparatus and the handling of genetically modified organisms.

Course and SP visitor badges:

Participants are kindly requested to wear their personal course badge during the course. In addition, in the Sciencepark building everyone requires a visitor badge that will also give you access to the research floors (2nd floor and higher) where the practicals and lunch will take place. During the first day you will obtain a visitor badge, valid for the whole week, that has to be returned at Friday afternoon.

Internet access:

Within the Sciencepark building one can access the wireless network using the Eduroam network in combination with your own login ID (only working when your institute is supporting Eduroam). Alternatively one could use the UvA account that has been made for you. Connect to the UVaCongress network and open your browser. Login with your emailaddress and the password that has been send to you. For more info contact Mark Hink.

Evaluation form:

We would appreciate if you could fill in the evaluation form at the end of the course. In this way we and ESF are able to further improve the quality of future courses. The enquiries will be distributed at the final Friday afternoon session at SciencePark.

Coffee, tea and lunch breaks:

Coffee and tea will be served in the lecture room during the coffee breaks and supplied by your instructor during the practical sessions. The lunch in SciencePark is served in the SILS common room that can be found at the 3rd floor (near lab A3.14) or in the AMC restaurant.

Course coordinators:

Information concerning the course registration, accommodation & payments

Mrs Laura M. Wind
Swammerdam Institute for Life Sciences
University of Amsterdam
Science Park 904 (room C2.202)
NL-1098 XH Amsterdam
The Netherlands
Tel: +31-20-525 7931
Fax: +31-20-525 7934
Email: L.M.Wind@uva.nl

Information concerning course content

Prof. dr. Theodorus W.J. Gadella Jr.
Chairman of section of Molecular Cytology
Director van Leeuwenhoek Centre for Advanced Microscopy
Swammerdam Institute for Life Sciences
University of Amsterdam
Science Park 904 (room C2.266)
NL-1098 XH Amsterdam
The Netherlands
Email: Th.W.J.Gadella@uva.nl

Dr. Mark Hink
section of Molecular Cytology
van Leeuwenhoek Centre for Advanced Microscopy
University of Amsterdam
room C2.264
Sciencepark 904
Tel: 020-525 6211
Email: M.A.Hink@uva.nl

Location:

The course will be organised at the three locations of the van Leeuwenhoek Centre of Advanced Microscopy (LCAM), spread throughout Amsterdam (see map next page). The course kicks off at Monday June 11th at room A1.10 (first floor) of the SciencePark building (LCAM-FNWI)

University of Amsterdam-Faculty of Science (FNWI)

Sciencepark 904
1098 XH Amsterdam

University of Amsterdam-Amsterdam Medical Centre (AMC)

Meibergdreef 9
1105 AZ Amsterdam

Netherlands Cancer Institute, Antoni van Leeuwenhoek Hospital (NKI)

Plesmanlaan 121
1066 CX Amsterdam

Diemen
Amsterdam Zuidoost
Duivendrecht
Ouderkerk aan de Amstel
Ouder-Amstel
Amstelveen
Bovenkerk
Nieuwe Meer
Amsterdamse Bos
Amsterdam-Zuid
Amsterdam-Oost
Oost en Watergraafsmeer
Diemerbos
Diemerpolder
Gaasperplas
Gaasperpark
Zuidoost
Bijlmerweide
Bijlmerpark
Overdiemen
Stammerdijk
Penbos
Middenmeer
Nieuwe Oosterbegraafplaats
Amsterdam Old Course
Amstelborgh/ Borchland
Bullewijk
Overamstel
Amstelpark
Het Loopveld
't Kleine Loopveld
Kleine Wetering
ZuiderAmstel
Vrije Universiteit Amsterdam
Amstelveenseweg
Beneluxbaan
Oranjebaan
Keizer Karelweg
Burgemeester van Sonweg
Handweg
Sportlaan Oost
De Braak
Het Amsterdams Bos
Speelweide
De Poel
Bosbaan
Bosbaanweg
Grote Vijver
Grote Speelweide
Nieuwemeerdijk
Schinkeldijk
Bosrandweg
Ruimzichtlaan
Ouderkerkerplas
Schoonhovendreef
Gaasperzoom
Tafelbergweg
Foppingadreef
Gooiseweg
Holterbergweg
Spaklerweg
Amsteldijk
Wibautstraat
Churchilllaan
Rivierenbuurt
President Kennedylaan
Ringweg Zuid
Ringweg Oost
Parnassusweg
Stadionweg
Beatrixpark
Vondelpark
Oud-Zuid
Hobbemakade
De Lairessestraat
Oosterpark
Flevopark
Universiteit van Amsterdam
Diemerpark
Rietveld West
Grote Rietveld
Havenrei
Ijburglaan
Ijburgbaan
Zuidas
Amstelglorie
Machineweg
Groenelaan
Mr. Jac. P. Thijsseweg
Cruquiusweg
Nieuwe Haagseweg
Ons Buiten
Amsterdam-Rijnkanaal
A1
A2
A4
A9
A10
E19
E22
E35
E231
N231
N522
s100
s106
s107
s108
s109
s110
s111
s112
s113

Course hotel:
If you Love City Life, Hampshire Hotel - Lancaster Amsterdam is exactly what you're looking for! Staying in the quiet and exclusive part of the city centre, opposite the Artis Zoo, the hotel can easily be reached by public transport and offers paid parking space in the direct vicinity. You are only a few minutes away from Amsterdam's highlights. For more details about the hotel check out www.hampshire-hotels.com/hotel_details.php?lan=en&hotelId=102.

Every morning at 8.30 a taxi is available at the hotel to bring you to the course at Sciencepark or AMC (on Thursday).

Traveling between LCAM locations:
The practicals will be organised at the three locations of the van Leeuwenhoek Centre of Advanced Microscopy (LCAM) and during the evening we will visit some restaurants which are spread throughout Amsterdam. This will require some traveling during the course day which we will do by cars, taxis, public transport or by walking. We will notify you during the morning sessions how we are traveling that day.

Sciencepark can be accessed directly via train station *Amsterdam Sciencepark* or using bus service nr 40 that is riding between trains stations *Amsterdam Muiderpoort* and *Amsterdam Amstel*. By car one has to take exit *Watergraafsmeer* from the A10 highway and follow the signs *Sciencepark*. Paid parking spots are available at parking region P3

AMC can be accessed by changing at trainstation *Duivendrecht* to metroline 9 and exit at stop *Holendrecht* or take buslines 45, 47, 120, 126 or 158 to *Holendrecht*. By car one can access the AMC via highways A2 or A9, taking exit *AMC* and park the car at one of the paid parking spots available.

NKI can be accessed via trainstation *Amsterdam Lelylaan* in combination with bus services 18,19, 23, 64 or 197. Alternatively one can use metroline 50 and exit at stop Heemstedestraat from where it's a 10 min walk. By car one approaches the NKI via highways A10 or A4 and take exit *Sloten (s107).* Follow the signs *Slotervaart Ziekenhuis* and park the car at the paid park centre Medical Centre Slotervaart.

Information about Amsterdam:
Amsterdam, capital of the Netherlands, became a metropolis since the second half of the sixteenth century. Amsterdam now hosts more than 750,000 residents from 175 different countries. 37% of the population belong to an ethnic minority. There is an open and tolerant atmosphere in the city. Amsterdam has a temperate climate with mild winters, cool summers and precipitation throughout the year. A good climate for the city makes it easy to visit throughout the year.

In the city you can discover something new each time, did you know that aside from 6 windmills there are 600,000 bicycles? In one of the 51 musea is very much to see and enjoy. And in June 2012 you have the chance to meet those Orange-mad Dutchmen, when they are watching and celebrating everywhere throughout the city their national football team during the European championship. For more info about Amsterdam check out www.iamsterdam.com

Programme:

Sunday June 10th 2012: Arrival

Monday June 11th 2012:

9.00-9.15	ScPark A1.10	Welcoming address (Dorus Gadella)
9.15-10.00	ScPark A1.10	Lecture confocal microscopy (Erik Manders)
10.00-11.00	ScPark A1.10	Lecture TIRF microscopy (Ulrike Engel)
11.00-11.30	ScPark A1.10	Coffee break
11.30-12.30	ScPark A1.10	Lecture Image correlation spectroscopy (Paul Wiseman)
12.30-13.30	ScPark SILS cr	Lunch
13.30-17.00	ScPark	Practicals of 4 groups of 4 students (confocal + TIRF)
17.30-19.00		Dinner in "De Polder", Sciencepark 205, A'dam
19.00-20.30	ScPark A1.10	Flash-presentations from participants

Tuesday June 12th 2012:

9.00-12.30	ScPark	Practicals of 4 groups of 4 students (confocal + TIRF)
12.30-13.30	ScPark SILS cr	Lunch
13.30-14.30	ScPark A1.10	Lecture fluorescent dyes and sensors (Carsten Schulz)
14.30-15.30	ScPark A1.10	Lecture fluorescent proteins (Vladislav Verkusha)
15.30-16.00	ScPark A1.10	Coffee break
16.00-17.00	ScPark A1.10	Lecture fluorescent membrane sensors (Tamas Balla)
18.00-20.00		Dinner in "Ponteneur", 1e van Swindenstraat 581, A'dam

Wednesday June 13th 2012:

9.00-10.00	ScPark A1.10	Lecture Fl. Lifetime Imaging Microscopy (Dorus Gadella)
10.00-11.00	ScPark A1.10	Lecture FRET in membrane systems (Kees Jalink)
11.00-11.30		Coffee break
11.30-12.30	ScPark A1.10	Lecture Fl. Recovery After Photobleaching (Adriaan Houtsmuller)
12.30-13.30	ScPark SILS cr	Lunch
13.30-17.00	ScPark & NKI	Practicals of 4 groups of 4 students (FCS, FLIM, FRET & FLIM)
18.00-20.00		Dinner in "Moeders", Rozengracht 251, A'dam

Thursday June 14th 2012:

9.00-10.00	AMC M3-108	Lecture Fluorescence fluctuation analysis in membrane (Mark Hink)
10.00-11.00	AMC M3-108	Lecture FRAP in membrane systems (Eric Reits)
11.00-11.30		Coffee break
11.30-12.30	AMC M3-108	Lecture Super-resolution microscopy (Thomas Schmidt)
12.30-13.30	AMC	Lunch
13.30-17.00	ScP, NKI, AMC	Practicals of 4 groups of 4 students (FRAP, FCS, FRAP, FRET)
18.00-20.00		Dinner in "Oude Gasthuis", Meibergdreef 23, A'dam

Friday June 15th 2012:

9.00-11.30	ScP, NKI, AMC	Practicals of 4 groups of 4 students (FRAP, FCS, FRAP, FRET)
11.45-12.45	ScPark SILS cr	Lunch
13.00-16.30	ScP, NKI, AMC	Practicals of 4 groups of 4 students (FRAP, FCS, FRAP, FRET)
17.00-17.30	ScPark A1.10	Closing remarks (Dorus Gadella)
18.00-20.30		Drinks and dinner in "Pompstation", Zeeburgerdijk 52, A'dam

Saturday June 16th 2012: Departure

The SILS common room (cr) is located at Sciencepark 3rd floor near lab 3.14

Practical groups:

Group 1:
Alexander Zwirzitz
Gülis Zengin
Valentina Bettio
Niels Heemskerk

Group 2:
Giulia De Luca
Anna Daniel
Marko Kamp
Kayode Salami

Group 3:
Rene Platzer
Kay Oliver Schink
Angelika Holm
Jenny Brinkmann

Group 4:
Lindsay Haarbosch
Nadezda Chakrova
Dion Richardson
Dimitra Touli

Practical sessions:

1. Confocal microscopy
2. Total Internal Reflection Fluorescence Microscopy (TIRF)
3. Fluorescence Fluctuation Spectroscopy (FFS)
4. Fluorescence Lifetime Imaging Microscopy (FLIM)
5. Förster Resonance Energy Transfer (FRET)
6. Fluorescence Recovery After Photobleaching (FRAP)

Date	Time	Group 1			Group 2			Group 3			Group 4		
		Subj	Room	Instr	Subj	Room	Instr	Subj	Room	Instr	Subj	Room	Instr
11-June-20	9.00-9.15	Welcome, Dorus Gadella, ScP A1.10											
	9.15-10.00	Confocal microscopy, Erik Manders, ScP A1.10											
	10.00-11.00	TIRF microcopy, Ulrike Engel, ScP A1.10											
	11.30-12.30	Image correlation spectroscopy, Paul Wiseman, ScP A1.10											
	13.30-17.00	Conf	ScP A2.34	EM	Conf	ScP A2.40	RB	TIRF	ScP A2.34	KC	TIRF	ScP A2.34	DG
12-June-20	9.00-12.30	TIRF	ScP A2.34	DG	TIRF	ScP A2.34	KC	Conf	ScP A2.34	EM	Conf	ScP A2.40	RB
	13.30-14.30	Fluorescent sensors, Carsten Schultz, ScP A1.10											
	14.30-15.30	Fluorescent proteins, Vlad Verkusha, ScP A1.10											
	16.00-17.00	Membrane sensors, Tamas Balla, ScP A1.10											
13-June-20	9.00-10.00	FLIM, Dorus Gadella, ScP A1.10											
	10.00-11.00	FRET, Kees Jalink, ScP A1.10											
	11.30-12.30	FRAP, Adriaan Houtsmuller, ScP A1.10											
	13.30-17.00	FCS	ScP A2.40	MH	FLIM	ScP A2.34	JG	FRET	NKI B5	KJ	FLIM	NKI B5	MR
14-June-20	9.00-10.00	FCS, Mark Hink, AMC											
	10.00-11.00	FRAP in membranes, Eric Reits, AMC											
	11.30-12.30	Super-resolution microscopy, Thomas Schmidt, AMC											
	13.30-17.00	FRAP	AMC M3-108	ER	FCS	ScP A2.40	MH	FRAP	ScP A2.40	JG	FRET	NKI B5	KJ
15-June-20	9.00-11.30	FLIM	ScP 2.34	DG	FRET	NKI B5	KJ	FCS	ScP A2.40	MH	FRAP	AMC M3-108	ER
	13.00-16.30	FRET	NKI B5	KJ	FRAP	AMC M3-108	ER	FLIM	ScP A2.34	JG	FCS	ScP A2.40	MH
	17.00-???	Evaluation and drinks, Dorus Gadella, ScP A1.10											

Section 2: Lecture courses

Erik Manders, Monday June 11th 2012, 9.15

For about 400 years the light microscope has been an instrument to observe small objects such as cells and to answer the question “What does it look like?”. The confocal microscope one of the steps in this long evolution (“what does it look like in 3D ”). And still new techniques are being developed to see where molecules are (super-resolution microscopy). In addition, during the last 2 decades new microscopy techniques have been developed to answer additional questions like: “What are molecules doing, where do they go to, how long do that stay there and who do they meet?”. In this course you will meet many of these technologies and you will learn how en when to use them.

In this first lecture we will discuss the fundamentals of light microscopy. After some history of microscopy technology and optical theory we will first focus on the limited resolving power of the light microscope. This limitation will briefly be explained by wave-theory of light (Huygens) and particle-theory (Heisenberg). We then will discuss the principles of confocal fluorescence microscopy, its limitations and applications in cell (membrane) biology.

Fluorescence Techniques to Study Lipid Dynamics

Erdinc Sezgin and Petra Schwille

Biophysics Group, BIOTEC, TU Dresden, 01307 Dresden, Germany

Correspondence: schwille@biotec.tu-dresden.de

Cold Spring Harbor Perspectives in Biology
www.cshperspectives.org

Biological research has always tremendously benefited from the development of key methodology. In fact, it was the advent of microscopy that shaped our understanding of cells as the fundamental units of life. Microscopic techniques are still central to the elucidation of biological units and processes, but equally important are methods that allow access to the dimension of time, to investigate the dynamics of molecular functions and interactions. Here, fluorescence spectroscopy with its sensitivity to access the single-molecule level, and its large temporal resolution, has been opening up fully new perspectives for cell biology. Here we summarize the key fluorescent techniques used to study cellular dynamics, with the focus on lipid and membrane systems.

To elucidate cellular processes in their native dynamic environment has been one of the main issues in cell biology over the past decades. The lack of appropriate techniques has long been the main limiting step for the research on dynamic systems, because it was impossible to acquire real time information with the well-known biochemical techniques. The key challenge in dynamically observing biological systems is to combine the ability to resolve moderate to very low concentrations of molecules—because they are simply limited in living cells—on relevant timescales. Relevant timescales in cell biology can be minutes and hours, on a systemic level of cell metabolism, down to the microsecond and even nanosecond regime in which molecular and intramolecular rearrangements take place. With respect to lipidic systems, relevant dynamics range from the local movements of lipids by diffusion to the mechanical transformations of whole membranes, spanning several orders of magnitude in time to be covered. Like for other cellular processes, the investigation of lipids and membranes also in general benefited greatly from the introduction of fluorescence microscopy and spectroscopy to biology. After the 1960s, great technological inventions based on the phenomenon of fluorescence were made, such as confocal microscopy, fluorescence recovery after photobleaching (FRAP), fluorescence correlation spectroscopy (FCS), Förster resonance energy transfer (FRET), total internal reflection fluorescence (TIRF), and two-photon microscopy, that not only revolutionized imaging but also yielded access to dynamics on previously inaccessible timescales. Another very big step was certainly taken after the introduction

Editor: Kai Simons

Additional Perspectives on The Biology of Lipids available at www.cshperspectives.org

 doi: 10.1101/cshperspect.a009803
Cite this article as *Cold Spring Harb Perspect Biol* 2011;3:a009803

of fluorescent proteins, which again accelerated the use of these techniques in living cells and organisms. Nowadays, the technical advancements of fluorescence-based methods allow us to explore systems as small as single molecules with temporal resolution down to the nanoseconds regime. Lately, even the resolution limit of optical microscopy, for a long time being one of the fundamental barriers in elucidating cellular processes, has been overcome by smart applications of the phenomenon of fluorescence.

This article aims at giving a short overview on mainly fluorescence-based methods that have in recent years propelled lipid and membrane research to fully new levels. We will give a short introduction to the modern fluorescence technology in general, referring to the techniques that allow addressing dynamics. A particular focus will be on fluorescence correlation spectroscopy, a technique that our lab works primarily on, but other important methods will also be discussed, including their promises, achievements, and caveats.

FLUORESCENCE TO STUDY LIPID DYNAMICS

The attempt to visualize the "living units" has progressed remarkably after Hooke's Micrographia. Starting from a simple light source, a mechanical stage, and up to three glass lenses, microscopy nowadays culminated in so-called super-resolution techniques with particle localization accuracies down to the nanometer range. Certainly, the involvement of the phenomenon of fluorescence is one of the biggest steps in this long journey.

Fluorescence is such a ubiquitous phenomenon that it is impossible to speculate about its first systematic observation. The first reported documentation of fluorescence is thought to be Nicolas Monardes' observation of wood extract. In 1845, John Herschel observed the fluorescent property of quinine sulphate which is believed to be the onset of modern fluorescence spectroscopy. After many more observations by several light philosophers in the 19th century, it was Stokes who actually termed this phenomenon "fluorescence" in 1838. The first application in biology was probably in 1914 Stanislav von Provazek who used fluorescence as a cell stain. August Koehler and Oskar Heimstadt were reportedly the first scientists who performed fluorescence microscopy in early 1900s. Today, a century later, fluorescence imaging and microscopy is one of the most powerful tools in the visualization and dynamic analysis of living structures, especially following the discovery of fluorescent proteins as cloneable markers, and the invention and widespread use of confocal microscopy. Minsky, its inventor, patented the idea of confocal microscopy already in the 1950s, and about 20 years later, the first commercial confocal microscopes appeared. Since then, many researchers and optical engineers step by step improved the technical realization (Brakenhoff et al. 1979; Davidovi and Egger 1973; Egger and Petran 1967; Hamilton and Wilson 1986; Sheppard and Wilson 1979). The rapid developments in laser and detector technology, along with the onset of fiber optics certainly helped in the rapid dissemination of confocal microscopy into cell biology laboratories around the world (Amos and White 2003).

When light interacts with matter, many photophysical phenomena may occur. Some molecules absorb light at a particular wavelength, whereas others predominantly scatter the light. On absorption, the molecules undergo vibrational relaxation on timescales between 10^{-14} and 10^{-12} sec, and then return to ground state, either by emitting a photon at a longer wavelength after 10^{-9} to 10^{-7} nsec, which is called fluorescence, or nonradiatively. Less probably, the molecules can jump to the quantum-mechanically forbidden triplet state or molecules transfer their energy to other molecules, by quenching or resonant energy transfer. After the molecules undergo the triplet state, they return to the ground state either by emitting light in longer time ranges than fluorescence or nonradiatively.

In the following sections, we will briefly touch on the task of fluorescently labeling lipids to be investigated, and then discuss, one by one, the most powerful biophysical techniques to study lipids and membranes in real time, along with some of their relevant applications.

Fluorescent Probes to Study Lipid Dynamics

After the invention of green fluorescent protein (GFP) as the first truly genetic fluorescent probe, visualizing proteins in their native environment became much more straightforward. From the perspective of the membrane researcher, this significantly improved our understanding of membrane proteins and their dynamics, but could help only marginally in better elucidating the functional dynamics of lipids. The first report on labeling lipids in living cells used azide-alkyne to label alkyne containing PA (Schultz et al. 2010). Besides this direct labeling, coupling the synthetic fluorescence molecules to lipids in vitro, and then reconstitute them to the cell membrane is getting more common in lipid field, enforcing the use of fluorescence also in lipid biology. Synthetic dye coupling has many advantages compared to fluorescent proteins, which nowadays represent the main strategy in protein labeling. First of all, one has theoretically a large choice of organic dyes in terms of their optical characteristics. It is possible, for instance, to use a far red dye; however, there is not yet a well-established monomeric far red protein. Second, the quantum efficiency and brightness of most of the organic dyes are higher than for fluorescent proteins. Cholesterol (Boldyrev et al. 2007; Holtta-Vuori et al. 2008; Marks et al. 2008; Oreopoulos and Yip 2009), Sphingomyelin (Marks et al. 2008; Eggeling et al. 2009; Tyteca et al. 2010), GM1 (Coban et al. 2007; Eggeling et al. 2009; Mikhalyov et al. 2009), PC, and PE (Baumgart et al. 2007; Juhasz et al. 2010) are some of the lipids that are often conjugated to organic dyes. Additionally, fluorescently labeled membrane-binders, like choleratoxin, are used to label, for example, the GMs on the cell surface (Middlebrook and Dorland 1984). However, taking into account that organic fluorophores are in comparison much larger handicaps to small lipid molecules than they are to proteins, and that the relatively tight packing of lipids in a membrane might be more easily disturbed by labeled lipids than in the case of soluble proteins, a careful control of the possible influence of labels on the functionality of lipids is of utmost importance.

Besides fluorescent lipid conjugates, there are some lipophilic fluorescent molecules frequently used to yield information on a specific lipid environment. They efficiently and selectively penetrate into lipid membranes, and to some extent even reflect on their physical properties, like viscosity, order, pH, or water content. DiO, DiD, DiI, Laurdan, and NAP are the lipophilic dyes most commonly used to visualize the lipid environment (Baumgart et al. 2007). Although the Di family of dyes is phase-preferring probes preferring either liquid-ordered (L_o) phase or liquid-disordered (L_d) phase in a specific setting, Laurdan has a different property. It partitions equally in both phases, but its emission spectrum changes according to the polarity of the membrane environment. Providing that L_d phase is more aqueous than L_o phase, on excitation the dye consumes some of its energy to reorient the water molecules in L_d phase, which shifts the emission to the red spectral region (emission maximum of 490 nm), whereas it is more blue shifted in L_o region (emission maximum of 440 nm). According to the ratio of fluorescence intensity in the blue-shifted (L_o phase) and the red-shifted region (L_d phase), one can calculate an order indicative value called generalized polarization (GP) calculated as

$$\mathrm{GP} = \frac{I_{440} - I_{490}}{I_{440} + I_{490}}, \qquad (1)$$

where I_x denotes the intensity at wavelength of x.

In addition to generalized polarization, fluorescence anisotropy is another important phenomenon that can be exploited to monitor rotational diffusion of the molecules by using the polarization of light. Because rotational diffusion is very sensitive to the size of molecules, binding constants can be efficiently derived from fluorescence anisotropy measurements. There have been comparative studies on the feasibility of several dyes for fluorescence anisotropy. Alexa and Oregon dyes conjugates with biological molecules (e.g., lipids), for instance, were found to be suitable for this method (Rusinova et al. 2002). Additionally, NBD and DHP lipid conjugates were used for fluorescence anisotropy to detect rafts in living cells (Gidwani et al. 2001). Laurdan generalized polarization

and fluorescence anisotropy were compared elsewhere (Engelke et al. 2001).

Besides lipid probes for the plasma membrane, there are also some tools to probe other lipidic environments in the cell, such as lipid droplets (Thiele and Spandl 2008). New fluorescent lipids were developed to visualize the intracellular and membrane lipids in their native environment without any external fluorescent labels (Kuerschner et al. 2005; Spandl et al. 2009).

Confocal Microscopy

Confocal microscopy may easily be the most widely applied imaging technique in cell and molecular biology field because it allows live cell imaging with high spatial and temporal resolution, as well as optical sectioning and 3D reconstruction of images. To start with the techniques for cell dynamics, confocal microscopy should therefore be briefly mentioned because it forms the basis (and often the gold standard) for most of the other techniques.

The confocal concept evolved as an alternative to wide-field microscopy. For wide-field microscopy, the so-called Koehler illumination guarantees a homogeneous illumination of the whole sample, which is then detected by area detectors. In contrast to this, confocal illumination occurs only at a resolution-limited point, which can then be sequentially scanned in three dimensions throughout the sample. As a technical difference, coherent light sources (lasers) are usually employed in confocal microscopy, whereas incoherent lamps are still mostly used in wide-field microscopy. However, the basic difference between wide-field and confocal microscopies is a so-called pinhole aperture which eliminates the out-of-focus light in the image plane, being the main source of background in wide field. The minimal size of the confocal illumination volume, and therefore the resolution that can be reached in confocal microscopy is usually determined by the so-called Rayleigh criterion. Here, resolution of the wide field is defined as the shortest distance d between two optically separable points:

$$d = \frac{0.61 \times \lambda}{\mathrm{NA}}, \tag{2}$$

where λ is the wavelength and NA is the numerical aperture of the objective. When the advantage of selective detection (pinhole) and selective illumination (diffraction limited spot by coherent light source) are applied, the resolution reaches a better point:

$$d = \frac{0.4 \times \lambda}{\mathrm{NA}}, \tag{3}$$

Taking above equation into consideration, the theoretical resolution of a confocal system with an NA of 1.4, at a wavelength of 500 nm should be ~160 nm. However, all theoretical calculations consider a perfect optical system and a pinhole of a laser spot size (i.e., Airy disc size). Yet, there are many aberrations caused by imperfect optics such as spherical aberrations, chromatic aberrations, astigmatism, comma etc. Moreover, pinhole size can never be as small as laser spot size. The biggest problem in confocal microscopy is, however, the large discrepancy between lateral (x–y) and axial resolution, resulting in image stacks that are usually quite blurred in the z dimension.

Axial resolution is given by

$$d_z = \frac{1.4 \times \lambda \times n}{\mathrm{NA}^2}, \tag{4}$$

where n is the refractive index of the medium. The axial resolution is usually three to five times worse than lateral resolution.

The limitation in axial resolution is a minor problem for pure membrane systems with little to no contribution of fluorescence light coming from the solution above and below the membrane. Thus, confocal microscopy has been particularly useful on supported membranes or giant unilamellar vesicles (GUVs) (Korlach et al. 1999). On the other hand, for the study of cellular membranes with their rather high background from cellular autofluorescence and labeled molecules that cannot easily be retained at the cell surface (e.g., because of endocytosis), limited z resolution can be a significant technical problem in studying lipid dynamics. For this reason, other illumination strategies established for fluorescence microscopy, such as total internal reflection (TIR), are

becoming increasingly popular for lipid and membrane research.

Total Internal Reflection Fluorescence (TIRF) Microscopy

Total internal reflection is a well-known phenomenon in everyday life. When a light beam passes from a medium with a refractive index n_1 to the other medium with a refractive index n_2, the relationship between the angle of incidence α_1 and the angle of refraction α_2 is determined by Snell's law:

$$n_1 \sin \alpha_1 = n_2 \sin \alpha_2. \quad (5)$$

When $n_1 > n_2$ (e.g., when light is propagating from water or glass into air), there exists a critical α_1 angle that would render the refraction angle to be 90° (i.e., parallel to the interface). At incidence angles equal to or greater than this critical angle, light cannot cross the boundary, and is internally reflected. This phenomenon is called total internal reflection (TIR). The critical angle (α_c) is determined by the refractive indices of the media:

$$\alpha_c = \sin^{-1}(n_2/n_1). \quad (6)$$

Although the light ray is totally reflected, its electrical field creates an evanescent wave whose intensity decreases exponentially in the axial direction (Fig. 1):

$$I(z) = I(0)e^{-z/d}, \quad (7)$$

where d is defined as

$$d = \left(\frac{\lambda}{4\pi}\right)\left(n_1^2 \sin^2 \alpha_1 - n_2^2\right)^{-1/2}, \quad (8)$$

and λ is the wavelength. The principle is schematically depicted in Figure 1.

The most remarkable feature of TIR illumination for membrane research is that the evanescent wave illuminates only a limited distance (~100 nm) along the z-axis, which reduces background coming from molecules above the surface substantially, thereby increasing the axial resolution and the signal-to-noise levels. The detailed physics behind TIR can be accessed from references Axelrod (2008) and Axelrod et al. (1983).

There are currently two methods to realize this illumination mode for fluorescence microscopy. The first, simpler, method is to use a high-NA TIRF objective. The light beam entering the objective is focused at the back focal plane of the objective with a displacement from the optical axis, such that it reaches the surface above the critical angle. Surface fluorescence is collected by the same objective and can be detected in the usual way.

The necessity for using a high-NA objective can be understood by considering that

$$\mathrm{NA} = n \sin \theta. \quad (9)$$

Then, Equation 8 can be rewritten as

$$d = (\lambda/4\pi)(\mathrm{NA}^2 - n_2^2)^{-1/2}. \quad (10)$$

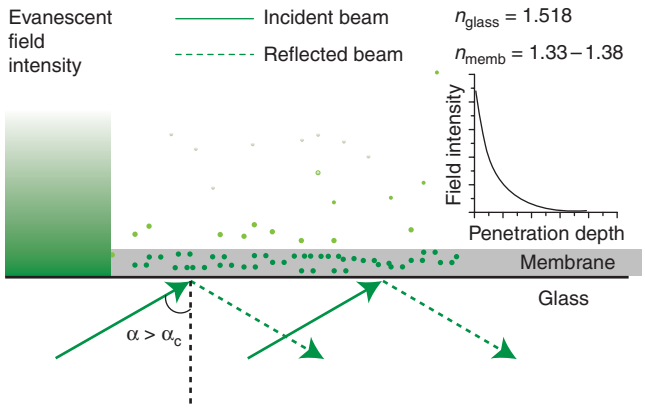

Figure 1. Evanescent wave and TIRF.

When NA $< n_2$, d is imaginary, which means light is refracted and TIR is lost. That is why the NA of TIRF objectives should be higher than the refractive index of the sample medium. A living cell has a refractive index of 1.33–1.38. Many current TIRF objectives thus have a NA of 1.45, which creates a penetration depth of the evanescent field of 82 nm at 488 nm excitation just above the critical angle.

The second way to create an evanescent wave is to use a prism. In this case, the sample is located between the prism and objective. The illumination is performed through the prism, while the objective collects the emission and transfers the signal to the camera. This decoupling of illumination and detection can be quite useful to create large illumination areas, but is less comfortable than objective-based TIR, which can be easily realized in any fluorescence microscope.

Further advantages of prism-based TIR are lower background and a better control on angle and polarization. It is also easy to set up for two colors. On the other hand, the free access to one side of the sample, safety of lasers, ease to use with cell culture plates can be counted as the advantages of objective-based system.

TIRF can be coupled to other techniques as a specific illumination mode when good z resolution is crucial. It has been combined with FCS, FRET, FRAP, AFM, fluorescent lifetime imaging, two-photon excitation, optical traps, and interference reflection. Some combinations of these techniques will be discussed later.

Polarized TIRF

The fluorophores can be excited only if their dipole is parallel to the excitation light dipole, which is called photoselection. A variation of TIRF called polarized TIRF uses polarized light perpendicular to the incidence plane (p-polarized) and parallel to the incidence plane (s-polarized) to overcome this limit. If the dipole of a fluorophore is always parallel to the membrane surface, p-polarized light can help to excite only the regions where the membrane is not parallel to the surface. The investigation of membrane curvature can be an important application field for polarized TIRF (Axelrod 2008).

TIRF Applications on Membrane Dynamics

There have been many studies to elucidate membrane dynamics using TIRF. Recently, it has been shown that TIRF has the capacity to show the adsorption of proteins and peptides to lipids in SLBs (Fox et al. 2009; Jorgensen et al. 2009). TIRF was combined with single-particle tracking to show the enrichment of GPI-anchored proteins in sphingolipid rich regions, as proposed by lipid raft theory (Pinaud et al. 2009). A new method has also been applied to detect lipid rafts, called LG-TIRF (Sohn et al. 2010). Other applications were to elucidate the role of ceramide in membrane restructuring (Ira et al. 2009), the organization of bacterial light harvesting complex 2 (Dewa et al. 2006), the role of cholesterol in antibody binding (Yu et al. 2009), EGFR activation by EGF (Sako et al. 2000; Cannon et al. 2005; Teramura et al. 2006), and the phase preference of peptides (Choucair et al. 2007). Membrane curvature, exocytosis, and endocytosis are some other topics in which TIRF is successfully applied (Merrifield et al. 2002, 2005; Byrne et al. 2008; Nagamatsu and Ohara-Imaizumi 2008; Joselevitch and Zenisek 2009; Ohara-Imaizume et al. 2009; Aoki et al. 2010; Gorg et al. 2010; Lam et al. 2010).

Two-Photon Microscopy

The theoretical basis of two-photon excitation was laid in a study of the early 1930s (Goppert 1929), although the experimental realization took almost three decades (Kaiser and Garrett 1961). It was first used in LSM in the 1970s (Hellwarth and Christensen 1975) but a convincing two-photon excitation fluorescence microscopy was only demonstrated in 1990 (Denk et al. 1990).

Two-photon microscopy, as the name implies, uses simultaneous absorption of two longer wavelength photons (at λ_1 and λ_2) to excite a fluorophore, which would be usually

excited by a single photon at a shorter wavelength (λ_3). The relationship between the wavelengths is

$$\lambda_3 = \frac{1}{\lambda_1^{-1} + \lambda_2^{-1}}. \qquad (11)$$

Because the two photons have to be absorbed simultaneously to excite the fluorophore, the excitation is dependent on the square of the light intensity. This could be thought as an equivalent of the double selection in confocal imaging, achieved by a selective illumination by the light source and selective detection by a pinhole. Therefore, in the two-photon illumination mode, a pinhole is no longer necessary. Moreover, it minimizes the out-of-focus photobleaching because the excitation only occurs in the vicinity of the focal plane (Fig. 2). Scattering is greatly reduced with two-photon excitation, and penetration depths for the long wavelength excitation are increased.

Because the emission does not have to pass through a pinhole, area detectors can be used and no descanning of the beam is necessary, making detection quite simple.

Another advantage of two-photon microscopy is its ability to excite fluorophores absorbing in the UV by two photons in visible range, which surpasses usual UV transmission problems with glass lenses. In combination with the reduced out-of-focus fluorescence, it also provides a suitable tool for UV uncaging in vivo without significant photo damage.

The photon density in two-photon excitation should be about one million times higher than is required for single-photon excitation, because of the square dependence of the absorption on intensity. Therefore, pulsed lasers should be used with sufficient photon flux in the pulses while having fairly low average power. Titanium-sapphire lasers are extensively used for two-photon microscopes because they provide a wide range of excitation wavelengths between 700 and 1100 nm. Because of different photophysical selection rules, two-photon absorption spectra are not identical with twice the spectra for one-photon excitation, and have therefore to be independently determined. In the same way as for TIR illumination, two-photon excitation can be combined with other single-molecule techniques.

Applications

Two-photon microscopy is very suitable to excite photosensitive, easily bleachable lipid probes in the blue to near-UV spectral range, such as Laurdan or C-Laurdan. These probes were used to detect the membrane domains in model membranes, as well as in living cells, by two-photon microscopy (Parasassi et al. 1997; Bagatolli and Gratton 1999, 2000a,b; Dietrich et al. 2001; Bagatolli 2003; Bagatolli et al. 2003; Kim et al. 2007; Kaiser et al. 2009). The order of different membrane systems was investigated (Gasecka et al. 2009), and new probes

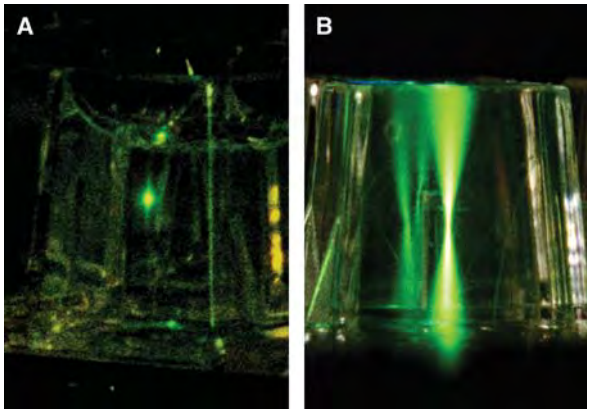

Figure 2. (*A*) Two-photon illumination and (*B*) single-photon illumination.

to visualize the membrane order were tested by two-photon microscopy (Jin et al. 2006; Kim et al. 2008; Klymchenko et al. 2009).

Fluorescence Recovery after Photobleaching (FRAP)

FRAP or, under its previous name, fluorescence photobleaching recovery (FPR) was first described in the late 1970s (Axelrod et al. 1976; Koppel et al. 1976) and got very popular in the 1990s because of the improvements in optics and the discovery of fluorescent proteins.

FRAP is a technique that exploits the photobleaching property of fluorophores. A region of interest (ROI) is bleached with a high laser power. Then, the ROI is observed for fluorescence recovery, caused by diffusion, interactions or reactions of the surrounding fluorophores, which yields a recovery curve. This curve typically looks like the one shown in Figure 3. Its most remarkable features are the bleaching step, an exponential-like recovery with characteristic half-time, and a recovery level usually lower than the initial level, whose offset is the so-called "immobile fraction."

According to the steepness of the recovery, diffusion coefficients, binding rates or turnover rates can be determined. The steeper the recovery is, the faster the molecules are, with diffusion coefficients (D) determined by the Stokes–Einstein relationship for spherical molecules:

$$D = \frac{k_B T}{6\pi\eta r}, \tag{12}$$

where k_B is the Boltzman constant, T is the absolute temperature, η is the viscosity, and r is the hydrodynamic radius of the spherical particles.

Because photobleaching is an irreversible process, immobile molecules will not recover at all. Therefore, one can obtain the immobile fraction of molecules as an additional information from FRAP curves. To get accurate quantitative information, the intensity profiles of bleached ROI, as well as an unbleached positive reference ROI on the same membrane, an empty ROI outside of the membrane, and the whole cell or membrane have to be derived. Then, the recovery should be normalized according to these values (Kenworthy 2007).

Normalized FRAP curves should be fitted to the appropriate models, to get the half time which is the time required for half of the recovery. The simplest fitting is by a single exponential:

$$f(t) = A(1 - e^{-\tau t}). \tag{13}$$

The diffusion coefficient can then be determined as

$$D = \frac{r_0^2 \gamma}{4\tau_{1/2}}, \tag{14}$$

where r_0 is $1/e^2$ radius of the Gaussian laser beam, γ is the parameter that depends on the photobleaching extend varying from 1.0 to 1.2 depending on ROI shape, and $\tau_{1/2}$ is the half-time. In case of a uniform circular spot ROI,

$$D = 0.224 r^2 / t_d. \tag{15}$$

Many fitting models for diffusion, interaction and reaction have been developed recently, some of which are listed in Table 1.

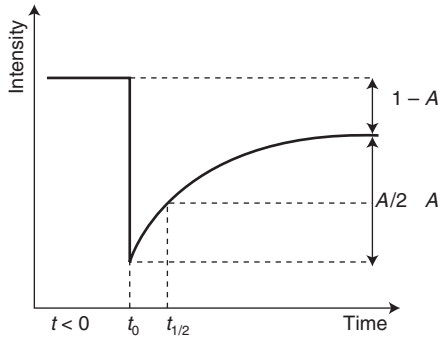

Figure 3. FRAP parameters. $0 < t$ is the time before the bleaching, t_0 is the time at which bleaching occurs, $t_{1/2}$ is the half-life (i.e., the time at $A/2$), A is the mobile fraction, and $1 - A$ is the immobile fraction.

TIR-FRAP

To measure the diffusion of molecules in a membrane, TIR illumination can be a better option than confocal microscopy for the same

Table 1. FRAP fitting models

Type of model	Function	Reference
Diffusion	$f(t) = f_f\left(1-\left(\frac{w^2}{w^2+4\pi Dt}\right)^{1/2}\right)$	Ellenberg et al. 1997
Diffusion	$f(t) = e^{-\frac{\tau_D}{2t}}\left[I_0\left(\frac{\tau_D}{2t}\right) + I_1\left(\frac{\tau_D}{2t}\right)\right]$	Soumpasis 1983
Chemical interaction dominant	$f(t) = y_0 + Ae^{\tau_1 t}$	Phair et al. 2004
Reaction dominant	$f(t) = 1-C_{eq}e^{-k_{off}t}$	Sprague et al. 2004

reasons as listed above. With TIR-FCS, complex binding-unbinding measurements are possible with high accuracy because of well-defined and background free illumination.

Challenges and Artifacts in FRAP

FRAP is usually implemented in laser scanning confocal microscopes (LSCMs), thus its ability is limited by the features of the respective microscope. In FRAP experiments, it is usually assumed that all the molecules are bleached at the same time, and no diffusion happens during photobleaching. But both assumptions may be wrong at nonideal settings in an LSCM. To guarantee proper photobleaching, more than one scan at high laser power may be needed. However, as the number of scanning cycles increases, diffusion into the ROI is nonnegligible, especially for fast diffusing molecules. This leads to a wrong initial starting point of recovery, and yields a wider and shallower bleaching profile. In other words, the required time for molecules to recover the bleached area appears to be higher. To get rid of this artifact, the initial point needs to be calibrated carefully (Snapp et al. 2003; Weiss 2004).

ROI Size. The shape and the area of the FRAP ROI are crucial for the extraction of diffusion coefficients. The ROI size should be much smaller than the total size of the sample, to keep the overall fraction of photobleached molecules fairly low, not to influence the fluorescence intensity profile of the sample. Moreover, ROI radius should not exceed 1 μm for Gaussian approximation to be valid.

Photobleaching Artifacts. During photobleaching, many chemical reactions can happen because of the high laser power, induced by radical (often reactive oxygen) formation, such as protein cross linking. This may affect the concentrations but also the diffusion coefficient notably. Another effect of high laser power, particularly in the red spectral range, can be a slight local temperature rise during photobleaching. Although it has been shown that the temperature increase is minor (Axelrod 1977) in solution, it may be important on membranes, specifically at critical temperature points (Honekamp-Smith et al. 2008).

Besides experimental parameters mentioned above, a proper fitting should be carefully applied (Sprague and McNally 2005).

Applications

The diffusion in native cell membranes has been addressed using the FRAP technique since long (Lippincott-Schwartz et al. 2001, 2003). The first studies were performed to see whether membrane heterogeneity affects the diffusion of proteins in the membrane (Edidin 1992; Jacobson et al. 1995; Feder et al. 1996; Lommerse et al. 2004; Kenworthy 2005; Lagerholm et al. 2005), which resulted in anomalous diffusion concept. In the context of lipid rafts, a continuous effort has been made to distinguish between the diffusion of raft and nonraft markers, as well as to characterize the factors that can influence the membrane organization, like cholesterol (Niv et al. 1999, 2002; Hao et al. 2001; Kenworthy et al. 2004; Rotblat et al. 2004; Goodwin et al. 2005; Roy et al. 2005; Meder et al. 2006; Nicolau

et al. 2006; Shvartsman et al. 2006). TIR-FRAP was applied to calculate the rates of binding and unbinding of hormones to and from the cell surface (Hellen and Axelrod 1991; Fulbright and Axelrod 1993).

Fluorescence Correlation Spectroscopy (FCS)

FCS is a method that has been extensively used and further developed by our group, being introduced and established as a very suitable approach to characterize model and cellular membranes (Schwille et al. 1999a; Bacia et al. 2004). It is, in a way, a single-molecule method, but provides sufficient statistical significance to also use it for general characterization of membranes, mainly through the diffusion properties of their constituents. It is thus related to FRAP, but provides several advantages, the most crucial of which is the dramatically improved sensitivity, allowing to work at significantly reduced fluorescence labeling densities. FCS has long been used to characterize domain-forming membranes (Korlach et al. 1999), and recently, by combination with super resolution illumination (Eggeling et al. 2009), was able to resolve nanometer-sized entrapment sites of labeled raft-markers. Because of our intensive efforts on FCS applied to membranes, this technique will be discussed in more detail in the following.

FCS measures small fluorescence intensity fluctuations in a defined volume. It provides accurate information about diffusion coefficients, concentrations, molecular brightness, intramolecular dynamics, and molecular interactions. It has been extensively used for a variety of biological applications, because of its great sensitivity. FCS has been combined with many different imaging methods, such as laser scanning confocal microscopy, two-photon microscopy, total internal reflection fluorescence microscopy, stimulated emission depletion nanoscopy, and others, making it particularly feasible for cell biology.

FCS was first established in the 1970s (Magde et al. 1972, 1974, 1978; Elson and Magde 1974) and technically greatly improved in the following years (Rigler et al. 1993; Eigen and Rigler 1994). Fluorescence intensity fluctuations, primarily addressed by FCS, can be caused by diffusion of the molecules through the observation volume, or by reversible brightness changes of the molecules because of some chemical or photophysical reactions (Petrov and Schwille 2007). FCS performs the statistical analysis of these fluctuations. In other words, it correlates a signal at a certain time t with the same signal after a lag time $t + \tau$, and takes the temporal average. This correlation can be described as self-similarity of the signal in time, which is represented by the autocorrelation function, a temporal decay function of average fluctuations. The basic formula for the fluctuation autocorrelation function is

$$G(\tau) = \frac{\langle \delta F(t) \cdot \delta F(t+\tau) \rangle}{\langle F(t) \rangle^2}, \qquad (16)$$

where $\delta F(t) = F(t) - \langle F(t) \rangle$ is the fluctuation around the average intensity and $\langle\ \rangle$ denotes the temporal average; τ is the lag time. The denominator is for normalization.

The basic steps of FCS experiments are as follows. First, the sample is illuminated by the appropriate illumination technique. Generally, in the simplest representation of FCS, confocal illumination without beam-scanning is used. The fluorescence signal is collected by the objective and detected by sensitive photodetectors, often by avalanche photodiodes (APDs). After detecting the fluorescence intensity for a certain time, a hardware correlator usually correlates the signal from subsequent time points according to the correlation function mentioned above, and forms the experimental FCS curve. This correlation step can also be performed retrospectively, if data is recorded in small enough ($<\mu$sec) time bins. Then, the correlation curve as in Equation 16 is fitted by an appropriate fitting model (some listed below) to get the numerical values of diffusion times, concentrations and molecular brightness, or other parameters governing fluctuation decay.

As seen in Figure 4, the amplitude of the curve is reciprocal to the concentration. The reason behind this is that for lag time zero,

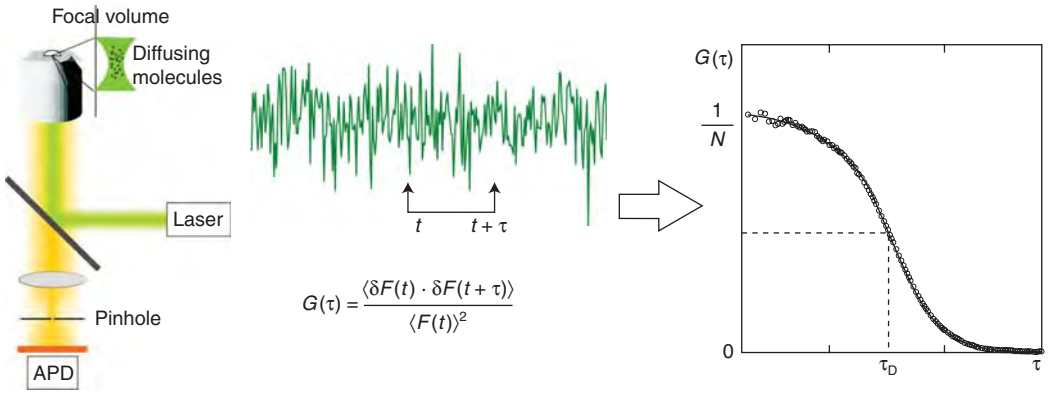

Figure 4. Principle of FCS. (Image courtesy of Jonas Ries.)

$G(\tau)$ is determined as

$$G(0) = \frac{\langle (\delta F)^2 \rangle}{\langle F \rangle^2}. \tag{17}$$

For random processes that are governed by Poisson statistics, the variance is

$$\mathrm{Var}(N) = \langle (\delta N)^2 \rangle = N. \tag{18}$$

Because the fluorescence intensity is directly proportional to the number of molecules,

$$\langle F \rangle = q \langle N \rangle, \tag{19}$$

when the intensity is normalized, we get

$$\frac{\langle (\delta F)^2 \rangle}{\langle F \rangle^2} = \frac{\langle (\delta N)^2 \rangle}{\langle N \rangle^2} = \frac{\langle N \rangle}{\langle N \rangle^2} = \frac{1}{\langle N \rangle}. \tag{20}$$

As stated above, the diffusion time and other variables are obtained from fitting the experimental data to the proper model function. From the diffusion time τ_D, the diffusion coefficient can be determined if the diameter of the focal volume is known:

$$\tau_D = \frac{\omega_o^2}{4D}. \tag{21}$$

Here, ω_o is the beam waist of focal volume (i.e., the radial distance of the optical axis), and D is the diffusion coefficient.

Besides the concentration and the diffusion time, the brightness of the molecule, η, can be calculated. This parameter is quite important for a good statistical accuracy, and can be used to assess the quality of FCS measurements in general. However, it can also reflect on the formation of higher molecular complexes and aggregates. η is directly proportional to the total photon count and to the amplitude of the correlation function:

$$\eta = \frac{\langle F(t) \rangle}{N} = \langle F(t) \rangle \cdot G(0). \tag{22}$$

In practice, FCS is quite a complicated and delicate technique to apply, with many parameters that have to be taken into account and carefully controlled.

- If the concentration of the fluorophores is too high (>100 nM) the contribution of correlated photons to the total intensity (or, the strength of the fluctuations) is only marginal, and precludes their analysis. If the concentration is too low (<1 pM) it gets difficult to register a molecule in the focal volume during a sensible measurement time. Background noise dominates the signal. In both cases, it is difficult to record decent FCS curves.
- Autofluorescence and (scattering) background may always affect the total fluorescence intensity, and there should be elaborate corrections for them. Besides, the sample should be kept in a nonautofluorescent medium.

- Low laser power should always be used to avoid photobleaching.
- The acquisition time should be long enough to collect enough photons to correlate, but not too long to avoid photobleaching.
- Fluorophore selection should be made carefully; more than other techniques FCS requires a high photostability.

The basic steps and tricks to do FCS on living cells are well described (Kim et al. 2007).

More problems, precautions, and corrections will be discussed later.

Fluorescence Cross-Correlation Spectroscopy (FCCS)

To quantitatively characterize molecular interactions is of prime importance for cell and molecular biologists. Biochemical assays that are usually employed for this purpose are particularly problematic for molecules embedded in or attached to cell membranes, because the physiological environment cannot be closely preserved in vitro. Video microscopy on fluorescently labeled molecules in life cells has helped to some extent, but often produces ambiguous results, because it largely relies on simple colocalization that does not really probe interaction, but rather spatial proximity. As the diffraction limit is much larger than a protein size, when two proteins are closer than the resolution of the microscope, it cannot be determined whether they are truly interacting. A much better approach is FRET, relying on the radiation-less transfer of excited state energy between two or more molecules that carry fluorescent labels with large spectral overlap. Here, the proximity needs to be in nanometer range, making it much more specific to probe true binding. FRET will be discussed in detail later. However, the key challenge with FRET is to attach the labels close enough to the binding site to yield high transfer efficiency, but far enough apart not to interfere with the binding. Here, a variant of FCS, called fluorescence cross-correlation spectroscopy (FCCS) often provides a valuable alternative.

FCS itself provides detailed information on the diffusion properties of labeled molecules. To probe binding or interaction of small molecules to large ones, or to immobile structures such as the cell membrane, the reduction in diffusional mobility may provide valuable information on the binding process. This has in the past been used to characterize binding events by standard one-color FCS (Icenogle and Elson 1983a,b). However, this approach breaks down when the interaction between molecules of approximately the same size are to be analyzed. Simulations show that for the minimum detectable difference in diffusion time of a molecule of at least 1.6-fold, an approximately sixfold change in mass is required, as implicitly seen in Equation 12, where the diffusion time is inversely proportional to the third root of mass (Meseth et al. 1999).

The principle of FCCS is to observe codiffusion of molecules, rather than colocalization. It can thus be employed to probe any phenomenon leading to or terminating such a comovement (Schwille et al. 1997). Direct interaction, complex formation, but also the clustering of molecules in microdomains or nanodomains can lead to such a codiffusion of two molecules of separate species. In contrast to standard FCS, the mathematical routine for FCCS is to correlate the fluorescence fluctuations from the first channel at time t with the fluorescence fluctuations in the second channel at time $t + \tau$ over a certain measurement interval (Fig. 5). The cross-correlation function $G_{cc}(\tau)$ for FCCS is given by

$$G_{cc}(\tau) = \frac{\langle \delta F_1(t) \cdot \delta F_2(t+\tau) \rangle}{\langle F_1(t) \rangle \langle F_2(t) \rangle}, \qquad (23)$$

where $\delta F_1(t)$ and $\delta F_2(t)$ are the fluctuations in the two fluorescence signals, and $\langle F_1(t) \rangle$ and $\langle F_2(t) \rangle$ are the mean intensities.

Scanning FCS (sFCS)

Although FCS is still mostly performed with a steady measurement volume (i.e., a confocal spot parked at a fixed position in solution or in a cell), many modern instruments, particularly combined FCS-LSM modules, feature

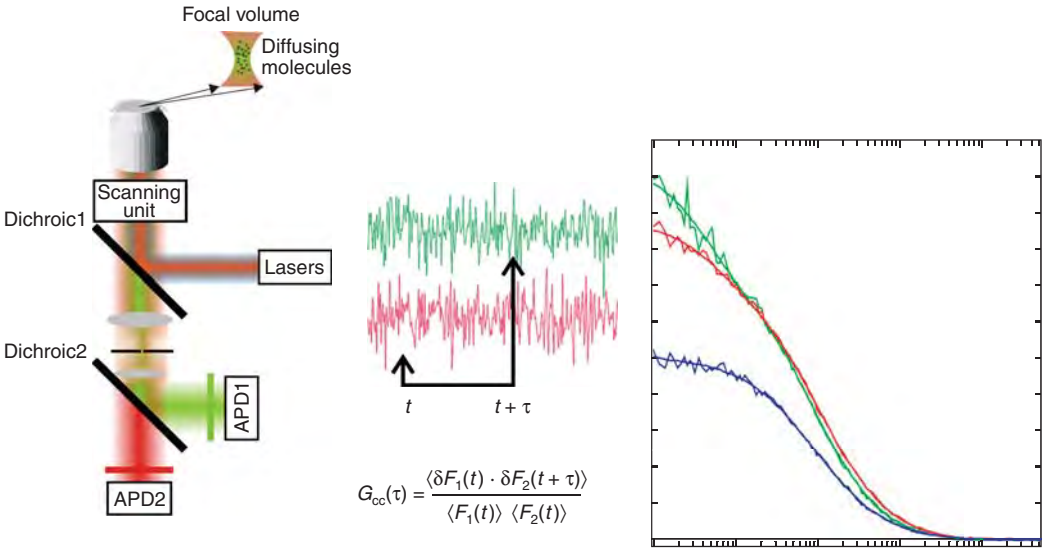

Figure 5. Principle of FCCS. (Image courtesy of Jonas Ries.)

the combination of correlation analysis with a scan beam. Here, the focal volume may be moving on a line (Petersen 1986; Petersen et al. 1986), a circle in lateral axis (Petrasek and Schwille 2008; Petrasek et al. 2010) or along *z*-axis (Benda et al. 2003). The basic principle of scanning FCS perpendicular to the membrane is shown in Figure 6.

In the line-scan mode, the laser focus moves perpendicularly to an axially aligned membrane (e.g., the side membrane of a giant vesicle). Because of the scan path being much larger than the actual intersection with the membrane, the focal spot will only be illuminating (membrane-bound) molecules for a small fraction of time. Thus, the recorded time-intensity trace cannot be directly fed into the hardware correlator but has to be processed by software to align the actual membrane intersections, before actually correlating the processed pseudo-real time signal and fitting the data (Ries and Schwille 2006). This procedure, although more

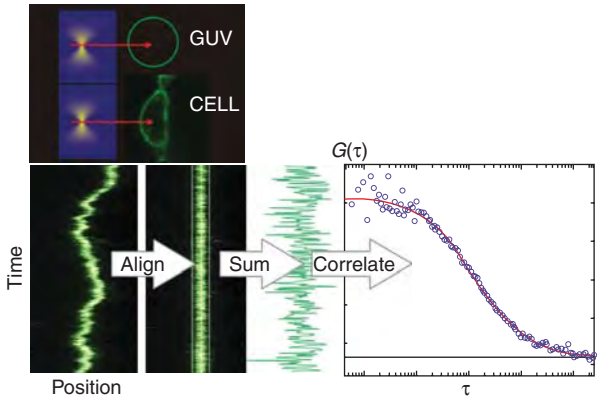

Figure 6. Principle of sFCS. (Image courtesy of Jonas Ries.)

elaborate than standard FCS, has the enormous advantage that sample drift or large-scale signal disturbance by autofluorescent particles can be efficiently suppressed. Although line-scan FCS has many advantages for membrane systems, which are going to be discussed later, it may cause out of focus bleaching, and its time resolution is limited by the software processing, rendering it unattractive to detect fast diffusing components in solution.

Besides a line scan in the lateral direction, there is an axial scanning approach in which the focal volume moves in the *z* direction, so that it can measure above the membrane, at the membrane and below the membrane sequentially (Humpolickova et al. 2006). Because of the laser divergence, the size of the illuminated area above and below the focal plane are larger, rendering the number of molecules and the diffusion time higher when moving the focal spot away from the focal plane. Also, the movement is usually performed by stage scanning, with much lower scan speed than available for lateral scanning, Consequently, this *z* scan is usually performed for other purposes: for example, to calibrate the focal volume in the *z* direction or to vary the size of the illuminated area on the membrane with minimal efforts.

Two-Focus FCS

Another modification of FCS that bears the characteristics of cross-correlation is two-focus FCS (or dual focus FCS). It can be implemented with two fixed confocal volume elements displaced with respect to each other at a spatial distance. This setup simplifies calibration—less measurements of diffusion coefficients (Dertinger et al. 2007). Spatial cross-correlation with two focal elements can, however, be conveniently combined with line scanning, in which two identical lines at a known distance *d* are scanned by two foci simultaneously, or alternately with very high frequency. When the distance is well known, one can extract autocorrelation curves as well as the spatial cross correlation curve between two foci. This mode is quite insensitive to artifacts that originate from the variations of the focal volume (e.g., because of different refractive indices within the sample [Dertinger et al. 2007; Loman et al. 2008]), and therefore particularly suited for cellular FCS. This will be discussed later.

TIR-FCS

As mentioned before, TIR illumination provides a great axial resolution, which makes it a very appropriate tool for membrane research. It can also be conveniently combined with FCS on membranes or surfaces in general. If there is a strong background from labeled molecules in the cytosol, or above and below the surface of interest, selective data processing in scanning FCS or two-focus FCS can only partly overcome this problem, which usually leads to a decrease in amplitude in the correlation curve. As a much more elegant strategy to eliminate the background caused by any other molecules away from the surface, objective-type TIRF illumination combined with standard confocal detection can be applied (Schwille 2003; Ries et al. 2008).

Two-Photon FCS

To combine FCS with two-photon excitation provides a number of interesting features and advantages. First of all, like for standard imaging, it limits cumulative photobleaching in out-of-focus areas, making it preferable for FCS measurements on samples with limited dye resources such as small cells and organelles (Schwille and Heinze 2001; Schwille et al. 2009). Two-photon excitation is, further, the method of choice for samples of high turbidity or high scattering cross sections, like multicellular systems or cells with thick cell walls. Additional advantages may be provided by the photophysical properties of the dyes, allowing to coexcite and correlate up to three spectrally distinct fluorophores with one two-photon excitation beam (Heinze et al. 2000, 2002). Caution has to be applied with regard to the photostability of dyes and the available count rate per molecule, as both seem to be significantly reduced under two-photon excitation (Schwille et al. 1999b).

Difficulties and Artifacts in FCS Applications

Background. Background can be caused by scattering, autofluorescence, or unwanted fluorophores in the sample because of nonspecific labeling. If the background is truly random and noncorrelated, a signal can be easily background-corrected after the measurement as follows (Petrasek et al. 2010):

$$g_c(\tau) = \left(\frac{\langle F\rangle}{\langle F\rangle - B}\right)^2 g(\tau), \qquad (24)$$

where $g_c(\tau)$ is corrected nonnormalized correlation, $g(\tau)$ is measured nonnormalized correlation, B is background fluorescence measured on the sample without fluorescent molecules, and $\langle F\rangle$ is the average intensity.

In case of correlating background, it has to be added to the fitting functions as a fixed second component in a two-component model after being carefully calibrated.

Membrane Heterogeneities, Blinking, Triplet, and Photobleaching. FCS usually assumes an equilibrated steady state in the focal volume around which fluctuations occur randomly. This means that the average count rate should not change over time when recording an FCS curve. In reality, this assumption is very rarely true. Many events, above all cumulative photobleaching, cause a continuous drop or other large scale drift in the average count rate, rendering the error-free recording of FCS curves quite complicated.

In measurements on live cell membranes, membrane undulations constitute the main problem. As the membrane may always be moving on a micron scale, the fraction of membrane occupying the detection volume can change drastically. This causes an increase or decrease in count rate, and results in major distortions of the curve, leading to erroneous values for autocorrelation amplitude and diffusion time.

Another cause of severe, although better controllable, distortion of FCS curves is the photophysical phenomenon of triplet state population, in which the molecules are trapped in a dark state for a few microseconds. Triplet-induced photophysical dynamics may lead to wrong fitting of diffusion times, particularly if the triplet fraction is high and the diffusion times are short (Davis and Shen 2006). Yet, this phenomenon can usually be corrected for in the fitting function, as seen in Table 2. Usually, triple dynamics can be easily distinguished from diffusion because it is independent of volume size, but dependent on illumination power. It can be easily evidenced as an additional shoulder in the FCS curve on short timescales.

Blinking on short timescales does not have to be of photophysical origin. Several fluorophores, particularly fluorescent proteins such as GFP, exhibit excitation independent dark state-bright state transitions which may, however,

Table 2. FCS fitting models

Diffusion type	Fitting function
3D diffusion	$G(\tau) = \frac{1}{N}\left(1+\frac{\tau}{\tau_D}\right)^{-1}\frac{1}{\sqrt{1+w_0^2\frac{\tau}{\tau_D}}}$
2D diffusion	$G(\tau) = \frac{1}{N}\left(1+\frac{\tau}{\tau_D}\right)^{-1}$
2D diffusion for elliptical Gaussian profile	$G(\tau) = \frac{1}{N}\left(1+\frac{\tau}{\tau_D}\right)^{-1/2}\frac{1}{\sqrt{1+\frac{\tau}{S^2\tau_D}}}$
2D diffusion with triplet	$G_{Tr}(\tau) = G(\tau)\left[1+T(1-T)^{-1}\exp\left(\frac{-\tau}{\tau_{Tr}}\right)\right]$
2D diffusion with blinking	$G_B(\tau) = G(\tau)\left[1+\frac{C_{dark}}{C_{bright}}e^{-k_{bl}\tau}\right]$
2D diffusion with two-component	$G_{2C}(\tau) = \frac{1}{N_{tot}}\frac{q_1^2Y_1G_1(\tau)+q_2^2Y_2G_2(\tau)}{q_1Y_1+q_2Y_2}$

be dependent on pH or ionic strength of the solution (Haupts et al. 1998). After careful calibration, this can be incorporated into the fitting function in the same way as the triplet dynamics (Table 2).

A more severe problem for FCS is dye photobleaching, as it not only leads to signal loss, but also compromises the determination of concentrations and diffusion coefficients, the key parameters in FCS applications. At too high illumination intensities, molecules will not stay fluorescent during their full diffusion path through the detection volume, but will be destroyed before leaving it again, leading to erroneously low diffusion times, and an overestimation of diffusion coefficients. In living cells, there is an additional problem with immobile fluorophores being unavoidably bleached during the measurements and leading to a drift in the overall count rate. To prevent this effect from destroying the correlation curve during real-time recordings, a prebleaching is usually performed. Although photobleaching can be usually diagnosed by decay in count rate, its effect is not necessarily visible on first sight, because an equilibrium state may be reached between bleaching and continuous supply of new fluorophores. To rule out photobleaching-induced artifacts in general, a laser power series of FCS measurements from minimum to a moderate power should be recorded. Only for power levels that do not show a change in the curve parameters, compared to very low power measurements, the intensity can be assumed safe (Dittrich and Schwille 2001; Delon et al. 2004). This "safe intensity" is, however, dramatically dependent on the diffusion characteristics of the labeled molecules (lower intensities required for slower molecules), and cannot just be inferred from pure dye measurements.

For measurements on extremely slow particles, scanning FCS as explained above represents an efficient solution to avoid photobleaching-induced artifacts, because the laser is not continuously exciting the same spot, reducing the interaction time with a specific region.

Detector Dead Time and Saturation. When a photon hits the APD detector, it creates an avalanche of electrons to amplify the signal. Before the next photon can be registered, there is a short interval of ~100 nsec, called the dead time of the detector. Events occurring on shorter scales than the dead time cannot be resolved. Sometimes, the detection of a single photon triggers the APD chip to create a second cascade during the dead time, the so-called "afterpulsing," which is an artifactual event, but highly correlated with the first one. As a result, a peak in the correlation curve is observed at very short timescales. The simplest solution for this (usually hardware-induced) problem is to split the light into two detection channels and record the cross-correlation between them. Cross-correlation does not include this after-pulsing peak because it is a hardware-induced phenomenon in only one of the detectors.

There is a photon count limit for the detector that it can process at a time. Above this value, electronic saturation occurs, which has a similar effect as optical saturation in the sample. Optical saturation happens when most of the molecules in the focal volume are not in the ground state, instead in excited state or triplet state. This effect usually leads to an enlarged focal volume and results in a slower decay of the correlation function (Gregor et al. 2005; Humpolickova et al. 2009). It should be ruled out in the same way as for photobleaching, by recording a laser power series and staying well below the intensity at which the curves change their shape.

Focal Volume Geometry and Positioning. The probe volume (composed of illumination by the laser and detection via the pinhole) is usually approximated as a 3D Gaussian profile. In one photon excitation, slightly underfilling the back aperture of the objective is a good way to satisfy this approximation. Overfilling the aperture to yield better excitation efficiencies, on the other hand, will for one-photon excitation result in diffraction fringes of the back aperture itself. This non-Gaussian volume is prone to produce artifacts in diffusion time, which may be misunderstood and taken as a second species or kinetics (Hess and Webb 2002).

There are several additional factors, like optical aberrations, that distort the geometry (shape or size) of the focal volume from the Gaussian profile.

Refractive index mismatch could be a common problem when dealing with cells, in which refractive indices vary from 1.33 to 1.38. When there is a mismatch between the immersion liquid, glass, and the sample, aberrations occur which cause a larger detection volume than assumed by the fitting model. This results in larger diffusion times and lower diffusion coefficients than the real values. Similar to this, displacement of the pinhole along the optical axis leads to larger detection volumes and larger diffusion times. Coverslip thickness also affects the focal volume. Objectives are usually designed for a certain range of coverslip thickness that has to be adjusted exactly. Deviations from the correct value again result in a larger detection area and underestimated diffusion coefficients (Enderlein et al. 2004, 2005).

Artifacts caused by refractive index mismatch, pinhole misalignment, or coverslip thickness affect the control experiments in the same way as the measurements, such that the ratio of control over sample is still correct. If absolute values are to be obtained and the optical system cannot be easily corrected, two-focus FCS provides a good solution to avoid problems with detection volume deformations. Two-focus FCS is insensitive to refractive index mismatch, cover-slide thickness variation, and optical saturation. Therefore, it happens to be a focal volume-calibration free technique for accurate dynamics measurements (Dertinger et al. 2007; Loman et al. 2008).

Correct axial positioning of the detection volume is crucial for membrane analysis. If the center of the focal volume is not exactly on the membrane, the divergent laser beam illuminates a bigger area of the membrane, mimicking a higher concentration (through the reduced count rate and higher occupation number) and a smaller diffusion coefficient. To minimize this artifact, the count rate should be maximized when adjusting the z position. For a more decisive solution, positioning-calibration free FCS variants like scanning FCS or z-scan FCS should be used.

Specific Artifacts in FCCS. One of the most crucial tasks for dual-color cross-correlation is the careful determination of measurement volumes. Because of the different wavelengths, the Airy disc sizes for the two detection channels vary in proportion to their wavelength. Consequently, in most FCCS instruments, the focal volumes do usually not completely overlap, even after eliminating all aberrations (Weidemann et al. 2002). For quantitative FCCS, this requires intensive calibration measurements (Schwille et al. 1997) (e.g., by using a "gold standard" of up to 100% cross-correlation [like a strong receptor-ligand or dsDNA] and comparing the experimental results with this reference).

One of the biggest problems in most optical systems featuring multicolor applications is spectral cross talk. FCCS is particularly prone to producing false positive results because of the cross talk induced by the leakage of the green dyes's emission into the red dyes' detection channel. In that case, the autocorrelation between the red and green spectral parts of the green dye results in false positive cross correlation.

As for other artifacts, cross talk can be taken care of by careful calibration. The cross talk coefficient of any fluorophore κ_x can be easily calculated by measuring the fluorescence simultaneously in both channels. This coefficient is specific for a particular set of optics (dichroics, filters, etc.):

$$\kappa_x = F_r/F_g, \tag{25}$$

where F_r is the fluorescence intensity in the red channel, and F_g is the fluorescence intensity of the same fluorophore in the green channel.

Cross-correlation can be corrected according to this coefficient in measurements with two fluorophores:

$$G_{CC}(\tau) = \frac{F_g F_r G_{rg}(\tau) - \kappa_x F_g^2 G_g(\tau)}{F_g(F_r - \kappa_x F_g)}. \tag{26}$$

In cases where cross talk constitutes a substantial portion of the fluorescence signal in the red channel, as is the case for most

combinations using fluorescent proteins (because of the limited availability of far red-emitting FPs), it may be more appropriate to eliminate cross talk already in the measurements, rather than correcting for it retrospectively. Here, alternating excitation schemes have proven to be very powerful. The best known scheme for FCS is pulsed interleaved excitation (Mueller et al. 2005; Sohn et al. 2010), and alternating excitation may also easily be combined with scanning FCS (Ries et al. 2009a).

FCS Applications on Membrane Dynamics

Over the last decade, FCS has been established as an extremely attractive tool for in vivo (Mütze et al. 2009) studies and on model membrane systems (Kahya and Schwille 2006a). Thus, lipid biology has widely exploited this technique. FCS experiments have been designed and appropriate models have been developed to distinguish free diffusion from diffusion in microdomains and meshwork structures in native membranes (Wawrezinieck et al. 2005; Lenne et al. 2006; Wenger et al. 2007). There have been many studies on phase separated model membranes, supported or free-standing, to determine the diffusion characteristics of lipids in different phases (Chiantia et al. 2008, 2009; Lingwood et al. 2008; García-Sáez and Schwille 2010; García-Sáez et al. 2010). It has been shown that the diffusion coefficient is influenced by environmental conditions such as ionic strength or sugar content of the medium (Bockmann et al. 2003; Sum et al. 2003; Doeven et al. 2005; van den Bogaart et al. 2007; Guo et al. 2008; Vacha et al. 2009). The role of cholesterol in membrane organization, a big issue in lipid biology, has been intensively addressed by FCS (Scherfeld et al. 2003; Bacia et al. 2004, 2005; Kahya and Schwile 2006b). Markers for more ordered lipid environments, such as sphingomyelin and ceramide, were other important molecules to be studied (Chiantia et al. 2007, 2008; Eggeling et al. 2009). Other membrane-dependent processes were also successfully investigated by FCS. For instance, the interaction of morphogen Fgf8 with its receptors on the cell surface in living embryos has been quantitatively determined by using scanning FCCS (Ries et al. 2009a; SR Yu e al. 2009). Another derivative of scanning FCS–line-scan FCS–was developed to address the questions related to membrane dynamics (Ries et al. 2009b). Moreover, reconstituted protein–protein interactions on GUV membranes were monitored by using FCCS. For example, active tBID and $BCL_{XL}\Delta Ct$ proteins were found to interact, and it was shown that membrane promotes their interaction (Fig. 7) (García-Sáez et al. 2009). In another example, helix–helix interaction was shown for *trans*-membrane domains using giant plasma membrane spheres by scanning FCCS (Worch et al. 2010).

The applications of FCS in lipid cell biology have been elaborately reviewed elsewhere (Machan and Hof 2010).

A Comparison between FRAP and FCS for Lateral Diffusion

As seen above, FRAP and FCS are alternative methods to measure lateral diffusion of molecules. Although their specific strengths and shortcomings have been briefly mentioned, a direct comparison may still be helpful for choosing the right technique for a particular experiment.

First, FRAP usually requires higher concentrations than does FCS. Numerically, approximately 100 labeled molecules should be on 1 μm^2 to obtain a reliable FRAP curve (Wolf 1989), and with increasing concentrations, the signal-noise ratio can be improved. In contrast, the FCS curve deteriorates with increasing concentration. One labeled molecule in the detection volume of 0.5 fL (which is almost 20 times less than probed by FRAP) is usually sufficient to record a decent FCS curve. FCS has a much better temporal resolution down to submicroseconds, thus can resolve very fast diffusions (Gordon et al. 1995). On the other hand, FCS is not well suited to analyze slow diffusion, which is quite vulnerable to photobleaching. The high temporal resolution makes FCS also much more susceptible to sample-induced noise, such as membrane

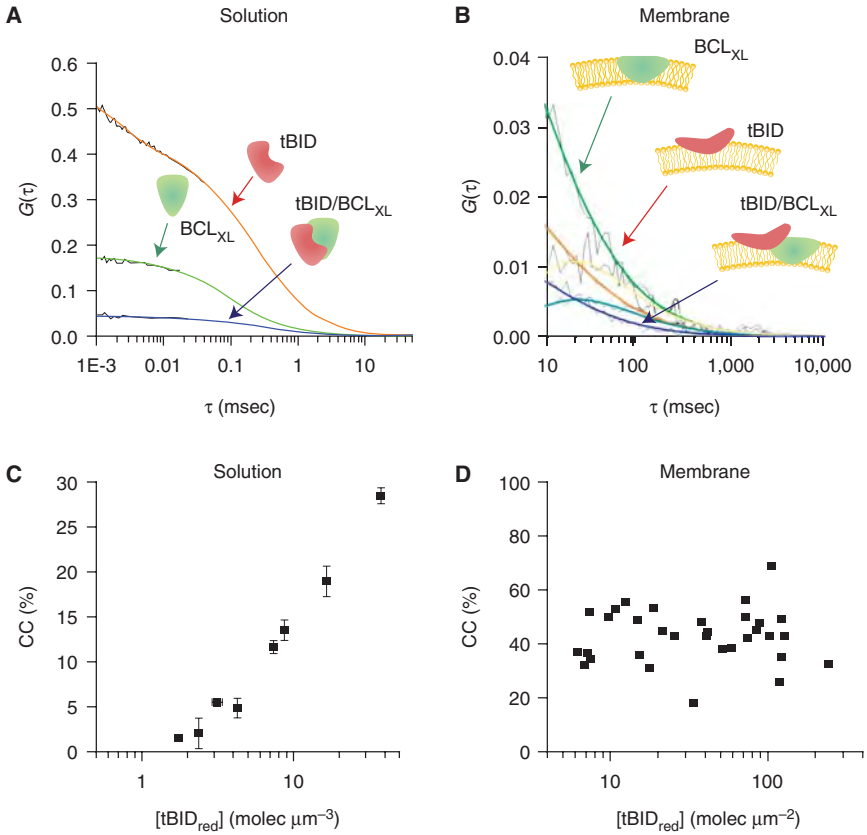

Figure 7. Stimulation of tBID and $BCL_{XL}\Delta Ct$ intereaction by membrane. Cross-correlation in solution is affected by concentration (*A*, *C*), whereas it is not changing and always higher in membrane (*B*, *D*). (Image courtesy of Ana García-Sáez.)

undulations, or autofluorescent objects floating around. However, FCS derivatives like scanning FCS can overcome these problems to some extent, still preserving the high sensitivity and precision of the method. The main issue about FRAP seems to be the high laser power which may easily destroy the living sample and change the dynamics of the molecular system. Finally, FRAP gives information about immobile fractions whereas FCS cannot.

Förster Resonance Energy Transfer (FRET)

FRET is not really a technique, but rather a well-established photophysical phenomenon used to monitor molecular dynamics and interactions down to the single-molecule level. The idea behind FRET was first proposed by Theodor Förster in 1948 (Förster 1948). The mechanism is based on the energy transfer of an excited fluorescent donor molecule to an acceptor molecule in a nonradiative fashion when they are in close proximity (10–100 Å).

The energy transfer not only depends on the distance between donor and acceptor, but also on the spectral properties of the dyes and the relative orientation of their transition dipole moments. The rate (k_t) and the efficiency (E) of the energy transfer in FRET are given by

$$k_t = \frac{1}{\tau_D}(R_0/r)^6, \tag{27}$$

$$E = \frac{1}{1+(r/R_0)^6}, \tag{28}$$

where τ_D is the donor lifetime in the absence of acceptor, r is the spatial distance between donor and acceptor, and R_0 is the Förster distance of the donor/acceptor pair, which is the distance at which the energy transfer efficiency is 50%. As seen, FRET efficiency highly depends on R_0, which is given by

$$R_0 = \left(\frac{9000 Q_D (\ln 10) \kappa^2 J(\lambda)}{128 \pi^5 n^4 N_A}\right)^{1/6}, \qquad (29)$$

where Q_D is the quantum yield of the donor in the absence of the acceptor, κ^2 is the dipole orientation factor, n is the refractive index of the medium, N_A is Avogadro's number, and J is the spectral overlap between the emission spectrum of the donor and the absorption spectrum of the acceptor (Fig. 8). J is calculated as

$$J(\lambda) = \int f_D(\lambda) \varepsilon_A(\lambda) \lambda^4 d\lambda, \qquad (30)$$

where f_D is the normalized donor emission spectrum, and ε_A is the acceptor molar extinction coefficient.

The dipole orientation factor κ^2 is often assumed to be 2/3, which is valid when the acceptor and donor molecules are freely rotating, and considered to be isotropically oriented during the excited state lifetime. If the donor and acceptor molecules are not free to rotate, then this assumption is not valid anymore. In most cases, however, even modest reorientation of donor and acceptor molecules results in enough orientational averaging that $\kappa^2 = 2/3$ does not result in a large error in the estimated energy transfer distance, because of the sixth-root dependence of R_0 on κ^2. Even when κ^2 is quite different from 2/3 the error can be associated with a shift in R_0, and thus, determinations of changes in relative distance for a particular system are still valid. Fluorescent proteins, for example, do not reorient on a timescale that is faster than their fluorescence lifetime. In this case, $0 \leq \kappa^2 \leq 4$ is a valid approximation.

There are several ways to detect FRET. Acceptor emission can be detected on donor excitation (Gordon et al. 1998). Because the energy is transferred to the acceptor from the donor, the emission intensity of acceptor is expected to increase on donor excitation. Alternatively, the emission of the donor can be observed while photobleaching the acceptor molecule (Jovin and Arndtjovin 1989; Kenworthy and Edidin 1998; Wouters et al. 1998). When the acceptor is optically saturated, the excitation energy of the donor molecule is no longer used by the acceptor molecule, such that the emission intensity of donor molecule increases on acceptor photobleaching, directly proportional to the FRET rate.

Besides the fluorescence intensity measurements mentioned above, the fluorescence life time of the donor can be also measured. FLIM-FRET is a technique to detect the decrease in the

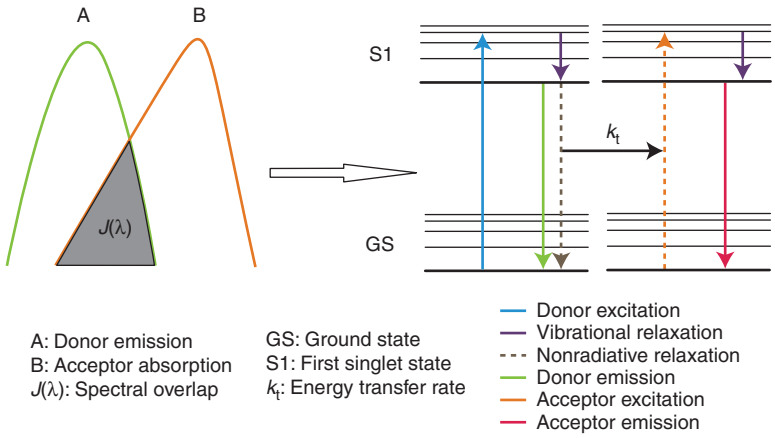

Figure 8. Principle of FRET.

donor's fluorescence lifetime on energy transfer (Gadella and Jovin 1995; Bastiaens and Squire 1999). This method is quite insensitive to many artifacts which are going to be discussed later, but its main disadvantage is the more involved instrumental setup required to detect on nanosecond timescales. FLIM-FRET appears to be more vulnerable to some artifacts caused by pH, temperature, and ionic strength of the medium, as these factors modify fluorescence lifetimes. However, with the proper controls, this method seems to be the most reliable one among others.

Fluorescence lifetime analysis can be performed in two ways, in time domain and in frequency domain. In the time domain approach, very short (picoseconds to femtoseconds) excitation pulses are used to excite the sample, and the lifetime is measured by collecting the resulting photons over time between the pulses, one by one. On the other hand, sinusoidally modulated light is used to excite the fluorophores in frequency domain. The emission is also sinusoidally modulated at the same frequency as the excitation, but there is a phase shift and reduction in the modulation depth, from which the fluorescence lifetime can be derived.

FRET can also be detected by fluorescence anisotropy (Runnels and Scarlata 1995; Gautier et al. 2001; Clayton et al. 2002; Lidke et al. 2003) which uses linearly polarized light to detect the orientation of the molecules. When there is no energy transfer, the orientation of excited molecule is highly correlated with the orientation of the emitting molecule. However, when there is FRET, the emitting molecules are not only the excited donors but also the acceptors, such that the correlation between the orientations of these two components will decrease remarkably. This method has a unique property to also determine FRET between identical molecules (so-called homo-FRET) which is very crucial in dimerization or oligomerization studies (Bader et al. 2009).

The FRET pair selection is an important issue. Theoretically, pairs are selected based on the spectral overlap criterion discussed above. The closer the spatial distance at closest proximity is expected to be, the larger the spectra may vary. Clearly, detection efficiency is maximized and cross talk minimized for spectrally more distinct probes. The most popular FRET pairs at present are GFP-RFP, CFP-YFP, BFP-GFP, GFP-mCherry for genetically modified proteins. There are also several classical FRET pairs based on chemical dyes, such as Cy3-Cy5 and Alexa488-Cy3. More FRET pairs and their properties can be found elsewhere (Sahoo et al. 2007).

Difficulties and Delicacy

In spite of its attractiveness of being a very intuitive technique with in principle rather straightforward experimental design and readout, FRET in praxis has many caveats to be considered carefully, some which are mentioned below.

To get reliable FRET results, spectral cross talk needs to be minimized. When the acceptor fluorescence intensity is used to assess FRET efficiency, spectral contamination always has to be corrected to some extent. Two major sources of this spectral contamination are the direct excitation of the acceptor, and the leakage of donor emission into the acceptor detection channel. As mentioned above, there is always a trade-off between minimal cross talk and a good spectral overlap factor *J*. The simplest way to correct for spectral contamination is to test the FRET signal in combinations of only acceptor, only donor and donor/acceptor combination, both with acceptor excitation and donor excitation.

Photoconversion is another problem often encountered with fluorescent proteins. Under certain conditions, emission spectra may change with time (e.g., on high laser power excitation) or sometimes spontaneously as a result of protein maturation. This is critical in FRET measurements, particularly when photobleaching is used as readout. It has been shown that on photobleaching of acceptor YFP, CFP-like emission is created without any FRET (Kirber et al. 2007).

Fluorescence lifetime-based FRET detection is insensitive to many of these problems as the life time is usually independent of excitation intensity. On the other hand, the big

practical advantage of FRET as a straightforward and intuitive method to complement imaging is also lost, and the instrumentation gets much more involved.

The interactions of donor or acceptor molecules with other components in the medium should be carefully tested. If there is an unwanted binding of one or both to other molecules, this can produce positive and false negative results. Other problems may arise from too complicated stoichiometry (van den Bogaart et al. 2007) and the impossibility to attach fluorescent tags close enough to the interaction region (Miyawaki and Tsien 2000).

As for other fluorescence techniques, photobleaching should be avoided, as it usually changes the molecular ratio of donor and acceptor, resulting in artifacts of FRET efficiency. The donor should be particularly photostable long enough to transfer its energy. It should also exhibit low polarization anisotropy to eliminate the κ^2 deviations.

The brightness of donor and acceptor should ideally be comparable, otherwise resulting in saturation in one channel, or enhanced noise in the other channel due (Piston and Kremers 2007).

Applications of FRET in Lipid Biology

Being such a powerful tool to detect dynamic molecular interaction, FRET has had a strong impact on membrane and lipid research. Particularly, lipid/protein clusters in membranes are interesting topics of study, and there are many applications of FRET in this context. It has been shown that GPI-anchored proteins are enriched in cholesterol-dependent clusters, whereas some putative nonraft proteins are not. Cross-linking of GPI-anchored proteins affects the protein distribution on the membrane and their endocytosis, which highlights the role of immobile, actin-driven nanoclusters in the membrane (Varma and Mayor 1998; Sharma et al. 2004; Goswami et al. 2008). However, there are also some contradicting reports on similar systems, proposing that there are no functional clusters in the cell membrane (Kenworthy and Edidin 1999; Kenworthy et al. 2000; Glebov and Nichols 2004). FLIM-FRET was used to detect the effect of cholesterol depletion on lipid order (Grant et al. 2007) as well as dynamic protein–lipid interactions in live cells (Larijani et al. 2003). TIR-FRET was used to visualize protein–protein interactions on cell membranes and insulin secreting cells (Lam et al. 2010; Sohn et al. 2010). Two-photon FRET was applied to visualize protein–protein colocalization (Mills et al. 2003) and free versus clustered receptor–ligand complexes in the membrane (Wallrabe et al. 2003).

Single-Particle Tracking (SPT)

As discussed above, information on the diffusion of molecules in a membrane can usually be obtained by either FRAP or FCS. However, there are certain disadvantages to both techniques. The lateral resolution of both techniques is limited by the diffraction barrier. Additionally, both techniques have to average over many molecular events to obtain a reliable diffusion time. This averaging, however, masks potential heterogeneities in the diffusion characteristics, induced by, for example, molecular interactions or a heterogeneous membrane environment. Therefore, a technique providing access to the randomly distributed tracks of individual particles is greatly desirable. With the possibility of resolving single molecules, the spatial precision at which lateral detection can be performed is only determined by the number of photons it takes to compute a spot-like image, which can then be fitted with a point-spread function to determine its geometrical center (Toprak et al. 2007).

This approach, which has in past years gained tremendous impact because of the availability of extremely sensitive charge-coupled device (CCD) cameras, is known under the name of single-particle tracking (SPT). The underlying idea is that single particles or even molecules are followed by computer-enhanced video microscopy with a spatial resolution of tens of nanometers and a temporal resolution of tens of milliseconds. Thus, it is a suitable technique to investigate the diffusion characteristics of lipid or membrane-attached proteins,

as well as factors influencing lipid dynamics and membrane order.

The first SPT experiment was performed in 1982 by Barak and Webb to follow the lipoprotein receptor (Barak and Webb 1982). Then, nanovid microscopy was developed, in which molecules are labeled with gold nanoparticles which can be more easily tracked by wide-field microscopy (Debrabander et al. 1985, 1991). The technique was further improved in terms of resolution in later years (Schnapp et al. 1988; Sheetz and Kuo 1993). A large body of work on imaging and tracking of single lipid molecules on artificial and cell membranes was further catalyzed by the work by Schütz et al. (1997). Later on, the technique was further developed by to track the particles 3D with different strategies (Digman and Gratton 2009; Katayama et al. 2009; Ragan et al. 2006).

The idea behind the technique is to follow the single-molecule movement over time, record it as trajectories and analyze these trajectories according to the diffusion theory. The main way to analyze the trajectories is to calculate the mean square displacement (MSD) defined as

$$\mathrm{MSD}(\tau) = \langle (x(t)-x(t+\tau))^2 + (y(t)-y(t+\tau))^2 + (z(t)-z(t+\tau))^2 \rangle, \quad (31)$$

where x, y, and z are the coordinates of the particles, τ is the lag time, and $\langle\ \rangle$ represents the temporal averaging.

The MSD represents the average distance that the molecule travels during the lag time and is thus directly related to the local mobility of the molecule. Once the trajectories are recorded and the MSD is obtained experimentally, it can be compared with theoretical models as listed in Table 3.

Of particular importance in membranes are usually the cases of subdiffusion or confined diffusion, which can be induced by corralling of the diffusing molecules in domains, or any other interactions slowing them down locally. To resolve the dynamics of small local constraints, one trajectory can be divided into different parts, to display the changes in mobility over time.

Table 3. SPT fitting models

Type of diffusion	Model
3D free diffusion	$6Dt$
3D anomalous subdiffusion	$6Dt^{\alpha}$
3D diffusion with directed motion	$6Dt + (Vt)^2$
2D free diffusion	$4Dt$
2D anomalous subdiffusion	$4Dt^{\alpha}$
2D diffusion with directed motion	$4Dt + (Vt)^2$
2D corralled motion	$r\,(1-A_1 e^{(4A_2 Dt/r)})$

Instrumentally, SPT can be performed by regular wide-field microscopy, as well as confocal, two-photon, and TIRF. The selection of the illumination method depends on the application.

Different labels can be used in SPT, according to the nature of the experiment and the temporal and spatial scales to be observed. Usually, the spatial precision scales with the signal-to-noise ratio that can be reached, but bright probes such as nanoparticles and beads have to be used with care, as they might also influence the mobility of molecules. The most commonly used labels are gold nanoparticles, quantum dots, and fluorescent microspheres. The most convenient way of labeling is to conjugate the probes with antibodies or adaptor proteins which specifically target the molecule of interest.

After the particle location is accurately determined in x–y or x–y–z (Levi and Gratton 2007), different algorithms can be applied to acquire the full trajectories. The basic algorithms are cross-correlating subsequent images (Gelles et al. 1988; Kusumi et al. 1993), calculating the center-of-mass of the labeled object (Lee et al. 1991; Ghosh and Webb 1994), or directly fitting the image to a Gaussian distribution (Anderson et al. 1992; Schutz et al. 1997). The correlation method compares the image with the Kernel of the successive image. This method gives the best performance at low signal-to-noise ratios. The centroid (center-of-mass) algorithm compares the center of mass of two subsequent images to determine the distance the molecule has travelled in between. A Gaussian fit algorithm directly fits the image of the object to a 2D Gaussian distribution

(as an approximation of the PSF):

$$G(x, y) = A \exp\left[-\frac{(x - x_0)^2 + (y - y_0)^2}{B}\right]. \quad (32)$$

This algorithm shows the greatest performance when the object is of subwavelength size. A detailed comparison of these algorithms, their potential problems, and performances can be found in Cheezum et al. (2001). There are also algorithms available which combine the correlation and Gaussian fit algorithms (Levi et al. 2006a,b).

Difficulties and Delicacy

There are many aspects to be taken into account to perform meaningful SPT analysis.

First, when using fluorescent probes rather than nanoparticles or beads, photodamage should be minimized. SPT requires a long time to record the trajectories. Therefore, photobleaching can be an important issue. The photostability of quantum dots or fluorescent beads is usually quite high, but when fluorescent lipid analogs or fluorescent proteins are used, the intensity has to be much reduced, limiting the spatial resolution. A very important strategy is to illuminate only while recording the photons, and shutting the laser during camera readout (i.e., frame transfer to the data storage).

A big argument in the SPT field is the effect of large labels on molecular motion. When a bead or nanoparticle is attached to small molecules such as lipids, the diffusion characteristics may change dramatically. Moreover, linkers to attach the label to the molecule can also be problematic. Generally, short linkers and small labels are desirable. Detailed work on this issue can be found in the literature (Dahan et al. 2003).

The determination of particle location is the most crucial aspect in SPT, and much work has been devoted to maximize the spatial precision. The accuracy of the spatial coordinates was in the last years improved drastically, down to 1.5 nm in recent studies (Yildiz et al. 2003, 2004a,b).

The tracking software must be sensitive to the particle brightness changes, because of changes in the particle location with respect to the focal plane. This effect can also be used to record z coordinates with moderate precision (Levi et al. 2005; Ragan et al. 2006). Needless to say, cameras should be fast and sensitive enough to catch the single-molecule signal.

The trajectory algorithm should be carefully chosen, taking all the advantages and disadvantages into consideration. The Gaussian fit algorithm, for instance, seems easy and robust to apply, but it just uses the brightest point as the center and does not take the topographical structure into account. Therefore, it may result in wrong results depending on the molecule topology (Cheezum et al. 2001).

The lag time τ used to record the MSD is also an important variable. It is supposed to be lower than one-fourth of the total trajectory time (Saxton and Jacobson 1997).

Scattering or autofluorescence background is usually quite low, but it decreases the localization accuracy of SPT. It is more dominant when the centroid algorithm is used, because center-of-mass is biased notably by the background (Cheezum et al. 2001; Levi and Gratton 2007).

Applications

SPT hfas been applied successfully to investigate different diffusion mechanisms and establish the models for active transport, free diffusion, anomalous diffusion, and confined diffusion, as seen in Figure 9 and Table 3 (Saxton 1994a,b,

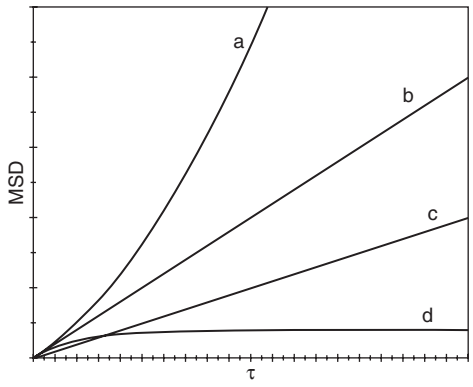

Figure 9. SPT models. (a) Active transport, (b) free diffusion, (c) anomalous diffusion, and (d) confined diffusion.

1995, 1996a,b, 1997; Saxton and Jacobson 1997). Lipid diffusion is found to be highly restricted in native plasma membranes, unlike in liposomes, highlighting the role of cytoskeleton in membrane dynamics (Kusumi et al. 2005). Another diffusion type was described according to these observations, called hop diffusion. It is claimed that both lipids and *trans*-membrane proteins diffuse in small compartments whose boundaries were mostly determined by cytoskeleton of the cell until they change the compartment by hop diffusion (Tomishige et al. 1998). Although there are many studies claiming that saturated lipids and GPI-anchored proteins show confined diffusion on cell membrane on islands of 80 nm and 700 nm in size (Schutz et al. 2000; Lenne et al. 2006; Wenger et al. 2007), some other SPT studies has recently claimed that the diffusion of saturated and unsaturated lipids is not different in cell membrane, which can be because of very small size (<16 nm) or very fast association/dissociation of the rafts. Recently, two-color SPT (Dunne et al. 2009) and micropatterning (Schwarzenbacher et al. 2008) was established to visualize the colocalization on a single-molecule level. A concise summary on many applications can be found elsewhere (Saxton and Jacaobson 1997; Levi and Gratton 2007).

ACKNOWLEDGMENTS

We would like to thank Senthil Arumugan, Fabian Heinemann, Grzegorz Chwastek, and Harekrushna Sahoo for their careful reading of and valuable comments on the manuscript.

REFERENCES

Amos WB, White JG. 2003. How the confocal laser scanning microscope entered biological research. *Biol Cell* **95:** 335–342.

Anderson CM, Georgiou GN, Morrison IEG, Stevenson GVW, Cherry RJ. 1992. Tracking of cell-surface receptors by fluorescence digital imaging microscopy using a charge-coupled device camera—Low-density-lipoprotein and influenza-virus receptor mobility at 4°C. *J Cell Sci* **101:** 415–425.

Aoki R, Kitaguchi T, Oya M, Yanagihara Y, Sato M, Miyawaki A, Tsuboi T. 2010. Duration of fusion pore opening and the amount of hormone released are regulated by myosin II during kiss-and-run exocytosis. *Biochem J* **429:** 497–504.

Axelrod D. 1977. Cell-surface heating during fluorescence photobleaching recovery experiments. *Biophys J* **18:** 129–131.

Axelrod D. 2008. Chapter 7: Total internal reflection fluorescence microscopy. *Methods Cell Biology* **89:** 169–221.

Axelrod D, Thompson NL, Burghardt TP. 1983. Total internal reflection fluorescent microscopy. *J Microsc* **129:** 19–28.

Axelrod D, Koppel DE, Schlessinger J, Elson E, Webb WW. 1976. Mobility measurement by analysis of fluorescence photobleaching recovery kinetics. *Biophys J* **16:** 1055–1069.

Bacia K, Schwille P, Kurzchalia T. 2005. Sterol structure determines the separation of phases and the curvature of the liquid-ordered phase in model membranes. *Proc Natl Acad Sci* **102:** 3272–3277.

Bacia K, Scherfeld D, Kahya N, Schwille P. 2004. Fluorescence correlation spectroscopy relates rafts in model and native membranes. *Biophys J* **87:** 1034–1043.

Bader AN, Hofman EG, Voortman J, Henegouwen P, Gerritsen HC. 2009. Homo-FRET imaging enables quantification of protein cluster sizes with subcellular resolution. *Biophys J* **97:** 2613–2622.

Bagatolli LA. 2003. Direct observation of lipid domains in free standing bilayers: From simple to complex lipid mixtures. *Chem Phys Lipids* **122:** 137–145.

Bagatolli LA, Gratton E. 1999. Two-photon fluorescence microscopy observation of shape changes at the phase transition in phospholipid giant unilamellar vesicles. *Biophys J* **77:** 2090–2101.

Bagatolli LA, Gratton E. 2000a. Two photon fluorescence microscopy of coexisting lipid domains in giant unilamellar vesicles of binary phospholipid mixtures. *Biophys J* **78:** 290–305.

Bagatolli LA, Gratton E. 2000b. A correlation between lipid domain shape and binary phospholipid mixture composition in free standing bilayers: A two-photon fluorescence microscopy study. *Biophys J* **79:** 434–447.

Bagatolli LA, Sanchez SA, Hazlett T, Gratton E. 2003. Giant vesicles, laurdan, and two-photon fluorescence microscopy: Evidence of lipid lateral separation in bilayers. *Biophotonics* **360:** 481–500.

Barak LS, Webb WW. 1982. Diffusion of low density lipoprotein-receptor complex on human fibroblasts. *J Cell Biol* **95:** 846–852.

Bastiaens PIH, Squire A. 1999. Fluorescence lifetime imaging microscopy: Spatial resolution of biochemical processes in the cell. *Trends Cell Biol* **9:** 48–52.

Baumgart T, Hunt G, Farkas ER, Webb WW, Feigenson GW. 2007. Fluorescence probe partitioning between L_o/L_d phases in lipid membranes. *Biochim Biophys Acta* **1768:** 2182–2194.

Benda A, Benes M, Marecek V, Lhotsky A, Hermens WT, Hof M. 2003. How to determine diffusion coefficients in planar phospholipid systems by confocal fluorescence correlation spectroscopy. *Langmuir* **19:** 4120–4126.

Bockmann RA, Hac A, Heimburg T, Grubmuller H. 2003. Effect of sodium chloride on a lipid bilayer. *Biophys J* **85:** 1647–1655.

Boldyrev IA, Zhai XH, Momsen MM, Brockman HL, Brown RE, Molotkovsky JG. 2007. New BODIPY lipid probes for fluorescence studies of membranes. *J Lipid Res* **48:** 1518–1532.

Brakenhoff GJ, Blom P, Barends P. 1979. Confocal scanning light-microscopy with high aperture immersion lenses. *J Microsc* **117:** 219–232.

Byrne GD, Pitter MC, Zhang J, Falcone FH, Stolnik S, Somekh MG. 2008. Total internal reflection microscopy for live imaging of cellular uptake of sub-micron non-fluorescent particles. *J Microsc* **231:** 168–179.

Cannon B, Weaver N, Pu QS, Thiagarajan V, Liu SR, Huang JY, Vaughn MW, Cheng KH. 2005. Cholesterol modulated antibody binding in supported lipid membranes as determined by total internal reflectance microscopy on a microfabricated high-throughput glass chip. *Langmuir* **21:** 9666–9674.

Cheezum MK, Walker WF, Guilford WH. 2001. Quantitative comparison of algorithms for tracking single fluorescent particles. *Biophys J* **81:** 2378–2388.

Chiantia S, Kahya N, Schwille P. 2007. Raft domain reorganization driven by short- and long-chain ceramide: A combined AFM and FCS study. *Langmuir* **23:** 7659–7665.

Chiantia S, Ries J, Schwille P. 2009. Fluorescence correlation spectroscopy in membrane structure elucidation. *Biochim Biophys Acta* **1788:** 225–233.

Chiantia S, Ries J, Chwastek G, Carrer D, Li Z, Bittman R, Schwille P. 2008. Role of ceramide in membrane protein organization investigated by combined AFM and FCS. *Biochim Biophys Acta* **1778:** 1356–1364.

Choucair A, Chakrapani M, Chakravarthy B, Katsaras J, Johnston LJ. 2007. Preferential accumulation of A β(1-42) on gel phase domains of lipid bilayers: An AFM and fluorescence study. *Biochim Biophys Acta* **1768:** 146–154.

Clayton AHA, Hanley QS, Arndt-Jovin DJ, Subramaniam V, Jovin TM. 2002. Dynamic fluorescence anisotropy imaging microscopy in the frequency domain (rFLIM). *Biophys J* **83:** 1631–1649.

Coban O, Burger M, Laliberte M, Ianoul A, Johnston LJ. 2007. Ganglioside partitioning and aggregation in phase-separated monolayers characterized by bodipy GM1 monomer/dimer emission. *Langmuir* **23:** 6704–6711.

Dahan M, Levi S, Luccardini C, Rostaing P, Riveau B, Triller A. 2003. Diffusion dynamics of glycine receptors revealed by single-quantum dot tracking. *Science* **302:** 442–445.

Davidovi P, Egger MD. 1973. Photomicrography of corneal endothelial cells in-vivo. *Nature* **244:** 366–367.

Davis LM, Shen. 2006. Accounting for triplet and saturation effects in FCS measurements. *Curr Pharm Biotechnol* **7:** 287–301.

Debrabander M, Geuens G, Nuydens R, Moeremans M, Demey J. 1985. Probing microtubule-dependent intracellular motility with nanometer particle video ultramicroscopy (nanovid ultramicroscopy). *Cytobios* **43:** 273–283.

Debrabander M, Nuydens R, Ishihara A, Holifield B, Jacobson K, Geerts H. 1991. Lateral diffusion and retrograde movements of individual cell-surface components on single motile cells observed with nanovid microscopy. *J Cell Biol* **112:** 111–124.

Delon A, Usson Y, Derouard J, Biben T, Souchier C. 2004. Photobleaching, mobility, and compartmentalisation: Inferences in fluorescence correlation spectroscopy. *J Fluorescence* **14:** 255–267.

Denk W, Strickler JH, Webb WW. 1990. 2-photon laser scanning fluorescence microscopy. *Science* **248:** 73–76.

Dertinger T, Pacheco V, von der Hocht I, Hartmann R, Gregor I, Enderlein J. 2007. Two-focus fluorescence correlation spectroscopy: A new tool for accurate and absolute diffusion measurements. *Chemphyschem* **8:** 433–443.

Dewa T, Sugiura R, Suemori Y, Sugimoto M, Takeuchi T, Hiro A, Iida K, Gardiner AT, Cogdell RJ, Nango M. 2006. Lateral organization of a membrane protein in a supported binary lipid domain: Direct observation of the organization of bacterial light-harvesting complex 2 by total internal reflection fluorescence microscopy. *Langmuir* **22:** 5412–5418.

Dietrich C, Bagatolli LA, Volovyk ZN, Thompson NL, Levi M, Jacobson K, Gratton E. 2001. Lipid rafts reconstituted in model membranes. *Biophys J* **80:** 1417–1428.

Digman MA, Gratton E. 2009. Imaging barriers to diffusion by pair correlation functions. *Biophys J* **97:** 665–673.

Dittrich PS, Schwille P. 2001. Photobleaching and stabilization of fluorophores used for single-molecule analysis with one- and two-photon excitation. *Appl Phys B* **73:** 829–837.

Doeven MK, Folgering JHA, Krasnikov V, Geertsma ER, van den Bogaart G, Poolman B. 2005. Distribution, lateral mobility and function of membrane proteins incorporated into giant unilamellar vesicles. *Biophys J* **88:** 1134–1142.

Dunne PD, Fernandes RA, McColl J, Yoon JW, James JR, Davis SJ, Klenerman D. 2009. DySCo: Quantitating associations of membrane proteins using two-color single-molecule tracking. *Biophys J* **97:** L5–L7.

Edidin M. 1992. Patches, posts and fences: Proteins and plasma membrane domains. *Trends Cell Biol* **2:** 376–380.

Egger MD, Petran M. 1967. New reflected-light microscope for viewing unstained brain and ganglion cells. *Science* **157:** 305–307.

Eggeling C, Ringemann C, Medda R, Schwarzmann G, Sandhoff K, Polyakova S, Belov VN, Hein B, von Middendorff C, Schonle A, et al. 2009. Direct observation of the nanoscale dynamics of membrane lipids in a living cell. *Nature* **457:** U1159–U1121.

Eigen M, Rigler R. 1994. Sorting single molecules—Application to diagnostics and evolutionary biotechnology. *Proc Natl Acad Sci* **91:** 5740–5747.

Ellenberg J, Siggia ED, Moreira JE, Smith CL, Presley JF, Worman HJ, Lippincott-Schwartz J. 1997. Nuclear membrane dynamics and reassembly in living cells: Targeting of an inner nuclear membrane protein in interphase and mitosis. *J Cell Biol* **138:** 1193–1206.

Elson EL, Magde D. 1974. Fluorescence correlation spectroscopy. 1. Conceptual basis and theory. *Biopolymers* **13:** 1–27.

Enderlein J, Gregor I, Patra D, Dertinger T, Kaupp UB. 2005. Performance of fluorescence correlation spectroscopy for measuring diffusion and concentration. *Chemphyschem* **6:** 2324–2336.

Enderlein J, Gregor I, Patra D, Fitter J. 2004. Art and artefacts of fluorescence correlation spectroscopy. *Curr Pharmaceut Biotech* **5:** 155–161.

Engelke M, Bojarski P, Bloss R, Diehl H. 2001. Tamoxifen perturbs lipid bilayer order and permeability: Comparison of DSC, fluorescence anisotropy, Laurdan generalized polarization and carboxyfluorescein leakage studies. *Biophys Chem* **90:** 157–173.

Feder TJ, BrustMascher I, Slattery JP, Baird B, Webb WW. 1996. Constrained diffusion or immobile fraction on cell surfaces: A new interpretation. *Biophysical J* **70:** 2767–2773.

Förster T. 1948. Intermolecular energy migration and fluorescence. *Ann Phys* **2:** 55–75.

Fox CB, Wayment JR, Myers GA, Endicott SK, Harris JM. 2009. Single-molecule fluorescence imaging of peptide binding to supported lipid bilayers. *Anal Chem* **81:** 5130–5138.

Fulbright RM, Axelrod D. 1993. Dynamics of nonspecific adsorption of insulin to erythrocyte membrane. *J Fluor* **3:** 1–16.

Gadella TWJ, Jovin TM. 1995. Oligomerization of epidermal growth-factor receptors on a431 cells studied by time-resolved fluorescence imaging microscopy—A stereochemical model for tyrosine kinase receptor activation. *J Cell Biol* **129:** 1543–1558.

García-Sáez AJ, Schwille P. 2010. Stability of lipid domains. *FEBS Lett* **584:** 1653–1658.

García-Sáez AJ, Ries J, Orzaez M, Perez-Paya E, Schwille P. 2009. Membrane promotes tBID interaction with BCLXL. *Nat Struct Mol Biol* **16:** U1178–U1179.

García-Sáez AJ, Carrer DC, Schwille P. 2010. Fluorescence correlation spectroscopy for the study of membrane dynamics and organization in giant unilamellar vesicles. *Meth Mol Biol* **606:** 493–508.

Gasecka A, Han TJ, Favard C, Cho BR, Brasselet S. 2009. Quantitative imaging of molecular order in lipid membranes using two-photon fluorescence polarimetry. *Biophys J* **97:** 2854–2862.

Gautier I, Tramier M, Durieux C, Coppey J, Pansu RB, Nicolas JC, Kemnitz K, Coppey-Moisan M. 2001. Homo-FRET microscopy in living cells to measure monomer-dimer transition of GFP-tagged proteins. *Biophys J* **80:** 3000–3008.

Gelles J, Schnapp BJ, Sheetz MP. 1988. Tracking kinesin-driven movements with nanometre-scale precision. *Nature* **331:** 450–453.

Ghosh RN, Webb WW. 1994. Automated detection and tracking of individual and clustered cell-surface low-density-lipoprotein receptor molecules. *Biophys J* **66:** 1301–1318.

Gidwani A, Holowka D, Baird B. 2001. Fluorescence anisotropy measurements of lipid order in plasma membranes and lipid rafts from RBL-2H3 mast cells. *Biochemistry* **40:** 12422–12429.

Glebov OO, Nichols BJ. 2004. Lipid raft proteins have a random distribution during localized activation of the T-cell receptor. *Nat Cell Biol* **6:** 238–243.

Goodwin JS, Drake KR, Remmert CL, Kenworthy AJ. 2005. Ras diffusion is sensitive to plasma membrane viscosity. *Biophys J* **89:** 1398–1410.

Goppert M. 1929. Über die Wahrscheinlichkeit des Zusammenwirkens zweier Lichtquanten in einem Elementarakt. *Naturwissenschaften* **17:** 932–932.

Gordon GW, Berry G, Liang XH, Levine B, Herman B. 1998. Quantitative fluorescence resonance energy transfer measurements using fluorescence microscopy. *Biophys J* **74:** 2702–2713.

Gordon GW, Chazotte B, Wang XF, Herman B. 1995. Analysis of simulated and experimental fluorescence recovery after photobleaching. Data for two diffusing components. *Biophys J* **68:** 766–778.

Gorg B, Morwinsky A, Keitel V, Qvartskhava N, Schror K, Haussinger D. 2010. Ammonia triggers exocytotic release of L-glutamate from cultured rat astrocytes. *Glia* **58:** 691–705.

Goswami D, Gowrishankar K, Bilgrami S, Ghosh S, Raghupathy R, Chadda R, Vishwakarma R, Rao M, Mayor S. 2008. Nanoclusters of GPI-anchored proteins are formed by cortical actin-driven activity. *Cell* **135:** 1085–1097.

Grant DM, McGinty J, McGhee EJ, Bunney TD, Owen DM, Talbot CB, Zhang W, Kumar S, Munro I, Lanigan PMP, et al. 2007. High speed optically sectioned fluorescence lifetime imaging permits study of live cell signaling events. *Opt Exp* **15:** 15656–15673.

Gregor I, Patra D, Enderlein J. 2005. Optical saturation in fluorescence correlation spectroscopy under continuous-wave and pulsed excitation. *Chemphyschem* **6:** 164–170.

Guo L, Har JY, Sankaran J, Hong YM, Kannan B, Wohland T. 2008. Molecular diffusion measurement in lipid bilayers over wide concentration ranges: A comparative study. *Chemphyschem* **9:** 721–728.

Hamilton DK, Wilson T. 1986. Scanning optical microscopy by objective lens scanning. *J Phys E-Scientific Instruments* **19:** 52–54.

Hao MM, Mukherjee S, Maxfield FR. 2001. Cholesterol depletion induces large scale domain segregation in living cell membranes. *Proc Natl Acad Sci* **98:** 13072–13077.

Haupts U, Maiti S, Schwille P, Webb WW. 1998. Dynamics of fluorescence fluctuations in green fluorescent protein observed by fluorescence correlation spectroscopy. *Proc Natl Acad Sci* **95:** 13573–13578.

Hein B, Willig KI, Hell SW. 2008. Stimulated emission depletion (STED) nanoscopy of a fluorescent protein-labeled organelle inside a living cell. *Proc Natl Acad Sci* **105:** 14271–14276.

Heinze KG, Koltermann A, Schwille P. 2000. Simultaneous two-photon excitation of distinct labels for dual-color fluorescence crosscorrelation analysis. *Proc Natl Acad Sci* **97:** 10377–10382.

Heinze KG, Rarbach M, Jahnz M, Schwille P. 2002. Two-photon fluorescence coincidence analysis: Rapid measurements of enzyme kinetics. *Biophys J* **83:** 1671–1681.

Hellen E, Axelrod D. 1991. Kinetics of epidermal growth factor/receptor binding on cells measured by total internal

reflection/fluorescence recovery after photobleaching. *J Fluor* **1:** 113–128.

Hellwarth R, Christensen P. 1975. Nonlinear optical microscope using second-harmonic generation. *Appl Opt* **14:** 247–248.

Hess ST, Webb WW. 2002. Focal volume optics and experimental artifacts in confocal fluorescence correlation spectroscopy. *Biophys J* **83:** 2300–2317.

Holtta-Vuori M, Uronen FL, Repakova J, Salonen E, Vattulainen I, Panula P, Li ZG, Bittman R, Ikonen E. 2008. BODIPY-cholesterol: A new tool to visualize sterol trafficking in living cells and organisms. *Traffic* **9:** 1839–1849.

Honerkamp-Smith AR, Cicuta P, Collins MD, Veatch SL, den Nijs M, Schick M, Keller SL. 2008. Line tensions, correlation lengths, and critical exponents in lipid membranes near critical points. *Biophys J* **95:** 236–246.

Honigmann A, Walter C, Erdmann F, Eggeling C, Wagner R. 2010. Characterization of horizontal lipid bilayers as a model system to study lipid phase separation. *Biophys J* **98:** 2886–2894.

Humpolickova J, Benda A, Enderlein J. 2009. Optical saturation as a versatile tool to enhance resolution in confocal microscopy. *Biophys J* **97:** 2623–2629.

Humpolickova J, Gielen E, Benda A, Fagulova V, Vercammen J, Vandeven M, Hof M, Ameloot M, Engelborghs Y. 2006. Probing diffusion laws within cellular membranes by Z-scan fluorescence correlation spectroscopy. *Biophys J* **91:** L23–L25.

Icenogle RD, Elson EL. 1983a. Fluorescence correlation spectroscopy and photobleaching recovery of multiple binding reactions. 1. Theory and FCS measurements. *Biopolymers* **22:** 1919–1948.

Icenogle RD, Elson EL. 1983b. Fluorescence correlation spectroscopy and photobleaching recovery of multiple binding reactions. 2. FPR AND FCS measurements at low and high DNA concentrations. *Biopolymers* **22:** 1949–1966.

Ira S Zou, Ramirez DMC, Vanderlip S, Ogilvie W, Jakubek ZJ, Johnston LJ. 2009. Enzymatic generation of ceramide induces membrane restructuring: Correlated AFM and fluorescence imaging of supported bilayers. *J Struct Biol* **168:** 78–89.

Jacobson K, Sheets ED, Simson R. 1995. Revisiting the fluid mosaic model of membranes. *Science* **268:** 1441–1442.

Jin L, Millard AC, Wuskell JP, Dong XM, Wu DQ, Clark HA, Loew LM. 2006. Characterization and application of a new optical probe for membrane lipid domains. *Biophys J* **90:** 2563–2575.

Johnson SA, Stinson BM, Go MS, Carmona LM, Reminick JI, Fang X, Baumgart T. 2010. Temperature-dependent phase behavior and protein partioning in giant plasma membrane vesicles. *Biochim Biophys Acta* **1798:** 1427–1435.

Jorgensen L, Wood GK, Rosenkrands I, Petersen C, Christensen D. 2009. Protein adsorption and displacement at lipid layers determined by total internal reflection fluorescence (TIRF). *J Lipo Res* **19:** 99–104.

Joselevitch C, Zenisek D. 2009. Imaging exocytosis in retinal bipolar cells with TIRF microscopy. *J Vis Exp* **9:** 1305.

Jovin TM, Arndtjovin DJ. 1989. Luminescence digital imaging microscopy. *Annu Rev Biophys Biophys Chem* **18:** 271–308.

Juhasz J, Davis JH, Sharom FJ. 2010. Fluorescent probe partitioning in giant unilamellar vesicles of 'lipid raft' mixtures. *Biochem J* **430:** 415–423.

Kaiser W, Garrett CGB. 1961. Two-photon excitation in CaF_2: Eu^{2+}. *Phys Rev Lett* **7:** 229.

Kahya N, Schwille P. 2006a. Fluorescence correlation studies of lipid domains in model membranes (Review). *Mol Membr Biol* **23:** 29–39.

Kahya N, Schwille P. 2006b. How phospholipid-cholesterol interactions modulate lipid lateral diffusion, as revealed by fluorescence correlation spectroscopy. *J Fluorescence* **16:** 671–678.

Kahya N, Scherfeld D, Bacia K, Poolman B, Schwille P. 2003. Probing lipid mobility of raft-exhibiting model membranes by fluorescence correlation spectroscopy. *J Biol Chem* **278:** 28109–28115.

Kahya N, Scherfeld D, Bacia K, Schwille P. 2004. Lipid domain formation and dynamics in giant unilamellar vesicles explored by fluorescence correlation spectroscopy. *J Struct Biol* **147:** 77–89.

Kaiser HJ, Lingwood D, Levental I, Sampaio JL, Kalvodova L, Rajendran L, Simons K. 2009. Order of lipid phases in model and plasma membranes. *Proc Natl Acad Sci* **106:** 16645–16650.

Katayama Y, Burkacky O, Meyer M, Brauchle C, Gratton E, Lamb DC. 2009. Real-time nanomicroscopy via three-dimensional single-particle tracking. *Chemphyschem* **10:** 2458–2464.

Kenworthy AK. 2005. Fleeting glimpses of lipid rafts: How biophysics is being used to track them. *J Invest Med* **53:** 312–317.

Kenworthy AK. 2007. Fluorescence recovery after photobleaching studies of lipid rafts. *Methods Mol Biol* **398:** 179–192.

Kenworthy AK, Edidin M. 1998, Distribution of a glycosylphosphatidylinositol-anchored protein at the apical surface of MDCK cells examined at a resolution of <100 angstrom using imaging fluorescence resonance energy transfer. *J Cell Biol* **142:** 69–84.

Kenworthy AK, Edidin M. 1999. Imaging fluorescence resonance energy transfer as probe of membrane organization and molecular associations of GPI-anchored proteins. *Methods Mol Biol* **116:** 37–49.

Kenworthy AK, Nichols BJ, Remmert CL, Hendrix GM, Kumar M, Zimmerberg J, Lippincott-Schwartz J. 2004. Dynamics of putative raft-associated proteins at the cell surface. *J Cell Biol* **165:** 735–746.

Kenworthy AK, Petranova N, Edidin M. 2000. High-resolution FRET microscopy of cholera toxin B-subunit and GPI-anchored proteins in cell plasma membranes. *Mol Biol Cell* **11:** 1645–1655.

Kim SA, Heinze KG, Schwille P. 2007. Fluorescence correlation spectroscopy in living cells. *Nat Methods* **4:** 963–973.

Kim HM, Choo HJ, Jung SY, Ko YG, Park WH, Jeon SJ, Kim CH, Joo TH, Cho BR. 2007. A two-photon fluorescent probe for lipid raft imaging: C-laurdan. *Chembiochem* **8:** 553–559.

Kim HM, Jeong BH, Hyon JY, An MJ, Seo MS, Hong JH, Lee KJ, Kim CH, Joo TH, Hong SC, et al. 2008. Two-photon fluorescent turn-on probe for lipid rafts in live cell and tissue. *J Am Chem Soc* **130:** 4246–4247.

Kirber MT, Chen K, Keaney JF. 2007. YFP photoconversion revisited: Confirmation of the CFP-like species. *Nat Methods* **4:** 767–768.

Koppel DE, Axelrod D, Schlessinger J, Elson EL, Webb WW. 1976. Dynamics of fluorescence marker concentration as a probe of mobility. *Biophys J* **16:** 1315–1329.

Korlach J, Schwille P, Webb WW, Feigenson GW. 1999. Characterization of lipid bilayer phases by confocal microscopy and fluorescence correlation spectroscopy. *Proc Natl Acad Sci* **96:** 8461–8466.

Kuerschner L, Ejsing CS, Ekroos K, Shevchenko A, Anderson KI, Thiele C.2005. Polyene-lipids: A new tool to image lipids. *Nat Methods* **2:** 39–45.

Klymchenko AS, Oncul S, Didier P, Schaub E, Bagatolli L, Duportail G, Mely Y. 2009. Visualization of lipid domains in giant unilamellar vesicles using an environment-sensitive membrane probe based on 3-hydroxyflavone. *Biochim Biophys Acta* **1788:** 495–499.

Kusumi A, Sako Y, Yamamoto M. 1993. Confined lateral diffusion of membrane-receptors as studied by single-particle tracking (NANOVID microscopy)—Effects of calcium-induced differentiation in cultured epithelial-cells. *Biophys J* **65:** 2021–2040.

Kusumi A, Nakada C, Ritchie K, Murase K, Suzuki K, Murakoshi H, Kasai RS, Kondo J, Fujiwara T. 2005. Paradigm shift of the plasma membrane concept from the two-dimensional continuum fluid to the partitioned fluid: High-speed single-molecule tracking of membrane molecules. *Annu Rev Biophys Biomol Struct* **34:** U351–U354.

Lagerholm BC, Weinreb GE, Jacobson K, Thompson NL. 2005. Detecting microdomains in intact cell membranes. *Annu Rev Phys Chem* **56:** 309–336.

Lam AD, Ismail S, Wu R, Yizhar O, Passmore DR, Ernst SA, Stuenkel EL. 2010. Mapping dynamic protein interactions to insulin secretory granule behavior with TIRF-FRET. *Biophys J* **99:** 1311–1320.

Larijani B, Allen-Baume V, Morgan CP, Li M, Cockcroft S. 2003. EGF regulation of PITP dynamics is blocked by inhibitors of phospholipase C and of the Ras-MAP kinase pathway. *Curr Biol* **13:** 78–84.

Lee GM, Ishihara A, Jacobson KA. 1991. Direct observation of Brownian-motion of lipids in a membrane. *Proc Natl Acad Sci* **88:** 6274–6278.

Lenne PF, Wawrezinieck L, Conchonaud F, Wurtz O, Boned A, Guo XJ, Rigneault H, He HT, Marguet D. 2006. Dynamic molecular confinement in the plasma membrane by microdomains and the cytoskeleton meshwork. *EMBO J* **25:** 3245–3256.

Levi V, Gratton E. 2007. Exploring dynamics in living cells by tracking single particles. *Cell Biochem Biophys* **48:** 1–15.

Levi V, Ruan QQ, Gratton E. 2005. 3-D particle tracking in a two-photon microscope: Application to the study of molecular dynamics in cells, *Biophys J* **88:** 2919–2928.

Levi V, Gelfand VI, Serpinskaya AS, Gratton E. 2006a. Melanosomes transported by myosin-V in *Xenopus* melanophores perform slow 35 nm steps. *Biophys J* **90:** L7–L9.

Levi V, Serpinskaya AS, Gratton E, Gelfand V. 2006b. Organelle transport along microtubules in *Xenopus* melanophores: Evidence for cooperation between multiple motors. *Biophys J* **90:** 318–327.

Lidke DS, Nagy P, Barisas BG, Heintzmann R, Post JN, Lidke KA, Clayton AHA, Arndt-Jovin DJ, Jovin TM. 2003. Imaging molecular interactions in cells by dynamic and static fluorescence anisotropy (rFLIM and emFRET). *Biochem Soc Trans* **31:** 1020–1027.

Lingwood D, Ries J, Schwille P, Simons K. 2008. Plasma membranes are poised for activation of raft phase coalescence at physiological temperature. *Proc Natl Acad Sci* **105:** 10005–10010.

Lippincott-Schwartz J, Snapp E, Kenworthy A. 2001. Studying protein dynamics in living cells. *Nat Cell Biol* **2:** 444–456.

Lippincott-Schwartz J, Altan-Bonnet N, Patterson GH. 2003. Photobleaching and photoactivation: Following protein dynamics in living cells. *Nat Cell Biol* Suppl: S7–S14.

Loman A, Dertinger T, Koberling F, Enderlein J. 2008. Comparison of optical saturation effects in conventional and dual-focus fluorescence correlation spectroscopy. *Chem Phys Lett* **459:** 18–21.

Lommerse PHM, Spaink HP, Schmidt T. 2004. In vivo plasma membrane organization: Results of biophysical approaches. *Biochim Biophys Acta* **1664:** 119–131.

Machan R, Hof M. 2010. Lipid diffusion in planar membranes investigated by fluorescence correlation spectroscopy. *Biochim Biophys Acta* **1798:** 1377–1391.

Magde D, Elson EL, Webb WW. 1974. Fluorescence correlation spectroscopy. 2. Experimental realization. *Biopolymers* **13:** 29–61.

Magde D, Webb WW, Elson E. 1972. Thermodynamic fluctuations in a reacting system—Measurement by fluorescence correlation spectroscopy. *Phys Rev Lett* **29:** 705.

Magde D, Webb WW, Elson EL. 1978. Fluorescence correlation spectroscopy. 3. Uniform translation and laminar-flow. *Biopolymers* **17:** 361–376.

Marks DL, Bittman R, Pagano RE. 2008. Use of Bodipy-labeled sphingolipid and cholesterol analogs to examine membrane microdomains in cells. *Histochem Cell Biol* **130:** 819–832.

Meder D, Moreno MJ, Verkade P, Vaz WLC, Simons K. 2006. Phase coexistence and connectivity in the apical membrane of polarized epithelial cells. *Proc Natl Acad Sci* **103:** 329–334.

Merrifield CJ, Perrais D, Zenisek D. 2005. Coupling between clathrin-coated-pit invagination, cortactin recruitment, and membrane scission observed in live cells. *Cell* **121:** 593–606.

Merrifield CJ, Feldman ME, Wan L, Almers W. 2002. Imaging actin and dynamin recruitment during invagination of single clathrin-coated pits. *Nat Cell Biol* **4:** 691–698.

Meseth U, Wohland T, Rigler R, Vogel H. 1999. Resolution of fluorescence correlation measurements. *Biophys J* **76:** 1619–1631.

Middlebrook JL, Dorland RB. 1984. Bacterial toxins—Cellular mechanisms of action. *Microbiological Rev* **48:** 199–221.

Mikhalyov I, Gretskaya N, Johansson LBA. 2009. Fluorescent BODIPY-labelled G_{M1} gangliosides designed for exploring lipid membrane properties and specific membrane–target interactions. *Chem Phys Lipids* **159:** 38–44.

Mills JD, Stone JR, Rubin DG, Melon DE, Okonkwo DO, Periasamy A, Helm GA. 2003. Illuminating protein interactions in tissue using confocal and two-photon excitation fluorescent resonance energy transfer microscopy. *J Biomed Opt* **8:** 347–356.

Miyawaki A, Tsien RY. 2000. Monitoring protein conformations and interactions by fluorescence resonance energy transfer between mutants of green fluorescent protein. *Appl Chim Genes Hybrid Prot Pt B* **327:** 472–500.

Mueller BK, Zaychikov E, Brauchle C, Lamb DC. 2005. Pulsed interleaved excitation. *Biophys J* **89:** 3508–3522.

Mütze J, Ohrt T, Schwille P. 2011. Fluorescence correlation spectroscopy in vivo. *Laser Photon Rev* **5:** 52–67.

Nagamatsu S, Ohara-Imaizumi M. 2008. Imaging exocytosis of single insulin secretory granules with TIRF microscopy. *Methods Mol Biol* **440:** 259–268.

Nicolau DV, Burrage K, Parton RG, Hancock JF. 2006. Identifying optimal lipid raft characteristics required to promote nanoscale protein–protein interactions on the plasma membrane. *Mol Cell Biol* **26:** 313–323.

Niv H, Gutman O, Henis YI, Kloog Y. 1999. Membrane interactions of a constitutively active GFP-Ki-Ras 4B and their role in signaling—Evidence from lateral mobility studies. *J Biol Chem* **274:** 1606–1613.

Niv H, Gutman O, Kloog Y, Henis YI. 2002. Activated K-Ras and H-Ras display different interactions with saturable nonraft sites at the surface of live cells. *J Cell Biol* **157:** 865–872.

Ohara-Imaizumi M, Aoyagi K, Akimoto Y, Nakamichi Y, Nishiwaki C, Kawakami H, Nagamatsu S. 2009. Imaging exocytosis of single glucagon-like peptide-1 containing granules in a murine enteroendocrine cell line with total internal reflection fluorescent microscopy. *Biochem Biophys Res Comm* **390:** 16–20.

Oreopoulos J, Yip CM. 2009. Probing membrane order and topography in supported lipid bilayers by combined polarized total internal reflection fluorescence–atomic force microscopy. *Biophys J* **96:** 1970–1984.

Parasassi T, Gratton E, Yu WM, Wilson P, Levi M. 1997. Two-photon fluorescence microscopy of Laurdan generalized polarization domains in model and natural membranes. *Biophys J* **72:** 2413–2429.

Petersen NO. 1986. Scanning fluorescence correlation spectroscopy. 1. Theory and simulation of aggregation measurements. *Biophys J* **49:** 809–815.

Petersen NO, Johnson DC, Schlesinger MJ. 1986. Scanning fluorescence correlation spectroscopy. 2. Application to virus glycoprotein aggregation. *Biophys J* **49:** 817–820.

Petrasek Z, Schwille P. 2008. Precise measurement of diffusion coefficients using scanning fluorescence correlation spectroscopy. *Biophys J* **94:** 1437–1448.

Petrasek Z, Ries J, Schwille P. 2010. Scanning FCS for the characterization of protein dynamics in live cells. *Meth Enzymol* **472:** 317–343.

Petrov E, Schwille P. 2007. State of the art and novel trends in fluorescence correlation spectroscopy. In *Standardization and quality assurance in fluorescence measurements II* (ed. Resch-Genger U), pp. 145–197. Springer-Verlag, Berlin.

Phair RD, Gorski SA, Misteli T. 2004. Measurement of dynamic protein binding to chromatin in vivo, using photobleaching microscopy. *Methods Enzymol* **375:** 393–414.

Pinaud F, Michalet X, Iyer G, Margeat E, Moore HP, Weiss S. 2009. Dynamic partitioning of a glycosyl-phosphatidylinositol-anchored protein in glycosphingolipid-rich microdomains imaged by single-quantum dot tracking. *Traffic* **10:** 691–712.

Piston DW, Kremers GJ. 2007. Fluorescent protein FRET: The good, the bad and the ugly. *Trends Biochem Sci* **32:** 407–414.

Ragan T, Huang HD, So P, Gratton E. 2006. 3D particle tracking on a two-photon microscope. *J Fluorescence* **16:** 325–336.

Ries J, Schwille P. 2006. Studying slow membrane dynamics with continuous wave scanning fluorescence correlation spectroscopy. *Biophys J* **91:** 1915–1924.

Ries J, Chiantia S, Schwille P. 2009b. Accurate determination of membrane dynamics with line-scan FCS. *Biophys J* **96:** 1999–2008.

Ries J, Petrov EP, Schwille P. 2008. Total internal reflection fluorescence correlation spectroscopy: Effects of lateral diffusion and surface-generated fluorescence. *Biophys J* **95:** 390–399.

Ries J, Yu SR, Burkhardt M, Brand M, Schwille P. 2009a. Modular scanning FCS quantifies receptor-ligand interactions in living multicellular organisms. *Nat Methods* **6:** U643–U631.

Rigler R, Mets U, Widengren J, Kask P. 1993. Fluorescence correlation spectroscopy with high count rate and low-background—Analysis of translational diffusion. *Euro Biophys J Biophys Lett* **22:** 169–175.

Rotblat B, Prior IA, Muncke C, Parton RG, Kloog Y, Henis YI, Hancock JF. 2004. Three separable domains regulate GTP-dependent association of H-ras with the plasma membrane. *Mol Cell Biol* **24:** 6799–6810.

Roy S, Plowman S, Rotblat B, Prior IA, Muncke C, Grainger S, Parton RG, Henis YI, Kloog Y, Hancock JF. 2005. Individual palmitoyl residues serve distinct roles in H-ras trafficking, microlocalization, and signaling. *Mol Cell Biol* **25:** 6722–6733.

Runnels LW, Scarlata SF. 1995. Theory and application of fluorescence homotransfer to melittin oligomerization. *Biophys J* **69:** 1569–1583.

Rusinova E, Tretyachenko-Ladokhina V, Vele OE, Senear DF, Ross JBA. 2002. Alexa and Oregon Green dyes as fluorescence anisotropy probes for measuring protein–protein and protein–nucleic acid interactions. *Anal Biochem* **308:** 18–25.

Sahoo H, Roccatano D, Hennig A, Nau WM. 2007. A 10-angstrom spectroscopic ruler applied to short polyprolines. *J Am Chem Soc* **129:** 9762–9772.

Sako Y, Minoghchi S, Yanagida T. 2000. Single-molecule imaging of EGFR signalling on the surface of living cells. *Nat Cell Biol* **2:** 168–172.

Saxton MJ. 1994a. Anomalous diffusion due to obstacles—A Monte Carlo study. *Biophys J* **66:** 394–401.

Saxton MJ. 1994b. Single-particle tracking—Models of directed transport. *Biophys J* **67:** 2110–2119.

Saxton MJ. 1995. Single-tracking-effects of corrals. *Biophys J* **69:** 389–398.

Saxton MJ. 1996a. Anomalous diffusion due to binding: A Monte Carlo study, *Biophys J* **70:** 1250–1262.

Saxton MJ. 1996b. Single-particle tracking: New methods of data analysis, *Biophys J* **70:** TU415–TU415.

Saxton MJ. 1997. Single-particle tracking: The distribution of diffusion coefficients. *Biophys J* **72:** 1744–1753.

Saxton MJ, Jacobson K. 1997. Single-particle tracking: Applications to membrane dynamics. *Annu Rev Biophys Biomol Struct* **26:** 373–399.

Scherfeld D, Kahya N, Schwille P. 2003. Lipid dynamics and domain formation in model membranes composed of ternary mixtures of unsaturated and saturated phosphatidylcholines and cholesterol. *Biophys J* **85:** 3758–3768.

Schnapp BJ, Gelles J, Sheetz MP. 1988. Nanometer-scale measurements using video light-microscopy. *Cell Motility Cytoskeleton* **10:** 47–53.

Schultz C, Neef AB, Gadella TW Jr, Goedhart J. 2010. Imaging lipids in living cells. *Cold Spring Harb Protoc* doi: 101101/pdbtop83.

Schutz GJ, Schindler H, Schmidt T. 1997. Single-molecule microscopy on model membranes reveals anomalous diffusion. *Biophys J* **73:** 1073–1080.

Schutz GJ, Kada G, Pastushenko VP, Schindler H. 2000. Properties of lipid microdomains in a muscle cell membrane visualized by single molecule microscopy. *EMBO J* **19:** 892–901.

Schwarzenbacher M, Kaltenbrunner M, Brameshuber M, Hesch C, Paster W, Weghuber J, Heise B, Sonnleitner A, Stockinger H, Schutz GJ. 2008. Micropatterning for quantitative analysis of protein–protein interactions in living cells. *Nat Methods* **5:** 1053–1060.

Schwille P. 2003. TIR-FCS: Staying on the surface can sometimes be better. *Biophys J* **85:** 2783–2784.

Schwille P, Heinze KG. 2001. Two-photon fluorescence cross-correlation spectroscopy. *Chemphyschem* **2:** 269–272.

Schwille P, Korlach J, Webb WW. 1999a. Fluorescence correlation spectroscopy with single-molecule sensitivity on cell and model membranes. *Cytometry* **36:** 176–182.

Schwille P, MeyerAlmes FJ, Rigler R. 1997. Dual-color fluorescence cross-correlation spectroscopy for multicomponent diffusional analysis in solution. *Biophys J* **72:** 1878–1886.

Schwille P, Haupts U, Maiti S, Webb WW. 1999b. Molecular dynamics in living cells observed by fluorescence correlation spectroscopy with one- and two-photon excitation. *Biophys J* **77:** 2251–2265.

Schwille P, Heinze K, Dittrich P, Haustein E. 2009. Two-photon fluorescence correlation spectroscopy. In *Biomedical optical imaging* (ed. Fujimoto JG, Farkas D). Oxford University Press, Oxford.

Sharma P, Varma R, Sarasij RC, Ira K, Gousset G, Krishnamoorthy M, Rao S, Mayor S. 2004. Nanoscale organization of multiple GPI-anchored proteins in living cell membranes. *Cell* **116:** 577–589.

Sheetz MP, Kuo SC. 1993. Tracking nanometer movements of single motor molecules. *Meth Cell Biol* **39:** 129–136.

Sheppard CJR, Wilson T.1979. Effect of spherical-aberration on the imaging properties of scanning optical microscopes. *Appl Opt* **18:** 1058–1063.

Shvartsman DE, Gutman O, Tietz A, Henis. 2006. Cyclodextrins but not compactin inhibit the lateral diffusion of membrane proteins independent of cholesterol. *Traffic* **7:** 917–926.

Snapp EL, Altan N, Lippincott-Schwartz J. 2003. Measuring protein mobility by photobleaching GFP chimeras in living cells. *Curr Protoc Cell Biol* **21:** 2121.

Sohn HW, Tolar P, Brzostowski J, Pierce SK. 2010. A method for analyzing protein–protein interactions in the plasma membrane of live B cells by fluorescence resonance energy transfer imaging as acquired by total internal reflection fluorescence microscopy. *Methods Mol Biol* **591:** 159–183.

Soumpasis DM. 1983. Theoretical analysis of fluorescence photobleaching recovery experiments. *Biophysical J* **41:** 95–97.

Spandl J, White DJ, Peychl J, Thiele C. 2009. Live cell multicolor imaging of lipid droplets with a new dye, LD540. *Traffic* **10:** 1579–1584.

Sprague BL, Pego RL, Stavreva DA, McNally JG. 2004. Analysis of binding reactions by fluorescence recovery after photobleaching. *Biophys J* **86:** 3473–3495.

Sprague BL, McNally JG. 2005. FRAP analysis of binding: Proper and fitting. *Trends in Cell Biol* **15:** 84–91.

Sum AK, Faller R, de Pablo JJ. 2003. Molecular simulation study of phospholipid bilayers and insights of the interactions with disaccharides. *Biophys J* **85:** 2830–2844.

Teramura Y, Ichinose J, Takagi H, Nishida K, Yanagida T, Sako Y. 2006. Single-molecule analysis of epidermal growth factor binding on the surface of living cells. *EMBO J* **25:** 4215–4222.

Thiele C, Spandl J. 2008. Cell biology of lipid droplets. *Curr Opin Cell Biol* **20:** 378–385.

Tomishige M, Sako Y, Kusumi A. 1998. Regulation mechanism of the lateral diffusion of band 3 in erythrocyte membranes by the membrane skeleton. *J Cell Biol* **142:** 989–1000.

Toprak E, Balci H, Blehm BH, Selvin PR. 2007. Three-dimensional particle tracking via bifocal imaging. *Nano Lett* **7:** 2043–2045.

Tyteca D, D'Auria L, Van Der Smissen P, Medts T, Carpentier S, Monbaliu JC, de Diesbach P, Courtoy PJ. 2010. Three unrelated sphingomyelin analogs spontaneously cluster into plasma membrane micrometric domains. *Biochim Biophys Acta* **1798:** 909–927.

Vacha R, Siu SWI, Petrov M, Bockmann RA, Barucha-Kraszewska J, Jurkiewicz P, Hof M, Berkowitz ML, Jungwirth P. 2009. Effects of alkali cations and halide anions on the DOPC lipid membrane. *J Phys Chem A* **113:** 7235–7243.

van den Bogaart G, Hermans N, Krasnikov V, de Vries AH, Poolman B. 2007. On the decrease in lateral mobility of phospholipids by sugars. *Biophys J* **92:** 1598–1605.

Varma R, Mayor S. 1998. GPI-anchored proteins are organized in submicron domains at the cell surface. *Nature* **394:** 798–801.

Veatch SL, Keller SL. 2002. Organization in lipid membranes containing cholesterol. *Phys Rev Lett* **89:** 268101–268104.

Veatch SL, Keller SL. 2003. Separation of liquid phases in giant vesicles of ternary mixtures of phospholipids and cholesterol. *Biophys J* **85:** 3074–3083.

Wallrabe H, Stanley M, Periasamy A, Barroso M. 2003. One- and two-photon fluorescence resonance energy transfer microscopy to establish a clustered distribution of receptor-ligand complexes in endocytic membranes. *J Biomed Opt* **8:** 339–346.

Wawrezinieck L, Rigneault H, Marguet D, Lenne PF. 2005. Fluorescence correlation spectroscopy diffusion laws to probe the submicron cell membrane organization. *Biophys J* **89:** 4029–4042.

Weidemann T, Wachsmuth M, Tewes M, Rippe K, Langowski J. 2002. Analysis of ligand binding by two-colour fluorescence cross-correlation spectroscopy. *Single Mol* **3:** 49–61.

Weiss M. 2004. Challenges and artifacts in quantitative photobleaching experiments. *Traffic* **5:** 662–671.

Wenger J, Conchonaud F, Dintinger J, Wawrezinieck L, Ebbesen TW, Rigneault H, Marguet D, Lenne PF. 2007. Diffusion analysis within single nanometric apertures reveals the ultrafine cell membrane organization. *Biophys J* **92:** 913–919.

Wolf DE. 1989. Designing, building, and using a fluorescence recovery after photobleaching instrument. In *Methods in cell biology* (ed. Taylor DL, Wang Y-L), pp. 271–332. Academic Press, New York.

Worch R, Bokel C, Hofinger S, Schwille P, Weidemann T. 2010. Focus on composition and interaction potential of single-pass transmembrane domains. *Proteomics* **10:** 4196–4208.

Wouters FS, Bastiaens PIH, Wirtz KWA, Jovin TM. 1998. FRET microscopy demonstrates molecular association of non-specific lipid transfer protein (nsL-TP) with fatty acid oxidation enzymes in peroxisomes. *EMBO J* **17:** 7179–7189.

Yildiz A, Forkey JN, McKinney SA, Ha T, Goldman YE, Selvin PR. 2003. Myosin V walks hand-over-hand: Single fluorophore imaging with 1.5-nm localization. *Science* **300:** 2061–2065.

Yildiz A, Park H, Safer D, Yang ZH, Chen LQ, Selvin PR, Sweeney HL. 2004a. Myosin VI steps via a hand-over-hand mechanism with its lever arm undergoing fluctuations when attached to actin. *J Biol Chem* **279:** 37223–37226.

Yildiz A, Tomishige M, Vale RD, Selvin PR. 2004b. Kinesin walks hand-over-hand. *Science* **303:** 676–678.

Yu CX, Hale J, Ritchie K, Prasad NK, Irudayaraj J. 2009. Receptor overexpression or inhibition alters cell surface dynamics of EGF-EGFR interaction: New insights from real-time single molecule analysis. *Biochem Biophys Res Commun* **378:** 376–382.

Yu SR, Burkhardt M, Nowak M, Ries J, Petrasek Z, Scholpp S, Schwille P, Brand M. 2009. Fgf8 morphogen gradient forms by a source-sink mechanism with freely diffusing molecules. *Nature* **461:** U533–U100.

Ulrike Engel, Monday June 11th 2012, 10.00

A REAL-TIME VIEW OF LIFE WITHIN 100 NM OF THE PLASMA MEMBRANE

J. A. Steyer and W. Almers‡*

The plasma membrane is a two-dimensional compartment that relays most biological signals sent or received by a cell. Signalling involves membrane receptors and their associated enzyme cascades as well as organelles such as exocytic and endocytic vesicles. Advances in light microscope design, new organelle-specific vital stains and fluorescent proteins have renewed the interest in evanescent field fluorescence microscopy, a method uniquely suited to image the plasma membrane with its associated organelles and macromolecules in living cells. The method shows even the smallest vesicles made by cells, and can image the dynamics of single protein molecules.

CAVEOLAE
Flask-shaped, cholesterol-rich invaginations of the plasma membrane, thought to be involved in cell signalling.

LIPID RAFTS
Micro-aggregates of cholesterol and sphingomyelin thought to occur in the plasma membrane.

GREEN FLUORESCENT PROTEIN
Isolated from the jellyfish *Aequorea victoria*. Can be genetically conjugated with proteins to make them fluorescent. The most widely used mutant, EGFP, has an emission maximum at 510 nm.

**Department of Molecular and Cell Biology, University of California, Berkeley, California 94720, USA.*
‡Vollum Institute, Oregon Health Sciences University, Portland, Oregon 97210, USA.
Correspondence to W.A.
e-mail: almersw@ohsu.edu

The plasma membrane is a busy place. Exocytic vesicles insert receptors into the plasma membrane and release ligands into the extracellular space. Endocytic vesicles carry receptors with bound ligand to internal processing stations. CAVEOLAE are plasma-membrane-associated vesicles with a presumed role in cell signalling[1]. LIPID RAFTS are thought to populate the plasma membrane as small floating islands[2] in which select membrane proteins meet in private to exchange signals. Finally, there is the universe of membrane receptors. Many are probably embedded in large molecular complexes that continually recruit and release downstream effector molecules.

Most or all these structures are highly dynamic, do their jobs in milliseconds to minutes and sometimes disperse soon thereafter. Only rarely do organelles of the same type act in synchrony. To observe single events mediated by single organelles and signalling complexes, we require *in vivo* methods that image single organelles, detect molecules in small numbers and report their function at high resolution in time and space. Fluorescence microscopy is a natural choice in so far as some organelles may be stained specifically with dyes, and more and more proteins have been conjugated with fluorescent proteins such as GREEN FLUORESCENT PROTEIN (GFP) without impairing their function[3]. However, most plasma membrane events involve interactions with cytosolic proteins that have been recruited to the plasma membrane transiently and in small numbers. And organelles of a given type often inhabit the entire cell. Because even CONFOCAL MICROSCOPES look into cells to a depth of nearly half a micron when focused on the plasma membrane, these and more conventional fluorescence microscopes show strong 'background' fluorescence from the cytosol that obscures the weaker fluorescence from small structures or molecular assemblies near the plasma membrane. Evanescent field (EF) fluorescence microscopy overcomes this problem because it provides depth discrimination of near-molecular dimensions. This review focuses on recent applications of this method to membrane dynamics and signal transduction. We ignore a large number of interesting papers with a more biophysical orientation[4], including those on cell–substrate contacts[5] and on single molecule imaging[6].

Evanescent fields

An EF can form when a beam of light travelling in a medium of high REFRACTIVE INDEX, such as glass, encounters one of lower refractive index such as the adjoining water or an adherent cell. When the angle of incidence α is small, light is refracted and propagates through the interface. But when α exceeds a certain 'critical angle',

Box 1 | **Evanescent fields**

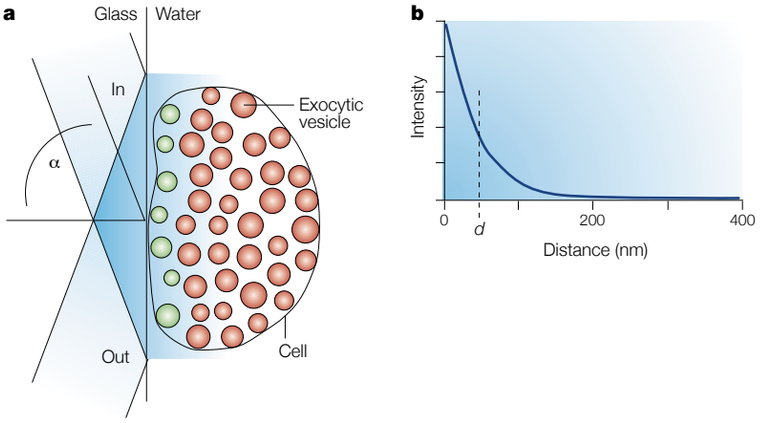

When a parallel beam of light in a medium of high refractive index (n_1) strikes an interface with a medium of lower refractive index (n_2) it suffers total internal reflection if the angle of incidence, α, exceeds the so-called critical angle. Total internal reflection generates an evanescent field in the medium of lower refractive index (**a**). The intensity of the evanescent field medium declines exponentially with distance from the interface (**b**), falling 37% within the so-called 'penetration depth' d:

$$d = \frac{\lambda}{4\pi\sqrt{NA_i^2 - n_2^2}} \qquad (1)$$

in which λ is the wavelength of light and $NA_i = n_1 \sin\alpha$ is the numerical aperture of incidence. The larger the difference between NA_i and n_2, the smaller is d.

In one example[33], light propagates through a coverslip of high refractive index glass ($n_1 = 1.8$) at an angle of $\alpha = 66°$ onto adhering cells (typically $n_2 = 1.37$). EQN 1 predicts $d = 43$ nm (**b**). EQN1 holds strictly in a homogenous medium such as water, and holds approximately in cells if local variations of n_2 are small compared to ($NA_i - n_2$). Otherwise light-scattering structures can significantly increase the apparent penetration depth of an evanescent field[43] and even cause it to become propagated[19,44].

CONFOCAL MICROSCOPE
A fluorescence microscope achieving improved depth discrimination by blocking fluorescence that originates outside the plane of focus by use of a 'confocal' pinhole. In most confocal microscopes, a laser beam focused to a small spot provides the excitation light and scans the image point by point.

REFRACTIVE INDEX
In a transparent medium, the refractive index is defined as the speed of light in a vacuum (or air) divided by the speed of light in the medium. It determines the change in direction undergone by a beam of light when it strikes an interface between two media of different refractive indices.

TOTAL INTERNAL REFLECTION
Highly efficient reflection occurring at the interface with a transparent medium of lower refractive index when light strikes the interface at a glancing angle.

light instead undergoes TOTAL INTERNAL REFLECTION (BOX 1). Classical electrodynamics does not allow an electromagnetic wave to vanish discontinuously at an interface, therefore total internal reflection sets up a thin layer of light in the water or cell, called the evanescent field (EF). An EF selectively illuminates fluorescent molecules near the interface and leaves more remote structures in the dark. In the example of BOX 1, the EF reaches from the plasma membrane into the cytosol for little more than 100 nm, a distance comparable to the thickness of ultrathin sections cut for electron microscopy. EF microscopes are extremely sensitive to movement of fluorescent objects vertical to the glass, as structures brighten when they approach the glass and dim when they retreat. Brightness is proportional to the illumination intensity within the evanescent field, but also to the availability of the emitted light for collection by a microscope objective (BOX 2). In the example of BOX 1, a 20-nm movement would produce a 37% change in illumination and, in the 'through-the-lens' configuration (see below), a 40% change in detected fluorescence (BOX 2b). In depth discrimination, EF fluorescence microscopy is up to tenfold better than confocal microscopy, the only other fluorescence microscopic technique developed for this purpose. Confocal and EF fluorescence microscopy are compared in TABLE 1.

There are two common configurations for EF microscopes — prism and through-the-lens (BOX 3). Prism microscopes can illuminate a larger field of view. This is an advantage when simultaneously imaging several cells or a single cell that spreads over large areas, such as a neuron with its axon and dendrites. Prism-type EF microscopes also have the least background light[7]. However, the sample is sandwiched in a narrow space between the prism and the objective lens and access to it is restricted. Moreover, the brightness of an object does not necessarily vary monotonically with its distance from the interface (BOX 2c). This is a disadvantage when interpreting brightness changes in terms of movement in and out of the evanescent field. The prism method is easy to implement, but we know of no commercial supplier.

Through-the-lens microscopes allow free access to the specimen, collect fluorescent light more efficiently from objects near the interface (BOX 2) and have higher image quality and spatial resolution. Good through-the-lens microscopes require unusual objectives that have become available only recently. So most early work with EF fluorescence has used the prism method (BOX 4). Attachments and objectives for through-the-lens microscopes are available from Olympus Co.

Imaging secretory granules

The molecular mechanism of exocytosis has been intensely studied biochemically[8]. Although ELECTROPHYSIOLOGY has been the method of choice in functional studies[9,10], this method directly assays only exocytosis, the last step in a long sequence of events. Precursor steps such as the docking of vesicles at the plasma membrane and their preparation for exocytosis must be inferred indirectly by kinetic modelling. Hence it was desirable to image SECRETORY VESICLES and granules before exocytosis. It is not difficult to make secretory vesicles fluorescent. Vesicle-resident proteins can be conjugated with GFP (FIG. 1)[11,12] or one may use the fact that most vesicles are acidic inside and therefore accumulate fluorescent weak bases such as acridine orange or quinacrine. In MAST CELLS of mutant mice, secretory granules are so large (1–3 μm diameter) that they could be observed with simple EPIFLUORESCENCE MICROSCOPY while they discharged quinacrine by exocytosis[13]. The large granules of sea urchin eggs could also be observed by epifluorescence microscopy[14]. But fluorescence imaging of the ten times smaller and more densely packed secretory granules of endocrine cells required EF fluorescence microscopy[15]. After CHROMAFFIN CELLS had accumulated acridine orange in their granules, stimulation caused the granules to release their fluorescence as a short-lived fluorescent cloud, and then to dim or vanish. Once the plasma membrane was stripped of docked granules, fresh granules arrived from the cytosol. Some of them approached by directed motion as if moving along filamentous tracks, and then lost mobility because they had either docked at the plasma membrane or become ensnared in the dense network of actin filaments that invests the plasma membrane of most cells.

Box 2 | **Light collection near a glass–water interface**

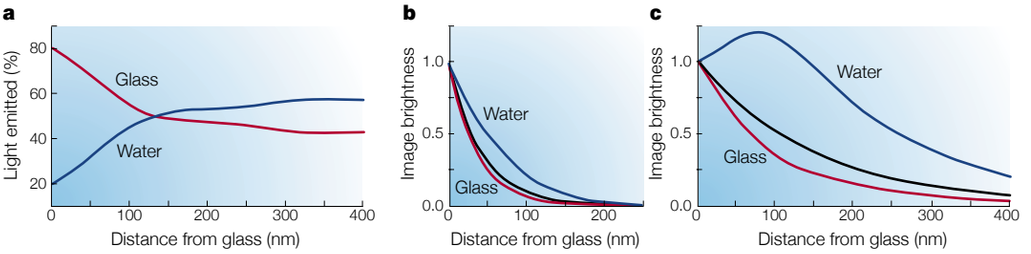

Apart from radiating light in all directions, a fluorescent molecule also generates an electromagnetic 'near field' that, like an evanescent field, does not propagate but declines rapidly with distance. Where the near field extends into the glass, it radiates into the glass as propagated light, entering at an angle larger than the critical angle[45]. In so far as the total fluorescence emitted by the molecule does not change, the energy thus captured from the near field diminishes the fluorescent light propagating elsewhere. Hence objects close to the interface emit most of their fluorescence into the glass at the expense of the aqueous phase. Objects at greater distance emit more fluorescence into the water, as propagated light is reflected from the glass back into the water. These effects occur regardless of whether fluorescence is excited by an EF or by propagated light. They are illustrated in panel **a**, which shows the light emitted into water (blue) and into glass (red). The blue curve was calculated for dipoles of random orientation as in References 46 and 47 but for $\lambda = 520$ nm and high refractive index glass ($n_1 = 1.8$) contacting water ($n_2 = 1.33$). The red curve is one minus the blue curve. A 1.65 *NA* objective is expected to collect most of the light emitted into the glass.

The red and blue curves in panel **b** show how bright a fluorescent object appears at various distances when it is illuminated with an evanescent field as in Box 1 (re-drawn as the black curve). Brightness depends both on the intensity of illumination (black) and on what portion of the emitted fluorescence is available for collection (red and blue in panel **a**). In glass, both factors combine in dimming the object as it retreats from the interface. This is shown in the red curve, which multiplies the black curve by the red curve in **a**. In water, the two factors oppose each other, and the blue curve is the black curve multiplied by the blue curve in **a**. All three curves were scaled to coincide at the interface. We assumed that ideal objectives collect all light emitted into glass on one side and water on the other. Light emitted into glass falls more steeply with distance than the illumination intensity, and light emitted into water less steeply. Panel c is similar to panel **b** but with a more deeply penetrating evanescent field ($d = 150$ nm, black). Note that light detected through water first rises and then falls as the object moves into water.

ELECTROPHYSIOLOGY
Three variants are used to study secretion. First, a glass micropipette penetrating a neuron records electric currents through plasma membrane ion channels opened by secreted neurotransmitter. Second, a carbon fibre placed near the surface of a secretory cell records a current as it oxidizes secreted catecholamines. Third, the increase in cell surface area following exocytosis is measured by monitoring the electrical capacitance of the plasma membrane. All three methods are sensitive enough to detect the exocytosis of single vesicles.

SECRETORY VESICLES
Used to sequester molecules within a cell and then deliver (secrete) them to the extracellular space by exocytosis.

MAST CELL
A type of leukocyte with large secretory granules containing histamine and various protein mediators. Granules are especially large in the *beige* mouse mutant.

EPIFLUORESCENCE
Most common fluorescence microscopy arrangement wherein excitation light is applied through the objective that is also used for viewing the fluorescent specimen. The method excites and collects fluorescence throughout the cell and has poor depth discrimination.

CHROMAFFIN CELLS
Cells of the medulla of the adrenal gland. They store and secrete adrenaline, noradrenaline and protein hormones. They are termed 'chromaffin' because they can be stained by chromium salts.

INS-1 CELLS
Cell line derived from pancreatic β-cells that secrete insulin.

PC-12 CELLS
A cell line derived from a tumour of CHROMAFFIN CELLS. Used as a substitute for chromaffin cells in secretion studies. Compared with chromaffin cells, they have smaller and fewer secretory granules, but also contain vesicles similar to synaptic vesicles.

Occasionally granules left the plasma membrane after remaining there for tens of seconds. The replenishment of the cell surface with fresh granules took some 10–20 min, a surprisingly long time considering that a docked and release-ready granule can undergo exocytosis in tens of milliseconds[16] or less[17] after a rise in internal Ca^{2+} concentration.

Related observations were made by others[18–20]. In INS-1 CELLS, the interior of secretory granules was labelled with acridine orange and their membrane was labelled with GFP-conjugated phogrin, a membrane protein whose function is unclear[20]. Both orange and green fluorescence were observed simultaneously. Interestingly, the green image of the empty granule membrane remained visible for several seconds after the release of acridine orange. Evidently the granule membrane does not flatten into the plasma membrane immediately after exocytosis. Sometimes the empty granule detached from the membrane and moved away, in direct support of the idea that empty granules can be retrieved intact by the cell[21,22].

Single secretory granules in live endocrine cells have also been observed by confocal microscopy[12,23]. Secretory granules were observed after deconvolution of epifluorescence images in live PC-12 (REF. 24) and pituitary cells[25]. Upon exocytosis, pituitary granule matrices stained brightly with FM1-43 and were retrieved intact in large endocytic vesicles[25].

Constitutive exocytosis

This process had previously been studied almost entirely by biochemical methods and electron microscopy. Neither method easily provides information on how often and how fast exocytic events happen. Two groups expressed a fluorescently labelled membrane protein in exocytic organelles (TRANSPORT CONTAINERS) of epithelial cells and observed the cells by EF fluorescence[26,27] and by epifluorescence[27]. To shorten the penetration depth, both groups plated cells on special high-refractive index glass and used special optics to achieve a large angle of incidence. Video imaging of single transport containers provided a wealth of new results. Transport containers undergoing exocytosis were both spherical and tube-shaped. Exocytosis was apparent as fluorescent membrane protein escaped from transport containers and spread into the plasma membrane by lateral diffusion. Transport containers moved around in the cytosol, arrived in the evanescent field, stopped at or close to the plasma membrane and then presumably docked. There they remained for tens of seconds or minutes until they either returned into the cytosol or underwent exocytosis. The large number of apparently docked vesicles was surprising, as it is normally a hallmark of REGULATED EXOCYTOSIS. As a second surprise, tubular transport containers released only a small portion of their membrane proteins as they fused transiently with the plasma mem-

Table 1 | **Comparison of two microscopic techniques**

Confocal	Evanescent field
Floods entire cell with excitation light, but rejects most fluorescence in confocal pinhole.	Illuminates only the plane of interest. No out-of-focus fluorescence. All fluorescence usable for imaging.
Extensive bleaching and photodamage throughout the cell. Tens of useful pictures per cell.	Less bleaching and photodamage per collected photon. Hundreds of useful pictures per cell.
Limited vertical resolution blurs a point into a vertical ellipse about 500-nm long.	Illumination declines exponentially over distances to 40–50 nm when high refractive index glass is used.
Pixels imaged sequentially in laser scanning microscopes. Imaging relatively slow.	All pixels imaged simultaneously. Rate of imaging limited only by speed of camera and photon collection.
Can image entire cell.	Images only cell surface.

brane and then closed their FUSION PORE. The time sequence in FIG. 2 shows an example, imaged both by epifluorescence to emphasize structures >100 nm from the plasma membrane, and by EF fluorescence for structures <100 nm. Both methods imaged the same fluorophore but the epifluorescence signal was coded red and the EF signal green. An arrow marks a transport container at some distance (red). At 7 s, part of it had turned green and hence had entered the evanescent field. Its red extension indicates that it was a tube extending beyond the evanescent field. Exocytosis appears as the spread of green fluorescence into the plasma membrane (8–12 s). After the green cloud faded (12 s), a green and red spot remained at the fusion site (41 s), indicating that the transport container remained

FM1-43
A water-soluble lipid that becomes fluorescent when it reversibly enters a lipid bilayer or the protein cores of some dense core granules.

TRANSPORT CONTAINERS
Vesicles or tubules derived from the *trans*-Golgi network that can either undergo exocytosis or give rise to vesicles capable of exocytosis.

REGULATED EXOCYTOSIS
In regulated exocytosis, vesicles accumulate beneath the plasma membrane and wait for a signal, such as an increase in cytosolic $[Ca^{2+}]_i$. By contrast, constitutive exocytosis is thought to occur as soon as vesicles arrive at the plasma membrane.

FUSION PORE
Small opening that allows flux of cargo between two membrane-bounded compartments. Fusion pores form at an early stage of membrane fusion and widen when they lead to full fusion.

DENSE CORE GRANULES
Large (100–1,000 nm diameter) secretory vesicles that concentrate and then secrete proteins. Because of their high protein content they stain heavily and hence appear to have a 'dense core' under the electron microscope.

Box 3 | **Two types of evanescent field microscope**

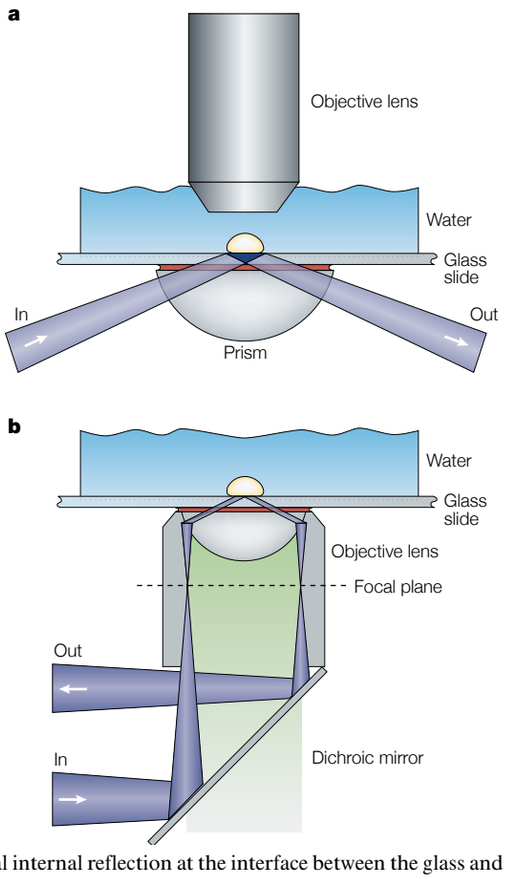

In prism-type microscopes (**a**), a prism directs light into a coverglass bearing cells. Fluorescence excited by the evanescent field (EF) is collected opposite the reflecting interface, either with an objective dipping into an open chamber as shown, or with an oil immersion objective if the chamber is covered by a coverslip. With a hemicylinder prism, light can easily be applied at various angles for varying the penetration depth of the EF[19,44]. Prism-type microscopes have completely separate paths for excitation and emission light and for this reason have the lowest background light. With a wide laser beam, it is easy to generate an EF over large areas, thereby illuminating a wide field of view. However, prism-type microscopes must look through a cell to see its bottom surface and this tends to degrade the image quality. They also tend to view cells through objectives of longer working distances and lower resolution.

Through-the-lens microscopes (**b**) generate the EF with the objective lens that is used for viewing the cell. How is this done? From basic optics, light diverging from a point source can be made parallel by placing the point source in the focal plane of a converging lens. The same is true for an objective lens and the focal plane at the back of the objective (dashed). The further off-axis the point source, the larger the angle at which the parallel beam leaves the objective. The largest angle α at which an objective can emit (and receive) light is expressed in terms of its numerical aperture (*NA*) as $NA = n \sin \alpha$, in which n is the refractive index for which the objective has been designed. Total internal reflection requires that the *NA* be higher than the refractive index of the specimen, $n_2 = 1.37$ for a typical cell. Until recently, the highest available *NA* was 1.4, barely enough to achieve total internal reflection at the interface between the glass and the cell[43]. However, a special objective with *NA* = 1.65 is now available (Olympus APO 100x O HR)[48].

Through-the-lens set-ups can be used like normal inverted epifluorescence microscopes and allow electrodes, pipettes or even an atomic force microscope on the stage without compromising optical quality. Because both the light collection efficiency and spatial resolution of an objective increase with its numerical aperture, through-the-lens set-ups automatically excel on both counts. Because they view cells through glass, through-the-lens set-ups have two advantages over prism set-ups. First, they collect more light from near-by objects (BOX 2). Second, light collected diminishes monotonically with distance, so brightness changes can be converted, at least approximately, into movements. This cannot be guaranteed for light emitted into water. However, the 1.65 *NA* objective requires special and costly coverslips of high-refractive index glass as well as special immersion oil that passes blue light poorly. But objectives using normal coverglass and immersion oil are becoming available from Olympus and Zeiss Co. Their numerical aperture is only 1.45, but this exceeds the refractive index of cells (1.37) sufficiently to be useful for this application. Through-the-lens set-ups have been discussed in recent articles[38,49].

Box 4 | Applications of the method

- First study reporting the imaging of cells by evanescent field microscopy[50].
- First through-the-lens evanescent field microscope[51].
- Imaging clusters of a fluorescently labelled plasma membrane protein[52].
- Adhesion of cells to substrates[52,53]; see REF. 5 for review.
- Imaging cells with through-the-lens evanescent field fluorescence[54].
- Theory of evanescent field microscopy[45,55,56].
- Measuring the distance between substrates, plasma membranes and organelles by variable-angle evanescent field illumination[19,44,47,57].
- Fluorimetric tracking of a cell's volume[58].
- Imaging Ca^{2+} concentration changes near the plasma membrane[59,60].

there and retained some or most of its cargo. The direct observation of an exocytic organelle fusing and then disconnecting adds to the extensive electrophysiological evidence on endocrine[21,22] and mast cells[28,29] in which DENSE CORE GRANULES undergo incomplete exocytosis as they open and then close transient fusion pores.

Synaptic vesicles

By virtue of their small size, SYNAPTIC VESICLES can release all their neurotransmitter in fractions of a millisecond. Indeed, synaptic vesicles are the smallest membranous organelles made in any cell (diameter 30–50 nm in brain). Whereas transport containers fuse continuously and at apparently random locations over the entire cell surface[26], synaptic vesicles dock preferentially at so-called ACTIVE ZONES, and fuse there within a millisecond after an electric stimulus. Synaptic vesicles have been intensely studied using biochemistry and electrophysiology but, as with secretory granules, no method existed to record signals from single synaptic vesicles before exocytosis. It therefore seemed desirable to image synaptic vesicles.

After exocytosis, the membrane of synaptic vesicles is retrieved by endocytosis[30,31], but may be loaded during its brief stay at the plasma membrane with a few hundred molecules of the fluorescent lipid FM1-43 (REF. 32). EF fluorescence was used to image FM1-43 stained giant synaptic terminals of RETINAL BIPOLAR NEURONS[33] where so-called SYNAPTIC RIBBONS tether vesicles near active zones[34]. Single vesicles were observed in terminals plated on high refractive index glass[33]. Many vesicles made brief visits to the plasma membrane, rapidly bouncing into and out of the evanescent field. Others were bright and immobile as if docked at the plasma membrane. A stimulus delivered with a VOLTAGE CLAMP caused the docked vesicles to undergo rapid exocytosis, visible as the release of FM1-43 from the vesicle and its spread into the plasma membrane by lateral diffusion (FIG. 3). The stimulus also caused new vesicles to dock and replace those lost through exocytosis. They were ready to fuse after being docked for 0.2–0.3 s. Although vesicles fused and docked mostly at discrete active zones of submicron diameter, they occasionally did so elsewhere on the plasma membrane. As in chromaffin and epithelial cells, capture of vesicles at or near the plasma membrane was reversible.

Interestingly, vesicles at active zones often appeared motionless but dim until a stimulus caused them to brighten as they moved to the plasma membrane and then fused. Evidently, active zones contain a cytosolic structure, probably the synaptic ribbon, that holds vesicles in reserve a short distance from the plasma membrane. Given the penetration depth of the evanescent field, it was calculated that vesicles were held about 20 nm away from the plasma membrane. This is close enough for v-SNARE proteins on the vesicle to reach out and touch t-SNARE proteins on the plasma membrane, and thereby initiate the formation of the SNARE complexes needed for fusion[35]. Whether or not the 20-nm movement actually reflects formation of the SNARE complex, the finding illustrates that EF fluorescence can image molecular-sized motions in living cells.

Organelle movement

Most organelles travel extensively within cells. Classical work with DIFFERENTIAL INTERFERENCE CONTRAST (DIC) MICROSCOPY has shown how microtubules transport organelles over long distances and how they segregate chromosomes. DIC is less well suited, however, to explore submicron movement of densely packed organelles in the very periphery of a cell. Such movement must occur if secretory granules are to occupy their docking site beneath the plasma membrane, and if endocytic vesicles at the plasma membrane are to reach their processing stations in the cytosol. In either direc-

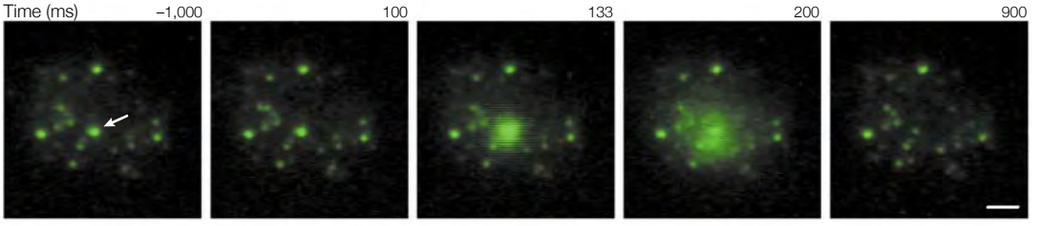

Figure 1 | **Chromaffin cell expressing GFP-conjugated pro-neuropeptide Y (p-NPY) in its granules.** p-NPY is normally contained in the secretory granules of chromaffin cells. Pictures taken at various times relative to a voltage jump from –70 mV to 0 mV that opened Ca^{2+} channels and stimulated exocytosis of a granule in the centre of the cell. Note the rapid spread of fluorescence, followed by disappearance of the granule. Scale bar, 2 μm. (Courtesy of I. Kleppe. Olympus APO 100x O HR 1.65 *NA* objective.)

SYNAPTIC VESICLES
Small-diameter (20–65 nm) secretory vesicles that store and secrete neurotransmitters. Capable of exocytosis within fractions of a millisecond after a stimulus. They do not enclose protein and hence lack a dense core.

ACTIVE ZONE
Structurally well-defined zone in presynaptic nerve terminals constituting a preferred site for the exocytosis of synaptic vesicles.

RETINAL BIPOLAR NEURONS
The predominant neurons in the inner nuclear layer of the retina. At the end of a short axon, they carry an unusually large synaptic terminal that can be directly studied by capacitance measurements.

SYNAPTIC RIBBON
Proteinaceous structure at the active zones of some sensory neurons. Thought to transport and/or capture synaptic vesicles in preparation for exocytosis.

VOLTAGE CLAMP
Electrophysiological amplifier that controls the plasma membrane voltage by electronic feedback, and reports the current that must pass across the plasma membrane to maintain the desired voltage. Used, for example, to open and close voltage-gated Ca^{2+} channels.

SNARES
Proteins required for membrane fusion in exocytosis and other membrane traffic events. Vesicle SNAREs on the vesicle membrane bind to target SNAREs on the target plasma membrane. When such *trans*-SNARE complexes are formed, they pull the two membranes close together and presumably cause them to fuse.

DIFFERENTIAL INTERFERENCE CONTRAST MICROSCOPY
Forms images of high contrast and resolution in unstained cells by using birefringent prisms and polarized light.

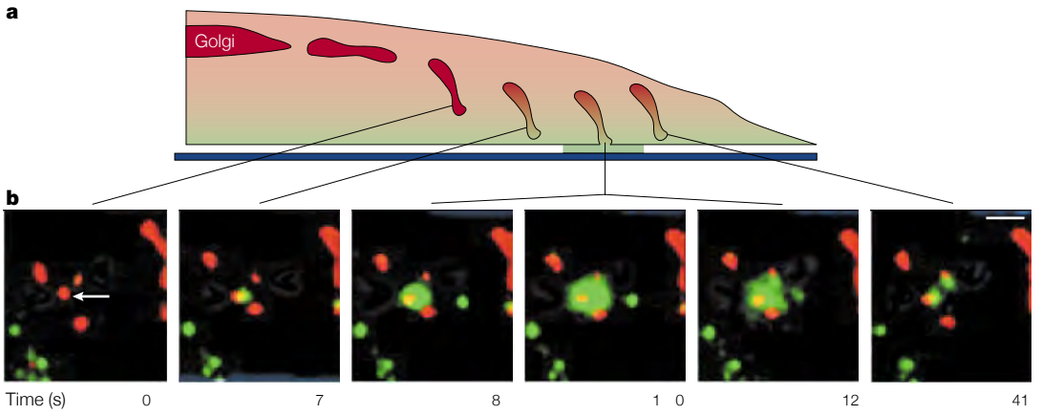

Figure 2 | **Constitutive exocytosis.** Epithelial cell expressing vesicular stomatitis virus glycoprotein tagged with yellow fluorescent protein and targeted to the plasma membrane. **a** | Schematic of the structures imaged in **b**. A tubular transport container approaches the plasma membrane, fuses and then disconnects. **b** | Pictures with evanescent field (EF) fluorescence showing structures <100 nm from the plasma membrane are overlaid on epifluorescence pictures that also show structures further away. Zone imaged with EF fluorescence in green, that with epifluorescence in red. Superimposed pairs of EF (green) and epifluorescence images (red) taken at indicated times. Structures illuminated both by the EF and by epifluorescence appear yellow. One transport container is marked with an arrow in the first image. Images of this transport container are hypothesized to be vertical projections of the structures drawn in **a**. Lines connect images with the structures they are hypothesized to represent. Images taken using the prism method[27]. Scale bar, 2 μm.

tion, organelles must penetrate the so-called actin cortex beneath the plasma membrane, a dense meshwork of actin filaments that is a few hundred nanometres thick. To the extent that actin filaments constantly assemble and disassemble, the meshwork is dynamic and permeable to organelles. Control mechanisms regulating the assembly and disassembly would also regulate the permeability of the actin cortex. To study them, a simple method to track organelle movement in the actin cortex would be useful.

EF fluorescence studies in PC-12 cells showed that granules beneath the plasma membrane come in three types[36,37]. A few move in a directed fashion over micron distances, others dither about without apparent direction and many do not measurably move at all. In resting chromaffin cells, all but a few per cent of the granules near the surface dither ~70 nm around a resting position as if tethered there or imprisoned in a cage[43], most likely the actin network. Movement over longer distances is extremely slow. By comparison, some giant synaptic terminals contain large reservoirs of mobile synaptic vesicles[33].

In permeabilized PC-12 cells[37], granule motion stopped when ATP was replaced by a non-hydrolysable analogue, or when the turnover of cortical actin was blocked by PHALLOIDIN. These results indicate that the movement of granules might require energy and might be hindered by actin filaments. Surprisingly, granule motion diminished also when most cortical actin was disassembled by LATRUNCULIN. Actin seems to both help and hinder granule motion, as previously shown in pancreatic ACINAR CELLS[39]. These studies are a modest beginning, but they promise that future work will provide important insights.

A surprising role for actin in endocytosis was found when MACROPINOCYTOSIS was observed in cultured mast cells expressing GFP-β-actin[40]. While separating from the plasma membrane, macropinocytic vesicles ignited a burst of actin polymerization that drove them into the cell interior much as actin 'comet tails' drive microorganisms such as *Listeria monocytogenes* through infected cells. Filamentous actin was long thought to function during endocytosis, but this was the first demonstration of actin-driven movement initiated by endocytosis.

PHALLOIDIN
Family of toxins present in the highly poisonous agaric fungus, *Amanita phalloides*. Phalloidin binds specifically to actin filaments and prevents their depolymerization.

LATRUNCULIN
Toxin present in the sponge *Latruncula magnifica*, which binds to monomeric actin and depolymerizes actin filaments.

ACINAR CELLS
Acinar cells in the mammalian pancreas are responsible for the secretion of digestive enzymes. Like mast cells, they have large secretory granules.

MACROPINOCYTOSIS
Actin-dependent process by which cells engulf large volumes of fluids.

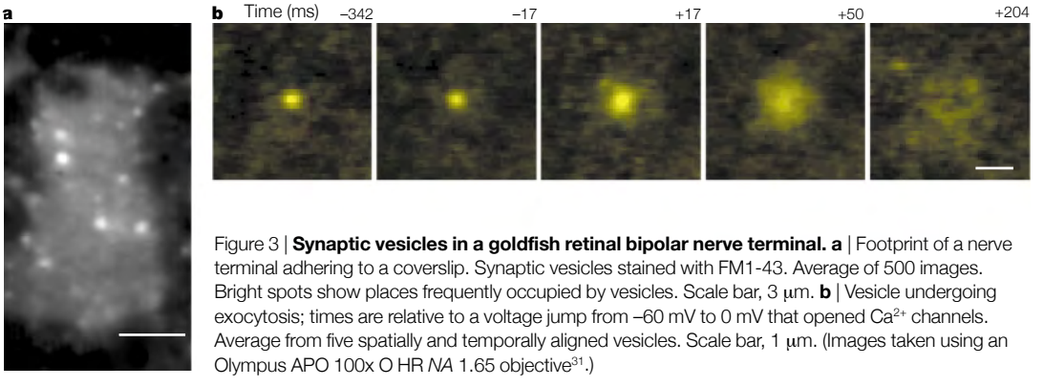

Figure 3 | **Synaptic vesicles in a goldfish retinal bipolar nerve terminal. a** | Footprint of a nerve terminal adhering to a coverslip. Synaptic vesicles stained with FM1-43. Average of 500 images. Bright spots show places frequently occupied by vesicles. Scale bar, 3 μm. **b** | Vesicle undergoing exocytosis; times are relative to a voltage jump from –60 mV to 0 mV that opened Ca^{2+} channels. Average from five spatially and temporally aligned vesicles. Scale bar, 1 μm. (Images taken using an Olympus APO 100x O HR *NA* 1.65 objective[31].)

DSRED
(dsRed). A red fluorescent protein (emission maximum at 583 nm) that, like GFP, can be genetically conjugated to proteins to make them fluorescent. First isolated from tropical corals of the *Discosoma* genus.

CFP
Variant of GFP engineered to fluoresce in cyan. Its emission maximum is at 474 nm.

YFP
Variant of GFP engineered to fluoresce in yellow. Its emission maximum is at 525 nm.

Signal transduction

An important use of EF fluorescence will be to image signal-transduction events. Although the potential of the method for this purpose remains to be fully exploited, it can be illustrated by two examples.

In one study[41], red fluorescent epidermal growth factor (Cy3–EGF) molecules were applied to cells. In an interesting but probably difficult variant of EF fluorescence, the authors sought to image the plasma membrane not where it adhered to the coverslip but instead at the opposite side where the cell faced the free solution. For generating the evanescent field, they took advantage of the minute refractive index differences between the cell and the surrounding medium. Dim spots of similar brightness appeared abruptly as epidermal growth factor (EGF) molecules were captured by the plasma membrane and then vanished some time later. Their persistence time varied inversely with the illumination intensity, as expected for the photobleaching of single molecules. Measurement of the fluorescence intensity of spots indicated two populations, one twice as bright as the other, as if the brighter spots originated from two EGF molecules bound to an EGF receptor dimer. These observations are a fine example of how single ligand molecules can be watched as they bind to the plasma membrane of an intact cell. Cells were next incubated with mixtures of red Cy3–EGF and deep-red Cy5–EGF, and then viewed with a camera system that separated the two fluorescence wavelengths. In spots emitting both wavelengths, fluorescence in the two channels fluctuated in opposite directions, indicating intermittent fluorescence energy transfer from a Cy3–EGF to a Cy5–EGF. Evidently pairs of chromophores can be imaged on the surface of living cells as they engage in fluorescence energy transfer with each other. The study shows that biochemistry can be done in living cells at the level of single molecules. Similar studies might directly reveal molecular insights that are not always possible with conventional biochemical methods.

In the second study[42], fibroblasts expressed a GFP-conjugated pleckstrin homology domain of the Akt protein kinase (GFP–Akt-PH). Akt binds to 3-phosphorylated phosphoinositides (3-PPI), relatively rare lipids used by membranes for signalling and protein recruitment. Platelet-derived growth factor (PDGF) is known to increase turnover of 3-PPIs in fibroblasts and to initiate a directed migration to the source of the hormone. PDGF turned the surface of fibroblasts expressing GFP–Akt-PH bright green in minutes, indicating the capture of GFP–Akt-PH by freshly generated 3-PPI at the plasma membrane. The construct was used to image the local plasma membrane concentration of 3-PPI. In a concentration gradient of PDGF, fluorescence (and hence 3-PPI local concentration) in any given cell was found highest on the side that faced the higher PDGF concentration.

Future perspectives

The most recent wave of experiments with EF fluorescence has emphasized secretory vesicles but this reflects more the interests of the investigators than the potential of the method. The number of articles using the technique on living cells has all but doubled during each of the past three years. As the method becomes more available, it will be applied to other problems in cell biology.

Perhaps the most promising development is the simultaneous EF imaging of two chromophores, each on a different molecule[20,41]. Pairs of genetically targetable chromophores, such as GFP and DSRED or CFP and YFP, will be particularly useful as they offer the opportunity to investigate protein–protein interactions on a nanometre scale. This will be particularly useful for studying reaction cascades at the plasma membrane with a spatially defined start or end point, such as exo- or endocytosis, the budding of a caveola or the assembly/disassembly of a lipid raft. Labelling the contents of an exocytic vesicle with a red chromophore, for instance, defines both the time and the place of the exocytic event. Any protein of interest may be labelled green so that it can be determined precisely how long before exocytosis it is recruited, and how soon afterwards it is dismissed. Because many events may be observed and averaged after temporal and spatial alignment, the recruitment and dismissal of arbitrarily few molecules can be detected. Next, another protein can be labelled and followed in the same way. In time, we may learn for each known member of a reaction cascade when and how long they are present at the reaction site. Such information can be obtained at the level of single events and at sub-second time resolution, and will help significantly in determining the function of each participating protein.

Links

FURTHER INFORMATION Almers home page
ENCYCLOPEDIA OF LIFE SCIENCES Light microscopy | Fluorescence microscopy | Synaptic vesicle traffic

1. Kurzchalia, T. V. & Parton, R. G. Membrane microdomains and caveolae. *Curr. Opin. Cell Biol.* **11**, 424–431 (1999).
2. Simons, K. & Toomre, D. Lipid rafts and signal transduction. *Nature Rev. Mol. Cell Biol.* **1**, 31–39 (2000).
3. Tsien, R. Y. The green fluorescent protein. *Annu. Rev. Biochem.* **67**, 509–544 (1998).
4. Thompson, N. L. & Lagerholm, C. B. Total internal reflection fluorescence: applications in cellular biophysics. *Curr. Opin. Biotechnol.* **8**, 58–64 (1997).
5. Burmeister, J. S., Olivier, L. A., Reichert, W. M. & Truskey, G. A. Application of total internal reflection fluorescence microscopy to study cell adhesion to biomaterials. *Biomaterials* **19**, 307–325 (1998).
6. Forkey, J. N., Quinlan, M. E. & Goldman, Y. E. Protein structural dynamics by single-molecule fluorescence polarization. *Prog. Biophys. Mol. Biol.* **74**, 1–35 (2000).
7. Ambrose, W. P., Goodwin, P. M. & Nolan, J. P. Single-molecule detection with total internal reflection excitation: comparing signal-to-background and total signals in different geometries. *Cytometry* **36**, 224–231 (1999).
8. Jahn, R. & Südhof, T. C. Membrane fusion and exocytosis. *Annu. Rev. Biochem.* **68**, 863–911 (1999).
9. Henkel, A. W. & Almers, W. Fast steps in exocytosis and endocytosis studied by capacitance measurements in endocrine cells. *Curr. Opin. Neurobiol.* **6**, 350–357 (1996).
10. Neher, E. Vesicle pools and Ca^{2+} microdomains: new tools for understanding their roles in neurotransmitter release. *Neuron* **20**, 389–399 (1998).
11. Lang, T. *et al.* Ca^{2+}-triggered peptide secretion in single cells imaged with green fluorescent protein and evanescent-wave microscopy. *Neuron* **18**, 857–863 (1997); erratum in **19**, 463 (1997).
12. Burke, N. V. *et al.* Neuronal peptide release is limited by secretory granule mobility. *Neuron* **19**, 1095–1102 (1997).
13. Breckenridge, L. J. & Almers, W. Final steps in exocytosis observed in a cell with giant secretory granules. *Proc. Natl Acad. Sci. USA* **84**, 1945–1949 (1987).
14. Whalley, T., Terasaki, M., Cho, M. S. & Vogel, S. S. Direct membrane retrieval into large vesicles after exocytosis in

sea urchin eggs. *J. Cell Biol.* **131**, 1183–1192 (1995).
15. Steyer, J. A., Horstmann, H. & Almers, W. Transport, docking and exocytosis of single secretory granules in live chromaffin cells. *Nature* **388**, 474–478 (1997).
16. Thomas, P., Wong, J. G., Lee, A. K. & Almers, W. A low affinity Ca^{2+} receptor controls the final steps in peptide secretion from pituitary melanotrophs. *Neuron* **11**, 93–104 (1993).
17. Heinemann, C., Chow, R. H., Neher, E. & Zucker, R. S. Kinetics of the secretory response in bovine chromaffin cells following flash photolysis of caged Ca^{2+}. *Biophys J.* **67**, 2546–2557 (1994).
18. Oheim, M., Loerke, D., Stuhmer, W. & Chow, R. H. The last few milliseconds in the life of a secretory granule. Docking, dynamics and fusion visualized by total internal reflection fluorescence microscopy (TIRFM). *Eur. Biophys. J.* **27**, 83–98 (1998).
19. Oheim, M. & Stuhmer, W. Tracking chromaffin granules on their way through the actin cortex. *Eur. Biophys. J.* **29**, 67–89 (2000).
20. Tsuboi, T., Zhao, C., Terakawa, S. & Rutter, G. A. Simultaneous evanescent wave imaging of insulin vesicle membrane and cargo during a single exocytotic event. *Curr. Biol.* **10**, 1307–1310 (2000).
Describes simultaneous evanescent field fluorescence imaging with two colours.
21. Albillos, A. *et al.* The exocytotic event in chromaffin cells revealed by patch amperometry. *Nature* **389**, 509–512 (1997).
22. Ales, E. *et al.* High calcium concentrations shift the mode of exocytosis to the kiss-and-run mechanism. *Nature Cell Biol.* **1**, 40–44 (1999).
23. Wacker, I. *et al.* Microtubule-dependent transport of secretory vesicles visualized in real time with a GFP-tagged secretory protein. *J. Cell Sci.* **110**, 1453–1463 (1997).
24. Lochner, J. E. *et al.* Real-time imaging of the axonal transport of granules containing a tissue plasminogen activator/green fluorescent protein hybrid. *Mol. Biol. Cell* **9**, 2463–2476 (1998).
25. Angleson, J. K., Cochilla, A. J., Kilic, G., Nussinovitch, I. & Betz, W. J. Regulation of dense core release from neuroendocrine cells revealed by imaging single exocytic events. *Nature Neurosci.* **2**, 440–446. (1999).
26. Schmoranzer, J., Goulian, M., Axelrod, D. & Simon, S. M. Imaging constitutive exocytosis with total internal reflection fluorescence microscopy. *J. Cell Biol.* **149**, 23–32 (2000).
27. Toomre, D., Steyer, J. A., Keller, P., Almers, W. & Simons, K. Fusion of constitutive membrane traffic with the cell surface observed by evanescent wave microscopy. *J. Cell Biol.* **149**, 33–40 (2000).
References 26 and 27 image for the first time the exocytosis of constitutive secretory vesicles.
28. Fernandez, J. M., Neher, E. & Gomperts, B. D. Capacitance measurements reveal stepwise fusion events in degranulating mast cells. *Nature* **312**, 453–455 (1984).
29. Spruce, A. E., Breckenridge, L. J., Lee, A. K. & Almers, W. Properties of the fusion pore that forms during exocytosis of a mast cell secretory vesicle. *Neuron* **4**, 643–654 (1990).
30. von Gersdorff, H. & Matthews, G. Dynamics of synaptic vesicle fusion and membrane retrieval in synaptic terminals. *Nature* **367**, 735–739 (1994).
31. Ryan, T. A., Reuter, H. & Smith, S. J. Optical detection of a quantal presynaptic membrane turnover. *Nature* **388**, 478–482 (1997).
32. Betz, W. J. & Bewick, G. S. Optical analysis of synaptic vesicle recycling at the frog neuromuscular junction. *Science* **255**, 200–203 (1992).
33. Zenisek, D., Steyer, J. A. & Almers, W. Transport, capture and exocytosis of single synaptic vesicles at active zones. *Nature* **406**, 849–854 (2000).
Describes results from imaging synaptic vesicles in a mature presynaptic terminal.
34. Raviola, E. & Gilula, N. B. Intramembrane organization of specialized contacts in the outer plexiform layer of the retina. A freeze-fracture study in monkeys and rabbits. *J. Cell Biol.* **65**, 192–222 (1975).
35. Sutton, R. B., Fasshauer, D., Jahn, R. & Brunger, A. T. Crystal structure of a SNARE complex involved in synaptic exocytosis at 2.4 Å resolution. *Nature* **395**, 347–353 (1998).
36. Han, W., Ng, Y. K., Axelrod, D. & Levitan, E. S. Neuropeptide release by efficient recruitment of diffusing cytoplasmic secretory vesicles. *Proc. Natl Acad. Sci. USA* **96**, 14577–14582 (1999).
37. Lang, T. *et al.* Role of actin cortex in the subplasmalemmal transport of secretory granules in PC-12 cells. *Biophys. J.* **78**, 2863–2877 (2000).
38. Steyer, J. A. & Almers, W. in *Imaging Neurons: A Laboratory Manual* (eds Yuste, R., Lanni, F. & Konnerth, A.) 54.1–54.8 (Cold Spring Harbor Laboratory Press, Cold Spring Harbor, 2000).
39. Muallem, S., Kwiatkowska, K., Xu, X. & Yin, H. L. Actin filament disassembly is a sufficient final trigger for exocytosis in nonexcitable cells. *J. Cell Biol.* **128**, 589–598 (1995).
40. Merrifield, C. J. *et al.* Endocytic vesicles move at the tips of actin tails in cultured mast cells. *Nature Cell Biol.* **1**, 72–74 (1999).
41. Sako, Y., Minoghchi, S. & Yanagida, T. Single-molecule imaging of EGFR signalling on the surface of living cells. *Nature Cell Biol.* **2**, 168–172 (2000).
Reports that two single molecules, each in a different colour, can be watched on a live cell as they engage in fluorescence resonance energy transfer.
42. Haugh, J. M., Codazzi, F., Teruel, M. & Meyer, T. Spatial sensing in fibroblasts mediated by 3' phosphoinositides. *J. Cell Biol.* **151**, 1269–1280 (2000).
43. Steyer, J. A. & Almers, W. Tracking single secretory granules in live chromaffin cells by evanescent-field fluorescence microscopy. *Biophys. J.* **76**, 2262–2271 (1999).
44. Rohrbach, A. Observing secretory granules with a multiangle evanescent wave microscope. *Biophys. J.* **78**, 2641–2654 (2000).
45. Axelrod, D., Hellen, E. H. & Fulbright, R. in *Topics in Fluorescence Spectroscopy* Vol. 3 (ed. Lakowicz, J. R.) 289–343 (Plenum, New York, 1992).
An excellent and readable review covering most aspects of evanescent field fluorescence microscopy.
46. Hellen, E. H. & Axelrod, D. Fluroescence emission at dieletric and metal-film interfaces. *J. Opt. Soc. Am.* **4**, 337–350 (1987).
47. Olveczky, B. P., Periasamy, N. & Verkman, A. S. Mapping fluorophore distributions in three dimensions by quantitative multiple angle-total internal reflection fluorescence microscopy. *Biophys. J.* **73**, 2836–2847 (1997).
48. Terakawa, S., Sakurai, T. & Abe, K. Development of an objective lens with a high numerical aperture for light microscopy. *Bioimages* **5**, 24 (1997).
49. Axelrod, D. Selective imaging of surface fluorescence with very high aperture microscope objectives. *J. Biomed. Opt.* **6**, 6–13 (2001).
50. Ambrose, E. J. The movements of fibrocytes. *Exp. Cell Res.* **8**, 54–73 (1961).
51. McCutchen, C. W. Optical systems for observing surface topography by frustrated total internal reflection and by interference. *The Review of Scientific Instruments* **35**, 1340–1345 (1964).
52. Axelrod, D. Cell–substrate contacts illuminated by total internal reflection fluorescence. *J. Cell Biol.* **89**, 141–145 (1981).
53. Lanni, F., Waggoner, A. S. & Taylor, D. L. Structural organization of interphase 3T3 fibroblasts studied by total internal reflection fluorescence microscopy. *J. Cell Biol.* **100**, 1091–1102 (1985).
54. Stout, A. L. & Axelrod, D. Evanescent field exitation of fluorescence by epi-illumination microscopy. *Appl. Opt.* **28**, 5237–5242 (1989).
55. Bryngdahl, O. in *Progress in Optics* (ed. Wolf, E.) 169–221 (North–Holland, Amsterdam, 1973).
56. Gingell, D., Heavens, O. S. & Mellor, J. S. General electromagnetic theory of total internal reflection fluorescence: the quantitative basis for mapping cell–substratum topography. *J. Cell Sci.* **87**, 677–693 (1987).
57. Burmeister, J. S., Truskey, G. A. & Reichert, W. M. Quantitative analysis of variable-angle total internal reflection fluorescence microscopy (VA-TIRFM) of cell/substrate contacts. *J. Microsc.* **173**, 39–51. (1994).
58. Farinas, J., Simanek, V. & Verkman, A. S. Cell volume measured by total internal reflection microfluorimetry: application to water and solute transport in cells transfected with water channel homologs. *Biophys. J.* **68**, 1613–1620 (1995).
59. Omann, G. M. & Axelrod, D. Membrane-proximal calcium transients in stimulated neutrophils detected by total internal reflection fluorescence. *Biophys. J.* **71**, 2885–2891 (1996).
60. Cleemann, L., DiMassa, G. & Morad, M. Ca^{2+} sparks within 200 nm of the sarcolemma of rat ventricular cells: evidence from total internal reflection fluorescence microscopy. *Adv. Exp. Med. Biol.* **430**, 57–65 (1997).

Acknowledgements
We acknowledge support from the Max Planck Society (J.A.S.) and a grant from the NIH (W.A.).

- Evanescent field (EF) fluorescence microscopy (also called total internal reflection fluorescence microscopy) is uniquely suited to image the plasma membrane with its associated organelles and macromolecules in living cells
- Total internal reflection of a light beam generates an evanescent field — a thin layer of light that typically penetrates about 40–200 nm from a coverslip into an adhering cell.
- EF fluorescence microscopy combines the specificity of confocal microscopy to detect fluorescent molecules with a depth discrimination of near-molecular dimensions. However, imaging is confined to the cell surface.
- A recent wave of applications was aimed at membrane transport events in living cells. EF fluorescence microscopy offers new insights for its abilities to resolve even the smallest vesicles made by cells and to detect molecular-sized motions of fluorescent objects vertical to the glass.
- In endocrine cells and synaptic nerve terminals, transport, exocytosis and replenishment of single secretory vesicles could be investigated. No method existed to record signals from single synaptic vesicles before the exocytic event.
- EF fluorescence imaging of transport containers undergoing constitutive exocytosis provided a wealth of new results, including evidence for incomplete exocytosis. Other studies enhanced our understanding about the role of actin filaments for the movement of small organelles near the plasma membrane.
- An important use of EF fluorescence microscopy will be to image signal-transduction events. Recent studies using EF fluorescence microscopy have shown that biochemistry can be done in living cells at the level of single molecules.

After studying physics in Mainz, Germany, Juergen A. Steyer moved into the field of cellular biophysics using two-photon microscopy during his yearlong stay at the AT&T Bell Laboratories in 1993/94. As a graduate student at the Max-Planck-Institute for Medical Research in Heidelberg, Germany, he explored, in the lab of Wolfhard Almers, the prospects of using evanescent field fluorescence microscopy to optically study transport and exocytosis of single vesicles in neuroendocrine cells.

After receiving his Ph.D. in physics from the University of Heidelberg in 1997, he refined the method to image, in collaboration with David Zenisek, single synaptic vesicles and their fusion with the plasma membrane. Thereafter he continued to work on neurobiological applications of evanescent field fluorescence microscopy as a postdoctoral fellow at the Vollum Institute in Portland, Oregon and most recently, at the University of California at Berkeley.

Wolfhard Almers received his Ph.D. from the University of Rochester, New York. He investigated excitation–contraction coupling in skeletal muscle, gating and permeability of ion channels and the mechanism of Ca^{2+} selectivity in Ca^{2+} channels, first at Cambridge, England and then at the University of Washington, Seattle, Washington. Since 1985, he focused on the mechanism of exocytosis in single cells and at the level of single secretory vesicles. In 1992, he became a Director at the Max Planck Institute for Medical Research in Heidelberg, Germany. He continued his interest in exo- and endocytosis of single vesicles. Since 1999, he has been a Senior Scientist at the Vollum Institute, Oregon Health Sciences University, Portland, Oregon.

ELS links

Light microscopy
http://www.els.net/elsonline/fr_article.jsp?id=A0002634

Fluorescence microscopy
http://www.els.net/elsonline/fr_article.jsp?id=A0002637

Synaptic vesicle traffic
http://www.els.net/elsonline/fr_loadarticle.jsp?available=1&ref=A0000215&orig=searching&page_number=1&page=search&Sitemap=exocytosis&searchtype=freetext&searchlevel=4

Wolhard Almers home page
http://www.ohsu.edu/vollum/faculty/almers.htm

Imaging with total internal reflection fluorescence microscopy for the cell biologist

Alexa L. Mattheyses[1,*], Sanford M. Simon[1] and Joshua Z. Rappoport[2,‡]

[1]Laboratory of Cellular Biophysics, The Rockefeller University, 1230 York Avenue, New York, NY 10065, USA
[2]The University of Birmingham, School of Biosciences, Edgbaston, Birmingham B15 2TT, UK
*Current address: Department of Cell Biology, Emory University School of Medicine, Atlanta, GA 30322, USA
‡Author for correspondence (j.rappoport@bham.ac.uk)

Journal of Cell Science 123, 3621-3628

doi:10.1242/jcs.056218

Summary

Total internal reflection fluorescence (TIRF) microscopy can be used in a wide range of cell biological applications, and is particularly well suited to analysis of the localization and dynamics of molecules and events near the plasma membrane. The TIRF excitation field decreases exponentially with distance from the cover slip on which cells are grown. This means that fluorophores close to the cover slip (e.g. within ~100 nm) are selectively illuminated, highlighting events that occur within this region. The advantages of using TIRF include the ability to obtain high-contrast images of fluorophores near the plasma membrane, very low background from the bulk of the cell, reduced cellular photodamage and rapid exposure times. In this Commentary, we discuss the applications of TIRF to the study of cell biology, the physical basis of TIRF, experimental setup and troubleshooting.

Key words: Total internal reflection fluorescence microscopy, Evanescent wave microscopy, Evanescent field microscopy, Fluorescence

Introduction

The plasma membrane is the barrier that all molecules must cross to enter or exit the cell, and a large number of biological processes occur at or near the plasma membrane. These processes are difficult to image with traditional epifluorescence or confocal microscopy techniques, because details near the cell surface are easily obscured by fluorescence that originates from the bulk of the cell. Total internal reflection fluorescence (TIRF) microscopy – also known as evanescent wave or evanescent field microscopy – provides a means to selectively excite fluorophores near the adherent cell surface while minimizing fluorescence from intracellular regions. This serves to reduce cellular photodamage and increase the signal-to-noise ratio. TIRF primarily illuminates only fluorophores very close (e.g. within 100 nm) to the cover-slip–sample interface. The background fluorescence is minimized because the excitation of fluorophores further away from the cover slip is reduced. The plasma membrane of an adherent cell lies well within the region of excitation, allowing imaging of processes occurring at or near the membrane. On the basis of these unique features, TIRF has been employed to address numerous questions in cell biology.

This Commentary details key issues for researchers who are using, or are considering using, TIRF for live cell imaging. We begin with a brief selection of specific areas of cell biological research in which the use of TIRF imaging has made a major impact. Subsequently, we describe the physical basis of TIRF, and discuss key issues to consider when setting up and employing TIRF. Finally, we identify several potential pitfalls and provide helpful suggestions. A basic knowledge of fluorescence microscopy is assumed. For general background on fluorescence microscopy, we refer readers to North (North, 2006) and Waters (Waters, 2009) For reviews containing an extensive treatment of TIRF theory and advanced applications, we refer readers to Axelrod (Axelrod, 2003; Axelrod, 2008).

Cellular processes visualized with TIRF

TIRF microscopy has been used in many different types of studies for the visualization of the spatial-temporal dynamics of molecules at or near the cell surface, particularly in cases in which the signal would otherwise be obscured by cytosolic fluorescence. Some of the advantages of TIRF for imaging near the cell surface are illustrated in Fig. 1. Actin (LifeAct–GFP in Fig. 1A,B), clathrin (GFP–clathrin light chain in Fig. 1C,D) and caveolin (caveolin-1–EGFP in Fig. 1E–G) have been imaged by both conventional epifluorescence (Fig. 1A,C,E) and TIRF (Fig. 1B,D,G). In each case, it is apparent that TIRF minimizes the out-of-focus intracellular fluorescence, resulting in images with a much higher signal-to-noise ratio. Similarly, although confocal microscopy (Fig. 1F) shows a reduced cytosolic signal relative to epifluorescence (Fig. 1E), the corresponding TIRF image (Fig. 1G) provides the greatest amount of information for fluorophores associated with the plasma membrane. The suppression of background fluorescence is crucial for studying each of the areas of cell biology on which TIRF has had a major impact.

TIRF has had an impact on many varied areas of cell biology, including HIV-1 virion assembly (Jouvenet et al., 2006) and intraflagellar transport in the *Chlamydomonas* flagella (Engel et al., 2009), and in single-molecule experiments. Below, we highlight several areas of cell biology – the cytoskeleton, endocytosis, exocytosis, cell–substrate contact regions and intracellular signaling – that have particularly benefited from investigation by TIRF.

Cytoskeleton

The dynamics of the cytoskeleton near the plasma membrane have been studied with TIRF (Fig. 1A,B), leading to new insights. Before TIRF was used to study vesicle trafficking, it was not known that a cortical microtubule network extended immediately adjacent to the plasma membrane, and that secretory vesicles remained attached to these microtubules until the moment of vesicle fusion (Schmoranzer

Journal of Cell Science

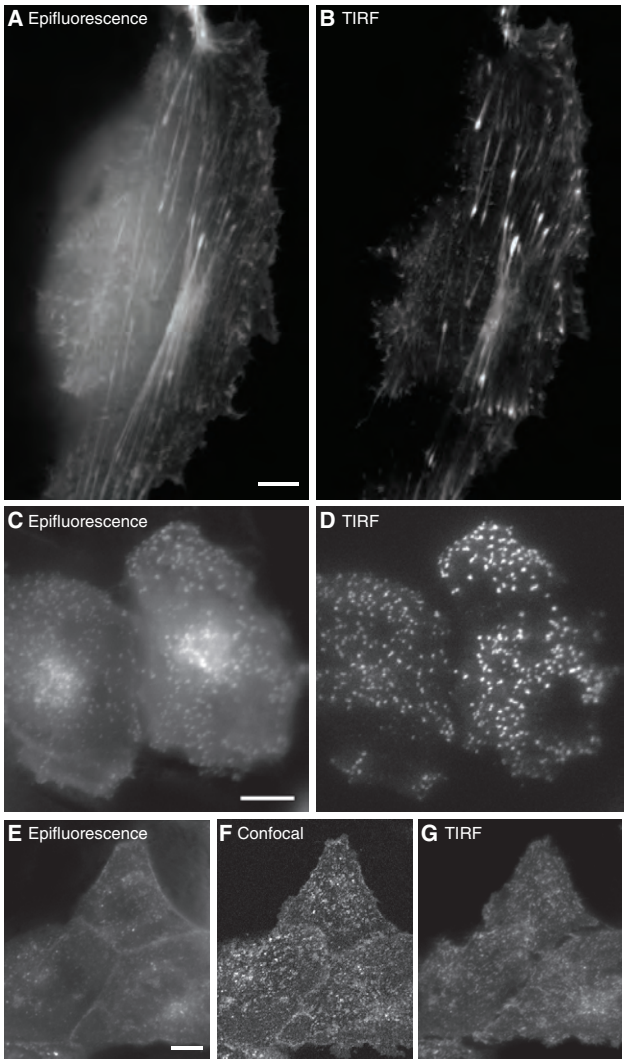

Fig. 1. Comparison of images obtained using epifluorescence and TIRF. In both cases, the microscope was focused at the adherent plasma membrane and images were acquired with one of three modes of excitation: epifluorescence, TIRF or confocal. (**A**,**B**) Actin (LifeAct–GFP) in a migrating MDCK cell. (**C**,**D**) Clathrin (clathrin light chain–GFP) in a HeLa cell. (**E–G**) Caveolin-1 (caveolin-1–EGFP) in MDCK cells. In each case, TIRF clearly eliminates of out-of-focus fluorescence and reveals details at or near the cell surface. Scale bars: 10 μm.

and Simon, 2003). This finding was made possible, in part, by the spatial restriction and high signal-to-noise ratio of the excitation field, as well as by the rapid acquisition rates that are possible when using wide-field acquisition. Furthermore, the increased excitation of fluorophores near the cover slip permitted the quantification of microtubule motility in the axial direction, revealing how microtubules are targeted to focal adhesions (Krylyshkina et al., 2003). TIRF also provided the spatial and temporal resolution to study the dynamics of actin and actin-associated proteins near the plasma membrane in several endocytosis studies (Kaksonen et al., 2005; Merrifield et al., 2002). Finally, fluorescence speckle microscopy, in which a limiting amount of cytoskeleton monomers are fluorescently labeled, combined with TIRF was able to deliver important information about the dynamics and flow of cytoskeleton filaments (Danuser and Waterman-Storer, 2006).

Endocytosis

The formation of endocytic vesicles involves the recruitment of cytosolic proteins to the adherent plasma membrane. When viewed with standard epifluorescence, the surface patches of the vesicle coat protein clathrin are difficult to discern from background fluorescence and intracellular clathrin structures (Fig. 1C). The initial report to image clathrin during endocytosis in live cells employed epifluorescence and was thus restricted to analyzing only those events that occurred in the cell periphery, because of out-of-focus signals (Gaidarov et al., 1999). By contrast, when TIRF is used, the clathrin patches on or near the membrane appear as distinct features (Fig. 1D). Imaging the dynamics of endocytosis is aided by rapid image acquisition, background elimination and the exponential decrease in excitation intensity with distance from the cover slip. TIRF has made it possible to gain insight into the components that are necessary for vesicle formation and the dynamics of this process (Rappoport, 2008). A main focus of studies that have applied TIRF to analyze endocytosis has been to determine the ‘life history’ of the formation of individual clathrin-coated vesicles. These studies have demonstrated that some proteins are present throughout the endocytosis process (e.g. clathrin and epsin) (Rappoport et al., 2006; Rappoport and Simon, 2003), whereas the localization of other proteins to the coated vesicle either increased over time (e.g. dynamin) (Merrifield et al., 2002; Rappoport et al., 2008; Rappoport and Simon, 2003) or decreased (e.g. AP-2) (Rappoport et al., 2003; Rappoport et al., 2005).

Exocytosis

The thin TIRF excitation field allows identification of secretory carriers near the membrane (Lang et al., 1997). Specific criteria, which involve quantifying the total fluorescence, as well as its peak and spread, have been established to quantify and characterize the fusion of vesicles with the plasma membrane (Schmoranzer et al., 2000). The exponential decay of the TIRF excitation field allows the small motions of individual fluorescence-marked secretory carriers in the direction normal to the substrate and plasma membrane (the axial or *z*-direction) to be manifested as intensity changes. The precision of tracking such axial movements can be as small as 2 nm, which is considerably smaller than the resolution limit of light microscopy (Allersma et al., 2006). Because of the high contrast and low background, the position of the centers of vesicles can be measured with an accuracy of about 10 nm and motions before fusion that are smaller than the granule diameter can be followed. By observing single vesicles as they approached and fused with a membrane, it was found that many of the vesicles did not deliver all of their cargo in a single fusion step, but required two or more fusions to fully discharge their cargo (Jaiswal et al., 2009; Schmoranzer et al., 2000).

Cell–substrate contact regions

TIRF has also been used to investigate cell–substrate contact regions using several different approaches. Similar to the examples above, the restricted excitation field was shown to be crucial for studying focal adhesions with regard to their location, composition, motion and specific biochemistry (Axelrod, 1981; Choi et al., 2008). One technique for identifying cell–substrate contacts involves adding a fluorophore to the surrounding solution (Todd et al., 1988). The intensity of fluorescence can be used to calculate the distance of the membrane from the surface and to ‘map’ the bottom surface of the cell (Gingell et al., 1987). This technique requires the thin excitation field of TIRF, as other imaging methods would result in

overwhelming background fluorescence. Recent work has analyzed focal adhesion disassembly in real time with TIRF and has demonstrated an unexpected role for clathrin in this process (Ezratty et al., 2009). This was made possible by the ability to rapidly acquire images of two spectrally distinct fluorophores, with axial information, at the adherent plasma membrane.

Intracellular signaling

TIRF has also been used to visualize different modes of intracellular signaling. For instance, TIRF has been instrumental in studies addressing plasma membrane recruitment and spatial distributions of signaling molecules such as phosphoinositide lipids (Haugh et al., 2000). Furthermore, a plasma-membrane-targeted biosensor revealed temporal oscillations of cAMP signaling, indicating a previously unidentified basis for regulation of upstream targets (Dyachok et al., 2006). Single plasma membrane Ca^{2+} channels have been imaged with good spatial and temporal resolution, providing information inaccessible to electrophysiological means, and revealing an uneven spatial distribution and diversity in kinetics (Demuro and Parker, 2004). TIRF and patch-clamp methods have been successfully combined to demonstrate the localization and coordination of open calcium channels and ER calcium-sensing molecules, revealing the spatial dynamics of intracellular Ca^{2+} signaling (Luik et al., 2006).

Physical basis of TIRF

To understand the setup, optimization and common pitfalls of TIRF, it is important to understand the physical basis of the technique. In the following section, we provide a brief description of some key parameters in the context of cellular imaging. We begin by considering the excitation light encountering the cover-slip–sample interface (Fig. 2). It is this interaction that produces the thin excitation field used in TIRF microscopy.

In the configuration most commonly used for cellular imaging, through-the-objective TIRF, the laser beam is focused off-axis at the back focal plane (BFP) of the objective lens. When the light exits the objective lens, it passes through the immersion oil and into the cover slip, which are matched in refractive index. When the excitation light beam propagating through the glass cover slip encounters the interface with the aqueous sample, the direction of travel of the light beam is altered (Fig. 2B). If the angle of incidence of the excitation light on the interface, θ, is greater than the 'critical angle', the light beam undergoes total internal reflection (TIR) and does not propagate into the sample. The critical angle, θ_c, is given by Snell's law:

$$\theta_c = \sin^{-1}(n_1 / n_2) ,$$

where n_1 and n_2 are the refractive indices of the sample and the cover slip, respectively. To achieve TIR, the refractive index of the sample must be less than that of the cover slip.

If the angle of incidence is less than θ_c, most of the excitation light propagates through the sample; this is what occurs in epifluorescence (Fig. 2). However, if the angle of incidence is greater than θ_c, the excitation light is reflected off the cover-slip–sample interface back into the cover slip. In this case, some of the incident energy penetrates through the interface, creating a standing wave called the evanescent field. This is the excitation field employed in TIRF microscopy.

The intensity (I) of the evanescent field decays exponentially with distance from the interface (z). Therefore, a fluorophore that is closer to the interface will be excited more strongly than a fluorophore that is further from the interface. The intensity of the evanescent field at any position z is described by:

$$I_z = I_0^{-z/d} ,$$

where I_0 is the intensity of the evanescent field at z=0. I_0 is related to the intensity of the incident beam by a complex function of θ and polarization (Axelrod, 1989). The depth of the evanescent field, d, refers to the distance from the cover slip at which the excitation intensity decays to 1/e, or 37%, of I_0. Depth d is defined by:

$$d = (\lambda_0 / 4\pi) * (n_2^2 \sin^2\theta - n_1^2)^{-1/2} ,$$

where λ_0 is the wavelength of the excitation light in a vacuum. Typical values for d are in the range 60–100 nm. The depth of the evanescent field is affected by several parameters, including incidence angle, wavelength, and the refractive indices of the sample and the cover slip. The depth decreases (i.e. the excitation field becomes more narrow) as the incidence angle increases. The longer the wavelength, the greater the depth (i.e. the thicker the excitation volume). In addition, for a given incidence angle, the depth depends on the refractive index of the sample. As the refractive index of the sample increases, the depth increases (Fig. 3).

Practically speaking, the excitation wavelength and refractive index of the cover slip are set, and the user controls the angle of incidence. Generally, this angle should be increased until it surpasses the critical angle. It is not advisable to 'set' a predefined angle of incidence without evaluating the evanescent field, because the critical

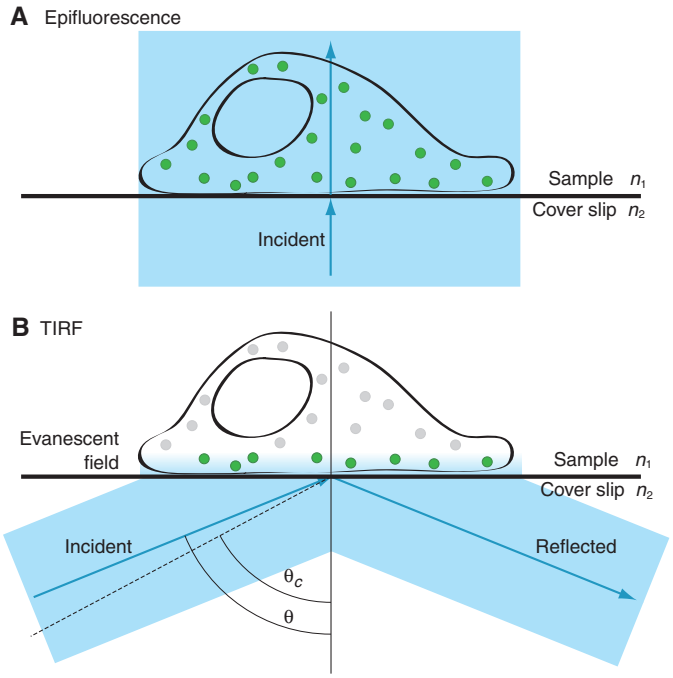

Fig. 2. The physical basis of epifluorescence and TIRF illumination. Schematic illustrating the cover-slip–sample interface. (**A**) Epifluorescence. The excitation beam travels directly through the cover-slip–sample interface. All of the fluorophores in the entire sample are excited. (**B**) TIRF. The excitation beam enters from the left at incidence angle θ, which is greater than the critical angle, θ_c (indicated by the dashed line). Angles are measured from the normal. The excitation beam is reflected off the cover-slip–sample interface and an evanescent field is generated on the opposite side of the interface, in the sample. Only fluorophores in the evanescent field are excited, as indicated by the green color. The refractive index of the sample (n_1) must be less than the index of refraction of the cover slip (n_2) to achieve TIR.

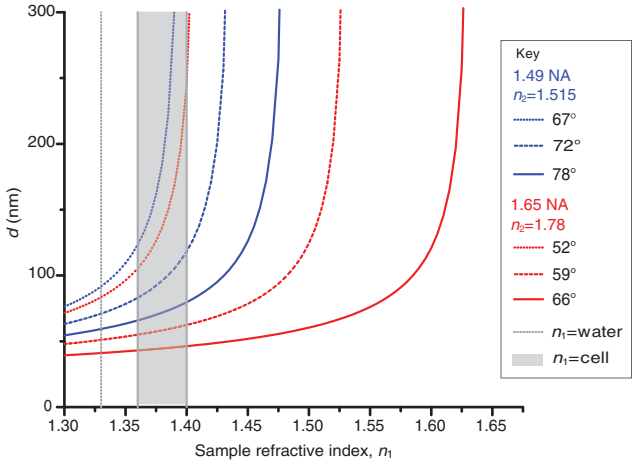

Fig. 3. The depth of the evanescent field depends on the refractive index of the sample. The depth of the evanescent field (d) is a function of the index of refraction of the sample (n_1). Incidence angles were chosen as 1.5° above the critical angle (dotted lines), the midpoint of all possible TIRF angles (dashed lines) and 1.5° less than the maximum incidence angle (solid lines). As the angle of incidence is increased, the sensitivity of d to the sample refractive index decreases in the range for cells. The 1.65 NA objective has a larger range with lower sensitivity to sample refractive index than the 1.49 NA objective.

angle will change depending on the refractive index of the sample. Biological samples have unknown and probably variable refractive indices. Moreover, the refractive index can vary within one sample as well as between samples. Thus, careful and repeated adjustment of the angle of incidence is strongly recommended because variations in sample refractive indices are the cause of many problems in TIRF microscopy, as discussed in detail below.

TIRF setup

Commercial TIRF systems are available; however, many researchers use 'homemade' TIRF setups. Some of these were constructed before major microscope manufacturers began selling off-the-shelf TIRF systems, whereas other setups are used by researchers who require flexible and easily modified platforms. Instructions on how to construct a homemade TIRF system are available (Axelrod, 2003). For the purpose of this article, we consider commercial TIRF systems, which are available from major microscopy companies (Leica, Nikon, Olympus and Zeiss) and third-party suppliers. These systems have the same basic ability to deliver through-the-objective TIRF illumination, but the individual system details vary. When evaluating different systems, we recommend viewing an experimental sample of interest, as well as each of the two test samples described in Box 1, to assess performance differences. In the best-case scenario, identical or very similar samples should be evaluated to exclude sample variation as a confounding variable.

When assembling a TIRF system, many of the same rules of thumb apply as when assembling any other high-resolution fluorescence microscopy system. Some important considerations include selection of an appropriate camera, dichroic mirror, emission filters, excitation light source, acquisition software and sample environment. Hardware considerations of particular importance in TIRF microscopy are described below.

TIRF excitation

In the majority of commercial systems, the excitation light is introduced to the sample through the same objective lens as the fluorescence is collected (Stout and Axelrod, 1989). However, there are various configurations for delivering the excitation beam to the sample, some of which use the objective and others a prism. The latter can be beneficial because it is generally inexpensive to set up and produces a 'cleaner' evanescent field with less scattered light, lower background and a greater range of incidence angles. Prism-based TIRF is often employed for in vitro studies, but is not the system of choice for most cell biologists because it can restrict sample accessibility and the choice of objectives. By contrast, through-the-objective TIRF allows rapid and easy access to the sample for changes to the media or drug addition, and exchange of samples is similarly quick and simple. Through-the-objective TIRF systems also tend to be more user friendly, requiring minimal maintenance and alignment. Thus, it is no surprise that through-the-objective TIRF is the configuration most commonly used by cell biologists.

Through-the-objective TIRF

To satisfy the physical requirements for TIRF, the excitation laser must be directed to the cover-slip–sample interface at an angle greater than the critical angle, as discussed above. In addition, all of the excitation light should be incident on the interface at the same angle. To achieve this uniform angle of illumination, the laser beam is focused on the BFP of the objective and therefore emerges in a collimated form, with all its 'rays' in parallel at a single angle. There is a one-to-one correspondence between the angle at which the light emerges from the objective and the position of the focused light on the BFP. The further off-axis the focused light is, the larger the angle of incidence. The angle of incidence is generally controlled either with a micrometer or through software.

High-numerical-aperture objective

One important requirement in through-the-objective TIRF is the numerical aperture (NA) of the objective. The NA of an objective describes its light-gathering power – specifically, the angle through which it is able to collect light. The NA also describes the maximum angle at which the excitation light can emerge from the objective. For an oil-immersion objective, this angle is also the maximum incidence angle of the excitation beam on the cover-slip–sample interface. The NA of the objective must be greater than the refractive index of the sample, preferably by a substantial margin. For example, if the sample is water (n_2=1.33), then a 1.4 NA objective is sufficient for TIR. However, the refractive index of a cell is greater than that of water and is variable. The refractive index of the cell interior is typically 1.38, although it varies among cell types, thus making TIRF imaging of cells challenging with a 1.4 NA objective (Fig. 3).

Fortunately, there are several commercial objectives available with a NA greater than 1.4; these are often marketed exclusively as TIRF objectives. The most common objectives are 1.45 NA and 1.49 NA, and are both available in 60×, 100× and 150× magnification. All these objectives should be used with standard glass cover slips (n=1.515) and standard immersion oil. In addition, a 100× 1.65 NA objective is also available from Olympus and has a number of advantages. First, the higher NA allows larger incidence angles, which can be crucial for imaging certain cell types (i.e. chromaffin cells) that have unusually high refractive indices. Second, there is a range of incidence angles where the depth of the evanescent field produced by the 1.65 NA objective is not very sensitive to the sample refractive index within the range of typical cellular refractive indices (Fig. 3). This is important because if there are any local variations in cellular refractive index (perhaps due to vesicles or

organelles), the 1.65 NA objective can create a uniform evanescent field. The major drawbacks of the 1.65 NA objective are that it requires a special and volatile immersion oil, and expensive non-standard cover slips (n=1.78).

Laser light source

It is possible to use either a laser or an arc lamp such as xenon or mercury for TIRF excitation. Some benefits of using an arc lamp are that it enables easy selection of excitation wavelengths with a filter wheel and the illumination field contains no interference fringes (see below). In this configuration, any light from the arc lamp that would arrive at the sample at less than the critical angle must be discarded. Therefore, a significant percent of the excitation power is lost, resulting in lower excitation intensity and dimmer images. Arc lamp sources for TIRF are commercially available and work well for samples that are intrinsically bright.

Lasers are the most common source for TIRF excitation and the TIRF system should have one laser line optimized for each fluorophore. The lasers can be mounted together and combined so that multiple fluorophores can be imaged either simultaneously or alternately. An acousto-optic tunable filter (AOTF) or filter wheel can be used for rapid switching between excitation wavelengths.

Camera

TIRF is a technique that captures the full field of an image, rather than scanning a single point. For the collection of images, a cooled charge-coupled device (CCD) camera is used. There is a wide range of CCD cameras to choose from, including electron multiplying (EM) CCDs. When rapid imaging in very low light situations is required, EMCCDs offer benefits over conventional CCDs. However, TIRF does not require an EMCCD and camera selection should be determined on the basis of the same considerations as for wide-field fluorescence imaging (Moomaw, 2007; Spring, 2007). When intensity changes are to be quantified, the linearity of the camera in response to incoming photons is an important consideration.

Image splitter

TIRF illumination is restricted within a single focal plane and relatively short exposure times (e.g. many frames per second) are routinely employed, making the technique especially useful for imaging dynamic processes. One of the developments that have made TIRF particularly powerful is the ability to image multiple fluorophores, either simultaneously or in very rapid succession. Image splitters, such as those sold by Cairn (Cairn Research Limited, UK) and Photometrics (Tucson, AZ, USA), allow simultaneous acquisition of emission from two to four spectrally distinct fluorophores on different regions of a CCD camera. This is an optimal method for imaging very rapid events; however, it reduces the size of the field that can be imaged. Alternatively, splitters that project two spectrally distinct images on two separate cameras are also available. Both methods can generate potential problems when aligning and overlaying the spectrally distinct channels, also known as image registration.

Sample environment

Live cell imaging often requires stable maintenance of the sample at 37°C, as temperature gradients can be a major source of focal drift. The thin optical section imaged with TIRF makes it particularly sensitive to small changes in focus, which degrade image quality. A number of solutions to this problem involve controlling temperature, and possibly also humidity and pCO_2 (partial pressure of CO_2). Stage-top incubators combined with objective heaters are one strategy for maintaining a stable temperature, although whole-scope incubators allow the entire system to equilibrate with fewer problems. Several companies are now offering focus-maintaining solutions, which reduce or eliminate focal drift resulting from temperature gradients.

Selection, preparation and analysis of TIRF samples

TIRF is ideal for imaging events occurring at a surface. However, there are several variables that must be considered before embarking on experiments.

Selection of cell type

The cells must be adherent, because TIRF illuminates only the region near the cover slip and cannot be used to image non-adherent cells. For some cell lines, it can be necessary to coat cover slips with extracellular matrix molecules or substances such as polylysine or collagen to ensure cell adherence. On the other hand, confluent monolayers of cells can generate areas of high refractive index, which can make imaging with TIRF difficult.

As outlined above, the refractive index of the cells should be below the NA of the objective. For example, chromaffin cells have a very high refractive index, which can make it difficult to obtain TIRF images using standard 1.45 NA or 1.49 NA objectives; the 1.65 NA objective was shown to yield good TIRF images (Allersma et al., 2004). Moreover, apoptotic cells generally have a higher index of refraction than non-apoptotic cells. Also, it is important to keep in mind that intracellular organelles have different refractive indices. Attempting TIRF imaging of a cell with a high refractive index can result in scattering of propagated light through the sample. To address this problem, it might be possible to increase the angle of incidence until the propagated light disappears. If this is not effective, the sample might require a 1.65 NA objective or the use of a prism-based system.

Sample preparation

TIRF is ideal for imaging live cells. Because of the thin excitation field, most of the imaged cell is not exposed to the excitation light, leading to fewer phototoxic effects. If cells are fixed, they should be mounted in a low refractive index media, such as PBS. Mounting medium that hardens or contains glycerol is useful for long-term sample storage, but it usually has a higher refractive index, rendering imaging of these samples with TIRF impossible. Finally, it should be noted that some dyes commonly used in cell biology (i.e. FM4-64 and DiI) adhere to the cover-slip surface and can obscure imaging unless the sample is properly washed after staining.

Data interpretation

When interpreting TIRF data, it is important to remember that the excitation field is not discrete, but exponentially decaying. The penetration depth, which is usually between 60 and 100 nm, describes the distance from the cover slip at which the excitation intensity is 1/e, or ~37%, of its value at the cover slip. The evanescent field exponentially decays, and objects located further than 100 nm from the surface of the cover slip can still be excited and imaged.

Particular care must be taken when interpreting the intensity of objects in an image obtained by TIRF. The intensity is affected by more than just the number of fluorophores; other factors include the axial (z) position and the orientation of the excitation dipole of the fluorophore relative to the polarization of the evanescent field. For example, 100 fluorophores positioned at z=0 will have the same

intensity as 370 fluorophores at $z=d$ ($I=1/e\times370=100$). Thus, intensity alone cannot be used to infer relative number of fluorophores or z positions between objects.

It follows that changes in intensity from a single object can be due to changes in multiple parameters, including the number of associated fluorophores, movements in z, the orientation of the object or the occurrence of photobleaching. The intensity of an object will increase if it gains fluorophores or moves closer to the cover slip, or if the excitation dipole rotates to align with the polarization of the evanescent field. In some cases, the specific biological context of the experiment can help to clarify the source of the intensity change; for example, the number of fluorophores on the inside of a secretory vesicle typically remains constant and, therefore, alteration in intensity can generally be interpreted as movement in z (Allersma et al., 2006). Also, in endocytosis, a loss of fluorescence can be interpreted as due to internalization only when it can be clearly distinguished from photobleaching. Alternatively, an epifluorescence image can be used for normalization and movement in z can be interpreted regardless of fluctuations in the number of fluorophores (Saffarian and Kirchhausen, 2008).

Troubleshooting and practical advice

In this section, we discuss commonly encountered problems when using TIRF microscopy. One of the most common is contamination of the image with propagating light, which can arise from a subcritical incidence angle or scattering from the sample. Both these scenarios significantly degrade the quality of TIRF images. Propagating light skimming at an angle through the sample will have similar characteristics to epifluorescence. Fig. 4A–D demonstrates the differences between TIRF and epifluorescence. The most notable characteristics are that, in epifluorescence, there is out-of-focus fluorescence and the sample can be focused in more than one plane. In TIRF, the background fluorescence is eliminated and the sample can only be focused in one plane. If a system is misaligned, it is possible for the image to appear to be half in TIR and half in epifluorescence. If a sample has areas of higher refractive index, 'comets' of propagating light can be seen. As a simple rule of thumb, if the image can be focused in more than one z plane, then propagating light is a problem (Fig. 4A–D; supplementary material Movie 1). The first step to overcome this problem is to vary the incidence angle. It is likely that the source of the problem is that the excitation angle is very close to the critical angle, or that dense organelles with a high refractive index found deeper in the cell are causing propagated light. This can be eliminated by increasing the incidence angle. However, if this is not the source of the problem, several other potential causes of propagating light can originate in the physical set up and/or the sample. It is simplest to begin by checking the parameters of the set up before exploring the sample itself as the cause of the propagated light.

Laser alignment

The most basic reason for contamination with propagated light is an improperly aligned excitation source. This will often manifest itself as a field that is half in and half out of TIRF, or the complete inability to obtain TIRF. As discussed above, the excitation laser beam must be focused on the BFP of the objective. If this is not the case, light will emerge from the objective at a variety of angles. It is important to follow manufacturer's instructions to check and correct the focus on the BFP.

Similarly, proper setting of the incidence angle is essential. The onset of TIRF should be obvious as a sudden darkening of the background and a flat two-dimensional look to the features near the surface (Fig. 1; supplementary material Movie 1). When the sample is viewed in TIRF, no new features should become apparent if the microscope is focused up into the sample, because there is only one plane of focus. Specific details of what should be observed for each of the two test samples are described in Box 1 and Fig. 4.

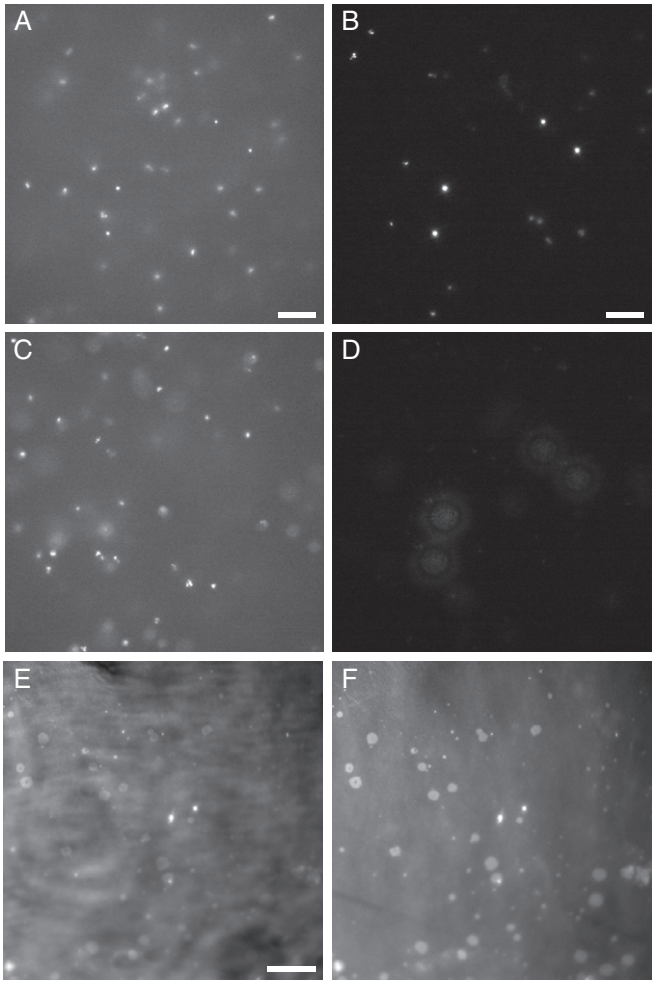

Fig. 4. TIRF test samples. The differences between epifluorescence and TIRF and the quality of the evanescent field can be examined using a test sample of fluorescent beads (**A–D**). In epifluorescence (incidence angle $\theta=0$), there is a large fluorescent background and beads appear in focus at both the cover slip $z=0$ (A) and deeper into the sample $z>0$ (C). In TIRF ($\theta>\theta_c$), the background is significantly less than in epifluorescence (B) and there are no beads in focus deeper into the sample ($z>0$) because the excitation field does not extend deep into the sample (D). The region imaged was constant, and identical exposure times and scalings were applied to all four images. DiI deposited on a cover slip reveals (**E**) interference fringes. For contrast, the same region is shown with elimination of the interference fringes (**F**). Scale bars: 10 μm.

Interference fringes

Laser illumination can produce interference fringes, which are caused by optical imperfections in the beam path. The interference fringes manifest themselves as an alternating light-dark pattern of excitation intensity at the sample plane (Fig. 4E). Although it is possible to obtain a correction image with which the image can be normalized, fringes are often specific to the sample and position in the xy plane, and are unlikely to be the same in the sample and the correction

image. There are several alterations to the TIRF set up that will eliminate fringes and create a uniform excitation field (Fig. 4F) (Fiolka et al., 2008; Inoue et al., 2001; Kuhn and Pollard, 2005; Mattheyses et al., 2006), although none are currently commercially available. When ordering filters and dichroics, it is recommended to specify that they will be used for TIRF imaging to reduce problems with interference fringes. Cleaning dust off optical surfaces, ensuring that the dichroic mirror is strain free and selecting the best of several objectives can reduce the number and severity of interference fringes. It is important to keep in mind that the excitation field might not be uniform; therefore, changes in intensity between objects located in different *xy* positions might be due to differences in excitation and not differences in the objects. The *xy* uniformity of the field can be examined with test samples, as detailed in Box 1 and Fig. 4.

Photobleaching

Photobleaching is the photon-induced decomposition of a fluorophore. It generally causes a permanent loss of fluorescence and dimming of the observed sample over time. In TIRF, it is important to keep in mind the unusual geometry of the excitation field. Fluorophores must be close to the origin of the evanescent field to be photobleached. Depending on the residence time of the fluorescent protein in the evanescent field, this will produce different effects. A fluorescently tagged membrane protein will be photobleached with normal kinetics because it resides in the excitation field. However, soluble fluorescently tagged proteins that diffuse in and out of the excitation field will not photobleach as quickly, because of the constant exchange between molecules in the evanescent field and those in the bulk of the cytoplasm. The intensity of the evanescent field is strongest closer to the cover slip and it is important to keep in mind the potential for photobleaching or photolysis when labeled molecules are present close to the cover slip (Jaiswal et al., 2007). Heat and free radicals generated by excitation light in any form of fluorescence microscopy can damage cellular proteins and structures, causing, for example, vesicle rupture or even cell death.

Conclusions

TIRF is a useful and accessible imaging technique used in cell biology for selective excitation of fluorophores at or near the cell membrane, while eliminating background fluorescence. TIRF facilitates the collection of information regarding processes in living cells that occur at the membrane, and enables the analysis of individual cellular and molecular events. This Commentary has provided a brief technical review of the physical basis of TIRF, highlighted some common issues that can arise when setting up and employing TIRF microscopy, suggested solutions to some of these potential problems, and provided examples of different types of cellular processes that can be effectively analyzed by TIRF imaging. The past few years have seen a great upswing in the application of TIRF microscopy in cell biology; of the nearly 1000 papers concerning TIRF published since approximately 1980, about 70% were written in the past five years! In the future, we can anticipate dissemination of this powerful technique to all areas of cell biology. Combining the ability to selectively probe dynamics at or near the cell membrane with different techniques, and the development of novel methods to make use of the properties of fluorophores and the geometry of TIRF will lead to great advances in our understanding of cell biology. Spectroscopic properties of fluorophores such as polarization (Anantharam et al., 2010; Sund et al., 1999) and anisotropic emission of fluorescence (Hellen and Axelrod, 1987) offer additional avenues for the development of novel techniques that will explore the environment and orientation of molecules. Furthermore, combining TIRF with other techniques, such as fluorescence recovery after photobleaching (FRAP) (Thompson et al., 1981), fluorescence correlation spectroscopy (FCS) (Lieto et al., 2003; Ohsugi et al., 2006),

Box 1. Determining the quality of a TIRF set up

The test samples described below can be used to check the quality of any TIRF set up. They should always be prepared using a cover slip with the correct thickness and refractive index for the objective.

Test samples

Fluorescent microbeads. These can be purchased from many sources, including Invitrogen (Carlsbad, CA) and Bangs Laboratories (Fishers, IN). The beads should be of subresolution size (100 nm diameter or less), and selected to have excitation and emission spectra that match typical experimental conditions. The beads should be diluted in water and applied to the cover slip. PBS can be added to increase the number of beads that adhere to the surface.

DiI. A convenient, uniform, fluorescent film can be easily made on a cover slip surface with the lipophilic fluorophore DiI (Invitrogen, Carlsbad, CA). Dissolve the DiI at 0.5 mg/ml in ethanol and place a single droplet of the solution on a glass cover slip. Then, before the solution dries, rinse the cover slip with distilled water. A monolayer of DiI fluorophore will remain adhered to the glass. Above the DiI-coated surface, add distilled water, being sure to add enough so that its upper surface is flat. The water-soluble fluorophore fluorescein (Invitrogen, Carlsbad, CA) can be used for this step instead of water. Fluorescein will allow detection of the critical angle. The fluorophores can be excited with a 488 nm laser and observed with a long-pass filter. DiI will appear red-orange and fluorescein green.

Evaluation criteria

The angle of illumination. Fluorescent microbeads are the ideal sample for evaluating TIRF. There are two populations of beads in the sample – immobile beads adhered to the surface and dynamic beads in solution moving by Brownian motion. If the angle of incidence is greater than the critical angle, the image will be overwhelmed by the dynamic beads in solution. When the incidence angle is increased, there should be a stark boundary at which the dynamic beads are no longer observed and the immobile surface-bound beads become visible. At this point, if you focus upwards into the sample, you should see the surface beads moving out of focus, but no new beads appearing – this is TIRF.

If it appears that TIRF is not achievable or that half of the field is in TIRF while the other half is in epi-illumination, a likely cause is that the excitation beam is not focused very well on the BFP. This can happen easily and is one of the first things to check when experiencing problems using TIRF.

Interference fringes. When the excitation light exceeds the critical angle, the DiI sample will reveal the interference fringe pattern, which usually manifests itself as concentric rings. The DiI will most likely have its own heterogeneities, which are distinguishable from the interference fringes; the sample heterogeneities will move as the sample is moved, whereas the interference fringes will remain for the most part unchanged.

It is important to keep in mind that it is not possible to set the angle of incidence on a test sample and expect it to be correct for an experimental sample. The test sample is used to verify the alignment of the system. Because of differences in the refractive indices between the test samples and experimental samples, the angle of incidence will need to be established for each experimental sample.

fluorescence resonance energy transfer (FRET) (Riven et al., 2006; Wang et al., 2008) or atomic force microscopy (AFM) (Brown et al., 2009; Kellermayer et al., 2006), will provide a wide variety of data on molecular dynamics in living cells. The superior background reduction provided by TIRF has allowed the development of several super-resolution techniques (Patterson et al., 2010). In the future, TIRF will continue to provide a unique view of cell biology.

J.Z.R. is funded through BBSRC grant BB/H002308/1. The authors thank Alexandre Benmerah for GFP-tagged clathrin, Ari Helenius for GFP-tagged caveolin-1 and Roland Wedlich-Soldner for GFP-tagged LifeAct. The authors also thank Natalie Poulter for assistance in the generation of Fig. 1. The TIRF microscope used in this research to generate Fig. 1 was obtained through the Birmingham Science City Translational Medicine Clinical Research and Infrastructure Trials Platform, with support from Advantage West Midlands (AWM). S.S.M. is funded through NIH grant R01 GM087977. Deposited in PMC for release after 12 months.

Supplementary material available online at
http://jcs.biologists.org/cgi/content/full/123/21/3621/DC1

References

Allersma, M. W., Wang, L., Axelrod, D. and Holz, R. W. (2004). Visualization of regulated exocytosis with a granule membrane probe using total internal reflection microscopy. *Mol. Biol. Cell* **15**, 4658-4668.

Allersma, M. W., Bittner, M. A., Axelrod, D. and Holz, R. W. (2006). Motion matters: secretory granule motion adjacent to the plasma membrane and exocytosis. *Mol. Biol. Cell* **17**, 2424-2438.

Anantharam, A., Onoa, B., Edwards, R. H., Holz, R. W. and Axelrod, D. (2010). Localized topological changes of the plasma membrane upon exocytosis visualized by polarized TIRFM. *J. Cell Biol.* **188**, 415-428.

Axelrod, D. (1981). Cell-substrate contacts illuminated by total internal reflection fluorescence. *J. Cell Biol.* **89**, 141-145.

Axelrod, D. (1989). Total internal-reflection fluorescence microscopy. *Methods Cell Biol.* **30**, 245-270.

Axelrod, D. (2003). Total internal reflection fluorescence microscopy in cell biology. *Biophotonics B* **361**, 1-33.

Axelrod, D. (2008). Total internal reflection fluorescence microscopy. In *Biophysical Tools for Biologists, Vol. 2, In Vivo Techniques* (ed. J. J. Correia and H. W. Detrich), pp. 169-221. San Diego, CA: Academic Press.

Brown, A. E. X., Hategan, A., Safer, D., Goldman, Y. E. and Discher, D. E. (2009). Cross-correlated TIRF/AFM reveals asymmetric distribution of force-generating heads along self-assembled, "synthetic" myosin filaments. *Biophys. J.* **96**, 1952-1960.

Choi, C. K., Vicente-Manzanares, M., Zareno, J., Whitmore, L. A., Mogilner, A. and Horwitz, A. R. (2008). Actin and alpha-actinin orchestrate the assembly and maturation of nascent adhesions in a myosin II motor-independent manner. *Nat. Cell Biol.* **10**, 1039-1050.

Danuser, G. and Waterman-Storer, C. M. (2006). Quantitative fluorescent speckle microscopy of cytoskeleton dynamics. *Annu. Rev. Biophys. Biomol. Struct.* **35**, 361-387.

Demuro, A. and Parker, I. (2004). Imaging the activity and localization of single voltage-gated Ca^{2+} channels by total internal reflection fluorescence microscopy. *Biophys. J.* **86**, 3250-3259.

Dyachok, O., Isakov, Y., Sagetorp, J. and Tengholm, A. (2006). Oscillations of cyclic AMP in hormone-stimulated insulin-secreting beta-cells. *Nature* **439**, 349-352.

Engel, B. D., Lechtreck, K. F., Sakai, T., Ikebe, M., Witman, G. B. and Marshall, W. F. (2009). Total internal reflection fluorescence (TIRF) microscopy of chlamydomonas flagella. *Methods Cell Biol.* **93**, 157-177.

Ezratty, E. J., Bertaux, C., Marcantonio, E. E. and Gundersen, G. G. (2009). Clathrin mediates integrin endocytosis for focal adhesion disassembly in migrating cells. *J. Cell Biol.* **187**, 733-747.

Fiolka, R., Belyaev, Y., Ewers, H. and Stemmer, A. (2008). Even illumination in total internal reflection fluorescence microscopy using laser light. *Microsc. Res. Tech.* **71**, 45-50.

Gaidarov, I., Santini, F., Warren, R. A. and Keen, J. H. (1999). Spatial control of coated-pit dynamics in living cells. *Nat. Cell Biol.* **1**, 1-7.

Gingell, D., Heavens, O. S. and Mellor, J. S. (1987). General electromagnetic theory of total internal-reflection fluorescence-the quantitative basis for mapping cell substratum topography. *J. Cell Sci.* **87**, 677-693.

Haugh, J. M., Codazzi, F., Teruel, M. and Meyer, T. (2000). Spatial sensing in fibroblasts mediated by 3′ phosphoinositides. *J. Cell Biol.* **151**, 1269-1279.

Hellen, E. H. and Axelrod, D. (1987). Fluorescence emission at dielectric and metal-film interfaces. *J. Opt. Soc. Am. B* **4**, 337-350.

Inoue, S., Knudson, R. A., Goda, M., Suzuki, K., Nagano, C., Okada, N., Takahashi, H., Ichie, K., Iida, M. and Yamanaka, K. (2001). Centrifuge polarizing microscope. I. Rationale, design and instrument performance. *J. Microsc.* **201**, 341-356.

Jaiswal, J. K., Fix, M., Takano, T., Nedergaard, M. and Simon, S. M. (2007). Resolving vesicle fusion from lysis to monitor calcium-triggered lysosomal exocytosis in astrocytes. *Proc. Natl. Acad. Sci. USA* **104**, 14151-14156.

Jaiswal, J. K., Rivera, V. M. and Simon, S. M. (2009). Exocytosis of post-Golgi vesicles is regulated by components of the endocytic machinery. *Cell* **137**, 1308-1319.

Jouvenet, N., Neil, S. J. D., Bess, C., Johnson, M. C., Virgen, C. A., Simon, S. M. and Bieniasz, P. D. (2006). Plasma membrane is the site of productive HIV-1 particle assembly. *PLoS Biol.* **4**, 2296-2310.

Kaksonen, M., Toret, C. P. and Drubin, D. G. (2005). A modular design for the clathrin- and actin-mediated endocytosis machinery. *Cell* **123**, 305-320.

Kellermayer, M. S. Z., Karsai, A., Kengyel, A., Nagy, A., Bianco, P., Huber, T., Kulcsar, A., Niedetzky, C., Proksch, R. and Grama, L. (2006). Spatially and temporally synchronized atomic force and total internal reflection fluorescence microscopy for imaging and manipulating cells and biomolecules. *Biophys. J.* **91**, 2665-2677.

Krylyshkina, O., Anderson, K. I., Kaverina, I., Upmann, I., Manstein, D. J., Small, J. V. and Toomre, D. K. (2003). Nanometer targeting of microtubules to focal adhesions. *J. Cell Biol.* **161**, 853-859.

Kuhn, J. R. and Pollard, T. D. (2005). Real-time measurements of actin filament polymerization by total internal reflection fluorescence microscopy. *Biophys. J.* **88**, 1387-1402.

Lang, T., Wacker, I., Steyer, J., Kaether, C., Wunderlich, I., Soldati, T., Gerdes, H. H. and Almers, W. (1997). Ca^{2+}-triggered peptide secretion neurotechnique in single cells imaged with green fluorescent protein and evanescent-wave microscopy. *Neuron* **18**, 857-863.

Lieto, A. M., Cush, R. C. and Thompson, N. L. (2003). Ligand-receptor kinetics measured by total internal reflection with fluorescence correlation spectroscopy. *Biophys. J.* **85**, 3294-3302.

Luik, R. M., Wu, M. M., Buchanan, J. and Lewis, R. S. (2006). The elementary unit of store-operated Ca^{2+} entry: local activation of CRAC channels by STIM1 at ER-plasma membrane junctions. *J. Cell Biol.* **174**, 815-825.

Mattheyses, A. L., Shaw, K. and Axelrod, D. (2006). Effective elimination of laser interference fringing in fluorescence microscopy by spinning azimuthal incidence angle. *Microsc. Res. Tech.* **69**, 642-647.

Merrifield, C. J., Feldman, M. E., Wan, L. and Almers, W. (2002). Imaging actin and dynamin recruitment during invagination of single clathrin-coated pits. *Nat. Cell Biol.* **4**, 691-698.

Moomaw, B. (2007). Camera technologies for low light imaging: overview and relative advantages. In *Digital Microscopy,* 3rd edn (ed. G. Sluder and D. E. Wolf), pp. 251-283. San Diego, CA: Elsevier Academic Press.

North, A. J. (2006). Seeing is believing? A beginners' guide to practical pitfalls in image acquisition. *J. Cell Biol.* **172**, 9-18.

Ohsugi, Y., Saito, K., Tamura, M. and Kinjo, M. (2006). Lateral mobility of membrane-binding proteins in living cells measured by total internal reflection fluorescence correlation spectroscopy. *Biophys. J.* **91**, 3456-3464.

Patterson, G., Davidson, M., Manley, S. and Lippincott-Schwartz, J. (2010). Superresolution imaging using single-molecule localization. *Annu. Rev. Phys. Chem.* **61**, 345-367.

Rappoport, J. Z. (2008). Focusing on clathrin-mediated endocytosis. *Biochem. J.* **412**, 415-423.

Rappoport, J. Z. and Simon, S. M. (2003). Real-time analysis of clathrin-mediated endocytosis during cell migration. *J. Cell Sci.* **116**, 847-855.

Rappoport, J. Z., Taha, B. W., Lemeer, S., Benmerah, A. and Simon, S. M. (2003). The AP-2 complex is excluded from the dynamic population of plasma membrane-associated clathrin. *J. Biol. Chem.* **278**, 47357-47360.

Rappoport, J. Z., Benmerah, A. and Simon, S. M. (2005). Analysis of the AP-2 adaptor complex and cargo during clathrin-mediated endocytosis. *Traffic* **6**, 539-547.

Rappoport, J. Z., Kemal, S., Benmerah, A. and Simon, S. M. (2006). Dynamics of clathrin and adaptor proteins during endocytosis. *Am. J. Physiol. Cell Physiol.* **291**, C1072-C1081.

Rappoport, J. Z., Heyman, K. P., Kemal, S. and Simon, S. M. (2008). Dynamics of dynamin during clathrin mediated endocytosis in PC12 cells. *PLoS ONE* **3**, e2416.

Riven, I., Iwanir, S. and Reuveny, E. (2006). GIRK channel activation involves a local rearrangement of a preformed G protein channel complex. *Neuron* **51**, 561-573.

Saffarian, S. and Kirchhausen, T. (2008). Differential evanescence nanometry: live-cell fluorescence measurements with 10-nm axial resolution on the plasma membrane. *Biophys. J.* **94**, 2333-2342.

Schmoranzer, J. and Simon, S. M. (2003). Role of microtubules in fusion of post-Golgi vesicles to the plasma membrane. *Mol. Biol. Cell* **14**, 1558-1569.

Schmoranzer, J., Goulian, M., Axelrod, D. and Simon, S. M. (2000). Imaging constitutive exocytosis with total internal reflection fluorescence microscopy. *J. Cell Biol.* **149**, 23-31.

Spring, K. R. (2007). Cameras for digital microscopy. In *Digital Microscopy,* 3rd edn (ed. G. Sluder and D. E. Wolf), pp. 171-187. San Diego, CA: Elsevier Academic Press.

Stout, A. L. and Axelrod, D. (1989). Evanescent field excitation of fluorescence by epi-illumination microscopy. *Appl. Opt.* **28**, 5237-5242.

Sund, S. E., Swanson, J. A. and Axelrod, D. (1999). Cell membrane orientation visualized by polarized total internal reflection fluorescence. *Biophys. J.* **77**, 2266-2283.

Thompson, N. L., Burghardt, T. P. and Axelrod, D. (1981). Measuring surface dynamics of biomolecules by total internal-reflection fluorescence with photobleaching recovery or correlation spectroscopy. *Biophys. J.* **33**, 435-454.

Todd, I., Mellor, J. S. and Gingell, D. (1988). Mapping cell glass contacts of dictyostelium amebas by total internal-reflection aqueous fluorescence overcomes a basic ambiguity of interference reflection microscopy. *J. Cell Sci.* **89**, 107-114.

Wang, L., Bittner, M. A., Axelrod, D. and Holz, R. W. (2008). The structural and functional implications of linked SNARE motifs in SNAP25. *Mol. Biol. Cell* **19**, 3944-3955.

Waters, J. C. (2009). Accuracy and precision in quantitative fluorescence microscopy. *J. Cell Biol.* **185**, 1135-1148.

Paul Wiseman, Monday June 11th 2012, 11.30

Cell Biochem Biophys
DOI 10.1007/s12013-007-9000-5

REVIEW PAPER

Advances in Image Correlation Spectroscopy: Measuring Number Densities, Aggregation States, and Dynamics of Fluorescently labeled Macromolecules in Cells

David L. Kolin · Paul W. Wiseman

Abstract A brief historical outline of fluorescence fluctuation correlation techniques is presented, followed by an in-depth review of the theory and development of image correlation techniques, including: image correlation spectroscopy (ICS), temporal ICS (TICS), image cross-correlation spectroscopy (ICCS), spatiotemporal ICS (STICS), k-space ICS (kICS), raster ICS (RICS), and particle ICS (PICS). These techniques can be applied to analyze image series acquired on commercially available laser scanning or total internal reflection fluorescence microscopes, and are used to determine the number density, aggregation state, diffusion coefficient, velocity, and interaction fraction of fluorescently labeled molecules or particles. A comprehensive review of the application of ICS techniques to a number of systems, including cell adhesion, membrane receptor aggregation and dynamics, virus particle fusion, and fluorophore photophysics, is presented.

Keywords Image correlation spectroscopy · Fluorescence correlation spectroscopy · Membrane dynamics · Fluorescence microscopy · Membrane receptors

D. L. Kolin · P. W. Wiseman
Department of Chemistry, McGill University, Montreal, QC, Canada H3A 2K6

P. W. Wiseman (✉)
Department of Physics, McGill University, Montreal, QC, Canada H3A 2T8
e-mail: Paul.Wiseman@McGill.ca

Introduction

The aggregation state of membrane proteins in living cells can be an important indicator of the underlying biology. For example, cytokines and growth factors are thought to exert their effect on cells by causing a dimerization or oligomerization of membrane receptors, which in turn initiate an intracellular signaling pathway [1, 2]. In addition to the aggregation state of cell-surface receptors, their rate and mode of transport can have a number of underlying biological determinants, including protein tethering or corralling by cytoskeletal elements or lipid rafts [3], binding of receptors to extracellular matrix proteins [4], and the membrane-substrate distance [5]. Clearly, to be able to fully understand and characterize the wide range of biochemical reactions which occur within living cells, there must be techniques available to probe the interactions and dynamics of biological macromolecules in situ. The introduction of green fluorescent protein (GFP) and its variants has revolutionized the field of cell biology by allowing an unprecedented specificity and efficiency of fluorescence labeling and live cell imaging [6]. This work will review a number of image correlation techniques which can measure the number densities, aggregation states, dynamics, and interactions of fluorescently labeled membrane proteins including those tagged with GFP or its variants.

The image correlation methods are imaging analogs of fluorescence correlation spectroscopy (FCS), a fluctuation technique developed over 30 years ago to probe the binding of ethidium bromide to DNA molecules in solution [7]. FCS monitors the spontaneous fluctuations of fluorescence intensity collected from fluorophores in a small, open excitation laser beam volume and records the detected fluctuations in photon counts as a time series. The

fluctuations in fluorescence arise from any process which changes the occupation number of fluorophores in the focal volume, such as molecular transport or chemical reactions. The time autocorrelation function of the fluctuation time series contains information regarding the dynamics, number density, and reaction kinetics of the system [8–10]. In a traditional FCS apparatus, the laser beam is kept stationary and the experiment is best suited for measuring molecules free in solution or in the cytoplasm. Scanning FCS (SFCS) was later developed as an extension of FCS, in which the laser beam was scanned in a line or circle across the sample, or the sample was translated under the beam, to obtain fluctuation measurements. It was initially used to measure the molecular weight of DNA in solution [11] and later extended to study the aggregation and number density of slowly moving or immobile fluorescent particles such as cell membrane proteins [12], virus particles [13] and lectins [14]. SFCS was also used to determine the diffusion coefficient of fluorescein-labeled proteins [15], and DNA labeled with ethidium bromide in solution as well as colloidal gold-tagged lipids in a planar bilayer [16].

Image correlation spectroscopy (ICS) was developed as the imaging analog of FCS, in which spatial autocorrelation functions are calculated from images of fluorophores (hence spatial fluorescence fluctuations) acquired on laser scanning microscopes [17]. Unlike single-point FCS, ICS does not require "fast" diffusion of fluorophores, making it amenable to the study of slow membrane receptors, receptor clusters, or even chemically fixed cells. The imaging modality is also advantageous because it acquires a large number of spatial samples (pixels) per frame, and does not require sample translation.

A number of fluorescence fluctuation correlation techniques, such as two-photon SFCS [18] and Fourier imaging correlation spectroscopy [19] have been developed which require custom-built apparatuses. While these techniques are powerful methods to measure molecular transport, this work will focus solely on techniques that have been applied to data acquired on commercial confocal or two-photon laser scanning microscopes (LSMs), or total internal reflection fluorescence microscopes (TIRFMs) used with high sensitivity CCD cameras for area detection.

This review will provide an introduction to the existing range of image correlation techniques, which can unlock a wealth of molecular information hidden in images and image time series of fluorescently labeled living or fixed cells recorded using now fairly standard fluorescence imaging systems (e.g., LSMs). The techniques described in this review all use correlation function analysis to extract a few meaningful parameters from a data set containing a huge amount of raw data (Fig. 1). The first part of this review will summarize the theory of the image correlation spectroscopy family of techniques and give guidelines for their practical application. The second part of the review will highlight their use in a wide range of biological and chemical applications, with an emphasis on quantifying the aggregation state and dynamics of membrane proteins and membrane-associated proteins.

Image Correlation Techniques

Most of the techniques described in this review can be expressed as a subset of a generalized spatiotemporal correlation function. We will first present the generalized function, and then show how the techniques are variations of this function. The raw data for image correlation analyses is an image series which is really fluorescence intensity, recorded as a function of space and time, $i(x, y, t)$, usually obtained from a confocal or two-photon LSM or evanescent wave imaging (TIRFM). We define a generalized spatiotemporal correlation function as [20]:

$$r_{ab}(\xi,\eta,\tau) = \frac{\langle \delta i_a(x,y,t)\delta i_b(x+\xi,y+\eta,t+\tau)\rangle}{\langle i_a(x,y,t)\rangle_t \langle i_b(x,y,t+\tau)\rangle_{t+\tau}}, \quad (1)$$

where a fluctuation in fluorescence, $\delta i(x, y, t)$, is given by:

$$\delta i(x,y,t) = i(x,y,t) - \langle i(x,y,t)\rangle_t, \quad (2)$$

where $i(x, y, t)$ is the intensity at pixel (x, y) in the image recorded at time t, and $\langle i(x, y, z)\rangle_t$ is the average intensity of that image. The subscripts a and b in Eq. 1 refer to two different emission wavelength detection channels. For the case of autocorrelation of single detection channel, $a = b$ and the subscripts are dropped. We will see that most of the techniques reviewed here are described by simplified versions of Eq. 1 for specified limits.

Every image acquired on a fluorescence microscope is a convolution of the microscope PSF with the point-source emission from the fluorophores due to diffraction [21]. This convolution causes the signal from a point-emitter to be spread over a number of pixels. All of the techniques described in this review exploit the microscope PSF to correlate fluorescence fluctuations over space, time, or both (cf. Eq. 1 and Fig. 1). These approaches are inherently powerful because they reduce a huge number of stochastic fluctuations to a few physically meaningful numbers by spatiotemporal averaging.

The act of correlating fluctuations arising from particles within the microscope PSF also confers some critical limitations on ICS approaches. For example, the use of correlation functions means almost all of the techniques presented here assume the system being studied is stationary (i.e., invariant) in either space or time. However, it is clear that this condition may not be met for all measurements in living cells since cells differ in behavior as a

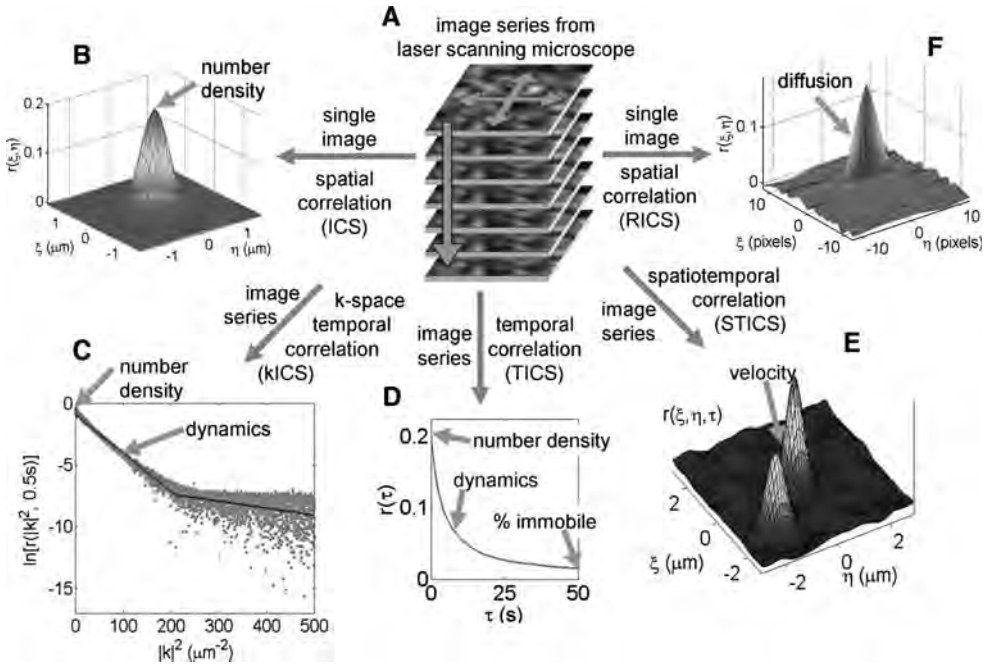

Fig. 1 An overview of the image correlation techniques described in this review. (**A**) All analyses are performed on an image or image series acquired on a confocal or two-photon laser scanning microscope, or a total internal reflection fluorescence microscope. Frequently, the sample is a cell membrane in which a macromolecule of interest is selectively tagged with a fluorophore, using either antibody labeling or transfection with a fluorescent protein. (**B**) Image correlation spectroscopy (ICS) is performed on an image, and can determine the number density and aggregation state of fluorescently labeled particles. (**C**) k-Space ICS (kICS) measures dynamics (i.e., diffusion and flow) of particles, and is completely insensitive to fluorophore "blinking" and photobleaching. (**D**) Temporal ICS (TICS) correlates an image series in time to determine dynamics, number densities, and the fraction of the fluorophores that are immobile on the time scale of the measurement. (**E**) Spatiotemporal ICS (STICS) calculates spatial and temporal correlations from an image series to determine the direction and magnitude of flow in the sample. (**F**) Raster ICS (RICS) uses spatial autocorrelation analysis of the fast and slow components of the laser raster scan for an image acquired on a laser scanning microscope to measure fast (e.g., cytosolic) transport dynamics

function of time and are spatially heterogeneous. For example, a membrane-bound protein involved in cell adhesion might exhibit different modes and rates of transport in the front compared to the rear of a migrating cell. The density of this protein may also depend on whether or not it is present in a nascent, mature, or disassembling focal adhesion. Thus, one key assumption in these analyses is that the system studied is at a steady state in the spatial region and over the time period, which is analyzed. Another limitation is introduced by the convolution of the microscope PSF. With the exception of particle ICS (discussed in Section "Particle Image Correlation Spectroscopy (PICS)"), the techniques described here are insensitive to particle movements and interactions below the diffraction limit ($\sim$200 nm). For example, temporal ICS cannot resolve the confined diffusion of particles in 50 nm corrals in the cell membrane, and image cross-correlation spectroscopy cannot differentiate between two species which are colocalized in a common 100 nm subcellular compartment and two species that are truly bound to each other. However, techniques such as single particle tracking (SPT) and fluorescence resonance energy transfer (FRET), respectively, are capable of spatially resolving these processes. Consequently, it is important to understand both the capabilities and limitations of a given method before attempting to study a process of interest.

For non-interacting (i.e., ideal) particles in a noise-free system, in which the measured fluorescence is proportional to the concentration of labeled species, the mean-squared intensity fluctuation divided by the squared mean image intensity is equal to the reciprocal of the mean number of independent fluorescent particles per laser beam volume or area (for two-dimensional (2D) systems such as membranes), $\langle n_p \rangle$ [8]:

$$\frac{\langle (\delta i)^2 \rangle}{\langle i \rangle^2} = \frac{1}{\langle n_p \rangle}. \tag{3}$$

"Independent particles" refers to separate fluorescent entities, so a linked cluster of monomers would constitute one entity or one independent fluorescent particle. In a real system, the fluctuations (cf. Eq. 2) contain contributions from both signal and noise. In a system without noise, $\langle (\delta i)^2 \rangle$ could be extracted from the image with a direct

calculation using the pixel intensities. However, in a system with noise, Eq. 3 no longer holds for two reasons. First, noise prevents a direct calculation of the number density because it adds spurious intensity counts to the image, increasing the average intensity. Second, the mean-squared fluctuation term in the numerator of Eq. 3 will also be perturbed, since both noise *and* signal fluctuations contribute to the recorded intensity fluctuations in an image. The noise in LSM images is usually uncorrelated between neighboring pixels or the same pixel in subsequent images. Such white noise contributions only correlate with themselves within a given pixel and will thus only contribute to the zero-lags value of the correlation function. However, signal measured from real physical sources is correlated in both space and time because of the point spread function (PSF) of the imaging system, which causes single-point emission source to be imaged onto a number of adjacent pixels in an image or at the same pixel location in subsequent images if the source has not moved significantly between images. The spatiotemporal persistence of the signal fluctuations can be exploited to separate them from noise fluctuations, by extrapolating the correlation function to its zero-lags amplitude. For example, in the case of Eq. 1 the autocorrelation function becomes:

$$\lim_{\xi\to 0,\eta\to 0,\tau\to 0} r(\xi,\eta,\tau) = \frac{\langle (i(x,y,t) - \langle i(x,y,t)\rangle_t)^2\rangle}{\langle i(x,y,t)\rangle_t \langle i(x,y,t)\rangle_t} = \frac{\langle (\delta i)^2\rangle}{\langle i\rangle^2} = \frac{1}{\langle n_p\rangle}. \quad (4)$$

In practice, this value is obtained by fitting the correlation function to an appropriate decay function without weighting the white-noise-containing zero-lags value in the fit. Even with extrapolation to obtain the magnitude of the correlation function, $\langle i\rangle$ must still be corrected for the signal background [22, 23]. The number of particles or clusters per beam area, $\langle n_p\rangle$ can be converted to the cluster density (CD), which is the number of particles per μm^2, by dividing by the area of the laser beam [17]:

$$\mathrm{CD} = \frac{\langle n_p\rangle}{\pi\omega_0^2}, \quad (5)$$

where ω_0 is the e^{-2} radius of the focused beam, which is the radius of the microscope PSF. The $\langle n_p\rangle$ is an indicator of the density of independent fluorescent clusters, but without additional calibration measurements or an estimate of the total number of monomers in the system, it cannot be determined if these particles exist as monomers, dimers, or oligomers. However, the average intensity of the image is proportional to the total number of fluorophores per beam area assuming quenching does not occur. Therefore, the ratio of $\langle i\rangle$ and CD provides a measure of the degree of aggregation (DA) [22]:

$$\mathrm{DA} = \frac{\langle i\rangle}{\mathrm{CD}} = c\frac{\langle n_m\rangle}{\langle n_p\rangle} \quad (6)$$

where the factor c is a proportionality constant, which depends on the spectral characteristics of the fluorophore and the light collection efficiency of the imaging system, and relates the average intensity to the number of monomers. When using antibody labeling, the value of c can be determined from control measurements of non-specific labeling with the assumption that the non-specifically labeled antibodies are monomers [22]. If the protein of interest is labeled with GFP, c can be found by imaging a control sample of dispersed GFP monomers under identical conditions as the regular samples [4]. Since the DA is calculated from an image, it can be calculated as a function of time from an image series to measure changes in the aggregation state of a protein [4, 24].

Image Correlation Spectroscopy

Using the original spatial image correlation spectroscopy (ICS) technique, it is possible to determine the CD and DA from an image of fluorophores acquired on a LSM or TIRFM [17]. As with all of the techniques presented in this review, a correlation function is first calculated from the raw data. This correlation function is then fit to an analytical model to extract the parameters of interest. With spatial ICS, a spatial autocorrelation function is calculated from the intensities recorded in the pixels of individual images.

The normalized intensity fluctuation spatial autocorrelation function of the image recorded at time t in a time series is given by Eq. 1 when $\tau = 0$:

$$r(\xi,\eta,0)_t = \frac{\langle \delta i(x,y,t)\delta i(x+\xi,y+\eta,t)\rangle}{\langle i(x,y,t)\rangle_t^2}, \quad (7)$$

where the angular brackets denote spatial averaging over the image, and ξ and η are spatial lag variables corresponding to pixel shifts of the image relative to itself in the x and y directions. The original ICS technique was a 2D method, and we have adopted the more encompassing notation here to reflect extensions of the method to the time domain. To minimize computation time, these functions are typically calculated using Fourier methods [17]:

$$r(\xi,\eta,0)_t = \frac{\mathcal{F}^{-1}[\mathcal{F}(i(x,y,t))\mathcal{F}^*(i(x,y,t))]}{\langle i(x,y,t)\rangle_t^2} - 1 \tag{8}$$

where $\mathcal{F}$ denotes the 2D spatial Fourier transform, $\mathcal{F}^*$ is the complex conjugate of this transform, and $\mathcal{F}^{-1}$ is the inverse 2D spatial Fourier transform. The correlation function is then fit to a 2D Gaussian using a three parameter nonlinear least squares algorithm (fit parameters are in bold):

$$r(\xi,\eta,0)_t = \mathbf{g}(\mathbf{0},\mathbf{0},\mathbf{0})_t \exp\left[-\frac{\xi^2+\eta^2}{\omega_0^2}\right] + \mathbf{g}_{\infty t}. \tag{9}$$

where $\mathbf{g}(\mathbf{0},\mathbf{0},\mathbf{0})_t$ is the zero-lags amplitude, and $\mathbf{g}_{\infty t}$ is the long-spatial lag offset to account for an incomplete decay of the correlation function. A Gaussian function is used because the laser beam acts as the spatial correlator and has a Gaussian intensity profile.

As described earlier, the zero-lags amplitude of the correlation function is inversely proportional to the number of independent fluorescent particles per beam area, $\mathbf{g}(\mathbf{0},\mathbf{0},\mathbf{0})_t = 1/\langle n_p\rangle$. Cluster densities can be calculated from $\langle n_p\rangle$, using the fit $\boldsymbol{\omega}_0$ (cf. Eq. 5) [17, 23]. The value of $\boldsymbol{\omega}_0$ obtained from the fit to Eq. 9 is usually the value used when calculating the CD (cf. Eq. 5), and is a useful indicator of the quality of the fit. If the fitted value of $\boldsymbol{\omega}_0$ differs by more than 30% from a measured value for the beam radius, the fit should be discarded [17, 25]. The beam radius of the microscope PSF can be determined using a number of methods, including imaging sub-diffraction-limit diameter fluorescent microspheres [26], or using the gold-foil edge technique [17]. Because the size of $\boldsymbol{\omega}_0$ is wavelength-dependent, the PSF should be measured at the same excitation wavelength as the fluorophore in the ICS experiment. An example ICS measurement, with the raw correlation function and fitted 2D Gaussian surface, is shown in Fig. 2.

Spatial ICS is usually applied to images acquired on LSMs. However, a variant was successfully used on images from a TIRFM [27]. Unlike a LSM, the evanescent wave used to excite the fluorophores in a TIRFM has a non-uniform Gaussian intensity profile, and this complication must be corrected for in a quantitative analysis [27].

Spatial ICS in Systems with Multiple Populations of Oligomers

When more than one population of fluorescent particles are present (e.g., monomers, dimers, and tetramers), $\mathbf{g}(\mathbf{0},\mathbf{0},\mathbf{0})_t$ can be interpreted as:

$$\mathbf{g}(\mathbf{0},\mathbf{0},\mathbf{0})_t = \frac{\sum_i \bar{N}_i\left(\sigma_i^2+\mu_i^2\right)}{\bar{N}_m^2} \tag{10}$$

where the sum is over all fluorescent species in the system, $\bar{N}_m$ is the average number of monomers in the beam volume, $\bar{N}_i$ is the average number of the ith species of aggregate in the volume, which has a mean number of monomers μ_i and a variance in the number of monomers σ_i^2 [12]. Equation 10 assumes that there is no quenching between the fluorophores in an aggregate. If quenching were present, the measured μ_i would be lower than the true value, and it would appear as if fewer monomers were present in each aggregate. Unless simplifying assumptions can be made or additional information about the system is available from outside sources, it is usually impossible to apply the multiple parameter dependent Eq. 10 to single ICS measurement, since only one parameter is determined from the experiment (the correlation function magnitude, $\mathbf{g}(\mathbf{0},\mathbf{0},\mathbf{0})_t$).

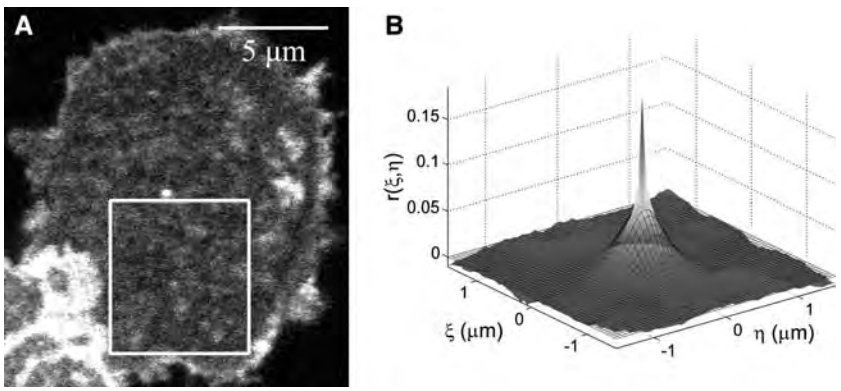

Fig. 2 (**A**) Confocal laser scanning image of CHO K1 cell expressing EGFR-eGFP. (**B**) Spatial autocorrelation function for the region outlined in (**A**). The raw correlation function is given by the colored surface, and the fitted 2D Gaussian function is denoted by the black mesh. The amplitude of the correlation function is the key parameter recovered from the fit, and it is inversely proportional to the number of independent fluorescent particles. From Ref. [23], with permission

Rocheleau et al. [28] developed an extension of ICS, which allows the fluctuations in an image associated with brightest aggregates to be separated from those of dimmer aggregates. The technique involves the sequential subtraction of intensity from LSM images, and is similar to that implemented by Wiseman et al. [29] to measure dendritic spine densities.

Ideally, one could determine the entire distribution of aggregation states, and not only the brightest aggregates (as in [28]), or a weighted average of the distribution (cf. Eq. 10). Such a determination is, in theory, possible. The full distribution of particle aggregation states can be calculated using higher order correlation functions, in which the relative number densities and brightnesses of species are measured (as demonstrated for FCS in [30]). This technique has been successfully applied to IgE distributions on supported planar membranes [31], in which the parameters extracted from the analysis qualitatively agreed with a visual inspection of the image. The accuracy and dynamic range of a related image moment technique applied to two-population systems was investigated by Sergeev et al. [32], who used it to measure oligomer distributions of imaged platelet-derived growth factor receptors (PDGF-βR) in fixed cells. They found that the density of the oligomeric population should not be higher than the monomer density, and that the monomer concentration should not be higher than an order of magnitude greater than the oligomeric population in order to extract accurate results from the image moment analysis. They also measured a tetrameric state for the PDGF-βR in agreement with ICS studies [22].

Accuracy and Precision of Spatial ICS

Costantino et al. [23] used computer simulations to determine the factors that affect the accuracy and precision of ICS measurements. They found that the two most important parameters are the number of sample laser beam areas in an image (i.e., the number of spatial intensity fluctuations) and background noise. The first criterion can be optimized by analyzing the largest homogeneous region in the sample. Although ICS can be performed on regions as small as 16×16 pixels^2 ($\sim$1.5 μm^2), larger regions will yield more accurate results. The whole region of analysis should be "on cell," since discontinuities in fluorescence, such as those caused by the edge of a cell, can introduce significant perturbations in the correlation function and its fit (see Section "Practical Guidelines for ICS Analysis"). In most cell measurements, background noise is the most important source of error, and can be minimized by the careful adjustment of microscope detectors, and a calibration of the fluorescence level from a monomeric unit of fluorophore either immobilized in a solid matrix or adsorbed on a coverslip (if possible within the detection limits of the microscope). It is of paramount importance to subtract the correct amount of background intensity from the data before the analysis to obtain an unbiased estimate of the number density. This background correction has been discussed for both single measurements [23] and population averages [22]. Both autofluorescence from within the cell and non-specific antibody labeling in the extracellular environment can contribute intensity counts to an image. Both of these effects can be corrected for in ICS measurements [22]. Photon counting head detectors usually have greater sensitivity than analog photomultiplier tubes typically found on confocal microscopes. However, the latter type of detectors are satisfactory for ICS measurements as long as they are operated in a linear regime.

The statistics of ICS measurements have also been examined from a theoretical statistics perspective [33].

Temporal Image Correlation Spectroscopy

Spatial ICS can measure the number density and aggregation state of fluorescently labeled macromolecules. However, spatial ICS cannot extract dynamics because it only analyzes the spatial fluctuations in an image. Temporal image correlation spectroscopy (TICS) was introduced as an alternative to SFCS and FCS for slow moving membrane proteins which allows the diffusion coefficient and flow speed to be measured from an image time series [25, 34]. Time correlation functions are sensitive to moving fluorescent particles if they stay within the area defined by the beam for a number of image frames. Both the transport mode and rate of the particles are manifested in the time correlation function.

TICS has also been referred to in the literature as image cross-correlation spectroscopy [34, 35] and dynamic image correlation spectroscopy [36]. We prefer to exclusively use the term TICS to refer to the technique described here, since "cross-correlation" often implies measurements with two different color detection channels.

The normalized intensity fluctuation temporal autocorrelation function of an image series as a function of time lag τ is obtained from Eq. 1 when ξ and $\eta = 0$:

$$r(0,0,\tau) = \frac{\langle \delta i(x,y,t)\delta i(x,y,t+\tau)\rangle}{\langle i(x,y,t)\rangle_t \langle i(x,y,t+\tau)\rangle_{t+\tau}} \tag{11}$$

where the angular brackets denote spatial and temporal averaging. Experimentally, τ values are determined by the time between subsequent images in the image series. Depending on the microscope system used, $\Delta\tau$ is usually between 0.03 and 10 s. As we will discuss in Section "Raster Image Correlation Spectroscopy," the imaging rate

must be appropriately matched to the time scale of the process of interest. An image series is discrete in both space and time, so a discrete approximation of the temporal autocorrelation function is calculated as follows:

$$r(0,0,s) = \frac{1}{N-s}\sum_{c=1}^{N-s}\frac{1}{XY} \sum_{x=1}^{X}\sum_{y=1}^{Y}\frac{\delta i(x,y,c)\delta i(x,y,c+s)}{\langle i(x,y,c)\rangle_c \langle i(x,y,c+s)\rangle_{c+s}} \tag{12}$$

where X and Y are the number of pixels spanning the region being analyzed, N is the number of images in the image series, s is the discrete analog of τ, and c is a dummy variable. The temporal correlation function calculated by Eq. 12 is then fit to the analytical decay model derived for the mode of transport present in the sample. Generally speaking, there are usually three parameters of interest determined from a time correlation function: its *amplitude*, which is inversely proportional to the number of particles (cf. Eq. 4); its decay *shape*, which describes the mode of transport the sample is undergoing (e.g., diffusion or flow); and its *rate of decay*, which describes how quickly the dynamic process is occurring.

For samples with 2D diffusion of the fluorescent particles, the temporal correlation function has the following decay form [8] (fit parameters in bold):

$$r(0,0,\tau) = \mathbf{g}(\mathbf{0},\mathbf{0},\mathbf{0})\left(1+\frac{\tau}{\boldsymbol{\tau}_d}\right)^{-1} + \mathbf{g}_\infty \tag{13}$$

where $\mathbf{g}(\mathbf{0},\mathbf{0},\mathbf{0})$ is the zero-lags amplitude, $\mathbf{g}_\infty$ is the long-time offset, and for confocal excitation, the characteristic diffusion time, $\boldsymbol{\tau}_\mathrm{d}$ is related to the diffusion coefficient, D by:

$$D = \frac{\langle \omega_0 \rangle}{4\tau_d}. \tag{14}$$

The mean fit e^{-2} radius, $\langle \boldsymbol{\omega}_0 \rangle$, for a particular analysis is usually determined by fitting the spatial autocorrelation function of each image to Eq. 9 and finding the average value of $\boldsymbol{\omega}_0$ for the time series [37]. As with spatial ICS (Section "Image Correlation Spectroscopy"), the value of $\boldsymbol{\omega}_0$ from the fits should be close to an independently measured value.

The correlation decay model of a sample with 2D flow is [10]:

$$r(0,0,\tau) = \mathbf{g}(\mathbf{0},\mathbf{0},\mathbf{0})\exp\left[-\left(\frac{\tau}{\boldsymbol{\tau}_f}\right)^2\right] + \mathbf{g}_\infty \tag{15}$$

where the characteristic flow time, $\boldsymbol{\tau}_f$, is used to calculate the flow speed, $|v|$:

$$|v| = \frac{\langle \omega_0 \rangle}{\tau_f}. \tag{16}$$

In the case where one population of particles simultaneously undergoes flow and diffusion, the autocorrelation function has the decay model:

$$r(0,0,\tau) = \mathbf{g}(\mathbf{0},\mathbf{0},\mathbf{0})\left(1+\frac{\tau}{\boldsymbol{\tau}_d}\right)^{-1}\exp\left[-\left(\frac{\tau}{\boldsymbol{\tau}_f}\right)^2\right] + \mathbf{g}_\infty. \tag{17}$$

If there are two populations in the sample, with one undergoing diffusion and the other flow, the decay model is:

$$r(0,0,\tau) = \mathbf{g}_1(\mathbf{0},\mathbf{0},\mathbf{0})\left(1+\frac{\tau}{\boldsymbol{\tau}_d}\right)^{-1} + \mathbf{g}_2(\mathbf{0},\mathbf{0},\mathbf{0})\exp\left[-\left(\frac{\tau}{\boldsymbol{\tau}_f}\right)^2\right] + \mathbf{g}_\infty. \tag{18}$$

The ability to resolve multiple populations in a sample is dependent on a number of factors including the relative concentrations and quantum yields of the different species. Although these limitations of ICS have not been studied, there has been an extensive investigation of the analogous restrictions in the context of FCS measurements [38].

The percentage of the population which is immobile can be calculated from the offset parameter $\mathbf{g}_\infty$ and the amplitude, $\mathbf{g}(\mathbf{0},\mathbf{0},\mathbf{0})$, obtained from the fits (Eqs. 13, 15, 17, or 18) [4]:

$$\%\,\text{immobile} = \frac{\mathbf{g}_\infty}{\mathbf{g}_\infty + \mathbf{g}(\mathbf{0},\mathbf{0},\mathbf{0})}. \tag{19}$$

There is evidence that the detection of an immobile fraction using fluorescence recovery after photobleaching (FRAP) is an artifact caused by anomalous subdiffusion [39]. This effect has not been examined in the context of TICS measurements, and it is possible that the long-time offset of a temporal autocorrelation function reflects anomalous subdiffusion occurring in the system instead of an immobile population.

Finally, assuming the laser excitation volume has a 3D Gaussian intensity profile, the functional form of the time correlation function for a system with 3D diffusion is [40]:

$$r(0,0,\tau) = \frac{\mathbf{g}(\mathbf{0},\mathbf{0},\mathbf{0})}{\left(1+\frac{\tau}{\tau_d}\right)\left(1+\frac{\langle \omega_0\rangle^2}{\langle z_0\rangle^2}\frac{\tau}{\tau_d}\right)^{1/2}} + \mathbf{g}_\infty \tag{20}$$

where $\langle z_0 \rangle$ is the mean e^{-2} radius of the laser focus in the axial direction. In practice, $\langle z_0 \rangle$ (and $\langle \boldsymbol{\omega}_0 \rangle$) can be obtained by 3D optical sectioning of a sample of sub-diffraction-limit fluorescent microspheres distributed on a glass coverslip. Experimental temporal autocorrelation

functions for diffusing and flowing microsphere samples are presented in Fig. 3, along with fits to Eqs. 20 and 15.

Comparison of TICS, Fluorescence Recovery after Photobleaching, and Single Particle Tracking

In addition to TICS, a number of other techniques have been developed to measure membrane dynamics, including SPT and FRAP. We will briefly discuss their relative advantages and disadvantages. SPT follows the location of one particle as a function of time to discern its mode of transport and diffusion coefficient or flow speed. Because the behavior of each particle is measured, subpopulations of particles can be clearly resolved [41]. In contrast, fluctuation correlation methods such as FCS and ICS measure, by their nature, an ensemble of particles and often report an average value, but not its distribution. Unlike single molecule techniques, such as SPT, fluctuation techniques may not be able to detect a subpopulation made up of a small fraction of the particles [38]. However, correlation techniques are generally more straightforward, and less time-consuming to implement (see supplemental material in [42] for a comparison of SPT and ICS). Another key advantage of fluctuation techniques is that they can by applied to both relatively low and high density samples [43], unlike SPT which requires individual particles to be well separated. This need for low-density labeling is often incompatible with GFP transfections of proteins expressed at native levels in cells where individual fluorophores are not well resolved. Because SPT requires a low-density, high quantum-yield fluorophore, quantum dots (QDs) or colloidal gold particles are often used to label proteins of interest [44]. However, most methods of labeling a cell surface protein with these probes involve multivalent ligands, which can lead to unintended clustering of proteins and a concomitant erroneous determination of the macromolecule's dynamics [41, 44].

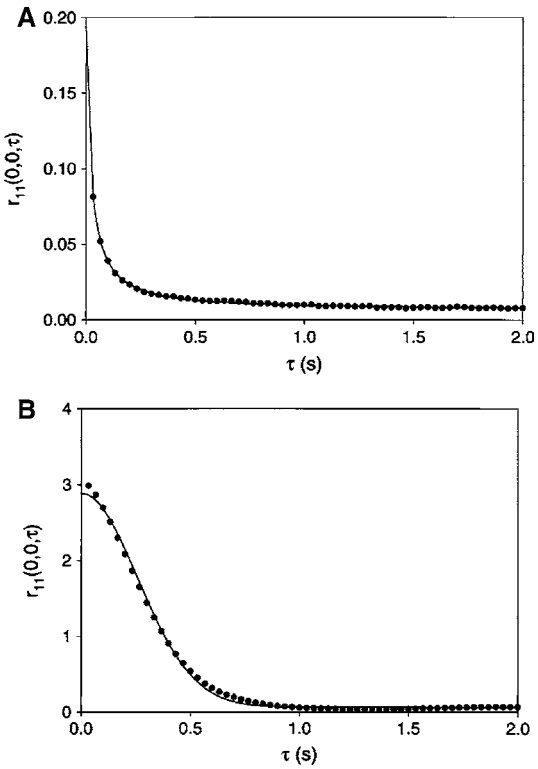

Fig. 3 Temporal image correlation decays for fluorescent microspheres in aqueous sucrose solution, imaged on a two-photon laser scanning microscope, undergoing (**A**) diffusion and (**B**) flow. From Ref. [25], with permission

FRAP monitors the spontaneous recovery of fluorescence in a region of the cell membrane after all fluorophores in the region have been bleached with a laser pulse [45]. FRAP is capable of determining both the diffusion coefficient and immobile fraction of a system of fluorescently tagged molecules [46]. However, the technique requires the introduction of a large external perturbation by using high intensity laser illumination. Some studies have suggested this light can potentially injure the cell or induce cross-linking of membrane receptors [47, 48], but the general consensus is that there is no such damage [49, 50]. In contrast, TICS uses a much lower laser excitation power, and studies the system at equilibrium or biological steady state.

Data in FCS and FRAP experiments are sometimes fit to anomalous subdiffusion models [39, 51], in which particles exhibit a restricted mobility, but are not immobilized. It is thought that this non-Brownian behavior is the result of fixed obstacles or lipid rafts in the membrane [52]. To date, TICS data have not yet been fit to anomalous subdiffusion models, and it would be beneficial to study systems with a number of techniques and over a range of time scales.

Accuracy of, and Photobleaching in, TICS

Kolin et al. [43] examined the accuracy of TICS measurements by using computer simulations of LSM imaging of point emitters undergoing diffusion and flow. They found that, as with spatial ICS, recovering accurate number densities from TICS autocorrelation functions was primarily limited by background noise in the sample. In contrast, diffusion coefficients and flow speeds could be recovered in the presence of high levels of background noise, and their accuracy was governed by spatiotemporal sampling (i.e., the number of pixels in the region of analysis, and the number of frames in the image time series). The effect of photobleaching on temporal autocorrelation

function decays was also studied in the same work, and it was found to cause a severe underestimation in number densities (by approximately a factor of 5), and a smaller, but still significant, overestimation of diffusion coefficients and flow speeds (roughly 20% for diffusion, and 5% for flow). For the case of irreversible monoexponential photobleaching, the authors provide a correction factor which can be used when fitting the data to recover unbiased values of $\langle n_p \rangle$, D, and v.

Cytosolic fluorophore populations should not interfere with TICS measurements of fluorescently labeled membrane proteins. Since proteins in the cytosol diffuse approximately two orders of magnitude faster than membrane-bound proteins, any concentration fluctuations due to fluorophores in the cytosol will be completely decorrelated in subsequent images, which are typically acquired at imaging rates below 10 Hz. Although the dynamics of these quickly diffusing species cannot be measured from LSM-acquired image series using TICS, we will describe a novel extension of ICS in Section "Raster Image Correlation Spectroscopy" that can measure such faster transport processes.

Image Cross-Correlation Spectroscopy

Image cross-correlation spectroscopy (ICCS) quantifies the coincident spatial fluctuations of two images collected in two different detection channels. Usually, two fluorophores with different emission wavelengths are attached to two different proteins of interest. The two fluorophores are imaged on a microscope that spectrally resolves the emissions, and an image is collected for each detection channel: $i_a(x, y)$ and $i_b(x, y)$. The normalized intensity 2D spatial cross-correlation function for these two images is given by Eq. 1 with $\tau = 0$:

$$r_{ab}(\xi,\eta) = \frac{\langle \delta i_a(x,y)\delta i_b(x+\xi,y+\eta)\rangle}{\langle i_a(x,y)\rangle\langle i_b(x,y)\rangle}, \tag{21}$$

and is calculated using Fourier methods, just as with a spatial autocorrelation function (Eq. 8). The average number of colocalized independent fluorescent particles in the beam area, $\langle n_{ab} \rangle$ is:

$$\langle n_{ab}\rangle = \frac{g_{ab}(0,0)}{g_{aa}(0,0)g_{bb}(0,0)}, \tag{22}$$

where $g_{ab}(0,0)$ is the amplitude of the cross-correlation function, and $g_{aa}(0,0)$ and $g_{bb}(0,0)$ are the amplitudes of the autocorrelation functions for channels a and b, respectively. All three amplitudes are determined by nonlinear curve fitting of their respective correlation functions to Eq. 9. The number density $\langle n_{ab} \rangle$ is usually transformed to a CD (as in Eq. 5), or the fraction of protein 1 interacting with protein 2 (or vice-versa) using $\langle n_a \rangle$ or $\langle n_b \rangle$.

A dual-labeled sample can be imaged as a function of time, and the fluorescence emissions imaged simultaneously in two detection channels to generate a dual-color image time series. A temporal cross-correlation function can be calculated from this image series, which is given by Eq. 1 with the spatial-lag variables ξ and η set to zero:

$$r_{ab}(0,0,\tau) = \frac{\langle \delta i_a(x,y,t)\delta i_b(x,y,t+\tau)\rangle}{\langle i_a(x,y,t)\rangle_t \langle i_b(x,y,t+\tau)\rangle_{t+\tau}}. \tag{23}$$

If a fraction of the two populations are interacting on the time scale of the measurement, $r_{ab}(0,0,\tau)$ can be fit to the same analytical models as the temporal autocorrelation decays (e.g., Eqs. 13, 15, 17, or 18 or 20) to determine the dynamics of the interacting complex. If there is no interaction between the species, the cross-correlation function will be zero for all τ if sampling of fluctuations is sufficient.

Advantages, Limitations, and Dynamic Range of ICCS

As alternatives to ICCS, protein–protein interactions can also be measured using automatic colocalization algorithms [53, 54]. These techniques calculate the interaction fraction for two protein species separately labeled with different color fluorophores based on the amount of signal overlap between pixels at the same image location for the two detection channels. Comeau et al. [55] and Costantino et al. [23] extensively studied the accuracy of ICCS and compared it to the automatic colocalization algorithms commonly found in commercial microscope software, and found the two techniques were complimentary and delivered accurate results under different experimental conditions. Specifically, spatial ICCS is able to accurately determine the fraction of proteins interacting over several orders of magnitude in concentration. In contrast, automatic colocalization usually provides accurate estimates at low fluorophore density, but can overestimate the fraction of interacting protein at higher concentration levels. Furthermore, spatial ICCS only works well when the interaction fraction is higher than 20% (for a typical image size of 256×256 pixels), while automatic colocalization will return an erroneous result if there is more than a factor of 2 difference between the concentration of the two populations being measured. Also, ICCS is substantially less affected by the signal-to-noise of the images than automatic colocalization algorithms [55].

An advantage of ICCS is its ability to automatically correct for different spatial alignments of the two channels. Chromatic aberrations in microscope objectives,

misalignment of optical components, and vibrations and mechanical instability of the scanning system can all cause a shift of more than one pixel between two color images acquired from the same sample [56]. Automatic colocalization techniques are greatly affected by systematic shifts since they directly compare pixels at the same image coordinate, so the raw data must be appropriately corrected for this shift. Although more sophisticated colocalization implementations include this pre-registration (such as the Medical Image Processing, Analysis, and Visualization (MIPAV)) software package developed by the Center for Information Technology, National Institutes of Health [57]), most do not automatically account for this shift. In contrast, a spatial shift between two images used for cross-correlation analysis would simply introduce a shift in the location of the cross-correlation function maximum, but would not alter the key parameter, its amplitude [55].

Automatic colocalization algorithms require that both channels in the optical setup have the same PSF [54], while cross-correlation calculations can be corrected for PSFs of different sizes [55, 58]. Additionally, the automatic colocalization algorithms force each pixel to be classified as either colocalized or non-colocalized, in contrast to ICCS, which takes into account that the PSF convolution causes intensity counts to be present in pixels adjacent to those where fluorophores are actually centered.

FRET has also been used to probe protein–protein interactions in live cells [59]. FRET measures the amount of non-radiative energy transfer between a donor and an acceptor fluorophore. In vitro measurements can give accurate distance measurements on the order of 1–10 nm, while measurements in live cells typically detect either the presence or absence of the transfer. Unlike FRET, cross-correlation cannot determine the average separation between two fluorophores. It can only give the fraction of the labeled species, which are located together spatially or travel together temporally in a common complex. However, some biomacromolecular complexes are so large that FRET cannot be used to measure the separation between two different components on opposite sides of the aggregate. Also, ICCS and automatic colocalization would find two components colocalized if they were in a common subcellular compartment, whose size was below the diffraction limit ($\sim$200 nm) and were imaged in the same pixel location. On the other hand, FRET could be used to differentiate between a true close interaction between two components, and a common compartmentalization.

As with ICS, the images analyzed must be relatively homogeneous, and without sharp bands of intensity or discontinuities. For example, ICS and ICCS may be appropriate for studying transmembrane proteins in the plasma membrane, but not the trans-Golgi network. Also, spectral bleed-through of signal (also known as cross-talk) between the detection channels must be corrected for to prevent artifacts in ICCS analyses.

Correlation Techniques for Non-Planar Regions of Cells

Image correlation techniques assume that the imaged membrane is perfectly flat. A small slope or undulations in the membrane would perturb the correlation functions. Petersen [12] examined the effect of a sloped membrane on spatial ICS measurements using simulations and found that while the $\mathbf{g}(\mathbf{0},\mathbf{0},\mathbf{0})_t$ value is not significantly affected, a degree of aggregation calculation (cf. Eq. 6) would be underestimated. The membrane slope causes this effect because the out-of-focus membrane contributes less to the intensity, and $\langle i \rangle$ is lower than if the membrane were entirely in focus. Milon et al. [60] investigated the effect of sloped, out-of-focus, or undulating membranes on FCS autocorrelation functions using simulations and measurements on large unilamellar vesicles, and found that these membrane characteristics could cause the diffusion coefficient could be underestimated by approximately a factor of 3 in FCS measurements on typical cells.

Some cell lines, such as leukocytes, are spherical and do not have flat areas appropriate for traditional ICS analysis. In this situation, a cell can be imaged on a LSM and using the microscope's inherent optical sectioning capability, and a z-slice can be obtained from an axially central region, in which neither the basal nor the apical membranes are visible yielding an image with "ring" staining for a membrane protein. Afterwards, a fluorescence trace around this "ring" can be extracted. This fluorescence record has been used to measure colocalization using a cross-correlation approach [61–63], as well as dynamics using a modified TICS analysis [64]. This technique is summarized in Fig. 4. A line trace around the perimeter of a cell membrane samples far fewer fluctuations than an image of a planar region of the membrane; therefore, these variants have an inherently lower signal-to-noise ratio than their imaging counterparts, and are best suited to round cell types which lack a large, relatively flat membrane region.

Spatiotemporal Image Correlation Spectroscopy

TICS is able to measure the *magnitude*, but not the *direction* of a concerted flux of flowing fluorophores (i.e., the flow speed). As first suggested in [65], the direction of the flow can be determined by calculating a full spatiotemporal correlation function. The technique was later fully developed and verified, and was named spatiotemporal ICS

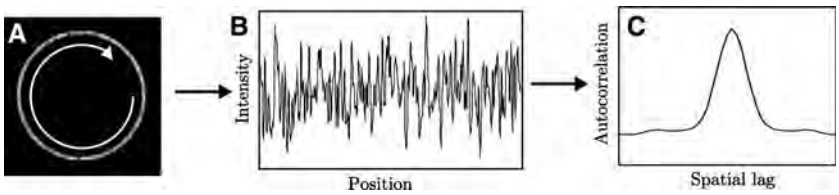

Fig. 4 An overview of ring correlation spectroscopy (RCS). (**A**) The image series collected in time from an optical section of the entire "spherical cell" at its equator. The resulting image series contains intensity rings for labeled membrane species. (**B**) In RCS, the intensity trace around the cell membrane is extracted for each image in the time series. (**C**) These membrane perimeter intensity records are correlated in space (for each ring) as well as time for a given membrane pixel location to measure the number density, dynamics, or interacting fractions of the fluorescently labeled proteins

(STICS) [20]. Recently, a similar technique has also been developed independently [66]. The theory of STICS analysis is similar to particle image velocimetry (PIV), a technique developed in 1984 to measure the turbulent flow of non-fluorescent micron-sized beads in fluids [67]. However, STICS incorporates greater temporal lag sampling into the calculation of the space–time correlation function from which velocity vectors are measured.

A spatiotemporal correlation function is defined in Eq. 1. As with ICS autocorrelation functions, this function is usually calculated with FFTs using the Wiener-Khinchin theorem (Eq. 8), because using the FFT is several times faster than the "direct" calculation [17]. The point spread function of laser scanning and TIRF microscopes is approximately Gaussian in the axial plane, so a STICS correlation function is usually a 2D Gaussian which moves from the zero-lags center as a function of time lag if there is a flow present (Fig. 5A(ii)). The velocity of the sample is determined by tracking the center of the moving peak at each time lag. Linear regressions of the x- and y-coordinates of the peak location as a function of time yield the x- and y-components of the velocity for uniform motion (Fig. 5C) [20]. As with PIV, using FFTs can introduce a significant bias in the correlation function if the PSF is on

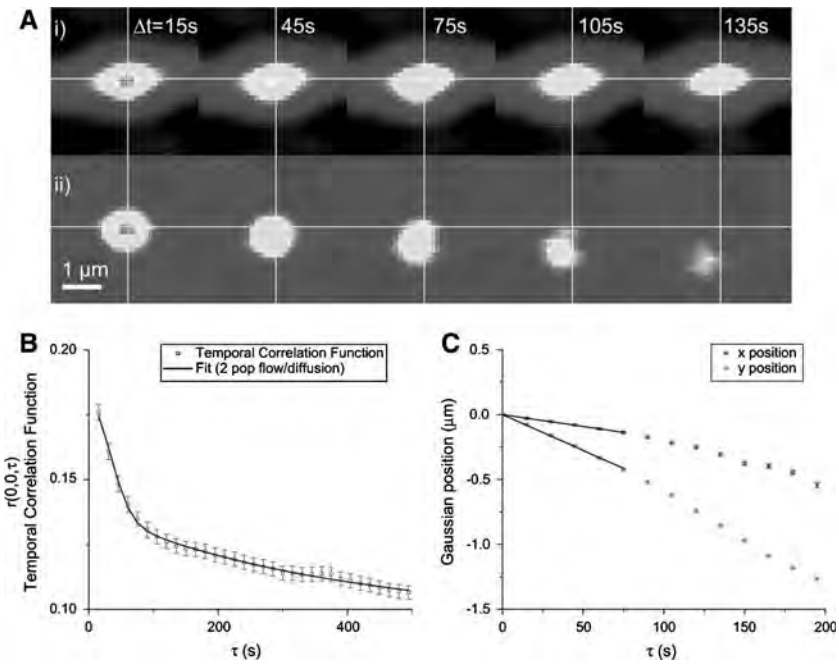

Fig. 5 STICS (**A**, **C**) and TICS (**B**) analysis of a region of the basal membrane of a living CHO cell expressing α-actinin-eGFP. The spatiotemporal correlation function without immobile population removal (**A**(i)) does not show a clear flowing population because the flowing component is masked by a slowly diffusing or immobile component. However, when the immobile filtering is applied (**A**(ii)), a flowing component becomes readily visible, and is easily tracked in the STICS correlation function. This peak location is tracked, and a linear regression of each of the x and y peak positions as a function of time lag, τ, gives the velocity vector components $v_x = (1.8 \pm 0.3) \times 10^{-3}$ μm/s and $v_y = (5.5 \pm 0.2) \times 10^{-3}$ μm/s, respectively (**C**). TICS analysis of the same region yields a temporal autocorrelation function best fit by a two-population flow/diffusion model, giving $v_{ICS} = (7.7 \pm 0.8) \times 10^{-3}$μm/s and $D = (6 \pm 1) \times 10^{-5}$ μm^2/s. From Ref. [20], with permission

the order of the size of the window used in STICS analysis [68]. This regime is usually not encountered with typical applications of STICS.

As with ICS, a STICS analysis is usually performed on different subregions of a cell (e.g., Fig. 6B). In the most recent application, a high-resolution variant has been used in which many small, partially overlapping regions are analyzed on the same sample (usually areas of 16×16 pixels^2, where each new region is offset 4 pixels from an adjacent region; see Fig. 7).

In many biological systems, two different proteins may interact periodically, but are not always colocalized. In such a case, a STICCS cross-correlation analysis will not yield a measurable Gaussian peak, because the correlation decays too quickly. In these situations, vector maps from each individual channel can be calculated (Fig. 7). The interaction between the two different proteins can then be quantified by comparing the relative magnitude and orientation of corresponding vectors in the velocity maps [69]. Brown et al. [69] hypothesize that this data treatment reveals the transient interaction between two different proteins because the binding and unbinding will lead to a fractional correlation in the two velocities. This method of analyzing dual-color STICS vector maps is thus a useful way to quantify transient protein–protein interactions when there is not a measurable cross-correlation.

Immobile Population Removal

The STICS theory presented to this point assumes there is only one population of fluorophores, which is flowing. However, in living cells, there is often a significant fraction of labeled protein that is either slowing diffusing or immobile in the plasma membrane on the measurement time scale. Either of these non-flowing populations, if present, are manifested in the STICS correlation function, and can prevent an accurate tracking of the flow correlation peak (Fig 5A(i)) [20].

The immobile population is usually removed from an image series prior to STICS analysis by subtracting the "mean image" of the image series from each image. This can be accomplished quickly by Fourier transforming in time each pixel trace in the image series, setting the DC component of the transforms to zero, and inverse Fourier transforming each pixel trace to recover the original movie with only the moving components preserved [20].

Slowly diffusing particles will also create a central lags peak in the STICS correlation function, which can mask the flow correlation peak which must be well-resolved to be tracked and to recover an accurate velocity. Using the previously described Fourier-based immobile population removal will only partially eliminate the contribution of the diffusing population to the correlation function [20]. An alternative method of removing slowly moving features in an image series is to use a moving average filter [70]. The variable temporal window size used in the filter determines which features are removed.

k-Space Image Correlation Spectroscopy

Concentration correlation techniques measure the underlying dynamics of a system by calculating a correlation function of spontaneous fluctuations observed as fluorophores move in and out of a small observation volume. To extract meaningful dynamics such as the diffusion coefficient or flow speed, these correlation functions are fit to different analytical models depending of the type of transport process the fluorophores are undergoing (e.g., Eqs. 13 and 15 for diffusion and flow, respectively). These analytical functions were derived assuming that the

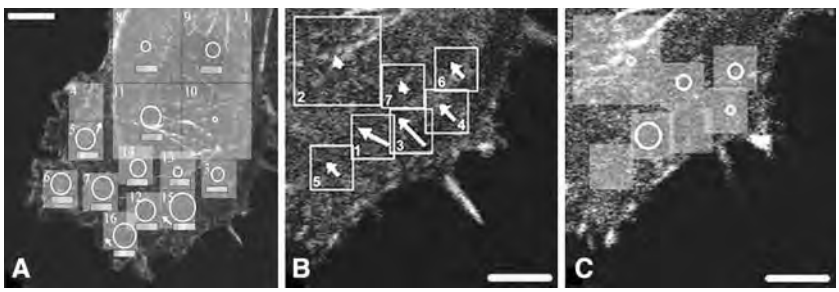

Fig. 6 (**A**) Dynamics of α-actinin-GFP fusion proteins in a live CHO-B2 cell, imaged on a two-photon LSM, were measured using TICS and STICS analysis. The region of the cell beneath area "3" in (**A**) was analyzed in more detail both before (**B**) and after (**C**) retraction of a microspike. There was a concerted flux of α-actinin away from the microspike during the retraction (**B**), while only diffusion was detected in those regions after the retraction (**C**). Circles indicate the average 10 min root-mean-square diffusion distance from the center of the circle. Arrows give the direction and average 10 min displacement for proteins undergoing flow in a particular region, as determined using STICS. The pixel size in all three image series was 0.118 μm, and images were acquired at 5 s intervals. Scale bars are 10 μm (**A**) and 5 μm (**B** and **C**). From Ref. [4], with permission

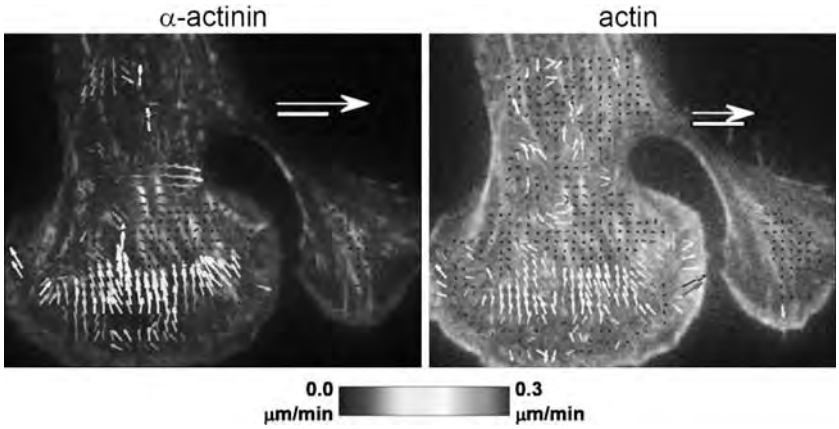

Fig. 7 High-resolution velocity maps of α-actinin-eGFP and actin-mRFP in an MEF cell plated on 1 μg/ml fibronectin. Image series were acquired on a TIRF microscope (Olympus IX70) with a Retiga EXi CCD camera. The color scale is common between both maps (see colorbar below images). The length scale of the velocity arrows varies between both maps; in both cases the velocity scale arrow represents 0.5 μm/min, and the spatial scale bar is 5 μm. Each analysis used 100 images, acquired at intervals of 10 s, with a pixel size of 0.215 μm. The relative directional correlation and relative velocity magnitude between both maps can be calculated. From Ref. [69], with permission

movement of fluorophores is the only process causing fluctuations in the collected fluorescence [8, 10]. However, many fluorophores have time dependent photophysical properties, such as fluorophore photobleaching [71] and intermittent fluorescence or "blinking" [72]. In fluorescence correlation techniques such as FCS and TICS, these intensity fluctuations due to the fluorophore photophysics must be taken into account when fitting the decay with an analytical model. If not, the experimental autocorrelation function may appear to be fit well by a model which only accounts for transport, but the transport coefficients recovered may be highly erroneous [43, 73].

Blinking of organic fluorophores occurs on the microsecond time scale, and is not sampled in the TICS autocorrelation functions because it occurs much faster than the imaging rate; any correlations due to triplet state photophysics are completely lost by the time a subsequent image is acquired. As described for TICS in Section "Accuracy of, and Photobleaching in, TICS," photobleaching of organic fluorophores can significantly affect the diffusion coefficient and flow speed obtained from temporal autocorrelation functions. This perturbation can be corrected for by fitting to an analytical model, which takes into account a first-order photobleaching contribution to the correlation function [43]. However, fluorescent proteins can also undergo reversible photobleaching [71], and this behavior is not easily measured from an image series of a live cell or corrected for in TICS studies. As well, QDs have recently emerged as novel fluorescent tags for biological macromolecules. Unlike organic fluorophores, QDs exhibit greatly reduced photobleaching under continuous laser excitation for extended periods of time (minutes to hours) [74, 75]. However, they do exhibit significant emission "blinking," in which individual QDs alternate between "on" and "off" states [76]. In contrast to organic fluorophores whose "on" and "off" distributions are characterized by exponential distributions [72], those of QDs are governed by extended power-law distributions in time [77]. These power-law distributions do not have a characteristic (i.e., average) "on" or "off" time. There have been recent efforts to derive an analytical model for temporal autocorrelation functions of QD blinking [78, 79]. However, their results are very complex, have not been yet tested experimentally, and are not directly amenable to experimentally measured correlation functions for blinking and diffusing QDs.

k-Space image correlation spectroscopy (kICS) is a useful new image correlation technique applicable when fluorophores undergo significant photobleaching or "blinking," because it always returns unbiased estimates of the fluorophore dynamics without any previous knowledge of the photophysics or PSF of the system [80]. As with the previously mentioned techniques, the seminal measurement in kICS is a microscope image time series, $i(\mathbf{r}, t)$. With kICS, each image is 2D Fourier transformed in space to yield $\tilde{i}(\mathbf{k}, t)$, before being correlated in time. (With modern computers, performing the transform prior to correlating imparts only a small increase in analysis time.) We define a reciprocal-space time correlation function, $r(\mathbf{k}, \tau)$, as:

$$r(\mathbf{k}, \tau) = \langle \tilde{i}(\mathbf{k}, t)\tilde{i}^*(\mathbf{k}, t+\tau) \rangle, \tag{24}$$

where the angular brackets denote a time average. The notation $\tilde{i}^*(\mathbf{k}, t+\tau)$ denotes the complex conjugate of the

2D spatial Fourier transform of image $i(\mathbf{r}, t + \tau)$. Assuming the system is imaged on a microscope with a Gaussian PSF, $r(\mathbf{k},\tau)$ has the following form for a 2D system of a population of fluorescent particles undergoing diffusion and flow [80]:

$$r(\mathbf{k},\tau) = N\frac{q^2 I_0^2 \omega_0^4 \pi^2}{4}\langle\Theta(t)\Theta(t+\tau)\rangle \times \exp\left[i\mathbf{k}\cdot\mathbf{v}\tau - |\mathbf{k}|^2\left(D\tau + \frac{\omega_0^2}{4}\right)\right], \quad (25)$$

where N is the number of particles in the image, q is the quantum yield, I_0 is the incident laser central peak intensity, $\mathbf{v}$ is the velocity of the particles, and $\Theta(t)$ is 1 if a particle is fluorescing at time t and 0 otherwise. The angular brackets denote an average over all particles in the image. For a sample undergoing diffusion, D is calculated by circularly averaging $r(\mathbf{k},\tau)$ and taking the natural logarithm:

$$\ln[r(|\mathbf{k}|^2,\tau)] = \ln\left[N\frac{q^2 I_0^2 \omega_0^4 \pi^2}{4}\langle\Theta(t)\Theta(t+\tau)\rangle\right] - |\mathbf{k}|^2\left(D\tau + \frac{\omega_0^2}{4}\right). \quad (26)$$

Note that the first term is constant for a given value of τ, and D can be extracted from $\ln[r(|\mathbf{k}|^2,\tau)]$ with several linear regressions (Fig. 8). In contrast to r-space correlation techniques, D can be calculated without any knowledge of the fluorophore photophysics [80, 81]. An application of kICS to QD blinking is described in Section "Fluorophore Photophysics."

We have recently shown that a new implementation of kICS can give a PSF-independent correlation function [81]. Therefore, kICS analysis does not require a calibration of the PSF of the imaging system, and automatically accounts for a non-Gaussian PSF, or an any asymmetry in the focal plane due to misalignment of optics.

One disadvantage of kICS is that it cannot be applied to arbitrarily small regions of cells. The analysis involves a linear regression (cf. Fig. 8), and depending on the sample size and noise level, a reliable fit may not be possible. Under typical imaging conditions, this usually limits analyses to image series 32×32 pixels^2 or larger, precluding the study of small cells such as yeast or bacteria.

The theory of kICS is very similar to that of dynamic light scattering [82], however the instrumental implementation and systems studied vary significantly. Fink et al. [19] and Hattori et al. [83] have developed techniques similar to kICS to selectively probe wavevectors using two interfering laser beams. These techniques can recover the same quantities as kICS; however, they require specialized equipment and cannot be applied directly to image series acquired on commercial imaging microscope, as can kICS.

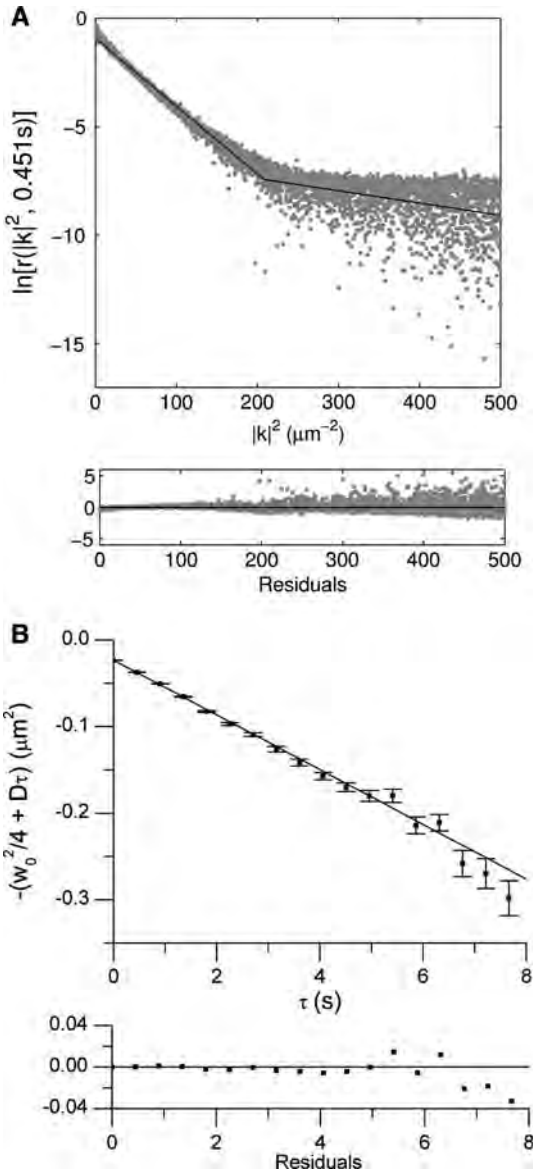

Fig. 8 (**A**) The circularly averaged, natural logarithm of the *k*-space time correlation function at $\tau = 0.451$ s for a sample of diffusing microspheres, with a radius of 0.1 μm, in sucrose solution. The image series was acquired on a confocal laser scanning microscope. The intercept of the correlation function as $|\mathbf{k}^2| \rightarrow 0$ is proportional to the number of particles in the image, and is also dependent on the photophysics of the fluorophore. The slope of the first segment (i.e., at low $|\mathbf{k}^2|$) is related to the diffusion coefficient (cf. Eq. 26). Noise is manifested in the second segment (i.e., at high $|\mathbf{k}^2|$). An analogous regression is performed for $r(\mathbf{k}, \tau)$ for each value of τ. (**B**) The slopes obtained from the plots of (**A**) at different τ values are plotted as a function of τ, and the diffusion coefficient is given by this slope. In this case, $D = (0.0316 \pm 0.0002)$ μm^2/s. From Ref. [80], with permission

Raster Image Correlation Spectroscopy

For TICS and kICS analysis, the imaging rate of the microscope dictates the maximum rate of a diffusive

process which can be measured [43]. On a typical LSM, this limits the largest diffusion coefficient measurable to approximately 10^{-9} cm^2/s. Most membrane proteins diffuse more slowly than this, so applying TICS to image series collected on an LSM is often an appropriate method to study this phenomenon. However, small molecules or proteins in solution diffuse far too quickly to be studied using either TICS or kICS, because fluorophores enter and leave the small focal volume long before a subsequent image is acquired, so intensity fluctuations in adjacent images in the image series are completely uncorrelated. Until recently, these fast dynamics could only be measured using FCS, which is not included with most commercial LSMs. A new approach, raster image correlation spectroscopy (RICS) allows fast dynamics to be probed on standard LSMs, which are common in life science research environments.

Digman et al. [84, 85] developed RICS, which allows one to measure rapid diffusion on a commercial LSM analogous to what can be measured with single-point FCS. These microscopes generate an image by using galvanometer mirrors to raster a laser beam across a sample, recording one pixel at a time. The raster-scanning used to generate an image introduces a time structure into the image since different parts of the image are acquired at different times (Fig. 9). RICS can therefore measure the diffusion coefficient of a sample of fluorophores imaged on a LSM by taking advantage of spatial correlations due to the raster pattern in which the image is constructed.

As with spatial ICS, the RICS autocorrelation function of an image collected on a confocal or two-photon laser scanning microscope is defined as in Eq. 7. If particles diffuse significantly on the time scale of image acquisition, the spatial autocorrelation function will not have an isotropic Gaussian shape (cf. Eq. 9, Fig. 2B). Instead, it will be "stretched" out in the fast scan direction, and the diffusion coefficient may be extracted by taking into account the time structure of the image introduced by the scanning mechanism (Fig. 10). In this case, the analytical form of the spatial autocorrelation function, $G_s(\xi,\eta)$, is:

$$G_S(\xi,\eta) = S(\xi,\eta) \times G(\xi,\eta) \tag{27}$$

where $S(\xi,\eta)$ is the correlation function due to the scanning of the laser beam, and $G(\xi,\eta)$ is the correlation function due to diffusion. Because the laser beam scanning and particle diffusion are independent processes, the correlation function $G_s(\xi,\eta)$ (Eq. 27) is the product of the correlation function for each process. A number of analytical forms of $S(\xi,\eta)$ exist for different scanning geometries [85]. When an image is collected on a commercial LSM, the laser is raster scanned across the sample line-by-line, and $S(\xi,\eta)$ has the following form:

$$S(\xi,\eta) = \exp\left[-\frac{\frac{\delta r^2}{\omega_0^2}\left(|\xi|^2+|\eta|^2\right)}{1+\frac{4D(\tau_p|\xi|+\tau_1|\eta|)}{\omega_0^2}}\right] \tag{28}$$

where τ_p is the pixel residence time, τ_1 is the line repetition time, δ_r is the pixel size, and

$$G(\xi,\eta) = \frac{\gamma}{N}\left(1+\frac{4D(\tau_p|\xi|+\tau_1|\eta|)}{\omega_0^2}\right)^{-1} \times \left(1+\frac{4D(\tau_p|\xi|+\tau_1|\eta|)}{\omega_z^2}\right)^{-1/2} \tag{29}$$

where γ is a factor describing the geometry of the laser beam [86]. It should be noted that the spatial lag variables ξ and η in Eqs. 28 and 29 are in pixel units, and not microns as in Eq. 9.

As with STICS, an immobile or slowly diffusing population can mask the correlation function of interest [20, 85]. Therefore, when RICS is used to measure cytosolic dynamics in living cells, either a Fourier or moving average filter may be required [85] (Fig. 10).

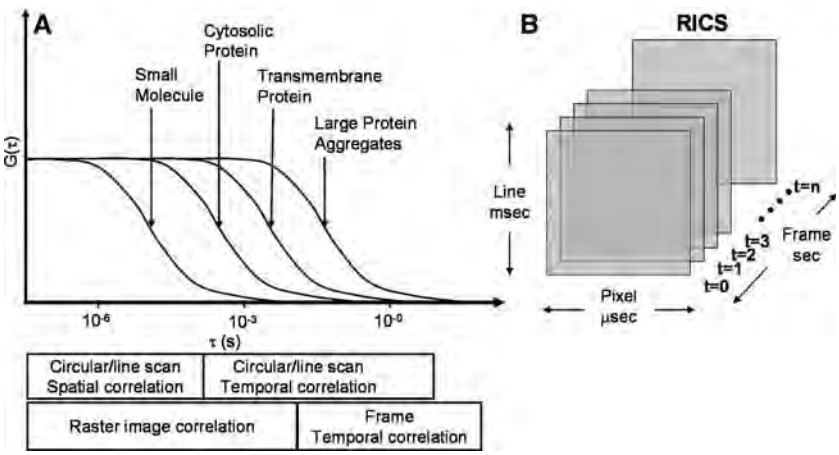

Fig. 9 (**A**) Dynamics of fluorophores attached to biomolecules ranging in size from small molecules to large protein aggregates in membranes can be measured using a LSM by applying a variety of correlation techniques. (**B**) An image series acquired on an LSM contains information on time scales from the microsecond to second regimes. Using RICS, it is possible to exploit this time structure to measure fast diffusion processes. From Ref. [85], with permission

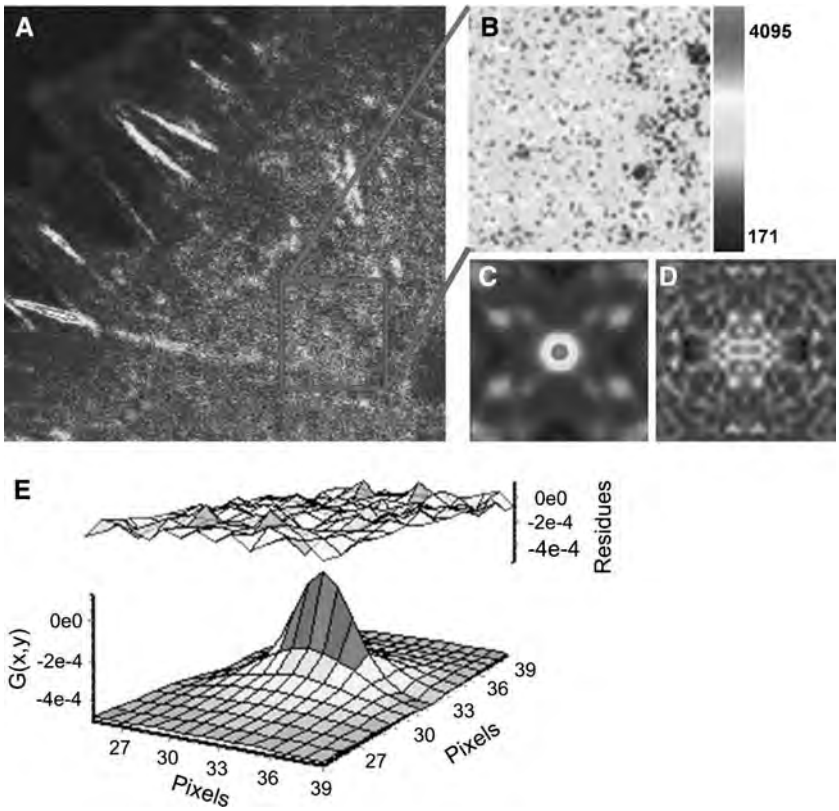

Fig. 10 (**A**) An image of a CHO K1 cell transfected with a paxillin-eGFP fusion protein, imaged on a confocal LSM. (**B**) An enlargement of the 64×64 pixel^2 region outlined in (**A**). The correlation function for the region shown in (**B**) both without (**C**) and with (**D**) immobile removal. (**E**) The correlation function in (**D**) was fit to Eq. 27, using Eqs. 28 and 29, giving $D = 8.3$ μm^2/s. The pixel dwell time was 8 μs, the pixel size was 0.09 μm, and the line scan time was 5.05 ms. To improve the measurement signal-to-noise, the average of correlation functions from 23 regions in identical locations in sequential images were used to calculate the correlation functions in (**C**) and (**D**). From Ref. [85], with permission

Particle Image Correlation Spectroscopy

Semrau and Schmidt [87] recently introduced PICS, a hybrid technique, which contains elements of both image correlation and particle tracking. One step in SPT data analysis is linking particle positions in subsequent images into particle trajectories. This process can be a challenge at high densities, when the inter-particle spacing approaches the step size of particle movements. One limitation of ICS is its insensitivity to movements below the diffraction limit of the imaging system. The PICS technique avoids these two pitfalls and permits the measurement of arbitrarily high diffusion coefficients at high densities, as long as individual particles can be resolved. PICS involves first identifying individual particles in each image of an image time series. A temporal cumulative correlation function is then generated from these particle positions, and the diffusion coefficient is calculated from this correlation function. PICS provides an attractive alternative to other techniques when high fluorophore densities prevent SPT analysis, or dynamics which occur on a sub-diffraction-limit length scale preclude traditional ICS measurements.

Software for ICS Analysis

To aid researchers in adopting ICS techniques, we have made MATLAB implementations freely available at http://wiseman-group.mcgill.ca/. The software includes command-line implementations of ICS, TICS, STICS and a basic simulation program. A brief tutorial is included with the distribution. As well, a full-featured high-resolution STICS program is provided with a graphical user interface. For implementing techniques not provided at the above website, we recommend MATLAB or IDL as programming languages which are relatively easy-to-learn for those without formal programming training. Also, researchers may find the programs SimFCS and Globals for Imaging useful for FCS and RICS analysis. These programs are available at http://www.lfd.uci.edu/globals/.

Practical Guidelines for ICS Analysis

The accuracy and precision of the results obtained from the techniques described in this review are strongly dependent on the quality of the data, which is analyzed. In Fig. 11, we present images, which are either acceptable or unacceptable for ICS analysis, and describe some of the most common pitfalls. Although microscopy techniques are beyond the scope of this review, some excellent guidelines for fluorescence microscopy of live cells in general are in Ref. [88], and for confocals specifically in Ref. [89].

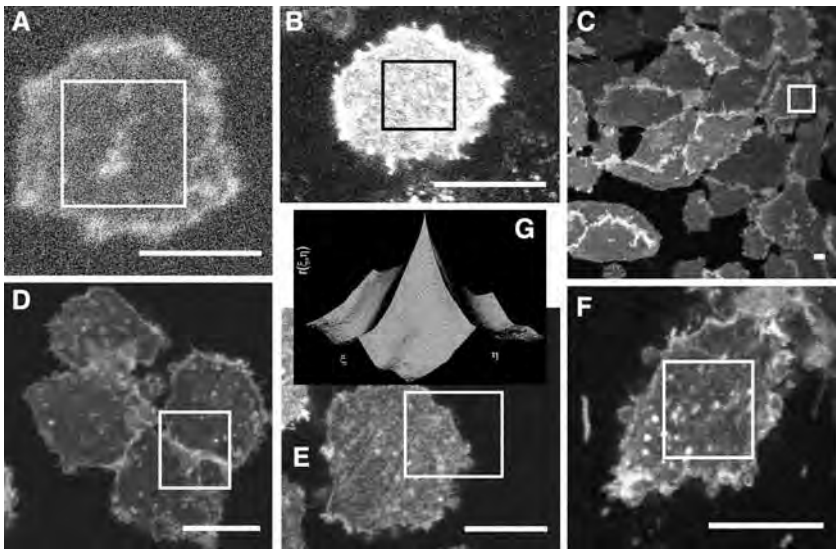

Fig. 11 Some common pitfalls in collecting suitable images for ICS analysis are illustrated with a series of images of CHO cells transfected with EGFR-eGFP imaged using a confocal LSM (Olympus FV300 IX71, with 60X 1.4 NA oil objective, and 488 nm line of an Ar^+ laser for excitation). These specific guidelines are given in the context of spatial ICS, although most are applicable to all of the forms of correlation analysis mentioned in the review. (**A**) Too much noise prevents an accurate determination of number density, and can be improved by averaging multiple frames in the series, changing the collection filters used, and by increasing the labeling efficiency, fluorophore brightness, detector sensitivity, or excitation intensity. (**B**) Detector saturation perturbs a correlation analysis by clipping the positive fluctuations. It can be avoided by decreasing the excitation intensity or detector sensitivity. An analogous effect occurs with negative fluctuations when a microscope offset setting is used to discard low intensity values. When collecting images for ICS analysis, the offset setting should be set to zero. (**C**) The microscope zoom used to collect this image gave a pixel size of ~0.5 μm/pixel, which is too large for ICS analysis because it does not sufficiently sample the decay of the beam PSF which acts as the correlator in the measurement. Appropriate pixel sizes for ICS are on the order of 0.05–0.1 μm/pixel. (**D**) The interface between the two cells in the region of interest creates a large, bright, heterogeneous signal, which yields an anisotropic correlation function that is fit poorly by Eq. 9. Analyzed areas should be relatively homogeneous with randomly distributed particles. (**E**) Similarly, analyzing a region which includes the edge of a cell introduces a significant artifact in the spatial correlation function (**G**). Regions analyzed with ICS should be entirely "on cell." (**F**) An acceptable region for ICS analysis. (**G**) The spatial autocorrelation function for the region outlined in (**E**). Compare the shape of this function to Fig. 2B

Applications

Image correlation techniques have been applied to a wide variety of biological systems, using a number of labeling methods and imaging modalities. This section of the review will provide a summary of this body of work. The ICS family of methods is relatively young, and some of the applications to date have been experiments to demonstrate the usefulness or accuracy of a given technique. It is hoped that with time, ICS will be used by more labs, especially in the areas of biology such as cell biology and neuroscience where there is an inherent advantage in observing processes across entire intact cells using imaging.

Cellular Adhesion and Migration

Cell adhesion and migration are important in a variety of biological processes including embryogenesis, wound healing, and metastasis [90]. Over 50 proteins have been implicated in adhesion, and their spatiotemporal coordination and localization in adhesion assembly and disassembly has yet to be fully understood [91]. Wiseman et al. [25] used a two-photon LSM and TICS to measure the diffusion of α5-integrin-GFP, a membrane protein known to bind to the extracellular matrix (ECM), in the basal membrane of a CHO cell. Two-photon excitation represents a significant advancement for live cell imaging, because the excitation light is less damaging to the cell than the equivalent one-photon wavelength [92]. As well, photobleaching outside the focal plane is reduced compared to single-photon excitation, since it is limited to the focal volume where the laser intensity is high enough to excite fluorophores. In an extension of the earlier work, Wiseman et al. [4] performed an extensive study on the aggregation state and dynamics of α5-integrin in living cells. ICS was used to characterize the degree of aggregation of α5-integrin, and a calibration with monomeric GFP allowed for a calculation of the absolute number of protein monomers in aggregates. TICS was used to measure the relative diffusing, flowing, and immobile fractions

of GFP constructs of α5-integrin and α-actinin (Fig. 6A). A temporal cross-correlation analysis showed that α5-integrin is colocalized with α-actinin, but not paxillin, throughout the cell outside of adhesions. Finally, STICS was used to map directed fluxes of α5-integrin and α-actinin (Fig. 6B).

The linkage between actin and the ECM plays a central role in regulating cell migration [93]. To understand this interaction, Brown et al. [69] used actin-mRFP constructs in CHO and mouse fibroblast cells also transfected with a GFP construct of α-actinin, α5-integrin, talin, paxillin, vinculin or focal adhesion kinase. By imaging time series of both fluorophores simultaneously, they were able to create velocity maps for both the actin (mRFP) and adhesion related protein (GFP) (Fig. 7). The similarity between the velocity maps for actin and the adhesion proteins was quantified by the relative magnitude of the velocity vectors, as well as their directional correlation [69]. This analysis probed the efficiency of the integrin-actin linkage in different cell types and under different conditions, such as various concentrations of ECM protein on the substrate. They conclude that the linkage is regulated at two levels: one proximal to the α-actinin in the adhesion, and another proximal to the integrins.

Platelet-Derived Growth Factor Receptors

Platelet-derived growth factor (PDGF) β-receptors are implicated in cell growth, chemotaxis, and actin reorganization. It is thought that their oligomerization plays a key role in their activation [94]. In the first application of ICS, Petersen et al. [17] compared the aggregation state of PDGF β2-receptors before and after the addition of PDGF β2-receptor antibodies. They quantified the antibody induced clustering of PDGF β2-receptors using ICS and found that the aggregates after the addition of antibody contained approximately 5 times as many receptors as before. Wiseman et al. [24] later used ICS to find that PDGF-β receptors were 3–4 times more clustered at 37°C than at 4°C, and that growth factor PDGF-BB addition did not induce a measurable aggregation at either temperature.

ICS was later optimized to correct for white noise, autofluorescence, and non-specific fluorescence [22]. Using these corrections, Wiseman and Petersen [22] showed using immunolabeling that PDGF β2-receptors on fixed human fibroblast cells were pre-aggregated at 4 °C. They also estimated these aggregates to be tetramers. A high-order moment analysis of LSM images of PDGF receptors in the same system also found the receptors to be in tetramers after addition of PDGF-BB [32], confirming the findings of the earlier study.

Epidermal Growth Factor Receptors

Activation of epidermal growth factor receptors (EGFR) has been shown to trigger cell migration, growth, differentiation, and apoptosis [95]. It is thought that there is a ligand-induced dimerization or oligomerization of receptors at the cell surface, which in turn activates a signaling pathway [96].

Petersen et al. [65] studied antibody-labeled EGFR on A431 cells, which are known to overexpress the receptors (2–3 million per cell). They found a temperature-dependent clustering of EGFR, in which the CD decreased by a factor of 2 while the number of receptors per cluster increased by a factor of 3 as the temperature was decreased from 37 to 4°C.

Clayton et al. [96] used ICS on EGFR-eGFP chimeras in BaF/3 cells to show that EGFR had, on average, 2.2 receptors/cluster in the absence of EGF, and increased to 3.7 receptors/cluster after being exposed to EGF. The cluster density was measured with ICS, and was converted to the number of receptors per cluster by estimating the total number of receptors per cell using comparative flow cytometry. In contrast to the antibody-labeled A431 cells used in [65], the BaF/3 cells expressed EGFR at the normal level of 50,000 copies/cell, and used GFP transfection to label EGFR. Saffarian et al. [97] recently used a modified fluorescence intensity distribution analysis (FIDA) approach to quantify the clustering of EGFR, and found that the values reported by Clayton et al. [96] are likely averages of a heterogeneous distribution of monomers, dimers, and tetramers. Clayton et al. [98] used ICS in conjunction with lifetime-based FRET to measure both sub-micron scale and nanoscale clustering of EGFR in A431 cells.

Intracellular Transport

Polyplexes, particles that are comprised of both synthetic polymers and nucleic acids, have recently been proposed as alternatives to viruses for gene delivery [99]. Kulkarni et al. [42] probed the dynamics of endosomes containing fluorescently labeled polyplexes, in living HeLa cells. They used TICS in conjunction with SPT to characterize the motion of an ensemble of polyplexes, and found that their motion was Brownian the majority of the time, with brief periods of directed motion, which they attributed to transport along microtubules.

Clathrin-Coated Pits

Clathrin-coated vesicles are the most common route of endocytosis in eukaryotic cells. There is strong evidence

that the AP-2 adapter protein plays a role in binding both clathrin, which forms the lining of the coated pit, and the cargo, which is internalized [100]. Brown and Petersen [101] used ICS to study the distribution of immunofluorescently labeled AP-2 in CV-1 cells, and found that one-third is found in large aggregates associated with clathrin-coated pits, and the remainder is in smaller aggregates with approximately one-third the brightness. Later, a similar system was used to show that ~35% of clathrin was free in the cytosol, while ~65% was in large aggregates in coated pit structures [102]. The same study showed that free clathrin in the cytosol was required for the stability of AP-2 coated pit nucleation sites. CV-1 cells are very appropriate for ICS studies because they are both large and flat [103].

Brown et al. [103] were interested in determining the order of association between clathrin, AP-2, and membrane receptors. Using ICS and ICCS, they found that AP-2 and the membrane receptor were colocalized in cells in which the clathrin lattice was disrupted with treatments. They propose that AP-2 binds membrane proteins prior to associating with clathrin. Later, Boyd et al. [104] used ICS to quantify the clustering and aggregation of AP-2 on different ECM proteins.

Fire et al. [105] found that the degree of clustering in coated pits was directly related to a membrane receptor's affinity for AP-2. This result suggests that the strength of a receptor's internalization signal could strongly influence both its endocytosis rate and lateral mobility.

Sendai Virus Fusion

Rasmusson et al. [106] studied the fusion of Sendai virus with living HEp-2 and BALB-3T3 cells. They were able to track the fusion of the viruses by labeling the viral membrane envelope with a fluorescent lipid probe. As the large, bright virus particles bound and then fused to the cell, the fluorescent probe diffused into the plasma membrane. This fusion was measured using ICS, and resulted in an increase in the CD as the lipid probe was dispersed from concentrated viral particles to a diffuse membrane population. Additionally, the effect of incorporating lipophosphoglycan (LPG), a known fusion inhibitor, in the cell membrane was measured quantitatively with ICS.

Rocheleau and Petersen [107] used a fluorescent derivative of the virus receptor GD1a, NBD-GD1a, to study the effect of Sendai virus addition on the aggregation state of the receptor in living CV-1 cells. The cluster density of NBD-GD1a was monitored using ICS, and exhibited a concentration-dependent clustering when virus was added. Furthermore, by labeling the virus with a different emission wavelength fluorophore, DiQ, and using ICCS, it was possible to show that the virus particles bound to the diffuse population of NBD-GD1a, because there was not a significant cross-correlation between the virus particles and receptor aggregates. Rocheleau and Petersen [108] later fluorescently labeled both the virus protein and lipid components with FITC and DiQ, respectively, and quantitatively followed their dispersion into the cell membrane upon fusion using ICS.

Caveolin-1 and Bone Morphogenetic Protein Receptors

Bone morphogenetic proteins (BMPs) have been shown to play key roles in a number of biological processes including embryonic development and postnatal bone formation [109]. Caveolae are membrane systems, often in the form of flask-shaped invaginations, that are involved in endocytosis and signal transduction [110]. Nohe et al. [111] used ICCS in conjunction with dual-color antibody labeling to show that ~25% of caveolin-1, a key protein in the formation of caveolae, is colocalized with BMP receptors type-Ia and -II, as well as EGFR. This was later extended to study the effect of BMP receptor stimulation with BMP-2 on the distribution of caveolin-1 isoforms and BMP receptors [112]. The aggregation of BMP-type-II and -type-Ia receptors and their role in activating the Smad signalling pathway, were also studied using ICS [113].

Counting Dendritic Spines

Changes in the number density of dendritic spines on neurons have been implicated as an indicator of synaptic plasticity [114]. Dendritic spines in light microscopy images of neuronal tissue are traditionally manually counted in a time-consuming procedure. Wiseman et al. [29] showed that ICS could yield number densities of spines, which agreed with the manual counting method, had a comparable precision, and could be obtained more quickly. This advance has not yet been adopted by other neuroscience groups probably due to the fact that it was communicated in a technical microscopy journal which would have a restricted readership amongst neuroscientists.

Membrane Domains

Bates et al. [115] studied the lateral diffusion of cystic fibrosis transmembrane conductance regulator (CFTR), a transmembrane protein, in living BHK cells using three different techniques: TICS, FRAP, and SPT. CFTR was labeled using streptavidin-Alexa488, -Alexa568, or -QD fluorophores bound to an enzymatically attached biotin

tag on an extracellular loop of the protein. Both FRAP and TICS found that >50% of the protein is immobilized at the cell surface. Interestingly, they found that FRAP consistently measured a higher diffusion coefficient than TICS measurements on the same system. SPT analysis of the QD-labeled protein revealed that a histidine tag mutant CFTR underwent transient confinement in the cell membrane. Computer simulations suggested that this transient confinement could be responsible for the difference in D measured using TICS and FRAP, since TICS was more sensitive than FRAP to the transiently confined population. Srivastava and Petersen [35] also found a similar difference between TICS and FRAP measurements of the diffusion of antibody-labeled transferrin receptors. They attributed this discrepancy to TICS measuring the diffusion of large aggregates of receptors, and FRAP probing the diffusion of receptor monomers, but the computer simulations do not support this interpretation.

In the first application of PICS, the mobility of a eYFP/H-Ras mutant in live 3T3 cells was measured [87]. The membrane-anchored protein was found to exist in two populations: one which exhibited a fast, free diffusion (0.73 ± 0.01 $\mu m^2/s$), and another which diffused more slowly (0.10 ± 0.01 $\mu m^2/s$), and was found to be confined to domains less than 200 nm in size. In the future, PICS should prove to be a useful alternative to SPT for detecting sub-micron confinement zones.

Putative lipid rafts in biological membranes are cholesterol enriched domains which are thought to play a role in signal transduction [44]. As a model raft protein, Nohe et al. [36] studied a glycosylphosphatidylinositol (GPI) lipid tagged with GFP. They found that the GPI-GFP is distributed in two populations: a homogeneous distribution, which moves too quickly to be measured via TICS, and a population of larger clusters that diffuses at a rate of 6×10^{-12} cm^2/s. They also studied the effect of cholesterol depletion and temperature on the measured diffusion coefficient and cluster density of the slower moving population.

Wang and Axelrod [116] used spatial autocorrelation functions to examine acetylcholine receptors (AChR) on rat myotubes. The size, periodicity, and spatial anisotropy of the AChR clusters were measured from the correlation function. As well, they introduced a novel method to prevent long range (i.e., low spatial frequency) variations in the image from masking short range (i.e., high spatial frequency) fluctuations.

Hwang et al. [117] used near-field scanning optical microscopy (NSOM) to image antibody labeled HLA-I membrane proteins. By calculating circularly averaged spatial autocorrelation functions from images, they were able to measure two distinct domain sizes of protein patches. A similar approach was used to characterize model membranes containing dipalmitoylphosphatidylcholine (DPPC), dilauroylphosphatidylcholine (DLPC), and cholesterol [118].

Fluorophore Photophysics

Bachir et al. [119] used TICS to characterize the blinking dynamics of QD ensembles. They immobilized QDs on a glass coverslip, and imaged them using a TIRFM and CCD camera. They found that while temporal correlation functions for single QDs were dominated by long "on" and "off" times (on the order of 100 s), the correlation functions for ensembles of dots were well-fit by a power law:

$$r(\tau) = A - B\tau^{\alpha}. \tag{30}$$

By changing the excitation laser intensity, the underlying blinking statistics of the QDs were altered, and these changes could be characterized by changes in the α fitting parameter.

Durisic et al. [81] used computer simulations and QDs in glycerol to show that TICS decays of samples containing blinking QDs are well fit by models taking only diffusion into account. However, the diffusion coefficient recovered from such analyses is significantly biased to higher diffusion coefficients because of the fluctuations introduced by the fluorophore blinking fluctuations. They showed that a kICS analysis of the same image time series measures the QD mobility independently of photophysics. Finally, they analyzed an image series of a QD-labeled GPI-anchored protein, CD73, in the membrane of fibroblast cells using both TICS and kICS and measured different diffusion coefficients, in agreement with the computer simulations and model system.

The kinetics of GFP photobleaching have been measured using kICS as a proof-of-principle to show that fluorophore photophysics could easily extracted independently of dynamics from a k-space time correlation function [80]. Although this demonstration measured monoexponential photobleaching, kICS could also be applied to more complex photophysics, such as QD blinking which is governed by a power-law distribution.

Conclusions

The progeny of ICS discussed in this review comprise a powerful toolbox for studying the dynamics, aggregation state, number density and interactions of membrane and cytosolic fluorescently labeled proteins in living cells. Importantly, they do not require custom made equipment, and can be applied to image series acquired on commercial LSMs and TIRFMs. Although we have presented

a number of varied applications of ICS techniques, their use is still in its infancy. With the further development of both methodology and microscopy, the power of the techniques and the breadth of their applications are bound to grow.

Acknowledgments We thank the reviewers for their careful reading of the manuscript, and excellent suggestions. Additionally, DLK thanks the Natural Sciences and Engineering Research Council (NSERC) of Canada for a Canada Graduate Scholarship and PWW acknowledges NSERC and the Canadian Institutes of Health Research.

References

1. Heldin, C.-H. (1995). Dimerization of cell surface receptors in signal transduction. *Cell, 80*, 213–223.
2. Lemmon, M. A., & Schlessinger, J. (1994). Regulation of signal transduction and signal diversity by receptor oligomerization. *Trends in Biochemical Sciences, 19*, 459–463.
3. Sheets, E. D., Simson, R., & Jacobson, K. (1995). New insights into membrane dynamics from the analysis of cell surface interactions by physical methods. *Current Opinion in Cell Biology, 7*, 707–714.
4. Wiseman, P. W., Brown, C. M., Webb, D. J., Hebert, B., Johnson, N. L., Squier, J. A., Ellisman, M. H., & Horwitz, A. F. (2004). Spatial mapping of integrin interactions and dynamics during cell migration by image correlation microscopy. *Journal of Cell Science, 117*, 5521–5534.
5. Tserkovnyak, Y., & Nelson, D. R. (2006). Conditions for extreme sensitivity of protein diffusion in membranes to cell environments. *Proceedings of the National Academy of Sciences of the United States of America, 103*, 15002–15007.
6. Tsien, R. Y. (1998). The green fluorescent protein. *Annual Review of Biochemistry, 67*, 509–544.
7. Magde, D., Elson, E., & Webb, W. W. (1972). Thermodynamic fluctuations in a reacting system—measurement by fluorescence correlation spectroscopy. *Physical Review Letters, 29*, 705–708.
8. Elson, E. L., & Magde, D. (1974). Fluorescence correlation spectroscopy. I. Conceptual basis and theory. *Biopolymers, 13*, 1–27.
9. Magde, D., Elson, E. L., & Webb, W. W. (1974). Fluorescence correlation spectroscopy. II. An experimental realization. *Biopolymers, 13*, 29–61.
10. Magde, D., Webb, W. W., & Elson, E. L. (1978). Fluorescence correlation spectroscopy. III. Uniform translation and laminar flow. *Biopolymers, 17*, 361–376.
11. Weissman, M., Schindler, H., & Feher, G. (1976). Determination of molecular weights by fluctuation spectroscopy: Application to DNA. *Proceedings of the National Academy of Sciences of the United States of America, 73*, 2776–2780.
12. Petersen, N. O. (1986). Scanning fluorescence correlation spectroscopy. I. Theory and simulation of aggregation measurements. *Biophysical Journal, 49*, 809–815.
13. Petersen, N. O., Johnson, D. C., & Schlesinger, M. J. (1986). Scanning fluorescence correlation spectroscopy. II. Application to virus glycoprotein aggregation. *Biophysical Journal, 49*, 817–820.
14. St-Pierre, P. R., & Petersen, N. O. (1990). Relative ligand binding to small or large aggregates measured by scanning correlation spectroscopy. *Biophysical Journal, 58*, 503–511.
15. Meyer, T., & Schindler, H. (1988). Particle counting by fluorescence correlation spectroscopy. Simultaneous measurement of aggregation and diffusion of molecules in solutions and in membranes. *Biophysical Journal, 54*, 983–993.
16. Koppel, D. E., Morgan, F., Cowan, A. E., & Carson, J. H. (1994). Scanning concentration correlation spectroscopy using the confocal laser microscope. *Biophysical Journal, 66*, 502–507.
17. Petersen, N. O., Hoddelius, P. L., Wiseman, P. W., Seger, O., & Magnusson, K. E. (1993). Quantitation of membrane receptor distributions by image correlation spectroscopy: Concept and application. *Biophysical Journal, 65*, 1135–46.
18. Berland, K. M., So, P. T., Chen, Y., Mantulin, W. W., & Gratton, E. (1996). Scanning two-photon fluctuation correlation spectroscopy: Particle counting measurements for detection of molecular aggregation. *Biophysical Journal, 71*, 410–420.
19. Fink, M. C., Adair, K. V., Guenza, M. G., & Marcus, A. H. (2006). Translational diffusion of fluorescent proteins by molecular Fourier imaging correlation spectroscopy. *Biophysical Journal, 91*, 3482–3498.
20. Hebert, B., Costantino, S., & Wiseman, P. W. (2005). Spatiotemporal image correlation spectroscopy (STICS) theory, verification, and application to protein velocity mapping in living CHO cells. *Biophysical Journal, 88*, 3601–3614.
21. Cannell, M. B., McMorland, A., & Soeller, C. (2006). Image enhancement by deconvolution. In J. B. Pawley (Ed.), *Handbook of biological confocal microscopy* (pp. 488–500). New York: Springer.
22. Wiseman, P. W., & Petersen, N. O. (1999). Image correlation spectroscopy. II. Optimization for ultrasensitive detection of preexisting platelet-derived growth factor-beta receptor oligomers on intact cells. *Biophysical Journal, 76*, 963–77.
23. Costantino, S., Comeau, J. W. D., Kolin, D. L., & Wiseman, P. W. (2005). Accuracy and dynamic range of spatial image correlation and cross-correlation spectroscopy. *Biophysical Journal, 89*, 1251–1260.
24. Wiseman, P. W., Höddelius, P., Petersen, N. O., & Magnusson, K. (1997). Aggregation of PDGF-β receptors in human skin fibroblasts: Characterization by image correlation spectroscopy (ICS). *FEBS Letters, 401*, 43–48.
25. Wiseman, P. W., Squier, J. A., Ellisman, M. H., & Wilson, K. R. (2000). Two-photon image correlation spectroscopy and image cross-correlation spectroscopy. *Journal of Microscopy, 200*, 14–25.
26. Yoo, H., Song, I., & Gweon, D.-G. (2006). Measurement and restoration of the point spread function of fluorescence confocal microscopy. *Journal of Microscopy, 221*, 172–176.
27. Huang, Z., & Thompson, N. L. (1996). Imaging fluorescence correlation spectroscopy: Nonuniform IgE distributions on planar membranes. *Biophysical Journal, 70*, 2001–2007.
28. Rocheleau, J. V., Wiseman, P. W., & Petersen, N. O. (2003). Isolation of bright aggregate fluctuations in a multipopulation image correlation spectroscopy system using intensity subtraction. *Biophysical Journal, 84*, 4011–22.
29. Wiseman, P. W., Capani, F., Squier, J. A., & Martone, M. E. (2002). Counting dendritic spines in brain tissue slices by image correlation spectroscopy analysis. *Journal of Microscopy, 205*, 177–86.
30. Palmer, A. G., & Thompson, N. L. (1989). High-order fluorescence fluctuation analysis of model protein clusters. *Proceedings of the National Academy of Sciences of the United States of America, 86*, 6148–6152.
31. Vanden Broek, W., Huang, Z., & Thompson, N. L. (1999). High-order autocorrelation with imaging fluorescence correlation spectroscopy: Application to IgE on supported planar membranes. *Journal of Fluorescence, 9*, 313–324.

32. Sergeev, M., Costantino, S., & Wiseman, P. W. (2006). Measurement of monomer–oligomer distributions via fluorescence moment image analysis. *Biophysical Journal, 91*, 3884–3896.
33. Benn, A. G., & Kulperger, R. J. (1997). Integrated marked poisson processes with application to image correlation spectroscopy. *The Canadian Journal of Statistics, 25*, 215–231.
34. Srivastava, M., & Petersen, N. O. (1996). Image cross-correlation spectroscopy: A new experimental biophysical approach to measurement of slow diffusion of fluorescent molecules. *Methods in Cell Science, 18*, 47–54.
35. Srivastava, M., & Petersen, N. O. (1998). Diffusion of transferrin receptor clusters. *Biophysical Chemistry, 75*, 201–211.
36. Nohe, A., Keating, E., Fivaz, M., van der Goot, F. G., & Petersen, N. O. (2006). Dynamics of GPI-anchored proteins on the surface of living cells. *Nanomedicine 39*, 159–169.
37. Petersen, N. (2001). FCS and spatial correlations on biological surfaces. In R. Rigler & E. S. Elson (Eds.), *Fluorescence correlation spectroscopy* (pp. 162–184). Heidelberg: Springer.
38. Ulrich, M., Wohland, T., Rigler, R., & Vogel, H. (1999). Resolution of fluorescence correlation measurements. *Biophysical Journal, 76*, 1619–1631.
39. Feder, T. J., Brust-Mascher, I., Slattery, J. P., Baird, B., & Webb, W. W. (1996). Constrained diffusion or immobile fraction on cell surfaces: A new interpretation. *Biophysical Journal, 70*, 2767–2773.
40. Aragón, S. R., & Pecora, R. (1976). Fluorescence correlation spectroscopy as a probe of molecular dynamics. *The Journal of Chemical Physics, 64*, 1791–1803.
41. Saxton, M. J., & Jacobson, K. (1997). Single-particle tracking: Applications to membrane dynamics. *Annual Review of Biophysics and Biomolecular Structure, 26*, 373–399.
42. Kulkarni, R. P., Wu, D. D., Davis, M. E., & Fraser, S. E. (2005). Quantitating intracellular transport of polyplexes by spatio-temporal image correlation spectroscopy. *Proceedings of the National Academy of Sciences of the United States of America, 102*, 7523–7528.
43. Kolin, D. L., Costantino, S., & Wiseman, P. W. (2006). Sampling effects, noise, and photobleaching in temporal image correlation spectroscopy. *Biophysical Journal, 90*, 628–639.
44. Lagerholm, B. C., Weinreb, G. E., Jacobson, K., & Thompson, N. L. (2005). Detecting microdomains in intact cell membranes. *Annual Review of Physical Chemistry, 56*, 309–336.
45. Axelrod, D., Koppel, D. E., Schlessinger, J., Elson, E., & Webb, W. W. (1976). Mobility measurement by analysis of fluorescence photobleaching recovery kinetics. *Biophysical Journal, 16*, 1055–1069.
46. Jacobson, K., O'Dell, D., & August, J. T. (1984). Lateral diffusion of an 80,000–dalton glycoprotein in the plasma membrane of murine fibroblasts: Relationships to cell structure and function. *The Journal of Cell Biology, 99*, 1624–1633.
47. Sheetz, M. P., & Koppel, D. E. (1979). Membrane damage caused by irradiation of fluorescent concanavalin. *Proceedings of the National Academy of Sciences of the United States of America, 76*, 3314–3317.
48. Lepock, J. R., Campbell, S. D., Gruber, M., & Kruuv, J. (1979). Photoinduced cell killing and crosslinking of fluorescein conjugated concanavalin A to cell surface proteins. *Biochemical and Biophysical Research Communications, 91*, 1157–1165.
49. Jacobson, K., Hou, Y., & Wojcieszyn, J. (1979). Evidence for lack of damage during photobleaching measurements of the lateral mobility of cell surface components. *Experimental Cell Research, 116*, 179–189.
50. Wolf, D. E., Edidin, M., & Dragsten, P. R. (1980). Effect of bleaching light on measurements of lateral diffusion in cell membranes by the fluorescence photobleaching recovery method. *Proceedings of the National Academy of Sciences of the United States of America, 77*, 2043–2045.
51. Schwille, P., Korlach, J., & Webb, W. W. (1999). Fluorescence correlation spectroscopy with single-molecule sensitivity on cell and model membranes. *Cytometry, 36*, 176–182.
52. Nicolau, J., Dan V., Hancock, J. F., & Burrage, K. (2007). Sources of anomalous diffusion on cell membranes: A Monte Carlo study. *Biophysical Journal, 92*, 1975–1987.
53. Manders, E. M. M., Verbeek, F. J., & Aten, J. A. (1993). Measurement of colocalization of objects in dual-color confocal images. *Journal of Microscopy, 169*, 375–382.
54. Costes, S. V., Daelemans, D., Cho, E. H., Dobbin, Z., Pavlakis, G., & Lockett, S. (2004). Automatic and quantitative measurement of protein–protein colocalization in live cells. *Biophysical Journal, 86*, 3993–4003.
55. Comeau, J., Costantino, S., & Wiseman, P. W. (2006). A guide to accurate colocalization measurements. *Biophysical Journal, 91*, 4611–4622.
56. Manders, E. M. M. (1997). Chromatic shift in multicolour confocal microscopy. *Journal of Microscopy, 185*, 321–328.
57. McAuliffe, M. J., Lalonde, F. M., McGarry, D., Gandler, W., Csaky, K., & Trus, B. L. (2001). Medical image processing, analysis & visualization in clinical research in 14th IEEE symposium on computer-based medical systems IEEE computer society (p. 0381).
58. Schwille, P. (2001). Cross-correlation analysis. In R. Rigler & E. S. Elson (Eds.), *FCS in fluorescence correlation spectroscopy: Theory and applications*. New York: Springer. Volume 65 of *Chemical Physics*.
59. Sekar, R. B., & Periasamy, A. (2003). Fluorescence resonance energy transfer (FRET) microscopy imaging of live cell protein localizations. *The Journal of Cell Biology, 160*, 629–633.
60. Milon, S., Hovius, R., Vogel, H., & Wohland, T. (2003). Factors influencing fluorescence correlation spectroscopy measurements on membranes: Simulations and experiments. *Chemical Physics, 288*, 171–186.
61. Stauffer, T. P., & Meyer, T. (1997). Compartmentalized IgE receptor-mediated signal transduction in living cells. *The Journal of Cell Biology, 139*, 1447–1454.
62. Sheets, E. D., Holowka, D., & Baird, B. (1999). Critical role for cholesterol in Lyn-mediated tyrosine phosphorylation of Fc ε RI and their association with detergent-resistant membranes. *The Journal of Cell Biology, 145*, 877–887.
63. Pyenta, P. S., Holowka, D., & Baird, B. (2001). Cross-correlation analysis of inner-leaflet-anchored green fluorescent protein co-redistributed with IgE receptors and outer leaflet lipid raft components. *Biophysical Journal, 80*, 2120–2132.
64. Hebert, B., Hulme, S. E., & Wiseman, P. W. (2005). Membrane protein dynamics measured by two-photon ring correlation spectroscopy: Theory and application to living cells in multiphoton microscopy in the biomedical sciences V. In A. Periasamy & P. T. So (Eds.) *Proceedings of S.P.I.E.* (Vol. 5700, pp. 109–117).
65. Petersen, N. O., Brown, C., Kaminski, A., Rocheleau, J., Srivastava, M., & Wiseman, P. W. (1998). Analysis of membrane protein cluster densities and sizes in situ by image correlation spectroscopy. *Faraday Discuss* (pp. 289–305); discussion 331–343.
66. Ji, L., & Danuser, G. (2005). Tracking quasi-stationary flow of weak fluorescent signals by adaptive multi-frame correlation. *Journal of Microscopy, 220*, 150–167.
67. Adrian, R. J. (2005). Twenty years of particle image velocimetry. *Experiments in Fluids, 39*, 159–169.
68. Gui, L., & Merzkirch, W. (2000). A comparative study of the MQD method and several correlation-based PIV evaluation algorithms. *Experiments in Fluids, 28*, 36–44.

69. Brown, C. M., Hebert, B., Kolin, D. L., Zareno, J., Whitmore, L., Horwitz, A. F., & Wiseman, P. W. (2006). Probing the Integrin-Actin Linkage using High Resolution Protein Velocity Mapping. *Journal of Cell Science, 119*, 5204–5214.
70. Hebert, B. (2006). Spatio-temporal image correlation spectroscopy: Development and implementation in living cells Ph.D. thesis McGill University.
71. Sinnecker, D., Voigt, P., Hellwig, N., & Schaefer, M. (2005). Reversible photobleaching of enhanced green fluorescent proteins. *Biochemistry, 44*, 7085–7094.
72. Dickson, R. M., Cubitt, A. B., Tsien, R. Y., & Moerner, W. E. (1997). On/Off blinking and switching behaviour of single molecules of green fluorescent protein. *Nature, 388*, 355–358.
73. Doose, S., Tsay, J. M., Pinaud, F., & Weiss, S. (2005). Comparison of photophysical and colloidal properties of biocompatible semiconductor nanocrystals using fluorescence correlation spectroscopy. *Analytical Chemistry, 77*, 2235–2242.
74. Bruchez, M., Moronne, M., Gin, P., Weiss, S., & Alivisatos, A. P. (1998). Semiconductor nanocrystals as fluorescent biological labels. *Science, 281*, 2013–2016.
75. Chan, W. C. W., & Nie, S. (1998). Quantum dot bioconjugates for ultrasensitive nonisotopic. *Detection Science, 281*, 2016–2018.
76. Yao, J., Larson, D. R., Vishwasrao, H. D., Zipfel, W. R., & Webb, W. W. (2005). Blinking and nonradiant dark fraction of water-soluble quantum dots in aqueous solution. *Proceedings of the National Academy of Sciences of the United States of America, 102*, 14284–14289.
77. Kuno, M., Fromm, D. P., Hamann, H. F., Gallagher, A., & Nesbitt, D. J. (2000). Nonexponential "blinking" kinetics of single CdSe quantum dots: A universal power law behavior. *The Journal of Chemical Physics, 112*, 3117–3120.
78. Margolin, G., & Barkai, E. (2004). Aging correlation functions for blinking nanocrystals, and other on–off stochastic processes. *The Journal of Chemical Physics, 121*, 1566–1577.
79. Margolin, G., & Barkai, E. (2005). Nonergodicity of blinking nanocrystals and other Lévy-walk processes. *Physical Review Letters, 94*, 080601.
80. Kolin, D. L., Ronis, D., & Wiseman, P. W. (2006). k-Space image correlation spectroscopy: A method for accurate transport measurements independent of fluorophore photophysics. *Biophysical Journal, 91*, 3061–3075.
81. Durisic, N., Bachir, A. I., Kolin, D. L., Hebert, B., Lagerholm, B. C., Grutter, P., & Wiseman, P. W. (2007). Detection and correction of blinking bias in image correlation transport measurements of quantum dot tagged macromolecules. *Biophysical Journal, 93*, 1338–1346.
82. Berne, B. J., & Pecora, R. (2000). Dynamic light scattering. New York: Dover.
83. Hattori, M., Shimizu, H., & Yokoyama, H. (1996). Fluorescence correlation spectroscopy with traveling interference fringe excitation. *The Review of Scientific Instruments, 67*, 4064–4071.
84. Digman, M. A., Sengupta, P., Wiseman, P. W., Brown, C. M., Horwitz, A. R., & Gratton, E. (2005). Fluctuation correlation spectroscopy with a laser-scanning microscope: Exploiting the hidden time structure. *Biophysical Journal, 88*, L33–L36.
85. Digman, M. A., Brown, C. M., Sengupta, P., Wiseman, P. W., Horwitz, A. R., & Gratton, E. (2005). Measuring fast dynamics in solutions and cells with a laser scanning microscope. *Biophysical Journal, 89*, 1317–1327.
86. Thompson, N. L. (1991). Fluorescence correlation spectroscopy in topics. In J. R. Lakowicz (Ed.), *Fluorescence spectroscopy, volume 1: Techniques* (pp. 337–378). New York: Plenum Press.
87. Semrau, S., & Schmidt, T. (2007). Particle image correlation spectroscopy (PICS): Retrieving nanometer-scale correlations from high-density single-molecule position data. *Biophysical Journal, 92*, 613–621.
88. Brown, C. M. (2007). Fluorescence microscopy—avoiding the pitfalls. *Journal of Cell Science, 120*, 1703–1705.
89. Hibbs, A. R., MacDonald, G., & Garsha, K. (2006). Practical confocal microscopy. In J. B. Pawley (Ed.), *Handbook of biological confocal microscopy* (pp. 650–671). New York: Springer.
90. Lauffenburger, D. A., & Horwitz, A. F. (1996). Cell migration: A physically integrated molecular process. *Cell, 84*, 359–369.
91. Webb, D. J., Parsons, J. T., & Horwitz, A. F. (2002). Adhesion assembly, disassembly and turnover in migrating cells—over and over and over again. *Nature Cell Biology, 4*, E97–E100.
92. Denk, W., Strickler, J. H., & Webb, W. W. (1990). Two-photon laser scanning fluorescence microscopy. *Science, 248*, 73–76.
93. Ridley, A. J., Schwartz, M. A., Burridge, K., Firtel, R. A., Ginsberg, M. H., Borisy, G., Parsons, J. T., & Horwitz, A. R. (2003). Cell migration: Integrating signals from front to back. *Science, 302*, 1704–1709.
94. Heldin, C.-H., Östman, A., & Rönnstrand, L. (1998). Signal transduction via platelet-derived growth factor receptors. *Biochimica et Biophysica Acta, 1378*, F79–F113.
95. Yarden, Y., & Sliwkowski, M. X. (2001). Untangling the ErbB signalling network. *Nature Reviews. Molecular Cell Biology, 2*, 127–137.
96. Clayton, A. H. A., Walker, F., Orchard, S. G., Henderson, C., Fuchs, D., Rothacker, J., Nice, E. C., & Burgess, A. W. (2005). Ligand-induced dimer-tetramer transition during the activation of the cell surface epidermal growth factor receptor—A multidimensional microscopy analysis. *The Journal of Biological Chemistry, 280*, 30392–30399.
97. Saffarian, S., Li, Y., Elson, E. L., & Pike, L. J. (2007). Oligomerization of the EGF receptor investigated by live cell fluorescence intensity distribution analysis. *Biophysical Journal, 93*, 1021–1031.
98. Clayton, A. H. A., Tavarnesi, M. L., & Johns, T. G. (2007). Unligated epidermal growth factor receptor forms higher order oligomers within microclusters on A431 cells that are sensitive to tyrosine kinase inhibitor binding. *Biochemistry, 46*, 4589–4597.
99. Haag, R., & Kratz, F. (2006). Polymer therapeutics: Concepts and applications. *Angewandte Chemie (International edition in English), 45*, 1198–1215.
100. Traub, L. M. (2003). Sorting it out: AP-2 and alternate clathrin adaptors in endocytic cargo selection. *The Journal of Cell Biology, 163*, 203–208.
101. Brown, C. M., & Petersen, N. O. (1998). An image correlation analysis of the distribution of clathrin associated adaptor protein (AP-2) at the plasma membrane. *Journal of Cell Science, 111*(Pt 2), 271–281.
102. Brown, C. M., & Petersen, N. O. (1999). Free clathrin triskelions are required for the stability of clathrin-associated adaptor protein (AP-2) coated pit nucleation sites. *Biochem. Cell Biol., 77*, 439–448.
103. Brown, C. M., Roth, M. G., Henis, Y. I., & Petersen, N. O. (1999). An internalization-competent influenza hemagglutinin mutant causes the redistribution of AP-2 to existing coated pits and is colocalized with AP-2 in clathrin free clusters. *Biochemistry, 38*, 15166–15173.
104. Boyd, N. D., Chan, B. M. C., & Petersen, N. O. (2002). Adaptor protein-2 exhibits $\alpha_1\beta_1$ or $\alpha_6\beta_1$ integrin-dependent redistribution in rhabdomyosarcoma cells. *Biochemistry, 41*, 7232–7240.
105. Fire, E., Brown, C. M., Roth, M. G., Henis, Y. I., & Petersen, N. O. (1997). Partitioning of proteins into plasma membrane microdomains. Clustering of mutant influenza virus

hemagglutinins into coated pits depends on the strength of the internalization signal. *The Journal of Biological Chemistry, 272*, 29538–29545.
106. Rasmusson, B. J., Flanagan, T. D., Turco, S. J., Epand, R. M., & Petersen, N. O. (1998). Fusion of Sendai virus and individual host cells and inhibition of fusion by lipophosphoglycan measured with image correlation spectroscopy. *Biochimica et Biophysica Acta, 1404*, 338–352.
107. Rocheleau, J. V., & Petersen, N. O. (2000). Sendai virus binds to a dispersed population of NBD-GD1a. *Bioscience Reports, 20*, 139–155.
108. Rocheleau, J. V., & Petersen, N. O. (2001). The Sendai virus membrane fusion mechanism studied using image correlation spectroscopy. *European Journal of Biochemistry, 268*, 2924–2930.
109. Chen, D., Zhao, M., & Mundy, G. R. (2004). Bone morphogenetic proteins. *Growth Factors, 22*, 233–241.
110. Anderson, R. G. W. (1998). The caveolae membrane system. *Annual Review of Biochemistry, 67*, 199–225.
111. Nohe, A., Keating, E., Loh, C., Underhill, M. T., & Petersen, N. O. (2004a). Caveolin-1 isoform reorganization studied by image correlation spectroscopy. *Faraday Discuss, 126*, 185–195.
112. Nohe, A., Keating, E., Underhill, M. T., Knaus, P., & Petersen, N. O. (2004b). Dynamics and interaction of caveolin-1 isoforms with BMP-receptors. *Journal of Cell Science, 118*, 643–650.
113. Nohe, A., Keating, E., Underhill, T. M., Knaus, P., & Petersen, N. O. (2003). Effect of the distribution and clustering of the type I A BMP receptor (ALK3) with the type II BMP receptor on the activation of signalling pathways. *Journal of Cell Science, 116*, 3277–3284.
114. Moser, M. B., Trommald, M., & Andersen, P. (1994). An increase in dendritic spine density on hippocampal CA1 pyramidal cells following spatial learning in adult rats suggests the formation of new synapses. *Proceedings of the National Academy of Sciences of the United States of America, 91*, 12673–12675.
115. Bates, I. R., Hebert, B., Luo, Y., Liao, J., Bashir, A. I., Kolin, D. L., Wiseman, P. W., & Hanrahan, J. W. (2006). Membrane lateral diffusion and capture of CFTR within transient confinement zones. *Biophysical Journal, 91*, 1046–1058.
116. Wang, M. D., & Axelrod, D. (1994). Microclustering patterns of acetylcholine receptors on myotubes studied by spatial fluorescence autocorrelation. *Bioimaging, 2*, 22–35.
117. Hwang, J., Gheber, L. A., Margolis, L., & Edidin, M. (1998). Domains in cell plasma membranes investigated by near-field scanning optical microscopy. *Biophysical Journal, 74*, 2184–2190.
118. Tokumasu, F., Hwang, J., & Dvorak, J. A. (2004). Heterogeneous molecular distribution in supported multicomponent lipid bilayers. *Langmuir, 20*, 614–618.
119. Bachir, A. I., Durisic, N., Hebert, B., Grütter, P. H., & Wiseman, P. W. (2006). Image correlation spectroscopy studies of blinking dynamics in semiconductor quantum dots. *Journal of Applied Physics, 99*, 064503.

Carsten Schultz, Tuesday June 12th 2012, 13.30

Principles for designing fluorescent sensors and reporters

Edward A Lemke & Carsten Schultz

Sensors and reporters are among the most exciting tools used in cell biology. Now, they are increasingly used in developmental biology and medicine because they allow us to spy on events in living cells and organisms, including humans, in real time and with high spatial resolution. Herein, we discuss multiple design options for fluorescent sensors and reporters as well as strategies to improve their properties and increase development.

Sensors and reporters are among the most fascinating and revealing tools available in today's laboratories. They permit us to do something that must have been considered a futuristic dream 50 years ago: follow events inside living cells and organisms, in real time and with spatial resolution. Although the first fluorescent sensors, such as voltage-dependent dyes, were introduced in the 1970s[1], the revolution truly began when the first ratiometric fluorescent calcium sensors[2,3] were combined with a method for delivering such molecules noninvasively and irreversibly across plasma membranes[4]. This provided the first technology routinely used to study ion homeostasis in living cells. Whereas sensors such as the calcium indicator Fura-2 were based on small molecules, the discovery and implementation of genetically encoded reporters—fluorescent proteins—was the next major step in expanding our repertoire of fluorescent probes[5]. The impact of the latter advances was recognized with the Nobel Prize for chemistry in 2008.

Sensors versus reporters

'Sensor', 'indicator', 'reporter' and 'tracer' are terms that are often used interchangeably in the literature. We define sensors and indicators as molecules that undergo a structural change when exposed to certain conditions, ions or molecules. The detector unit of a sensor is coupled to another part of the molecule and acts almost like a display, communicating changes through, say, an increase in fluorescence. The structural change a sensor undergoes is always reversible, allowing us to follow dynamic processes over time. By our definition, reporter or tracer molecules are somewhat different; they also have a detector unit, such as a paramagnetic metal complex or a fluorescent protein, but they are usually insensitive to the external environment and are often used to gather spatial information. A third group of molecules is sensitive to external changes but lacks the reversibility of sensors. This group consists mostly of fluorescent reporters that react to changes in the environment but become localization detectors immediately after the change. Such reporters include fluorescent substrates for enzymes that are cleaved irreversibly and activity-based probes (ABPs) that covalently react with an enzyme[6,7]. Although their lack of dynamic readout might appear to be (and sometimes is) a drawback, these reporters have the advantage of producing an accumulating signal that provides information about even very small changes that develop over long periods of time, and they can potentially provide spatial resolution as well. These molecules are commonly called memory probes.

Making a good sensor

Apart from simple labeled proteins, it is estimated that there are over 100 sensors and reporters available that have been used in living cells or animals. Of these, only a small number have been used outside of their lab of origin. Many genetically encoded sensors originated from the discovery of a molecular mechanism underlying a biological process, such as calcium binding or GTPase activity. Thanks to decades of fundamental biological research, there are numerous biological processes waiting to be adapted for sensor or reporter design.

Bacterial and plant proteins, as well as proteins that are common in only one cell type, are particularly useful for building sensors in mammalian cells because they are less likely to show cross-reactivity. Alternatively, isolated protein domains that lack enzyme activity can often be starting points for the development of intramolecular sensors[8]. Fluorescence-based sensors are typically successful if a protein changes conformation or when molecular assembly or disassembly occurs. In such cases, Förster resonance energy transfer (FRET)-based reporters, which rely on a fluorophore pair that senses proximity and or dipole orientation, are a common choice (**Fig. 1**). For genetically encoded FRET-based sensors, much attention has to be paid to the position and properties of the peptide linkers between the sensor protein and the somewhat large fluorescent proteins[9]. Often, this involves an educated guess, based on substituting amino acids and varying overall linker composition until a sensor shows a useful sensitivity (a large structural change induced between the two fluorescent proteins) in response to the underlying biological process. However, as the barrels that make up the core of fluorescent proteins never allow the chromophores to come into truly close proximity, FRET changes are typically small, even for the best sensors.

To overcome these limitations, a semisynthetic approach was recently developed using SNAP and CLIP tags to introduce small-molecule fluorophores into sensors for drugs or metabolites (**Fig. 1**)[10]. This strategy is based on genetically fusing

an enzyme (SNAP or CLIP) to a protein of interest, yielding a fusion protein that is able to label itself in the presence of a suitable substrate. The result is similar to a genetically encoded fusion protein, but the fluorophores are synthetic, small and photostable. As a result, FRET changes in response to conformational changes were in the order of 30–100% and are expected to reach values as high as 500% in the future, significantly higher than with the average fluorescent proteins. In the future, a less intrusive and more sophisticated solution could be provided by fluorescent tags that covalently react with small residues inside the living cells. Examples are the FlAsH tag that reacts with tetracysteine motifs[11] and unnatural amino acids (UAAs) that provide bioorthogonally reactive chemistry via cyclooctyne groups[12]. UAAs can be genetically encoded by re-engineering the host translation system, allowing site-specific replacement of a single natural amino acid in a protein of choice with a customized artificial amino acid[13] (such as a 'clickable' UAA; **Box 1**). This technology offers a straightforward route to minimize changes to the native protein.

When protein conformational changes are not involved, small and nonratiometric sensors might be considered. However, care needs to be taken with this approach, as nonratiometric intensity-based sensors suffer frequently from the influences of environmental factors, including pH and ions. Even more problematic is the variation in sensor copy number from one cell to the next. Furthermore, the variability and stability of equipment often complicates experiments and makes comparisons between studies almost impossible, as there is usually no internal reference for standardization. Nonratiometric tools are most commonly applied if a ratiometric sensor does not exist or if an additional readout, such as spatial redistribution, makes it possible to generate ratios of intensities between two regions within the cell[14].

Small-molecule sensors, which are widely used to detect metal ions such as calcium and zinc, come in different varieties, including ratiometric and nonratiometric variants; their major advantages are their small size and tunable biophysical properties. Their much higher performance has a two-fold cost: preparation of these reagents requires organic and/or peptide chemistry and significant purification, and cell penetration of sensors is not always achieved by small-chemical, enzyme-sensitive masking groups. In general, cell delivery is often difficult because what is able to enter is also able to leave. Solutions include the use of cell-penetrating peptides[15] and noncovalent tricks to force the molecular tool into cells or tissue[16]. The issue of cell and tissue penetration is generally one of the most basic bottlenecks in all strategies for the biological application of synthetic 'spying' tools.

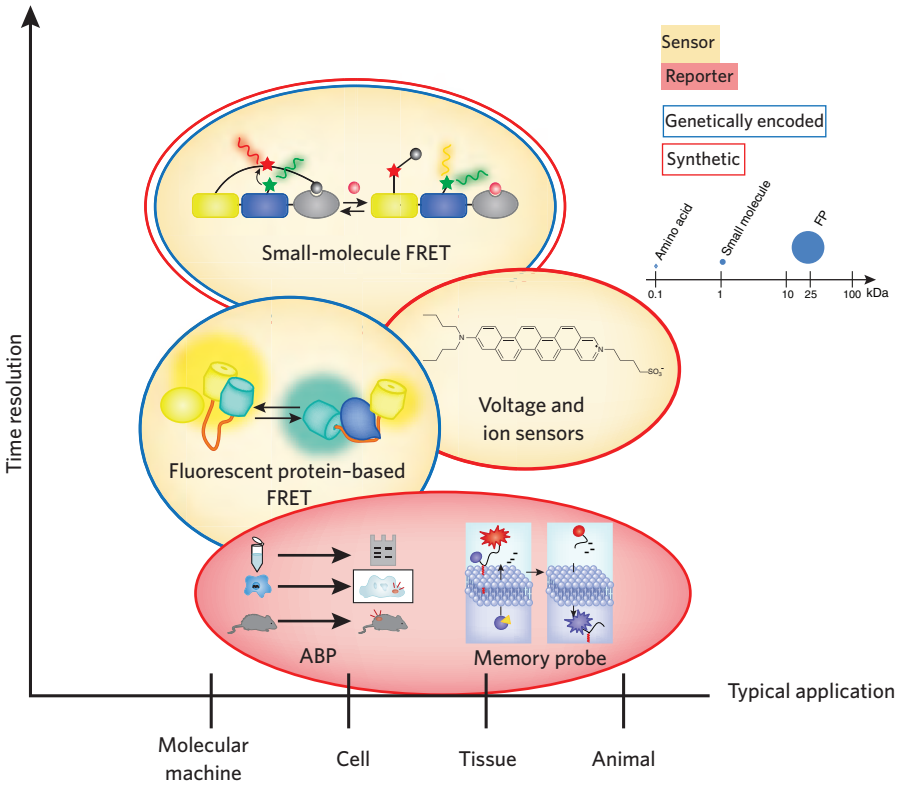

Figure 1 | Example reporters and sensors with typical time resolution and application range. In small-molecule FRET, small synthetic molecule dye pairs are used to probe ligand and or metabolite binding. In FP-based FRET, genetically encoded FRET sensors are frequently used to measure conformational changes induced by, for example, post-translational modifications or ligand binding. Voltage and ion sensors report dynamic behavior by changes in emission intensities or ratiometric readouts. Shown here is the voltage sensor ANNINE-6, which inserts into plasma membranes. Activity-based probes have applications *in vitro*, in cells and within living organisms (left). Internalization of a fluorescent fragment after cleavage of a lipidated small-molecule protease FRET reporter on cell surfaces produces a memory effect (right).

Making a good reporter

The design of fluorescent substrates to serve as reporters for enzymes is in theory straightforward. Once a suitable enzyme substrate has been identified, a useful FRET-dye pair can be attached to either end of the substrate such that a bond cleavage (for example, elimination or hydrolysis) results in total separation of the dye pairs and thus, complete loss of FRET instead of a gradual change. However, as with small-molecule probes in general, this comes at the cost of decreased cell penetration as well as cell- or tissue-specificity issues. Even more importantly, those probes need to be synthesized by organic chemistry procedures, and any modification to the reporter requires more or less sophisticated chemistry and the ability to make fresh batches over time. As a result, there are currently many more genetically encoded sensors than small-molecule reporters available.

Toward spatial resolution of enzyme activities

Enzyme activity is at the core of biological function and many activities central to cell viability. The number of reactions going on in a single cell per unit of time is enormous. The constant forming and breaking of bonds thus presents an ideal environment for studying protein function using ABPs (**Fig. 1**). A particularly elegant approach is the development of a compound that perfectly mimics the original substrate and acts as a suicide inhibitor. The active enzyme consumes the artificial substrate—by

our definition, a reporter—immediately stalling enzyme function, thus providing a global snapshot of cellular enzyme activity. If a fluorescence marker is linked to the artificial substrate, a spatial target profile can be generated by advanced imaging technologies. The power of this technique can be enhanced even further if a purification handle, which allows a scientist to 'fish' for the inactivated enzymes[17], is also linked to the probe. Advanced proteomics analysis then reveals the identity of the targets. Owing to the high sensitivity of such approaches, even rare events and heterogeneous populations can be resolved.

An alternative to ABP use is to directly monitor the formation of enzyme-substrate complexes by fluorescence lifetime imaging. In one published example of this technique, a tyrosine phosphatase PTP1B sensor was able to reveal localized enzyme activity at the endoplasmic reticulum[18].

Memory reporters

The search for memory probes has been going on for decades, and the above mentioned ABPs could be considered a special class of these probes**.** In neurobiology, it would be very helpful to know which cells in a neuronal network in an intact organism have fired under a specific set of environmental and temporal conditions. To our knowledge, however, there is no calcium sensor that can provide this information in organisms. In the future, it might be possible to use annexins to do this, as these proteins polymerize irreversibly after a specific intracellular calcium level is reached[19]. The readout intensity will be improved when enzyme substrates are used, owing to intrinsic amplification and irreversibility. The challenge in this case is to preserve the products of the enzymatic reaction locally. In some examples, this has been achieved by generating an entity that can penetrate cell membranes after cleavage of a FRET reporter. The fluorescent fragment is then trapped, staining the cell interior (**Fig. 1**)[20,21].

Demand versus delivery

The need to understand molecular functions in cells is increasing the demand for sensors and reporters enormously. For some common organisms, the number of fluorescent fusion proteins used to localize proteins of interest in cells reaches into the thousands, although there are issues maintaining endogenous protein levels with these reporters. Still, there are only a few probes available for monitoring enzyme activities. Ideally, we would have sensitive reporters and sensors for most biochemical reactions happening in cells, but ten years of hard work have clearly failed to achieve this goal. Therefore, high-throughput approaches need to be developed to make more probes available. For genetically encoded sensors, this means that most expressed sequence tags need to be placed between a selected set of fluorescent proteins, including circular permutated versions with a variety of dipole moment orientations, serving as FRET pairs. To do this for large libraries, automated cloning and automated microscopy are required. The latter was recently established at the European Molecular Biology Laboratory in Heidelberg, where cDNAs bearing FRET constructs were spotted on cover slips[9]. Reverse transfection of cells growing on these spots in a multiwell format permitted the examination of larger sensor libraries by automated confocal microscopy under identical conditions, thereby helping to increase the throughput in sensor production.

Sensors and reporters in animal models

Application of sensors to animal models is not just limited by the technological state of sensor development: genetic sensors require time-consuming knock-in strategies, whereas faster gene-delivery strategies, such as viral infection, are still subject to problems with issues such as controlled expression, infectivity and tissue specificity. In addition, fluorescence imaging in living animals is still a nascent field. However, two-photon imaging[22] and sheet-illumination approaches[23] have the potential to overcome many of the current challenges. Particularly advanced sensors have already been applied in neurobiology, where voltage-sensitive small-molecule dyes (**Fig. 1**) can facilitate visualization of action-potential firing[24]. Using genetically encoded sensors, we can envision a future where we can see brains think. Given the growing potential of genetically encoded and neuron-specific sensors, a time-resolved atlas of neuronal network activity does not just seem like fiction anymore.

Parting perspectives

Analogous to drug screening, combinatorial approaches may also be used to screen for small-molecule sensors. These efforts do not face the same hurdles as screening for genetically encoded probes but instead face the possibility that the resulting probes lack a targeting device for *in vivo* applications. A possible solution would be to use semisynthetic strategies that incorporate the advantages of both approaches, which we envision will define the future. New sensors can be identified in chemical screens, and as part of a pipeline process, target compounds will be selected for membrane permeability. Using 'click chemistry', selected compounds can then be linked to a genetically encoded 'click counterpart', assuring proper integration into host cells and living organisms (**Box 1**).

We also want to stress that the improvement of fluorescent sensors and reporters is necessarily linked to technological advances in fluorescence detection and microscopy. There are many more exciting advances that could be

Box 1 | "Click Chemistry"

An optimal biocompatible chemical reaction proceeds rapidly in water and is absolutely specific. In order for it also to work within the context of a living cell, another prerequisite is that that both reaction partners must be completely bioorthogonal, meaning that they do not cross-react with any biological specimen. Very few chemical reactions fulfill these requirements, and these are often summed up under the term 'click chemistry'. One of the most prominent types of biocompatible click reactions is the reaction between an ideally strained alkyne and an azide. Both chemical groups are not naturally occurring, are fairly inert, are nontoxic and react with each other quite rapidly. The high biocompatibility of this type of chemistry has even enabled applications within living embryos[26].

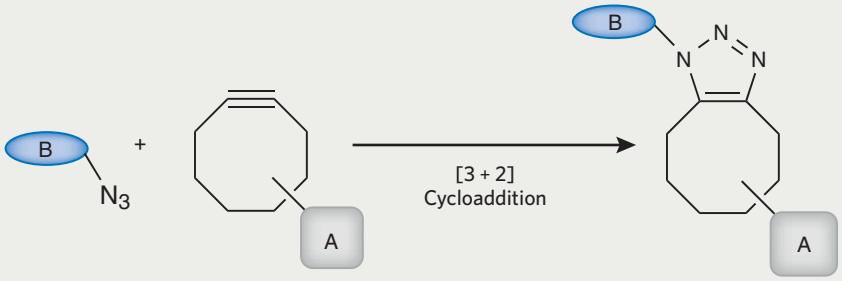

Basic reaction for strain-promoted azide-alkyne activated click chemistry (SPAAC).

discussed: for example, the development of switching-based technologies[25], which will have a dramatic impact on future sensor and reporter studies.

In the future, there will be the need for an objective quality standard for sensors and reporters. In many analytical fields, general quality criteria have been established. For instance, X-ray crystallographers use R_{free} values and resolution as standard scales by which to judge the quality of a model. Sensors and reporters also have recurring characteristics that provide information about their utility, such as sensitivity, signal strength and stability. What has been less fully investigated is whether they are sensitive to other cellular perturbations unrelated to their intended application—a factor that is often only taken into account during the application of the sensor. The process of 'learning by doing' is long and winding, making it especially helpful to establish common quality criteria for a given variable, especially to facilitate the application of the expected wave of new sensors and reporters in live cells and organisms.

Edward A. Lemke is in the Structural & Computational Biology Unit at the European Molecular Biology Laboratory, Heidelberg, Germany. Carsten Schultz is in the Cell Biology & Biophysics Unit at the European Molecular Biology Laboratory, Heidelberg, Germany.
**e-mail: lemke@embl.de or schultz@embl.de*

References

1. Waggoner, A. *J. Membr. Biol.* **27**, 317–334 (1976).
2. Tsien, R.Y. *Biochemistry* **19**, 2396–2404 (1980).
3. Grynkiewicz, G., Poenie, M. & Tsien, R.Y. *J. Biol. Chem.* **260**, 3440–3450 (1985).
4. Tsien, R.Y. *Nature* **290**, 527–528 (1981).
5. Chalfie, M., Tu, Y., Euskirchen, G., Ward, W.W. & Prasher, D.C. *Science* **263**, 802–805 (1994).
6. Fonović, M. & Bogyo, M. *Expert Rev. Proteomics* **5**, 721–730 (2008).
7. Cravatt, B.F., Wright, A.T. & Kozarich, J.W. *Annu. Rev. Biochem.* **77**, 383–414 (2008).
8. Zhang, J., Campbell, R.E., Ting, A.Y. & Tsien, R.Y. *Nat. Rev. Mol. Cell Biol.* **3**, 906–918 (2002).
9. Piljić, A., de Diego. I., Wilmanns, M., & Schultz, C. *ACS Chem. Biol.* 6, doi:10.2021/cb100402n (2011).
10. Brun, M.A., Tan, K.T., Nakata, E., Hinner, M.J. & Johnsson, K. *J. Am. Chem. Soc.* **131**, 5873–5884 (2009).
11. Adams, S.R. *et al. J. Am. Chem. Soc.* **124**, 6063–6076 (2002).
12. Plass, T., Milles, S., Koehler, C., Schultz, C. & Lemke, E.A. *Angew. Chem. Int. Edn Engl.* **50**, 3878–3881 (2011).
13. Liu, C.C. & Schultz, P.G. *Annu. Rev. Biochem.* **79**, 413–444 (2010).
14. Piljic, A. & Schultz, C. *ACS Chem. Biol.* **3**, 156–160 (2008).
15. Joliot, A. & Prochiantz, A. *Nat. Cell Biol.* **6**, 189–196 (2004).
16. Ozaki, S., DeWald, D.B., Shope, J.C., Chen, J. & Prestwich, G.D. *Proc. Natl. Acad. Sci. USA* **97**, 11286–11291 (2000).
17. Greenbaum, D. *et al. Mol. Cell. Proteomics* **1**, 60–68 (2002).
18. Yudushkin, I.A. *et al. Science* **315**, 115–119 (2007).
19. Gerke, V., Creutz, C.E. & Moss, S.E. *Nat. Rev. Mol. Cell Biol.* **6**, 449–461 (2005).
20. Jiang, T. *et al. Proc. Natl. Acad. Sci. USA* **101**, 17867–17872 (2004).
21. Cobos-Correa, A., Trojanek, J.B., Diemer, S., Mall, M.A. & Schultz, C. *Nat. Chem. Biol.* **5**, 628–630 (2009).
22. Kuhn, B., Denk, W. & Bruno, R.M. *Proc. Natl. Acad. Sci. USA* **105**, 7588–7593 (2008).
23. Keller, P.J. *et al. Nat. Methods* **7**, 637–642 (2010).
24. Bradley, J., Luo, R., Otis, T.S. & DiGregorio, D.A. *J. Neurosci.* **29**, 9197–9209 (2009).
25. Patterson, G., Davidson, M., Manley, S. & Lippincott-Schwartz, J. *Annu. Rev. Phys. Chem.* **61**, 345–367 (2010).
26. Laughlin, S.T., Baskin, J.M., Amacher, S.L. & Bertozzi, C.R. *Science* **320**, 664–667 (2008).

Competing financial interests

The authors declare no competing financial interests.

Vladislav Verkusha, Tuesday June 12th 2012, 14.30

Directed molecular evolution to design advanced red fluorescent proteins

Fedor V Subach[1,2], Kiryl D Piatkevich[1,2] & Vladislav V Verkhusha[1]

Fluorescent proteins have become indispensable imaging tools for biomedical research. Continuing progress in fluorescence imaging, however, requires probes with additional colors and properties optimized for emerging techniques. Here we summarize strategies for development of red-shifted fluorescent proteins. We discuss possibilities for knowledge-based rational design based on the photochemistry of fluorescent proteins and the position of the chromophore in protein structure. We consider advances in library design by mutagenesis, protein expression systems and instrumentation for high-throughput screening that should yield improved fluorescent proteins for advanced imaging applications.

The discovery of homologs of GFP, which emit not only green but also yellow, orange and red fluorescence, has provided a powerful boost for *in vivo* labeling[1]. Similarly to GFP, these fluorescent proteins have been developed into monomers suitable for protein tagging: this includes conventional fluorescent proteins, fluorescent proteins with a large Stokes shift of fluorescence emission (LSS-FPs), photoactivatable and photoswitchable fluorescent proteins (PA-FPs and PS-FPs, respectively) and fluorescent timers[2]. Several advances in the design of red-shifted—such as orange, red, and far-red—fluorescent proteins (here generally referred to as red fluorescent proteins (RFPs)), and RFP-based biosensors with new spectral and photochemical properties have also been achieved: reduced autofluorescence, low light scattering and minimal absorbance at the longer wavelengths make RFPs superior probes for super-resolution, deep-tissue and two-photon imaging. However, no existing RFP is perfect; each still has some suboptimal key characteristics such as brightness, pH stability, photostability, maturation rate, photoactivation, photoswitching contrast or monomeric state (**Supplementary Table 1**). Some RFPs undergo undesirable photochromism and photoconversion during imaging or complex photobehavior during switching, and few attempts have been made to optimize such properties as intracellular life span and cytotoxicity. Although many RFPs have properties that are optimal for specific applications, no single RFP combines several of them (**Supplementary Table 2**). Moreover, there is a large demand for RFPs with improved brightness. Also, monomeric LSS-FPs and PA-FPs are available in green and red colors only[2,3]. Finally, red-shifted fluorescent proteins also hold a great potential for the engineering of biosensors, but this has not been exploited in full as yet. Thus, we expect that new strategies for generating enhanced RFPs will have an impact on many fields.

Here we first describe chemical transformations of the RFP chromophores, the understanding of which gives the basis for a knowledge-guided design of new red-shifted fluorescent proteins. The chemistry of the RFP chromophores is more diverse and complex than that of the GFP-like chromophore and thus has substantially more potential for selection and fine-tuning. Nonetheless, although we focus on the development of new RFPs, the general themes we discuss apply to fluorescent proteins of all colors. Based on in depth analysis of the dependence of RFP properties on amino acids surrounding the chromophore, we describe approaches for the development of new red-shifted fluorescent proteins with desired phenotypes. Finally, we consider new methods to improve molecular evolution and discuss possible resulting RFPs for emerging imaging techniques.

Rational design of fluorescent proteins

A typical process for the development of fluorescent proteins with desired properties includes rational

[1]Department of Anatomy and Structural Biology, and Gruss-Lipper Biophotonics Center, Albert Einstein College of Medicine, Bronx, New York, USA. [2]These authors contributed equally to this work. Correspondence should be addressed to V.V.V. (vladislav.verkhusha@einstein.yu.edu).

PUBLISHED ONLINE 29 NOVEMBER 2011; DOI:10.1038/NMETH.1776

design followed by several steps of directed molecular evolution (**Fig. 1** and **Supplementary Note**). Rational design relies on knowledge about chromophore transformations in RFPs.

Chromophore transformations. The chemistry of RFPs is determined by the chromophore-forming tripeptide and its immediate environment. Although most chemical transformations occur in the chromophore, its amino acid microenvironment has a crucial role for catalysis. Currently known red-shifted fluorescent proteins have one of two major types of red chromophores, called the DsRed-like chromophore 5a, 6a (see **Fig. 2** for chromophore structure and numbering) and the Kaede-like chromophore 14, after the first proteins in which they had been found[1,2].

Two chemical mechanisms for DsRed-like chromophore formation have been discovered[2]: it is formed either through autocatalytic post-translational modifications of a blue monomeric (m)TagBFP-like chromophore 4 (refs. 4,5) (found in mTagBFP[6] and in the blue form of fluorescent timers[7]) or via induction by irradiation with violet light[8], as in the case of PAmCherry[9], PATagRFP[10] and PAmKate[11]. The DsRed-like chromophore can exist in neutral 5b, 6b or anionic 5a, 6a states, which interconvert upon pH changes and excited-state proton transfer[3,12]. Cyclization of the N-acylimine group in the DsRed-like chromophore results in an mOrange-like or mKO-like 10 chromophore or a zFP538-like 9 chromophore, exhibiting orange emission[1,2]. Formation of the zFP538-like chromophore 9 is accompanied by backbone cleavage. The photoconversion of the DsRed-like chromophore 5a, 6a into the GFP-like chromophore 12 has been demonstrated for mKate, HcRed and DsRed using high-power irradiation[13]. The converse transition 12 to 5a, 6a, called 'redding', was autocatalytic[14] or induced by oxidants for several different GFPs[15]. Unlike the GFP-like chromophore, the illumination of mOrange-like or mKO-like chromophores 10 resulted in an appearance of far-red 11 and red 5a species, respectively[13,16]; the absorbance (610 nm) and emission (650 nm) of these far-red species suggested formation of new type of chromophore (**Supplementary Table 3**). The far-red–shifted spectral properties of chromophore 7 observed in mRouge[17], E2-Crimson[18], mNeptune[19] and TagRFP657 (ref. 20) result from the realization of hydrogen bonding, stacking interactions and/or hydrophobic residues surrounding the DsRed-like chromophore.

The Kaede-like chromophore 14 is characteristic for the red state of green-to-red PS-FPs including Kaede, EosFP, mEos2, mIrisFP, Dendra2, mKikGR and mClavGRs[1,2,21]. In the green state, these Kaede-like PS-FPs have the GFP-like chromophore 12. The formation of the Kaede-like chromophore requires a histidine residue at the first position of the chromophore-forming tripeptide Xnn65-Tyr66-Gly67 (where Xnn is any amino acid and numbering of amino acids follows that of GFP), limiting its possible chemical transformations.

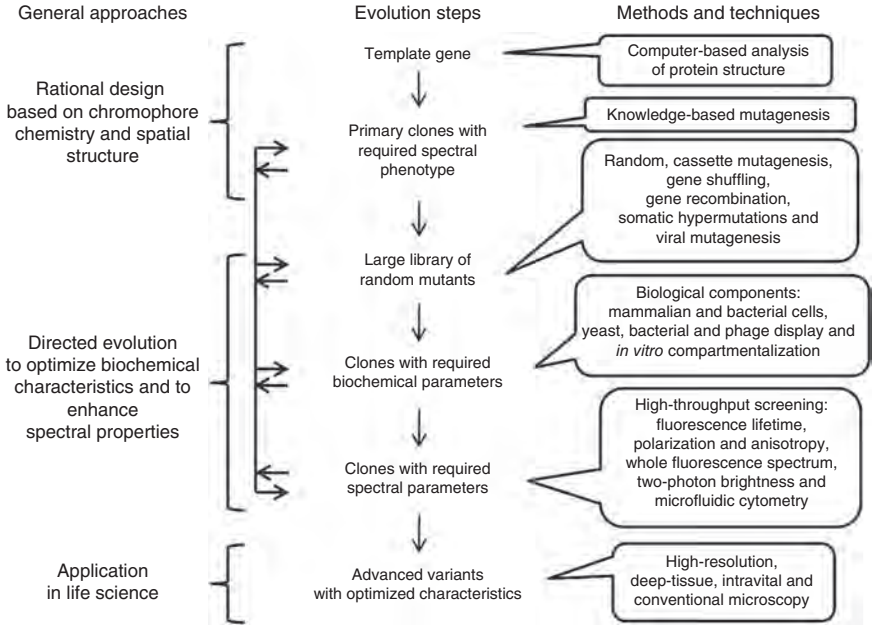

Figure 1 | Steps in the directed molecular evolution of fluorescent probes. Vertical arrows indicate the typical order of steps. Horizontal arrows represent possible transitions between the steps of molecular evolution, which can be repeated several times in different order.

Based on the current data on fluorescent proteins, three conclusions can be formulated: (i) most chemical transitions between chromophore structures occur autocatalytically, photochemically (by photoinduction) or are blocked; (ii) the same chromophore structure can be either in a fluorescent state (that absorbs and emits) or in a chromo state (that absorbs but does not emit); and (iii) autocatalytic versus photoinduced versus blocked states and fluorescent versus chromo states are mainly determined by amino acid residues in the chromophore and in its nearby environment. Some of these conclusions can be illustrated by two RFP subfamilies, derived from mCherry and TagRFP (**Fig. 2b,c**). These observations form the physicochemical basis for the development of RFPs with new photochemical behavior.

Choosing a template. Choosing an appropriate starting template for development of fluorescent proteins is an important step that strongly influences the final results of the process. A list of possible templates is made based on their spectral and biochemical properties, using as criteria both the required phenotype and the availability of three-dimensional structures. High amino acid homology between potential precursors and already known RFPs with the desired phenotype but having different spectral characteristics or other suboptimal properties can be used as an additional screening criterion. It is preferable to select templates with beneficial characteristics such as high brightness, pH stability, photostability, fast maturation and low cytotoxicity. For example, the brightness, maturation and pH stability of PATagRFP and PAmCherry1 proteins correlates with those characteristics of their precusors[10].

Knowledge-based mutagenesis. The knowledge of chromophore chemistry and overall protein structure enables the directed engineering of variants with required phenotypes (**Table 1** and **Supplementary Table 4**). As stated above, the diverse chemical

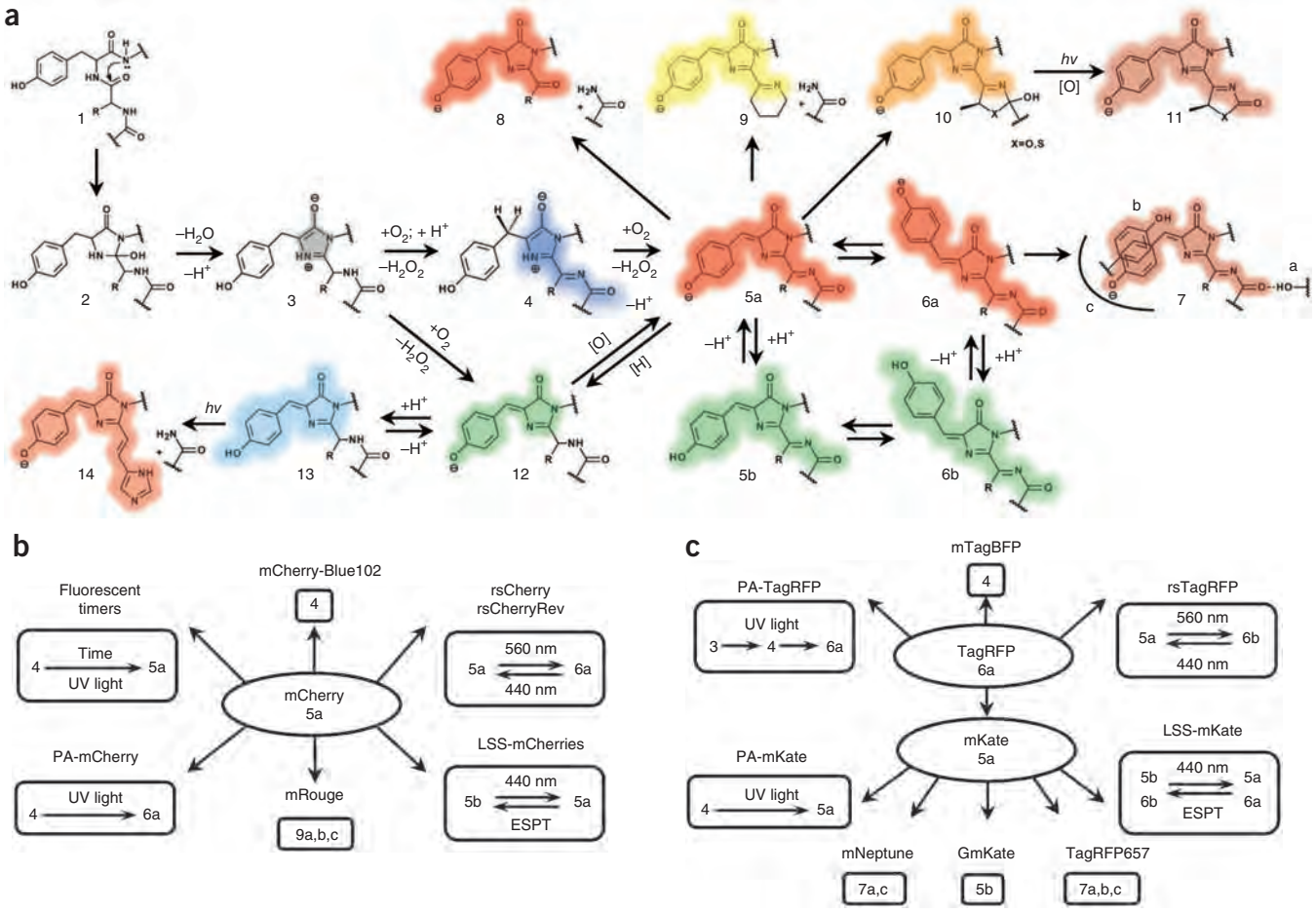

Figure 2 | Major chemical transformations of the chromophores in red fluorescent proteins. (**a**–**c**) Transformations in fluorescent protein subfamilies derived from red fluorescent protein (**a**), mCherry (**b**) and TagRFP (**c**). The colored shading of the chemical structures (**a**) and chromophore numbers (**b**,**c**) correspond to the spectral range of the chromophore fluorescence emission. Gray shading denotes the nonfluorescent state; [H] denotes reduction; and [0] denotes oxidation. The chromo states (structures 5, 10 and 13) are not necessarily caused by a *cis-trans* chromophore isomerization but may result from modifications of the chromophore environment of the same isoform that decrease quantum yield. *hv*, photon.

transitions and spectral and photochemical properties of red-shifted fluorescent proteins are mainly due to the interactions between the chromophore and its immediate environment. The main targets for rational design are therefore the amino acid residues around the chromophore.

There are currently ~80 red-shifted fluorescent proteins of different phenotypes. An analysis of the properties of these existing RFPs and of their chromophore's immediate environment suggests key and supporting positions for each phenotype. Amino-acid residues at the key positions provide a principal RFP phenotype, whereas residues at the supporting positions tune the RFP properties (**Supplementary Note**). Both key and supporting residues are responsible for the different photoinduced or autocatalytic chromophore transitions, photophysical chromophore properties and oligomeric state of RFPs (**Table 1**, **Supplementary Table 4** and **Supplementary Fig. 1**). For example, an alignment of the amino acid sequences of red-shifted PA-FPs with those of the parental RFPs and with each other reveals positions at which the residues were substituted. This allows us to identify positions such as 69 and 203, minimally required for the photoactivatable-like phenotype, as key positions (**Table 1**). Additional analysis of literature on available mutants and on X-ray structures of the related RFPs allowed us to determine ten supporting positions responsible for this phenotype (**Supplementary Table 4**). We note that there are many examples where a particular property (for example, red color in DsRed) is a synergistic effect of the large number of residues, including many that are remote from the chromophore. How these positions control fluorescence properties via coupling to each other is poorly understood.

Based on suggested residues at the key (**Table 1**) and supporting positions (**Supplementary Table 4**), the template can be subjected to multiple site-specific mutagenesis at the chosen positions, beginning with residues at key positions and, in subsequent rounds, targeting supporting positions to optimize properties of fluorescent proteins. The PAmCherry[9], PATagRFP[10], rsTagRFP[22], mRouge[17] and mTagBFP-like[6] and LSS-FP–like[3] fluorescent proteins have different colors and photochemical behavior, and all of them were developed using rational mutagenesis at amino acids around the chromophore to find a weak phenotype, followed by random mutagenesis for the improvement of mainly brightness, maturation and photostability. A computer-based approach using the PHOENIX protein design software and FASTER algorithm can be used to eliminate amino acids incompatible with the β-barrel protein fold and generate focused small-size combinatorial libraries of RFP mutants[17].

Table 1 | Residues responsible for RFP phenotypes and properties

Phenotype or property	Structure or transition	Key positions			
mTagBFP-like	4	84[a] Phe, Trp, Leu	148[a] Phe, Ile	203[a] Ile, Tyr, Phe	
Fluorescent timer-like	4 → 5a, 6a	69[a] Arg		84[a] Trp	
Photoactivatable-like	4 → 5a,6a	69[a] Asn, Ser, Lys, Gln		203[a] Arg	
Photoswitchable-like	5a ↔ 6a	148[a] Cys, Ala, Thr, Ser	165[a] Ser, Gly, Ile	167[a] Met, Gln	203[a] His, Ile
Far-red shifted–like					
Hydrogen bonding to N-acylimine	7a	14[b] Thr, Phe	16[b] Thr, Glu, Gln, Val	44[b] Gly, Gln, Glu, Ala, Cys, Met	
Hydrophobic packing	7c	84[c] Phe, Leu, Trp	148[c] His, Ser, Cys, Asn	165[c] Met,T,C, Asn, Ser	167[c] Mer, Leu, Gln
π stacking	7b	65[c] Phe, Met, Gln	69[c] His	148[c] His, Ser, Cys, Asn	203[c] Tyr, His, Arg, Thr, Ile
Large Stokes shift–like	5b, 6b ↔ 5a, 6a	148[b] Asp	165[b] Asp, Glu	167[b] Asp, Glu, Lys	
High quantum yield		70[c] Thr	148[c] Ser, Asn	167[c] Met	
High photostability		64[a] His	99[a] Tyr	165[c] Thr, Ala, Ile	
High pH stability		69[b] Arg		167[b] Lys	
Fast maturation		42[c] Gln	69[c] Lys, Arg	179[c] Val, Ala, Cys	224[c] Ser, Ala
Monomeric state		126[c] Arg	162[c] Glu, Lys, Arg	166[c] Asp, Lys, His	168[c] Ala, Arg

[a]Residues at this position provide the respective phenotype in a concerted manner (residue numbering follows that for jellyfish GFP). [b]Residues at this position provide the respective phenotype independently. [c]Residues at this position provide the respective phenotype either in a concerted manner or independently.

Directed evolution of fluorescent proteins

Creation of large libraries of mutants. Once rational design has resulted in primary clones with a required spectral phenotype, researchers typically take advantage of directed evolution for optimization. The first step in each round of molecular evolution is the generation of a large number (>10^5) of mutant genes. *In vitro* random mutagenesis, coupled with bacterial expression, has been effectively used to develop new red-shifted fluorescent proteins. In eukaryotic systems, different approaches must be taken to generate large mutant libraries. A recombinant vesicular stomatitis virus was recently reported to generate randomly mutated fluorescent proteins amenable to screening in mammalian cells[23]. The mutation rate and the size of the library were controlled by regulating the number of infected cells and the number of rounds of viral replication. However, the likely presence and continuous replication of several viral genomes per cell may hamper efficient screening of clones for specific spectral phenotypes (**Fig. 3**). Gene-diversification processes, such as somatic hypermutation and gene conversion, occur naturally in B lymphocytes via an introduction of random point mutations in a certain gene and through random shuffling of complex genetic domains, respectively. These approaches have been introduced for high-throughput screening of non-antibody proteins and have been applied to develop RFPs[24].

The main advantages of *in vivo* mutagenesis are expression of the protein library in the context of intracellular networks, substantially shorter time of sequence evolution and high diversity of mutants; viral mutagenesis is applicable to a wide spectrum of cell types and has advantage over somatic hypermutation and gene conversion approaches, which are limited to B lymphocytes. Furthermore, because these mutagenesis techniques use mammalian cells as hosts, they should result in the selection of mutants with low cytotoxicity and ones that are optimized for expression and stability in these cells.

Biological components of molecular evolution. New systems for the expression of gene libraries may help to improve directed evolution of fluorescent proteins and increase the number of biochemical parameters screened. With the exception of the above examples in eukaryotic cells, to date the molecular evolution of fluorescent proteins is mainly carried out via expression in *Escherichia coli*.

One property that could be substantially improved in new expression systems is intracellular half-life. Currently available fluorescent proteins typically have an intracellular half-life in mammalian cells of about 20–30 h (ref. 25). Short-lived fluorescent proteins variants with lifetimes of 0.5–10 h have been developed by fusing them with ubiquitinatable peptides[25]. However, fluorescent proteins with an extended intracellular lifespan are still in demand. Use of bacterial hosts other than *E. coli*, such as *Thermus thermophilus* that grow at 70 °C (ref. 26), could allow high-throughput screening for thermally stable fluorescent proteins, but this approach has not been implemented yet (**Fig. 3**). With some exceptions, a longer intracellular lifespan of proteins correlates with their higher thermostability in bacteria[27] and mammalian cells, so that this approach could complement expression in mammalian cells as a way to screen for variants with longer half-lives and those that are more suitable for long-term monitoring of proteins *in vivo*.

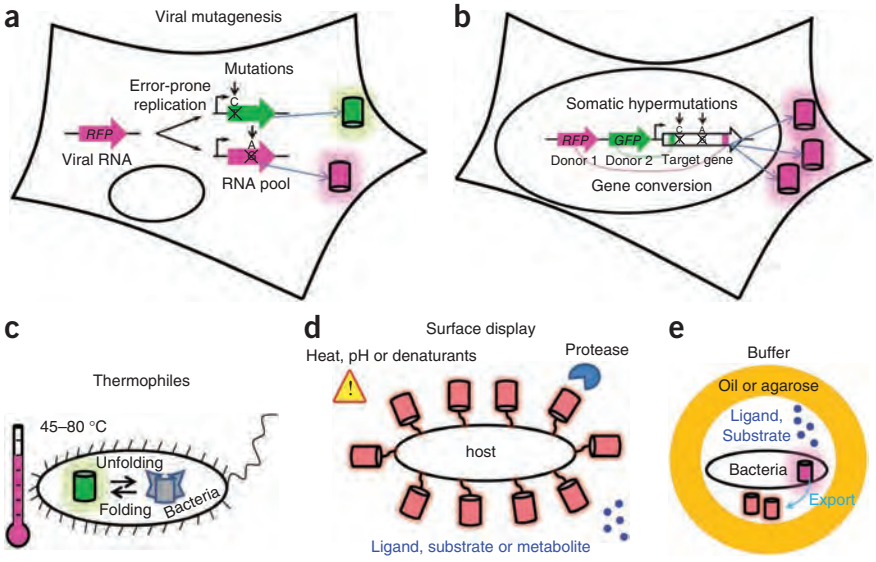

Figure 3 | Methods that could improve molecular evolution of fluorescent proteins. (**a**–**e**) Schematics depict eukaryotic cell–based mutagenesis methods (**a**,**b**) and advanced protein expression systems (**c**–**e**). Cylinders denote fluorescent protein molecules. Error-prone replication of virus (**a**) causes point mutations in the viral genome containing a target fluorescent protein gene; after several rounds of replication, the cell expresses mutated fluorescent protein genes. Somatic hypermutations and gene conversion in eukaryotic cells (**b**) allow for creation of large random mutant gene libraries during cell proliferation (note that only one type of fluorescent protein mutant is produced per cell). Expression of fluorescent protein libraries (**c**) in thermophilic bacteria for selection of more stable fluorescent proteins. Surface display (**d**) of fluorescent protein libraries could facilitate screening for fluorescent protein stability under different environmental conditions or for fluorescent protein–based biosensors. *In vitro* compartmentalization (**e**) of bacteria in water-oil-water or water-agarose-water droplets should enable screening for fluorescent protein–based biosensors.

Phage, bacterial and yeast surface display of a fluorescent protein library offers a spectrum of screening conditions (proteases, temperature and denaturants) for higher stability of the displayed protein[28]. In particular, surface display of fluorescent proteins could provide an important future tool for screening of biosensors. Surface display of biosensor variant libraries would enable screening for interactions with potential ligands, substrates or metabolites. Surface displays of large proteins are well developed in yeast eukaryotic cells[29], but typical library sizes are limited to about 10^5 clones. Bacterial surface display is not well established for large proteins and requires improvement[30]. The *Bacillus subtilis* endospore system (proteins are targeted to the endospore surface) may be promising in this regard because the expressed proteins do not need to cross a cytoplasmic membrane, but the low transformation efficiency of *B. subtilis* is a substantial limitation. An approach that could in the future complement bacterial display for RFP-biosensor screening is *in vivo* compartmentalization[31], based on compartmentalization of bacterial cells secreting RFP constructs in water-in-oil emulsions. But problems with ensuring the presence of single constructs per 'cell', with limiting the number of empty 'cells' and with preventing exchange of small molecules between compartments limit this approach and will need to be solved.

Instrumentation for high-throughput screening. The major high-throughput screening approach for evolution of fluorescent proteins is sorting of bacterial libraries using a fluorescence-activated cell sorter. However, it is limited by the available excitation sources[32] and to the detection of essentially three parameters: (i) wavelength of fluorescence emission, (ii) fluorescence intensity and (iii) intensity of light-scattering at two angles. The substantial improvements of the optical detection modes and fluidics formats discussed below have been implemented in proof-of-principle experiments, but these achievements have not been applied for RFP screening yet.

Fluorescence-activated cell sorter optical components can be developed by introducing new types of excitation and detection formats (**Fig. 4**). Recording the whole fluorescence spectrum[33] during fluorescence-activated cell sorting (FACS) may enable efficient screening for far-red– and near-infrared–shifted fluorescent proteins. Detection of polarization or anisotropy would enable screening for monomeric RFPs lacking fluorescence resonance energy transfer (FRET) between similar chromophores (homo-FRET). Incorporating sequential irradiation with several synchronized lasers will make it possible to sort for high-speed photoswitching PA-FPs for photoactivated localization microscopy (PALM) of live cells.

FACS with fluorescence lifetime detection[34] will permit additional improvement of FRET pairs of fluorescent proteins. It will accelerate the development of RFPs with distinctive lifetimes, which would provide new possibilities for imaging proteins *in vivo*, using a single excitation source and emission channel[35]. The fluorescence lifetime is proportional to quantum yield, and fluorescence lifetime measurements are independent of changes in probe concentration, excitation intensity and other factors that limit intensity-based measurements[36]. Thus we believe that fluorescence lifetime screening either in a low-throughput format[36], or using FACS[34], holds great promise for the improvement of RFP brightness.

Finally, coupling a two-photon laser with a fluorescence-activated cell sorter[37] provides a way to develop a new class of RFPs with greater two-photon excitation efficiency. Current RFPs have suboptimal two-photon brightness and photostability[38], which are important properties for intravital imaging in animals.

Developments in the fluidics components of fluorescence-activated cell sorters could provide advanced platforms for screening of molecular fluorescent biosensors that include (i) rapid switching between buffers with distinctive properties or concentrations of substances to be 'sensed', (ii) automatic sampling from multiwell plates pretreated with such substances and (iii) use of biphasic unmixable suspensions of one liquid in another, such as aqueous drops in a nonpolar carrier for bead-based *in vitro* transcription-translation systems. Several recent approaches such as those using microfluidic cytometers[39] and a combination of imaging scanning cytometers[40] with cell-isolation technologies[41] could provide additional options for screening.

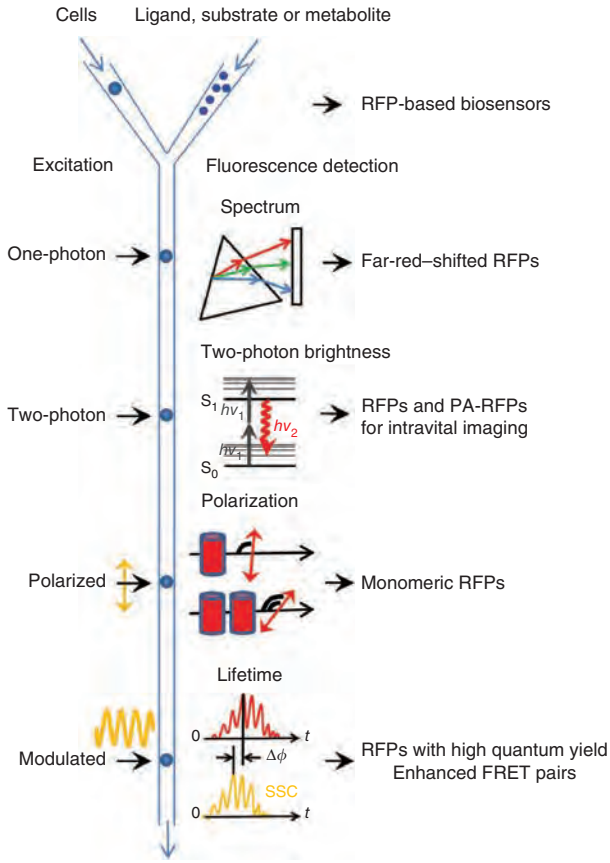

Figure 4 | Possible FACS-based screening approaches for red-shifted fluorescent proteins. The respective red fluorescent proteins expected to result from each method are listed on the right. The schematic depicts cells or other hosts expressing fluorescent proteins being mixed with ligand, substrate or metabolite with different delays before fluorescence screening. A standard one-photon laser excites flowing cells, and the resultant fluorescent signal is dispersed with a diffraction grating (triangle) and projected onto an array detector (rectangle) for recording of a complete emission spectrum. A two-photon laser excites the cells with two low-energy photons (hv_1) and the resulting fluorescence emission (hv_2) is detected. Linearly polarized laser excitation and the emitted fluorescence signals have different degrees of polarization depending on the size of fluorescent molecules and FRET efficiency between them. Cylinders denote fluorescent proteins in monomeric and dimeric states. Modulated excitation (yellow sinusoid) results in a phase shift, $\Delta\phi$, between the fluorescence emission (red) and side-scattered excitation light (SSC; yellow), which is used to compute the average fluorescence lifetime of fluorescent proteins in a cell.

Compared to FACS, these techniques are slower, but they provide longer time periods for cell detection and manipulations such as buffer exchange.

Installing cell lysis[42] and PCR microfluidic chips[43] at the output of fluorescence-activated cell sorters or microfluidic cytometers could accelerate re-cloning of fluorescent protein genes from eukaryotic, viral and phage expression systems into bacterial systems, for high-throughput screening gene sequencing and protein production. Growing of cells in microdroplets[44] would increase screening sensitivity, particularly for surface displays with a limited number of molecules of fluorescent proteins on the cell surface.

Advanced probes for emerging imaging approaches

Approaches such as super-resolution microscopy including stimulated emission depletion (STED) microscopy and PALM, deep-tissue imaging, intravital microscopy and two-photon microscopy demand fluorescent proteins with particular properties.

Commercial super-resolution STED microscopy requires far-red fluorescent proteins excitable with red lasers, such as 633 nm HeNe and 635–640 nm laser diodes[18,20]. Similarly, far-red or near-infrared fluorescent proteins are necessary for deep-tissue and whole-animal imaging, as oxy-hemoglobin, deoxy-hemoglobin and melanin do not absorb light at these wavelengths (650–900 nm), and light scattering from cellular components is decreased as well. To date the most far-red shifted fluorescent proteins, such as E2-Crimson[18], mNeptune[19] and TagRFP657 (ref. 20), have in common a DsRed-like chromophore, and have excitation and emission maxima limited to about 610 nm and 650 nm, respectively. The 'cost' of the far-red shift of the DsRed-like chromophore is a substantial drop in its quantum yield. Furthermore, quantum yield also decreases with the increasing Stokes shift of emission. As there is a correlation between the absorbance and emission wavelengths and the number of the conjugated double bonds (**Supplementary Table 3**), one possible way to develop far-red fluorescent proteins could be to design a chromophore with more double bonds than in the DsRed-like chromophore. The Kaede-like chromophore 14 is a good candidate; it has more double bonds than DsRed-like chromophore 5a, 6a and a far-red shoulder at 627 nm. Kaede-like far-red fluorescent proteins could be developed by causing the light-inducible transition from structure 12 to 14 to proceed autocatalytically. Another approach may be to exploit the fact that the mOrange-like chromophore 10 undergoes photoconversion to far-red species 11. Thus, far-red fluorescent proteins could be developed by causing the transition from structure 10 to 11 to occur autocatalytically, with no light. A third approach may exploit hydrogen bonding, stacking and hydrophobic interactions around the DsRed-like chromophore to obtain a far-red–shifted chromophore 7a,b,c.

STED microscopy is typically limited to fixed cells because of the extremely high light intensity (10 MW cm^{-2})—which is harmful to live cells—required for the depletion of the excited state of fluorescent proteins[45]. However, a STED microscopy modification, called reversible saturable optical transitions (RESOLFT), can be applied for live cell super-resolution microscopy. RESOLFT uses RS-FPs, which typically require relatively low photoswitching intensity of 1–10 W cm^{-2}, but scanning is typically performed several tens of times. Presently available RS-FPs have low photostability, which does not allow their use for many switching cycles of RESOLFT. RS-FPs with substantially higher photostability need to be engineered. RS-FPs with photoswitchable absorbance spectra could be also used as acceptors in photochromic FRET approaches[22]. This should facilitate detection of protein-protein interactions, provide internal controls for FRET and could enable the determination of the distance between interacting protein pairs.

Finally, multicolor localization microscopy of single molecules, such as PALM and its variants, requires PA-FPs of different colors[46]. Currently, monomeric PA-FPs are limited to green and red[1,9,10,46–49]. Analysis of chemical transformations of the RFP chromophores provides putative rational strategies to develop orange and far-red PA-FPs photoactivatable with violet light, for instance via making

light-inducible the autocatalytic steps from structure 4 to 10 and from structure 4 to 7a,b,c (**Fig. 2**). PA-FPs with photoactivation bands in the near-UV or green wavelength ranges could expand the palette of single-molecule super-resolution approaches even further[16]. For example, a blue PA-FP, photoactivatable with near-UV light and excitable with violet light, could be engineered by blocking the photoinducible transition from structure 4 to 5a,b (**Fig. 2**).

PALM with PA-FPs is limited to a localization precision of 15–20 nm[9] that allows for estimation of co-localization of two proteins but makes it difficult to determine whether the proteins physically interact with each other. Combining FRET with two-color PALM could solve this problem, but it is difficult because simultaneous photoactivation of the PA-FP donor and PA-FP acceptor in the interacting protein pair is highly unlikely. However, an acceptor PA-FP photoactivatable via FRET from a conventional fluorescent protein donor could allow super-resolution imaging of protein-protein interactions. A PA-FP acceptor with the photoactivation band in a green-orange wavelength range would be required for this purpose. Such PA-FPs could be also useful for intravital photoactivation experiments because green-orange light is substantially less phototoxic than violet[50].

Multicolor fluorescence imaging using a single excitation wavelength could be possible with LSS-FPs of different emission wavelengths. The excitation of such LSS-FPs with the same one-photon laser would permit researchers to image several probes simultaneously. Determination of chromophore environments in green and red LSS-FPs[3] resulted in the elucidation of several excited-state proton transfer pathways that cause the LSS emission. Engineering of these pathways into existing conventional RFPs could yield LSS probes with orange and far-red fluorescence. Moreover, multicolor LSS-FPs with close excitation maxima could be applied for intravital imaging using two-photon excitation with a single wavelength of the two-photon laser.

Conclusions

Despite the availability of increasingly sophisticated rational design software, it is unlikely that the structure-based approaches alone will be sufficient to solve all future demands for engineering of fluorescent proteins. Analysis of chromophore transformation mechanisms suggests that fluorescent probes with novel features can be designed based on existing monomeric fluorescent proteins, using a combination of rational engineering and high-throughput screening techniques. Improvements both in the biological and instrumental components of directed molecular evolution should increase the palette of red-shifted fluorescent proteins with advanced biochemical and photochemical properties. Advanced fluorescent proteins will not only solve some of the limitations of current microscopy methods but will in turn stimulate the development of novel fluorescence-detection technologies, *in vivo* imaging approaches and image-processing techniques.

Note: Supplementary information is available on the Nature Methods website.

ACKNOWLEDGMENTS

This work was supported by US National Institutes of Health grants GM073913 and CA164468 to V.V.V.

COMPETING FINANCIAL INTERESTS

The authors declare no competing financial interests.

Published online at http://www.nature.com/naturemethods/.
Reprints and permissions information is available online at http://www.nature.com/reprints/index.html.

1. Chudakov, D.M., Matz, M.V., Lukyanov, S. & Lukyanov, K.A. Fluorescent proteins and their applications in imaging living cells and tissues. *Physiol. Rev.* **90**, 1103–1163 (2010).
2. Piatkevich, K.D. & Verkhusha, V.V. Advances in engineering of fluorescent proteins and photoactivatable proteins with red emission. *Curr. Opin. Chem. Biol.* **14**, 23–29 (2010).
3. Piatkevich, K.D., Malashkevich, V.N., Almo, S.C. & Verkhusha, V.V. Engineering ESPT pathways based on structural analysis of LSSmKate red fluorescent proteins with large Stokes shift. *J. Am. Chem. Soc.* **132**, 10762–10770 (2010).
4. Pletnev, S., Subach, F.V., Dauter, Z., Wlodawer, A. & Verkhusha, V.V. Understanding blue-to-red conversion in monomeric fluorescent timers and hydrolytic degradation of their chromophores. *J. Am. Chem. Soc.* **132**, 2243–2253 (2010).
5. Subach, O.M. *et al.* Structural characterization of acylimine-containing blue and red chromophores in mTagBFP and TagRFP fluorescent proteins. *Chem. Biol.* **17**, 333–341 (2010).
6. Subach, O.M. *et al.* Conversion of red fluorescent protein into a bright blue probe. *Chem. Biol.* **15**, 1116–1124 (2008).
7. Subach, F.V. *et al.* Monomeric fluorescent timers that change color from blue to red report on cellular trafficking. *Nat. Chem. Biol.* **5**, 118–126 (2009).
8. Subach, F.V. *et al.* Photoactivation mechanism of PAmCherry based on crystal structures of the protein in the dark and fluorescent states. *Proc. Natl. Acad. Sci. USA* **106**, 21097–21102 (2009).
9. Subach, F.V. *et al.* Photoactivatable mCherry for high-resolution two-color fluorescence microscopy. *Nat. Methods* **6**, 153–159 (2009).
10. Subach, F.V., Patterson, G.H., Renz, M., Lippincott-Schwartz, J. & Verkhusha, V.V. Bright monomeric photoactivatable red fluorescent protein for two-color super-resolution sptPALM of live cells. *J. Am. Chem. Soc.* **132**, 6481–6491 (2010).
11. Gunewardene, M.S. *et al.* Superresolution imaging of multiple fluorescent proteins with highly overlapping emission spectra in living cells. *Biophys. J.* **101**, 1522–1528 (2011).
12. Wang, Q. *et al.* Molecular mechanism of a green-shifted, pH-dependent red fluorescent protein mKate variant. *PLoS ONE* **6**, e23513 (2011).
13. Kremers, G.J., Hazelwood, K.L., Murphy, C.S., Davidson, M.W. & Piston, D.W. Photoconversion in orange and red fluorescent proteins. *Nat. Methods* **6**, 355–358 (2009).
14. Mishin, A.S. *et al.* The first mutant of the *Aequorea victoria* green fluorescent protein that forms a red chromophore. *Biochemistry* **47**, 4666–4673 (2008).
15. Bogdanov, A.M. *et al.* Green fluorescent proteins are light-induced electron donors. *Nat. Chem. Biol.* **5**, 459–461 (2009).
16. Subach, O.M. *et al.* A photoswitchable orange-to-far-red fluorescent protein, PSmOrange. *Nat. Methods* **8**, 771–777 (2010).
17. Chica, R.A., Moore, M.M., Allen, B.D. & Mayo, S.L. Generation of longer emission wavelength red fluorescent proteins using computationally designed libraries. *Proc. Natl. Acad. Sci. USA* **107**, 20257–20262 (2010).
18. Strack, R.L. *et al.* A rapidly maturing far-red derivative of DsRed-Expres2 for whole-cell labeling. *Biochemistry* **48**, 8279–8281 (2009).
19. Lin, M.Z. *et al.* Autofluorescent proteins with excitation in the optical window for intravital imaging in mammals. *Chem. Biol.* **16**, 1169–1179 (2009).
20. Morozova, K.S. *et al.* Far-red fluorescent protein excitable with red lasers for flow cytometry and superresolution STED nanoscopy. *Biophys. J.* **99**, L13–L15 (2010).
21. Hoi, H. *et al.* A monomeric photoconvertible fluorescent protein for imaging of dynamic protein localization. *J. Mol. Biol.* **401**, 776–791 (2010).
22. Subach, F.V. *et al.* Red fluorescent protein with reversibly photoswitchable absorbance for photochromic FRET. *Chem. Biol.* **17**, 745–755 (2010).
23. Davis, J.N. & van den Pol, A.N. Viral mutagenesis as a means for generating novel proteins. *J. Virol.* **84**, 1625–1630 (2010).
24. Arakawa, H. *et al.* Protein evolution by hypermutation and selection in the B cell line DT40. *Nucleic Acids Res.* **36**, e1 (2008).
25. Corish, P. & Tyler-Smith, C. Attenuation of green fluorescent protein half-life in mammalian cells. *Protein Eng.* **12**, 1035–1040 (1999).
26. Cava, F., Hidalgo, A. & Berenguer, J. *Thermus thermophilus* as biological model. *Extremophiles* **13**, 213–231 (2009).
27. Kwon, W.S., Da Silva, N.A. & Kellis, J.T. Jr. Relationship between thermal stability, degradation rate and expression yield of barnase variants in the periplasm of *Escherichia coli*. *Protein Eng.* **9**, 1197–1202 (1996).

28. Martin, A., Schmid, F.X. & Sieber, V. Proside: a phage-based method for selecting thermostable proteins. *Methods Mol. Biol.* **230**, 57–70 (2003).
29. Pavoor, T.V., Cho, Y.K. & Shusta, E.V. Development of GFP-based biosensors possessing the binding properties of antibodies. *Proc. Natl. Acad. Sci. USA* **106**, 11895–11900 (2009).
30. Daugherty, P.S. Protein engineering with bacterial display. *Curr. Opin. Struct. Biol.* **17**, 474–480 (2007).
31. Bergquist, P.L., Hardiman, E.M., Ferrari, B.C. & Winsley, T. Applications of flow cytometry in environmental microbiology and biotechnology. *Extremophiles* **13**, 389–401 (2009).
32. Telford, W.G., Subach, F.V. & Verkhusha, V.V. Supercontinuum white light lasers for flow cytometry. *Cytometry A* **75**, 450–459 (2009).
33. Goddard, G. *et al.* Single particle high resolution spectral analysis flow cytometry. *Cytometry A* **69**, 842–851 (2006).
34. Houston, J.P., Naivar, M.A. & Freyer, J.P. Digital analysis and sorting of fluorescence lifetime by flow cytometry. *Cytometry A* **77**, 861–872 (2010).
35. Kim, J., Kwon, D., Lee, J., Pasquier, H. & Grailhe, R. The use of Cyan Fluorescent Protein variants with a distinctive lifetime signature. *Mol. Biosyst.* **5**, 151–153 (2009).
36. Goedhart, J. *et al.* Bright cyan fluorescent protein variants identified by fluorescence lifetime screening. *Nat. Methods* **7**, 137–139 (2010).
37. Buschke, D.G. *et al.* Multiphoton flow cytometry to assess intrinsic and extrinsic Fluorescence in cellular aggregates: applications to stem cells. *Microsc. Microanal.* **17**, 540–554 (2010).
38. Drobizhev, M., Makarov, N.S., Tillo, S.E., Hughes, T.E. & Rebane, A. Two-photon absorption properties of fluorescent proteins. *Nat. Methods* **8**, 393–399 (2011).
39. Godin, J. *et al.* Microfluidics and photonics for Bio-System-on-a-Chip: a review of advancements in technology towards a microfluidic flow cytometry chip. *J. Biophotonics* **1**, 355–376 (2008).
40. Heng, X., Hsiung, F., Sadri, A. & Patt, P. Serial line scan encoding imaging cytometer for both adherent and suspended cells. *Anal. Chem.* **83**, 1587–1593 (2011).
41. Pai, J.H., Xu, W., Sims, C.E. & Allbritton, N.L. Microtable arrays for culture and isolation of cell colonies. *Anal. Bioanal. Chem.* **398**, 2595–2604 (2010).
42. Kim, J. *et al.* Cell lysis on a microfluidic CD (compact disc). *Lab Chip* **4**, 516–522 (2004).
43. Zhang, C., Xing, D. & Li, Y. Micropumps, microvalves, and micromixers within PCR microfluidic chips: advances and trends. *Biotechnol. Adv.* **25**, 483–514 (2007).
44. Barbulovic-Nad, I., Au, S.H. & Wheeler, A.R. A microfluidic platform for complete mammalian cell culture. *Lab Chip* **10**, 1536–1542 (2010).
45. Hofmann, M., Eggeling, C., Jakobs, S. & Hell, S.W. Breaking the diffraction barrier in fluorescence microscopy at low light intensities by using reversibly photoswitchable proteins. *Proc. Natl. Acad. Sci. USA* **102**, 17565–17569 (2005).
46. Lippincott-Schwartz, J. & Patterson, G.H. Photoactivatable fluorescent proteins for diffraction-limited and super-resolution imaging. *Trends Cell Biol.* **19**, 555–565 (2009).
47. Wu, B., Piatkevich, K.D., Lionnet, T., Singer, R.H. & Verkhusha, V.V. Modern fluorescent proteins and imaging technologies to study gene expression, nuclear localization, and dynamics. *Curr. Opin. Cell Biol.* **23**, 310–317 (2011).
48. Davidson, M.W. & Campbell, R.E. Engineered fluorescent proteins: innovations and applications. *Nat. Methods* **6**, 713–717 (2009).
49. Nienhaus, G.U. & Wiedenmann, J. Structure, dynamics and optical properties of fluorescent proteins: perspectives for marker development. *ChemPhysChem* **10**, 1369–1379 (2009).
50. Post, J.N., Lidke, K.A., Rieger, B. & Arndt-Jovin, D.J. One- and two-photon photoactivation of a paGFP-fusion protein in live *Drosophila* embryos. *FEBS Lett.* **579**, 325–330 (2005).

Tamas Balla, Tuesday June 12th 2012, 16.00

Visualization of Cellular Phosphoinositide Pools with GFP-Fused Protein-Domains

Tamas Balla[1] and Péter Várnai[2]

[1]National Institutes of Health, Bethesda, Maryland
[2]Semmelweis University of Medical School, Budapest, Hungary

ABSTRACT

This unit describes the method of following phosphoinositide dynamics in live cells. Inositol phospholipids have emerged as universal signaling molecules present in virtually every membrane of eukaryotic cells. Phosphoinositides are present in only tiny amounts as compared to structural lipids, but they are metabolically very active as they are produced and degraded by the numerous inositide kinase and phosphatase enzymes. Phosphoinositides control the membrane recruitment and activity of many membrane protein signaling complexes in specific membrane compartments, and they have been implicated in the regulation of a variety of signaling and trafficking pathways. It has been a challenge to develop methods that allow detection of phosphoinositides at the single-cell level. The only available technique in live cell applications is based on the use of the same protein domains selected by evolution to recognize cellular phosphoinositides. Some of these isolated protein modules, when fused to fluorescent proteins, can follow dynamic changes in phosphoinositides. While this technique can provide information on phosphoinositide dynamics in live cells with subcellular localization, and it has rapidly gained popularity, it also has several limitations that must be taken into account when interpreting the data. This unit summarizes the design and practical use of these constructs and also reviews important considerations for interpretation of the data obtained by this technique. *Curr. Protoc. Cell Biol.* 42:24.4.1-24.4.27. © 2009 by John Wiley & Sons, Inc.

Keywords: phosphoinositide • FRET • live-cell imaging • green fluorescent proteins • pleckstrin homology domain • fluorescence microscopy

INTRODUCTION

The first established role of phosphoinositides was recognized in the mid-80s as precursors for two important second messengers, the calcium mobilizing inositol 1,4,5-trisphosphate and the protein kinase C activator diacylglycerol (Berridge and Irvine, 1984). However, starting with the discovery of PI 3-kinases (Whitman et al., 1988), several new inositol lipid isomers have been identified and a much broader role of these lipids as organizers of membrane-associated signaling complexes were uncovered (Di Paolo and De Camilli, 2006). The highly compartmentalized nature of inositol lipid signaling processes demanded new methods that allow detection of the presence of the various inositide isomers with subcellular resolution. The idea of how this can be achieved was born out from discoveries that identified protein modules capable of inositol lipid recognition with reasonable specificity in proteins that are regulated by phosphoinositides (Lemmon et al., 1997).

Visualization of phosphoinositide changes in single living cells was then based on the premise that protein modules that possess high enough affinity and specificity to bind the inositide headgroup of specific phosphoinositides can find the lipids within the cell and visualize it when expressed in the form of a green fluorescent protein (GFP) fusion protein (Balla et al., 2000). As simple as it sounds, the short history of this method has

Published online March 2009 in Wiley Interscience (www.interscience.wiley.com).
DOI: 10.1002/0471143030.cb2404s42

already raised several important technical and theoretical questions that one needs to be aware of when attempting to use these methods. The protocols in this unit provide some practical guidance to users who are not experienced with live cell microscopy. Also included are sections that deal with theoretical considerations and interpretational issues highly relevant to these measurements (see Commentary). The protocols will not detail common laboratory practices but try to concentrate on aspects that are unique to these applications. The technical comments are intended for less experienced users and not intended for experts of this research field.

STRATEGIC PLANNING

Selecting Fusion Proteins for Detection of Selected Inositol Lipids

Table 24.4.1 summarizes protein domains that have been used for imaging purposes. Some of these are better established, while a consensus has yet to be reached for others. These protein domains are widely available and also can be easily duplicated. This section discusses the most important issues related to the individual lipid species for which the authors have accumulated experience.

PtdIns(4,5)P_2

Almost all imaging work for this lipid has used the pleckstrin homology (PH) domain of PLCδ_1 (PLCδ_1PH-GFP) construct developed independently in the Meyer laboratory and in the authors' laboratory (see references in Table 24.4.1). This construct expresses very well and decorates the plasma membrane and some vesicular structures but no other organelles. This has raised the question of whether PtdIns(4,5)P_2 is only present in detectable amounts in the plasma membrane, or is the probe biased against the plasma membrane pool of the lipid. Few reliable works have compared PLCδ_1PH-GFP distribution with staining with PtdIns(4,5)P_2 antibodies, and some have found the lipid in the Golgi with antibody staining but not with PLCδ_1PH-GFP (Matsuda et al., 2001), while others have seen no discrepancy and no Golgi staining with PtdIns(4,5)P_2 antibody either (Hammond et al., 2006). Also, EM studies showed some PtdIns(4,5)P_2 in the Golgi using GST-fused PLCδ_1PH-GFP post fixation (Watt et al., 2002). These data demonstrate one of the possible limitations of this method, namely, that not all pools of the lipids might be equally seen by the domain and this will be even more apparent when imaging other inositol lipid forms (see below).

In spite of this lingering question, the plasma membrane pool of PtdIns(4,5)P_2 can be monitored by PLCδ_1PH-GFP. This probe reports changes in this lipid either following phospholipase C (PLC) activation or after degradation by a phosphoinositide-sensitive 5-phosphatase (Stauffer et al., 1998; Várnai and Balla, 1998; Várnai et al., 2006). However, there is another question that complicates what these changes mean when following PLC-mediated hydrolysis of these lipids. Since PLCδ1PH-GFP recognizes the phosphorylated inositol headgroup within the lipid, the corresponding soluble inositol phosphate [in this case, Ins(1,4,5)P_3] can compete with the membrane PtdIns(4,5)P_2 for binding the PH-domain GFP fusion protein. Because of this competing effect, some research groups treat the changes in PLCδ_1PH-GFP membrane localization as a faithful index of InsP_3 elevations rather than lipid changes within the cell (Nash et al., 2001). A recent detailed review of the authors' opinion on this topic is available (Varnai and Balla, 2006). The bottom line is that inositol phosphates can compete with lipid binding of the PH-domain constructs and their effects on changing localization could be quite significant under certain conditions and cannot be ignored. At the same time, it would be just as misleading to treat the PLCδ_1PH-GFP translocation response as an index of InsP_3 change, and differences between the two have been recently demonstrated by simultaneous measurements of InsP_3 and PLCδ_1PH-GFP

Table 24.4.1 Phosphoinositide Binding Modules in Use for Imaging Purposes in Live Cells

Lipid protein domain	In vitro reference	Live cell localization	Reference
PtdIns(4,5)P_2			
PLCδ_1-PH	Lemmon et al., 1995	Plasma membrane	Stauffer et al., 1998; Várnai and Balla, 1998
Tubby domain	Santagata et al., 2001	Plasma membrane plus cleavage furrow	Santagata et al., 2001; Field et al., 2005
PtdIns(3,4,5)P_3			
GRP1-PH	Klarlund et al., 1997; Rameh et al., 1997a	Plasma membrane	Venkateswarlu et al., 1998a; Klarlund et al., 2000
ARNO-PH	Klarlund et al., 2000	Plasma membrane	Venkateswarlu et al., 1998b
Cytohesin-1-PH	Klarlund et al., 2000	Plasma membrane	Nagel et al., 1998; Venkateswarlu et al., 1999
Btk-PH	Salim et al., 1996; Rameh et al., 1997a	Plasma membrane	Varnai et al., 1999
PtdIns(3,4,5)P_3 /PtdIns(3,4)P_2			
Akt-PH	Franke et al., 1997	Plasma membrane	Watton and Downward, 1999; Servant et al., 2000
PDK1	Komander et al., 2004	Plasma membrane	Komander et al., 2004
CRAC	Huang et al., 2003	*Dictyostelium* plasma membrane	Dormann et al., 2002
PtdIns(3,4)P_2			
TAPP1-PH	Dowler et al., 2000	Plasma membrane	Kimber et al., 2002
PtdIns(3,5)P_2			
Ent3p-ENTH[a]	Friant et al., 2003	Yeast pre-vacuole	Friant et al., 2003
Svp1p[a]	Dove et al., 2004	Yeast vacuole	Dove et al., 2004
PtdIns3P			
FYVE (Hrs, EEA1)	Burd and Emr, 1998; Simonsen et al., 1998	Early endosome	Gillooly et al., 2000
(Vps27)		Yeast vacuole	Burd and Emr, 1998
P40phox-PX	Ellson et al., 2001; Kanai et al., 2001	Early endosome	Ellson et al., 2001
PtdIns4P			
OSH2-2xPH[b]	Yu et al., 2004	Plasma membrane	Roy and Levine, 2004; Yu et al., 2004; Balla et al., 2007
OSBP-PH	Levine and Munro, 1998; Dowler et al., 2000	Golgi plus plasma membrane	Levine and Munro, 1998, 2002; Balla et al., 2005
FAPP1-PH	Dowler et al., 2000	Golgi plus plasma membrane	Munro, 2002; Godi et al., 2004; Levine and Balla, 2005
PtdIns5P			
3xPHD (ING2)	Gozani et al., 2003	Nucleus plus plasma membrane	Gozani et al., 2003; Pendaries et al., 2006

[a]The usefulness of these domains for imaging purposes is questionable (see Michell et al., 2005).

[b]The OSH2-PH shows little discrimination between PtdIns4P and PtdIns(4,5)P_2 based on in vitro binding (Yu et al., 2004) and it is still uncertain whether it actually reports on both of these molecules in some proportions.

translocation (Matsu-ura et al., 2006). Another PtdIns(4,5)P_2 binding module called the Tubby domain was described from the Tubby protein (Santagata et al., 2001; Field et al., 2005; Yaradanakul and Hilgemann, 2007). Two recent studies using a full-length Tubby protein (Nelson et al., 2008) or a mutant form of the Tubby domain have shown that these domains are less sensitive to $InsP_3$ changes than the PLCδ_1PH-GFP (Nelson et al., 2008; Quinn et al., 2008).

The third complication to remember when using these methods is the inhibitory effect of the expressed domain on cellular responses regulated by the inositol lipids. Binding of the PH (or other) domain-GFP reporters to phosphoinositides should inhibit the lipid-mediated cellular process since it competes with the lipid binding of endogenous effectors. High expression of the PLCδ_1PH-GFP causes morphological changes that include rounding of the cells, loss of attachment, and development of intracellular vesicles (Fig. 24.4.1). These "toxic" effects are due to the inhibition by the construct of the connections between the cytoskeleton and the plasma membrane (Raucher et al., 2000). This problem can be minimized by choosing cells that express low levels of the protein and using a sensitive microscope that can resolve the weak signals that such cells will possess (Fig. 24.4.1A).

PtdIns4P

Several PH domains have been used to detect PtdIns4P in living cells. The two most popular ones are the PH domains of the oxysterol binding protein (OSBP) and four-phosphate-adaptor protein (FAPP1) that were first identified as specific binders to PtdIns4P by fat blots (Dowler et al., 2000). Based on lipid vesicle–binding assays, these domains not only bind PtdIns4P but also PtdIns(4,5)P_2 (Levine and Munro, 1998; Roy and Levine, 2004; Yu et al., 2004). These PH domains, as well as their close relative found in the ceramide transfer (CERT) protein, were indeed localized to the Golgi pool of PtdIns4P both in yeast and in mammalian cells (Levine and Munro, 2002), but not to the plasma membrane, where PtdIns(4,5)P_2 is abundant. These data suggest that within the cells these PH domains do not recognize PtdIns(4,5)P_2 efficiently. Moreover, it was also found that both the OSBP- and FAPP1-PH domains require active (GTP-bound) Arf1 for Golgi localization, and their Golgi targeting requires binding to both PtdIns4P and Arf1-GTP (Levine and Munro, 2002). Neither interaction alone is sufficient for efficient membrane recruitment. This also means that brefeldin A treatment that prevents the formation of Arf1-GTP in the Golgi causes release of these PH domains from these locations. The limited lipid-binding specificity and the need for additional protein interaction for membrane targeting make these probes less than optimal for lipid imaging in live cells. However, because of the lack of better probes, they have been used in many laboratories including the authors (see Table 24.4.1 for references).

Two additional PH domains, namely those of OSH1 and OSH2 (oxysterol binding protein homologs of *S. cerevisiae*) were found to show cellular localization consistent with binding to PtdIns4P in yeast (Roy and Levine, 2004; Yu et al., 2004). Remarkably, the OSH2-PH (used in tandem to increase its apparent affinity) showed both the plasma membrane and the Golgi pool of PtdIns4P in yeast, while the OSH1-PH domain only detected the pool in the Golgi (Roy and Levine, 2004; Yu et al., 2004). This spatial discrimination was the more surprising as these PH domains showed very little discrimination between PtdIns4P and several other inositides including PtdIns(4,5)P_2 in various in vitro lipid-binding assays (Yu et al., 2004). Studies in the authors' laboratory on mammalian cells with these two PH domains yielded somewhat different results: while the OSH1-PH is found as a very good marker for PtdIns4P in the Golgi (as it was in the yeast), the OSH2-2xPH (or the single PH domain) construct only localizes to the plasma membrane but does not show Golgi localization (Fig. 24.4.2C). In spite of its very limited in vitro lipid-binding specificity, the OSH2-2xPH appears to be biased towards PtdIns4P

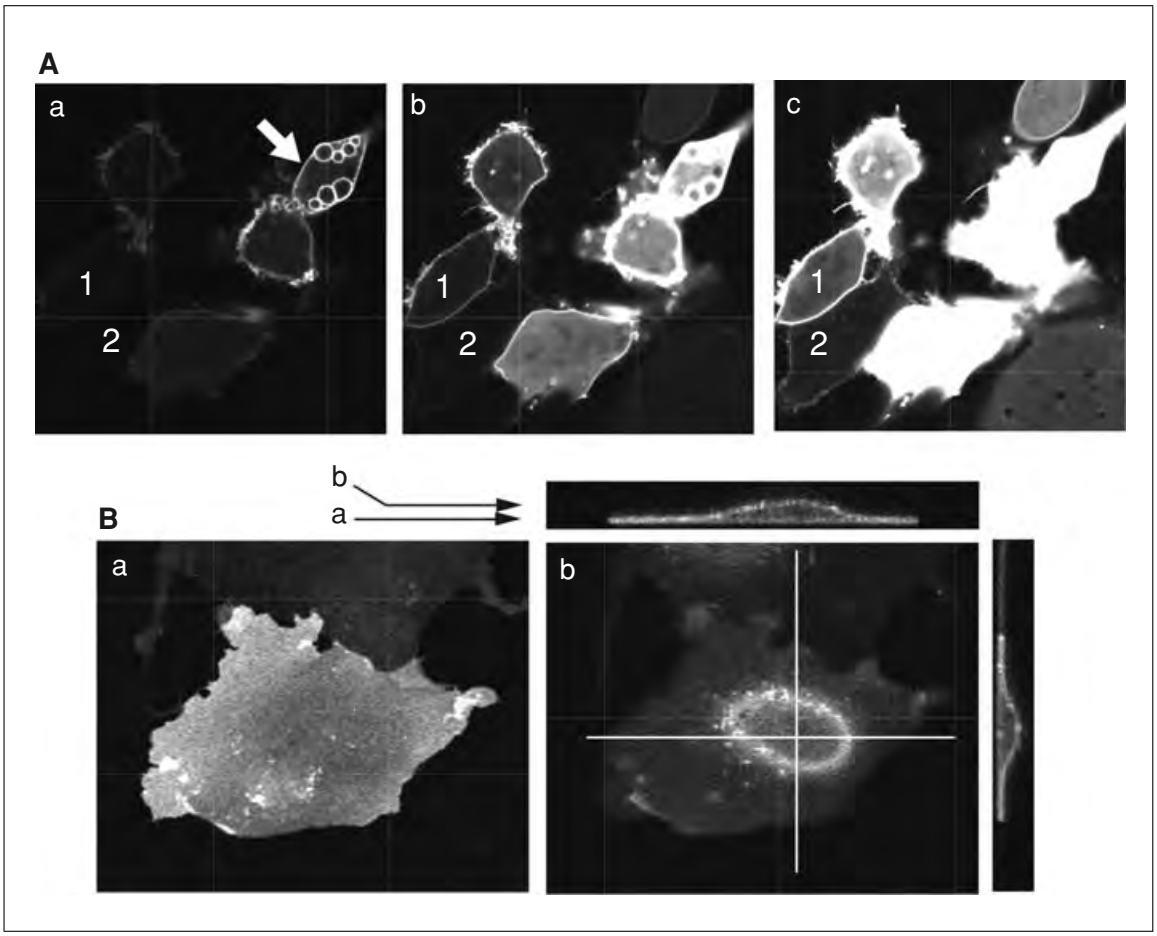

Figure 24.4.1 Cellular localization of the PLCδ_1PH-GFP. (**A**) Clusters of HEK293 cells transfected for 24 hr, and expressing the domain at various levels. Note the vesicular structures in the cell (arrow) that expresses a high level of the fusion protein. This is an example of toxic effects of the protein. Also note that with these illumination settings (panel a), cells 1 and 2 are not even visible, yet these are the cells that should be chosen for analysis as shown by higher illumination, which saturates the signal in other cells (b and c). (**B**) Confocal images of a COS-7 cell transfected with PLCδ_1PH-GFP for 24 hr and analyzed by z-sectioning. Panel a shows an image taken close to the bottom of the cell where it attaches to the coverslip. Note that there is no sharp outline of the cell and the signal covers the whole area of the cell. In panel b, the picture is taken at a z-plane higher up in the cell and again, there is no clear outline of the plasma membrane. Compare it with HEK293 cells that are not as flat and show a clear image of the plasma membrane (**A**). The side views of this COS-7 cell at the cross-sections (top and right side) show a better image of plasma membrane localization and the shape of the cell.

over PtdIns(4,5)P_2 in the plasma membrane, based on the resistance of its membrane localization to phosphoinositide 5-phosphatases that eliminate PtdIns(4,5)P_2 (Balla et al., 2008). The extent of this discrimination as well as the mechanism underlying its interaction with other proteins that would restrict access to PtdIns(4,5)P_2 but not PtdIns4P; however, requires further investigation.

It is clear that only specific pools of PtdIns4P can be monitored with these domains and there is not a single domain identified as yet that would detect all PtdIns4P pools within a cell. A domain that recognizes the PtdIns4P produced by type-II PI 4-kinases on endosomes has not been found. Even within the Golgi, PtdIns4P is produced by different PI 4-kinases (De Matteis et al., 2005), and it is possible that the different PH domains do not detect these pools equally. Moreover, there is an effect of the overexpression of the domains on the Golgi itself. For example, the FAPP1-PH localizes primarily in the trans-side of the Golgi (Godi et al., 2004), but its localization between the cis- and trans- side depends on the expression level (Weixel et al., 2005). In COS-7 cells, an increased level

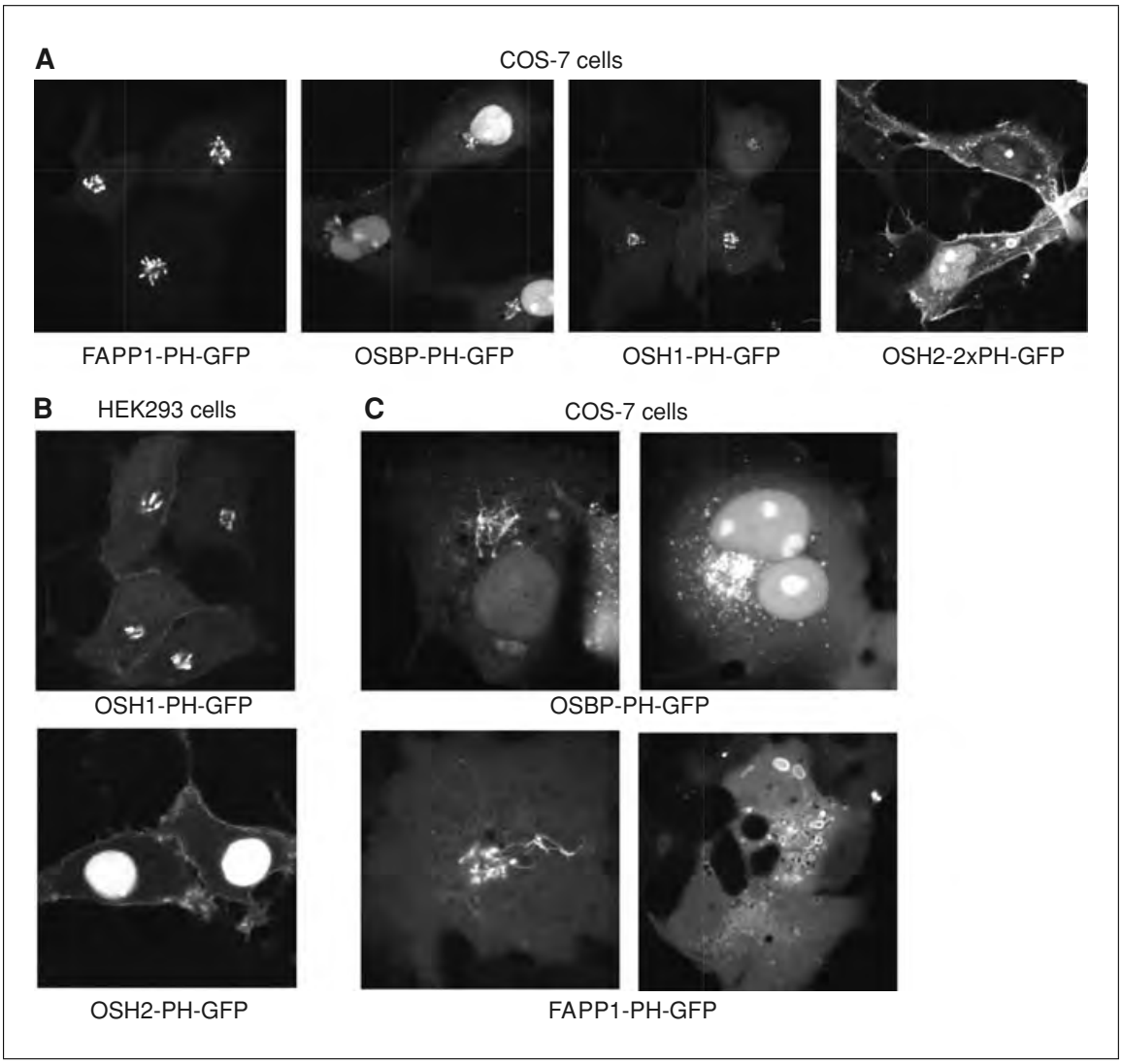

Figure 24.4.2 Localization of the various domains used for imaging PtdIns4P in COS-7 and HEK293 cells. (**A**) COS-7 cells transfected with the indicated domains for 24 hr. Note the sharp contrast and prominent recruitment of the FAPP1-PH domain and the higher nuclear staining of the OSBP-PH domain. The yeast OSH1-PH-GFP also shows the Golgi but is also localized to a small extent to the plasma membrane (better seen in **B**). The OSH2-2xPH-GFP prominently labels the plasma membrane but does not show Golgi localization. For this picture cells were selected that are not so flat, to demonstrate better plasma membrane localization. (**B**) Localization of the OSH1-PH-GFP and OSH2-PH-GFP constructs in HEK293 cells. Note the Golgi and moderate plasma membrane localization of the OSH1-PH and the lack of Golgi localization and high nuclear signal with the OSH2-PH domain. The nuclear localization is less prominent with the OSH2-2xPH-GFP construct. (**C**) Examples for interference of the domains with cellular functions. Both the OSBP- and FAPP1-PH domains cause tubulation of the Golgi. Remarkably, this always occurs at moderate levels of expression and never at high expression levels and only in a fraction of cells. This indicates that this effect is conditional and requires a certain functional state of the Golgi. At high expression levels, the two constructs have very different effects: the OSBP-PH breaks the Golgi into small vesicles that eventually cover the whole cytoplasm. These are completely resistant to brefeldin A, a treatment that rapidly eliminates the Golgi localization of the construct indicating the Arf1-GTP requirement of the localization (not shown). In contrast, the FAPP1-PH domain shows no Golgi localization at high expression levels and instead produces large vacuoles in the cell with FAPP1-PH domain attached to their limiting membranes.

of expression of FAPP1 and OSBP causes distinct morphological changes (Fig. 24.4.2B) suggesting that they interact with distinct proteins (in addition to PtdIns4P and Arf1) and indicating that even though they may appear in the same Golgi compartment at low expression levels, they still detect functionally distinct pools of the lipids. These are all important signs to indicate that not all PtdIns4P are created equal and cannot simply be imaged by a single probe.

PtdIns(3,4,5)P_3

There are a large number of studies imaging PtdIns(3,4,5)P_3 dynamics due to the high interest in phosphatidylinositol (PI) 3-kinase signaling and its role in polarized cell movements such as chemotaxis. In *Dictyostelium*, a widely used model for polarization migration, the PH domain of the CRAC protein (cytosolic regulator of adenyl cyclase, not to be mistaken with calcium release activated channels, as the same acronym is often used in mammalian cells) has been a very good reporter of PtdIns(3,4,5)P_3 distribution (Dormann et al., 2002; Huang et al., 2003). In mammalian cells, the Akt-PH domain has served best for following polarized PtdIns(3,4,5)P_3 production (Servant et al., 2000), even though this PH domain also recognizes PtdIns(3,4)P_2. The Btk-PH domain that is more specific for PtdIns(3,4,5)P_3 and detects lipid increases after PDGF or insulin stimulation in the plasma membrane (Varnai et al., 1999) has not seen similar popularity presumably because it does not show this polarization so effectively. This already suggests that in addition to PtdIns(3,4,5)P_3, protein-protein interactions probably also play a role in the effective recruitment of these PH domains to the plasma membrane. Because of its good in vitro specificity, the Grp1-PH domain (or its close relative, ARNO-PH) is considered to be the most specific probe to detect PtdIns(3,4,5)P_3. However, the authors' experiences have not been positive with this construct. In many cells it shows a relatively poor response, e.g., by showing high nuclear localization [independent of PtdIns(3,4,5)P_3] and membrane recruitment is largely dependent on active (GTP-bound) Arf6 (Cohen et al., 2007). Because membrane recruitment is largely dependent on active Arf6, the Grp-PH is also relatively toxic to the cells and inhibits several Arf6-dependent functions including attachment and spreading of cells (Varnai et al., 2005). A recent study compared several PtdIns(3,4,5)P_3-binding PH domains for their in vitro binding specificity and cellular localization response (Manna et al., 2007). This study found strikingly different membrane recruitment kinetics between the various domains in PDGF-stimulated NIH3T3 cells also suggesting that in addition to inositide lipid binding, membrane penetration and possibly protein-protein interactions have a role in membrane association of the domains. Based on all of the measurements presented, the Btk-PH appeared to be the best probe for the detection of PtdIns(3,4,5)P_3 in intact cells.

PtdIns3P

PtdIns3P was one of the first inositol lipids for which a recognition domain other than a PH domain was found. No PH domain that recognizes PtdIns3P specifically has been reported to date. It was the FYVE domain (the acronym originates from the first four proteins in which the domain was described: Fab1p, YOTB, Vac1p, and EEA1) that was found to be responsible for PtdIns3P recognition and shown to recognize this lipid in its isolated form fused to GFP (Burd and Emr, 1998). Since the strictly defined FYVE domain will recognize PtdIns3P very specifically in vitro, but poorly localizes without some adjacent residues that help its dimerization (and partially may also bind Rab5), the most widely used construct from the Stenmark laboratory is based on a tandem FYVE domain of the Hrs protein (Gillooly et al., 2000). The construct the authors have made from the EEA1 (early endosome-associated antigen) FYVE domain is the slightly longer version (Hunyady et al., 2002). Both of these constructs decorate an early endosomal compartment and will fall off from the vesicles upon inhibition of PI 3-kinases consistent with the view that the Class III PI 3-kinase (the mammalian Vps34p homolog) constitutively generates PtdIns3P on early endosomes.

The other domain that recognizes PtdIns3P is the PX domain of several proteins, but most prominently that of p40phox (Kanai et al., 2001). Expression of this PX domain as a GFP fusion protein also labels the early endosomes. However, in contrast to the FYVE domains, this construct leads to the accumulation of very brightly stained aggregated vesicles in many cells that express higher amounts of the protein. Moreover, these bright vesicles do not lose their signal after addition of PI 3-kinase inhibitors (while the solitary vesicles labeled in cells with low expression do), suggesting that the PX domain is part of a more stable protein complex that cannot disassemble and is probably responsible for the aggregation of vesicles. This again is an indication of protein-protein interactions that clearly differ between the FYVE and PX domains and a good example of why cells with low expression levels should be used in these studies.

PtdIns(3,4)P_2, PtdIns(3,5)P_2, and PtdIns5P

The authors have not had much experience with visualizing any of these lipids; therefore, a summary of what is known in the literature is presented. The only PH domains that showed in vitro specificity to binding PtdIns(3,4)P_2 were those of the TAPP1 and TAPP2 proteins (Dowler et al., 2000). The crystal structure of the TAPP1 PH domain clearly revealed the structural features responsible for this specificity (Thomas et al., 2001). The GFP-tagged TAPP1 PH domain has been shown to detect the lipid in live cells in the plasma membrane under conditions where PtdIns(3,4)P_2, but not PtdIns(3,4,5)P_3, was elevated (Kimber et al., 2002). In addition, a GST-fused TAPP1 PH domain labeled the membrane of internal vesicles and the multivesicular body in fixed cells processed for EM analysis (Watt et al., 2004). Moreover, this domain does not show membrane association when only PtdIns(3,4,5)P_3 is elevated, indicating that it can discriminate between these two otherwise closely related lipid products within the cell. Other studies also found this domain useful in detecting the formation of PtdIns(3,4)P_2 in phagocytic cups in macrophages (Horan et al., 2007). The PX domain of p47phox has also been claimed as a PtdIns(3,4)P_2-recognizing module (Zhan et al., 2002) and used to detect the lipid as a GFP fusion protein (Stahelin et al., 2003). However, in the authors' hands the p47phox PX domain-GFP chimera does not show any indication of binding to membranes in a lipid-dependent manner (T. Balla and P. Várnai, unpub. observ.) and its binding to other phospholipids such as phosphatidic acid (Karathanassis et al., 2002) and proteins (Zhan et al., 2002) may limit the usefulness of this PX domain as an imaging tool.

The formation of PtdIns(3,5)P_3 and its role in trafficking to the vacuole in yeast and to the multivesicular body in higher eukaryotes (Gary et al., 1998; Ikonomov et al., 2003; Jefferies et al., 2008) has made this lipid a highly interesting target for imaging studies. Unfortunately, in spite of several attempts and claims, there are no established tools to accomplish this task reliably. Two proteins, the yeast Ent3p (Friant et al., 2003) and Svp1p (Dove et al., 2004) have been found to be targets of PtdIns(3,5)P_2. The inositide binding site was located within the ENTH domain of Ent3p, while it was attributed to a cluster of basic residues on a beta propeller within Svp1p. To the authors' knowledge there has been no systematic analysis on the intracellular distribution of any isolated domains extracted from these molecules with the aim of localizing PtdIns(3,5)P_2 in live cells.

PtdIns5P is a lipid that was first identified as a substrate of the type II PIP kinases (PI5P 4-kinase; Rameh et al., 1997b). The main route(s) of its production in cells is highly debated, but most likely is the result of dephosphorylation of polyphosphoinositides (Coronas et al., 2007; Zou et al., 2007) rather than direct phosphorylation of PtdIns. The only domain that recognizes PtdIns5P has been identified in the nuclear protein ING2 within a domain (PHD as for plant homeodomain) that binds PtdIns5P, and to a lesser degree PtdIns3P, in vitro (Gozani et al., 2003). A GFP fusion protein made of the 3xPHD domain of ING2 detected PtdIns5P in the plasma membrane in response to overexpressed bacterial 4-phosphatase, IpgD (Gozani et al., 2003; Pendaries et al., 2006)

and did not show endosomal localization suggesting that it does not bind PtdIsn3P in the cells. Nevertheless, more experience is needed with this domain to determine where PtdIns5P is found in the cells and whether its role in the nucleus is associated with detectable changes in its nuclear level.

The common message from these examples is that none of these tools is useful as general lipid reporters without specific constraints that vary from probe to probe. However, if treated with caution and after performing proper controls, these reporters are very useful in answering questions that no other technique can provide.

Selecting the Fluorescent Protein to be Fused

Most of these fluorescent reporters have been originally created as fusion proteins with the enhanced green fluorescent protein (EGFP). However, over the past few years, a large number of fluorescent proteins were introduced now offering a wide variety of colors and other unique features (*UNIT 21.5*). In addition to the spectral variants that allow multicolor imaging of several probes in parallel, new features include photoactivation (*UNIT 21.6*), photoswitching, spectral change during maturation, pH stability, resistance to photobleaching or dimerization, etc. These have been summarized in several recent reviews and will not be detailed in this unit (Shaner et al., 2005; Giepmans et al., 2006; Wiedenmann and Nienhaus, 2006). These proteins are often very useful for a particular application but there is considerable confusion as to the source of these proteins. In addition to the GFP variants based on the pioneering work of the Tsien laboratory, many new proteins originate from the Miyawaki laboratory, and the company Evrogen. These proteins have been cloned from a variety of species and are not derivatives of the jellyfish *Aequorea victoria* GFP. A good summary of these proteins and their features are found in Muller-Taubenberger and Anderson (2007) and *UNIT 21.5*. However, these proteins do not only differ in their optical behavior and they cannot be replaced with one another without any problems. In the authors' experience, occasionally a probe behaves quite differently depending on whether an EGFP, an mRFP, or EosFP molecule is attached to it. Therefore, it is better to start with a few colors that are proven to work similarly with a particular lipid-binding domain than to generate a whole series of colors assuming that they will behave identically within the cells. As most studies were done with the pEGFP plasmids and their initial color versions, it is recommended to use these for initial experiments. Unfortunately, the original pEGFP-N and -C series plasmids are no longer available because Clontech has become part of Takara and these companies now offer their own fluorescent proteins that originate from a different species. The original EGFP and its color variants are now sold by Invitrogen in a different plasmid backbone. This often causes confusion among novices beginning their fluorescent protein collections that do not realize that a green fluorescent molecule now can mean different entities depending on the manufacturer.

EXPRESSION OF FLUORESCENT PROTEINS IN MAMMALIAN CELLS

BASIC PROTOCOL 1

The following procedure describes the general methods for analyzing cells expressing EGFP or GFP-fusion proteins by microscopic techniques.

Materials

98% ethanol
0.1% (w/v) poly-L-lysine in water (Sigma cat. no. P-8920)
Cultured cells of interest
Culture medium with serum and antibiotics (depending on the cells)
Plasmid DNA (usually a midiprep)
Transfection reagents (depending on the cells in use; *UNITS 20.3, 20.4, 20.5, 20.6, & 20.7*)
Phosphate buffered saline (PBS)

2% (w/v) paraformaldehyde (see recipe)
Blocking solution (10% FBS in PBS made fresh)
Primary antibody against fluorescent protein (available from several commercial sources)
0.2% saponin
Fluorophore-conjugated secondary antibody
Aqua-Poly/Mount (Polysciences)
Clear nail polish
25-mm coverslips (PGC Scientific cat. no. 60-4884-25 or Warner Instruments cat. no. 64-0705) for TIRF applications
6-well culture dishes
Glass microscope slides
Fluorescent microscope

Prepare poly-L-lysine-coated coverslips

1. Rinse 25-mm coverslips with 98% ethanol in a cell culture hood and air dry.
2. Place one coverslip in each well of a 6-well culture dish.
3. Add 2 ml of 1:50 or 1:100 dilution of poly-L-lysine in filter-sterilized deionized water to cover the entire surface of each coverslip and allow to stand 1 hr at room temperature.

   In a pilot study, plate cells on coverslips coated at each poly-L-lysine concentration to determine which is best for the cells being studied.

   Because most plastic-ware used for cell culture work has high autofluorescence, it is recommended that cells be cultured and transfected on poly-L-lysine-coated glass coverslips so that they can be viewed under the microscope after transfection without replating. For certain cell types and transfections, it is more advantageous to transfect the cells in culture dishes and re-plate the transfected cells on the poly-L-lysine-coated coverslips before microscopy. Some cells can be grown on coverslips without the coating (e.g., cost-7, CHO)

4. Aspirate the solution from the coverslip and air dry (~ 1hr) before plating cells.

Transfect cells with plasmid DNA

5. Plate ~50,000 cells directly onto the poly-L-lysine-coated coverslips in 2 ml of the appropriate culture medium and grow to the density best suited for transfection (usually 2 days).
6. Transfect the cells with the desired plasmid DNA construct using a method that is most appropriate for the cells.

   The authors usually use 2 μl Lipofectamine 2000 and 0.5 μg plasmid DNA per coverslip.

   Transfection protocols are available for different reagents (UNITS 20.3–20.6), and for each cell type, the reagent and the procedure that produce the best results can differ considerably (UNIT 20.7). Therefore, refer to the manufacturer's instructions as far as specifics for cell transfection are concerned. The optimal level of expression must be determined for each cell type and expression construct. It is important to remember that the expressed proteins often interfere with the functions of the lipids that they recognize, and in high concentrations, the lipid-binding fusion proteins are often toxic to the cells.

   Initial transfection of cells with a mutant version of the lipid-binding domain that does not bind lipids is recommended. For example, many constructs localize to the nucleus, but this localization is not dependent on lipid binding; thus, lipid-mediated localization can be confirmed by comparing the distribution of the native lipid-binding domain to that of the non-lipid binding mutant. Transfection of cells with the GFP protein alone without the lipid-binding domain is also recommended. These two controls help to track phenotypic changes and potential cellular toxicity associated with overexpression of the lipid-binding domain, as well as to serve as controls for monitoring localization that accurately reflects lipid binding.

7. Grow cells 24 hr to allow expression of the transfected protein.
8. Incubate cells in serum-free culture medium for 6 to 10 hr to render them quiescent before microscopy.

   Growing cells for >34 hr after transfection is not recommended because of the potential toxicity of the lipid-binding fusion protein and the ability of the expressed protein to interfere with the functions of the lipids that they bind. Not every experiment requires serum deprivation of cells.

Immunostain cells to detect expressed GFP fusion protein

9. Rinse the transfected cells with 2 ml of PBS.
10. Add 2 ml of 2% paraformaldehyde and incubate 10 min at room temperature.
11. Wash cells three times with 2 ml of PBS, 10 min each wash.
12. Cover cells with 2 ml of blocking solution to block nonspecific antibody binding. Incubate 10 min at room temperature.
13. Add primary antibody diluted appropriately in blocking solution supplemented with 0.2% saponin. Incubate 1 hr at room temperature.

    A volume of 100 μl of diluted antibody should be sufficient for a 25-mm circular or 22 × 2–mm square coverslip, if it is inverted on a glass slide and incubated in a humidified Petri dish.

    This step can be skipped when performing live cell microscopy (see below). However, it may be necessary to confirm expression of the fusion protein, especially if the GFP signal is not bright enough. This confirmation can be accomplished by immunocytochemistry with antibodies to the GFP portion of the fusion protein. Co-localization of the GFP-fused domain with other molecular markers may also require immunostaining.

14. Wash cells three times with 2 ml of blocking solution, 5 min each wash.
15. Add the fluorphore-conjugated secondary antibody diluted in blocking solution containing 0.2% saponin. Incubate 1 hr at room temperature protected from light.
16. Wash cells three times with 2 ml of PBS, 1 min each wash.
17. Air dry until coverslips are only damp.
18. Mount coverslips with cells down on a glass slide using Aqua-Poly/Mount.
19. Seal coverslips on the side with clear nail polish to prevent drying.
20. View the slides to detect expression of the GFP/fluorescent protein.

VERIFYING STRUCTURAL INTEGRITY OF THE FUSION CONSTRUCT

BASIC PROTOCOL 2

This protocol describes how to determine whether the fluorescent protein construct remains intact when expressed in the cells. This is an important control in addition to sequencing the DNA construct before performing any microscopy work. Often the fusion protein is cleaved within the cell so that the green fluorescence is not coming from the molecule that was designed. In the authors' experience, free EGFP is more often present when using pEGFP-N1 plasmids than with the pEGFP-C1-variant. (This can happen if an internal ribosomal entry site allows the translation of GFP itself, which can be prevented by removing the start codon of the original GFP.) In one case, a fusion protein expressed in COS-7 cells was proteolytically cleaved when placed COOH-terminal to EGFP. Analyzing cell lysates by sodium dodecyl sulfate polyacrylamide gel electrophoresis (SDS-PAGE) either using a phosphorimager equipped with a blue laser line (described below) or by conventional immunoblotting (*UNIT 6.2*) techniques using

antibodies against the GFP portion of the fusion protein is recommended. In many cases, samples that are boiled and analyzed by immunoblotting show more degraded product than those analyzed directly from the gel. The electrophoretic mobility of the EGFP molecule is clearly different when expressed from pEGFP-C1 versus pEGFP-N1. This may be due to altered migration of the non-denatured protein by extra amino acids encoded within the multiple cloning site of the pEGFP-C1 plasmid.

Materials

Cultured cells of interest
Culture medium with serum and antibiotics (depending on the cells)
Plasmid DNA (usually a midiprep)
Transfection reagents (depending on cells used)
Phosphate buffered saline (PBS)
Laemmli buffer
10-cm SDS-PAGE acrylamide gel
Gel running buffer

12-well culture plates
1.5-ml microcentrifuge tubes
Sonicator
SDS gel apparatus
Phosphorimager (or reagents and apparatus for immunoblotting)

1. Seed COS-7 (or other cells to be studied) at 2×10^5 cells/2 ml medium onto 12-well culture plates and incubate 24 hr.
2. Transfect cells with the method of choice and incubate 1 day (or equal to the time the experiments would be done).
3. Wash cells with 2 ml PBS and aspirate the PBS.
4. Dissolve cells in 100 µl Laemmli buffer and transfer to 1.5-ml microcentrifuge tubes. Do not boil, but briefly sonicate to disrupt DNA.
5. Load 40 µl of the sample per lane of a small (10-cm) SDS-PAGE gel with an acrylamide concentration that will resolve proteins in the size range of interest.
6. Run the gel at 100 V until the front reaches the bottom of the gel.
7. Remove gel from cassette and place in running buffer.
8. Place the wet gel directly onto a phosphorimager and scan using the appropriate laser line (blue for GFP and red for mRFP or similar colors)

Alternatively, if no phosphorimager is available, the fluorescent proteins can be detected with immunoblotting using an anti-GFP (or other appropriate) antibody. In this case, boil the samples before SDS gel analysis. It is also important to remember that the anti-GFP antibody does not recognize proteins that are derived from other species than Aequorea victoria.

BASIC PROTOCOL 3

OBSERVE GFP SIGNAL BY MICROSCOPY

Provided here are practical suggestions on what to pay attention to when observing cells by microscopy. This is not intended for experienced users but for researchers who have limited practical knowledge of microscopes and want to observe their proteins as GFP-fusion constructs in live cells. This protocol is not a substitute for training on any specific microscope system but rather an aid to help commonsense practices.

Wide field or confocal microscopy?

The first question to be answered is whether to view the cells with a conventional fluorescence microscope or with a confocal microscope. The authors suggest that the distribution of GFP fluorescence and other initial experiments such as assessing transfection efficiency should be performed with a conventional fluorescence microscope using filters suitable for fluorescein isothiocyanate (FITC) detection (excitation at 470 to 490 nm, emission at 500 to 550 nm). It is not necessary to examine the cells immediately with a confocal microscope, and it is more difficult to obtain a general impression of what the cells look like in a confocal microscope when expressing the construct. Individual cells, especially COS cells, show enormous variability in their shape, size, and general appearance, and often the level of expression changes their appearance. Conventional fluorescence microscopy is a significantly more efficient way to browse through many cells and notice trends in cellular morphology. In addition, many cells are flat in culture (especially COS cells), so there is little benefit from analyzing the cells in a confocal microscope. Confocal microscopy can be saved for recording cells and changes in fluorescence distribution once the conditions have been optimized with a fluorescence microscope. A further advantage of viewing cells in a fluorescence microscope is that autofluorescence often can be distinguished from the GFP signal because its color is different from the green color of GFP. It is important to remember that confocal microscopes detect light intensity without colors and the "color" given is artificial. Therefore, in each case, the autofluorescence has to be determined so that the GFP signal can be reliably used. For this, observation of untransfected cells is a useful control.

Fixed or live cells?

The next question is whether to analyze live or fixed cells. EGFP fluorescence can persist in fixed cells under proper fixation conditions (see Basic Protocol 1, steps 9 to 19). Fixed cells can be processed for immunostaining, which is often necessary to determine co-localization with organelle markers for which antibodies are available. Also, fixed cells can be stored and studied whenever convenient. On the other hand, changes cannot be followed as they happen in real time when using fixed cells. Moreover, fixation and permeabilization procedures may distort cellular morphology. For example, vesicular structures shrink during fixation, and long canaliculi can turn into small vesicles. The use of live cells is the most reliable way of assessing undistorted morphology, but it is also the most time-consuming and least efficient. For live-cell imaging, it is best to use an inverted microscope. New water-immersion objectives make it possible to look at cells under upright microscopes, but the objective has to be in culture medium. In addition, live-cell imaging would generally require some form of temperature control with all the complications associated with it while fixed cells do not.

When analyzing live cells, one major advantage is to record time-lapsed images sequentially after a stimulus is applied to the cells. In confocal microscopes, the speed of scanning determines how fast one can record an image, and generally the faster the scan, the poorer the quality of the individual pictures. Finally, one of the greatest difficulties is to keep the cell in focus after stimulation, because of shape changes that often occur in response to the stimulus (HEK 293 cells are especially lively). This change in position of the originally imaged plane can make the entire recorded process unsuitable. Software programs are being developed to compensate for "focal-drift" due to cell movements. These new developments may already be available for some confocal imaging systems.

BASIC PROTOCOL 4

LIVE-CELL IMAGING

This protocol describes steps to help guide a less-experienced user during the live-cell imaging process.

Materials

Coverslips holding transfected cells
Medium appropriate for cells (e.g., modified Krebs-Ringer solution; see recipe)
Immersion oil

Chambers to hold coverslips (e.g., metal Atto chambers, Invitrogen)
Kimwipes
Wide-field fluorescence microscope equipped with sensitive camera and appropriate software for data acquisition or confocal microscope
Lens cleaning paper
Objective heater and heated stage (Bioptechs, *http://www.bioptechs.com*) or a complete temperature control enclosure
Computer controlled valve-system and perifusion (optional)
Forceps

Mount transfected cells

1. Place coverslip with transfected cells face-up into metal chambers. Tighten the upper part with the O-ring in place gently but firmly so no leaks occur. Wash cells with medium and add 1 or 2 ml medium to the cells. Clean the bottom of coverslip with a clean Kimwipe.

   Ensure that the coverslip is in the grooved area of the chamber otherwise it will break during tightening. Test for leakage using a clean paper where the metal meets the glass coverslip. Leakage can worsen as the temperature changes on the stage. In any case, the use of a lens protector against leakage is advised when using live-cell imaging.

2. Dust off the objective and clean with a cleaning solution provided by the manufacturer (or isopropanol) using a lens cleaning paper.

   Cleaning the lens is important but it can do more damage than good if not done properly. Consult an expert before performing this task. Do not use Kimwipes or any other paper or cotton swab for this purpose. Never clean the lens with dry lens paper and do not use solutions containing ammonia (e.g., Windex) or organic solvents other than recommended.

3. Add one small drop of immersion oil to the lens without allowing it to flow down along the surface.

4. Place the metal chamber on the stage and slowly elevate the objective with eye control until it touches the coverslip.

Select cells

5. Observe the transfected cells and, if necessary, the control non-transfected cells using the fluorescence setting of the confocal microscope fitted with filters suitable for the chosen fluorophore (470 to 490 nm excitation and 500 to 550 nm emission for EGFP).

   Looking into the fluorescence microscope, one can usually see cells with a wide range of fluorescence intensities. Depending on the quality of the microscope and the intensity of the light source, sometimes only the cells with the highest expression levels are visible and these are the cells to avoid. It is recommended to study cells in which the GFP signal is as low as possible but clearly distinguishable from the autofluorescence of non-transfected control cells. Since microscopes are very different, there are no arbitrary rules.

   Often a separate non-transfected cell control is not necessary, because even in the transfected samples, not all cells express the fusion proteins. The non-transfected cells in the

population can usually be distinguished by their autofluorescence, allowing easy identification of transfected and non-transfected cells from the same sample when viewed using the fluorescent setting.

6. Choose cells in which expression levels are just high enough to be resolved above the background autofluorescence, and that are not obviously unhealthy.

   A good quality image should be obtained in confocal microscopy using 3% to 5% of the maximum laser power (assuming a 30-mW, 488-nm laser; see Fig. 24.4.1A).

   Analysis of cells that are unhealthy and suffer from toxicity induced by the expression of the fusion protein should be avoided. For example, cells that have rounded up and are about to detach—a common phenomenon with cells expressing high levels of a fusion protein consisting of the PH domain of PLC and GFP (PLCδ_1PH-GFP) are not likely to behave normally. Another indication of toxicity is the appearance of large intracellular vesicles.

Perform time-lapse analysis of live cells

7. Record and store an image before applying any stimulus.

   An important and often unappreciated problem in live-cell imaging is the proper temperature of the cells that are being observed. Even with a heated stage, an objective acts as a heat sink, keeping the cells in the observation field at a temperature near that of the objective. This temperature is closer to room temperature especially when rooms are kept on the cold side because of the lasers. Many trafficking processes in the cells slow down or do not work properly below 34°C. Therefore, use an objective heater. Unfortunately, the heater collar does not fit all objectives, and heating may be damaging to the objective if it is warmed very fast from a cold temperature. Alternative methods of maintaining the proper temperature include perfusion of cells with a high flow of warm medium or the use of a hair dryer to keep the objective at the proper temperature. Complete incubator enclosures are also available from various companies that can keep both the temperature and CO_2 concentration and humidity of cells on the stage at the desired levels. Unfortunately, they make manipulations of the cells often difficult.

8. Set the software to record time-lapsed images.

   The speed of recording must be decided based on the expected speed of the response and the scan speed that is required to generate an image. Phospholipase C activation by receptors is a fast event, but it can be followed by obtaining an image every 5 sec. Depending on the software, the scanning time (1.0 to 2.5 sec/image for one color) is taken into account when setting up the speed of image acquisition. It is important to remember that frequent scanning leads to fast photobleaching but including a break between scans helps to counter the bleaching problem.

9. Start data acquisition and add stimuli or inhibitors after a control period (five to ten images depending on the speed).

   Addition of a treatment is more complicated than it seems. The best method is to use a computer-controlled valve-system linked to constant perfusion of the cells with prewarmed medium. This ensures proper mixing, timing, and keeping the composition of the medium not affected by evaporation. However, the authors' experience is that many of the lipophylic compounds (ionomycin, thapsigargin, rapamycin, etc.) stick to the plastic tubing and to the valve components to such an extent that it is almost impossible to clean them even with organic solvents. This is also true for the metal chambers including the plastic O-ring seal. This may cause significant problems, especially in multi-user settings. Because of this potential problem, simply use a pipet to stimulate the cells. For this, remove 200 μl warm medium from the cells and add it to a microcentrifuge tube that contains the desired amount of drug in 1 to 5 μl, and after mixing, add the medium back to the cells. With practice, one can pipet the medium back at an angle that will yield proper mixing, which may be further mixed by pipetting up and down one time. This takes ~2 sec, which is acceptable for many applications but may be too slow for others. It is the investigator's choice whether to follow the manual pipetting procedure or to use the more sophisticated valve-controllers.

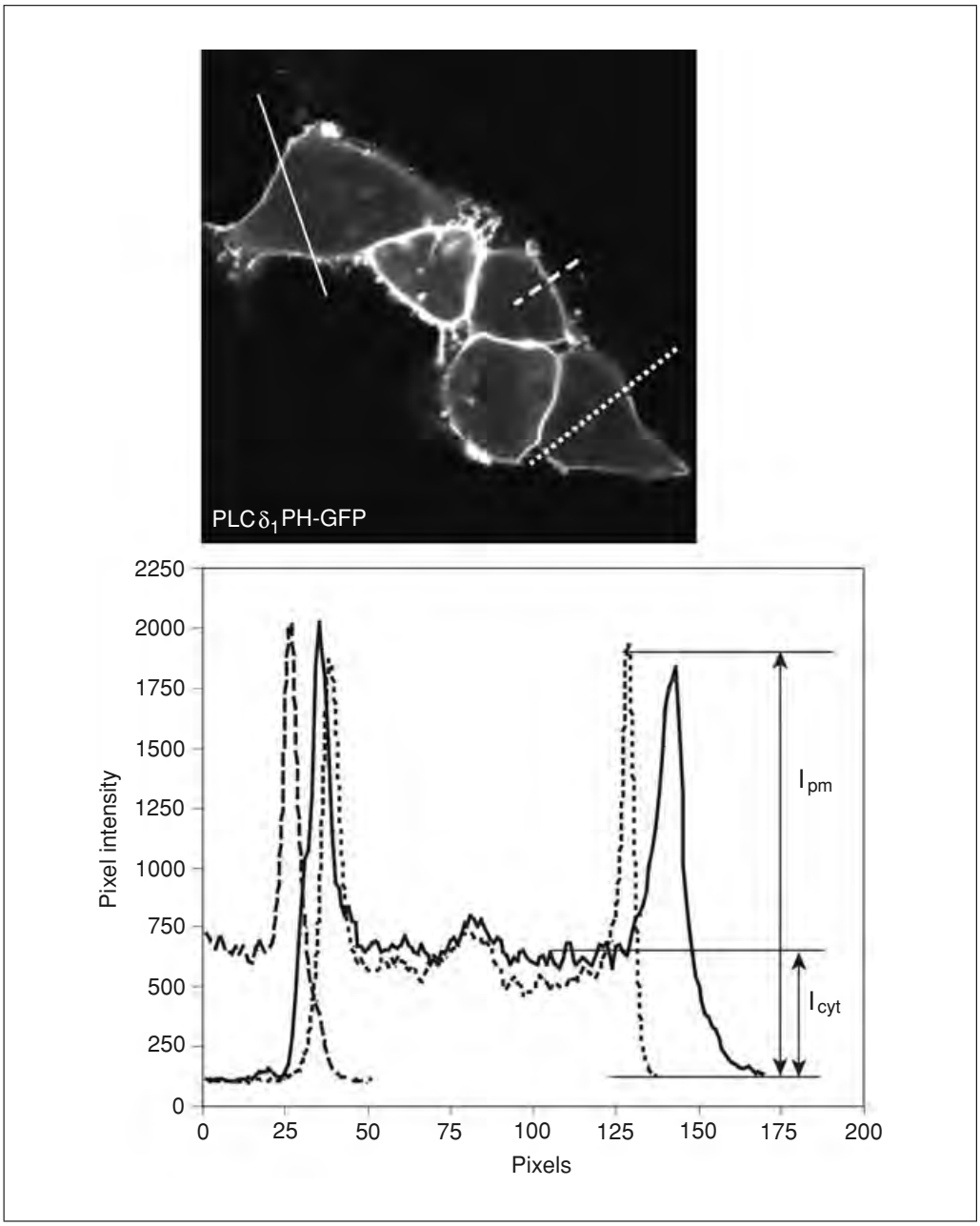

Figure 24.4.3 Quantification of the plasma membrane localization of an inositide binding domain. HEK293 cells are shown expressing the PLCδ_1PH-GFP. The pixel intensity histograms are calculated for the three lines placed on this recording. Note that the scale shows that this is a 12-bit image. An 8-bit image would only have 256 levels of intensities. Also note that the peak intensities are not at saturation. The lower panel shows how the intensity values from the membrane and the cytosol are calculated. Their ratio is then a good measurement of localization. Also note that no lines are placed over areas where two cells are joined. These calculations must be made for each picture from a sequence to obtain a full time-course of change. It is recommended that more than one line be placed on a cell to obtain a more accurate value as the intensities vary along the perimeter.

10. Once the scanning sequence is complete, save the results.

11. Quantify the data using appropriate software.

The most demanding part of the analysis of time-lapsed sequences is the quantification of data. Obvious changes can be documented in a series of pictures or movies that describe what is happening. However, as imaging tools are improving, some of the changes are not so obvious to the eye, especially when the number of vesicles, their movement patterns, or intensities all show some changes. Quantification is necessary when determining a dose-response relationship, comparing the relative effectiveness of two stimuli, or investigating the efficacy or potency of an inhibitor. It is difficult to provide recommendations that would cover all of these areas. In most of the applications dealing with plasma membrane phosphoinositides, it is necessary to assess the extent of plasma membrane recruitment; therefore, methods that determine plasma membrane association are focused upon. The simplest way is to monitor the cytosolic intensity since it will significantly increase as a domain translocates from the membrane to the cytosol. It is more demanding to calculate the ratio of membrane to cytosolic intensities. This can be done after creating a line-intensity histogram through a selected line across the cell. It is important that the highest intensities should not be in saturation, which requires a fine optimization of the dynamic range before recording in 8-bit systems (256 levels of gray intensity; Fig. 24.4.3). This is less of a problem with the newer 12-bit systems (4096 levels of intensity) or with a higher dynamic range. A more accurate but also more demanding way of quantification of the extent of membrane association of fluorescent proteins is to use fluorescence resonance energy transfer (FRET; UNITS 17.1 & 17.9) or total internal reflection fluorescence (TIRF; UNIT 4.12) microscopy as detailed in Varnai and Balla (2006) and Balla (2007). The latter is able to detect the radiationless energy transfer between two appropriate fluorophore pairs when they are within an optimal distance, while the former only detects fluorescence originating from the plane of the membrane attached to the coverslips. The variability of the cell population and the requirement for analysis of a large number of cells to obtain quantitative estimates of the fluorescence changes remains the most laborious parts of obtaining reliable, reproducible results.

REAGENTS AND SOLUTIONS

Use deionized, distilled water in all recipes and protocol steps. For common stock solutions, see ***APPENDIX 2A****; for suppliers, see* ***SUPPLIERS APPENDIX****.*

Krebs-Ringers solution

120 mM NaCl
4.7 mM KCl
1.2 mM Na_2HPO_4
1.2 mM $CaCl_2$
0.7 mM $MgSO_4$
10 mM glucose
20 mM Na-HEPES, pH 7.4
0.1% bovine serum albumin (BSA; not added when lipofilic druqs are to be added)
Store up to 4 to 5 weeks at 4°C

Paraformaldehyde

Prepare paraformaldehyde fresh by dissolving the appropriate amount of EM-grade paraformaldehyde in PBS and heating (in a chemical hood) until the aldehyde goes into solution. Keep the bottle cap loosened so that pressure does not build up. Cool down to 20°C and pH to 7.4 with NaOH.

COMMENTARY

Background Information

The classical methods to study phosphoinositides relied upon metabolic labeling of phosphoinositides. Labeling cells with myo-[^{3}H]inositol or ^{32}P-phosphate followed by lipid extraction and separation by TLC (or other methods) has been widely used to measure phosphoinositide changes (e.g., Christy

et al., 1998). However, these techniques require millions of cells to obtain a sufficient signal. Moreover, depending on the labeling time and the turnover rate of the metabolically distinct inositide pools, it is not certain whether isotopic equilibrium is reached. Determination of the subcellular location of inositides requires even more cells and cell fractionation procedures, and by the end it is still questionable whether the distribution really reflects what was present in the intact cell. Total cellular mass of inositides have also been measured based on quantitation of the inositide headgroup that is liberated from the extracted lipid species (Pearson et al., 2000). Detection of phosphoinositides or inositol phosphate mass separated on HPLC has been done with metal dye-detection (Pittet et al., 1989) or suppressed conductivity detection (Nasuhoglu et al., 2002). Excellent collections of the conventional methods have been published (Irvine, 1990; Shears, 1997). In the meantime, newer methods have been introduced for mass measurement of inositides without extensive purification with the aid of protein domains that specifically recognize the inositide headgroup (Luo et al., 2003; Guillou et al., 2007). However, even in their most simple forms these methods are cumbersome and are unable to resolve the small changes that occur in subcellular compartments, especially against the higher background of nonresponsive inositide pools. The realization that inositides are rapidly changing in restricted cellular compartments brought about the desire to detect them at the single-cell level preferably in live cells where the dynamics can be followed in real time.

Since the method employing protein domain fluorescent protein (FP) chimeras in live cells has certain limitations, there is a legitimate need for alternative methods in which the lipids are detected post-fixation without interfering with the biological process. Moreover, none of the live-cell imaging techniques can compete with the resolving power of electron microscopy. Post-fixation detection of the lipids has been achieved with anti-phosphoinositide antibodies or recombinant GST-fused inositol lipid–binding domains in immuno-cytochemical or -electron microscopy applications (Watt et al., 2002, 2004). The value of these techniques is clear; theoretically they would tell us where the lipids are in an intact cell without any distortion caused by the detection process and many cells can be analyzed with no time constraints. EM studies revealed the presence of lipids in compartments where in vivo PH domain imaging failed to do so, e.g., PtdIns(4,5)P2 in the Golgi (Watt et al., 2002). However, these techniques also have their drawbacks. First, the fixation process has a major influence on what inositide pools are visible to the antibodies or the GST-fused inositide-binding module. Second, the sensitivity of these methods is hard to evaluate. The fixation process is even more critical than in proteins in preserving the lipids and yet to make them accessible to the antibodies or protein modules. This technical difficulty explains the variability of the results obtained in different laboratories with the antibodies and their failure to work in some cases. The specificity of the antibodies should be a rigorous criterion and the data should be consistent with already existing knowledge on the distribution of phosphoinositides.

Assessing membrane localization by FRET

A quantitative assessment of the membrane localization of fluorescent probes is not always easy based on confocal images. An increase in the fluorescent intensity of the membrane can reflect a change in membrane volume or shape and not a real recruitment. Similarly, the cytosolic intensity of the probe can increase due to shrinkage instead of its release from the membranes. To overcome these problems, the FRET principle was used in several studies to obtain a signal that reflects true binding of the inositide binding domain to membranes. The method developed in the Jalink laboratory and also used in the authors' studies is based on co-expression of the CFP- and YFP-tagged versions of the same PH domain (e.g., PLCδ_1-PH). These fluorophores are the most widely used pairs for FRET studies although the more pH-resistant Venus replaces YFP and cerulean replaces CFP in newer applications. Newer fluorophore pairs are also available now for FRET studies but they are not as well established as the GFP derivatives. Nevertheless, the principle is the same; when the donor (CFP) and the acceptor (YFP) are within FRET distance (<8 nm) there will be energy transfer from CFP to YFP causing a decrease in CFP emission (475 nm) and an increase in YFP emission (525 nm) when using CFP excitation only (430 nm). In the so-called sensitized emission method, the efficiency of the energy transfer is numerically calculated after making all necessary corrections (such as bleed through of the CFP and YFP signals into the other pair's emission channels). However, for all practical purposes, the simple

fluorescence ratio of 525/475 can be used if the two wavelengths show opposite changes. This principle is applicable to the lipid binding PH domains when expressed both as a CFP or YFP fusion protein. The two fluorophores will show efficient energy transfer when their attached PH domains are bound to the lipids at the membrane. However, upon PLC activation, the PtdIns(4,5)P_2 molecules are hydrolyzed and the PH domains leave the membrane decreasing the FRET signal (van Der Wal et al., 2001). This method is quite sensitive and even small PLC activation can be detected and quantified. The method does not require a confocal microscope and can be used either in individual cells or in cell suspensions (Balla et al., 2005). A disadvantage of the method is that the FRET efficiency is not very high at low expression levels (which would be desirable to minimize the ill effects of the presence of the probes) and even at high probe concentrations there could be low FRET signal if the density of the lipids is below a certain level. Although the authors have not used this application, FRET can also be assessed by fluorescence life-time imaging microscopy (FLIM; *UNIT 4.14*) that calculates the half life of the excited state of the fluorophore that is very different when the energy is emitted in the form of photons or is transferred to an acceptor by FRET (Bastiaens and Squire, 1999). FLIM has many advantages over sensitized emission to evaluate FRET but it requires separate special instrumentation that is not as easily available as fluorescence microscopes.

In the above examples, two separate molecules are used to detect FRET between neighboring molecules (intermolecular FRET). A better solution would be to have inositol lipid probes based on intramolecular FRET in which case both fluorophores are attached to the same inositide-recognizing domain. Lipid binding then induces a molecular rearrangement that changes the distance (or more likely the dipole orientation) of the two fluorophores and, hence, the FRET signal. Such a probe based on the Grp1-PH domain was targeted to different membranes for PtdIns(3,4,5)P_3 detection (Sato et al., 2003) and a similar principle was utilized to generate FRET probes for monitoring InsP3 concentrations in the cytoplasm (Matsu-ura et al., 2006). The difficulty here is to ensure a large enough conformational change upon lipid binding to substantially change the FRET efficiency. Construction of a useful probe requires lots of experimentation with the domains themselves as well as with the linkers to connect the fluorophores. In a recent study, the AktPH domain was used to detect PtdIns(3,4,5)P_3/PtdIns(3,4)P_2 changes using a clever molecular design. The conformational change between the lipid-bound and unbound stages was achieved by inserting a negatively charged "pseudoligand" into the probe that binds to the PH domain (presumably to the lipid-binding site) when lipids are not present. Binding of the appropriate lipids abolishes this intramolecular interaction amplifying the conformational change and amplifying the change in the FRET signal (Ananthanarayanan et al., 2005). These single-molecule FRET probes do not require co-expression, their readout does not depend on their expression level (once above reliable detection limits) or on lipid density in the membrane. It is expected that more efforts will be made to generate similar probes for the detection of lipid production in the various cellular compartments.

More detailed technical and theoretical background on FRET measurements either with sensitized emission or with FLIM are covered in recent publications (Sekar and Periasamy, 2003; van Rheenen et al., 2004; Thaler et al., 2005).

Membrane localization based on TIRF analysis

Total internal reflection fluorescence (TIRF; *UNIT 4.12*) analysis has also been used to monitor plasma membrane association of inositol lipid binding domains (Tengholm et al., 2003). The basis of this technique is a special form of illumination where the light is shot at the sample at a shallow angle in a way that the photons do not illuminate the specimen beyond a ~200-nm thickness above the coverslip. This way the excitation is limited to the fluorescence molecules that are found close to the membrane of the cell attached to the coverslip, which makes this method suitable to detect membrane-associated events and also useful to study association and dissociation of molecules from the membrane. If the footprint of the cell changes, it could cause a change in fluorescence intensity unrelated to the actual amount of fluorescent molecules at the membrane. For this reason, use of a fluorescent membrane marker as a control and then evaluation of fluorescence changes against this reference signal are recommended.

Live-cell imaging of inositol lipids has become a standard approach in many laboratories. It has generated some controversy with examples for its uncritical use as well as for its complete dismissal as an unreliable method.

The truth is that this method—as every other—has its unique benefits as well as its limits. The authors emphasize that the phosphoinositides imaged with these molecular tools are only representative of a pool associated with certain processes and not necessarily representative of all of that particular inositide within the cell. This is especially true and obvious for PtdIns4P and may be less notable but still true for the other inositides. Also be cautious about high expression levels, which inhibit and distort cellular processes. Generating quantitative data with these methods is an added challenge but a very important necessity. As more domains that interact with inositides are identified in proteins it is important to remember that many of these will not work as reporters because their cellular localization is more dependent on protein-protein interaction than on lipid binding. However, some other probes should be compared for their imaging properties, especially for PtdIns(4,5)P_2 and PtdIns4P. Development of FRET-based probes relying on intramolecular rearrangements should also be facilitated. This research area will be in high demand for the near future. The high interest in phosphoinositides also demands constant improvement of the tools to further the knowledge on these molecules.

Troubleshooting

Described here are the most common problems that are encountered—starting from plasmid propagation to the final microscopy steps.

No bacterial colonies

The pEGFP plasmids have the kanamycin selection marker so transformed bacteria must be grown on kanamycin-containing plates and not on ampicillin-containing plates. However, companies are selling various forms of plasmids that one cannot assume that all GFP constructs are kanamycin selectable. Moreover, some laboratories add GFP to their chosen domain in ampicillin-resistance plasmids, and oftentimes researchers make wrong assumptions when selecting colonies of transformed bacteria. This should be the first consideration when no colonies are found after transformation of bacteria during subcloning or propagation of plasmids. Problems with subcloning, ligation reaction, or bacterial transformation can also result in no bacterial growth, but discussion of these variables is beyond the scope of this unit.

No green fluorescence

It may sound trivial but the most common reason for not seeing fluorescence is due to inappropriate microscope settings. Confocal microscopes used for fluorescence imaging can be intimidating for novices, with several filters and light directions that must be set properly to see the fluorescent signal. It is good practice to find the right focus of the cells with transmitted light. Switching to fluorescence, the blue (or other color) light coming through the objective must be visible to be sure that the illumination and the light path is properly set. It is very useful to have a slide of fixed GFP-expressing cells to use as a control. If the microscope settings are correct and there are still no GFP-positive cells (yet the autofluorescence is visible with a 40× or higher objective), then the problem lies with the transfection. Transfection problems can be caused by several factors, including inaccurate subcloning, impure plasmid for transfection, unsuitable transfection conditions for the cells. Even transfected primary cultured cells should have a few positive cells. Using cells transfected with the original pEGFP plasmid as control should help to determine whether the transfection procedure or the DNA construct is the source of the problem. If these cells are positive for GFP fluorescence, then the most likely source of the problem is the construct itself. The DNA construct could be defective by having an unwanted stop codon or a frame-shift either due to a flaw in the design or by a mutation. The plasmids should always be confirmed by DNA sequencing and the expression of the full-length protein should be confirmed by SDS-PAGE as described.

Weak fluorescence

If there are positive cells but their fluorescence is weak, the microscope may not be set up properly. Compare the cells with fixed cells transfected with EGFP alone to determine if the problem is with the microscope or the construct to be studied. If the EGFP-expressing cells are bright, but the fusion protein–expressing cells are weakly fluorescent, then the problem is inherent to the fusion protein. The authors' experience is that the larger the protein fused to GFP, the weaker its fluorescence. This could be because of the difficulty in the folding of GFP as part of a larger protein or that the translation of longer proteins is less efficient. Since the constructs listed in Table 24.4.1 express well, low levels of fluorescence usually indicates a transfection problem, which is also corroborated by few cells showing fluorescence. Many cells showing weak fluorescence indicates good transfection efficiency but low yield of the fluorescent protein.

Large aggregates present in cytoplasm

The localization of the lipid-binding domains listed in Table 24.4.1 is well documented. However, from time to time, one will encounter a problem when making a new probe or introducing mutations or deletions in any of these probes. This is a "localization" that is not related to interactions with phospholipids but is due to technical problems. High concentrations or more often folding problems of the expressed fusion proteins are usually responsible for this phenomenon, which results in the formation of large fluorescent aggregates that are found in various parts of the cell but mostly associated with the perinuclear area and could overlap with the Golgi. Very often this localization corresponds to the ER-associated protein degradation and represents the proteosome (Hitchcock et al., 2003). The authors experienced such problems with the EBFP-fused PLCδ1PH and with some chimeric constructs. In such cases, a fraction of the expressed protein still could fold properly and function as expected, and there are also cells that express less of the protein or, for a shorter time, do not display this problem. It is important to recognize this aggregation artifact and not to interpret it as a true localization. Sometimes it helps to reduce expression by using a less active promoter or to lower the temperature by 5° to 7°C during transfection and culture. However, the authors were not successful with these manipulations once the construct showed this aggregation behavior.

No localization is observed on the membrane where the lipid is expected to be

If GFP fluorescence is observed, but it is not associated with the membrane, it should be confirmed that the expression construct contains the sequence for the lipid-binding domain. Plasmid preparations of pEGFP-based plasmids often contain a ~600-bp DNA piece that is present without digestion by restriction enzymes. This band is usually faint but can be mistaken for an insert when confirming the DNA construct by restriction enzyme digestion analysis. This is especially problematic because many PH domains are encoded by DNA sequences of ~500 bp.

It also has to be realized that the amount of lipid produced and available for binding by a fluorescent probe is limited. Therefore, the membrane-bound fraction may not be distinguishable from the high cytosolic background of the unlocalized fusion protein when a cell expresses high amounts of the fusion protein. This is another reason to study cells that express low concentrations of the fusion protein. When PtdIns(4,5)P_2 is monitored with PLCδ_1PH-GFP, saturation within a wide range of expression level was not observed. We assume that there is a compensatory increase in the amount of PtdIns(4,5)P_2 in the cells expressing larger amounts of the lipid-binding protein. Compensatory increases are less likely to occur with lipids that are only formed in response to acute stimulation, such as PtdIns(3,4,5)P_3.

Nuclear localization

All of the domains listed in Table 24.4.1 can penetrate the nuclear pore and enter the nucleus, although their movement in and out is clearly limited. Many of the PH domains (Grp1-PH, ARNO-PH, Btk-PH, OSBP-PH, OSH2-PH) show very prominent nuclear localization. With the increased interest in nuclear phosphoinositides (Irvine, 2006) and the clear presence of these lipids in the nuclear matrix (in a still poorly understood physical form), localization of PH domains sparks the interest of many researchers. However, nuclear localization of these domains is also observed with mutants that do not bind the inositol lipids. This does not rule out that the wild-type constructs do have some nuclear binding components, but it shows that the major force of nuclear enrichment is not a reflection of lipid binding. It is very likely that the numerous basic residues characteristic of these domains are responsible for their nuclear localization; this is supported by the fact that algorithms based on the primary sequences of these proteins accurately predict their nuclear localization. However, if the protein binds to a lipid that is already present and abundant during expression, such as PtdIns(4,5)P_2, it will keep the domain out of the nucleus, provided that the amount of the expressed protein does not saturate the lipid available for binding. Again, choosing cells in which the expression levels are low also ensures less localization in the nucleus.

Plasma membrane localization—true or false?

The authors believe that many investigators have wrong ideas about how plasma membrane localization can be recognized especially under a confocal microscope. They expect a strong fluorescence signal outline of cells and no signal over the cytoplasm. This is true for cells that are round in shape or arranged as cobblestones such as MDCK cells. However, plasma membrane localization can

be more difficult to recognize in cells that are solitary and very flat such as COS cells. In such flat cells, one could see even fluorescence when imaging the glass-attached membrane surface giving the impression that the probe is also present in the cytoplasm. Moving upwards on the cell can change the view to a very fuzzy ring with some worm-like intensity (representing ruffles and microfilopodia) as the membrane covering the nucleus appears in the z-plane (Fig. 24.4.1B). It requires a trained eye to differentiate between plasma membrane and cytosolic constructs in such cells. A good guide is to see if the fluorescence clearly outlines the nucleus and its intensity is diminishing toward the periphery of the cells, both being signs of cytosolic localization.

In an opposing way, cytosolic proteins can show a phenomenon that the authors call "pseudo membrane localization," which gives the impression that the protein is in the membrane. In very flat cells, the edge of the cell and the membrane ruffles often appear as high-intensity lines or wrinkles because of the way the membrane appears in the imaged plane. Since membrane ruffling is a common response of cells to stimuli that activate PI 3-kinases and can be reversed with PI3K inhibitors, this "apparent" localization will show the same PI 3-kinase dependence as the real plasma membrane recruitment of PtdIns(3,4,5)P_3 recognizing domains. Therefore, it can give the impression that the construct localizes to the membrane ruffles in stimulated cells even when it does not actually bind to PtdIns(3,4,5)P_3. Comparing the fusion protein–expressing cells with control cells expressing only GFP is essential to resolving true versus false membrane localization. A useful measure of true plasma membrane recruitment is to monitor the decrease in intensity of the probe in the cytoplasm. The authors find that often this decrease can be best judged by the increased contrast between the cytoplasm and the nucleus, which appears sharper as the cytoplasmic fluorescence decreases. True membrane localization also has to fulfill several criteria. The localization of the fusion protein should follow the lipid changes that are evoked by physiological or pharmacological means. For example, PI 3 kinase inhibitors, such as wortmannin or LY294002 prevent the formation of 3-phosphorylated lipid products, so treatment of the transfected cells with these inhibitors should eliminate localization of fluorescent probes that recognize 3-phosphorylated lipids. Also, robust activation of PLC should cause a decrease in the localization of probes detecting PtdIns(4,5)P_2. However, the extent of change often is smaller than what can be detected by the eye or even with more sensitive quantification. For example, many G protein–coupled receptors evoke a Ca^{2+} signal (indicating PLC activation), yet no detectable change in PLCδ_1PH-GFP distribution. This does not mean that the probe does not work. It only means that the PLC activation is not robust enough, or the PIP 5 kinase activity is so active that there is little change in the concentration of the PtdIns(4,5)P_2 in the membrane.

A further observation of practical importance is that live cells lose localization of the PLCδ1PH-GFP (and some other domains) when they are kept at room temperature for >15 to 20 min. The reason for this has not been explored in detail, but it may be that lipid synthesis is slowed because of either ATP depletion or the physicochemical properties of the membrane change. Warming the cells to 37°C does not correct the situation within 30 min. Thus, live-cell imaging should be performed using a temperature-controlled microscope system within a short period of time after placing the cells in the observation medium.

Anticipated Results

Expression of GFP-fused inositol lipid binding domains should yield a fluorescent signal that is easy to recognize and distinguishable from background autofluorescence. In fact, the larger problem often is too high of expression, especially in COS-7 cells. In these cells, the biology is greatly distorted; therefore, these cells should not be used for analysis (see Fig. 24.4.1 for an example). HEK293 or HeLa cells will express more moderate levels of the same constructs since they do not express the large T antigen that generates many copies of the plasmid in COS cells. The distribution of the individual domains will reflect the localization of the lipid to which it binds except additional interactions of the domain with other membrane components or proteins may significantly alter the localization of the probe. Lastly, the lipid changes are not always large enough to be observed by the eye or even by quantification of the data. Many cells generate clearly detectable Ca^{2+} signals by PLC activation without a noticeable change in PLCδ1PH-GFP localization. These negative data do not necessarily mean that the probe is not working. A positive control is always a useful way to check a newly studied construct.

Time Considerations

Performing a live-cell imaging experiment is not particularly time consuming. A typical experiment starts out by preparing the coverslips (~2 hr with drying) and seeding cells for the experiment. Cells are transfected on the following day with plasmid DNA (~1 hr depending on the number of coverslips). For most phosphoinositide-binding domains, the transfection begins at ~1400 hr and the transfection medium is changed to one with serum ~1900 hr for experiments that are planned for the following day. It is not recommended to use cells after >24 to 30 hr after transfection with these domains. The actual experiment requires setting up the microscope and the heated stage (~30 min) and waiting for equilibration (~30 min). Depending on the type of experiment, a sample is rarely on the stage >30 min. Data analysis is done off-line and can be more time consuming than the actual experiment depending on the application. Design and generation of a new construct is a more time-consuming process that can take from 1 week (optimal) to several weeks.

It is important to remember that the time-consuming part of live-cell imaging is the many times an experiment must be repeated. Many recordings cannot be used because of technical problems such as moving cells or focus-drift occurring during time-lapse imaging. Also, one must repeat experiments many times before being confident that the chosen pictures actually represent a reproducible biological process. Due to individual variations among cells, this is often not appreciated by users who are used to methods that give averaged cell responses.

Acknowledgments

The authors would like to thank Dr. Mark Lemmon (Univ. Pennsylvania, Philadelphia) for the OSH1-PH-GFP and OSH2-PH-GFP constructs. The confocal imaging was performed at the Microscopy & Imaging Core of the National Institute of Child Health and Human Development, NIH with the kind assistance of Drs. Vincent Schram and James T. Russell. This research was supported in part by the Intramural Research Program of the National Institute of Child Health and Human Development of the National Institutes of Health. Péter Várnai is also a Bolyai Fellow of the Hungarian Academy of Science and was also supported by the Hungarian Scientific Research fund (OTKA NF-68563) and the Medical Research Council (ETT 440/2006).

Literature Cited

Ananthanarayanan, B., Ni, Q., and Zhang, J. 2005. Signal propagation from membrane messengers to nuclear effectors revealed by reporters of phosphoinositide dynamics and Akt activity. *Proc. Natl. Acad. Sci. U.S.A.* 102:15081-15086.

Balla, T. 2007. Imaging and manipulating phosphoinositides in living cells. *J. Physiol.* 582:927-937.

Balla, A., Tuymetova, G., Tsiomenko, A., Varnai, P., and Balla, T. 2005. A plasma membrane pool of phosphatidylinositol 4-phosphate is generated by phosphatidylinositol 4-kinase type-III alpha: Studies with the PH domains of the oxysterol binding protein and FAPP1. *Mol. Biol. Cell* 16:1282-1295.

Balla, A., Kim, Y.J., Varnai, P., Szentpetery, Z., Knight, Z., Shokat, K.M., and Balla, T. 2008. Maintenance of hormone-sensitive phosphoinositide pools in the plasma membrane requires phosphatidylinositol 4-kinase III{alpha}. *Mol. Biol. Cell* 19:711-721.

Bastiaens, P.I. and Squire, A. 1999. Fluorescence lifetime imaging microscopy: Spatial resolution of biochemical processes in the cell. *Trends Cell Biol.* 9:48-52.

Berridge, M.J. and Irvine, R.F. 1984. Inositol trisphosphate, a novel second messenger in cellular signal transduction. *Nature* 312:315-321.

Burd, C.G. and Emr, S.D. 1998. Phosphatidylinositol(3)-phosphate signaling mediated by specific binding to RING FYVE domains. *Mol. Cell* 2:157-162.

Christy, A.H., Kim, A.C., Marfatia, S.M., Lutchman, M., Hanspal, M., Jindal, H., Liu, S.C., Low, P.S., Rouleau, G.A., Mohandas, N., Chasis, J.A., Conboy, J.G., Gascard, P., Takakuwa, Y., Huang, S.C., Benz, E.J. Jr., Bretscher, A., Fehon, R.G., Gusella, J.F., Ramesh, V., Solomon, F., Marchesi, V.T., Tsukita, S., Arpin, M., Louvard, D., Tonks, N.K., Anderson, J.M., Fanning, A.S., Bryant, P.J., Woods, D.F., and Hoover, K.B. 1998. The FERM domain: A unique module involved in the linkage of cytoplasmic proteins to the membrane. *Trends Biochem. Sci.* 23:281-282.

Cohen, L.A., Honda, A., Varnai, P., Brown, F.B., Balla, T., and Donaldson, J.G. 2007. Active Arf6 recruits ARNO/cytohesin GEFs to the PM by binding their PH domains. *Mol. Biol. Cell* 18:2244-2253.

Coronas, S., Ramel, D., Pendaries, C., Gaits-Iacovoni, F., Tronchere, H., and Payrastre, B. 2007. PtdIns5P: A little phosphoinositide with big functions? *Biochem. Soc. Symp.* 74:117-128.

De Matteis, M.A., Di Campli, A., and Godi, A. 2005. The role of the phosphoinositides at the Golgi complex. *Biochim. Biophys. Acta* 1744:396-405.

Di Paolo, G. and De Camilli, P. 2006. Phosphoinositides in cell regulation and membrane dynamics. *Nature* 443:651-657.

Dormann, D., Weijer, G., Parent, C.A., Devreotes, P.N., and Weijer, C.J. 2002. Visualizing PI3 kinase-mediated cell-cell signaling during *Dictyostelium* development. *Curr. Biol.* 12:1178-1188.

Dove, S.K., Piper, R.C., McEwen, R.K., Yu, J.W., King, M.C., Hughes, D.C., Thuring, J., Holmes, A.B., Cooke, F.T., Michell, R.H., Parker, P.J., and Lemmon, M.A. 2004. Svp1p defines a family of phosphatidylinositol 3,5-bisphosphate effectors. *EMBO J.* 23:1922-1933.

Dowler, S., Currie, R.A., Campbell, D.J., Deak, M., Kular, G., Downes, C.P., and Alessi, D.R. 2000. Identification of pleckstrin-homology-domain-containing proteins with novel phosphoinositide-binding specificities. *Biochem. J.* 351:19-31.

Ellson, C.D., Gobert-Gosse, S., Anderson, K.E., Davidson, K., Erdjument-Bromage, H., Tempst, P., Thuring, J.W., Cooper, M.A., Lim, Z.Y., Holmes, A.B., Gaffney, P.R.J., Coadwell, J., Chilvers, E.R., Hawkins, P.T., and Stephens, L.R. 2001. PtdIns(3)P regulates the neutrophil oxidase complex by binding to the PX domain of p40phox. *Nat. Cell Biol.* 3:679-682.

Field, S.J., Madson, N., Kerr, M.L., Galbraith, K.A., Kennedy, C.E., Tahiliani, M., Wilkins, A., and Cantley, L.C. 2005. PtdIns(4,5)P2 functions at the cleavage furrow during cytokinesis. *Curr. Biol.* 15:1407-1412.

Franke, T.F., Kaplan, D.R., Cantley, L.C., and Toker, A. 1997. Direct regulation of the Akt protooncogene product by PI3,4P2. *Science* 275:665-668.

Friant, S., Pecheur, E.I., Eugster, A., Michel, F., Lefkir, Y., Nourrisson, D., and Letourneur, F. 2003. Ent3p Is a PtdIns(3,5)P2 effector required for protein sorting to the multivesicular body. *Dev. Cell* 5:499-511.

Gary, J.D., Wurmser, A.E., Bonangelino, C.J., Weisman, L.S., and Emr, S.D. 1998. Fab1p is essential for PtdIns(3)P 5-kinase activity and the maintenance of vacuolar size and membrane homeostasis. *J. Cell Biol.* 143:65-79.

Giepmans, B.N., Adams, S.R., Ellisman, M.H., and Tsien, R.Y. 2006. The fluorescent toolbox for assessing protein location and function. *Science* 312:217-224.

Gillooly, D.J., Morrow, I.C., Lindsay, M., Gould, R., Bryant, N.J., Gaullier, L.M., Parton, G.P., and Stenmark, H. 2000. Localization of phosphatidylinositol 3-phosphate in yeast and mammalian cells. *EMBO J.* 19:4577-4588.

Godi, A., Di Campi, A., Konstantakopoulos, A., Di Tullio, G., Alessi, D.R., Kular, G.S., Daniele, T., Marra, P., Lucocq, J.M., and De Matteis, M.A. 2004. FAPPs control Golgi-to-cell-surface membrane traffic by binding to ARF and PtdIns(4)P. *Nat. Cell Biol.* 6:393-404.

Gozani, O., Karuman, P., Jones, D.R., Ivanov, D., Cha, J., Logovskoy, A.A., Baird, C.L., Zhu, H., Field, S.J., Lessnick, S.L., Villasenov, J., Mehrotra, B., Chen, J., Rao, V.R., Brugge, J.S., Ferguson, C.G., Payrastre, B., Myszka, D.G., Cantley, L.C., Wagner, G., Divecha, N., Prestwich, G.D., and Yuan, J. 2003. The PHD finger of the chromatin-associated protein ING2 functions as a nuclear phosphoinositide receptor. *Cell* 114:99-111.

Guillou, H., Stephens, L.R., and Hawkins, P.T. 2007. Quantitative measurement of phosphatidylinositol 3,4,5-trisphosphate. *Methods Enzymol.* 434:117-130.

Hammond, G.R., Dove, S.K., Nicol, A., Pinxteren, J.A., Zicha, D., and Schiavo, G. 2006. Elimination of plasma membrane phosphatidylinositol (4,5)-bisphosphate is required for exocytosis from mast cells. *J. Cell Sci.* 119:2084-2094.

Hitchcock, A.L., Auld, K., Gygi, S.P., and Silver, P.A. 2003. A subset of membrane-associated proteins is ubiquitinated in response to mutations in the endoplasmic reticulum degradation machinery. *Proc. Natl. Acad. Sci. U.S.A.* 100:12735-12740.

Horan, K.A., Watanabe, K., Kong, A.M., Bailey, C.G., Rasko, J.E., Sasaki, T., and Mitchell, C.A. 2007. Regulation of FcgammaR-stimulated phagocytosis by the 72-kDa inositol polyphosphate 5-phosphatase: SHIP1, but not the 72-kDa 5-phosphatase, regulates complement receptor 3 mediated phagocytosis by differential recruitment of these 5-phosphatases to the phagocytic cup. *Blood* 110:4480-4491.

Huang, Y.E., Iijima, M., Parent, C.A., Funamoto, S., Firtel, R.A., and Devreotes, P. 2003. Receptor-mediated regulation of PI3Ks confines PI(3,4,5)P3 to the leading edge of chemotaxing cells. *Mol. Biol. Cell* 14:1913-1922.

Hunyady, L., Baukal, A.J., Gaborik, Z., Olivares-Reyes, J.A., Bor, M., Szaszak, M., Lodge, R., Catt, K.J., and Balla, T. 2002. Differential PI 3-kinase dependence of early and late phases of recycling of the internalized AT1 angiotensin receptor. *J. Cell Biol.* 157:1211-1222.

Ikonomov, O.C., Sbrissa, D., Foti, M., Carpentier, J.L., and Shisheva, A. 2003. PIKfyve controls fluid phase endocytosis but not recycling/degradation of endocytosed receptors or sorting of procathepsin D by regulating multivesicular body morphogenesis. *Mol. Biol. Cell* 14:4581-4591.

Irvine, R.F. 1990. Methods in Inositide Research. Raven Presss, New York.

Irvine, R.F. 2006. Nuclear inositide signalling—Expansion, structures and clarification. *Biochim. Biophys. Acta* 1761:505-508.

Jefferies, H.B., Cooke, F.T., Jat, P., Boucheron, C., Koizumi, T., Hayakawa, M., Kaizawa, H., Ohishi, T., Workman, P., Waterfield, M.D., and Parker, P.J. 2008. A selective PIKfyve inhibitor blocks PtdIns(3,5)P(2) production and disrupts endomembrane transport and retroviral budding. *EMBO Rep.* 9:164-170.

Kanai, F., Liu, H., Field, S.J., Akbary, H., Matsuo, T., Brown, G.E., Cantley, L.C., and Yaffe, M.B. 2001. The PX domains of p47phox and p40phox bind to lipid products of PI(3)K. *Nat. Cell Biol.* 3:675-678.

Karathanassis, D., Stahelin, R.V., Bravo, J., Perisic, O., Pacold, C.M., Cho, W., and Williams, R.L. 2002. Binding of the PX domain of p47phox to phosphatidylinositol 3,4-bisphosphate and phosphatidic acid is masked by an intramolecular interaction. *EMBO J.* 21:5057-5068.

Kimber, W.A., Trinkle-Mulcahy, L., Cheung, P.C., Deak, M., Marsden, L.J., Kieloch, A., Watt, S., Javier, R.T., Gray, A., Downes, C.P., Lucocq, J.M., and Alessi, D.R. 2002. Evidence that the tandem-pleckstrin-homology-domain-containing protein TAPP1 interacts with Ptd(3,4)P2 and the multi-PDZ-domain-containing protein MUPP1 in vivo. *Biochem. J.* 361:525-536.

Klarlund, J.K., Guilherme, A., Holik, J.J., Virbasius, J.V., Chawla, A., and Czech, M.P. 1997. Signaling by phosphoinositide-3,4,5-trisphosphate through proteins containing plekstrin and Sec7 homology domains. *Science* 275:1927-1930.

Klarlund, J.K., Tsiaras, W., Holik, J.J., Chawla, A., and Czech, M.P. 2000. Distinct polyphosphoinositide binding selectivities for pleckstrin homology domains of GRP1-like proteins based on diglycine versus triglycine motifs. *J. Biol. Chem.* 275:32816-32821.

Komander, D., Fairservice, A., Deak, M., Kular, G.S., Prescott, A.R., Peter Downes, C., Safrany, S.T., Alessi, D.R., and van Aalten, D.M. 2004. Structural insights into the regulation of PDK1 by phosphoinositides and inositol phosphates. *EMBO J.* 23:3918-3928.

Lemmon, M.A., Falasca, M., Ferguson, K.M., and Schlessinger, J. 1997. Regulatory recruitment of signalling molecules to the cell membrane by plekstrin-homology domains. *Trends Cell Biol.* 7:237-242.

Lemmon, M.A., Ferguson, K.M., O'Brian, R., Sigler, P.B., and Schlessinger, J. 1995. Specific and high-affinity binding of inositol phosphates to an isolated plekstrin homology domain. *Proc. Natl. Acad. Sci. U.S.A.* 92:10472-10476.

Levine, T.P. and Munro, S. 1998. The pleckstrin-homology domain of oxysterol-binding protein recognizes a determinant specific to Golgi membranes. *Curr. Biol.* 8:729-739.

Levine, T.P. and Munro, S. 2002. Targeting of Golgi-specific pleckstrin homology domains involves both PtdIns 4-kinase-dependent and -independent components. *Curr. Biol.* 12:695-704.

Luo, H.R., Huang, Y.E., Chen, J.C., Saiardi, A., Iijima, M., Ye, K., Huang, Y., Nagata, E., Devreotes, P., and Snyder, S.H. 2003. Inositol pyrophosphates mediate chemotaxis in *Dictyostelium* via pleckstrin homology domain-PtdIns(3,4,5)P3 interactions. *Cell* 114:559-572.

Manna, D., Albanese, A., Park, W.S., and Cho, W. 2007. Mechanistic basis of differential cellular responses of phosphatidylinositol 3,4-bisphosphate- and phosphatidylinositol 3,4,5-trisphosphate-binding pleckstrin homology domains. *J. Biol. Chem.* 282:32093-32105.

Matsuda, M., Paterson, H.F., Rodriguez, R., Fensome, A.C., Ellis, M.V., Swann, K., and Katan, M. 2001. Real time fluorescence imaging of PLC gamma translocation and its interaction with the epidermal growth factor receptor. *J. Cell Biol.* 153:599-612.

Matsu-ura, T., Michikawa, T., Inoue, T., Miyawaki, A., Yoshida, M., and Mikoshiba, K. 2006. Cytosolic inositol 1,4,5-trisphosphate dynamics during intracellular calcium oscillations in living cells. *J. Cell Biol.* 173:755-765.

Michell, R.H., Heath, V.L., Lemmon, M.A., and Dove, S.K. 2005. Phosphatidylinositol 3,5-bisphosphate: Metabolism and cellular functions. *Trends Biochem. Sci.* 31:52-63.

Muller-Taubenberger, A. and Anderson, K.I. 2007. Recent advances using green and red fluorescent protein variants. *Appl. Microbiol. Biotechnol.* 77:1-12.

Nagel, W., Schilcher, P., Zeitlmann, L., and Kolanus, W. 1998. The PH domain and the polybasic c domain of cytohesin-1 cooperate specifically in plasma membrane-association and cellular function. *Mol. Biol. Cell* 9:1981-1994.

Nash, M.S., Young, K.W., Willars, G.B., Challiss, R.A., and Nahorski, S.R. 2001. Single-cell imaging of graded Ins(1,4,5)P3 production following G-protein-coupled-receptor activation. *Biochem. J.* 356:137-142.

Nasuhoglu, C., Feng, S., Mao, J., Yamamoto, M., Yin, H.L., Earnest, S., Barylko, B., Albanesi, J.P., and Hilgemann, D.W. 2002. Nonradioactive analysis of phosphatidylinositides and other anionic phospholipids by anion-exchange high-performance liquid chromatography with suppressed conductivity detection. *Anal. Biochem.* 301:243-254.

Nelson, C.P., Nahorski, S.R., and Challiss, R.A. 2008. Temporal profiling of changes in phosphatidylinositol 4,5-bisphosphate, inositol 1,4,5-trisphosphate and diacylglycerol allows comprehensive analysis of phospholipase C-initiated signalling in single neurons. *J. Neurochem.* 107:602-615.

Pearson, M.A., Reczek, D., Bretscher, A., and Karplus, P.A. 2000. Structure of the ERM protein moesin reveals the FERM domain fold and extended actin binding tail domain. *Cell* 101:259-270.

Pendaries, C., Tronchere, H., Arbibe, L., Mounier, J., Gozani, O., Cantley, L., Fry, M.J., Gaits-Iacovoni, F., Sansonetti, P.J., and Payrastre, B. 2006. PtdIns5P activates the host cell PI3-kinase/Akt pathway during *Shigella flexneri* infection. *EMBO J.* 25:1024-1034.

Pittet, D., Schlegel, W., Lew, D.P., Monod, A., and Mayr, G.W. 1989. Mass changes in inositol tetrakis- and pentakisphosphate isomers induced by chemotactic peptide stimulation in HL-60 cells. *J. Biol. Chem.* 264:18489-18493.

Quinn, K.V., Behe, P., and Tinker, A. 2008. Monitoring changes in membrane phosphatidylinositol 4,5-bisphosphate in living cells using a

domain from the transcription factor tubby. *J. Physiol.* 586:2855-2871.

Rameh, L.E., Arvidsson, A., Carraway, K.L. III, Couvillon, A.D., Rathbun, G., Crompton, A., VanRentherghem, B., Czech, M.P., Ravichandran, K.S., Burakoff, S.J., Wang, D.S., Chen, C.S., and Cantley, L.C. 1997a. A comparative analysis of the phosphoinositide binding specificity of plekstrin homology domains. *J. Biol. Chem.* 272:22059-22066.

Rameh, L.E., Tolias, K.F., Duckworth, B.C., and Cantley, L.C. 1997b. A new pathway for synthesis of phosphatidylinositol-4,5-bisphosphate. *Nature* 390:192-196.

Raucher, D., Stauffer, T., Chen, W., Shen, K., Guo, S., York, J.D., Sheetz, M.P., and Meyer, T. 2000. Phosphatidylinositol 4,5-bisphosphate functions as a second messenger that regulates cytoskeleton-plasma membrane adhesion. *Cell* 100:221-228.

Roy, A. and Levine, T.P. 2004. Multiple pools of phosphatidylinositol 4-phosphate detected using the pleckstrin homology domain of Osh2p. *J. Biol. Chem.* 279:44683-44689.

Salim, K., Bottomley, M.J., Querfurth, E., Zvelebil, M.J., Gout, I., Scaife, R., Margolis, R.L., Gigg, R., Smith, C.I.E., Driscoll, P.C., Waterfield, M.D., and Panayotou, G. 1996. Distinct specificity in the recognition of phosphoinositides by the plekstrin homology domains of dynamin and Bruton's tyrosine kinase. *EMBO J.* 15:6241-6250.

Santagata, S., Boggon, T.J., Baird, C.L., Gomez, C.A., Zhao, J., Shan, W.S., Myszka, D.G., and Shapiro, L. 2001. G-protein signaling through tubby proteins. *Science* 292:2041-2050.

Sato, M., Ueda, Y., Takagi, T., and Umezawa, Y. 2003. Production of PtdInsP3 at endomembranes is triggered by receptor endocytosis. *Nat. Cell Biol.* 5:1016-1022.

Sekar, R.B. and Periasamy, A. 2003. Fluorescence resonance energy transfer (FRET) microscopy imaging of live cell protein localizations. *J. Cell Biol.* 160:629-633.

Servant, G., Weiner, O.D., Herzmark, P., Balla, T., Sedat, J.W., and Bourne, H.R. 2000. Polarization of chemoattractant receptor signaling during neutrophil chemotaxis. *Science* 287:1037-1040.

Shaner, N.C., Steinbach, P.A., and Tsien, R.Y. 2005. A guide to choosing fluorescent proteins. *Nat. Methods* 2:905-909.

Shears, S.B. 1997. Signalling by Inositides. Oxford University Press, Oxford.

Simonsen, A., Lippe, R., Christoforidis, S., Gaullier, J.M., Brech, A., Callaghan, J., Toh, B.H., Murphy, C., Zerial, M., and Stenmark, H. 1998. EEA1 links PI(3)K function to Rab5 regulation of endosome fusion. *Nature* 394:494-498.

Stahelin, R.V., Burian, A., Bruzik, K.S., Murray, D., and Cho, W. 2003. Membrane binding mechanisms of the PX domains of NADPH oxidase p40phox and p47phox. *J. Biol. Chem.* 278:14469-14479.

Stauffer, T.P., Ahn, S., and Meyer, T. 1998. Receptor-induced transient reduction in plasma membrane PtdIns(4,5)P2 concentration monitored in living cells. *Curr. Biol.* 8:343-346.

Tengholm, A., Teruel, M.N., and Meyer, T. 2003. Single cell imaging of PI3K activity and glucose transporter insertion into the plasma membrane by dual color evanescent wave microscopy. *Sci. STKE* 2003:PL4.

Thaler, C., Koushik, S.V., Blank, P.S., and Vogel, S.S. 2005. Quantitative multiphoton spectral imaging and its use for measuring resonance energy transfer. *Biophys. J.* 89:2736-2749.

Thomas, C.C., Dowler, S., Deak, M., Alessi, D.R., and van Aalten, D.M. 2001. Crystal structure of the phosphatidylinositol 3,4-bisphosphate-binding pleckstrin homology (PH) domain of tandem PH-domain-containing protein 1 (TAPP1): Molecular basis of lipid specificity. *Biochem. J.* 358:287-294.

van Der Wal, J., Habets, R., Varnai, P., Balla, T., and Jalink, K. 2001. Monitoring phospholipase C activation kinetics in live cells by FRET. *J. Biol. Chem.* 276:15337-15344.

van Rheenen, J., Langeslag, M., and Jalink, K. 2004. Correcting confocal acquisition to optimize imaging of fluorescence resonance energy transfer by sensitized emission. *Biophys. J.* 86:2517-2529.

Várnai, P. and Balla, T. 1998. Visualization of phosphoinositides that bind pleckstrin homology domains: Calcium-and agonist-induced dynamic changes and relationship to myo-[3H]inositol-labeled phosphoinositide pools. *J. Cell Biol.* 143:501-510.

Várnai, P. and Balla, T. 2006. Live cell imaging of phosphoinositide dynamics with fluorescent protein domains. *Biochim. Biophys. Acta* 1761:957-967.

Várnai, P., Rother, K.I., and Balla, T. 1999. Phosphatidylinositol 3-kinase-dependent membrane association of the Bruton's tyrosine kinase pleckstrin homology domain visualized in single living cells. *J. Biol. Chem.* 274:10983-10989.

Várnai, P., Bondeva, T., Tamas, P., Toth, B., Buday, L., Hunyady, L., and Balla, T. 2005. Selective cellular effects of overexpressed pleckstrin-homology domains that recognize PtdIns(3,4,5)P3 suggest their interaction with protein binding partners. *J. Cell Sci.* 118:4879-4888.

Várnai, P., Thyagarajan, B., Rohacs, T., and Balla, T. 2006. Rapidly inducible changes in phosphatidylinositol 4,5-bisphosphate levels influence multiple regulatory functions of the lipid in intact living cells. *J. Cell Biol.* 175:377-382.

Venkateswarlu, K., Gunn-Moore, F., Oatey, P.B., Tavare, J.M., and Cullen, P.J. 1998a. Nerve growth factor- and epidermal growth factor-stimulated translocation of the ADP-ribosylation factor-exchange factor GRP1 to the

plasma membrane of PC12 cells requires activation of phosphatidylinositol 3-kinase and the GRP1 pleckstrin homology domain. *Biochem. J.* 335:139-146.

Venkateswarlu, K., Oatey, P.B., Tavare, J.M., and Cullen, P.J. 1998b. Insulin-dependent translocation of ARNO to the plasma membrane of adipocytes requires phosphatidylinositol 3-kinase. *Curr. Biol.* 8:463-466.

Venkateswarlu, K., Gunn-Moore, F., Tavare, J.M., and Cullen, P.J. 1999. EGF-and NGF-stimulated translocation of cytohesin-1 to the plasma membrane of PC12 cells requires PI 3-kinase activation and a functional cytohesin-1 PH domain. *J. Cell Sci.* 112:1957-1965.

Watt, S.A., Kular, G., Fleming, I.N., Downes, C.P., and Lucocq, J.M. 2002. Subcellular localization of phosphatidylinositol 4,5-bisphosphate using the pleckstrin homology domain of phospholipase C delta1. *Biochem. J.* 363:657-666.

Watt, S.A., Kimber, W.A., Fleming, I.N., Leslie, N.R., Downes, C.P., and Lucocq, J.M. 2004. Detection of novel intracellular agonist responsive pools of phosphatidylinositol 3,4-bisphosphate using the TAPP1 pleckstrin homology domain in immunoelectron microscopy. *Biochem. J.* 377:653-663.

Watton, J. and Downward, J. 1999. Akt/PKB localisation and 3′ phosphoinositide generation at sites of epithelial cell-matrix and cell-cell interaction. *Curr. Biol.* 9:433-436.

Weixel, K.M., Blumental-Perry, A., Watkins, S.C., Aridor, M., and Weisz, O.A. 2005. Distinct Golgi populations of phosphatidylinositol 4-phosphate regulated by phosphatidylinositol 4-kinases. *J. Biol. Chem.* 280:10501-10508.

Whitman, M., Downes, C.P., Keeler, M., Keller, T., and Cantley, L. 1988. Type-I phosphatidylinositol kinase makes a novel inositol phospholipid, phosphatidylinositol-3-phosphate. *Nature* 332:644-646.

Wiedenmann, J. and Nienhaus, G.U. 2006. Live-cell imaging with EosFP and other photoactivatable marker proteins of the GFP family. *Expert Rev. Proteomics.* 3:361-374.

Yaradanakul, A. and Hilgemann, D.W. 2007. Unrestricted diffusion of exogenous and endogenous PIP(2) in baby hamster kidney and Chinese hamster ovary cell plasmalemma. *J. Membr. Biol.* 220:53-67.

Yu, J.W., Mendrola, J.M., Audhya, A., Singh, S., Keleti, D., DeWald, D.B., Murray, D., Emr, S.D., and Lemmon, M.A. 2004. Genome-wide analysis of membrane targeting by *S. cerevisiae* pleckstrin homology domains. *Mol. Cell* 13:677-688.

Zhan, Y., Virbasius, J.V., Song, X., Pomerleau, D.P., and Zhou, G.W. 2002. The p40phox and p47phox PX domains of NADPH oxydase target cell membranes via direct and indirect recruitment by phosphoinositides. *J. Biol. Chem.* 277:4512-4518.

Zou, J., Marjanovic, J., Kisseleva, M.V., Wilson, M., and Majerus, P.W. 2007. Type I phosphatidylinositol-4,5-bisphosphate 4-phosphatase regulates stress-induced apoptosis. *Proc. Natl. Acad. Sci. U.S.A.* 104:16834-16839.

Dorus Gadella, Wednesday June 13th 2012, 9.00

Journal of Microscopy

Journal of Microscopy, Vol. 241, Pt 2 2011, pp. 111–118
Received 6 May 2010; accepted 9 July 2010

doi: 10.1111/j.1365-2818.2010.03437.x

FRET microscopy: from principle to routine technology in cell biology

A. PIETRASZEWSKA-BOGIEL & T.W.J. GADELLA
Section of Molecular Cytology and Centre for Advanced Microscopy, Swammerdam Institute for Life Sciences, University of Amsterdam, Amsterdam, The Netherlands

Key words. Acceptor photobleaching, anisotropy, fluorescence lifetime imaging microscopy (FLIM), fluorescence resonance energy transfer (FRET), homo-FRET.

Summary

The phenomenon of resonance energy transfer first described by Theodor Förster presents the opportunity of retrieving information on molecular proximity, orientation and conformation on the nanometre scale from (living) samples with conventional fluorescence microscopes (or even macroscopic devices). During the past 10 years Förster (or fluorescence) resonance energy transfer (FRET) microscopy has been revolutionized by the vast progress in fluorescent protein and *in situ* fluorescent labelling technology as well as by the commercial availability of advanced quantitative microscopy instrumentation. FRET microscopy is now routinely used in modern cell biology research. This short review will guide the reader through the most established FRET microscopy techniques, their inherent strengths and limitations, potential pitfalls, and assist the reader in making an educated choice on the FRET microscopy method most suited for their specific application.

FRET basics

FRET is the physical phenomenon whereby energy is transferred from an excited fluorophore, called the donor (D), to a nearby chromophore, called the acceptor (A), by non-radiative dipole–dipole coupling (through space). FRET only occurs when D and A are in close proximity (nanometre range), when there is sufficient spectral overlap between donor emission and acceptor absorption and when the acceptor transition dipole moment is not perpendicular to the electric field of the dipole field of the donor. The amount of energy transfer, usually expressed as the FRET efficiency (E), is defined as the fraction of photons absorbed by donors whose energy is transferred to acceptors, and is highly dependent on the distance between donor and acceptor (r_{DA}). For a single DA pair this dependence is described in Eq. (1), where R_0 is the Förster radius at which 50% energy is transferred:

$$E = \frac{R_0^6}{R_0^6 + r_{DA}^6} \qquad (1).$$

The Förster radius R_0 depends on the fluorescence quantum yield of D (Q_D), the absorption coefficient of A (ε_A) (through the parameter J, the overlap integral), the refractive index (n) and on the relative angular dispositions of the donor emission and the acceptor absorption dipole moments (through the parameter: κ^2), see Eq. (2) in which C is a constant of 8.79×10^{-11} (units M cm nm^2):

$$R_0^6 = C\, n^{-4} Q_D \kappa^2 J \quad \text{(units nm}^6\text{)} \quad \text{and}$$
$$J = \int F_D(\lambda) \cdot \varepsilon_A(\lambda) \cdot \lambda^4 d\lambda \Big/ \int F_D(\lambda) d\lambda \qquad (2)$$

The overlap integral J (units M^{-1} cm^{-1} nm^4) depends on the donor fluorescence emission ($F_D(\lambda)$, arbitrary units), the acceptor absorption ($\varepsilon_A(\lambda)$, units M^{-1} cm^{-1}) and the wavelength (λ, in nanometre units).

Given the steep distance dependency of FRET (Eq. 1) and Förster radii of 3–6 nm for most DA pairs, FRET is only observed at DA separation of less than 10 nm, which is at the biomolecular scale. Therefore, FRET microscopy offers unique opportunities for studying static and dynamic molecular proximity (through r_{DA}) and conformation (through κ^2) with a resolution far below the diffraction limit of optical microscopy. Together with the revolution in fluorescent genetic encoded labelling [e.g. visible fluorescent proteins (FPs)] and the increasing availability of commercial quantitative fluorescence microscopy instrumentation, FRET microscopy has become a routine technology in modern cell biology with its most profound application being the study of

Correspondence to: T.W.J. Gadella. Section of Molecular Cytology and Centre for Advanced Microscopy, Swammerdam Institute for Life Sciences, University of Amsterdam, Science Park 904, 1098 XH Amsterdam, The Netherlands. Tel: +31-20-5256259; fax: +31-20-5257934; e-mail: th.w.j.gadella@uva.nl

cellular signalling phenomena. For more detailed description of Förster's theory, the reader is referred to the original literature and the many excellent reviews offer clear and helpful graphical visualizations (e.g. Vogel *et al.*, 2006; Clegg, 2009).

Intriguingly, the rate of energy transfer cannot be determined directly (because it is a dark process), and hence all FRET measurement techniques are indirect and monitor subtle changes in donor and/or acceptor photophysical properties. In order to appreciate the multitude of FRET microscopy techniques a thorough understanding of the changed properties of donor and acceptor molecules due to FRET is required. After absorption of a photon, the excited fluorescent donor molecule can relax back to the ground state through several different kinetically competing pathways. In case of FRET (donor in presence of acceptor, DA), the donor quantum yield is diminished ($Q_{DA} < Q_D$), resulting in reduced donor fluorescence intensity ($I_{DA} < I_D$). Because FRET offers an additional deactivation pathway from the donor-excited state, the donor fluorescence lifetime (τ_D), which is proportional to the average amount of time the fluorophore spends in the excited state, is shortened ($\tau_{DA} < \tau_D$). Other competing deactivation pathways from the singlet excited state (like intersystem crossing to triplet state and/or subsequent photobleaching) similarly become less probable in case of FRET. Therefore, FRET results in slower photobleaching kinetics (longer donor photobleaching time, $\tau_{bl,D}$) of the donor (i.e. $\tau_{bl,DA} > \tau_{bl,D}$). If the acceptor is a fluorophore, FRET will increase the acceptor fluorescence (I_A), called sensitized emission (SE), because the non-radiative energy transfer excites the acceptor in addition to direct excitation of the acceptor through absorbance of photons (hence $I_{AD} > I_A$). FRET is not dependent on the acceptor quantum yield (Q_A). FRET can also be observed by measuring the anisotropy of the fluorescence emission after exciting the donor with polarized light.

The efficiency of energy transfer (E) can be calculated from altered photophysical parameters, such as intensity, lifetime or bleaching kinetics (see Eq. 3). The subscripts denote donor in the presence (DA) or absence (D) of the acceptor and acceptor in the presence (AD) or absence (A) of donor.

$$E = 1 - \frac{Q_{DA}}{Q_D} = 1 - \frac{I_{DA}}{I_D} = 1 - \frac{\tau_{DA}}{\tau_D} = 1 - \frac{\tau_{bl,D}}{\tau_{bl,DA}} = \frac{\varepsilon_A}{\varepsilon_D}\left(\frac{SE}{I_A}\right) = \frac{\varepsilon_A}{\varepsilon_D}\left(\frac{I_{AD}}{I_A} - 1\right) \quad (3)$$

In this review, we will restrict ourselves to the most established FRET microscopy techniques. However, for an overview of many more (exotic) FRET detection methods, some of which even not tested yet in practice, we refer to Jares-Erijman and Jovin (2003). Detailed considerations on the choice of fluorophores, either organic fluorescent dyes or visible FPs, although crucial for the success of a FRET experiment, are beyond the scope of this review, and can be found elsewhere. However, some specific characteristics of fluorophores will be highlighted if they are essential for execution of a particular technique.

Intensity-based FRET methods

Fluorescence intensity-based FRET methods determine the increased (i.e. sensitized) acceptor fluorescence (as compared to the donor and/or direct excited acceptor signal). For a comprehensive list of filter FRET techniques and original references, see Berney and Danuser (2003). An advantage of intensity-based FRET methods is that they can be implemented on conventional wide-field or confocal fluorescence microscopes. Filter FRET is the method of choice if intramolecular ratiometric FRET sensors are employed and fast dynamic measurements are required. In this case the DA labelling ratio is constant in the image and a simple ratio-image procedure can provide FRET contrast (because probe concentration and spatial variations of excitation light distribution and/or detection efficiency are largely divided out). The common ratio-imaging technique is emission ratioing, where excitation is done at a donor absorption wavelength and the fluorescence is recorded at the D and A emission wavelengths using bandpass filters. On confocal microscopes this is most easily implemented using simultaneous dual channel emission detection. On a wide-field microscope usually a filter wheel is required to change the emission bandpass filter to acquire two consecutive images with a charge-coupled device (CCD) camera, in which case the filter changes can limit the time resolution. The fastest and most sensitive FRET recording system can be achieved by using image splitters with dichroic mirrors projecting the D and A images side by side onto the same CCD. Ratiometric FRET can also be done using single emission wavelength recordings at the acceptor emission wavelength and performing dual excitation at the D and A absorption bands. For wide-field implementation this can be beneficial because image registration problems due to changing emission filters are avoided. The ratio values show FRET contrast and can be calibrated [e.g. by fluorescence lifetime imaging microscopy (FLIM) or acceptor photobleaching, see below] to provide quantitative images of E. However, for most ratiometric experiments such images are not required.

Although advantageous for ratiometric sensors, quantitative intensity-based FRET methods are highly problematic for situations, where D, A and E are distributed differentially in the specimen (as is the case for all intermolecular FRET studies). Here three-filter cube methods are necessary, requiring acquisition of three separate images with the settings allowing the detection of sensitized emission (S, using excitation at the donor absorption wavelength and detection at the acceptor emission wavelength), as well as donor (D, at donor excitation and emission wavelengths) and

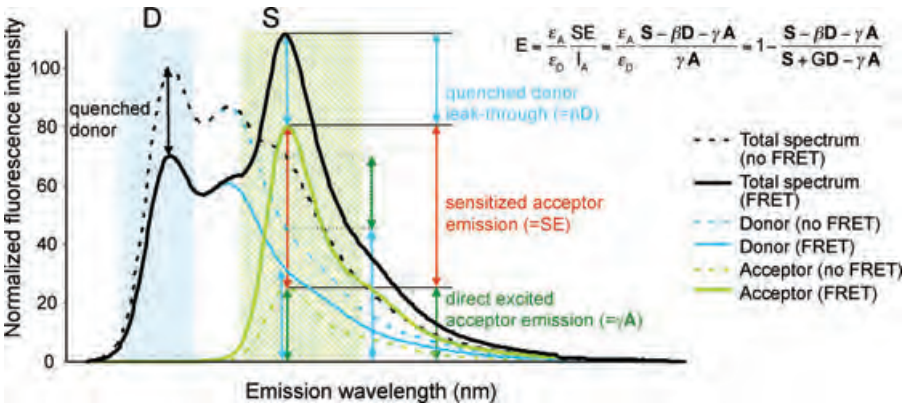

Fig. 1. Intensity-based and spectral FRET. Fluorescence emission spectra of donor (cyan line) and acceptor (green line) in absence (dashed line) and presence (solid line) of FRET are shown. Note the quenched donor and sensitized acceptor emission as a result of energy transfer. For intensity-based FRET small spectral regions (blue and green shaded areas) are selected for detection (e.g. by using bandpass emission filters). In the absence of FRET, the detected intensity in the sensitized emission image (S) contains direct acceptor excitation and donor emission contribution (bleed-through) (green and blue dashed arrows, respectively). In case of FRET, the S image contains direct acceptor excitation, donor bleed-through and sensitized emission (green, blue and red solid arrows, respectively). Here the donor emission filter to acquire the D image was chosen to avoid acceptor emission bleed-through. The calculation of net sensitized emission and E requires careful calibration with reference samples and determination of several correction factors (β, γ and G in the formula, see Jalink & van Rheenen, 2009).

acceptor (A, at acceptor excitation and emission wavelengths) images (Gordon *et al.*, 1998). In theory, from these three images and several calibration images and correction factors, E can be quantified (Jalink & van Rheenen, 2009) (see Fig. 1). In practice the method is beset with a number of problems, difficulties and error propagation in calculations. First, the S image, besides sensitized emission, contains inadvertent direct excitation of acceptor molecules. Second, the S image contains bleed-through of donor emission into the acceptor filter (see Fig. 1). Third, acceptor fluorescence (including sensitized emission) can leak into the D image, which can be avoided by choosing a restrictive donor emission filter. To calculate correction factors to cope with these problems and to obtain the fully corrected FRET image, a total of nine images are required. The accuracy of the FRET estimation will therefore be highly dependent on the reliability of the correction factors (please note that the correction factors are derived from measuring other samples than the FRET sample, and therefore might not yield exactly correct values, even if performed under exactly the same acquisition conditions). Detrimental for accurate calculation is the presence of different background intensities in the sample and calibration samples due to autofluorescence, scattered excitation light as well as possible inner filtering (absorption of excitation light or reabsorption of emission by highly concentrated absorbing molecules). Moreover, the method is very sensitive to slight photobleaching, image artefacts caused by the instrumental drift, excitation intensity fluctuations (both spatial and temporal), registration problems due to changing of filters, and dichroic beam splitters, dye photochromicity and chromatic aberrations (Jalink & van Rheenen, 2009). Also detector gain and laser intensities (in case of confocal filter FRET) need to be constant for the acquisition of all nine images, and each experiment needs its own calibration, precluding easy day-to-day comparisons. In practice, because of the large amounts of corrections required, obtaining quantitative results with filter FRET methods is very complicated, and requires a thorough knowledge of the setup being used and excellent microscopy and image processing skills from the researcher. For a full description of many challenges present in filter FRET techniques and considerations of its quantitative possibilities (aiming also at the unification of the correction factors nomenclature) the reader is referred to Jalink and van Rheenen (2009). Although quantitative filter-FRET menus and wizards are advertised by confocal microscope manufacturers, and may seem simple as a push-button computer application, we strongly suggest trying more robust techniques (like acceptor bleaching or FLIM, see below) unless acquisition speed and low fluorescent signals become a limitation, and the aforementioned issues can be addressed.

Spectral FRET

FRET can also be calculated from spectral images (spectral FRET) in which each pixel encodes the composite spectrum from all different fluorescent species present at the corresponding location in the specimen. The spectra from the different fluorescent species are extracted with linear unmixing algorithms and used for the calculation of E (Zimmerman *et al.*, 2002; Thaler *et al.*, 2005). Spectral FRET microscopy requires the availability of specialized instrumentation, but in return offers several advantages over three-filter cube FRET method: (1) the possibility to use D and A fluorophores with highly overlapping emission spectra

(generally characterized by higher R_0 values and hence enhanced FRET); (2) background fluorescence including autofluorescence can be attributed to distinct spectral components and adequately corrected for by unmixing and (3) the entire emission spectrum is collected whereas in filter FRET methods large portions of the emission are discarded by selective bandpass filters (see Fig. 1). However, because some spectral detectors display relatively low quantum efficiencies (especially in confocal imaging), and emission photons are inherently distributed into several parallel detector channels to acquire the spectrum, the method requires relatively long integration times and/or high fluorescence levels in the specimen. Quantitative spectral FRET with linear unmixing requires careful acquisition of reference spectra under the same excitation conditions as the FRET sample (needs frequent calibration), and similar restrictions apply as compared to filter FRET. Spectral FRET is sensitive to photobleaching, photochromicity (see below) and possible inner filtering.

Intensity-based and spectral FRET methods require relatively photostable donor and acceptor molecules, and both techniques benefit from acceptors with high quantum yield, which increases sensitized emission, but has no effect on E. Furthermore, to perform meaningful FRET quantification, the donor and acceptor signals should be within the same order of magnitude, especially for unmixing in spectral FRET.

Acceptor depletion FRET methods

Acceptor depletion methods aim at quantifying the reduced donor quantum yield or intensity due to FRET. In practice, the donor emission (usually in terms of intensity or spectrum but also τ_D can be determined) is measured before (providing I_{DA}) and after (providing I_D) selective photodestruction of the acceptor. The relative increase in donor emission – or lifetime – after complete acceptor photobleaching is proportional to E (see Fig. 1) (Bastiaens *et al.*, 1996; Bastiaens & Jovin, 1998). The advantages of acceptor depletion methods are: the ease of implementation and compatibility with standard (confocal) microscopes; the ease of FRET estimation and insensitivity to inner filtering artefacts. In addition, the method, unlike FLIM, is very effective when (part of) the donor molecules display very high transfer efficiencies causing their 'disappearance'. After acceptor depletion these molecules contribute most to the detected FRET signal. However, this technique can be relatively slow and therefore is most often applied to fixed samples. In addition, it is inherently destructive precluding dynamic measurements, and it can induce severe phototoxic effects when applied to live samples. Fast photobleaching requires a relatively low photostable acceptor and a strong and selective excitation source that does not affect donor photostability. Inadvertent bleaching of the donor during the acquisition of I_{DA} and I_D images, results in erroneous (under-)estimation of E. Moreover, measurements are affected by scattering, autofluorescence and by movement in the sample between the acquisition of the pre- and post-bleach images. The quantification of E using acceptor photobleaching strictly relies on complete photobleaching of the acceptor (Berney & Danuser, 2003). However, continuous monitoring of donor and acceptor intensities during acceptor photobleaching and subsequent curve fitting of donor and acceptor bleaching kinetics eliminates the need of performing additional correction measurements. This technique improves the determination of FRET efficiency and allows measurements with partially bleached acceptors (van Munster *et al.*, 2005). For acceptor depletion methods it is assumed that photobleaching of the acceptor also destroys its absorption. Some acceptor fluorophores however can be converted to (reversible) absorbing dark states with low quantum yield. In this case acceptor fluorescence is lost (temporarily), but FRET remains, leading to an underestimation of E. Photochromic acceptor behaviour can also be used for FRET microscopy if the acceptor absorption can be switched (cycled) repeatedly between FRET competent 'on' and FRET incompetent 'off' states using specific excitation wavelengths (photochromic FRET, pcFRET). In the past a few organic probes have been used as reversible switching FRET acceptors (Jares-Erijman *et al.*, 1997). The recent development of a reversible photoswitchable red fluorescent protein rsTagRFP enabled excellent intra- and intermolecular pcFRET using YFP as donor (Subach *et al.*, 2010) and holds great prospects for dynamic pcFRET microscopy of live cells in the future.

Donor photobleaching FRET method

Another technique employing photodestruction is based on altered donor photobleaching kinetics in the presence of FRET (photobleaching FRET, pbFRET; Jovin & Arndt-Jovin, 1989). pbFRET can be applied if photodestruction of the donor fluorophore involves and depends on the population of the donor singlet excited state. In this case the reduced donor fluorescence lifetime due to FRET decreases the probability/rate of donor bleaching. In practice, the technique requires recording of the donor fluorescence intensity as a function of time, and the kinetics of donor bleaching is compared in presence and absence of FRET (Young *et al.*, 1994). Because bleaching occurs generally in the seconds to minutes range, the kinetic measurements can be performed using conventional fluorescence microscopes. Another advantage of the method is that high excitation power and long integration times can be used which gives rise to high signal to noise data. Disadvantages of this technique are the requirement of fixed samples, the need for a photostable acceptor and the influence of factors other than FRET influencing the photobleaching rate like presence of oxygen, radical scavengers and (spatial dependent) excitation light intensity in the sample (e.g. introduced by inner filtering). Even if all these can be controlled photobleaching can be a

rather complex process and the accuracy of FRET estimation relies on the correctly fitted decay of donor intensity. Final caveats of methods employing photobleaching strategies are the induction of photodamage and/or photochromicity, and their inherent destructiveness, which is not compatible with dynamic (live cell) FRET measurements.

FLIM–FRET method

FLIM is a technique used to resolve the spatial distribution of nanosecond (ns) excited state lifetimes within microscopic images (Gadella & Jovin, 1995; van Munster & Gadella, 2005). The two most common implementations are the frequency- and time-domain FLIM. Measurements in the time-domain employ ultra short excitation pulses and recording of the (ns) time-resolved donor fluorescence emission decay from which the donor fluorescence lifetime (τ_D) can be determined. In the frequency domain, (sinusoidally) intensity-modulated excitation light and a gain-modulated detector are used, and τ is derived from the phase shift and demodulation of the fluorescence emission as compared to the excitation light. Because of the frequency-domain technique is most easily implemented on wide-field microscopes (using a gain-modulated intensified-CCD detector) and the time-domain technique is usually implemented on a confocal scanning microscope (using time-correlated single photon counting), they are often described separately. However, both methods can be implemented on either confocal scanning or wide-field microscopes and the wide-field FLIM implementations are compatible with Nipkow disc multi-beam techniques.

Although FLIM–FRET requires specialized instrumentation, the independence of τ from fluorescence intensity makes the technique very robust because variations in excitation intensity, inner filtering, moderate donor photobleaching and detector sensitivity do not influence τ. Furthermore, by contrast to the bleaching methods, the method is non-destructive, not particularly phototoxic and hence can be applied to living cells and used for monitoring dynamic FRET changes. Factors possibly affecting the measurements are scattered excitation light and autofluorescence. Although the latter is a general problem for any form of quantitative fluorescence microscopy, the former problem can be reduced by usage of a proper emission filter or accounted for by FLIM analysis because scattering is an ultrafast process ($\tau = 0$). A disadvantage of FLIM analysis is that it requires the detection of relatively large numbers of photons in order to get accurate results, especially for (time-correlated single photon counting) confocal imaging. This can result in long acquisition times (generally >30 s/frame). Wide-field FLIM, despite its usage of low quantum yield (gated or frequency modulated) intensified detectors, is usually one to two orders of magnitude faster than confocal FLIM because all time-resolved measurements in the image are done in parallel: even video-rate FLIM systems have been described. So depending on the type of instrumentation FRET–FLIM can be compatible with monitoring dynamic processes.

There are two concerns related to the process of photodestruction for FLIM measurements. First, (partial) acceptor bleaching leaves the donor unquenched, leading to underestimation of E. Second, photoconversion of the donor fluorophore can alter its fluorescent lifetime. Therefore the ideal FRET pair for FLIM consists of two relatively photostable fluorophores with well-separated emission spectra (because FLIM requires the donor-only part of the spectrum). For FRET–FLIM one has to rule out the possibility of lifetime changes due to altered pH, ion concentration or viscosity in the sample. Small organic fluorophores are especially affected whereas most recent monomeric FPs are far less sensitive to such artefacts. Furthermore, donor fluorophores with long lifetimes, increasing the dynamic range of the lifetime measurement, and monoexponential decay, for easier fitting and quantification, are preferred (Goedhart *et al.*, 2010). Assumptions involved in curve fitting, such as the appropriateness of specific decay models for a particular sample, or even the specific method used for fitting must be considered to attain reasonable results. Although multispecies fitting procedures in FLIM such as global analysis (Verveer & Bastiaens, 2002) or phasor/polar plot analysis (Clayton *et al.*, 2004) can be complicated, they enable the identification of fractions of molecules involved in FRET, which is impossible for methods like filter FRET, spectral FRET, pbFRET, pcFRET or acceptor bleaching.

Anisotropy FRET method

Another powerful and still underappreciated parameter reporting on energy transfer is the anisotropy of the fluorescence emission. Upon excitation of the sample with polarized light, only molecules that, by chance, have their excitation dipole moment oriented favourably (i.e. parallel) to the excitation light polarization direction are excited (a process called photoselection). If rotational movement of the molecule within its fluorescence lifetime is limited or negligible (as is the case for visible FPs due to their size), the emitted light will also be polarized, the extent of which depends on the angle between excitation and emission dipole moments. In case of FRET to a fluorescent acceptor, the ensuing sensitized emission is partially depolarized because it results from acceptor molecules whose emission dipoles can be differently orientated with respect to the excitation polarization direction (see Fig. 2). Both steady-state emission anisotropy and (life)time-resolved anisotropy decay measurements are possible. In practice, the sample is excited using linearly polarized light and the fluorescence intensity is measured in both parallel and perpendicular polarization directions (Clayton *et al.*, 2002). Anisotropy measurements can be performed using scanning or wide-field microscopes. Complicating

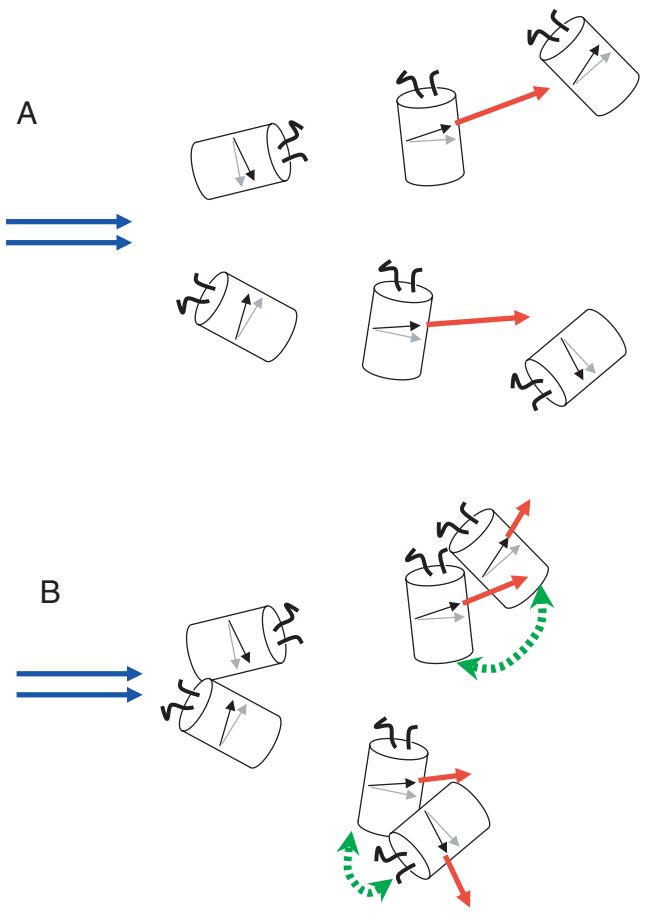

Fig. 2. Homo-FRET by fluorescence anisotropy measurement. A population of randomly oriented FPs is excited with linearly polarized light (the polarization direction is indicated by the leftmost blue arrows). In situation A, no FRET occurs because of extended distance between the FPs (here, photoselection only excites two molecules). Due to a small intrinsic angle between excitation (grey) and emission (black) dipole moments, the total resulting fluorescence emission (red arrows) will have nearly the same polarization direction as the excitation light. In case of homo-FRET (in situation B, note the close proximity of FPs), the resulting fluorescence emission consists of remaining highly polarized emission from the initial photoselected FPs and a much less polarized sensitized emission from their interacting partner FPs. This mixed polarization results in reduction of the detected anisotropy. Note that FRET (green arrow) can be bidirectional and that the total emission (summed lengths of the red arrows) is identical for situation A and B, i.e. no overall quenching or fluorescence lifetime reduction will occur.

instrumental factors are (de)polarizing effects of filters, mirrors and lenses (especially lenses with high numerical aperture), leading to a G factor (= relative detection efficiency of parallel and perpendicular directions) substantially deviating from 1. As a result, microscopy-based anisotropy measurements are restricted to lenses with numerical aperture ≤ 1, usually limiting the possible magnification for the measurement. Furthermore, contrast techniques such as phase contrast and Nomarski differential image contrast that utilize polarization and interference to enhance contrast, perturb with the anisotropy measurement. Hence, the microscopy setup should be free of these functional elements in order to ensure correct anisotropy calculations. Besides these hardware considerations, the anisotropy measurement is sensitive to background autofluorescence and scattered excitation light. In hetero-FRET applications (different spectral properties of D and A), both direct excitation of the acceptor and bleed-through of the donor emission will introduce highly polarized components. Hence, three-filter cube-like corrections are required for isolation of the partially depolarized sensitized emission in hetero-FRET anisotropy.

Importantly, anisotropy measurement holds a unique advantage over all other FRET methods in that it is the only technique that can detect homo-FRET: the energy migration between spectrally identical fluorophores (see Fig. 2). A requirement for homo-FRET (also called energy migration) is a fluorophore with a small Stokes shift and hence overlapping excitation and emission spectra. Homo-FRET is particularly useful for the investigation of oligomerization (Varma & Mayor, 1998). Homo-FRET (employing 1 type of fluorophore) provides a higher sensitivity than hetero-FRET (employing two different types of fluorophores) for studying homo-oligomerization. In hetero FLIM–FRET pairing of two acceptor-tagged molecules will not be detected and worse, pairing of two donor-tagged molecules will dilute the FRET signal from donor-acceptor paired molecules. Other advantages of homo-FRET are that it relieves the researcher from dual labelling, from controlling relative expression levels of differently labelled but otherwise identical proteins and from using narrow emission bandpass filters, because the entire donor spectrum can be used.

Choosing the best FRET microscopy method

Considering the many different methods and principles for detecting FRET in a microscope, choosing the best microscopy technique for a FRET measurement can be a daunting task. There is no overall best method, because each has its own pros and cons. Furthermore, the choice will be determined by the microscopy instrumentation available, including (excitation/emission) filters and excitation options (laser lines), the specimen and probes used. To assist the interested reader in selecting the best FRET microscopy technique we included Fig. 3 in which answering a few questions will guide you to the most straightforward and applicable techniques. The figure is presented without pretensions: by no means other choices, solutions or new options considering new hardware developments are excluded, it should be regarded as a well-meant advice after 20 years of FRET experimentation in practice.

Some general considerations to keep in mind are: regard the use of a simple technique in case only a qualitative answer is needed (a FRET change over time) or in case

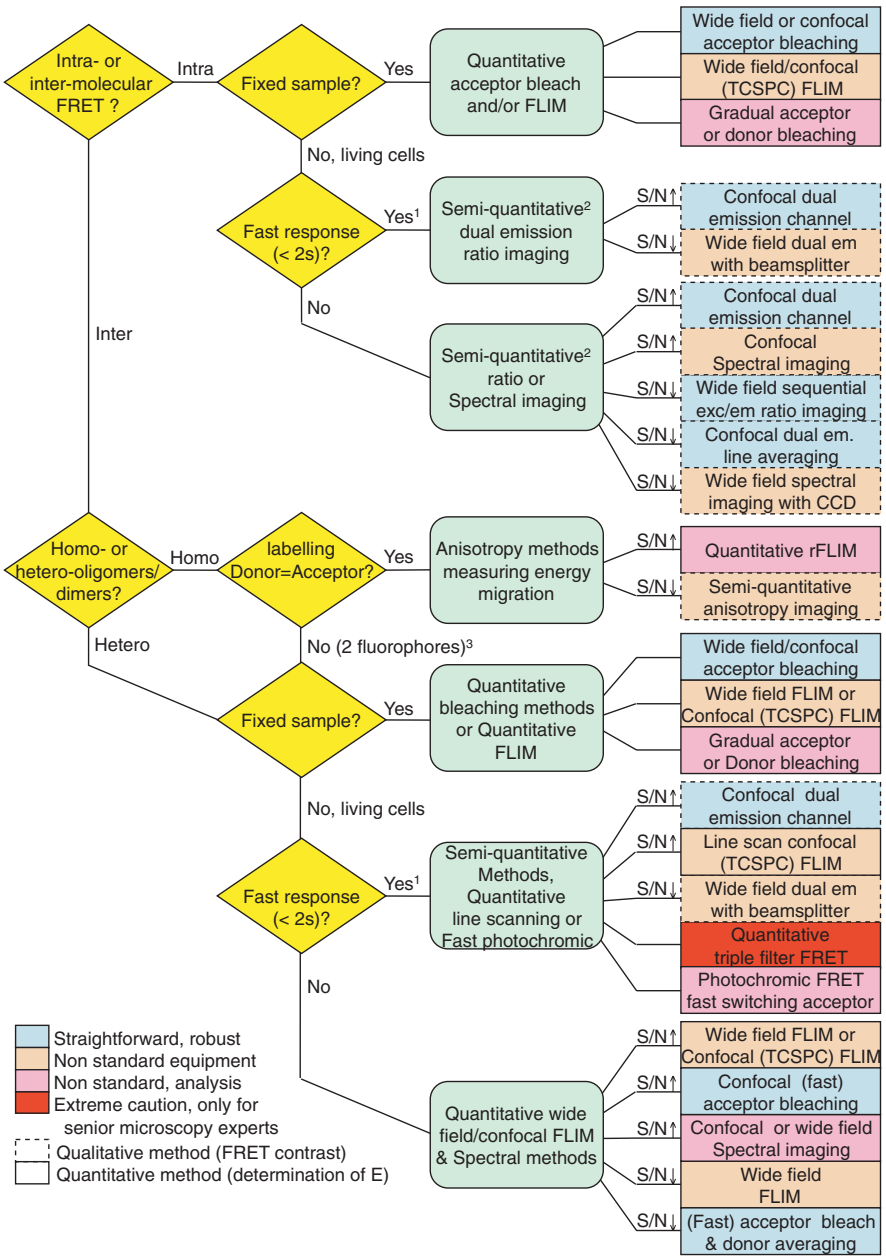

Fig. 3. FRET-microscopy method selector. [1]Or slow response with fast moving cells or subcellular structures. [2]Can be made quantitative after calibration using ratiometric constructs with known E. [3]In this case donor-only and acceptor-only labelled oligomers will not contribute to the FRET signal. S/N↑ means the method of choice in case of high fluorescence levels and S/N↓means the method of choice in case of low fluorescence levels (noisy images).

where a ratiometric intramolecular FRET sensor (with fixed donor to acceptor labelling ratio) is used. Another advice is to pay particular attention to setting up the proper set of controls – also perform measurements of non-labelled, donor-only, acceptor-only and dual-labelled non-FRET and FRET samples, even if they do not seem necessary (like acceptor bleaching of a donor-only labelled specimen). Such controls will report on autofluorescence, scattering, bleed-through, photochromicity, registration problems, etc. Upon awareness of these problems, measures can be taken to reduce or eradicate them by changing the experimental conditions, like filters, laser intensity, fixation method, medium, immersion oil, etc. Finally, if possible, try to confirm results with two different techniques, i.e. one based on donor quenching and one on sensitized emission. In case of intermolecular FRET, methods monitoring only the donor (like acceptor bleaching and FLIM) are less prone to artefacts because acquisition with only one excitation wavelength circumvents registration problems, chromatic aberrations and allows usage of so-called dirty acceptors (e.g. labelled antibodies recognizing multiple

epitopes) or even dark non-fluorescing acceptors. On the other hand, methods monitoring both donor and acceptor populations provide an invaluable control for the behaviour of both interacting species. This can be of great importance in a situation where the distribution of molecules changes during the measurement.

Acknowledgements

This work was supported by the EC Nodperception TMR network MRTN-CT-2006–035546. We thank Kevin C. Crosby, Joachim Goedhart and Mark A. Hink for proofreading of the manuscript.

References

Bastiaens, P.I.H. & Jovin, T.M. (1998) Fluorescence resonance energy transfer microscopy. *Cell Biology: A Laboratory Handbook*, vol. **3** (ed. by J.E. Celis), pp. 136–146. Academic Press, New York.

Bastiaens, P.I.H., Majoul, I.V., Verveer, P.J., Söling, H.-D. & Jovin, T.M. (1996) Imaging the intracellular trafficking and state of the AB 5 quaternary structure of cholera toxin. *EMBO J.* **15**, 4246–4253.

Berney, C. & Danuser, G. (2003) FRET or no FRET: a quantitative comparison. *Biophys. J.* **84**, 3992–4010.

Clayton, H.A., Hanley, Q.S., Arndt-Jovin, D.J., Subramanian, V. & Jovin, T.M. (2002) Dynamic fluorescence anisotropy imaging microscopy in the frequency domain (rFLIM). *Biophys. J.* **83**, 1631–1649.

Clayton, A.H.A., Hanley, Q.S. & Verveer, P.J. (2004) Graphical representation and multicomponent analysis of single-frequency fluorescence lifetime imaging microscopy data. *J. Microsc.* **213**, 1–5.

Clegg, R.M. (2009) Förster resonance energy transfer – FRET: what is it, why do it, and how it's done. *FRET and FLIM Techniques* (ed. by T.W.J. Gadella). Series: *Laboratory Techniques in Biochemistry and Molecular Biology*, vol. **33** (series ed. S. Pillai & P. C. van der Vliet), pp. 1–57. Elsevier, Amsterdam.

Gadella Jr., T.W.J. & Jovin, T.M. (1995) Oligomerization of epidermal growth factor receptors on A431 cells studied by time-resolved fluorescence imaging microscopy. A stereochemical model for tyrosine kinase receptor activation. *J. Cell Biol.* **129**, 1543–1558.

Goedhart, J., van Weeren, L., Hink, M.A., Vischer, N.O., Jalink, K. & Gadella Jr., T.W.J. (2010) Bright cyan fluorescent protein variants identified by fluorescence lifetime screening. *Nat. Methods* **7**, 137–139.

Gordon, G.W., Berry, G., Liang, X.H., Levine, B. & Herman, B. (1998) Quantitative fluorescence resonance energy transfer measurements using fluorescence microscopy. *Biophys. J.* **74**, 2702–2713.

Jalink, K. & van Rheenen, J. (2009) Filter FRET: quantitative imaging of sensitized emission. *FRET and FLIM Techniques* (ed. by T.W.J. Gadella). Series: *Laboratory Techniques in Biochemistry and Molecular Biology*, vol. **33** (series ed. S. Pillai & P. C. van der Vliet), pp. 289–349. Elsevier, Amsterdam.

Jares-Erijman, E.A. & Jovin, T.M. (2003) FRET imaging. *Nature Biotech.* **21**, 1387–1395.

Jares-Erijman, E.A., Song, L. & Jovin, T.M. (1997) Photochromism-FRET (phFRET): modulation of fluorescence resonance energy transfer by a photochromic acceptor. *Mol.Cryst. Liq. Cryst.* **298**, 151–159.

Jovin, T.M. & Arndt-Jovin, D.J. (1989) FRET microscopy: digital imaging of fluorescence resonance energy transfer. Application in cell biology. *Cell Structure and Function by Microspectrofluorimetry* (ed. by E. Kohen, J.S. Ploem & J.G. Hirschberg), pp. 99–117. Academic Press, Orlando.

Subach, F.V., Zhang, L., Gadella, T.W.J., Gurskaya, N.G., Lukyanov, K.A. & Verkhusha, V.V. (2010) Red fluorescent protein with reversibly photoswitchable absorbance for photochromic FRET. *Chem. Biol.*, **17**, 745–755.

Thaler, C., Koushik, S.V., Blank, P.S. & Vogel, S.S. (2005) Quantitative multiphoton spectral imaging and its use for measuring resonance energy transfer. *Biophys. J.* **89**, 2736–2749.

van Munster, E.B. & Gadella, T.W.J. (2005) Fluorescence lifetime imaging microscopy (FLIM). *Microscopy Techniques* (ed. by J. Rietdorf). Series: *Advances in Biochemical Engineering/Biotechnology*, vol. **95** (series ed. T. Scheper), pp. 143–175. Springer, Heidelberg.

van Munster, E.B., Kremers, G.J., Adjobo-Hermans, M.J.W. & Gadella Jr., T.W.J. (2005) Fluorescence resonance energy transfer (FRET) measurement by gradual acceptor photobleaching. *J Microsc.* **218**, 253–262.

Varma, R. & Mayor, S. (1998) GPI-anchored proteins are organized in submicron domains at the cell surface. *Nature* **394**, 798–801.

Verveer, P.J. & Bastiaens, P.I.H. (2003) Evaluation of global analysis algorithms for single frequency fluorescence lifetime imaging microscopy data. *J. Microsc.* **209**, 1–7.

Vogel, S.S., Thaler, C. & Koushik, S.V. (2006) Fanciful FRET. *Sci. STKE* **331**, DOI:10.1126/stke.3312006re2.

Young, R.M., Arnette, J.K., Roess, D.A. & Barisas, B.G. (1994) Quantitation of fluorescence energy transfer between cell surface proteins via fluorescence donor photobleaching kinetics. *Biophys. J.* **67**, 881–888.

Zimmermann, T., Rietdorf, J., Girod, A., Georget, V. & Pepperkok, R. (2002) Spectral imaging and linear un-mixing enables improved FRET efficiency with a novel GFP2-YFP FRET pair. *FEBS Lett.* **531**, 245–249.

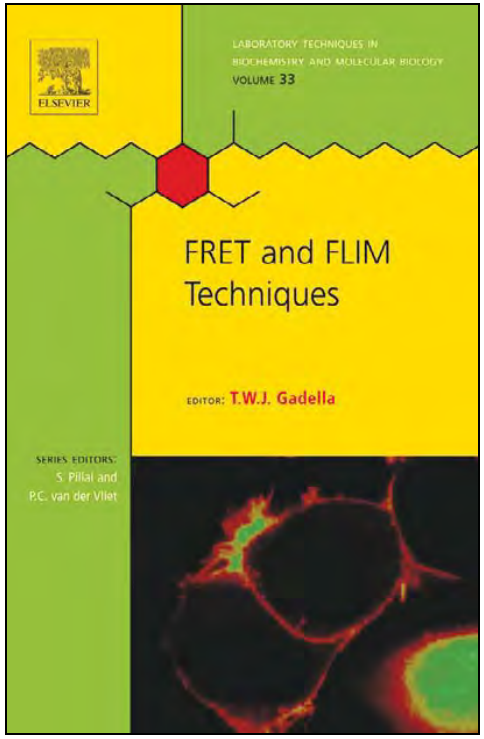

From: Peter J. Verveer and Quentin S. Hanley, Frequency domain FLIM theory, instrumentation, and data analysis.
In T. W. J. Gadella, editor, Laboratory Techniques in Biochemistry and Molecular Biology, Vol 33, Burlington: Academic Press, 2009, pp.59-94.
ISBN: 978-0-08-054958-3

Laboratory Techniques in Biochemistry and Molecular Biology, Volume 33
FRET and FLIM Techniques
T. W. J. Gadella (Editor)

CHAPTER 2

Frequency domain FLIM theory, instrumentation, and data analysis

Peter J. Verveer[1] and Quentin S. Hanley[2]

[1]*Department of Systemic Cell Biology, Max Planck Institute of Molecular Physiology, Otto Hahn Straße 11, D-44227 Dortmund, Germany*
[2]*School of Science and Technology, Nottingham Trent University, Nottingham NG11 8NS, UK*

Practical frequency domain fluorescent lifetime imaging microscopy has enjoyed considerable success in the analysis of biological systems. Appreciation of the strength of the method requires an understanding of kinetics, instrumentation, calibration, data processing, and subsequent analysis. This chapter presents an overview of the governing equations of frequency domain lifetime imaging, specifically: apparent lifetimes, fluorophore mixtures, chi-squared minimization, discrete Fourier processing, and treatment of binary mixtures. Emphasis is placed on instrumentation variations, trends in the field, and finishes with methods of interest for the future.

While publications on fluorescence lifetime imaging microscopy (FLIM) have been relatively evenly divided between time and frequency domain methods, a majority of the 10 most highly cited papers using FLIM have taken advantage of the frequency domain method [1, 2–9]. Both techniques have confronted similar challenges as they have developed and, as such, common themes may be found in both approaches to FLIM. One of the most important criteria is to retrieve the maximum information out of a FLIM

DOI: 10.1016/S0075-7535(08)00002-8

measurement in the shortest period of time. There are many reasons for this interest: minimization of motion artifacts, reduction of sample changes during measurement, generation of time series data sets, and photochemical damage to the specimen [9–15].

In the time domain, this has driven investigations of methods for sampling the fluorescence decay with time in a variety of ways—a topic treated elsewhere in this book. Similarly, in the frequency domain, rapid and minimally intrusive measurement involves a set of tradeoffs between lifetime accuracy and speed. Recently, considerable effort has gone into obtaining the most information about a sample from measurements made at a single frequency [16–20]. To better appreciate these developments and the instrumentation that underpins them, this chapter will review the theory of frequency domain measurements, describe instrumentation for making the measurement, look at some of the emerging areas in the technique, and discuss analysis strategies. The analysis of fluorescence resonance energy transfer using FLIM in single cells is demonstrated with an example.

The chapter will present data primarily from wide field frequency domain measurements; however, a wide range of confocal solutions in the frequency domain have been reported, including: point scanning [21], programmable arrays [22], and spinning disks [23]. The principles of frequency domain lifetime imaging in both wide field and confocal measurements are the same, so the treatment is this chapter is general. The implementation of all types is very similar with the exception of the point scanning reference [21], which uses a lock-in technique. Readers interested in the lock-in approach should consult the original report. The goal of this chapter is to present the collection and processing of frequency domain data and briefly describe subsequent processing of single or multiple lifetime images to provide information to users. This last part is particularly important as there are a growing number of FLIM users who have little or no fundamental interest in fluorescence lifetimes. These users are interested in answers to questions such as: "Is my protein phosphorylated?" "Are my proteins interacting?" "Has my receptor dimerized?" "Where and when is my protein activating its

Author's personal copy

partner?" For these users, the fluorescence lifetime is simply a tool to answer a biological question and the goal is to provide these users with answers as unambiguously as possible.

2.1. *Rates, time constants, and lifetimes*

When a molecule absorbs a photon of light, this mediates a process in which an electron is promoted from a ground state to an excited state. The energy difference between the two states is equal to the energy of the photon absorbed. The molecule spends some period of time in the excited state before returning to the ground state. The amount of time that the molecule, on an average, spends in the excited state is called the fluorescence lifetime. The excited state may deactivate through a variety of processes (see also Chapters 1 and 12). If the molecule returns to the ground state with the emission of a photon, the process is said to be radiative. If no light is released, it is said to be nonradiative. Lifetime imaging makes it possible to investigate the rates of molecules returning to the ground state by observing the behavior of emitted light. Measured fluorescence lifetimes change in response to a variety of processes. Chemical changes in the structure of a molecule, such as addition of a proton, can result in a fundamental change in the rate constant of emission. More commonly, measured fluorescence lifetimes change in response to nonradiative processes competing with the radiative rate constant for deactivation of the excited state. The two most important nonradiative processes are dynamic quenching of the fluorophore and fluorescence resonance energy transfer (FRET). Quenching effects assess the degree of accessibility of a fluorophore to a quencher. FRET is an indicator of proximity between a fluorophore and the molecule that accepts the excited state energy.

For a simple fluorophore, the release of light proceeds through a first-order process. By this we mean that the rate of return to the

ground state depends on the number of molecules in the excited state times a rate constant.

$$\frac{dM^*}{dt} = -kM^* \tag{2.1}$$

In this expression, M^* is the number of molecules in the excited state and k is the first-order rate constant. The differential equation has a solution of the form (see also Chapter 1, Section 1.5.2):

$$M(t) = M_0 e^{-kt} \tag{2.2}$$

The fluorescence lifetime, τ, is the reciprocal of the rate constant k and is the parameter of interest for lifetime imaging:

$$\tau = \frac{1}{k} \tag{2.3}$$

An intuitive way to measure the rate constant, k, is to prepare some number of molecules in the excited state, perhaps with a pulse of light, and observe the amount of light given off per unit of time after the pulse. A logarithmic plot of intensity with time will give a straight-line graph with a slope of $-k$. This approach is the basis of time domain measurements.

If, instead of a pulse of light, a light source modulated at a particular frequency or set of frequencies is used to excite the molecules, the result is a frequency domain measurement. Although frequency domain methods for the analysis of fluorescence decays appeared as early as 1927 with the work of Gaviola [24], the modern development of this approach began with the work of Spencer and Weber [25]. The structure of the modulation function with time can provide information from one or many frequencies. Typically, experiments are done by modulating the excitation light source using a sinusoidal function with a single frequency. This results in a modification of Eq. (2.1) to include a driving function that adds a time-dependent increase in the number of excited state molecules [26, 27].

$$\frac{dM^*}{dt} = -kM^* + f(t) \tag{2.4}$$

The term $f(t)$ is the time-dependent driving function provided by the modulated light source. This differential equation may be solved in terms of the measured signal relative to the driving function. Details of the solutions to these types of equations for a variety of systems may be found in the literature (c.f.: [27]). For lifetime imaging, the goal is a set of measurements allowing the recovery of the rate constant or set of constants. For a single k, the lifetime may be computed from the modulation and phase of the driving function and the equivalent values obtained from the sample. The apparent decay rates are computed from m and ϕ:

$$k = \frac{\omega}{\tan\phi} \text{ and } k = \omega\sqrt{\frac{m^2}{1-m^2}} \tag{2.5}$$

With the rate constant in hand, the lifetime can be reported. Rearrangement of these expressions yields the more familiar expression for phase and modulation lifetimes in terms of τ.

$$\tau_\phi = \frac{1}{\omega}\tan\phi \tag{2.6}$$

$$\tau_m = \frac{1}{\omega}\sqrt{\frac{1}{m^2} - 1} \tag{2.7}$$

where ω is the circular frequency of modulation ($= 2\pi \times$ frequency in Hz). These two estimations yield the same value if only a single lifetime is present, that is, if the decay is truly monoexponential. This will be the case if there is a single fluorescent species of fluorophore with a monoexponential decay. In special cases, including energy transfer or excited state reactions, a complex mixture may also cause the two estimators to yield a single value. In most cases of interest, there will be multiple species that possibly have nonexponential decays. In such a case, these single-frequency lifetime estimations are a function of the lifetimes of the various

fluorescent species and their respective amounts. Nevertheless, Eqs. (2.6 and 2.7) are informative, as with an increasing amount of short-lifetime species, these estimations will become lower. For a single species, the lifetimes are reasonably constant with wavelength. However, mixtures of fluorophores will exhibit wavelength-dependent behavior.

Similar expressions can be derived for systems of fluorophores having different rate constants, the details of the mathematics are not important here. A few rules have been derived for mixing of signals from such systems. The modulation and phase for a system of multiple noninteracting fluorophores that are not undergoing excited state reactions can be computed from a sum related to the fractional contribution of the individual fluorophores, the lifetime, and the modulation frequency. The fractional contributions f_i, for the ith fluorophore in a mixture is given by:

$$f_i = \frac{I_{0i}}{\sum_{i=1}^{n} I_{0i}} = \frac{\alpha_i \tau_i}{\sum_{i=1}^{n} \alpha_i \tau_i} \tag{2.8}$$

In this expression, I_{0i} is the fluorescence intensity calculated for the ith fluorophore at a particular wavelength and α_i is the corresponding amplitude of its exponential decay.

For a mixture of n directly excited noninteracting fluorophores, the apparent phase and modulation may be calculated according to Eqs. (2.9–2.11):

$$N = \frac{\sum_{i=1}^{n} \dfrac{\alpha_i \omega \tau_i^2}{1 + \omega^2 \tau_i^2}}{\sum_{i=1}^{n} \alpha_i \tau_i} \tag{2.9a}$$

$$D = \frac{\sum_{i=1}^{n} \dfrac{\alpha_i \tau_i}{1 + \omega^2 \tau_i^2}}{\sum_{i=1}^{n} \alpha_i \tau_i} \tag{2.9b}$$

$$\phi = \tan^{-1}\left(\frac{N}{D}\right) \tag{2.10}$$

$$m = \sqrt{N^2 + D^2} \tag{2.11}$$

Practically speaking, these expressions allow the prediction of the phase and modulation for an arbitrary mixture of noninteracting fluorophores and the respective modulation and phase lifetimes.

It is important to note that if a mixture of fluorophores with different fluorescence lifetimes is analyzed, the lifetime computed from the phase is not equivalent to the lifetime computed from the modulation. As a result, the two lifetimes are often referred to as "apparent" lifetimes and should not be confused with the true lifetime of any particular species in the sample. These equations predict a set of phenomena inherent to the frequency domain measurement.

Consequences of Eqs. (2.9–2.11) are:

1. A mixture of noninteracting fluorophores might be observed by spatially variant FRET in a specimen, which is blurred because of optical resolution issues, will result in different lifetimes being measured for τ_m and τ_f and $\tau_m > \tau_f$. In many instances, a single frequency measurement will be insufficient to determine the number of fluorophores or the number of fluorophore environments in a sample.
2. Equations (9–11) are dependent on three parameters: ω, α_i, and τ_i. All may be exploited in the analysis of mixtures of fluorophores; however, ω is the only one that can be systematically varied without altering the sample.
3. Most reported measurements are a tradeoff between speed of image collection, photobleaching, and operator convenience. The limitations of variously designed instruments are consequences of these defining equations.

In the next section of this chapter, we will review a variety of instrumentation approaches to the FLIM experiment. In particular, we describe conventional systems as well as those designed to observe variation in α, and systems designed for the collection of multifrequency data. In this context, we will also look at data collection strategies and the subsequent first pass analysis of the acquired

images using Fourier transforms or sinusoidal fitting. The two strategies have slightly different needs for data collection. Sinusoidal fitting will be successful for any number of phase steps, the phase steps need not be equally spaced, and the sum of the phase steps can be quite flexible (e.g., π, 2π, 4π, etc.), with no special conditions placed on the subsequent analysis. Discrete Fourier transform (DFT) processing requires equally spaced phase steps. Depending on the implementation, changing the number of steps and the total distance over which those steps are taken may require special processing and programming.

2.2. Instrumentation

The instrumentation for frequency domain fluorescence lifetime imaging consists of a modulatable light source, the microscope and associated optics, and a modulatable detector. Traditionally, the FLIM light source has been a laser modulated with an acousto-optic modulator (AOM) [15, 28, 29], although pulsed laser sources have also been used in frequency domain systems [30]. Recently, LEDs have appeared as an alternative to lasers in frequency domain FLIM [31–34]. There are a variety of advantages of the LED over the laser. The cost of LEDs and repair of LED equipment is substantially less than that of lasers. Various publications have described the use of LEDs and advances in LED sources have produced devices with high output across wide ranges of the UV–vis spectrum. Integrated LED systems are available commercially for the determination of lifetimes. [35] A disadvantage of LEDs is the more extended nature of the LED as a source. This tends to lead to a lower flux reaching the sample. In comparison, traditional systems using AOMs and ion lasers will be more costly. A few noteworthy points about light sources for the frequency domain lifetime measurement:

1. Although LEDs are emerging as a likely dominant light source for FLIM, there are some regions of the spectrum where lasers are still the best choice. Since the technologies are advancing rapidly, before purchasing components for the UV portion of the spectrum, a quick review of the literature should be done.
2. In the UV, standard LEDs are still relatively untested and either the UV lines of the Ar+ ion laser or directly modulatable LED lasers are likely the component of choice at time of writing.
3. Use of a laser that is not directly modulatable will require the use of a suitable modulator. Although a number of technologies are available for FLIM, the only one in widespread use is the AOM. The AOM must be on resonance and finding a suitable frequency is facilitated by access to a high-speed photodetector. AOMs must be temperature controlled or the modulation depth and phase will drift (perhaps rapidly). The modulated signal from an AOM is at twice the driving frequency and is found in the zero-order position of the AOM output. The zero- and higher-order beams exiting the AOM diverge at relatively low angles and require roughly 1–2 meters to separate. As a result, the AOM modulated system is likely to require more space, an optical bench, and occasional beam adjustment.
4. High-power argon ion or similar lasers require cooling, high voltage, and skilled technical assistance. These points should be taken into account when computing the cost of a system.

Over the next 1–5 years, it is likely that nearly all frequency domain FLIM will migrate to LED light sources. Unless a user has a specialty application requiring a traditional high-power laser, the added cost will likely be unjustified. Specialty applications that might justify the laser are very high speed—the best LEDs do not, at present, bring as much light to the object plane of a microscope as a laser—or UV-excitation in the range required to excite the intrinsic fluorescence of proteins or molecules with similar UV-excitation requirements.

2.3. Instrumentation: Frequency domain FLIM

FLIM systems can be purchased as an add-on for a standard fluorescence microscope. Such a system will consist of a CCD camera coupled to a modulatable image intensifier, an LED light source, and driver electronics. This system will modulate the LED and image intensifier while shifting the phase between them as it takes a series of images (Fig. 2.1).

An alternative to purchasing a turnkey system is to construct a similar system from components. CCD cameras are available from a wide range of suppliers. For FLIM applications, the CCD need not have particularly high QE or exceptionally low noise.

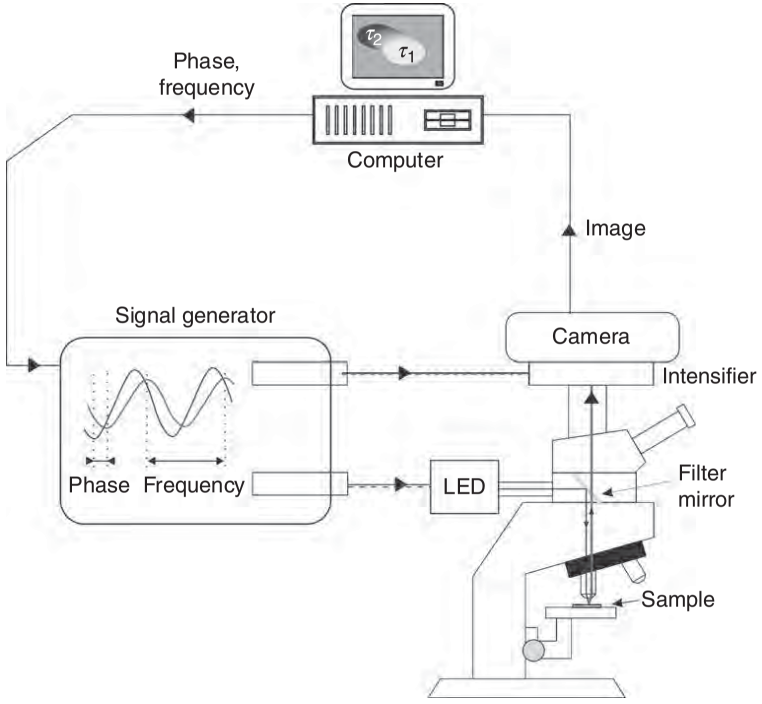

Fig. 2.1. Frequency domain FLIM system.

The image intensifier will define the overall noise characteristics and QE of the system. The CCD camera should be chosen so as to have a good response at the emission wavelengths of the phosphor in the intensifier and, if there is a demand for high frame rates, the CCD should be chosen to support this. Image intensifiers suitable for frequency domain FLIM are available from Hamamatsu, Kentech, and Lambert Instruments. There is wide variation in cost and flexibility between these suppliers. If camera and intensifier are purchased separately, thought should be given to coupling the intensifier to the camera. A pair of standard high-quality camera lenses can be used to accomplish this task. Usually this will require c-mount adapters and a small amount of machining. Some manufacturers provide a unit consisting of a suitable intensifier precoupled to a CCD camera.

The intensifier manufacturers listed above provide electronics to drive the intensifier at the frequency of an input signal. Generation of the input signal requires a precisely controlled frequency synthesizer. Two such synthesizers will be needed for many applications to independently control the intensifier and the light source. For example, when modulating an AOM, the frequency must be half the desired modulation frequency and may need to be at higher power than the signal driving the image intensifier. In the literature, units made by Marconi [3, 22], Hewlett Packard, and Rhode & Schwarz [29] are often cited; however, some of these brands are currently available. The Marconi synthesizers are currently sold by Aeroflex under the IFR Systems name. The test and measurement portion of Hewlett Packard has been reorganized under the Agilent name.

A similar arrangement may be used for driving an AOM to modulate a laser. An AOM and amplifier may be purchased together. The main difference between driving an LED and an AOM from an operational point of view is that the AOM is driven at half the frequency of modulation. As noted earlier, the AOM does not support continuous frequency modulation. A frequency must be chosen close to the desired frequency at the position of a node in the AOM response. Typically, these are regularly spaced about 100–200 kHz apart. This makes finding a convenient node

relatively straightforward; however, the position of the AOM nodes must be found and tabulated and the temperature of operation matched to that of the test conditions.

2.4. Systems for measuring lifetimes at multiple frequencies

Examination of Eqs. (2.9–2.11) suggests that having frequency domain lifetimes measured at a variety of frequencies is desirable, as it will allow a mixture of fluorophores to be determined. With this in mind, two approaches may be taken to obtain multifrequency results. The first of these is simply to make a series of FLIM measurements while stepping through a predetermined set of frequencies. In practice, this is of limited utility for biological systems because of photo-induced damage to the specimen.

A second multiplexed approach is to use a nonsinusoidal excitation source, by employing pulsed light sources or multiple AOMs and a nonsinusoidal modulation of the detector, which leads to the presence of multiple harmonics in the FLIM signal. These harmonics can be separated using Fourier methods, allowing measurement at several frequencies. This approach appears to have been reported only once by Squire *et al.* where he used two AOMs placed in series, and modulated an image intensifier in a block-wave fashion [36]. From a theoretical point of view, there appear to be few disadvantages of the multiplexed approach to obtaining multiple frequencies. The barrier to more widespread application is, at present, the complexity of the hardware.

2.5. Spectral FLIM

Spectral FLIM involves measuring the apparent lifetimes in a preparation at many wavelengths with the assistance of a spectrograph or a series of filters (see also Chapter 4, Figs. 4.7 and 4.8 depicting hyperspectral FLIM in the time domain). The goal of the measurement is similar to that of the multifrequency approach:

determining a mixture of lifetimes with the assistance of Eqs. (2.9–2.11), except exploiting spectral variations in α rather than using variations in frequency. Provided the fluorophores are spectrally dissimilar enough, variation in α is of similar value to variation in frequency. However, variations in α in a sample or a set of dyes tend to be fortuitous rather than systematically adjustable like the modulation frequency.

Instrumentally, spectral FLIM generates a spectrally resolved set of lifetimes by either introducing filters to provide spectral resolution or a spectrograph between the sample and image intensifier. The first such system was created for looking at the long lifetimes of lanthanide dyes [37]. Later, a spectral FLIM system was described for measuring from a two-dimensional (2D) area of a microscope field [38]. Simpler systems have also been described and adopted by others [39]. Introducing the spectrograph is relatively straightforward compared with the difficulty of assembling and programming a FLIM system and may be completed at reasonable cost (Fig. 2.2).

There are a number of practical issues associated with introduction of a spectrograph. A spectrograph disperses the light from a single point into a spectrum, which is measured as several points. As a result, the total light in the spectrum will be equal to the light from a single point in a standard FLIM image. The more spectral elements the system has, the less signal will be observed in each of

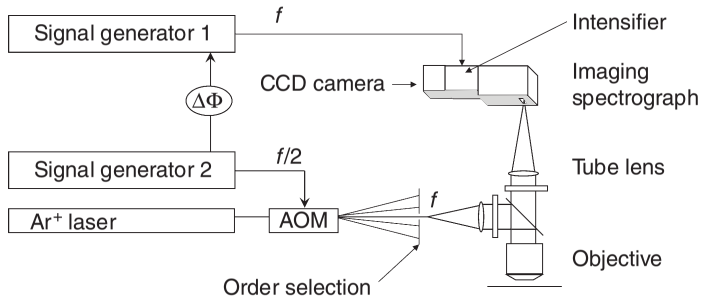

Fig. 2.2. Imaging Spectroscopic FLIM system.

them. As a result, users should plan on taking longer to acquire data, should be realistic about the number of spectral segments they wish to collect, and should bin the camera in the spectral direction. The only alternative to longer exposures and binning is to increase the slit width of the spectrograph. Increasing the slit width is best avoided, since microscope optics can produce features smaller than the slit width if it is increased too much. Often this will not be a problem; however, it can result in small shifts in the position of spectral features in the resulting images. To avoid this, a slit width should be selected that samples the image plane of the microscope well. A slit around 10 μm will work well for many cases.

2.6. Data acquisition strategies

A serious practical limitation on lifetime measurements of all types is photodestruction of the sample. Photodamage can take many forms. The primary fluorophore of interest may simply bleach making the sample unusable. This is perhaps the least worrying because it is readily apparent. Other mechanisms of light-induced change may be more subtle. An acceptor may bleach, leaving the donor apparently unaffected but the measurement altered. Fluorescent proteins have been shown to undergo photoconversion between different forms with different lifetimes. This may be sufficient to alter a result. Most of the time this photon-induced change is undesirable.

A variety of strategies to mitigate sample photodamage have been described. The most widely used is a procedure in which the data is collected twice while reversing the direction of the phase steps. This approach works for minimal photobleaching. Photobleaching is a kinetic process similar to the first-order kinetics discussed earlier in the chapter and exhibits an exponential decrease with time. Over a short time period, the exponential decay because of photobleaching may be treated as approximately linear. By summing up the two measurements at a particular phase shift in the acquisition sequence, approximately linear photobleaching and related processes can be corrected.

The disadvantage of this procedure is that it doubles the amount of time required to acquire a data set, doubles the size of the data set, and exposes the sample to twice as much excitation light. More recently, an approach has been described in which phase step acquisition is randomized so that there is no trend in photobleaching or related effects in the analysis [29]. This approach is relatively new, is reported to work very well, and should see more widespread use in the future.

2.7. Calibration and measurement validation

Frequency domain requires careful calibration and spending time to test and validate the results is worth the effort. Users should be aware that an error in the standard lifetime, using the standard lifetime, or transferring a calibration inappropriately does not propagate linearly to the resulting measured lifetimes. Frequency domain measurements are relative measurements insofar as the lifetime of the sample is made relative to the lifetime of a reference standard of known lifetime. Three methods have been described for calibrating the measurement. Each one seeks to determine the modulation depth and the zero-phase position of the excitation light source. The phase of a sample is the difference between the raw measured phase of the sample and the zero-phase position of the light source standard. Similarly, the corrected modulation depth of the sample is the raw measured value divided by the modulation depth of the excitation light. All three of these methods attempt to determine the modulation and zero-phase position of the light source by using a sample of known "lifetime."

2.8. Calibration by comparison with a scattering solution

In this case, the excitation and emission filters and dichroic mirror used with the sample are removed and replaced with a beam splitter [3, 36]. A scattering solution is placed on the microscope and a

measurement series is collected. Scattering of light is a fast process and as such the "lifetime" of the scattering solution is assumed to be 0 ns. The computed phase and modulation depths obtained are therefore equivalent to the position of zero phase and modulation depth of the light source. This method has the advantage of providing a stable reference value and the scattering solution will mimic fluorescence better than a reflecting surface.

This procedure should be used cautiously as image intensifiers can be damaged by too much light. When the standard microscope filters are replaced by the beam splitter, a neutral density filter should be inserted to protect the intensifier.

2.9. Calibration by use of reflecting surfaces

This approach works similar to the scattering solution. The filters are replaced with a beam splitter and a mirrored surface is placed in the position of the sample [36, 40]. Similar to the scattering solutions, the "lifetime" of the reflection process is assumed to be 0 ns. The remaining aspects of the approach are the same as for the scatterer.

There is a variation on this approach in which a specialized filter cube is constructed consisting of a true mirror rotated 90 ° from the way a dichroic mirror is typically installed such that the incident beam is directed to the camera without passing through the objective [41]. This gives a reference phase for a path length that does not include the trip through the objective to the sample and back. The phase delays and demodulation factors for this additional distance are calibrated independently for each objective. Reflecting surfaces are advantageous because they are readily available, provide a robust mimic of a very short lifetime, and will be stable over time.

Both versions of this procedure should be done with care to avoid damaging the image intensifier.

2.10. Calibration by use of fluorophores of known lifetime

This procedure involves selecting a fluorophore of known lifetime and placing it in the microscope and measuring the phase and modulation depth [11]. Rearranging Eqs. (2.5 and 2.6) allows the expected phase and modulation to be predicted. These may then be used to compute the position of zero phase and the modulation depth of the light source. An advantage of the method is that it may be done under conditions exactly matching those of a sample.

2.11. Comparison of calibration methods

All three methods work and have yielded good results when done properly, but none is ideal. Deciding which is best for a particular purpose will depend mostly on personal preference and the traditions of the group doing the measurement. There are a few points to note in each case, which are worth keeping in mind.

1. When implementing methods based on reflection and scattering from the object plane, reflecting surfaces inside the microscope must be kept to a minimum. Phase rings inside an objective can cause spurious reflections, which may cause small changes in phase and modulation depth. Some objectives have polished metal surfaces, which can generate a signal at the intensifier, which interferes with the signal from the object plane.
2. The calibration should be done for the specific objective in use. Some objectives have been shown to be interchangeable with minimal effect on the modulation depth and phase; however, this is not easily predicted in advance and should never be assumed to be negligible.
3. Introduction of metalized neutral density filters in FLIM systems should be done cautiously as artifacts have been observed due to single or multiple reflections between pairs of ND filters.

4. When using fluorophores of known lifetime, it is important to validate the lifetime used. Fluorescence lifetimes can be sensitive to concentration, temperature, pH, and other environmental variables. Fluorophores from different suppliers can have variable purity. As a result, one should not assume that a value reported in the literature will be exactly transferable to other labs and conditions. Users of the method should be particularly careful to use low concentrations of fluorophore ($<10\ \mu$M) to avoid a variety of processes which can perturb lifetimes in solution. There are a limited number of well characterized fluorophores. If one is not available for a particular wavelength this will require a change of filters leaving the method with nothing to recommend it over reflection and scatter.
5. The reflection calibration method with the specialized filter block has the advantage that it does not require the sample to be moved to recalibrate. As a result it might be particularly useful for long time scale time series data.
6. Most of the calibration methods described in the literature have been on systems using laser excitation and AOM modulation. There is much reason to believe that directly modulated LEDs are more stable; however, the base of experience with LEDs is currently less.
7. On the RF time scale, the transit times of electrons in long coaxial cables and the time of flight of photons in optical paths as short as a few centimeters are significant. These effects become more pronounced as the modulation frequency increases. Even simple changes made to a system will affect the resulting measurements.

2.12. Validation after calibration

Once familiar with methods for calibrating the FLIM system, it is worthwhile to verify the range over which a given FLIM system performs well. This is particularly useful for persons new to the method to

build confidence and an intuition for conditions likely to cause problems. One approach to doing this is with a set of quenched solutions. The use of Rhodamine 6G solutions quenched with variable amounts of iodide has been well investigated, both in cuvettes and in imaging arrangements [11, 42]. Detailed approaches to this may be found in the literature and it has been used successfully in a number of labs.

2.13. First pass analysis—data to modulation depth and phase shift

To analyze frequency domain FLIM data, first the phase shift and demodulation of the fluorescence light with respect to the excitation light are estimated. In the case of single frequency data, this reduces the FLIM data to only three parameters: phase shift, demodulation, and total intensity. This step can be done in various ways as described in the following sections. From these parameters, the lifetimes can be estimated either by Eqs. (2.6 and 2.7), or by more elaborate approaches as described below.

2.14. Fourier methods for estimating phase and modulation

When analyzing a data set using Fourier methods to estimate the phase shift and demodulation, a stack of images is transformed along the stack direction using a DFT. When using DFTs, there is some computational advantage of using a radix-2 type Fast Fourier transform (FFT); however, for practical work on the data lengths typical of FLIM, other considerations may outweigh any computational advantage these might have. For example, a user may find that collection of eight images does not give the desired results but not wish to expose the sample to a full 16. Twelve images may be processed instead using a DFT.

When using a DFT, the images in the stack must be collected at equal phase intervals and it is convenient to restrict the full

sampling to multiples of 2π. For proper sampling of the sinusoidally modulated waveform, the highest frequency in the data set must be sampled greater than or equal to twice per period; a condition dictated by the Nyquist limit.

Processing of the output of one of these algorithms allows recovery of phase and modulation depth from the Fourier coefficients. As an example, assume that a series of N images has been collected. Each point in an image can be designated by an indexing system (x, y) where x and y are the pixel positions in the image in the horizontal and vertical directions, respectively. If the data are measured as a function of wavelength, as has been done in some specialized applications, the data may be indexed further to include (x, y, λ). For the transform, the raw data are treated as a function $g(x, y, n)$, where x and y represent the pixel position in the image, and n is the index into the N evenly spaced phase samples. The data are transformed over n to obtain the discrete Fourier coefficients $G(x, y, \omega)$, where ω is the frequency corresponding to particular component of the sinusoidal driving function:

$$G(x, y, \omega) = \sum_{n=0}^{N-1} g(x, y, n) e^{i\omega n/N} \tag{2.12}$$

It should be recognized that the discrete Fourier coefficients $G(x, y, \omega)$ are represented by complex numbers. The real part $\mathrm{Re}(G(x, y, \omega))$ of the complex number represents the amplitude of the cosine part of the sinusoidal function and the imaginary part $\mathrm{Im}(G(x, y, \omega))$ represents the amplitude of the sine wave.

DFT methods are valuable for determining the magnitude and phase of a complex mixture of frequency components simultaneously such as might be encountered in the multiplexed systems for collection of several frequencies. Once the discrete Fourier coefficients have been computed the uncorrected values of m and ϕ may be computed for every pixel in the sample image:

$$m(x,y) = \frac{|\, G(x,y,\omega_0)\,|}{|\, G(x,y,0)\,|} \tag{2.13}$$

$$\phi(x,y) = \tan^{-1}\left[\frac{\mathrm{Im}\Big(G(x,y,\omega_0)\Big)}{\mathrm{Re}\Big(G(x,y,\omega_0)\Big)}\right] \tag{2.14}$$

$\mathrm{Re}(\cdot)$ and $\mathrm{Im}(\cdot)$ refer to the real and imaginary parts of discrete Fourier coefficients $G(x, y, \omega)$. $G(x, y, \omega_0)$ and $G(x, y, 0)$ refer to the Fourier coefficients corresponding to the frequency of excitation and to zero frequency, respectively, and $|G(x,y,\omega)| = \sqrt{\mathrm{Re}\Big(G(x,y,\omega)\Big)^2 + \mathrm{Im}\Big(G(x,y,\omega)\Big)^2}$. A variety of methods for using Fourier methods have been presented in the literature, which are optimized for specific purposes. For the purposes of this chapter, the discussion will be limited to the treatment given. Users desiring assistance with particular methods and optimizations are encouraged to consult the original literature.

2.15. Sine fitting methods for estimating phase and modulation

The Fourier method is not a requirement, and direct sinusoidal fitting procedures are also used to fit the data from a set of images. A number of specialized procedures have been described over the years and it is worth noting that extracting the amplitude and phase may be done as a simple extension to conventional linear regression.

Linear least squares fitting of sine and cosine data may be accomplished using a similar indexing system to those used for the Fourier methods. Suppose that a data set consisting of N images may be indexed as $g(x, y, n)$, where x and y represent the pixel position in the image, and n is the index into the N phase samples. If the frequency of modulation and the sampling is known (as is usually the case) this becomes a standard multilinear regression problem. Of the form:

$$f(x,y,n) = A(x,y)\cos(\omega n) + B(x,y)\sin(\omega n) + C(x,y) \tag{2.15}$$

Presented in this manner, the analysis may proceed similarly to the treatment obtained from the Fourier analysis. C is the zero frequency component of the fit and A and B may be treated as the real and imaginary parts of the complex number.

$$m(x,y) = \frac{\sqrt{A(x,y)^2 + B(x,y)^2}}{C(x,y)} \tag{2.16}$$

$$\phi(x,y) = \tan^{-1}\left[\frac{B(x,y,\lambda)}{A(x,y,\lambda)}\right] \tag{2.17}$$

Sinusoidal fitting is more flexible than Fourier methods, as it does not require evenly spaced phase steps. There is no special convenience associated with sampling of an angle of 2π and estimation of errors in parameters is somewhat more straightforward.

2.16. *Two-component analysis of FLIM data*

With some further assumptions, it is possible to use single frequency FLIM data to fit a two-component model, and calculate the relative concentration of each species, in each pixel [16]. To simplify the analysis, we will assume that in each pixel of the sample we have a mixture of two components with single exponential decay kinetics. We assume that the unknown fluorescence lifetimes, τ_1 and τ_2, are invariant in the sample. In each pixel, the relative concentrations of species may be different and are unknown. We first seek to estimate the two spatially invariant lifetimes, τ_1 and τ_2. We make a transformation of the estimated phase-shifts and demodulations as follows:

$$N_i = m_i \sin(\Delta\phi_i) \tag{2.18a}$$

$$D_i = m_i \cos(\Delta\phi_i) \tag{2.18b}$$

We have added a subscript i, to indicate the number of the pixel that is being considered. From Eq. (2.9) we get:

$$N_i = \frac{f_i \omega\tau_1}{1+\omega^2\tau_1^2} + \frac{(1-f_i)\omega\tau_2}{1+\omega^2\tau_2^2} \tag{2.19a}$$

$$D_i = \frac{f_i}{1+\omega^2\tau_1^2} + \frac{1-f_i}{1+\omega^2\tau_2^2} \tag{2.19b}$$

where f_i is the relative contribution of the first component to the steady-state fluorescence in pixel i. Eliminating f_i from Eq. (2.19), we find a linear relation between N_i and D_i:

$$N_i = u + vD_i \tag{2.20}$$

where

$$u = \frac{1}{\omega(\tau_1+\tau_2)} \tag{2.21a}$$

and

$$v = \frac{\omega^2\tau_1\tau_2 - 1}{\omega(\tau_1+\tau_2)} \tag{2.21a}$$

The only unknowns in these equations are the two fluorescence lifetimes, which considerably reduces the complexity of the problem. Figure 2.3 shows a plot of N versus D for all possible monoexponential decays, and for all possible mixtures of two monoexponential species with lifetimes equal to 2.5 and 1 ns. The half-circle though (0,0) and (0,1) represents the values of N and D that correspond to all possible monoexponential decay kinetics [13, 16, 43]. All the values of N_i and D_i for a mixture of two species lie on a straight line connecting the two points on the half-circle that correspond to the lifetimes of the two species. The offset and the slope of this straight line are given by Eq. (2.21).

Figure 2.3 suggests a simple strategy to recover the fluorescence lifetimes τ_1 and τ_2: Given estimated phase shifts and demodulations,

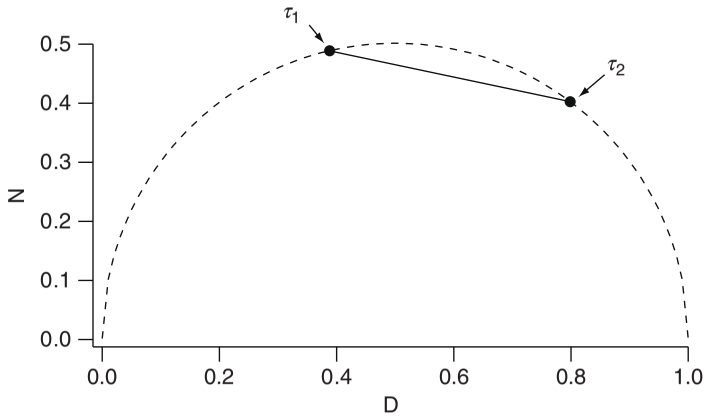

Fig. 2.3. Plot of N versus D for a mixture of two monoexponential species, with fluorescent lifetimes equal to τ_1 and τ_2. Single exponential lifetimes are found on the half-circle passing trough the points (0,0) and (0,1). All possible fluorescent lifetimes of a mixture of free donor and complex are found on the straight line connecting the two points on the half-circle that correspond to the lifetimes of both species.

we calculate the corresponding N_i and D_i values and fit a straight line through them to obtain the slope v and the offset u [16]. The estimated fluorescence lifetimes of the two species are then found by inverting Eq. (2.21):

$$\tau_{1,2} = \frac{1 \pm \sqrt{1 - 4u(u+v)}}{2\omega u} \tag{2.22}$$

Knowing the values of the two lifetimes, the fractions f_i can be recovered in each pixel, by solving Eq. (2.19) in a least squares sense:

$$f_i = \frac{N_i + \omega\tau_1 - \omega D_i \tau_1 - \omega(D_i + \omega N_i \tau_1)\tau_2}{\omega(\tau_1 - \tau_2)} \tag{2.23}$$

The fraction f_i is the fractional contribution of the first species to the total fluorescence in pixel i. The *molar fraction* c_i of the first species

in each pixel can be derived from it by dividing by its quantum yield, and renormalizing, which for a two-component system yields:

$$c_i = \frac{f_i Q_2}{Q_1 + (Q_2 - Q_1) f_i} \tag{2.24}$$

where Q_1 and Q_2 are the quantum yields of the first and the second species, respectively. To apply Eq. (2.24), the quantum yields of the two species, or at least their relative magnitudes, must be known. This is straightforward for the case where the two species are the same donor fluorophore in the presence and absence of fluorescent resonance energy transfer. In this case, $Q_1 \propto \tau_1$ and $Q_2 \propto \tau_2$ were given by the lifetimes in the presence and absence of FRET.

This approach, derived first by Clayton *et al.* [16] and subsequently developed further by others [9, 10, 13, 17–19] is conceptually very simple and gives analytical solutions for the lifetimes of the two species in the mixture and the relative concentrations in each pixel. To be able to fit a straight line, it is crucial that the lifetimes (and thus u and v) are invariant over all pixels, and that there is sufficient variation in f_i (and thereby in N_i and D_i). These requirements of invariance in some parameters and of sufficient variation in at least one other parameter also form the basis of the so-called global analysis methods [44, 45] that were applied earlier to fit FLIM images [20]. In these approaches, nonlinear least squares fitting were used to estimate the lifetimes and molar fractions of each species. The relation of these global analysis methods to the approach described above can be seen, if we introduce error weighting. Both N_i and D_i are distorted by errors, and any proper fit should include those in the estimation of the lifetimes. However, since both N_i and D_i have errors, standard error weighting methods for linear fitting methods cannot be applied. Instead, we directly formulate a least square criterion that we minimize:

$$\chi^2(u,v) = \sum_i \frac{(N_i - u - vD_i)^2}{\sigma_{N,i}^2 + v^2 \sigma_{D,i}^2} \tag{2.25}$$

where $\sigma_{N,i}$ and $\sigma_{D,i}$ are the standard deviations of N_i and D_i, respectively. They can be found by propagation of the errors found for the estimated phase and modulation. This least squares criterion can be minimized to find u and v, which is a nonlinear problem, that is, however, not computationally complicated since only two parameters need to be estimated. In practice, we use a different function that is obtained by substituting Eq. (2.21) into (2.25), and minimize directly for τ_1 and τ_2:

$$\chi^2(\tau_1,\tau_2) = \sum_i \frac{\left((\omega^2\tau_1\tau_2 - 1)D_i - \omega(\tau_1+\tau_2)N_i + 1\right)^2}{\omega^2(\tau_1+\tau_2)^2\sigma_{N,i}^2 + (\omega^2\tau_1\tau_2 - 1)\sigma_{D,i}^2} \qquad (2.26)$$

This function is identical to the one that was derived earlier using global analysis methods [46].

2.17. *Application: Semi-quantitative FRET analysis*

As an example of the usefulness of simple estimations of the lifetime from phase and modulation, we consider the case of donor quenching by FRET. Figure 2.4 shows the results of FLIM measurements on epidermal growth factor receptor tagged with GFP or YFP (EGFR-GFP and EGFR-YFP) [47]. Cells were stimulated with epidermal growth factor for 1 min, and then fixed, permeabilized, and incubated with PY72, a generic antibody against phosphorylation. The antibody was tagged with Cy3 (in the case of EGFR-GFP) or Cy3.5 (in the case of EGFR-YFP). Binding of the antibody to phosphorylated EGFR can be detected specifically by FRET from the donor-tagged receptor to the acceptor-tagged antibody. This can be observed in intact cells by measuring the fluorescence lifetime of the donor. Figure 2.4a shows the result for EGFR-GFP. Both the phase and modulation lifetimes of EGFR-GFP are lower in cells that are incubated with PY72-Cy3, near the plasma membrane of the cells. Similar results are shown for EGFR-YPF in Fig. 2.4b.

To summarize the results of multiple cells, 2D histograms of the phase and modulation lifetimes can be used (Fig. 2.4c). Such 2D

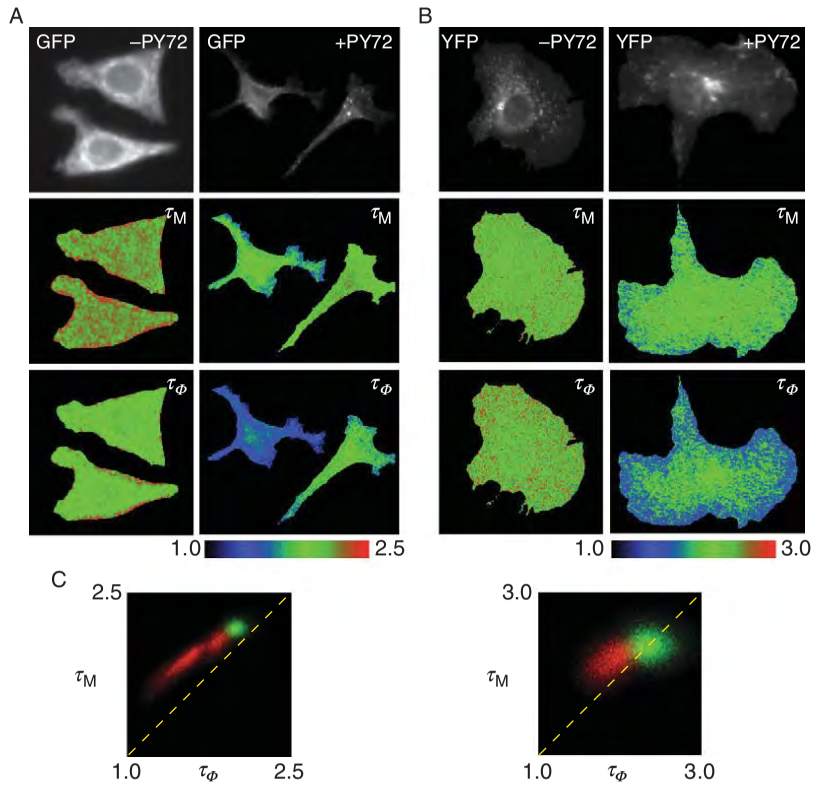

Fig. 2.4. (A) FLIM measurements of EGFR-GFP in the absence (left panels) and presence (right panels) of PY72-Cy3. (B) FLIM measurements of EGFR-YFP in the absence (left panels) and presence (right panels) of PY72-Cy3.5. The scaling of the pseudocolored lifetime images in panel (A) and (B) are indicated with the color bar in ns. Top panels: GFP intensity; Middle: modulation lifetimes; Bottom: phase lifetimes. (C) 2D histograms of τ_ϕ versus τ_M for EGFR-GFP (left) and EGFR-YFP (right). Red: samples incubated with PY72-Cy3 or PY72-Cy3.5, respectively; Green: control samples without PY72.

histograms can be calculated from many images and represent a joint distribution of the phase and modulation lifetimes. These 2D histograms demonstrate some general properties of the GFP and YFP kinetics in the absence and presence of FRET. For EGFR-GFP,

the values of the lifetimes in the absence of acceptor do not center on the diagonal of the histogram. This indicates that EGFR-GFP does not have monoexponential decay kinetics. However, in the case of EGFR-YPF, the values of the phase and modulation lifetimes, in the absence of FRET, are located on the diagonal of the 2D histogram showing that the phase and modulations lifetimes are equal within the precision of the measurement. From this we can conclude that within the precision of the instrument EGFR-YFP has essentially monoexponential decay kinetics. In the presence of acceptor, the 2D histograms show that both phase and modulation lifetimes are lower compared to the control, where the phase lifetime is generally lower than the modulation lifetime. In this particular analysis, it does not matter much that the lifetime of GFP alone is not monoexponential, since the occurrence of FRET can be inferred by this drop of both phase and modulation lifetimes. If, however, a more quantitative analysis of the data is required, this issue becomes more important as we will show below.

2.18. *Application: Quantitative FRET analysis*

We can apply the quantitative analysis of two-component mixtures to the FRET data from Fig. 2.4 [20]. In this case, the two lifetimes are equal to the lifetimes of the donor in the absence and presence of acceptor. Figure 2.5a shows the results for EGFR-GFP. It can be seen that in the control sample, the relative concentrations of the short-lifetime component are not equal to zero, as would be expected for a monoexponential donor in the absence of FRET. Indeed, if we look at the plot of N_i versus D_i for a subset of the pixels of the EGFR-GFP data, we see that the data for the control are not centered on a point on half-circle of monoexponential decays. In contrast, if we look at the results of EGFR-YFP (Fig. 2.5b), we find that the relative concentrations of the short-lifetime component are indeed much closer to zero. Indeed, the plot of N_i versus D_i shows that the data for the control are centered on a

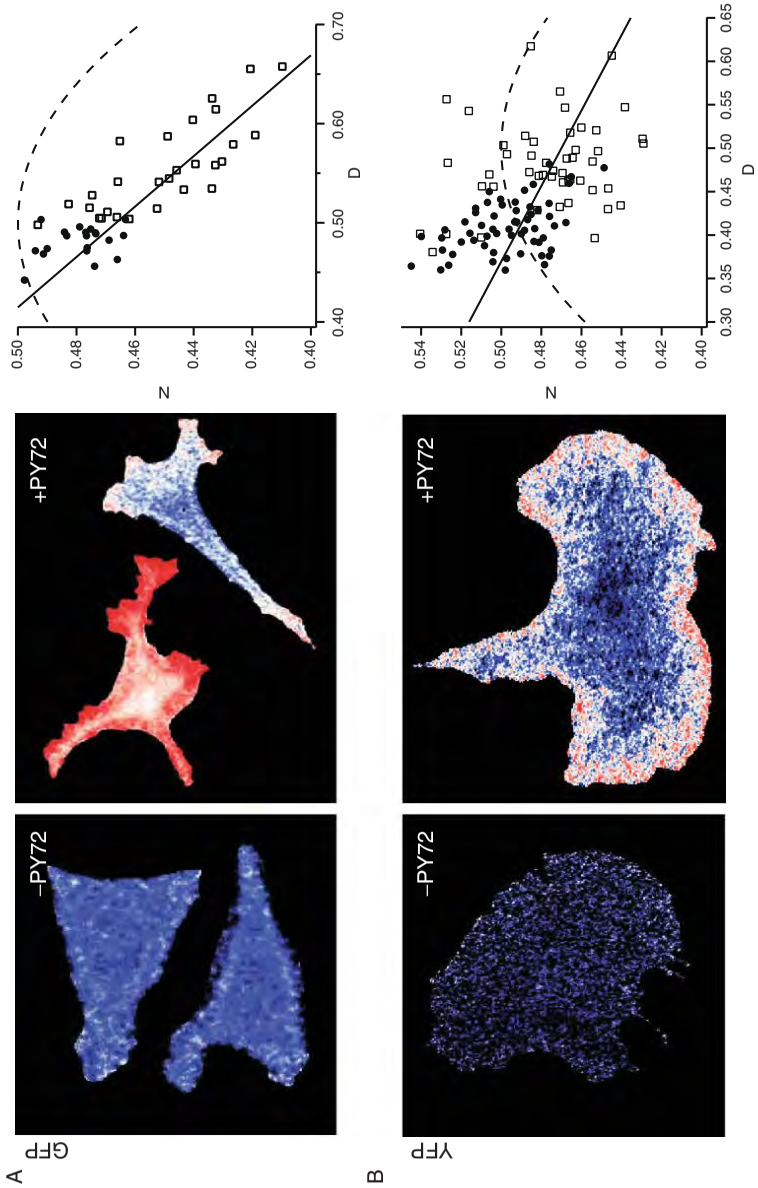

Fig. 2.5. (A) The relative concentrations of the short lifetime component, in samples expressing EGFR-GFP in the absence (left panel) and presence (middle panel) of PY72-Cy3. The calculated lifetimes values of the two species

point on the half-circle of monoexponential decays. This confirms our earlier observations that EGFR-YFP has a monoexponential decay and is therefore more suitable for quantitative analysis than EGFR-GFP. For EGFR-GFP, a systematic error must be expected, but as shown in Fig. 2.5a, the results may still be useful. For biological experiments where a relatively big error is acceptable, this approach can still be used successfully if GFP is used as a donor tag. Indeed GFP tagged donors have been used successfully in several biological applications [8, 48, 49], although YFP tagged donors have proven more reliable for the purpose of quantitative analysis [50]. It should be stressed that not all fluorophores are suitable for this type of analysis, even in approximation. For instance, CFP has a far more pronounced biexponential decay than GFP and is unsuitable for this type of quantitative analysis.

2.19. *Emerging techniques*

A few methods have been described worth following over the next few years as they represent potentially significant advances. Most of these have to do with improvements in the modulated intensifiers or attempts to remove them altogether. At present, none of these have a sufficient base of users to evaluate their significance but all are intriguing concepts in FLIM instrumentation.

2.20. *Segmented intensifiers*

One limitation of frequency domain and other FLIM systems is the time of acquisition. For example, a frequency domain FLIM

were 0.7 and 2.2 ns. (B) The relative concentrations of the short lifetime component, in samples expressing EGFR-YFP in the absence (left panel) and presence (middle panel) of PY72-Cy3.5. The calculated lifetimes values of the two species were 1.0 and 2.4 ns. The right panels show a plot of N_i versus D_i for a subset of the pixels from the samples shown.

system requiring four or eight phase steps to generate a lifetime image typically takes a second or more to collect. During the data acquisition cycle, the specimen can move or bleach. Earlier in the chapter, the notion of randomizing the phase steps was introduced as a method to limit the impact of photobleaching. Given that the images at the different phase steps are not done coincident in time, randomization is perhaps the best approach; however, this only assures that the computed results are not systematically affected.

One approach to rectify this problem has been to divide an intensifier into segments [51]. Each segment is provided with a different time delay. In the current arrangement, the system has been described with four segments and was demonstrated for use with time domain measurements, however, the approach is significant for frequency domain FLIM. To use the segmented intensifier, the image arriving from the microscope is put into a beam splitter dividing the light into four separate images, each of which is directed to a different segment of the intensifier. This allows four time delays to be collected simultaneously. This seems to be a useful technology as the other approaches to FLIM require multiple exposures to be taken at different times.

2.21. *Directly modulated detection schemes*

Another problem of widely used instrumentation for FLIM has been the intensifier. In general, the intensifier is a necessary evil required to make the FLIM experiment work. A typical image intensifier can resolve around 12.5 line pairs/mm (about 80 μm). This is a very significant degradation of image quality relative to direct measurements with a CCD camera. The overall effect can be summarized as a process in which a good image goes in one side of an intensifier and a bad image emerges out the other side. Replacing the modulated image intensifier with an alternative with less degradation (and perhaps lower cost) is worth considerable effort.

Two approaches to intensifier-free detection have been described but neither has been used extensively. In one approach, the CCD is modulated by the application of a high-frequency signal to the device and using it to shuffle charge in and out of light sensitive areas of the CCD [33, 52]. This remains an intriguing approach and as CCDs advance this approach may provide users of frequency domain methods with a viable alternative to the intensifier. As with the segmented image intensifier, the pioneering work on this instrument has been done on time domain lifetime measurements; however, the approach holds promise for the frequency domain as well.

A related technology is a so-called "time-of-flight" imager that was originally designed for 3D-vision applications [40]. This can be thought of as a "lock-in" approach to the measurement of a signal at a particular frequency. The time-of-flight imager has the property that a pixel has two gates, which collect charge generated by light striking the detector depending on the phase of the signal applied to the gate. The two gates operate 180 ° out of phase from each other. The approach has some advantages in that the light effectively rejected by an image intensifier would be collected in the out-of-phase image. Although this technology is at an early stage of development, it holds promise for the future.

Acknowledgments

The authors thank Bert van Geest of Lambert Instruments for Fig. 2.1 and permission to use it in this publication.

References

[1] Bastiaens, P. I. H. and Squire, A. (1999). Fluorescence lifetime imaging microscopy: Spatial resolution of biochemical processes in the cell. Trends Cell Biol. *9*, 48–52.

Author's personal copy

[2] Gadella, T. W. J. and Jovin, T. M. (1995). Oligomerization of epidermal growth-factor receptors on A431 cells studied by time-resolved fluorescence imaging microscopy—a stereochemical model for tyrosine kinase receptor activation. J. Cell Biol. *129*, 1543–58.

[3] Gadella, T. W. J., Jr. Jovin, T. M. and Clegg, R. M. (1993). Fluorescence lifetime imaging microscopy (Flim)—spatial-resolution of microstructures on the nanosecond time-scale. Biophys. Chem. *48*, 221–39.

[4] Lakowicz, J., Szmacinski, H., Nowaczyk, K., Berndt, K. and Johnson, M. (1992). Fluorescence lifetime imaging. Anal. Biochem. *202*, 316–30.

[5] Lakowicz, J. R. and Berndt, K. W. (1991). Lifetime-selective fluorescence imaging using an Rf phase-sensitive camera. Rev. Sci. Instrum. *62*, 1727–34.

[6] Ng, T., Shima, D. S., Hansra, G., Bornancin, F., Prevostel, C., Hanby, A., Harris, W., Barnes, D., Schmidt, S., Mellor, H., Bastiaens, P. I. H. and Parker, P. J. (1999). PKC alpha regulates beta 1 integrin-dependent cell motility through association and control of integrin traffic. EMBO J. *18*, 3909–23.

[7] Ng, T., Squire, A., Hansra, G., Bornancin, F., Prevostel, C., Hanby, A., Harris, W., Barnes, D., Schmidt, S., Mellor, H., Bastiaens, P. I. H. and Parker, P. J. (1999). Imaging protein kinase Cα activation in cells. Science *283*, 2085–9.

[8] Verveer, P. J., Wouters, F. S., Reynolds, A. R. and Bastiaens, P. I. H. (2000). Quantitative imaging of lateral ErbB1 receptor signalling propagation in the plasma membrane. Science *290*, 1567–70.

[9] Colyer, R. A., Lee, C. and Gratton, E. (2008). A novel fluorescence lifetime imaging system that optimizes photon efficiency. Microsc. Res. Tech. *71*, 201–13.

[10] Digman, M. A., Caiolfa, V. R., Zamai, M. and Gratton, E. (2008). The phasor approach to fluorescence lifetime imaging analysis. Biophys. J. *94*, L14–L16.

[11] Hanley, Q. S., Subramaniam, V., Arndt-Jovin, D. J. and Jovin, T. M. (2001). Fluorescence lifetime imaging: Multi-point calibration, minimum resolvable differences, and artifact suppression. Cytometry *43*, 248–60.

[12] Kremers, G. J., Van Munster, E. B., Goedhart, J. and Gadella, T. W. (2008). Quantitative lifetime unmixing of multi-exponentially decaying fluorophores using single-frequency FLIM. Biophys. J. *95*, 378–89.

[13] Redford, G. I. and Clegg, R. M. (2005). Polar plot representation for frequency-domain analysis of fluorescence lifetimes. J. Fluoresc. *15*, 805–15.

[14] Redford, G. I., Majumdar, Z. K., Sutin, J. D. B. and Clegg, R. M. (2005). Properties of microfluidic turbulent mixing revealed by fluorescence lifetime imaging. J. Chem. Phys. *123*, 224504.
[15] Schneider, P. C. and Clegg, R. M. (1997). Rapid acquisition, analysis, and display of fluorescence lifetime-resolved images for real-time applications. Rev. Sci. Instrum. *68*, 4107–19.
[16] Clayton, A. H. A., Hanley, Q. S. and Verveer, P. J. (2004). Graphical representation and multicomponent analysis of single-frequency fluorescence lifetime imaging microscopy data. J. Microsc. *213*, 1–5.
[17] Esposito, A., Gerritsen, H. C. and Wouters, F. S. (2005). Fluorescence lifetime heterogeneity resolution in the frequency domain by lifetime moments analysis. Biophys. J. *89*, 4286–99.
[18] Forde, T. and Hanley, Q. S. (2006). Spectrally resolved frequency domain analysis of multi-fluorophore systems undergoing energy transfer. Appl. Spectrosc. *60*, 1442–52.
[19] Hanley, Q. S. and Clayton, A. H. A. (2005). AB-plot assisted determination of fluorophore mixtures in a fluorescence lifetime microscope using spectra or quenchers. J. Microsc. *218*, 62–7.
[20] Verveer, P. J., Squire, A. and Bastiaens, P. I. H. (2000). Global analysis of fluorescence lifetime imaging microscopy data. Biophys. J. *78*, 2127–37.
[21] Carlsson, K. and Liljeborg, A. (1998). Simultaneous confocal lifetime imaging of multiple fluorophores using the intensity-modulated multiple-wavelength scanning (IMS) technique. J. Microsc. *191*, 119–27.
[22] Hanley, Q. S., Lidke, K. A., Heintzmann, R., Arndt-Jovin, D. J. and Jovin, T. M. (2005). Fluorescence lifetime imaging in an optically sectioning programmable array microscope (PAM). Cytometry A *67A*, 112–8.
[23] van Munster, E. B., Goedhart, J., Kremers, G. J., Manders, E. M. M. and Gadella, T. W. J. (2007). Combination of a spinning disc confocal unit with frequency-domain fluorescence lifetime imaging microscopy. Cytometry A *71A*, 207–14.
[24] Gaviola, E. (1927). Ein fluorometer. Zeitschrift fur Physik *42*, 853–61.
[25] Spencer, R. D. and Weber, G. (1969). Measurement of subnanosecond fluorescence lifetimes with a cross-correlation phase fluorometer. Ann. N. Y. Acad. Sci. *158*, 361–76.
[26] Lakowicz, J. R. (1999). Principles of fluorescence spectroscopy. Kluwer/Plenum,** New York.
[27] Lakowicz, J. R. and Balter, A. (1982). Theory of phase-modulation fluorescence spectroscopy for excited-state processes. Biophys. Chem. *16*, 99–115.
[28] Marriott, G., Clegg, R. M., Arndtjovin, D. J. and Jovin, T. M. (1991). Time resolved imaging microscopy—phosphorescence and delayed fluorescence imaging. Biophys. J. *60*, 1374–87.

Author's personal copy

[29] van Munster, E. B. and Gadella, T. W. J. (2004). Suppression of photobleaching-induced artifacts in frequency-domain FLIM by permutation of the recording order. Cytometry A *58A*, 185–94.
[30] Hanson, K. M., Behne, M. J., Barry, N. P., Mauro, T. M., Gratton, E. and Clegg, R. M. (2002). Two-photon fluorescence lifetime imaging of the skin stratum corneum pH gradient. Biophys. J. *83*, 1682–90.
[31] Dinish, U. S., Fu, C. Y., Chao, Z. X., Seah, L. K., Murukeshan, V. M. and Ng, B. K. (2006). Subnanosecond-resolution phase-resolved fluorescence imaging technique for biomedical applications. Appl. Opt. *45*, 5020–6.
[32] Elder, A. D., Matthews, S. M., Swartling, J., Yunus, K., Frank, J. H., Brennan, C. M., Fisher, A. C. and Kaminski, C. F. (2006). The application of frequency-domain fluorescence lifetime imaging microscopy as a quantitative analytical tool for microfluidic devices. Opt. Express *14*, 5456–67.
[33] Mitchell, A. C., Wall, J. E., Murray, J. G. and Morgan, C. G. (2002). Direct modulation of the effective sensitivity of a CCD detector: A new approach to time-resolved fluorescence imaging. J. Microsc. *206*, 225–32.
[34] Moser, C., Mayr, T. and Klimant, I. (2006). Filter cubes with built-in ultrabright light-emitting diodes as exchangeable excitation light sources in fluorescence microscopy. J. Microsc. *222*, 135–40.
[35] Anonymous. (2003). LIFA system for fluorescence lifetime imaging microscopy (FLIM). J. Fluoresc. *13*, 365–7.
[36] Squire, A., Verveer, P. J. and Bastiaens, P. I. H. (2000). Multiple frequency fluorescence lifetime imaging microscopy. J. Microsc. *197*, 136–49.
[37] Vereb, G., Jares-Erijman, E., Selvin, P. R. and Jovin, T. M. (1998). Temporally and spectrally resolved imaging microscopy of lanthanide chelates. Biophys. J. *74*, 2210–22.
[38] Hanley, Q. S., Arndt-Jovin, D. J. and Jovin, T. M. (2002). Spectrally resolved fluorescence lifetime imaging microscopy. Appl. Spectrosc. *56*, 155–66.
[39] Hanley, Q. S. and Ramkumar, V. (2005). An internal standardization procedure for spectrally resolved fluorescence lifetime imaging. Appl. Spectrosc. *59*, 261–6.
[40] Esposito, A., Oggier, T., Gerritsen, H. C., Lustenberger, F. and Wouters, F. S. (2005). All-solid-state lock-in imaging for wide-field fluorescence lifetime sensing. Opt. Express *13*, 9812–21.
[41] Van Munster, E. B. and Gadella, T. W. J. (2004). phi FLIM: A new method to avoid aliasing in frequency-domain fluorescence lifetime imaging microscopy. J. Microsc. *213*, 29–38.
[42] Harris, J. M. and Lytle, F. E. (1977). Measurement of subnanosecond fluorescence decays by sampled single-photon detection. Rev. Sci. Instrum. *48*, 1469–76.

[43] Jameson, D. M., Gratton, E. and Hall, R. D. (1984). The measurement and analysis of heterogeneous emissions by multifrequency phase and modulation fluorometry. Appl. Spectrosc. Rev. *20*, 55–106.
[44] Beechem, J. M. (1992). Global analysis of biochemical and biophysical data. Methods Enzymol. *210*, 37–54.
[45] Beechem, J. M., Knutson, J. R., Ross, B. A., Turner, B. W. and Brand, L. (1983). Global resolution of heterogeneous decay by phase/modulation fluorometry: Mixtures and proteins. Biochemistry *22*, 6054–8.
[46] Verveer, P. J. and Bastiaens, P. I. H. (2003). Evaluation of global analysis algorithms for single frequency fluorescence lifetime imaging microscopy data. J. Microsc. *209*, 1–7.
[47] Wouters, F. S. and Bastiaens, P. I. H. (1999). Fluorescence lifetime imaging of receptor tyrosine kinase activity in cells. Curr. Biol. *9*, 1127–30.
[48] Ng, T., Parsons, M., Hughes, W. E., Monypenny, J., Zicha, D., Gautreau, A., Arpin, M., Gschmeissner, S., Verveer, P. J. Bastiaens, P. I. H. *et al.* (2001). Ezrin is a downstream effector of trafficking PKC-integrin complexes involved in the control of cell motility. EMBO J. *20*, 2723–41.
[49] Reynolds, A. R., Tischer, C., Verveer, P. J., Rocks, O. and Bastiaens, P. I. H. (2003). EGFR activation coupled to inhibition of tyrosine phosphatases causes lateral signal propagation. Nat. Cell. Biol. *5*, 447–53.
[50] Rocks, O., Peyker, A., Kahms, M., Verveer, P. J., Koerner, C., Lumbierres, M., Kuhlmann, J., Waldmann, H., Wittinghofer, A. and Bastiaens, P. I. H. (2005). An acylation cycle regulates localization and activity of palmitoylated Ras isoforms. Science *307*, 1746–52.
[51] Elson, D. S., Munro, I., Requejo-Isidro, J., McGinty, J., Dunsby, C., Galletly, N., Stamp, G. W., Neil, M. A. A., Lever, M. J. Kellett, P. A. *et al.* (2004). Real-time time-domain fluorescence lifetime imaging including single-shot acquisition with a segmented optical image intensifier. New J. Phys. *6*. 1–13.
[52] Mitchell, A. C., Wall, J. E., Murray, J. G. and Morgan, C. G. (2002). Measurement of nanosecond time-resolved fluorescence with a directly gated interline CCD camera. J. Microsc. *206*, 233–8.

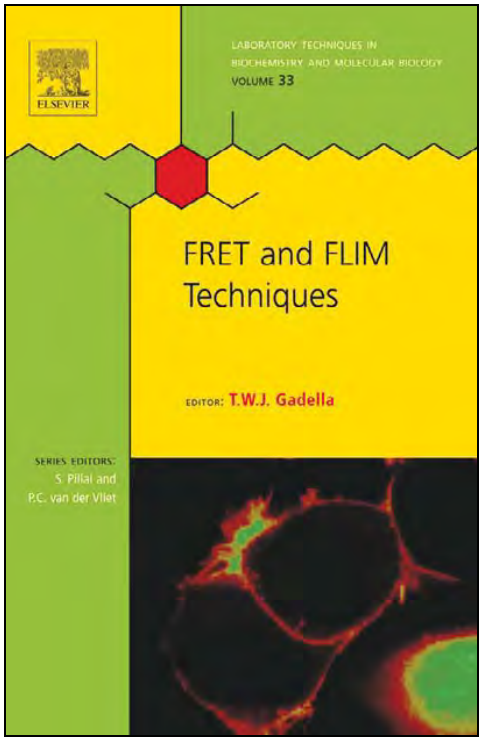

From: H. C. Gerritsen, A. V. Agronskaia, A. N. Bader, and A. Esposito,
Time domain FLIM: Theory, instrumentation, and data analysis.
In T. W. J. Gadella, editor, Laboratory Techniques in Biochemistry and Molecular Biology, Vol 33, Burlington: Academic Press, 2009, pp.95-132.
ISBN: 978-0-08-054958-3

Laboratory Techniques in Biochemistry and Molecular Biology, Volume 33
FRET and FLIM Techniques
T. W. J. Gadella (Editor)

CHAPTER 3

Time domain FLIM: Theory, instrumentation, and data analysis

H. C. Gerritsen,[1] A. V. Agronskaia,[1]
A. N. Bader,[1] and A. Esposito[1,2]

[1]*Molecular Biophysics Group, Debye Institute, Utrecht University, NL 3508 TA, Utrecht, The Netherlands*
[2]*Laser Analytics Group, Department of Chemical Engineering and Biotechnology, University of Cambridge, Cambridge, UK*

The lifetime of the excited state of fluorophores may be altered by physical and biochemical properties of its environment. Fluorescence lifetime imaging microscopy (FLIM) is thus a powerful analytical tool for the quantitative mapping of fluorescent molecules that reports, for instance, on local ion concentration, pH, and viscosity. the fluorescence lifetime of a donor fluorophore, Förster resonance energy transfer can be also imaged by FLIM. This provides a robust method for mapping protein–protein interactions and for probing the complexity of molecular interaction networks.

Quantitative fluorescence imaging techniques and FLIM in particular are becoming increasingly important in biological and biomedical sciences. Knowledge of instrumentation and data analysis is required to avoid misinterpretation of the experimental results and to exploit the wealth of information provided by these techniques.

DOI: 10.1016/S0075-7535(08)00003-X

In this chapter, instrumentation and methods of analysis for FLIM in the time domain will be described. Advantages and limitations of time-correlated single photon counting (TCSPC) and time-gated imaging techniques will be discussed together with general issues on photon efficiency of detection schemes, data analysis, and practical experimental examples.

3.1. Introduction

Because of the underlying photophysics, fluorescence lifetimes are intrinsically short, usually on the order of a few nanoseconds. Detection systems with a high timing resolution are thus required to resolve and quantify the fluorescence decays. Developments in electronics and detector technology have resulted in sophisticated and easy to use equipment with a high time resolution. Fluorescence lifetime spectroscopy has become a popular tool in the past decades, and reliable commercial instrumentation is readily available.

At present, two main streams of techniques exist for the measurement of fluorescence lifetimes, time domain based methods, and frequency domain methods. In the frequency domain, the fluorescence lifetime is derived from the phase shift and demodulation of the fluorescent light with respect to the phase and the modulation depth of a modulated excitation source. Measurements in the time domain are generally performed by recording the fluorescence intensity decay after exciting the specimen with a short excitation pulse.

At the end of the 1980s and early 1990s, first experiments were carried out to combine fluorescence lifetime measurements with imaging using both time domain [1–4] and frequency domain [5–7] based approaches. This chapter will deal exclusively with time domain based fluorescence lifetime imaging methods. For the frequency domain based methods, refer Chapter 2.

Lifetime imaging can be implemented both in wide field and in scanning microscopes such as confocal microscopes and two-photon excitation microscopes. The most common implementations in time-domain fluorescence lifetime imaging microscopy (FLIM) are based on TCSPC [8, 9] and time-gating (TG) [2, 10].

3.2. Lifetime detection methods

3.2.1. Time-correlated single photon counting

In TCSPC, the fluorescent molecules are excited with very short light pulses. Typically picosecond and femtosecond excitation pulses are used, and the time delays between the excitation pulse and the detection of a single-photon is recorded. By repeating this procedure many times, the probability distribution for the emission of a single photon, and thus the fluorescence decay curve, is obtained. TCSPC is characterized by a high overall time resolution of 25–300 ps and a wide dynamic lifetime range. The TCSPC electronics often have a very high timing accuracy (<1–200 ps). In almost all cases, the time resolution with which photons are being detected is limited by the timing jitter of the detector (25–300 ps). At present, plug-in boards for PCs are commercially available that contain all the TCSPC electronics [8].

A schematic diagram of a typical TCSPC setup is shown in Fig. 3.1. The sample is excited by a short excitation pulse usually provided by a pulsed laser. A trigger signal that is synchronized with the excitation light pulse is used to start an accurate timing device such as a time-to-amplitude converter (TAC). The fluorescence emitted by the specimen is then selected by an emission filter and detected by a fast detector (e.g., a photomultiplier tube (PMT) or an avalanche photodiode) that is able to detect single photons (single photon counting (SPC)). The output pulses of the detector are sent through a discriminator and used to stop the TAC.

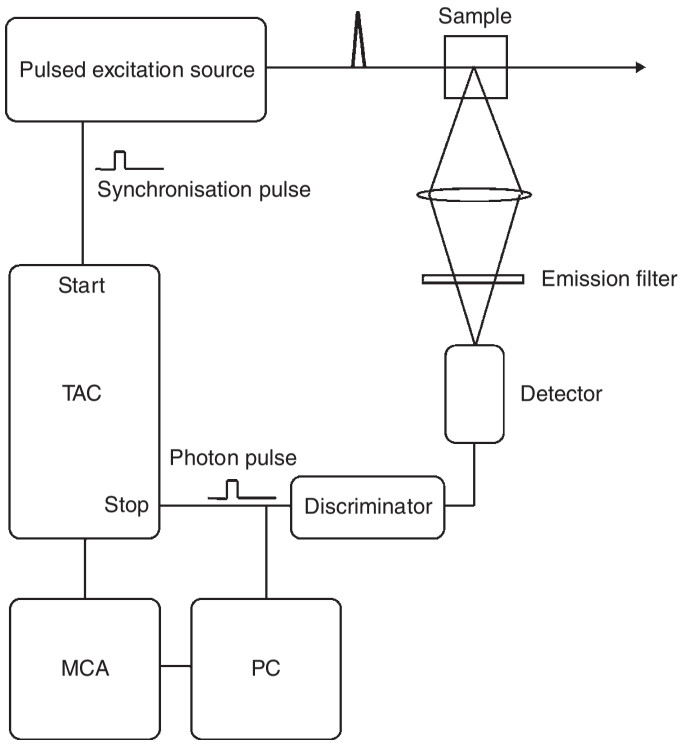

Fig. 3.1. Schematic diagram of a TCSPC setup. Using a fast timing device (e.g., time-to-amplitude-converter) the time is measured between the excitation pulse and the detection of a photon. By repeating this procedure many times a decay curve is measured. TAC: time to amplitude convertor, MCA: multi channel analyzer, PC: personal computer.

The output from the TAC is an analog signal that is proportional to the time difference between the start and stop pulses. The next step consists of digitizing the TAC output and storing the event in a multichannel analyzer (MCA). After repeating this process many times, a histogram of the arrival times of photons is accumulated in the memory of the MCA. In fluorescence lifetime spectroscopy the histogram usually contains 512–2048 channels

and represents the fluorescence decay curve of the specimen (see Fig. 3.2). Note that the recorded decay curve is convoluted with the total timing response of the instrument, the instrument response function (IRF). Nowadays, there are other timing devices used for TCSPC such as time to digital converters (TDCs) [11]. These devices directly convert the timing difference between start and stop signals into a digital word. To this end, a series of solid state delay lines is used and, in practice, TDCs have similar timing accuracies and limitations as TACs.

Importantly, the dead-time of TACs and TDCs is comparatively long, typically 125–350 ns. When a photon arrives within this time interval after the detection of a photon, it will not be observed. Therefore, care must be taken that the count rate of the experiment is sufficiently low to prevent this pulse-pileup. TACs and TDCs usually operate in reversed start–stop geometry. Here, the TAC is started by the fluorescence signal and stopped by the laser trigger.

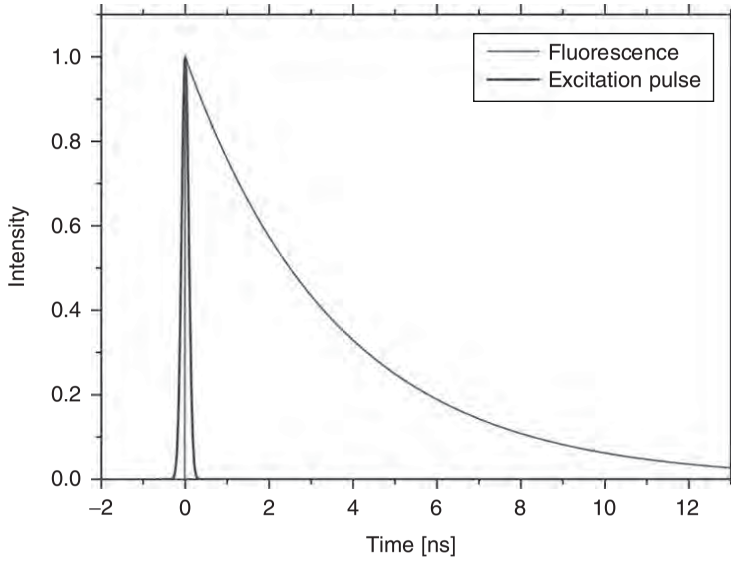

Fig. 3.2. A decay curve of a fluorescent dye and an IRF.

In this way the TAC is only triggered by usable events, and not by laser trigger pulses that do not result in a detected fluorescence photon. This mode of operation suffers less from dead-time effects. If two photons arrive within a period equal to the dead-time of the system, pulse-pileup occurs and the second photon cannot be detected. In the reversed start–stop geometry, pile-up is minimized by reducing the excitation intensity to about 1–5 detected photons per 100 excitation pulses. Furthermore, in spectroscopy applications excitation frequencies not exceeding 10 MHz are used to ensure that the fluorescence decay signal from one excitation pulse is not affected by the tail of the fluorescence decay produced by other excitation pulses. The maximum count rate employed in conventional spectroscopy applications of TCSPC is less than 100 kHz. The time required to access the histogramming memory and to transfer the decay curve from the histogramming memory to the computer system can be substantial in particular for TCSPC electronics designed for spectroscopic application.

In general the decay curves recorded by TCSPC are fitted to a (multi)exponential decay employing an iterative deconvolution technique to account for the time response of the instrument [9]. This requires the recording of the timing response of the system (see Fig. 3.2) and can be done by, for instance, the recording of excitation light from a scattering sample or fluorescence from a fast decaying dye such as Rose Bengal ($\tau \sim$80 ps) [12, 13].

3.2.2. Time gating

In TG methods, the fluorescence emission is detected in two or more time-gates each delayed by a different time relative to the excitation pulse (see Fig. 3.3). In the case of a detection scheme equipped with two time-gates, the ratio of the signals acquired in the two time-gates is a measure of the fluorescence lifetime. For a decay that exhibits only a single exponent, the fluorescence lifetime is given by:

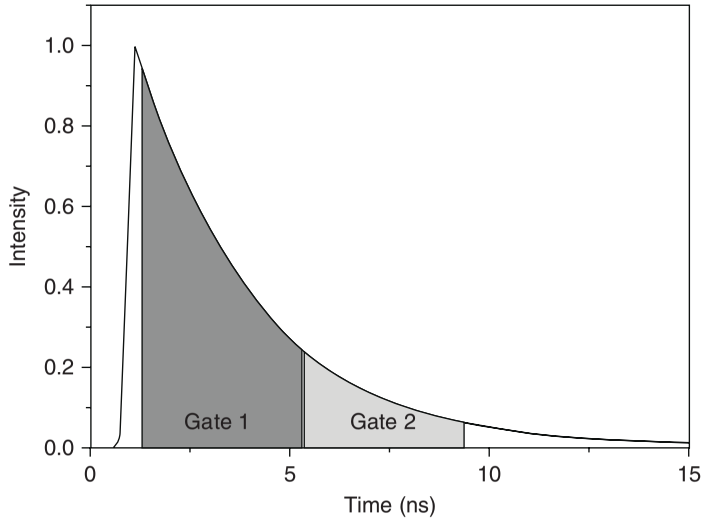

Fig. 3.3. Principle of time gating (TG). After exciting the specimen with a short light pulse, the fluorescence is detected in a number of time gates that open after a specific delay with respect to the excitation pulse.

$$\tau = \Delta T / \ln(I_1/I_2) \tag{3.1}$$

where ΔT is the time-offset between the start of the two time-gates and I_1 and I_2 are the corresponding fluorescence intensities accumulated in the gates. In this "rapid lifetime determination method," the assumption is made that the two time-gates are of equal width [14]. In the case of a multiexponential fluorescence decay (Eq. (3.1)), yields only an "average" fluorescence lifetime. This limitation can be circumvented by increasing the number of time-gates enabling the recording of multiexponential decays (de Grauw and Gerritsen, 2001; [15, 16]. Increasing the number of gates requires more sophisticated data analyses approaches like fitting the decay to (multi)exponential functions.

Practical implementation of TG requires careful synchronization of the opening of the gates with respect to the laser pulses, see

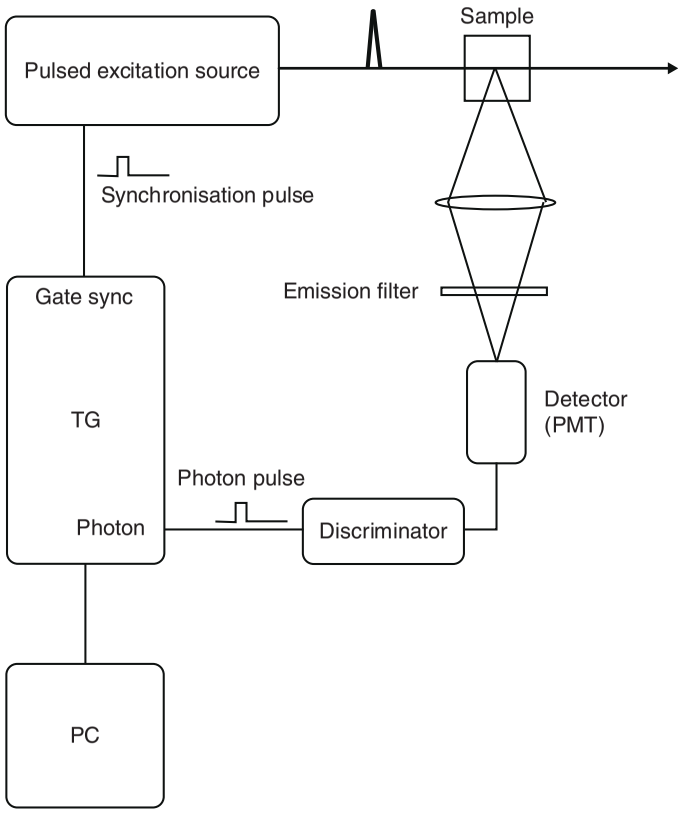

Fig. 3.4. Schematic diagram of a TG setup. The TG electronics need careful synchronization with the excitation pulse. Here, time-gated single photon counting is shown.

Fig. 3.4. In addition, if TG is implemented using SPC, a discriminator is required to separate the photon signal from background noise.

Time-gated detection offers the possibility to suppress background signals correlated with the excitation pulse. Direct and multiple scattered excitation light as well as Raman scattering reaches the detector at $t \approx 0$, and can be effectively suppressed by opening the first gate a few hundred picoseconds after $t = 0$.

This can improve the signal-to-background ratio of the images without a significant loss of signal. Furthermore, TG can be employed to discriminate autofluorescence in biological specimens. Often, autofluorescence has a comparatively short fluorescence lifetime and the signal-to-background ratio of the images can be improved by offsetting the first gate with respect to the excitation pulse [17].

In Fig. 3.5A a comparison between time-gated detection and TCSPC is shown. The time-gated detection system was based on four 2 ns wide gates. The first gate opened about 0.5 ns after the peak of the excitation pulse from a pulsed diode laser. The TCSPC trace was recorded using 1024 channels of 34.5 ps width. The specimen consisted of a piece of fluorescent plastic with a lifetime of about 3.8 ns. In order to compare the results, approximately 1700–1800 counts were recorded in both experiments. The lifetimes obtained with TG and TCSPC amounted to 3.85 ± 0.2 ns and 3.80 ± 0.2 ns respectively, see Fig. 3.5B. Both techniques yield comparable lifetime estimations and statistical errors.

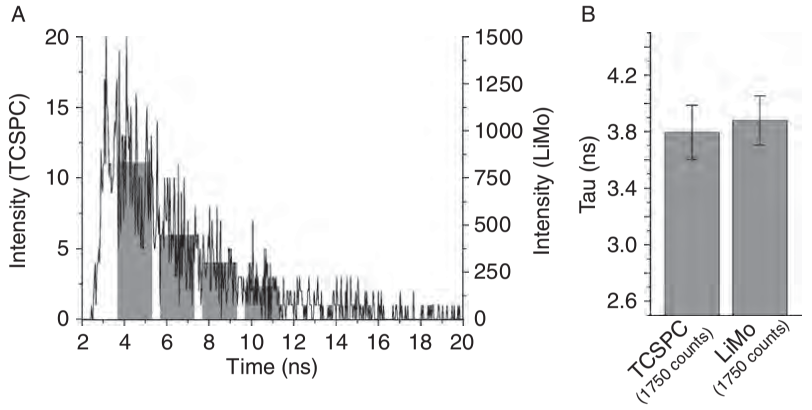

Fig. 3.5. A comparison between TG and TCSPC using the same number of detected photons. (A) The distribution of photons over the time bins. (B) Bar plot of the lifetimes including errors ($n = 4$).

3.3. Point scanning time domain FLIM implementations

Implementation of time domain FLIM methods is comparatively straightforward in laser scanning microscopes (LSMs). Here, point-scanning is used so that single channel lifetime detection suffices. In principle, standard fluorescence lifetime detection equipment developed for spectroscopy can be used in combination with point-scanning systems and a pulsed laser.

3.3.1. Point scanning TCSPC-based FLIM

Conventional TCSPC equipment has been successfully employed in LSM for fluorescence spectroscopy on discrete microscopic volumes [18, 19] and for fluorescence lifetime imaging at a low acquisition speed [1]. The use of conventional TCSPC equipment for imaging results in very long acquisition times, several to many minutes per (time-resolved) image. Importantly, operating the TCSPC detection system at too high detection rates, above 5% of the excitation frequency, results in distortion of the recorded decay curve [20].

At present dedicated TCSPC FLIM boards are commercially available. They are compatible with most LSMS and are easily synchronized with the scanning microscope and pulsed laser. These boards, often plug-in cards for PCs, have a lower dead-time than do the conventional TCSPC electronics intended for use in spectroscopy and the memory bottle neck of the histogramming memory has been removed [21, 22]. Consequently, these dedicated boards provide higher acquisition speeds.

Dedicated TCSPC electronics is used in all practical TCSPC–FLIM implementations [21, 22]. There are several issues that should be noted. First of all, the lifetime acquisition has to be synchronized with the scanning of the confocal or multiphoton microscope. To this end, the pixel clock and often the line and frame synchronization signals of the scanning microscope are used.

After each and every pixel clock pulse, the MCA memory is transferred to buffer memory (either on the TCSPC board or on the PC memory), the MCA memory is reset and accumulation is (re) started. The repetition rate of the laser is typically in the range 20–80 MHz, much higher than common pixel clock rates in lifetime imaging of 10^4–10^5 Hz. Therefore, no synchronization is required between the pulse train coming out of the laser and the pixel clock. The frame synchronization signal can be used to provide an overall start signal for the acquisition and the line synchronization signal can be used to stop acquisition during the retrace of the laser beam.

In TCSPC imaging, the number of time channels is usually restricted to 32–128. In general, a higher number of channels do not provide additional information because only a limited number of detected photons are accumulated per pixel, often several hundred to a few thousand.

3.3.2. Point scanning TG-based FLIM

TG-based FLIM in LSMs is usually implemented using SPC. Here, fast and efficient detection schemes can be employed where the detected photons are counted in the time-gates that are opened sequentially after each and every laser pulse (de Grauw and Gerritsen, 2001; [23]). Similarly to TCSPC, the fluorescence signal from hundreds to thousands of excitation pulses is accumulated at each pixel to obtain sufficient signal level for reliable lifetime analysis. Also TG data acquisition needs to be synchronized with the pixel clock of the scanning microscope. Again, frame and line synchronization signals are used as overall start and line start triggers, respectively.

For the simple TG scheme with only two time-gates, the optimum gate-width amounts to $2.5\,\tau$. Consequently, the total integration time per pulse amounts to $5\,\tau$ and approximately 99% of all photons in the decay are detected. The detected fraction decreases when an offset is applied between the laser pulse and the opening of

the first gate. Such an offset is often used to avoid detection of the signal corresponding with the tail of the excitation pulse.

In time-gated photon counting, comparatively high photon count rates can be employed; count rates as high as 10 MHz are often used. TG has the advantage of virtually no dead-time of the detection electronics (~1 ns), whereas the dead-time of the TCSPC electronics is usually on the order of 125–350 ns. This causes loss of detected photons, and a reduced actual photon economy of TCSPC at high count rates.

3.3.3. Detectors for single photon counting

Detector properties determine to a great extent the performance of TCSPC and TG experiments. In TCSPC the timing resolution of the electronics is in general much better than that of the detector. Often, fast PMTs are used. Here, the timing resolution is limited by the timing jitter in the arrival of electrical pulses at the output of the PMT. This transit time spread (TTS) of fast PMTs is in the order of 25–300 ps, much smaller than the width of the pulses coming out of the PMT, which are usually on the order of <1–3 ns. We note that the standard PMTs used in commercial confocal microscopes are not suitable for the detection of fluorescence lifetimes. These PMTs are selected for sensitivity and not for timing resolution. Often they exhibit a TTS of several nanoseconds, which makes them useless for fluorescence lifetime imaging.

Another important property of PMTs is the pulse height distribution. The amplification of individual photoelectrons by the PMT is a stochastic process that causes variations in the gain of individual photoelectrons. As a result significant jitter in the amplitude of the output pulses is observed, see Fig. 3.6. These pulse height variations can be more than a factor of 10. The lowest pulse heights mainly consist of (thermal) noise, indicated by the dashed line in Fig. 3.6. The pulse height distribution exhibits a peak corresponding to detected photons. The threshold level of the

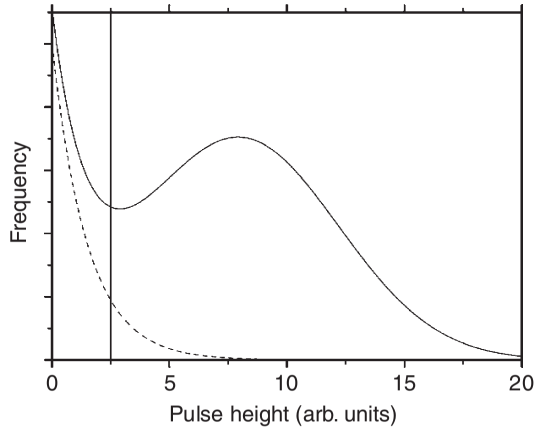

Fig. 3.6. The pulses produced by PMTs show a distribution in pulse heights. The lowest pulses are caused by noise (dashed line) and the higher pulses are due to detected photons. The vertical line indicates the position of the valley in the pulse height distribution. This position would correspond to the optimal setting for the discriminator.

discriminator should be set at the appropriate level to suppress the background signal. Setting the threshold level at the position of the valley between background pulses and the photon pulses is a good compromise between sensitivity and noise suppression (vertical line in Fig. 3.6).

Special "constant fraction" discriminators (CFDs) are being used to realize the highest timing accuracy. This type of discriminator determines the position of the maximum of the pulse coming out of the detector. Conventional discriminators trigger at a constant level of the detector pulses. Because of pulse height variations, constant level triggering results in timing jitter as high as 1–2 ns. In contrast, CFDs yield timing jitter, depending on the type of detector, of 25 to a few hundred ps.

After the detection of a single photon, PMTs need a specific recovery time before they are sensitive again. During this dead-time, no photons can be detected. Because of the stochastic nature

of the fluorescence signals, the dead-time reduces the detection probability when the count rate goes up. The relative detection efficiency for a system with a (overall) dead-time t_d at an incident count rate C_i amounts to:

$$f = 1/(1 + t_d C_i) \tag{3.2}$$

At low count rates $C_i \ll 1/t_d$, the detection sensitivity is not affected by the dead-time ($f = 1$). However, at a count rate of $C_i = 1/t_d$ the detection sensitivity is reduced to 50% of its sensitivity at low count rates, see Fig. 3.7. Typical values for dead-times of PMTs are on the order of 50–100 ns.

Not only PMTs and other detectors such as avalanche photodiodes suffer from dead-time effects also the detection electronics may have significant dead-times. Typical dead-times of TCSPC electronics are in the range 125–350 ns. This may seriously impair the efficiency of detection at high count rates. The dead-time effects of the electronics in time-gated single photon detection are usually negligible.

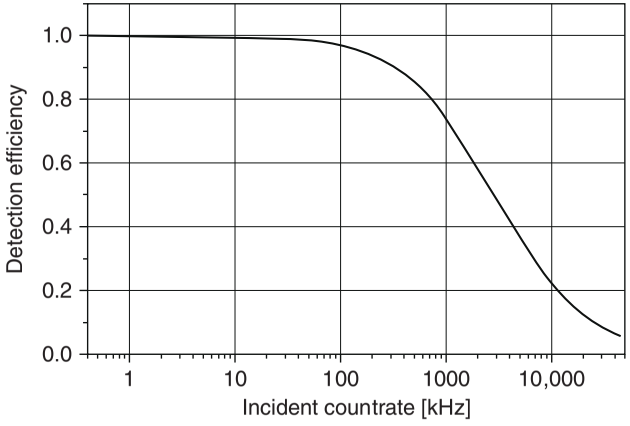

Fig. 3.7. The detection efficiency of a system with a dead-time 350 ns as a function of the incident count rate. At high count rates the detection efficiency reduces due to pileup effects.

Therefore, the throughput of current systems based on time-gated SPC is somewhat higher than in TCSPC-based systems.

Both TCSPC and TG benefit from operation in SPC mode. SPC results in little or no noise and a high photon-economy [10]. Therefore, TCSPC and TG are ideal for high spatial and lifetime resolution imaging [24]. Both techniques offer high image contrast also on dim samples. However, the dead-time of the detectors and the point scanning character limit the throughput of these systems.

Imaging in biology is often affected by other uncertainties than the instrumental sensitivity and precision. Therefore, detectors with very low dead-times, for example PMTs capable of counting at high count rates ($\sim 10^7$ Hz), may be preferred to achieve higher throughputs at the cost of higher timing jitter.

Often, experiments are carried out on specimens that emit only very weak fluorescence. For these cases, the most sensitive detectors should be used, for instance fast avalanche photodiodes or high quantum yield PMTs. These detectors may have somewhat longer dead-times causing longer exposure times but maximal sensitivity.

3.4. *Wide field time-domain FLIM implementations*

In wide field microscopy, spatial information of the entire image is acquired simultaneously thus providing comparatively short acquisition times compared with scanning microscopy implementations. Combining TCSPC with wide field microscopy is not straightforward. However, a four quadrant anode multichannel plate (MCP) has been used for time- and space-correlated SPC experiments [25, 26]. This detector has excellent timing properties that make it very suitable for FLIM. Unfortunately, it can be operated only at low count-rates ($\sim 10^5$–10^6 Hz); therefore, it requires comparatively long acquisition times (minutes).

A more common approach to time domain wide field FLIM is based on a time-gated image intensifier MCP in combination with a CCD camera (see Fig. 3.8). After every excitation pulse the gated

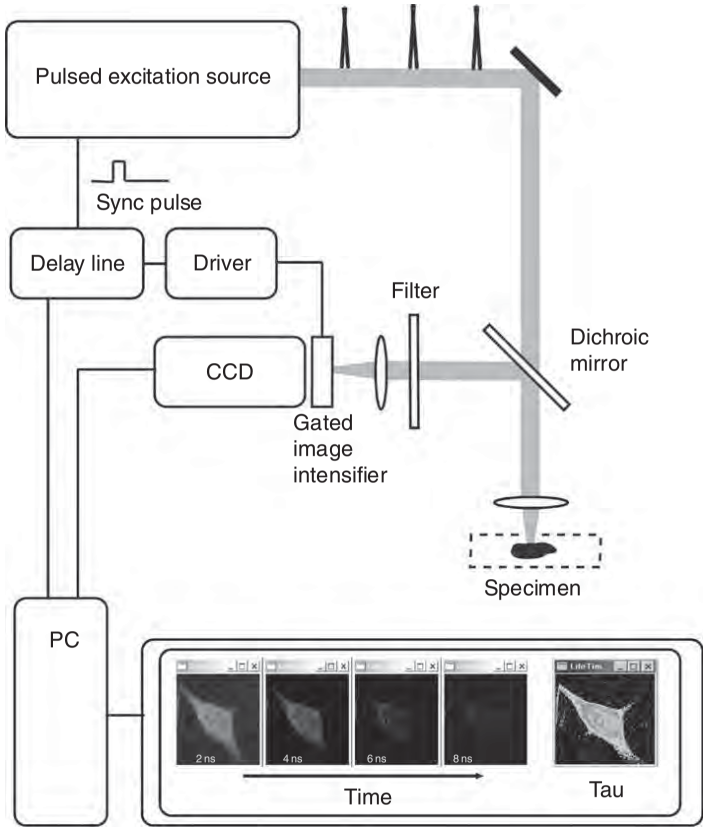

Fig. 3.8. Wide field time-gated FLIM based on a gated image intensifier in combination with a CCD camera.

image intensifier is triggered and its output detected by the CCD camera. After a large number of excitation pulses sufficient signal is detected by the CCD chip and the time-gated image is transferred to the computer. This procedure is repeated for every gate setting. Finally, the lifetime image is calculated from the series of time-gated images. The gate width is determined by the voltage pulse that is applied to the photocathode of the image intensifier. Furthermore, the time offset between the excitation pulse and

the opening of the gate is set by a delay line. Data acquisition and gate settings are controlled by the computer.

In contrast to point scanning implementation of TG discussed earlier, wide field TG is an analog detection technique. The sensitivity of analog detection methods is in general lower than that of SPC-based methods. Both the intensifier and the CCD camera introduce noise that reduces the sensitivity of the system. The image intensifier in particular strongly deteriorates the performance of the system. The quantum efficiency and noise properties of the intensifier determine to a great extend the sensitivity; furthermore, the rise time is a critical parameter for the timing properties of the system.

In most implementations of wide field time-gated detection, multiple images are recorded sequentially at different time offsets with respect to the excitation pulse. At present, only few custom-built systems [27, 28] offer the combined advantage of spatial and TG parallelization. This can be implemented by using image splitters and offers the possibility of high speed lifetime imaging at acquisition speeds of hundreds of hertz without artifacts due to sequential opening of gates. In Fig. 3.9, the principle of such a parallelized approach is shown [27]. The fluorescence image generated by pulsed excitation is split into two images by means of a

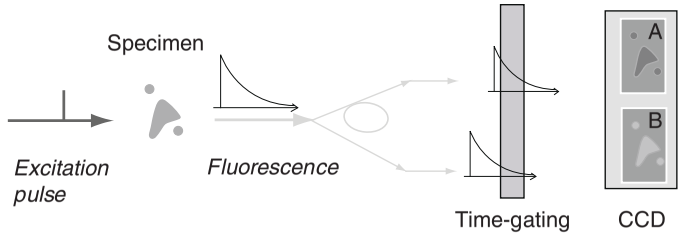

Fig. 3.9. Principle of a wide field FLIM system with simultaneous detection of two time gates. The fluorescence image is split into two images and one of the images is optically delayed with respect to the other. Both images are detected simultaneously with the same time-gated detector.

beam splitter. One of the images is (optically) delayed with respect to the other and both images are projected onto the same gated image intensifier. The gating process results in the simultaneous recording of two time-gated images. The images have the same gate width but a different time offset with respect to the excitation pulse. Based on this approach, fluorescence lifetime images could be recorded at a rate of 100 Hz.

Although new emerging technologies may provide more efficient applications in the future [29, 30], so far in all wide field TG-based FLIM systems, the gating process results in the loss of photons and a consequent reduction of the sensitivity (photon-economy).

In contrast to point scanning TG, wide field TG is comparatively inefficient; only a (small) fraction of the decay is recorded per time-gate acquisition. Nevertheless, this approach generally results in acquisition times that are significantly shorter than in LSM-based FLIM (0.1–10 s).

3.5. Signal considerations and limitations

3.5.1. Noise

There are many sources of noise that affect the performance of fluorescence imaging systems. The sources of noise can be classified into [31]:

(i) *Intrinsic noise* caused by statistics related to the number of detected quanta. This type of noise is often referred to as Poissonian noise or shot-noise. For specific number of detected photons, N_e, the standard deviation of the detected signal will be never less than $N_e^{1/2}$. Consequently, the highest achievable signal-to-noise ratio (SNR) equals $N_e/N_e^{1/2} = N_e^{1/2}$.

(ii) *Subtractive noise* caused by the loss of photons because of inefficiencies in the collection and detection of the fluorescence emission. If the efficiency of the total system equals η, the number of detected photons will be $N_d = \eta N_e$ and the SNR ratio relative to the ideal case will be reduced to $(\eta N_e)^{1/2}$. An important cause for subtractive noise is the limited solid angle (α) of microscope objectives. A high numerical aperture objective may have an α as high as 72 °. This results in detected fraction of ~30% of all photons. Other contributions to subtractive noise include inefficiencies of the optics (e.g., band pass filters) and the limited quantum efficiency of detectors.

(iii) *Additive noise* caused by background light, dark counts (current) of the detector and noise of the electronics. Additive noise only increases the noise and not the signal, therefore reducing the SNR of the system.

(iv) *Multiplicative noise* caused by the uncertainty in the gain of detectors, which results in the increase of noise by a factor a; a will be between 1 and 2. This noise is usually absent in SPC and dominates in systems that employ analog detection.

(v) *Digitization noise* is caused by the digitization of the detector output. Photon counting is not affected by digitization noise due to the discrete nature of the detection.

Noise can be also introduced by *biochemical heterogeneity* of the specimen. This can be a major cause of uncertainty in biological imaging. The high (three-dimensional) spatial resolution of fluorescence microscopy results in low numbers of fluorophores in the detection volume. In a typical biological sample, the number of fluorophores in the detection volume can be as low as 2–3 fluorophores for a confocal microscope equipped with a high NA objective at a fluorescent dye concentration of 100 nM. This introduces another source of noise for imaging applications, chemical or *molecular noise*, related to the inherent randomness of diffusion and the interaction of molecules.

There are several other sources of noise that are specific to lifetime imaging. In particular, noise related to the *timing jitter* of

detector and electronics. This causes uncertainties in the time-resolved detection of photons. In absence of timing jitter, the IRF equals the laser pulse shape. The timing jitter of detector and electronics broadens the IRF and deteriorates the lifetime sensitivity and resolution, in particular for short lifetimes.

3.5.2. Photon economy

The performance of a lifetime detection system can be conveniently quantified by a figure-of-merit F, which is defined as the ratio of the SNR in a lifetime measurement and the SNR in an intensity measurement both carried out with the same number of photons. Based on this definition, F can be written as:

$$F = \frac{\Delta\tau}{\tau}\left(\frac{\Delta N}{N}\right)^{-1} = \frac{\sigma_\tau}{\tau}\sqrt{N} \tag{3.3}$$

where $N^{1/2}$ is the intrinsic Poissonian noise for N detected photons. When $F = 1$, lifetime estimations will exhibit the minimal possible noise, whereas $F > 1$ implies a reduced SNR for the lifetime estimation compared to a perfect system. An increase in F can be compensated for by collecting F^2-fold more photons. This will result in the same SNR at the expense of F^2-fold longer exposure times (or higher excitation intensities). Therefore, F^{-2} is a measure for the efficiency with which information is collected and used by an imaging application; F^{-2} can be defined as the photon-economy of a system.

The photon-economy depends on extrinsic sources of noise, the characteristics and settings of the instrument and also on the analysis method. Usually, the photon-economy depends on the lifetime; therefore it is instructive to construct graphs of F as a function of the lifetime. The photon-economy of time-domain techniques has been extensively characterized [10, 14, 32, 33].

SPC techniques are hardly affected by additive noise and multiplicative noise is absent. However, subtractive noise due to the collection efficiency and transmission of optics and the quantum efficiency of the detector do play a role. In addition, at high count rates, the efficiency goes down due to pileup effects.

$$F_{\mathrm{SPC}} = EF = \sqrt{\frac{1 + C_\mathrm{i} t_\mathrm{d}}{\eta}}\frac{\sigma_\tau}{\tau}\sqrt{N} \tag{3.4}$$

E represents the combined collection and detection efficiency of the system and F the intrinsic photon-economy of the technique. The factor η accounts for the subtractive noise, t_d is the dead-time of the detector and C_i the count rate of the system.

Methods based on analog detection are usually configured to not suffer from rate-dependent (saturation) effects. Therefore, such effects only occur at very high signal intensities, much higher than used in SPC. Multiplicative (a) and additive noise do make a contribution to the photon economy in analog detection. The effect of additive noise is not straightforward to include in the photon economy description and is here ignored. Inclusion of multiplicative noise in F results in:

$$F_{\mathrm{analog}} > \frac{a}{\sqrt{\eta}}\frac{\sigma_\tau}{\tau}\sqrt{N} = EF \tag{3.5}$$

a is usually in the range 1–2.

An analytical description of the photon-economy and additive noise could be carried out by the estimation of the Fisher-information matrix of the used estimators [34].

Also the relationship between the F-value and imaging parameters such as the number of time-bins, the width of the time-bins and the repetition rate have been studied in detail (de Grauw and Gerritsen, 2001); [10, 14, 32, 33, 35, 36].

When high repetition rate pulsed laser (40–80 MHz) are employed, the fluorescence decay can be resolved over the 12–25 ns

between adjacent excitation pulses with high time-resolution. Commercial electronics for TCSPC can digitize the photon arrival time with (sub) picosecond time resolution and the overall time resolution is determined by the detector. Because of the high time resolution and the large number of time-bins, TCSPC exhibits excellent F-values, close to one when the excitation frequency is sufficiently low [33]. TG with SPC can achieve equivalent efficiencies. However, TG is typically implemented with a low number of time-gates (2–8). When only two gates (I_0, I_1) of equal width are employed the rapid lifetime determination algorithm (Eq. 3.2) can be used to calculate the (average) lifetime of the fluorescence decay.

The optimum gate width ΔT for a specific lifetime amounts to 2.5τ. In Fig. 3.10 a typical F–τ curve is shown for time domain lifetime detection with a variable number of time bins and a total detection window (sum of all the time bins/gate widths) of 10 ns (de Grauw and Gerritsen, 2001). The curves are representative for both TCSPC and TG operating in a high excitation frequency mode of

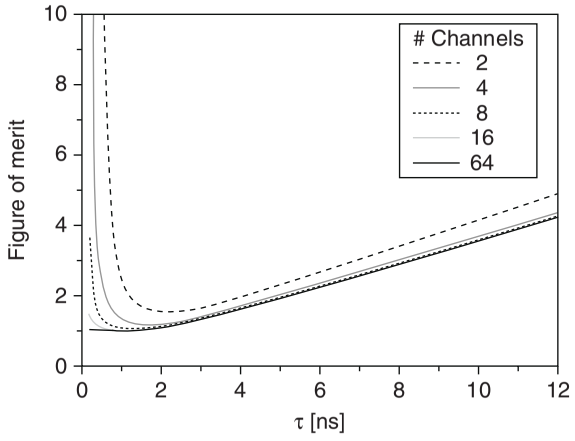

Fig. 3.10. Figure of merit curves for time domain lifetime detection with a variable number of gates. For all the curves the total detection window, the sum of all the gate widths, is 10 ns.

operation. The curves were calculated assuming that no pulse-pileup occurs and that all the TG gates are opened sequentially after the excitation pulse. Moreover, only the intrinsic photon-economy of the technique is taken into account and no additional noise contributions. Also, the effect of the IRF is not taken into account.

The two-gate curve has its minimum ($F \sim 1.5$) at 2 ns and below 1 ns the F-value rapidly increases. Interestingly, the minimum F-values for four and more channels hardly differ at 2 ns. The value is 1.18 and 1.10 for 4 and 64 gates respectively. Only for (very) short lifetimes <500 ps the advantage of a large number of (narrow) gates/time bins shows up. Interestingly, in the case of long detection windows ($\gg\tau$), F converges to 1 for high numbers of gates.

3.5.3. Calibration and accuracy

The accuracy with which a system can measure lifetimes depends on a number of different factors including: calibration of the instrument, the number of detected photons and also the efficiency of the analysis routines. In addition, sources of background and scattered light should be eliminated. Emission filters should be chosen with great care to make sure that no scattered laser light reaches the detector. Detection of scattered excitation light results in a spurious fast component in the decay and complicates the interpretation of the data. The choice of emission filters is much more critical in FLIM than in conventional fluorescence intensity imaging methods.

The time-domain IRF can be comparatively broad and skewed functions. The IRF needs to be taken into account in the data acquisition procedure and analyses to minimize systematic errors in the lifetime determination, in particular if the lifetimes are short.

TCSPC is inherently self-referenced and therefore, with the exception of the regular recording of the IRF, a TCSPC system requires practically no day-to-day calibration. In TCSPC the recording

of the decay is started well before the rise of the fluorescence signal and the high timing resolution allows measuring the entire fluorescence rise and decay of the fluorophore. This makes TCSPC insensitive to long-term drift of reference timing signals from, for instance, the lasers source. A (slow) drift in the timing is automatically accounted for in the data analyses procedure.

TG-based microscopes make use of a comparatively low number of gates and only a part of the decay is sampled. The opening of the first gate should be carefully chosen to start after the initial rise of the fluorescence emission. Opening the first gate before or during the rise of the fluorescence will cause a reduction of counts in the first gate relatively to the second and therefore a bias in the lifetime. This needs to be taken into account in the analyses. A further delay of the opening of the first gate can be used for the suppression of (fast) background lifetime contributions, but at the expense of loss of detected photons. Due to the scale-invariant properties of exponentials, a time-shift in the opening of the gates will not alter the measured lifetimes.

A common cause of inaccuracy in SPC-based time domain detection is pulse-pileup, that is, the arrival of photons during the dead-time of the detection system. Because the higher probability of emission (and detection) in the earlier part of the decay, pulse-pileup is more probable in this part of the decay. Consequently, the decay will be distorted and the lifetime will be biased towards higher values. Moreover, pulse-pileup will also result in a reduction of the detection efficiency (see Fig. 3.7 and Eq. (3.4)). Therefore, care should be taken to avoid excitation rates too close to the efficacy count rate (i.e., the inverse of the dead-time) in order to minimize these effects.

For comparatively high repetition-rates (period $T < 5\tau$) fluorescence decays could also overlap between adjacent pulses. Thanks to the scale-invariant properties of the exponentials, no error is introduced when the decay is a pure single-exponential. Conversely, the preexponential factors can be altered when multiple lifetime decays

are present, causing bias in the estimation of the (average) lifetimes of the sample.

Finally, it is interesting to note that biases can be introduced by data fitting at low counts even with the use of ordinarily unbiased estimators like the maximum likelihood estimator [37].

Day-to-day drifts of instrumental characteristics, differences in temperature and sample preparation may affect the recorded lifetimes. For instance, differences in temperature can affect both the excited state lifetime of the fluorophore and instrument properties like noise or delays of wirings and electronics.

Importantly, the intrinsic heterogeneity of biological samples can cause lifetime differences between different preparations [38]. Although the broadness of estimated lifetime distributions of single-exponential fluorophores can be narrowed by collecting higher numbers of photons, in biological imaging there will be often broader lifetime distribution because of biochemical intracellular heterogeneity and differences among cells and preparations.

It is recommended to characterize these errors in order to estimate the statistical relevance of the measurement. Importantly, relative estimates are usually less prone to errors and may offer higher sensitivities. For example, in FRET–FLIM experiments the ratio of the donor lifetime in the absence and presence of an acceptor is measured. This offers a higher precision than absolute lifetime values.

3.5.4. Lifetime resolution and lifetime heterogeneity

The lifetime resolution is the smallest variation in lifetime that can be detected. If external noise sources are ignored, the lifetime resolution depends essentially on the photon-economy of the system. For instance, if a 2 ns lifetime is measured with a 4 gate TG single-photon counting FLIM ($F = 1.3$) and 1000 photons, variations of about 80 ps can be resolved. However, for reasons discussed earlier, in biological samples these values could be higher.

To optimize resolution in lifetime-based assays, a comparison of relative estimates is always favorable. If the FLIM experiment is carried out in an environment where temperature cannot be tightly controlled, it is also convenient to cycle between different samples during the same experimental session, in order to average out thermal and other instrumental drifts. When applicable, this practice may be useful to suppress any nonrandom variation in the detection.

Lifetime heterogeneity can be analyzed by fitting the fluorescence decays with appropriate model function (e.g., multiexponential, stretched exponential, and power-like models) [39]. This, however, always requires the use of additional fitting parameters and a significantly higher number of photons should be collected to obtain meaningful results. For instance, two lifetime decays with time constants of 2 ns, 4 ns and a fractional contribution of the fast component of 10%, requires about 400,000 photons to be resolved at 5% confidence [33].

3.5.5. Shortest lifetimes

The shortest lifetime that an instrument can measure is mainly determined by the instrument characteristics and for sufficiently short excitation pulses it is limited by the timing-jitter of detector and electronics. The most accurate detectors are MCP–PMTs that exhibit TTSs as low as 25 ps but other commonly used detectors may have values as high as 300 ps. At very high count numbers, the lifetime resolution can be virtually infinitely high; however, the timing jitter of the system is a practical detection limit for the shortest measurable lifetime at any realistic SNR. Moreover, the IRF needs to be taken into account to measure lifetimes that are on the order of the width of the IRF or shorter. Contrary to time-resolved spectroscopy, measuring lifetimes on the order of the width of the IRF is challenging in lifetime imaging due to the significantly lower numbers of photons per pixels that are typically detected.

3.5.6. Acquisition throughput

The acquisition throughput of a microscope is often determined by photon statistics, but depends also on many parameters including instrumental limitations, for example, the read-out and dead-time of the detector and electronics [40].

For instance, a time-gated SPC microscope with four gates exhibits a better maximal ($F_{TG4} = 1.3$) photon-economy than a two-gated system ($F_{TG2} = 1.5$). The latter setup will thus require $(F_{TG2}/F_{TG4})^2 = 1.7$-fold longer acquisition time than the former because of photon-statistics alone.

Throughput also depends on the degree of parallelization of the detection system. In wide-field imaging the fluorescence emission needs to be acquired and gated sequentially by a MCP or simultaneously by the use of image splitters. In both the cases, however, only a fraction of photons equal to the inverse of the number of gates is collected because of the gating process. Based on the sequential acquisition setup, a two gate system will be $(4/2)(F_{TG4}/F_{TG2})^2 \sim 1.5$ times faster than a four-gate system. On the other hand, the importance of parallelization lies in the minimization of read-out time-lags, photobleaching, and motion artefacts, which could affect wide-field imaging when performed by the sequential acquisition of the images. Such systems proved capable of acquisition rates in excess of 100 Hz [27, 41]. TCSPC can be also performed using wide-field detectors. These detectors cannot, however, sense more than one photon at a time and are inherently slow [26]. Therefore, at present wide-field TCSPC systems do not take advantage of the parallelization in terms of acquisition speed.

SPC techniques offer the advantage of low noise detection, providing F-values of 1–2 times lower than in analog detection. Although this can in principle result in four times faster acquisition speed this gain in speed is not realized in practice. In SPC, the comparatively high dead-times of detectors and electronics limits the acquisition speed. SPC system should be operated at count rates below the inverse of the dead-time of the system (electronics

or detector). Above this count rate the lifetime may be distorted. Moreover, the efficiency of the system goes down because of pileup effects (see Fig. 3.7)

Because of the low timing-jitter (down to 25 ps) TCSPC-based systems are often equipped with a MCP-PMT at detriment of acquisition speed ($<10^6$ counts per second). On the other hand, a TG-SPC system equipped with four gates and a fast PMT (10 MHz) could be slower than a TCSPC at low count-rates (<100 kHz), because of a lower photon-economy. However, already at 1 MHz, the former would be almost three times faster and more the one order of magnitude faster at 10 MHz.

The above limitations are implementation dependent and no intrinsic limitations. The throughput of TCSPC can for instance be improved by the use of multiple detectors, and multiple TCSPC boards [42]. The photon-economy of TGSPC could be optimized somewhat by increasing the number of gates.

3.6. Data analysis

Time-domain detection results in histograms of photon arrival times. In time-correlated SPC, the time-bins correspond to the analog-to-digital conversion levels, whereas in time-gated SPC, the time-bins are the time-windows during which the photon-counting gate is activated.

The analysis of the histograms of photon arrival times is equivalent in both cases and relies on fitting appropriate model functions to the measured decay. The selection of the fitting model depends on the investigated system and on practical considerations such as noise. For instance, when a cyan fluorescent protein (CFP) is used, a multi-exponential decay is expected; furthermore, when CFP is used in FRET experiments more components should be considered for molecules exhibiting FRET. Several thousands of photons per pixel would be required to separate just two unknown fluorescent

decay times; a signal level that can often not be realized in biological imaging.

On the basis of a priori knowledge of the system, the number of fit parameters can be sometimes constrained. In the case of a FRET imaging experiment, the lifetime component corresponding to the donor molecules that do not exhibit FRET can be assumed constant. Now, the fitting would require one fit parameter less and consequently fewer detected photons per pixel are required for a reliable fit.

Lifetime heterogeneity itself can be the target of the measurement. In this case, high photon counts and alternative model functions like stretched exponentials and power-distribution-based models can be used [39, 43]. These provide information on the degree of heterogeneity of the sample with the addition of only one fit parameter compared with single exponential fits.

It is not uncommon to detect only a few hundred photons per pixel or less. Therefore, spatial binning of the data may be necessary to obtain the sufficient signal for a reliable fit. At low counts, also rebinning of the time histograms may be beneficial to avoid "empty bins" and increase the efficiency of the fit. TD-FLIM can be implemented with only two time-gates. By using Eq. (3.1)—the rapid lifetime determination method—the average lifetime of the sample can be estimated without any fitting. This method offers high speed in both acquisition and analysis, but a comparatively low photon-economy and accuracy. The latter is partly due to lack of background correction.

Generally, inaccuracies can also be expected at low photon counts ($N < 100$). Besides comparatively large statistical fluctuations, also a bias in lifetime is introduced by the data fitting procedure [37].

As a criterion for the quality of the fit usually the reduced χ^2 is used by the fitting algorithm. This function is defined as:

$$\chi^2 = \sum_{i=1}^{N} \frac{1}{\sigma_i^2} \Big(y_i - f(x_i) \Big)^2 \tag{3.6}$$

Here, N is the number of data points (time bins), y_i the measured intensity in time bin i, σ_i^2 the measurement error (variance) for y_i, x_i the time position of bin i, and f the theoretical function describing the decay.

The fitting algorithm minimizes the χ^2, or another goodness-of-fit function [44], to minimize the difference between the experimental data and the fit model. In spectroscopic measurements, high values of the reduced χ^2 (>1.4) indicate that the model may be not a good representation of the experimental data and a different fit function may have to be selected. However, in lifetime imaging experiments even values higher than 2 may be acceptable because systematic errors cannot be always excluded in FLIM data sets [20]. On the other hand, a reduced χ^2 close to one implies only that the model fits the data with high accuracy within the experimental errors. This does not necessarily mean that the model itself is a realistic model. If the model has too many fit parameters, the fitting function will yield low χ^2 values without reliable values for the estimated parameters.

Furthermore, at very low photon counts in general low values of the reduced χ^2 ($\approx$1) are obtained because of the high noise level in the data. Therefore, the reduced χ^2 and other goodness of parameters should be used with caution.

Also global fitting techniques, where the space invariance (or any other invariance property) of one or more fitting parameters is exploited, have been successfully used to analyze fluorescence lifetime images [45, 46]. When applicable, global analysis techniques provide more homogeneous SNRs and reduce the number of fitted parameters.

In the analyses of the FLIM data, it is important to set an appropriate threshold on the number of counted photons above which the data is fitted. If a pixel contains a number of counts below the threshold, the fit parameters are usually set to 0, that is, those pixels are masked out.

When for a single exponential fit an error of <5% is required, the threshold should be set at 400–700 counts, depending on the

F-value of the system. The exact number of total counts per (eventually binned) pixel can be calculated from the F-value using Eq. (3.3). For precise measurements, care should be taken that the contribution of autofluorescence to the measurement is negligible. This may mean that the threshold has to be raised to comparatively high values.

The inspection of the fit residuals, that is, the (normalized) differences between the experimental and fitted data point, is a reliable tool to check for deviations from the fitted model. Residuals should be statistically noncorrelated and randomly distributed around zero. For example, if a bi-exponential decay is fitted to a single exponential function, the residuals will show systematic errors. Therefore, correlations in the residuals may indicate that another fit model should be used.

Recently, a method used for the analysis of frequency-domain data has been proposed for the analysis of time-domain images. The AB-plot or phasor plot provides a useful graphical representation of lifetime data that can be used for the segmentation of the images prior to data fitting [47, 48]. With this method, data fitting may be avoided in many instances.

3.7. FRET–FLIM example application

An important application of fluorescence lifetime imaging is the imaging of molecular colocalization based on FRET imaging, see Chapters 1 and 2). The energy transfer from a fluorescent donor molecule to a matched acceptor introduces an additional deactivation pathway for the donor's excited state. As a result, the donor's fluorescence lifetime is reduced. Therefore, the occurrence of FRET can be imaged using FLIM. Figure 3.11, shows an example of a FRET-FLIM experiment in which two lipid raft markers, GPI-GFP (donor) and CTB-Alexa594 (acceptor), are present in the plasma membrane of NIH 3T3 cells. The lifetime images were recorded using a confocal microscope equipped with a four channel

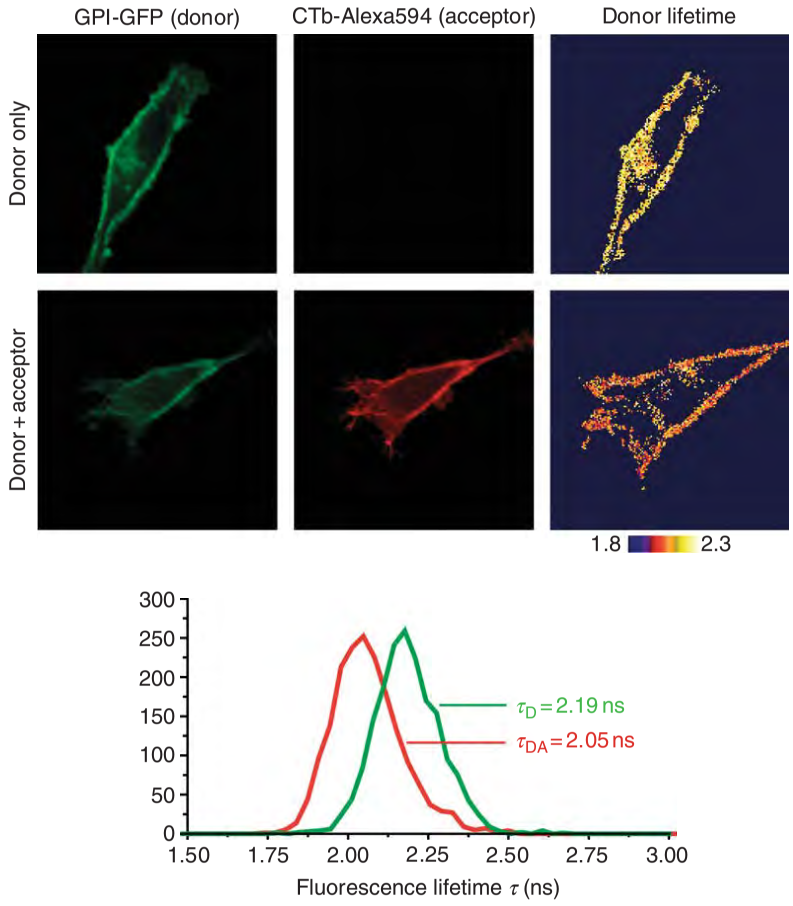

Fig. 3.11. FRET–FLIM experiment to study colocalization of two lipid raft markers, GPI-GFP and CTB-Alexa594. The rows of images show intensity and lifetime images of donor-labeled and donor + acceptor-labeled cells. The histogram shows the lifetime distribution of the whole cells. The FRET efficiency is ~6%.

time-gated photon counting module with 2-ns wide time gates (LIMO) [23]. A low power pulsed 440 nm laser diode was used with a pulse width of about 100 ps and the power at the specimen

was approximately 50 μW. Because of the low excitation power the acquisition time was comparatively long, about 60 s.

The top series of images in Fig. 3.11 was recorded on a specimen containing donor only. Left and middle images show the intensity images of donor and acceptor channel respectively. As expected no signal is present in the acceptor channel and the donor channel shows clear labeling of the plasma membrane. On the right, the donor-only FLIM image is shown. Here, a threshold was set at 900 counts and the maximum number of counts amounted to about 2500 counts. Only above the threshold the lifetimes were calculated. The donor-only image shows a fairly constant lifetime over the whole image. From the lifetime histograms of the image, an average lifetime over the whole cell of 2.19 ns was found.

The presence of the acceptor, lower row of images, results in a clear reduction in the lifetime to about 2.05 ns. The reduction corresponds to a 6% FRET efficiency. Experiments on more cells ($N = 4$, not shown) confirms that this reduction is indeed significant and that the two lipid raft markers colocalize in the plasma membrane.

A closer look at the data shows the lifetime distributions are comparatively broad, about 0.25 ns for both distributions. This is in fact much broader than what one would expect from photon statistics alone. Based on realistic F-values (1.2–1.5) lifetime images recorded with this many counts are expected to yield distributions with widths on the order of 0.1 ns. The broadening is therefore not because of photon statistics. Variations in the microenvironment of the GFP are the most likely source of the lifetime heterogeneities. Importantly, such sensitivity for local microenvironment may be the source of apparent FRET signals. In this particular FRET–FLIM experiment, we found that the presence of CTB itself without the acceptor dye already introduced a noticeable shift of the donor lifetime. Therefore, in this experiment the donor-only lifetime image was recorded after unlabeled CTB was added to the cells. The low FRET efficiency and broadened lifetime distribution call for careful control experiments and repeatability checks.

For this particular experiment, we also carried out additional photobleaching measurements. Here, the acceptor was photo bleached and it was found that the donor lifetime returned to the donor only lifetime of about 2.19 ns. This confirms that the observed lifetime reduction is indeed due to FRET [49].

References

[1] Bugiel, I., König, K. and Wabnitz, H. (1989). Investigation of cells by fluorescence laser scanning microscopy with subnanosecond time resolution. Laser Life Sci. *3*, 1–7.

[2] Buurman, E. P., Sanders, R., Draaijer, A., Gerritsen, H. C., Van Veen, J. J. F., Houpt, P. M. and Levine, Y. K. (1992). Fluorescence lifetime imaging using a confocal laser scanning microscope. Scanning *14*, 155–9.

[3] Schneckenburger, H. and Konig, K. (1992). Fluorescence decay kinetics and imaging of Nad(P)H and flavins as metabolic indicators. Opt. Eng. *31*, 1447–51.

[4] Wang, X. F., Uchida, T., Coleman, D. M. and Minami, S. (1991). A 2-dimensional fluorescence lifetime imaging-system using a gated image intensifier. Appl. Spectrosc. *45*, 360–6.

[5] Gadella, T. W., Jovin, T. M. and Clegg, R. M. (1993). Fluorescence lifetime imaging microscopy (FLIM) - spatial resolutions of microstructures on the nanosecond time scale. Biophys. Chem. *48*, 221–39.

[6] Lakowicz, J. R. and Berndt, K. W. (1991). Lifetime-selective fluorescence imaging using an Rf phase- sensitive camera. Rev. Sci. Instrum. *62*, 1727–34.

[7] Morgan, C. G., Mitchell, A. C. and Murray, J. G. (1990). Nano-second time-resolved fluorescence microscopy: principles and practice. Trans. R. Microsc. Soc. *1*, 463–6.

[8] Becker, W., Bergmann, A., Hink, M. A., Konig, K., Benndorf, K. and Biskup, C. (2004b). Fluorescence lifetime imaging by time-correlated single-photon counting. Microsc. Res. Tech. *63*, 58–66.

[9] O'Connor, D. V. and Phillips, D. (1984). Time-Correlated Single Photon Counting. Academic press, London.

[10] Gerritsen, H. C., Asselbergs, M. A., Agronskaia, A. V. and Van Sark, W. G. (2002a). Fluorescence lifetime imaging in scanning microscopes: Acquisition speed, photon economy and lifetime resolution. J. Microsc. *206*, 218–24.

[11] Bohmer, M., Pampaloni, F., Wahl, M., Rahn, H. J., Erdmann, R. and Enderlein, J. (2001). Time-resolved confocal scanning device for ultrasensitive fluorescence detection. Rev. Sci. Instrum. *72*, 4145–52.

[12] Esposito, A., Gerritsen, H. C., Wouters, F. S. and Resch-Genger, U. (2007b). Fluorescence lifetime imaging microscopy: Quality assessment and standards. In: Standardization in Fluorometry: State of the Art and Future Challenges (Wolfbeis, O. S., ed.). Springer, Berlin Heidelberg New York.

[13] Stiel, H., Teuchner, K., Paul, A., Leupold, D. and Kochevar, I. E. (1996). Quantitative comparison of excited state properties and intensity- dependent photosensitization by rose bengal. J. Photoch. Photobiol. B *33*, 245–54.

[14] Ballew, R. M. and Demas, J. N. (1989). An error analysis of the rapid lifetime determination method for the evaluation of single exponential decays. Anal. Chem. *61*, 30–3.

[15] Scully, A. D., Ostler, R. B., Phillips, D., O'Neill, P. O., Townsend, K. M., Parker, A. W. and MacRobert, A. J. (1997). Application of fluorescence lifetime imaging microscopy to the investigation of intracellular PDT mechanisms. Bioimaging *5*, 9–18.

[16] Siegel, J., Elson, D. S., Webb, S. E. D., Lee, K. C. B., Vlanclas, A., Gambaruto, G. L., Leveque-Fort, S., Lever, M. J., Tadrous, P. J., Stamp, G. W. H., Wallace, A. L., Sandison, A., *et al.* (2003). Studying biological tissue with fluorescence lifetime imaging: microscopy, endoscopy, and complex decay profiles. Appl. Optics *42*, 2995–3004.

[17] Vroom, J. M., De Grauw, K. J., Gerritsen, H. C., Bradshaw, D. J., Marsh, P. D., Watson, G. K., Birmingham, J. J. and Allison, C. (1999). Depth penetration and detection of pH gradients in biofilms by two-photon excitation microscopy. Appl. Environ. Microb. *65*, 3502–11.

[18] Ghiggino, K. P., Harris, M. R. and Spizzirri, P. G. (1992). Fluorescence lifetime measurements using a novel fiberoptic laser scanning confocal microscope. Rev. Sci. Instrum. *63*, 2999–3002.

[19] Van der Oord, C. J. R., Gerritsen, H. C., Rommerts, F. F. G., Shaw, D. A., Munro, I. H. and Levine, Y. K. (1995). Microvolume time-resolved fluorescence spectroscopy using a confocal synchrotron-radiation microscope. Appl. Spectrosc. *49*, 1469–73.

[20] Lakowicz, J. R. (1999). Principles of Fluorescence Spectroscopy. Plenum press, New York.

[21] Becker, W., Bergmann, A., Biskup, C., Kelbauskas, L., Zimmer, T., Klöcker, N. and Benndorf, K. (2003). High resolution TCSPC lifetime imaging. Proc. SPIE *4963*, 175–84.
[22] Kwak, E. S. and Vanden Bout, D. A. (2003). Fully time-resolved near-field scanning optical microscopy fluorescence imaging. Anal. Chim. Acta *496*, 259–66.
[23] Van der Oord, C. J., de Grauw, C. J. and Gerritsen, H. C. (2001). Fluorescence lifetime imaging module LIMO for CLSM. Proc. SPIE *4252*, 119–23.
[24] Gratton, E., Breusegem, S., Sutin, J., Ruan, Q. and Barry, N. (2003). Fluorescence lifetime imaging for the two-photon microscope: time-domain and frequency-domain methods. J. Biomed. Opt. *8*, 381–90.
[25] Jose, M., Nair, D. K., Reissner, C., Hartig, R. and Zuschratter, W. (2007). Photophysics of clomeleon by FLIM: Discriminating excited state reactions along neuronal development. Biophys. J. *92*, 2237–54.
[26] Kemnitz, K., Pfeifer, L. and Ainbund, M. R. (1997). Detector for multi-channel spectroscopy and fluorescence lifetime imaging on the picosecond timescale. Nucl. Instrum. Meth. Phy. Res. A *387*, 86–7.
[27] Agronskaia, A. V., Tertoolen, L. and Gerritsen, H. C. (2003). High frame rate fluorescence lifetime imaging. J. Phys. D: Appl. Phys. *36*, 1655–62.
[28] Elson, D. S., Munro, I., Requejo-Isidro, J., McGinty, J., Dunsby, C., Galletly, N., Stamp, G. W., Neil, M. A. A., Lever, M. J., Kellett, P. A., Dymoke-Bradshaw, A., Hares, J., *et al.* (2004). Real-time time-domain fluorescence lifetime imaging including single-shot acquisition with a segmented optical image intensifier. New J. Phys. *6*, 180–93.
[29] Mosconi, D., Stoppa, D., Pancheri, L., Gonzo, L. and Simoni, A. (2006). CMOS single-photon avalanche diode array for time-resolved fluorescence detection. IEEE ESSCIRC. 564–67.
[30] Niclass, C., Gersbach, M., Henderson, R., Grant, L. and Charbon, E. (2007). A single photon avalanche diode implemented in 130-nm CMOS technology. IEEE J. Sel. Top. Quant. Electron *13*, 863–9.
[31] Pawley, J. (2006). Handbook of Biological Confocal Microscopy, 3rd edition. Springer Verlag, New York.
[32] Gerritsen, H. C., Draaijer, A., van den Heuvel, D. J. and Agronskaia, A. V. (2006). Fluorescence lifetime imaging in scanning microscopy. In: Handbook of Biological Confocal Microscopy (Pawley, J., ed.). Plenum Press, New York, pp. 516–33.
[33] Kollner, M. and Wolfrum, J. (1992). How many photons are necessary for fluorescence-lifetime measurements? Chem. Phys. Lett. *200*, 199–204.

Author's personal copy

[34] Watkins, L. P. and Yang, H. (2004). Information bounds and optimal analysis of dynamic single molecule measurements. Biophys. J. *86*, 4015–29.
[35] Ballew, R. M. and Demas, J. N. (1991). Error analysis of the rapid lifetime determination method for single exponential decays with a non-zero base-line. Anal. Chim. Acta *245*, 121–7.
[36] Moore, C., Chan, S. P., Demas, J. N. and DeGraff, B. A. (2004). Comparison of methods for rapid evaluation of lifetimes of exponential decays. Appl. Spectrosc. *58*, 603–7.
[37] Tellinghuisen, J. and Wilkerson, C. W. (1993). Bias and precision in the estimation of exponential decay parameters from sparse data. Anal. Chem. *65*, 1240–6.
[38] Grailhe, R., Merola, F., Ridard, J., Couvignou, S., Le Poupon, C., Changeux, J. P. and Laguitton-Pasquier, H. (2006). Monitoring protein interactions in the living cell through the fluorescence decays of the cyan fluorescent protein. Chemphyschem *7*, 1442–54.
[39] Lee, K. C. B., Siegel, J., Webb, S. E. D., Leveque-Fort, S., Cole, M. J., Jones, R., Dowling, K., Lever, M. J. and French, P. M. W. (2001). Application of the stretched exponential function to fluorescence lifetime imaging. Biophys. J. *81*, 1265–74.
[40] Esposito, A., Gerritsen, H. C. and Wouters, F. S. (2007a). Optimizing frequency-domain fluorescence lifetime sensing for high-throughput applications: photon economy and acquisition speed. J. Opt. Soc. Am. *24*, 3261–73.
[41] Agronskaia, A. V., Tertoolen, L. and Gerritsen, H. C. (2004). Fast fluorescence lifetime imaging of calcium in living cells. J. Biomed. Opt. *9*, 1230–7.
[42] Becker, W., Bergmann, A., Biscotti, G., König, K., Riemann, I., Kelbauskas, L. and Biskup, C. (2004a). High-speed FLIM data acquisition by time-correlated single photon counting. Proc. SPIE *5223*, 1–9.
[43] Wlodarczyk, J. and Kierdaszuk, B. (2003). Interpretation of fluorescence decays using a power-like model. Biophys. J. *85*, 589–98.
[44] Awaya, T. (1979). New method for curve fitting to the data with low statistics not using the Chi-2-method. Nucl. Instrum. Methods *165*, 317–23.
[45] Barber, P. R., Ameer-Beg, S. M., Gilbey, J. D., Edens, R. J., Ezike, I. and Vojnovic, B. (2005). Global and pixel kinetic data analysis for FRET detection by multi-photon time-domain FLIM. *In* Multiphoton Microscopy in the Biomedical Sciences V.Vol. 5700. SPIE, San Jose, CA, USA, pp. 171–81.

[46] Pelet, S., Previte, M. J., Laiho, L. H. and So, P. T. (2004). A fast global fitting algorithm for fluorescence lifetime imaging microscopy based on image segmentation. Biophys. J. *87*, 2807–17.
[47] Clayton, A. H., Hanley, Q. S. and Verveer, P. J. (2004). Graphical representation and multicomponent analysis of single-frequency fluorescence lifetime imaging microscopy data. J. Microsc. *213*, 1–5.
[48] Digman, M., Caiolfa, V. R., Zamai, M. and Gratton, E. (2007). The Phasor approach to fluorescence lifetime imaging analysis. Biophys. J. *94*, L14–16.
[49] Barzda, V., de Grauw, C. J., Vroom, J., Kleima, F. J., van, G. R., van, A. H. and Gerritsen, H. C. (2001). Fluorescence lifetime heterogeneity in aggregates of LHCII revealed by time-resolved microscopy. Biophys. J. *81*, 538–46.
[50] de Grauw, C. J. and Gerritsen, H. C. (2001). Multiple time-gate module for fluorescence lifetime imaging. Appl. Spectro. *55*(6), 670-78.

Kees Jalink, Wednesday June 13th 2012, 10.00

Imaging membrane constituents by intensity-based FRET approaches

Cellular signals that are either very local or short-lived (transient) can easily escape detection by conventional biochemistry. A detailed understanding of these signals requires techniques with high spatiotemporal resolution that can be used in single living cells. Imaging techniques offer this high resolution, and the introduction of Green Fluorescent Protein (GFP) has begun to rapidly add to the number of targets that can be monitored. In addition, the isolation of spectral mutants of GFP allows direct imaging of molecular interactions within the cell through Fluorescent Resonance Energy Transfer (FRET). FRET, which occurs when suitable donor and acceptor fluorophores come into close proximity, serves to visualize protein-protein interactions, and it is also well suited as the read-out is so-called biological "sensors". Such sensors are genetically encoded constructs engineered to allow monitoring of signaling events by a change in energy transfer.

Several fundamentally different ways are used to detect FRET in microscopic images. I will introduce in detail ratio-imaging and 'FilterFRET' (quantitative determination of FRET from sensitized emission) as means to resolve FRET efficiency in living cells. I will describe what I perceive as strenths but also weaknesses of these methods, and make some remarks on the necessary equipment. Focusing on sensors to detect membrane lipids in living cells, I will then describe some of the work done in our lab in developing FRET sensors, as well as some of our past results with them.

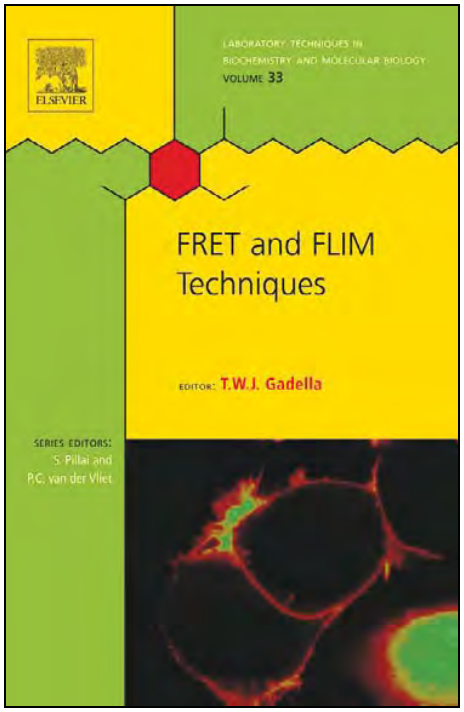

From: Kees Jalink and Jacco van Rheenen, FilterFRET: Quantitative imaging of sensitized emission.
In T. W. J. Gadella, editor, Laboratory Techniques in Biochemistry and Molecular Biology, Vol 33, Burlington: Academic Press, 2009, pp.289-349.
ISBN: 978-0-08-054958-3

Laboratory Techniques in Biochemistry and Molecular Biology, Volume 33
FRET and FLIM Techniques
T. W. J. Gadella (Editor)

CHAPTER 7

FilterFRET: Quantitative imaging of sensitized emission

Kees Jalink[1] and Jacco van Rheenen[2]

[1]*Department of Cell Biology, The Netherlands Cancer Institute, Plesmanlaan 121, 1066 CX Amsterdam, The Netherlands*
[2]*Hubrecht Institute-KNAW and University Medical Center Utrecht, Uppsalalaan 8, 3584CT, Utrecht, The Netherlands*

Previous chapters in this volume were dedicated to advanced imaging techniques such as fluorescence lifetime imaging (FLIM) that require complicated, dedicated, and expensive equipment. Fluorescence resonance energy transfer (FRET) can also be assessed from simple fluorescence images taken with conventional wide-field or confocal microscopes readily available in most research institutes. To this goal, cells expressing donor- and acceptor-tagged proteins ("FRET cells") are imaged, along with control cells expressing either donor- or acceptor alone, under different spectral recording conditions (i.e., with different filter sets). Quantitative FRET images are then calculated by mathematically correcting for filter leak-through terms. Algorithms for "filterFRET" with wide-field microscopes have been reported by several groups but for confocal imaging, separate formalisms had to be developed.

In this chapter, we intend to give the reader an understanding of the possibilities and pitfalls of filterFRET. Following a brief historical overview describing early nonquantitative incarnations of FRET imaging, the theory that allows quantitative wide-field and

DOI: 10.1016/S0075-7535(08)00007-7

confocal FRET imaging will be treated. Special emphasis will be on calibration of the FRET setup and images. Next, major sources of error and noise that have hampered, until recently, application of these algorithms in a very quantitative way will be discussed. Finally, image enhancement strategies, their possible bias on the results and some useful presentation aids will be treated. Taken together, with proper attention for image recording conditions and enhancement strategies, imaging of sensitized emission is a quantitative, fast, photon-efficient, and easy way to determine FRET.

7.1. Introduction

7.1.1. Definition

The term filterFRET here refers to intensity-based methods for calculating fluorescence resonance energy transfer (FRET) from sets of images of the preparation collected at different excitation and/or emission wavelength. The term is not intended to imply that interference filters are actually present in the setup; very similar considerations apply when donor- and acceptor fluorophores are spectrally resolved by other means, such as monochromators or spectral detectors.

7.1.2. Sensitized emission

In previous chapters it was shown that FRET can be reliably detected by donor fluorescence lifetime imaging. Here, we will focus on what is perhaps the most intuitive and straightforward way to record FRET: imaging of sensitized emission (s.e., that is, the amount of acceptor emission that results from energy transferred by the donor through resonance) by filterFRET. While simple in principle, determinations of s.e. are complicated by overlap of excitation and emission spectra of the donors and acceptors, and by several imperfections of the recording optics, light sources and detectors.

7.1.3. The sensitized emission problem

To explain what problems complicate filterFRET, consider the model neuronal cell in Fig. 7.1A. It contains two independently expressed fluorophores: donor molecules at the membrane and in the nucleus, and acceptor molecules at the membrane and around the nucleus. Thus, FRET is only possible at the membrane and sensitized emission should be restricted to the membrane. However, if we collect an s.e. image (**S**) by exciting donors while collecting the fluorescence of acceptors (Fig. 7.1A) the intensity distribution differs from the predicted FRET distribution (compare the s.e. panel, bottom right, to the FRET panel). In particular, **S** also shows some signal from donors in the nucleus and from acceptors in the region around the nucleus. This is due to overlap of the excitation and emission spectra (Fig. 7.1B), which is particularly apparent when genetically encoded fluorescent proteins (FPs) are used as labels. First, overlap of the donor emission spectrum with the acceptor detection channel causes some emission of the donor to appear in the **S** image (leak-through; Fig 7.1C), and second, due to overlap of the acceptor excitation spectrum, some acceptors are directly (inappropriately) excited at the donor excitation wavelength (cross-excitation; Fig 7.1C) and this causes acceptor fluorescence independent from FRET. Thus, the first problem is:

> **FilterFRET Problem 1: Spectral overlap**
>
> **S** *is a mixture of sensitized emission, donor- and acceptor fluorescence.*

Even if we forget, for a moment, the overlap problem and assume that we obtained a "pure" sensitized emission image, interpretation of this image is still ambiguous. That is because first, the intensity of **S** varies linearly with the excitation intensity and with the detector sensitivity. The exact same preparation will, when measured on a different microscope, yield different s.e. intensities. In fact, as much as renewing the arc lamp would impede comparison of results obtained on the same microscope. Second, the interpretation

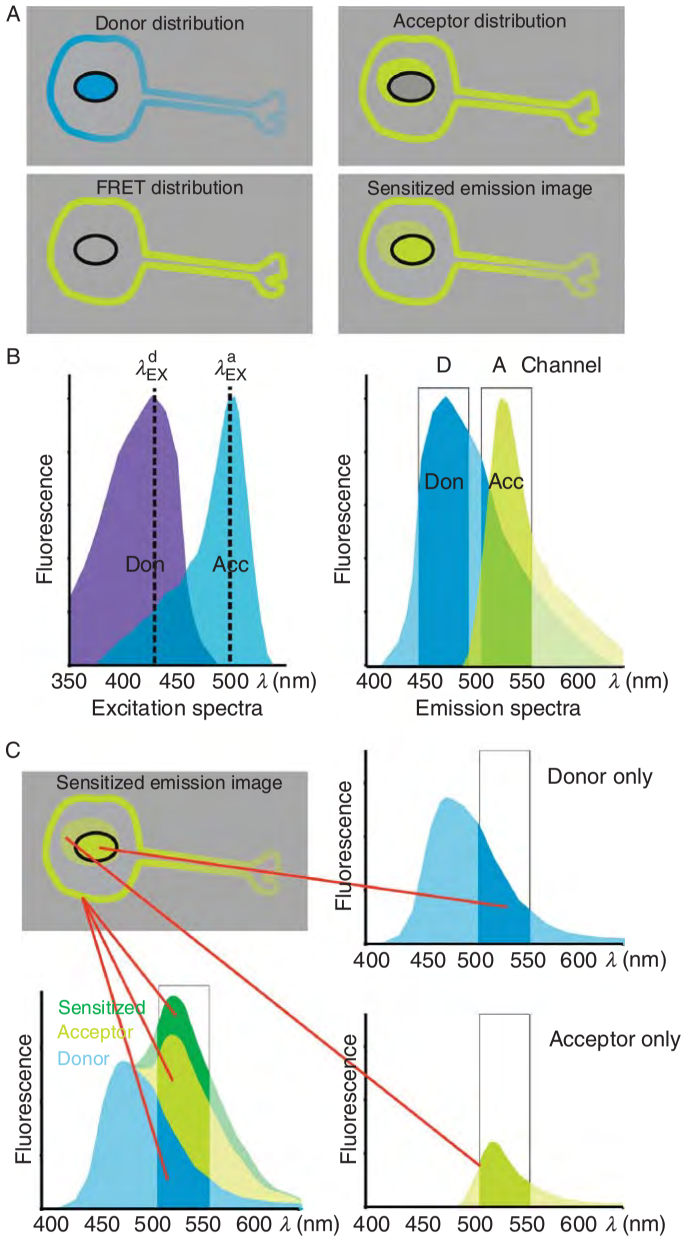

Fig. 7.1. (*Continued*)

of local differences in s.e. within a single image is also ambiguous. For example, the diminished s.e. in the axon of our model neuron (Fig. 7.1C) may either stem from less efficient interaction between donors and acceptors or from locally decreased abundance of donors and/or acceptors. As one often is interested in the distribution of the *degree* of protein interaction, the s.e. image must thus be normalized by relating it to the local concentration of the donor, the acceptor, or both. Thus:

FilterFRET Problem 2: Normalization

S *depends on FRET efficiency but also on fluorophore concentration, donor excitation, and detector sensitivity.*

To perform such normalization, images of the distribution of the donors and acceptors are needed. For the donor image (**D**), donor emission is collected while exciting at donor wavelength, and for the acceptor image (**A**), the acceptor fluorescence is imaged while exciting at acceptor wavelength. Unfortunately, these images also contain components of spectral overlap. In addition, **D** also contains a (negative) component of FRET because inevitably some donor emission will be lost due to resonance. This creates a recurrent problem: we cannot calculate s.e. because we do not know the

Fig. 7.1. *Detecting sensitized emission.* (A) Neuronal cell expressing donors (blue) at the membrane and in the nucleus, and acceptors (green) at the membrane and around the nucleus. Lower abundance of the donor in the axon is also depicted. FRET can only occur at the membrane of this cell (lower left panel). (B) Normalized excitation spectra of donors (CFP) and acceptors (YFP). Indicated are the donor- and acceptor excitation lines (left panel) and the two detection channels (bandpass filters). (C) Appearance of signals in the s.e. image. Whereas FRET is restricted to the membrane, due to leak-through of donor signal in the s.e. channel (e.g., in the nucleus; rightmost spectrum) and false excitation of acceptors (e.g., around the nucleus; lower right spectrum and figure B) additional signals are apparent. Note that leak-through and cross-excitation are not restricted to areas stained with either donors or acceptors alone (lower left panel).

donor distribution, and the reason that we do not know this is that we cannot correct it for the unknown s.e. Similarly, the acceptor levels may not be directly derived from **A** if this image also contains some emission of donor molecules that have been cross-excited at the acceptor excitation wavelength and that bleed into the acceptor channel. It would appear that this latter term is always very small, but as we will see later on in this chapter its contribution may become significant when acceptors are present very sparsely and the sensitivity of the acceptor channel is increased to cope with that fact. Thus:

FilterFRET Problem 3: Reference donor- and acceptor images

Relative donor and acceptor levels cannot be determined directly from **D** *and* **A** *images.*

Once proper corrections have been applied to donor, acceptor, and s.e. images (i.e., Problems 1 and 3 have been tackled), we can proceed with Problem 2 and normalize the data. Here, a final important issue is raised: that of absolute quantification. Let us define here the apparent donor FRET efficiency E_D as the fraction of energy quanta absorbed by all donors (whether in complex with an acceptor or not) in a given pixel that is transferred to acceptors (note the difference with FRET efficiency E as defined in other chapters, which is the chance that excitation of the donor in a *donor–acceptor complex* leads to transfer to the acceptor). By definition, both E_D and E should be corrected, normalized, and quantitative measures for interactions. However, the quantitative E_D cannot be simply obtained by dividing corrected **S** and **D** images because **S** and **D** are not to the same scale. That is, even if **S** and **D** share the same excitation settings (which cancels out excitation changes as a source of variance), **D** and **S** are obtained with different "sensitivity" because filter settings, detector gain, and quantum yields of fluorophores are not the same. To be able to directly compare results obtained in different labs and with different setups, we thus have to find a scaling parameter that relates the sensitivity of the setup for donors to that for acceptors.

FilterFRET Problem 4: Getting it quantitative

Corrected s.e. and donor images are not to the same scale because they have been recorded under different conditions.

Luckily, a mathematical framework to solve these problems has been worked out by several groups [1–6] who showed that from just three acquired images **S**, **D**, and **A** quantitative FRET efficiency images can be calculated. This framework relies on calibrations taken from cells expressing either donors only or acceptors only and it allows direct comparison of results obtained around the world.

Before embarking on a detailed treatment of filterFRET, for completion we will briefly treat earlier nonquantitative FRET imaging methods that rely on calculating the ratio of **S** and either **D** or **A**. While not quantitative, ratio imaging is still widely in use because it is very simple and, depending on the biological application, it often gives enough information to provide answers.

7.2. Two-channel ratio imaging

7.2.1. Emission ratio

Emission ratio imaging is extremely popular due to its simplicity and speed. In essence, cells expressing donors and acceptors are illuminated at the donor wavelength and fluorescence intensity data are collected both at donor (**D**) and at acceptor (**S**) channels. Collected data may be either images, or, in case high acquisition speed is crucial and spatial information is not required, dual-channel photometer readings (see Textbox 1). **S** and **D** are not overlap-corrected and "FRET" is simply expressed as the ratio of intensities[1] as: ratio = **S/D**.

[1]Variations on the simple ratio are also encountered in literature, for example, S/(S + D).

Emission ratioing yields some form of normalization (provided that the FRET efficiency is small) and it nicely cancels out light source intensity fluctuations. It does not, however, provide sufficient data to calculate FRET quantitatively in most cases. Nevertheless, there are cases where quantitative FRET data are not needed to still be able to draw biological conclusions. For example, to study agonist-induced changes in FRET, emission ratio data from time-lapse series provide good information on the time course and localization of the induced FRET changes, and a reasonable impression about the magnitude. In addition, a better quantitative feel for the data can be obtained if endpoint calibrations are applicable, for example, if FRET can be experimentally maximized (see Textbox 1) [7–9].

Ratio imaging is particularly suited for single-polypeptide FRET sensors. In these constructs FRET changes are due to altered distance and/or orientation of the donor and acceptor, and since the fluorophores are tethered their stoichiometry is always fixed. Thus, the filterFRET problems are easier to address and, assuming full maturation of both FPs [4], it can in fact be shown that under these circumstances two images suffice to calculate FRET quantitatively (see Textbox 1 and Appendix 7.A.6).

7.2.2. Excitation ratio

In principle, similar information can be obtained from excitation ratioing where acceptor images are acquired at both donor (**S**) and acceptor (**A**) excitation wavelength, and FRET is apparent from ratio = **S**/**A**.

Because of the double exposure, the preparation suffers from increased bleaching and photodamage. Furthermore, split-imaging on charge-coupled-device (CCD) systems (see Textbox 1) is not an option. Nevertheless, excitation ratioing may be an economic choice for laboratories that have an old Fura-imaging setup. These microscopes often allow very fast excitation switching

Textbox 1. **Ratio imaging**

Emission ratio imaging involves collection of **S** and **D** images from the preparation. On wide-field microscopes, **D** and **S** can be sequentially acquired by emission filter switching, for example, using a filter wheel. This requires two consecutive exposures, causing unnecessary photobleaching and raising the risk of errors due to cell movements (Fig. 7.T1). Therefore it is better to collect the images simultaneously, for example, using a commercially available image-splitting device (Fig. 7.T1B) that projects the channels on two halves of the same CCD camera chip. Note, however, that these devices require precise calibration to ensure perfect co-registration of the images. On point-scanning confocal microscopes, simultaneous acquisition of **D** and **S** is also possible and the two images will usually overlap quite well.

Ratio imaging nicely cancels out some of the main complications in the interpretation of wide-field images in that it normalizes fluorescence intensity differences caused by for example, cell height (Fig. 7.T1) as well as possible slow drift in excitation intensity. Light sources invariably are much less stable than detectors. Incidentally, for these reasons emission ratio imaging has been applied for over 3 decades by the Ca^{2+} imaging community.

In Fig. 7.T1C, a special case of emission ratioing is shown. Rather than forming an image, the objective is used to project the emission on a beamsplitter/dual-photometer assembly that simply records the total emission in **S** and **D** channels. Pooling of all the emission photons allows for dimming of the excitation intensity by several orders of magnitude, effectively eliminating photodamage. Whereas spatial resolution is given up, this setup is ideally suited for fast kinetic experiments because it can easily be tuned for sub-ms temporal resolution.

(*Continued*)

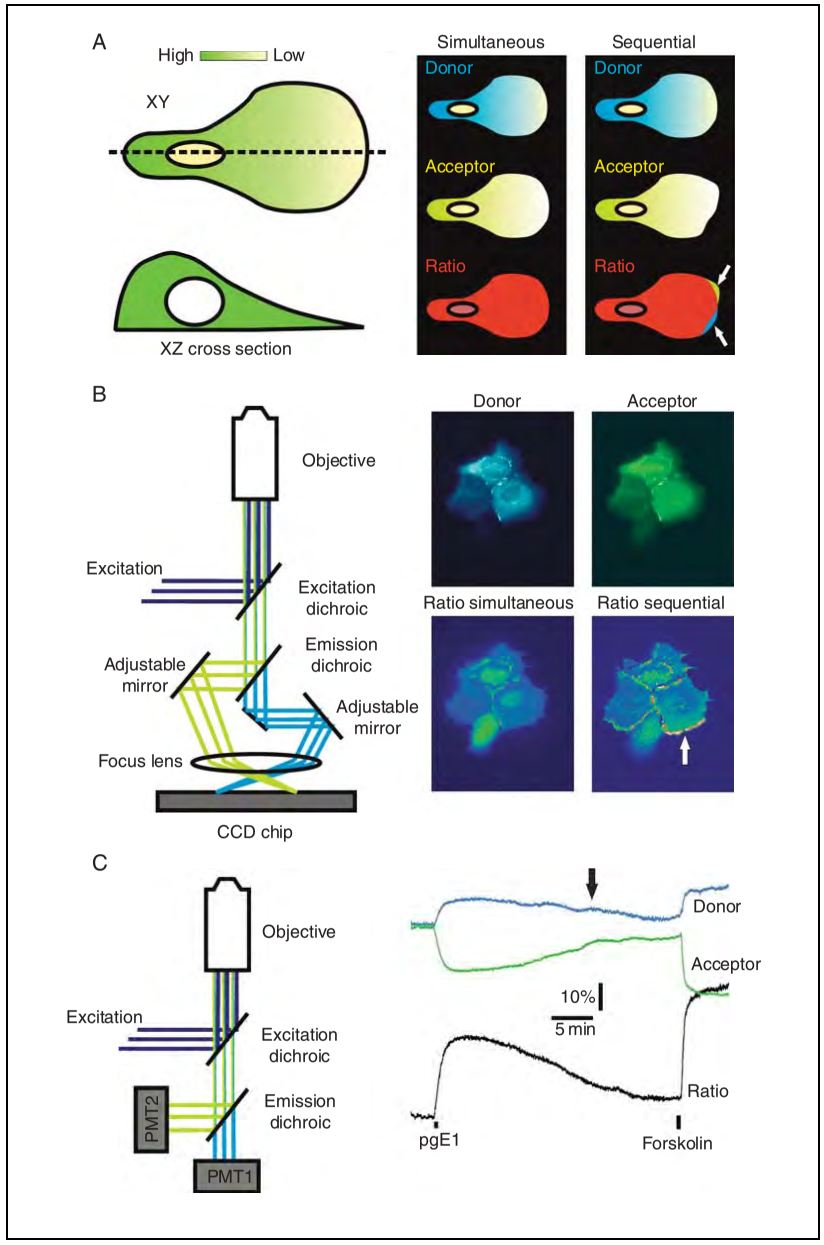

The traces in Fig. 7.T1C show a typical result and also illustrate the use of FRET endpoint calibrations by manipulating the preparation to a state of maximal FRET.

In general, ratio imaging is not quantitative nor is it, strictly spoken, normalized because the acquired data do not permit Problems 1–4 (see Sect. 7.1.1) to be properly addressed. One important exception is the case where donors and acceptors are present at a fixed stoichiometry. Examples of that are the popular single-polypeptide FRET sensors. In this case, the normalization problem (2) is inherently solved and the overlap- and reference-image problems (1 and 3) simplify considerably. It can be shown [1 and Appendix 7.A.6] that in that case FRET efficiency (E) can be calculated from **D** and **S** images.

Fig. 7.T1. *Emission ratio imaging of the cAMP FRET sensor CFP-Epac-YFP* [8]. (A) Ratio imaging largely corrects intensity differences that are due to cell morphology. However, if channels are collected consecutively, any shape changes of the cells cause errors (arrows) in the ratio image that may easily be mistaken for FRET differences. (B). Simultaneous image collection. **D** and **S** are projected side by side on a CCD chip using a commercially available image splitting device fitted to a widefield epifluorescence microscope. The ratio image (lower left photomicrograph) is calculated using Image J; no attempt was made to correct for bleed-through. The lower right ratio image shows errors due to cell movement (images taken 5 s apart) (C) Emission ratioing using a beam splitter and dual photometer setup. Traces represent **D** (blue), **S** (green), and the ratio (black). Since the Epac sensor looses FRET upon binding to cAMP, in this case the ratio was calculated as **D**/**S** to have upward ratio changes correspond with increased [cAMP]. Note that excitation fluctuations (arrow) disappear in the ratio. All data courtesy of B. Ponsioen.

and may be adapted for FRET by a mere filter change. Furthermore, unlike the emission ratio, the ratio **S**/**A** changes linearly with FRET.

7.3. Three-channel measurements: FilterFRET

In this section, FRET will be calculated from sets of three separately acquired images that are chosen to optimally detect s.e. (**S**), donor emission (**D**), and acceptor emission (**A**). Because both the excitation and emission spectra of donor and acceptor overlap extensively, **S**, **D,** and **A** likely also contain leak-through components that have to be subtracted (Fig. 7.2). Just how much leak-through needs to be subtracted depends on calibration values that must be calculated from measurements obtained with special reference samples. Note that in essence our treatment follows and builds on the work of several authors [1–3, 5, 6, 10–12]. Most of the published correction schemes have been worked out for images acquired with a wide-field fluorescence microscope equipped with digital camera [1, 2, 5, 6, 10]; however, a variety of mathematical terminologies has been used. For confocal images, we showed that correction is distinctly more complex because the sensitivities of the detection channels are varied independently [3]. We here present a generalized mathematical framework, with an attempt to arrive at a compromise in terminology.

7.3.1. Sensitized emission

In the following treatment it is assumed that detector gain and offset are correctly adjusted, and that autofluorescence of cells is either negligible or properly subtracted. In addition, it is assumed that the images are shading-corrected; see Sect. 7.4.4. For details on shading techniques, the reader is referred to Nagy et al. and Tomazevic et al. [10, 13]. Provided that independent measurements on the magnitude of cross talk terms can be made, straightforward corrections can be carried out from three acquired images:

- Donor excitation with donor emission, **D**
- Donor excitation with acceptor emission, **S**
- Acceptor excitation with acceptor emission, **A**

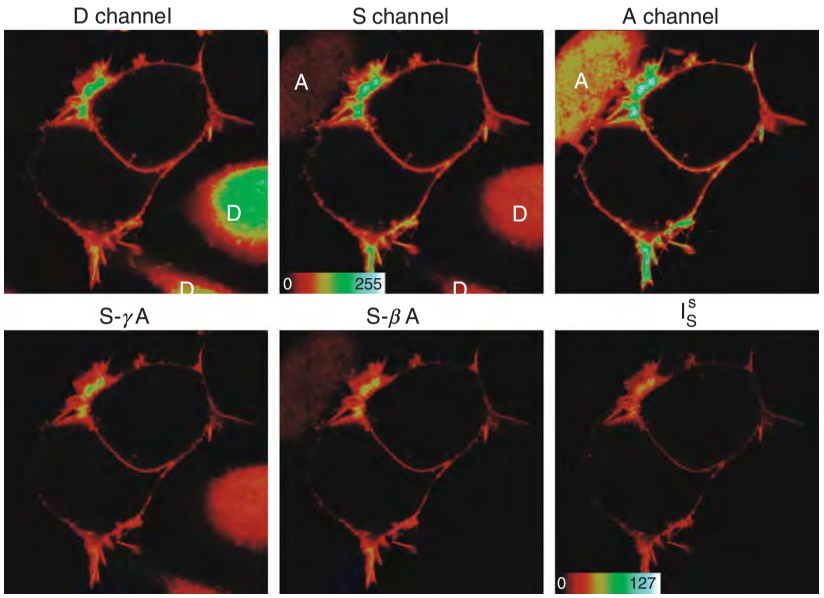

Fig. 7.2. *Sensitized emission calculated from confocal images*. Cells expressing CFP- and YFP-tagged Pleckstrin homology (PH) domains were seeded together with control cells expressing either CFP (marked "D") or YFP (marked "B"). Top row shows raw input files and illustrates donor leak-through (middle panel, "D") and cross-excitation (middle panel, "A"). In the bottom row, **S** images are corrected for cross-excited YFP (left), for CFP leak-through (middle) or according to Eq. (7.8) (right panel). The contrast of the I_S^S panel is stretched twofold as indicated. All images in this chapter are collected with Leica TCS SP2 or SP5 confocal microscopes except for Fig. 7.T1, which was acquired with a Leica ASMDW wide-field epifluorescence microscope equipped with dual-view adapter (Optical Insights). Image acquisition and specimen refocusing were automated from within a custom-made Visual Basic (v6.0) program by calling commands from the Leica macro tool package. ROIs were manually assigned to cells expressing only CFP or YFP and from these, correction factors were measured and calculated. Using these factors, sensitized emission was calculated as outlined in the text.

The acquired images are composite images that consist of fluorescence stemming from different molecular species: donors, acceptors, or FRET pairs (Figs. 7.1 and 7.2). These fluorescent

components are denoted by I (intensity) followed by a capitalized subscript ($_D$, $_A$, or $_S$, for respectively donors, acceptors, or donor/acceptor FRET pairs) to indicate the particular population of molecules responsible for emission of I, and a lower-case superscript (^{d,} ^{a,} or ^{s}) that indicates the detection channel (or filter cube). For example, I_D^d denotes the intensity of the donors as detected in the donor channel and reads as "Intensity of donors in the donor channel," etc. (see Table 7.1).

The terms in the composite images thus are as follows:

- **D** is the sum of the remaining donor fluorescence in the donor channel $\left(I_{D-S}^d\right)$, and of leak-through components of sensitized emission back into the donor channel $\left(I_S^d\right)$ and of cross-excited acceptors back into the donor channel $\left(I_A^d\right)$.

$$\mathbf{D} = I_{D-S}^d + I_S^d + I_A^d \tag{7.1}$$

- **S** contains energy transfer $\left(I_S^s\right)$, leak-through from the "donor minus FRET" population $\left(I_{D-S}^s\right)$ and emission from cross-excited acceptors $\left(I_A^s\right)$.

$$\mathbf{S} = I_{D-S}^s + I_S^s + I_A^s \tag{7.2}$$

- Finally, **A** contains acceptor fluorescence $\left(I_A^a\right)$ and two usually very minor leak-through components: that of the (partially quenched) donor population inappropriately excited at acceptor wavelength and leaking into the acceptor channel $\left(I_{D-S}^a\right)$, and the small amount of sensitized emission that stems from FRET after inappropriate excitation of donors at acceptor wavelength $\left(I_S^a\right)$.

$$\mathbf{A} = I_{D-S}^a + I_S^a + I_A^a \tag{7.3}$$

In the majority of cases, the two cross-terms in this equation can be ignored (i.e., are $\ll 0.01$) and Eq. (7.3) simplifies to:

$$\mathbf{A} = I_A^a \tag{7.3'}$$

TABLE 7.1
Glossary of terms

Symbol	Excitation	Emission	Fluorophore	Indicates
D	Don	Don		raw donor image collected at λ_{ex}^d with donor emission filter (donor channel)
S	Don	s.e.		raw sensitized emission image collected at λ_{ex}^d with the sensitized emission filter (s.e. channel)
A	Acc	Acc		raw acceptor image collected at λ_{ex}^a with the acceptor emission filter (acceptor channel)
I_D^d	Don	Don	Don	unquenched donor signal in the donor channel
I_S^d	Don	Don	s.e.	(acceptor) s.e. leaking through in the donor channel
I_A^d	Don	Don	Acc	cross-excited (at λ_{ex}^d) acceptor emission leaking through in the donor channel
I_D^s	Don(S)[1]	s.e.[2]	Don	leak-through of unquenched donor excited at λ_{ex}^d in s.e. channel
I_S^s	Don(S)	s.e.	s.e.	(acceptor) s.e. signal detected in the s.e. channel
I_A^s	Don(S)	s.e.	Acc	emission of acceptors cross-excited at λ_{ex}^d in the s.e. channel
I_D^a	Acc	Acc	Don	cross-excited (at λ_{ex}^a) signal of unquenched donors leaking through in the acceptor channel
I_S^a	Acc	Acc	s.e.	(acceptor) s.e. in acceptor channel at λ_{ex}^a; this signal derives from the small population of cross-excited donors that leads to FRET

(*Continued*)

TABLE 7.1 (*Continued*)

Symbol	Excitation	Emission	Fluorophore	Indicates
I_A^a	Acc	Acc	Acc	(directly excited) acceptor signal in the acceptor channel
I_{D-S}^d	Don	Don	Don[3]	(partly) quenched donor signal in the donor channel
I_{D-S}^s	Don(S)	s.e.	Don[3]	leak-through of the (partly) quenched donor signal in the s.e. channel
I_{D-S}^a	Acc	Acc	Don[3]	leak-through of the cross-excited, (partly) quenched donor signal in the s.e. channel

The fluorescent components are denoted by I (intensity) followed by a capitalized subscript ($_{D,\,A,}$ or $_S$, for respectively Donors, Acceptors, or s.e.) to indicate the particular population of molecules responsible for emission and a lower-case superscript ($^{d,\,a,}$ or ^{s}) that indicates the detection channel (or filter cube). For example, I_D^d denotes the intensity of the donors as detected in the donor channel and reads as "Intensity of donors in the donor channel," etc. Notes: (1) The excitation in the s.e. channel is generally set up to be equal to that in the donor channel. In case a separate filter cube is used, slight differences may occur, which is denoted by Don(S). See the text and appendix for further details. (2) The s.e. emission filter is usually the same as the acceptor emission filter in confocal determinations. We here designate a different filter to accommodate those wide-field/digital camera experiments that employ different filters for A and S. (3) Here the notation D–S indicates the residual (quenched) donor fluorescence in the presence of the acceptor. In the other chapters this is indicated as DA. Hence: $I_{D-S}^d = I_{DA}^d$; $I_{D-S}^s = I_{DA}^s$; and $I_{D-S}^a = I_{DA}^a$.

For those cases where cross-terms cannot be ignored, we derive an expression in Sect. 7.A.5.

Now, note that each of the leak-through terms in Eqs. (7.1) and (7.2) is just a fixed fraction of the intensity in its "own" channel:

$$I_A^d = \alpha I_A^a \ (= \alpha A) \tag{7.4}$$

$$I_{D-S}^s = \beta I_{D-S}^d \tag{7.5}$$

$$I_A^s = \gamma I_A^a \ (= \gamma A) \tag{7.6}$$

$$I_S^d = \delta I_S^s \tag{7.7}$$

where α is the ratio of pure acceptor fluorescence detected using donor/acceptor filters, β is the leak-through of pure donor fluorescence in the acceptor (s.e.) channel, δ that for leak-through of sensitized emission back into the donor channel, and γ relates acceptor fluorescence excited at donor wavelength and detected in the s.e. channel to the acceptor fluorescence excited at acceptor wavelength and detected in the acceptor channel. Further, it can be easily shown that $\alpha = \gamma\delta$ (see Textbox 2 and Appendix).

We can thus rewrite Eqs. (7.1) and (7.2) to:

$$\mathbf{D} = I_{D-S}^d + \delta I_S^s + \gamma\delta\mathbf{A} \tag{7.1B}$$

$$\mathbf{S} = \beta I_{D-S}^d + I_S^s + \gamma\mathbf{A} \tag{7.2B}$$

which rearranges to [3]:

$$I_S^s = \frac{\mathbf{S} - \beta\mathbf{D} - \gamma(1-\beta\delta)\mathbf{A}}{1-\beta\delta} \tag{7.8}$$

Sensitized emission $\left(I_S^s\right)$, as defined in Eq. (7.8), reliably measures the *relative* amount of energy transfer occurring in each pixel (Fig. 7.2, lower right panel). I_S^s is corrected for spectral overlap (i.e., Problem 1 has been taken care of); however, unlike E, it is not a normalized measure for interaction nor is it quantitative in absolute terms. It depends on the specific biological question which of the two yields the most relevant information.

7.3.2. FRET efficiency

Having obtained the s.e. image I_S^s, which provides a spatial map of molecular interactions in the cell, the next steps are normalization and absolute quantification of the interactions. Normalization can

Textbox 2. **The leak-through parameters**

The correction factors α, β, γ, and δ must be determined independently. From Eqs. (7.4) to (7.7), it is clear that estimates for α, γ, and δ can be obtained by imaging a sample with only acceptor molecules and calculating:

$\alpha = \mathbf{D}/\mathbf{A}$ leak-through of cross-excited acceptors back into the donor channel
$\gamma = \mathbf{S}/\mathbf{A}$ cross excitation of acceptors
$\delta = \mathbf{D}/\mathbf{S}$ leak-through of s.e. back into the donor channel

Similarly, β is estimated from a sample with only donor molecules:

$\beta = \mathbf{S}/\mathbf{D}$ leak-through of donors into the s.e. channel

Note that parameters β and δ depend on signal amplifications in the utilized detectors and on the elements in the optical path (optical filter, spectral detection bands) only, while α and γ are additionally influenced by relative excitation intensity. This is usually a fixed constant in wide-field microscopy but in confocal imaging laser line intensities are adjusted independently. Furthermore, note that the α factor equals δ multiplied by γ (see Appendix for further detail).

be carried out through division of the s.e. image by a pure donor image to arrive at the "*apparent* FRET efficiency" (not to be confused with the quantitative E_D):

$$^{\text{app}}\text{FRET}_D = I_S^{\text{s}}/I_D^{\text{d}} \tag{7.9}$$

where the denominator represents the total donor fluorescence as it would appear in the absence of FRET. That is, the pure donor image in the denominator has to be corrected for leak-through components and for loss of donor emission due to FRET (Problem 3) [1, 3, 5, 6].

Sometimes normalization to the acceptor image is encountered:

$$^{\text{app}}\text{FRET}_A = I_S^{\text{s}}/I_A^{\text{a}} \tag{7.10}$$

This is easier because the acceptor image is readily available (Eq. (7.3′)) without further corrections. $^{\text{app}}\text{FRET}_A$ and $^{\text{app}}\text{FRET}_D$ are not quantitative in that nominator and denominator images are acquired in different channels. Thus, their relative magnitude depends on filter settings, detector gain, on donor and acceptor quantum yield and, in the case of $^{\text{app}}\text{FRET}_A$, also on relative excitation intensities. While neither $^{\text{app}}\text{FRET}_A$ nor $^{\text{app}}\text{FRET}_D$ solve the problem of quantification, both are frequently encountered in the literature and both do allow quantitative comparison of interactions *within the same image*.

In order to obtain the desired quantitative measure of FRET (Fig. 7.3), an additional correction factor must scale the nominator to the denominator in Eq. (7.9) [1–3, 6]. In other words, we must relate the FRET-induced sensitized emission in the **S** channel to the loss of donor emission in the **D** channel as in:

$$E_D = \frac{\text{Loss in donor emission due to FRET}}{\text{Total donor emission in the absence of FRET}} \tag{7.11}$$

or in our terminology:

$$E_D = \frac{I_D^{\text{d}} - I_{D-S}^{\text{d}}}{I_D^{\text{d}}} = 1 - \frac{I_{D-S}^{\text{d}}}{I_D^{\text{d}}} \left(= 1 - \frac{I_{DA}}{I_D} \right) \tag{7.11A}$$

Note that the "*Loss in donor emission due to FRET*" (Eq. (7.11)) is just a constant times the "*sensitized emission*" (Eq. (7.8)) for given acquisition settings, or $I_{\text{Loss}}^{\text{d}} = \phi I_S^{\text{s}}$. Thus (noting that both $I_{\text{Loss}}^{\text{d}}$ and ϕ have negative values):

$$I_{D-S}^{\text{d}} = I_D^{\text{d}} + I_{\text{Loss}}^{\text{d}} = I_D^{\text{d}} + \phi I_S^{\text{s}} \tag{7.12}$$

Now it is straightforward to solve for I_D^{d} and I_{D-S}^{d}. Substituting Eq. (7.12) in Eq. (7.2B), **S** and **D** become:

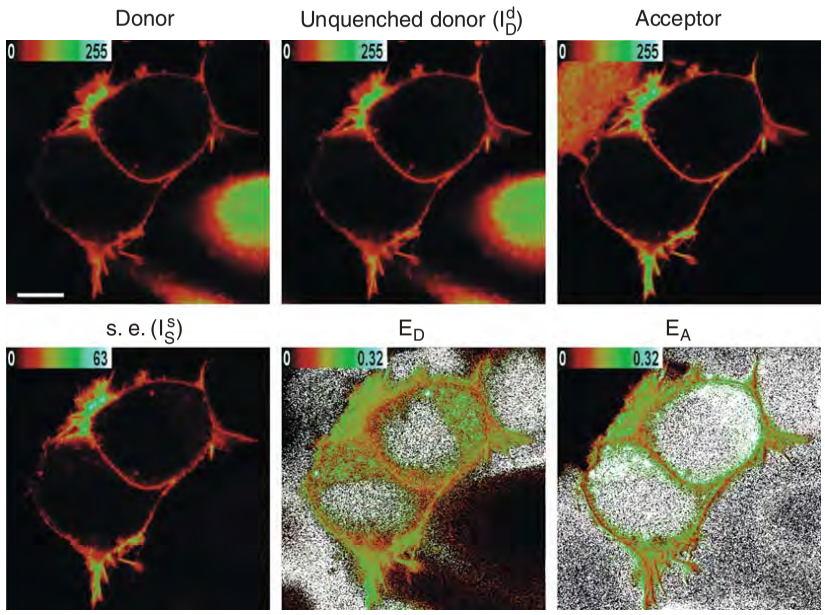

Fig. 7.3. Fret efficiency. The unquenched donor image (top row, middle panel), as calculated according to Eq. (7.13), and the acceptor image (top right panel) are used to normalize the s.e. image. The resulting images E_D and E_A (Eqs. (7.10) and (7.11), respectively) are quantitative, as detailed in the text. Unfiltered, raw data are shown. Scale bar is 12 μm.

$$\mathbf{D} = I_D^{\mathrm{d}} + (\phi + \delta) I_S^{\mathrm{s}} + \gamma\delta\mathbf{A} \tag{7.1C}$$

$$\mathbf{S} = \beta I_D^{d} + (\beta\phi + 1) I_S^{s} + \gamma\mathbf{A} \tag{7.2C}$$

Combining Eqs. (7.8) and (7.1C):

$$I_D^{\mathrm{d}} = \frac{\beta\phi + 1}{1 - \beta\delta}\mathbf{D} - \frac{\phi + \delta}{1 - \beta\delta} S + \gamma\phi\mathbf{A} \tag{7.13}$$

defining

$$\zeta = \frac{\beta(\phi + \delta)}{1 - \beta\delta} \tag{7.14}$$

then:

$$I_D^{\mathrm{d}} = (\zeta + 1)\mathbf{D} - \frac{\zeta}{\beta}\mathbf{S} + \gamma\left(\delta - \frac{\zeta}{\beta} + \delta\zeta\right)\mathbf{A} \tag{7.13B}$$

Note that this equation is identical to the expression for unquenched donor fluorescence of van Rheenen et al. (Eq. (A17)).

And for I_{D-S}^{d} we can derive the following expression after combining Eqs. (7.1B) and (7.2B):

$$I_{D-S}^{\mathrm{d}} = \frac{\mathbf{D} - \delta\mathbf{S}}{1 - \beta\delta} \tag{7.15}$$

Thus, we now have the results to express E_D as:

$$E_D = 1 - \frac{I_{D-S}^{\mathrm{d}}}{I_D^{\mathrm{d}}} = 1 - \frac{\mathbf{D} - \delta\mathbf{S}}{(\beta\phi + 1)\mathbf{D} - (\delta + \phi)\mathbf{S} + \phi(1 - \alpha\beta)\mathbf{A}} \tag{7.16}$$

7.3.3. Making it quantitative

One final step is needed to wrap things up: the factor ϕ (which relates the s.e. in **S** to loss of donor fluorescence in **D**) that was introduced to solve for I_D^{d} must be determined. Note that for a given combination of filter settings and fluorophores ϕ is a constant, independent from expression levels and excitation intensity. For the popular cyan fluorescent protein (CFP)/yellow fluorescent protein (YFP) FRET pair, we have mostly used a very intuitive approach that employs Yellow Cameleon, the well-known single-polypeptide intracellular Ca^{2+} sensor. This construct shows significant FRET change upon raising intracellular Ca^{2+} concentration with, for example, ionomycin [7]. Recording **D** and **S** before and after ionomycin-induced Ca^{2+} saturation of Yellow Cameleon gives paired observations for Eqs. (7.1C) and (7.2C) that differ only in FRET efficiency. The increase in **S** is:

$$\begin{array}{r} \mathbf{S}(\text{post}) = \beta I_D^{\text{d}} + (\beta\phi + 1) I_S^{\text{s}}(\text{post}) + \gamma \mathbf{A} \\ \mathbf{S}(\text{pre}) \;\; = \beta I_D^{\text{d}} + (\beta\phi + 1) I_S^{\text{s}}(\text{pre}) \;\; + \gamma \mathbf{A} \\ \hline \mathbf{S}(\text{post}) - \mathbf{S}(\text{pre}) = (\beta\phi + 1)\big(I_S^{\text{s}}(\text{post}) - I_S^{\text{s}}(\text{pre})\big) \end{array} \text{subtract} \quad (7.17)$$

And for the change in D:

$$\begin{array}{r} \mathbf{D}(\text{pre}) \;\; = I_D^{\text{d}} + (\delta + \phi) I_S^{\text{s}}(\text{pre}) \;\; + \gamma\delta \mathbf{A} \\ \mathbf{D}(\text{post}) = I_D^{\text{d}} + (\delta + \phi) I_S^{\text{s}}(\text{post}) + \gamma\delta \mathbf{A} \\ \hline \mathbf{D}(\text{pre}) - \mathbf{D}(\text{post}) = -(\delta + \phi)\big(I_S^{\text{s}}(\text{post}) - I_S^{\text{s}}(\text{pre})\big) \end{array} \text{subtract} \quad (7.18)$$

Dividing Eq. (7.17) by Eq. (7.18) gives:

$$\frac{\mathbf{S}(\text{post}) - \mathbf{S}(\text{pre})}{\mathbf{D}(\text{pre}) - \mathbf{D}(\text{post})} = -\frac{\beta\phi + 1}{\phi + \delta} \equiv G \quad (7.19)$$

or[2]

$$\phi = -\frac{1 + \delta G}{\beta + G} \quad (7.20)$$

Note that G as derived here relates the FRET-induced sensitized emission in the **S** channel to the loss of donor emission in the **D** channel and that it is identical to the correction factor γ/ξ [2] or G [6, 14]. Note however, that if the correction factors β or δ change, G and ϕ change as well. In contrast, our correction factor ζ [3] is a constant that depends only on fluorophore properties and filter settings, and therefore it does not change with excitation intensity or detector gain. This is a clear advantage for confocal filterFRET. ζ (Eq. (7.14)) and G (Eq. (7.19)) are related as:

$$G = -\beta\left(1 + \frac{1}{\zeta}\right) \quad (7.21)$$

[2]Note that we have slightly rearranged the math from van Rheenen et al, BJ 2004 to adopt the correction factor G that is used in several publications.

and

$$\zeta = -\frac{\beta}{\beta + G} \quad (7.22)$$

Of course any of the many cytosolic constructs that can be forced to change FRET are useful for calibration, as long as the fluorophores are the same as those used in the experiments. We have for example also successfully used caspase-cleavable GFP-mRFP chimera (unpublished results).

Several other approaches to solve the quantitation problem have been proposed. Hoppe et al. [2] determined γ/ξ by calibrating it against constructs with known FRET efficiency. We and others [3, 6] have used data from a cell before and after acceptor photobleaching to relate the FRET-induced sensitized emission in the **S** channel to the loss of donor emission in the **D** channel by factors termed ζ or G, respectively. For the CFP/YFP pair this works very well on confocal microscopes with a 514-nm Argon ion laser line, but on wide-field systems, selective acceptor photobleaching reportedly causes problems [14]. Finally, G can also be determined by comparison of several constructs that differ in FRET efficiency, a bit analogous to the Yellow Cameleon calibration described above [10, 14].

7.3.4. Stoichiometry

The FRET efficiency E_D as determined above is the fraction of energy quanta absorbed by all donor molecules that is transferred to acceptors. For a given pixel, E_D effectively reflects both the efficiency with which paired donor–acceptors transfer energy (E) and the fraction of molecules in that pixel that pair up (f_D). This means, for example, that a pixel with $E_D = 0.2$ may result from 100% of donors having $E = 0.2$, or from 20% of donors having $E = 1$, or anything in between. The FRET efficiency E of a donor/acceptor pair (termed characteristic FRET efficiency, E_c in some literature [2, 3]) is most often unknown.

However, if a good estimate of E can be made, the fraction of donors in complex can be readily calculated as

$$f_D = \frac{E_D}{E} \tag{7.23}$$

The cases where reliable determination of E is possible are those where good assumptions can be made based on known fluorophore dipole alignment and distance and those where the donors and acceptors can be induced to quantitatively engage in interactions (for example, by determining FRET in an (in vitro) preparation of a 1:1 donor–acceptor mix, or by inducing maximal interaction in a single-polypeptide FRET sensor such as Yellow Cameleon or CFP-Epac-YFP, see Figure in Textbox 1). In vivo, usually many uncertainties exist that prevent determination of E. For example, distance and orientation of donors and acceptors may be variable and FRET may also occur between molecules that just happen to come within resonance range (sometimes called spurious- or collision FRET). This latter effect is very small for molecules in solution, but it dramatically increases when the donors and acceptors are concentrated in cell organelles. For example, even donor- and acceptor-tagged molecules that are distributed randomly (i.e., not clustered) at the membrane will yield significant FRET despite moderate expression levels (for analysis, see Appendix of van Rheenen et al. [15]). Thus, E_D reflects both intra- and inter FRET-pair resonance, and consequently f_D would be overestimated (which incidentally also holds true for the determination of E or f_D using FLIM). Usually I_S^s, E_D, and E_A can be reliably determined, but in the vast majority of FilterFRET or FLIM experiments E and f_D will be unknown.

Unlike donor-based FRET methods like FLIM, filterFRET also yields spatial information on the acceptor population. This means that in addition to querying donor-FRET (by solving for E_D or I_D^d), we can also assess the relationship between sensitized emission and the acceptor population. At 1:1 stoichiometry obviously E_D should equal the acceptor-normalized efficiency E_A. In other cases, E_A deviates from E but sometimes can yield biologically more relevant information than E_D or E. For example, dislocation of 50% of the donors from an organelle decorated with donor–acceptor pairs into the cytosol might leave 50% of acceptors unpaired at the organelle. E_D would in this case report that the remaining 50% donors still interact just as efficiently, whereas E_A clearly reveals the lowered acceptor occupation by dropping with 50%.

What is the donor/acceptor ratio in a given cell? Again, this ratio cannot be directly derived because it concerns two quantities that stem from fluorophores with different properties (absorption coefficient, quantum yield, spectra) and that emit into two channels differing in gain, filters, and excitation intensity. Thus, the (overlap corrected) intensity of acceptors in channel **A** will be a factor k times that of donors in D, at equimolar concentrations,[3] or:

$$kI_A^a = I_D^d \tag{7.24}$$

For a first approximation, k can be simply calculated by dividing I_D^d by I_A^a for a donor–acceptor fusion construct, because both quantities are corrected for overlap and FRET. Note however that this requires ϕ to be known (see Sect. 7.3.3). For the ratio of donor to acceptor concentration, we simply find:

$$\frac{[\text{donor}]}{[\text{acceptor}]} = k\frac{I_D^d}{I_A^a} \tag{7.25}$$

Or, in the case of confocal acquisition[4]

$$\frac{[\text{donor}]}{[\text{acceptor}]} = \gamma\sigma\frac{I_D^d}{I_A^a} \tag{7.25B}$$

[3]Termed k in [1]; α in [10]; R in [7], $\kappa\gamma$ in [17].

[4]For confocal imaging with tunable gains, k is not constant. Rather, we can distinguish a fixed part (which relates the efficiency of donor excitation at donor wavelength to that of acceptor excitation at acceptor wavelength) and a part that depends on relative excitation intensities and gains. The former was termed κ in van Rheenen et al. [3] but to keep κ in line with the terminology used in this volume that factor will here be renamed to σ, such that $k = \gamma\sigma$. Also, see Appendix.

Of actual interest to the biologist is usually not the quantification of donor, acceptor, and donor–acceptor, but rather to estimate the concentrations of the interacting proteins and the extent of their interactions, regardless of their labeling state. It is obvious that if the interacting proteins are incompletely labeled (for example, due to the presence of an endogenous population of untagged proteins, or due to imperfect maturation of FP labels) FRET recordings will significantly underestimate the amount of interactions between the proteins. Formalisms to cope with incomplete labeling have been put forward by several groups [2, 4, 16].[5] Inasmuch as such formalisms rely on calibration using donor–acceptor tandem constructs, it is important to note that we observed that speed of maturation of a given FP may dramatically vary from construct to construct [17].

7.4. Optimizing image acquisition

As the I_S^s, E_D, and E_A images are calculated from the raw input images, it is extremely important that **D**, **S,** and **A** are of the best possible quality. In addition, care must be taken that correction factors are derived from reference images taken at exactly the same

[5]Wlodarczyk and coworkers consider that labeling may be incomplete for 2 two reasons: first, not all proteins may become labeled (either in the chemical crosslinking process, or in the case of FP-labeling, due to the presence of endogenous proteins), and second, existing labels may be non-fluorescent, for example due to poor maturation of FPs, or due to photobleaching. Be p_d and p_a the probability that a given molecule of type a and d receive a functional label, respectively, then the concentration of fluorescent donors equals p_d times the total concentration of d plus $(1–p_d)$ times the concentration of complexes, or, in their terminology,

$[D] = p_d.[d] + (1–p_a)[da]$. Analogously,
$[A] = p_a.[a] + (1–p_d)[da]$ and
$[AD] = p_d p_a[da]$.

Provided that proper estimates of p_a and p_d are present, quantitative estimates of interactions can be readily achieved for certain types of experiments.

imaging conditions. In this part, possible pitfalls will be discussed and strategies to improve image quality will be lined out.

7.4.1. Wide-field versus confocal FilterFRET: A comparison

FRET imaging differs enough between wide-field fluorescence microscopes and confocal microscopes to warrant a comparison of the two techniques in this chapter. Confocal imaging offers significant advantages over wide-field imaging because it produces crisp optical sections of the preparation. Furthermore, point-scanning confocals offer greater freedom in image acquisition by allowing free choice of zoom and resolution and independent tuning of channel sensitivities through adjustment of the voltage of the photomultiplier tubes (PMTs). Confocal imaging is also more easily combined with acceptor photo bleaching and with fluorescence recovery after photobleaching (FRAP) experiments. On the other hand, wide-field fluorescence setups offer the freedom to filter-select whatever excitation wavelength desired, and the CCD detectors are more sensitive than PMTs. CCD imaging also is less harsh for the cells than laser point-scanning, although careful tuning of the confocal excitation regime can remedy that for a large part.

These differences have important consequences for filterFRET imaging. The major complication posed by confocal acquisition is that relative sensitivities for **D**, **S**, and **A** are tunable. This is true even if identical filter and pinhole settings are used from experiment to experiment since in general the user wants to fine-tune the excitation line intensities and to control individual PMT gain (high voltage) and offset settings for the channels. With CCD acquisition, weaker fluorescent cells are imaged by increasing the integration time, which causes both I_D^d, I_S^s, and I_A^a as well as the leak-through terms to increase linearly. As a result, when leak-through factors for particular fluorophores and a particular filter set have been quantified once, alterations in integration time can be easily compensated for. In the confocal case, however, unless laser

intensity and PMT settings are kept fixed, this is not possible, due to the nonlinear dependence of gain and offset on the PMT high voltage. This necessitates that β, γ, and δ are determined after each change in setting. The advantage—on the other hand—is that the added flexibility allows simultaneous optimized acquisition of the often weak FRET signals without compromising acquisition time.

Because on CCD setups excitation for **D**, **S**, and **A** images is usually filter-selected from a single white light source the relative intensity of excitation is approximately fixed. Confocal microscopes use separate laser lines, often from distinct lasers, that can (and for optimal imaging should) be independently adjusted. Thus, on CCD setups γ (Eq. (7.6)) is constant for a given set of filters whereas on the confocal, it varies from image to image (also, see Sect. 7.4.2).

A final distinction is that on confocal microscopes **S** and **A** images are commonly acquired with the exact same emission filter settings whereas for CCD microscopes they typically involve physically separate- and therefore slightly different—filter cubes.[6] This simplifies the calculation of leak-through terms [3]. In Appendix of this chapter, we rather generalized the treatment of filterFRET by not making assumptions on the filter settings for **S** and **A**.

These differences add up to one major distinction: on wide-field imaging setups, it suffices to calibrate the setup *just once* for a given set of filters and fluorophores, and then use it for weeks or months without bothering about it. In contrast, for confocal filterFRET imaging, calibrations must be made every time a gain setting or laser line is adjusted, and preferably, for every image.

7.4.2. Temporal errors: Laser intensity fluctuation

On a variety of confocal microscopes, we and others [3, 18] observed considerable drift as well as oscillations (on a time scale of

[6]Unless a dual-excitation filter cube is used, in combination with a excitation switcher.

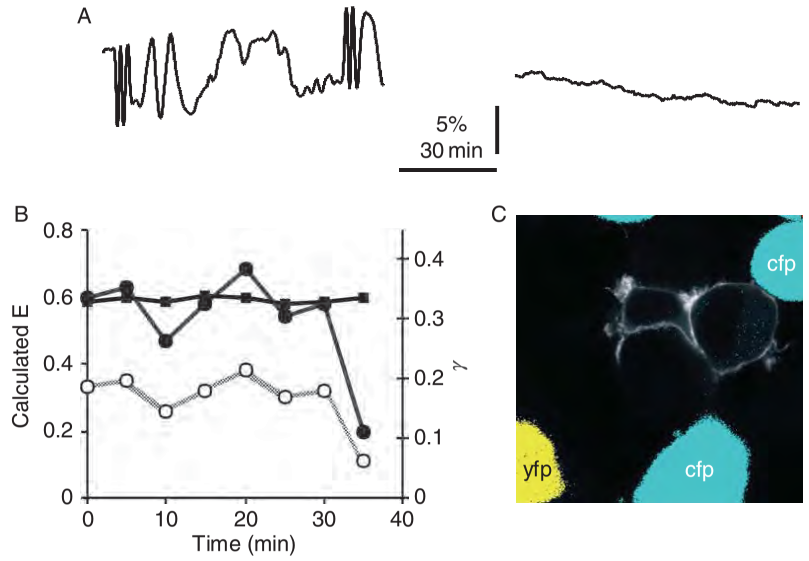

Fig. 7.4. *Correcting excitation fluctuations by inclusion of reference cells.* (A) Fluctuations in the intensity of a 514-nm argon ion laser line (left) and a mercury arc lamp (right), measured every 20 s for a 3 h time period. (B) Calculated E_D (solid circles; left axis) is seen to fluctuate significantly in time-lapse experiments. After 30 min a large intensity fluctuation in acceptor excitation was simulated by manually diminishing laser power with 60%. The open circles depict the correction factor γ, calculated according to Eq. (7.6) from cells expressing acceptors only. Calculating E_D with the online-updated γ-factor (solid squares) abolished the effects of excitation fluctuations. (C) Preparation containing FRET cells (gray) and CFP- and YFP reference cells (blue and yellow), as recognized by automated segmentation based on the ratio of intensity of donors and acceptors.

one to a few minutes) in excitation line intensity (Fig. 7.4A). Changes of several percent are common, while worst-case variations of up to 20% were found in poorly aligned systems. Importantly, individual laser lines fluctuate independently, even when derived from the same laser. Excitation stability is extremely important because it influences γ. While intensity variations may also occur in arc lamps on wide-field fluorescence microscopes, these changes are often much smaller (compare Fig. 7.4 A left and right

panels). Furthermore, slow arc lamp intensity variations affect **D**, **S,** and **A** to the same degree if images are gathered in rapid succession, and thus have no effect on the apparent FRET image (Eqs. (7.9) and (7.10)).

The independent variations in laser line intensity on confocal systems pose a major problem for time-lapse FRET measurements. The supplier of our TCS-SP2 confocal installed a stabilization loop that improved the stability considerably, but not completely. In particular when expected FRET signals are a small fraction of the total fluorescence, the realized stability of ~3% will prevent acquisition of meaningful results. We therefore implemented online correction by recalculating the leak-through factors α, β, γ, and δ for each image [3], as well as G or ϕ (Eqs. (7.4)–(7.19)). To this goal, the cells under study are plated together with a mix of cells expressing either donors or acceptors on the same cover slip (Figs. 7.2 and 7.3). In an image taken at low zoom factor, regions of interest (ROIs) are assigned to single donor- or acceptor transfected cells (Fig. 7.4B and C). Then correction factors are determined from these ROIs as detailed in Eqs. (7.4)–(7.7). E_D and s.e. images are thus calculated using correction factors taken simultaneously with (or just before, in case one wants to zoom in) the FRET cell. This procedure completely removes the effect of laser fluctuations, resulting in superior registration of FRET during acquisition of time-lapse series.

As an alternative, changes in relative intensity of the laser lines may be directly recorded using for example, reflection images or a transmission detector, and γ may be adjusted accordingly. In our experience, this works significantly less reliable.

7.4.3. Co-registration of the input images

Obviously, it is of the utmost importance that the three input channels spatially overlap tightly, both in lateral and in axial direction. Co-registration (i.e., the precise, pixel-by-pixel correspondence of

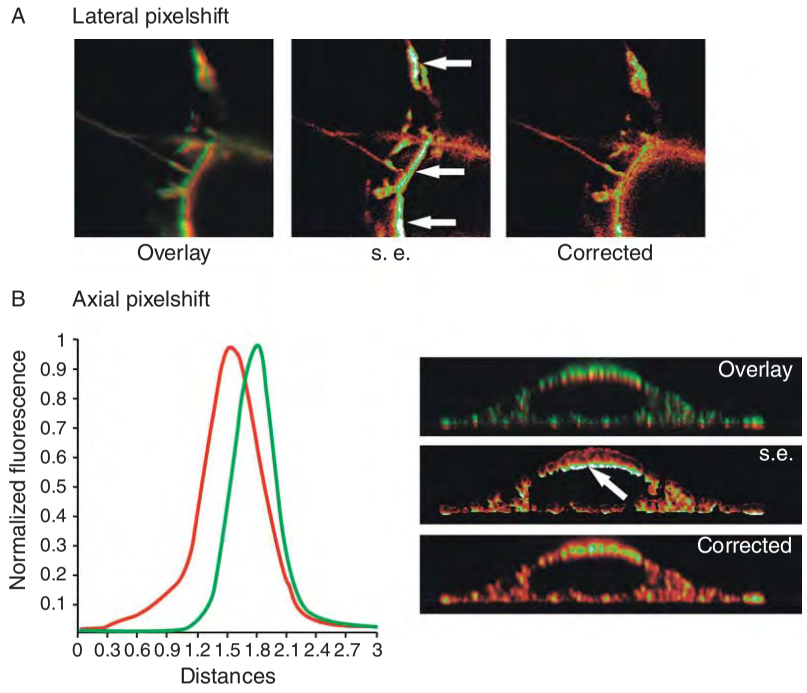

Fig. 7.5. *Effects of poor co-registration on calculated FRET images.* (A) Typical artifacts due to improper alignment (left) of raw input images caused by switching between unmatched filter cubes. The consistent appearance of high FRET values at the right side of bright structures (middle) is a sure indication to check image alignment. Right panel, proper alignment of the images corrects FRET artifacts. (B) Left panel, profiles of fluorescence intensities in a confocal X/Z image of the green emission (525 nm) of a 0.17-microm bead was registered using a HCX PL APO CS 63× objective upon 430-nm (blue line) and 514-nm (red line) excitation. Both scans use detection at 525 nm, demonstrating the extent of axial offset. Right panels, confocal images were acquired from a cell expressing CFP- and YFP-tagged membrane anchors. Top image, green–red overlay illustrates axial offset. Erroneous values (middle image) in the calculated I_S^s (s.e.) image are effectively corrected by using the refocusing macro routine (lower image). Shown are extreme examples.

D, **S,** and **A**) has to be checked meticulously by the experimenter, using for example, color overlay images (Fig. 7.5A). Pixel-shift deviations are common on CCD imaging setups where they are

caused by slight differences in filter cube alignment. When image-splitting devices are used, extensive adjustment for optimal co-registration is always necessary. In contrast, lateral overlay of confocal channels should be excellent for a well-maintained instrument. If needed, co-registration of channels can be easily optimized postacquisition by software pixel-shift algorithms.

Axial co-registration is also important, although it is often completely ignored. Compared with wide-field microscopy, possible focusing deviations (deviations due to offset of donor- and acceptor images in the axial direction) are emphasized by the confocals inherent optical sectioning. When the input images are effectively taken from slightly different planes in the cell, erroneous results occur during calculation of the sensitized emission that are often apparent as margins of unexpected high or low FRET values around an object (Fig. 7.5B).

Two main sources for this type of deviation exist: chromatic aberrations within the objective and other optics, and, for confocals, slight differences in the collimation of the laser beams. Chromatic aberrations are due to the wavelength dependency of the refractive index of optical glasses, which causes axial misregistration of images taken at different wavelengths [19]. Depending on the objective used, chromatic aberrations may be several micrometers (worst case). Chromatically corrected objectives are available, but it should be stressed that these are optimized only for a limited part of the spectrum, typically the mid-visible range. Therefore, significant chromatic aberration may still be present outside this range. For example, using a good, standard corrected 63×, 1.32 NA oil immersion objective (HCX PL APO CS, #506180, Leica), we noticed focusing deviations of about 400 nm (Fig. 7.5B) between the 430 and 514 nm laser lines used to excite the CFP/YFP FRET pair. Use of a UV-corrected 63× objective (HCX PL APO lbd.BL, #506192, Leica) significantly, but not completely, remedied this chromatic aberration. Chromatic focusing deviations are not limited to violet wavelengths because significant deviations exist for dye pairs excited throughout the visible

spectrum (Table 7.1 in [3]). In addition, chromatic aberrations vary with lens types, and even for different objectives of the same type (L. Oomen and K.J., unpublished; [18]). Axial focusing errors also exist in CCD images but here they usually go unnoticed because of the poor axial resolution of wide-field fluorescence microscopes.

A more generic approach to overcome focusing deviations can be implemented if the setup is equipped for fast fine-focusing. First, **D** and **S** images are recorded at donor excitation. Then, before taking the **A** image at acceptor excitation, the preparation is refocused to minimize chromatic aberration. Because for a given combination of objective and excitation lines the focus deviation is constant, the correction distance needs to be determined only once. We used XZ-scanning of fixed cells or fluorescent beads for this goal. Applying this focus correction in an automated acquisition routine (macro), **D**, **S,** and **A** images are collected from the same focal plane in the biological sample (Fig. 7.5B).

7.4.4. Shading

Lateral intensity errors may be present over the entire image and occur on CCD and confocal systems alike. For CCD systems, a standard correction algorithm exists: corrections are carried out by normalizing pixel intensities using a reference image, a procedure called shading correction [13]. On the confocal system with independent excitation lines, these deviations are often more pronounced because spatial excitation intensities vary independently (L. Oomen, L. Brocks and K.J., unpublished; [18]). For example, when measuring excitation inhomogeneities for the 430 and 514 nm CFP/YFP lines by imaging a solution of the FRET calcium sensor Yellow Cameleon [7], we observed very significant deviations from unity flatness (Fig. 7.6). The 430 nm excitation intensity dropped by as much as 50% at the image corners, while 514 nm deviated by about 15% (data not shown). Importantly, significant differences (up to 20%) also occurred in the center of the images. Deviations of

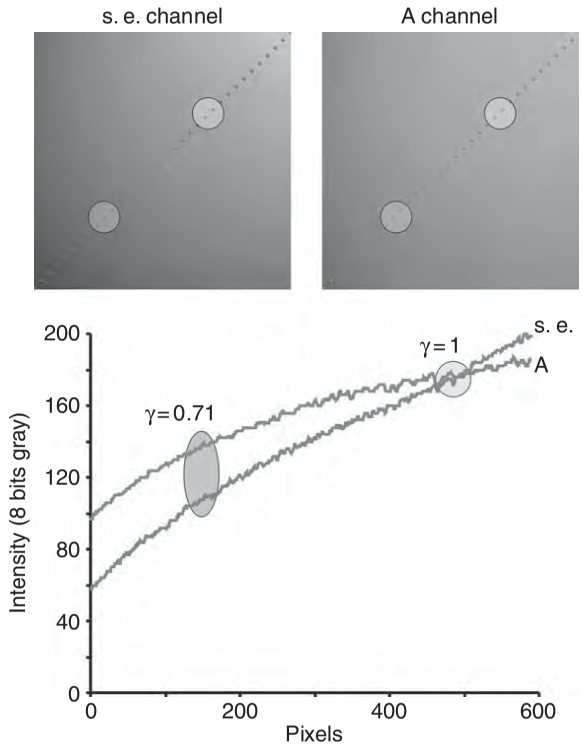

Fig. 7.6. *Shading errors: Lateral image intensity errors*. Shown are parts of reference images (1024 × 1024) that were acquired by averaging eight confocal images of a solution of Yellow Cameleon at 430-nm excitation (upper left panel) and at 514-nm excitation (upper right panel), both detected at 525–570 nm. Note that due to significant differences in shading at these two excitation wavelengths, the γ value (calculated according to Eq. (7.6)) may vary by ~25% in either direction, causing significant errors in calculated FRET. Images were collected with a 63× oil immersion objective without zooming. Note that similar, albeit smaller, differences were observed when 458 and 514 nm laser lines (both derived from the same argon ion laser) were compared.

this magnitude are not uncommon in confocal systems [18], and they are often diminished by increasing the zoom factor.

Shading correction is simply carried out by measuring the fluorescence of solutions of dyes that are spectrally similar to the donor and acceptor. The fluorescence of these reference images is then

normalized to a standard, and all **D**, **S,** and **A** images are divided by their cognate reference standard. Correction factors and FRET images are only calculated after applying the shading correction. In our experience, shading correction is crucial to obtain good FRET images.

7.5. *Postacquisition improvements and analysis*

When optimal input pictures are obtained whilst observing all the above corrections and precautions, the raw calculated FRET images nonetheless often are quite disappointing and complicated to interpret. See for example the I_S^s, E_D, and E_A images in Fig. 7.3. To blame are noise in the FRET images and the way our eyes handle that.

7.5.1. *Noise in FRET images*

Even in the nominal absence of laser fluctuations or other image-degrading aberrations, the number of photons that hit the detector during the data collection period of the image (i.e., the exposure time for a CCD image or the pixel dwell time for a confocal image) will contain considerable noise. The photon count x follows a Poisson distribution (Fig. 7.7A) with mean value μ as

$$p(x) = \frac{\mu^x e^{-\mu}}{x!} \tag{7.26}$$

It can be shown that the standard deviation (SD) of this distribution is also just $\sqrt{\mu}$. In other words, if one would repeatedly measure the same pixel that on average collects 100 photons during a single dwell time (a normal value for a rather bright confocal image!!) one would record less than $100–2\times\sqrt{100} = 80$ photons or more than $100 + 2\times\sqrt{100} = 120$ photons just by coincidence in ~5% of the measurements. This uncertainty is expressed as the

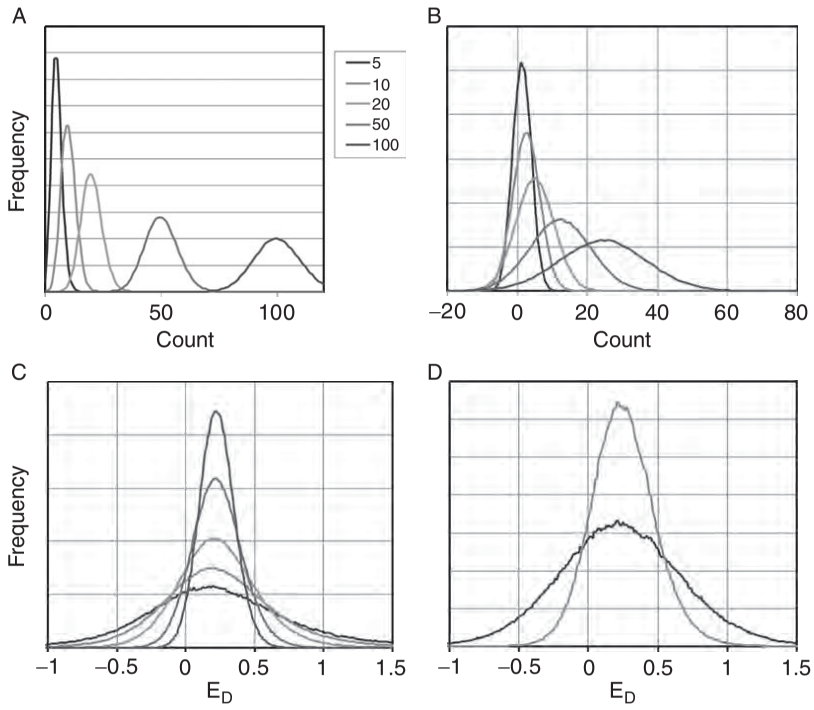

Fig. 7.7. *Effects of Poisson photon noise on calculated SE and FRET values.* (A) Statistical distribution of number of incoming photons for the mean fluorescence intensities of 5, 10, 20, 50, and 100 photons/pixel, respectively. For $n = 100$ (rightmost curve), the SD is 10; thus the relative coefficient of variation (RCV; this is SD/mean) is 10 %. In this case, 95% of observations are between 80 and 120. For example, $n = 10$ the RCV has increased to 33%. (B) To visualize the spread in s.e. caused by the Poisson distribution of pixel intensities that averaged 100 photons for each **A**, **D**, and **S** (right-most curve), s.e. was calculated repeatedly using a Monte Carlo simulation approach. Realistic correction factors were used ($\alpha = 0.0023, \beta = 0.59, \gamma = 0.15, \delta = 0.0015$) that determine 25% FRET efficiency. Note that spread in s.e. based on a population of pixels with RCV = 10 % amounts to RCV = ~60 % for these particular settings! Other curves: for photon counts decreasing as in (A), the uncertainty further grows and an increasing fraction of calculated s.e. values are actually below zero. (C) Spread in E_D values for photon counts as in (A). Note that whereas the value of the mean remains the same, the spread (RCV) increases to several hundred percent. (D) Spread depends not only on photon counts but also on values of the correction

relative coefficient of variation (RCV, defined as the SD divided by the mean value). In this example, RCV = 10%. The situation becomes considerably worse for dimmer pixels (Fig. 7.7A). Thus, in dim sections of the image the degrading influence of noise is worst (Fig. 7.3; see also Fig. 7.8).

As the s.e. values are calculated from individual images, each subject to noise, the errors multiply. This leads to a dramatic spreading of calculated values (Figs. 7.7B and 7.8). Thus, calculated E_D pixel values less than 0 or larger than 1 may be quite common, depending on the intensities of individual images in that pixel and the values of the correction factors. Clearly, such outliers cannot be simply rejected as this would introduce systematic errors in the calculated FRET results. For E_D, s.e. is divided by I_D^d which further increases the spread (Fig. 7.7C). In such pictures, single-pixel RCVs in the order of 100% are not uncommon. It is obvious that the RCV strongly depends on the values of the correction factors α, β, γ, and δ (Fig. 7.7D) and on the magnitude of the FRET efficiency.

Clearly, a major route towards better pictures is to maximize the photon count. On confocal microscopes this can be accomplished in different ways. More photons are collected when increased laser power is used (which incidentally also allows using lower PMT voltages which reduces detector noise). Furthermore, the pinhole can be opened, the dwell time can be increased by lowering the scan speed and acquired images can be averaged. However, these measures come at the expense of increased fluorophore bleaching, prolonged imaging time, and degraded resolution. As this is usually not desired, we will next cover alternative procedures to clear up the images in an—as much as possible—unbiased manner.

In performing the operations described in the next sections, it is absolutely necessary to use imaging software that can handle

factors. For the green trace, mean photon counts for **A**, **D**, and **S** were 30 each. The factors were $\beta = 0.645$ and $\gamma = 0.11$. For the lower trace, counts for **A**, **D**, and **S** were 100, 100, and 30, and correction factor values were $\beta = 0.81$ and $\gamma = 0.4$. Despite higher photon counts, the spread in this example is significantly larger.

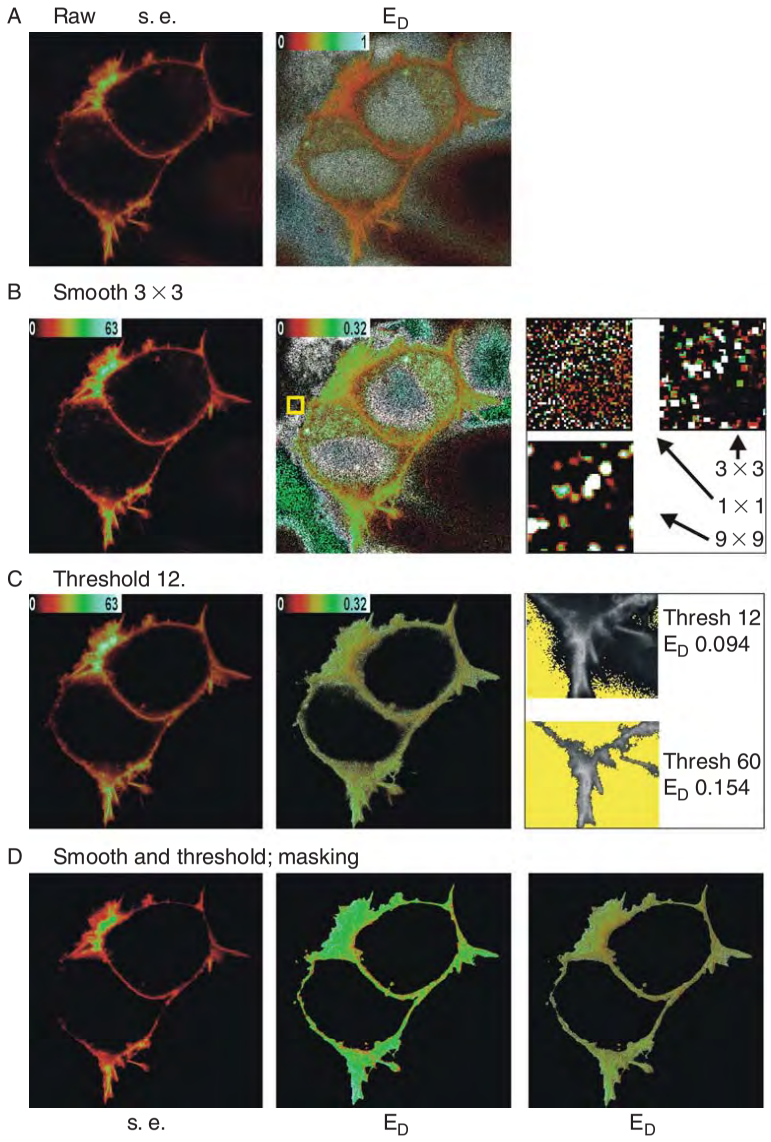

Fig. 7.8. *Postacquisition improvements.* (A) Unaltered "raw" 1024 × 1024 confocal s.e. and E_D images. Note the appearance of excessive noise in E_D at low-signal locations. (B) Lateral averaging (smoothing) using a 3 × 3 kernel cleans up the s.e. image but is less effective on the E_D image. Note the difference in Look-Up Table. Right panel: detail of the middle panel (yellow box) showing how smoothing with the indicated kernel sizes influences E_D. (C) Application of lower threshold on the input images rejects any pixels for which either donor or acceptor intensity is below 12 gray levels. Right panel: the detail taken from the lower portion of the middle panel demonstrates that thresholding significantly influences calculated E_D values. Yellow pixels are excluded from the calculations. (D) A combination of smoothing and thresholding with settings as in B and C cleans up the s.e. and E_D images. Right panel, a mask, derived from the smoothed and thresholded E_D image, is applied to the unfiltered E_D data to preserve fine details in the FRET image.

Author's personal copy

floating point (Negative and broken numbers) calculations. The freeware package Image J (Rasband, W., NIH, Bethesda, Md; *http://rsb.info.nih.gov/ij*) for example performs the described image analysis steps excellently, if 8- or 12-bit images are converted to 32-bit images, and it allows automation of frequently occurring analysis sequences.

7.5.2. Smoothing/filtering

Lateral averaging of the pixel values of the raw images ("smoothing") is the easiest way to reduce the noise effects due to photon statistics significantly, but of course it also reduces the resolution of the picture. A simple mathematical averaging with a 3 × 3 kernel applied to the background-subtracted, shading-corrected input images already reduces photon noise by ~3-fold (Fig. 7.8A and B). On the other hand, smoothing also spreads out the effect of incidental very high noise pixels that are present in just one of the images (Fig. 7.8B, right detail panels). The effect of this is that it replaces a single outlier pixel in the FRET image with an island of (albeit less pronounced) outliers. To our eye, the effect is the same. Smoothing works better on s.e. images than on the FRET efficiency image. As an alternative, smoothing may be applied to the calculated images as well. It depends on the raw input images which approach gives the best results.

7.5.3. Thresholding

As the effects of photon noise are most confusing in very dim regions in the image, significant improvements may be expected from simply setting a low-end threshold for each of the input images (Fig. 7.8C). Commonly, separate thresholds have to be set for each of the images, depending on background level and brightness of the image. Indeed thresholding clears up a lot of the noise in background areas, but the highest outliers will still exceed the threshold, and conversely any accidental low-value pixels in the regions that are of interest will be removed. In addition, if the FRET efficiency depends on the expression level of the donor and acceptor constructs [15] thresholding is guaranteed to bias the results. Independent estimation of the magnitude of this bias is necessary. This can be simply performed by comparing calculated FRET values from images differing only in threshold setting (Fig. 7.8C, right detail panels).

Setting an upper threshold may also be necessary. This is evident when saturated pixels are present in the image, a situation that can not always be avoided because expression of some GFP-tagged constructs sometimes causes appearance of extremely bright aggregates in the cytosol that outshine the structures of interest. To retain full dynamic range in the ROI, it is best to allow image saturation in the aggregates while rejecting them from the analysis using an upper threshold. Note that the upper threshold has to be set well below the highest gray level to prevent systematic bias, in particular when the input images are acquired with averaging.

7.5.4. Masking

A masking strategy may be used to dismiss false high FRET values in dim and therefore noisy image regions while simultaneously preventing loss of resolution in the brighter regions (Fig. 7.8D, right panel). In the apparent FRET image, resonance can be distinguished from incidental noise pixels by smoothing the image with a

spatial filter. Isolated noise pixels become averaged out, while consecutive adjacent pixels with positive FRET remain visible. Setting thresholds for each image to just above background intensity generates a mask that contains only regions of true FRET. The thus obtained binary mask may be further edited by for example, erosion, dilation, or floodfill if necessary. The mask is subsequently applied to the original, unfiltered FRET image resulting in near-complete rejection of noise pixels (Fig. 7.8D). Masking tends to be a very powerful way to clean up the images, but since it involves thresholding one has to verify that it does not bias the results in experiments where dimmer pixels are likely to contain less FRET.

7.5.5. Unbiased cleaning up: Mixing FRET efficiency with image intensity information

Completely unbiased visualization of FRET results with strong rejection of noise in dim regions is possible by combining the FRET efficiency picture with the original image intensity (Fig. 7.9A). Here, a pseudocolor RGB FRET image is made from the unprocessed (i.e., without any thresholding or masking) FRET image by overlaying it with a pseudocolor table, also called Look-Up Table or LUT. The intensity of the RGB image is then modulated with the intensity information present in the original input images (see Fig. 7.9). Intensity information may be derived from **D**, **A**, I_S^s or a combination thereof (e.g., the maximum value of **D** or **A**). Thus, background noise pixels that yield high FRET values are still retained in the image, but they will be displayed very dim, just as they appear to the eye.[7] Prior to the modulation step the intensity

[7]Many image analysis packages are not capable to perform this operation correctly in a single step. One approach is to unravel the pseudocolor FRET image into individual R, G, and B channel images. Each of these images is then multiplied with the normalized intensity image, and the final image is regenerated by combining the channels to an RGB image.

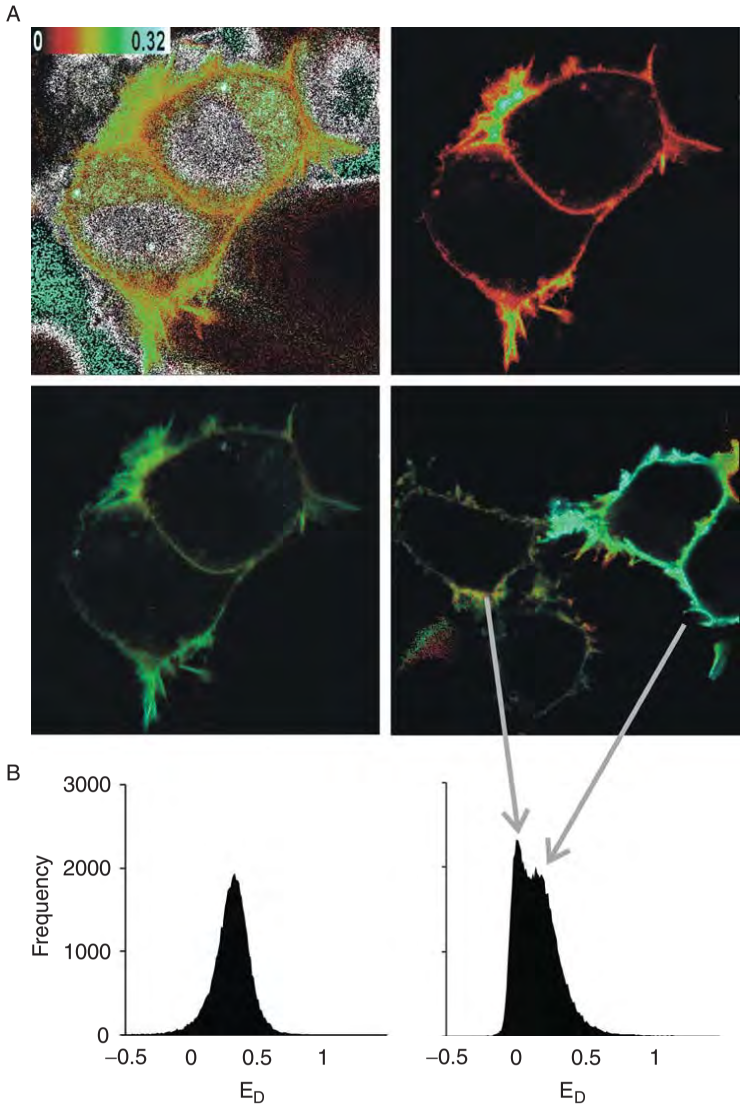

Fig. 7.9. *Further FRET efficiency analysis.* (A) Unbiased display of FRET efficiency. The E_D image (upper left panel) is modulated with an intensity picture (in this case, s.e., upper right panel) to yield the lower left image. See text for further details. Lower right panel, example with several cells displaying different E_D. (B) Frequency histograms of E_D in the pictures in the lower panels in A. Note that whereas the distribution on the left hand displays merely stochastic noise (compare Fig. 7.7C), the rightmost histogram reveals the heterogeneous FRET efficiency in the cells of the corresponding image.

image may optionally be enhanced by smoothing, brightness/contrast adjustment, and masking.

7.5.6. FRET efficiency histograms

A final postanalysis step that helps interpreting the data is to present frequency histograms of pixel FRET values in selected ROI (Fig. 7.8B). As outlined before, correctly acquired and calculated FRET results are expected to display a Gaussian distribution, in first approximation. Inspection of the distribution of FRET values is a quick way to identify possible deviations from this rule. For example, failing to apply proper shading correction may lead to significant broadening of the distribution. In addition, multimodal or very skewed distributions may draw attention to specific problems with the input images or, alternatively, to interesting cell-to-cell variability.

7.6. Discussion

In this chapter, it was shown that filterFRET is an easy, intuitive and quantitative alternative to record sensitized emission and FRET efficiency. The major advantages of filterFRET over donor-based FRET detection methods (FLIM) are that it can be carried out with standard wide-field or confocal fluorescence microscopes that are available in most laboratories, and that it yields additional data on the acceptor population. FilterFRET is also fast, requiring just two confocal scans (if need be on a line-by-line basis) which minimizes the risk of artifacts due to, for example, organelle movement in living cells, and acquisition can be optimized for each channel independently. However, quantitative

filterFRET requires significant attention for corrections and calibration, whereas FLIM-based FRET techniques are inherently quantitative from first physical principles.

The corrections and calibration of filterFRET differ significantly for CCD microscopes and confocal microscopes. This is because in confocal experiments, channel sensitivities are adjusted at will by the experimenter, and because relative excitation intensities show intended–as well as unintended variations (adjustments and drift, respectively). Confocal filterFRET therefore requires frequent, if not in-line, recalibration; however, if properly streamlined this should not take more than 15 min a day. It also slightly complicates the mathematical framework, as compared to CCD imaging filterFRET. We aimed to arrive at a comprehensive theory that is equally applicable to both imaging modes. We also proposed mathematical jargon that is a compromise between the widely differing terminologies used in the various publications on this topic.

What degree of precision is to be expected from filterFRET? Obviously, precision is governed by the quality of the input pictures, in particular by the lateral and axial co-registration, shading correction, and by photon Poisson noise. For typical confocal images, averaging around a 100 pictures is necessary to arrive at 1% uncertainty in each pixel value of the input pictures, and the FRET calculation will further degrade that figure. Clearly, excessive averaging is not realistic for live-cell imaging. In addition, FPs perform poorly by displaying ill-characterized behavior such as bleaching, maturation, excitation-induced dark states, and pH dependence. Thus, going for one percent variance in pixel FRET values almost certainly stretches the data. However, when multiple pixels can be pooled (average of a ROI), this type of precision may be obtained even without image averaging. Of course, these considerations also hold true for FLIM. From a noise-point of view, simple 2-channel ratio determinations (Sect. 7.22) are preferred. We also want to emphasize again that quantitative FRET efficiency images are not necessarily the "holy grail" for cell biologists. For example, if in the soma of the neuron in Fig. 7.1, a kinase-FRET construct would be 100 times more abundant but only half as active

as in the axon, E_D images would suggest half the kinase activity in the soma, whereas sensitized emission images would correctly report a 50-fold enhanced kinase activity.

The area of filterFRET is evolving actively. Recent developments include its combination with other imaging modes including total internal reflection microscopy (TIRF, see also Chap. 9) and FRAP [20]. Furthermore, several laboratories are testing novel FP donor/acceptor combinations to minimize spectral overlap and issues related to FP maturation. In our hands, especially poor red FP (mRFP1, mCherry, and Tomato) maturation interferes with reliable FRET imaging because of the green emission of the immature proteins [17]. In addition, reliable photo-switchable acceptors [21] are an obvious idea with potential. Likewise, correction algorithms keep evolving. For example, Zal and Gasgoigne [6] included correction for photo bleaching in their treatment, and Elangovan et al. [22] introduced concentration-dependency in the leak-through factors. The applicability of such corrections depends very much on imaging conditions and equipment, and we therefore choose not to incorporate them in this chapter. With all these developments, filterFRET has emerged as a full-grown, adaptable, efficient, and fun way to study molecular interactions in vivo.

7.A. Appendix

7.A.1. Factorization

In this appendix, we will assume that a cell expressing donor- and acceptor molecules is excited at appropriate wavelength λ_{ex}^{d} and λ_{ex}^{a} to image FRET. As detailed in the main text, three images are collected that allow independent estimates of cross talk magnitude to perform correction of leak-through:

- **D**, excitation and emission at donor wavelength
- **S**, excitation at donor wavelength and emission at acceptor wavelength
- **A**, excitation and emission at acceptor wavelength

Furthermore, we assume the more general, but also more complex case in which confocal detection is used. This allows for example flexibility in setting independent detector gains for **D**, **S,** and **A**. When this flexibility is not required the expressions simplify considerably.

Before proceeding, an important note must be made. In literature, two different but fully equivalent approaches have been taken in s.e. The first approach considers a cell that contains (unknown) numbers of donors and acceptors N_D and N_A. When energy transfer takes place (be it from collisional encounters or because a stable population of FRET pairs exist with FRET efficiency E) this diminishes the *effective* number of emitting donors with N_S [3]; that is, the FRET efficiency for this population is unity. Thus, the residual donor emission results from $(N_D - N_S)$ unquenched donor molecules, and the N_S population emits *only* sensitized emission. This approach is intuitive in case no assumptions are being made on the presence of a stable population of FRET pairs or on the magnitude of E in a donor–acceptor complex.

A second approach also considers three populations: free (unquenched) donors N_D, free acceptors N_A, and a population engaged in FRET pairs N_S that transfer energy with characteristic efficiency E (between 0 and 1). However, in this case, the N_S population emits *both* donor fluorescence (quenched by a fraction $(1 - E)$) *and* sensitized emission (proportional to EN_S). To keep in line with the treatment and terminology in other chapters in this volume, this latter approach will be followed here. Note, however, that in other chapters the population of FRET pairs is indicated by the subscript $_{DA}$ whereas we stick to the notation N_S to indicate that this quantity is based on photons emitted from sensitized emission (**S** image) and to keep the close synonymy with the former approach. Thus, our I_{D-S} equals I_{DA} and $I_S + I_A$ equals I_{AD}. Both ways yield essentially identical results.

Bearing this in mind, the acquired images are composite images that consist of multiple terms (see Fig. 7.1; for symbols, see Appendix Table 7.A1) as follows:

TABLE 7.A1
Factorization of symbols

Symbol	Factorization
I_D^{d}	$N_D \ell^{\mathrm{d}} \varepsilon_D^{\mathrm{d}} Q_D F_D^{\mathrm{d}} g^{\mathrm{d}}$
I_A^{d}	$N_A \ell^{\mathrm{d}} \varepsilon_A^{\mathrm{d}} Q_A F_A^{\mathrm{d}} g^{\mathrm{d}}$
I_S^{d}	$N_S E \ell^{\mathrm{d}} \varepsilon_D^{\mathrm{d}} Q_A F_A^{\mathrm{d}} g^{\mathrm{d}}$
I_{D-S}^{d}	$(N_D - N_S) \ell^{\mathrm{d}} \varepsilon_D^{\mathrm{d}} Q_D F_D^{\mathrm{d}} g^{\mathrm{d}} + N_S (1 - E) \ell^{\mathrm{d}} \varepsilon_D^{\mathrm{d}} Q_D F_D^{\mathrm{d}} g^{\mathrm{d}}$
I_{D-S}^{s}	$(N_D - N_S) \ell^{\mathrm{s}} \varepsilon_D^{\mathrm{d}} Q_D F_D^{\mathrm{s}} g^{\mathrm{s}} + N_S (1 - E) \ell^{\mathrm{s}} \varepsilon_D^{\mathrm{d}} Q_D F_D^{\mathrm{s}} g^{\mathrm{s}}$
I_S^{s}	$N_S E \ell^{\mathrm{s}} \varepsilon_D^{\mathrm{d}} Q_A F_A^{\mathrm{s}} g^{\mathrm{s}}$
I_A^{s}	$N_A \ell^{\mathrm{s}} \varepsilon_A^{\mathrm{d}} Q_A F_A^{\mathrm{s}} g^{\mathrm{s}}$
I_A^{a}	$N_A \ell^{\mathrm{a}} \varepsilon_A^{\mathrm{a}} Q_A F_A^{\mathrm{a}} g^{\mathrm{a}}$

The fluorescent components are denoted by I (intensity) followed by a capitalized subscript ($_D$, $_A$, or $_S$, for respectively Donors, Acceptors, or Donor/Acceptor FRET pairs) to indicate the particular population of molecules responsible for emission of$I$and a lower-case superscript ($^{d,\ a,}$ or ^{s}) that indicates the detection channel (or filter cube). For example, I_D^{d} denotes the intensity of the donors as detected in the donor channel and reads as "Intensity of donors in the donor channel," etc. Similarly, properties of molecules (number of molecules, N; quantum yield, Q) are specified with capitalized subscript and properties of channels (laser intensity, ℓ; gain, g) are specified with lowercase superscript. Factors that depend on both molecular species and on detection channel (excitation efficiency, ε; fraction of the emission spectrum detected in a channel, F) are indexed with both. Note that for all factorized symbols it is assumed that we work in the linear (excitation-fluorescence) regime with negligible donor or acceptor saturation or triplet states. In case such conditions are not met, the FRET estimation will not be correct. See Chap. 12 (FRET calculator) for more details.

– **D** is the output gray scale value after amplification[8] in the donor channel (g^{d}) of the sum of the fraction $\left(F_D^{\mathrm{d}}\right)$ of donor fluorescence in the donor channel and the fraction $\left(F_A^{\mathrm{d}}\right)$ of acceptor fluorescence in the donor channel. The fluorescence of donors depends on the number of donor molecules (N_D) diminished by

[8]The factor g may account for integration time and electron multiplication in CCD imaging, or for the PMT gain in confocal imaging.

those donors that lose their excited state energy due to FRET (EN_S), the molar extinction coefficient of the donor ($\varepsilon_D^{\mathrm{d}}$), the laser intensity ($\ell^{\mathrm{d}}$) at $\lambda_{\mathrm{ex}}^{\mathrm{d}}$, and the donor quantum yield (Q_D). The fluorescence of acceptors depends on their quantum yield (Q_A), and on the sum of the number of acceptor molecules (N_A) cross-excited at $\lambda_{\mathrm{ex}}^{\mathrm{d}}$ ($\ell^{\mathrm{d}}\varepsilon_A^{\mathrm{d}}$) and those excited by FRET ($N_S E$).

$$\mathbf{D} = (N_D - \mathrm{EN_S})\ell^{\mathrm{d}}\varepsilon_D^{\mathrm{d}}Q_D F_D^{\mathrm{d}}g^{\mathrm{d}} + N_A\ell^{\mathrm{d}}\varepsilon_A^{\mathrm{d}}Q_A F_A^{\mathrm{d}}g^{\mathrm{d}} + EN_{\mathrm{S}}\ell^{\mathrm{d}}\varepsilon_D^{\mathrm{d}}Q_A F_A^{\mathrm{d}}g^{\mathrm{d}} \tag{7.A1}$$

– **S** is the output gray value after the s.e. channel detector scaling (g^{s}) of the sum of the fractions of donor fluorescence in the s.e. channel (F_D^{s}) and of acceptor fluorescence in the s.e. channel (F_A^{s}). The donor fluorescence depends on Q_D, the excitation efficiency at $\lambda_{\mathrm{ex}}^{\mathrm{d}}$ (that is, $\ell^{\mathrm{s}}\varepsilon_D^{\mathrm{d}}$), the number of donors (N_D), and the population of donors that lose their energy by FRET (EN_S). The fluorescence of acceptors depends on Q_A, the amount of acceptor molecules (N_A) excited with $\lambda_{\mathrm{ex}}^{\mathrm{d}}$ ($\ell^{\mathrm{s}}\varepsilon_A^{\mathrm{s}}$) and on the amount of acceptor molecules excited by FRET ($\mathrm{EN_S}$, which is linear to $\ell^{\mathrm{s}}\varepsilon_D^{\mathrm{s}}$).

$$\mathbf{S} = (N_D - \mathrm{EN_S})\ell^{\mathrm{s}}\varepsilon_D^{\mathrm{s}}Q_D F_D^{\mathrm{s}}g^{\mathrm{s}} + N_A\ell^{\mathrm{s}}\varepsilon_A^{\mathrm{s}}Q_A F_A^{\mathrm{s}}g^{\mathrm{s}} + \mathrm{EN_S}\ell^{\mathrm{s}}\varepsilon_D^{\mathrm{s}}Q_A F_A^{\mathrm{s}}g^{\mathrm{s}} \tag{7.A2}$$

– Finally, **A** is the output gray value after the acceptor channel[9] scaling (g^{a}) of the fraction of acceptor fluorescence in the acceptor channel (F_A^{a}), which depends on the acceptor quantum yield (Q_A) and on the amount of acceptors N_A excited at $\lambda_{\mathrm{ex}}^{\mathrm{a}}$ ($\ell^{\mathrm{a}}\varepsilon_A^{\mathrm{a}}$), of (usually very minor) contributions of donor fluorescence cross-excited at $\lambda_{\mathrm{ex}}^{\mathrm{a}}$ and leaking into the acceptor channel ($(N_D - \mathrm{EN_S})\ell^{\mathrm{a}}\varepsilon_D^{\mathrm{a}}Q_D F_D^{\mathrm{a}}g^{\mathrm{a}}$) and of sensitized emission resulting from cross-excitation at $\lambda_{\mathrm{ex}}^{\mathrm{a}}$ ($\mathrm{EN}_S\ell^{\mathrm{a}}\varepsilon_D^{\mathrm{a}}Q_A F_A^{\mathrm{a}}g^{\mathrm{a}}$). However, as

[9]Note that in confocal imaging, the PMT will generally be the same physical detector as that of the s.e. channel, but operated at a different gain setting.

$\ell^{\mathrm{a}}\varepsilon_D^{\mathrm{a}}$ is very small, the latter two (leakthrough and FRET) terms in most cases essentially are zero.

$$\mathbf{A} = (N_D - \mathrm{EN_S})\ell^{\mathrm{a}}\varepsilon_D^{\mathrm{a}}Q_D F_D^{\mathrm{a}}g^{\mathrm{a}} + N_A\ell^{\mathrm{a}}\varepsilon_A^{\mathrm{a}}Q_A F_A^{\mathrm{a}}g^{\mathrm{a}} + \mathrm{EN_S}\ell^{\mathrm{a}}\varepsilon_D^{\mathrm{a}}Q_A F_A^{\mathrm{a}}g^{\mathrm{a}} \tag{7.A3}$$

As mentioned before, we will assume that a cell expressing donor- and acceptor molecules is excited at appropriate wavelength $\lambda_{\mathrm{ex}}^{\mathrm{d}}$ and $\lambda_{\mathrm{ex}}^{\mathrm{a}}$ in all three channels, so that the donor and acceptor extinction coefficients in **D** and **S** are the same:

$$\varepsilon_D^{\mathrm{s}} = \varepsilon_D^{\mathrm{d}} \text{ and } \varepsilon_A^{\mathrm{s}} = \varepsilon_A^{\mathrm{d}} \tag{7.A4}$$

Note that this is always the case for wide-field and confocal determination where **D** and **S** are collected simultaneously using the same excitation filters or lasers. In case three separate filters are used, care should be taken to match the filters so as to fulfill Eq. (7.A4).

By taking (7.A4) in account, (7.A1)–(7.A3) can be simplified as:

$$\mathbf{D} = pN_D + q\mathrm{EN_S} + rN_A$$
$$\mathbf{S} = tN_D + u\mathrm{EN_S} + vN_A,$$
$$\mathbf{A} = xN_D + y\mathrm{EN_S} + zN_A$$

$$p = \ell^{\mathrm{d}}\varepsilon_D^{\mathrm{d}}Q_D F_D^{\mathrm{d}}g^{\mathrm{d}} \quad q = -p + \ell^{\mathrm{d}}\varepsilon_D^{\mathrm{d}}Q_A F_A^{\mathrm{d}}g^{\mathrm{d}} \quad r = \ell^{\mathrm{d}}\varepsilon_A^{\mathrm{d}}Q_A F_A^{\mathrm{d}}g^{\mathrm{d}}$$
$$t = \ell^{\mathrm{s}}\varepsilon_D^{\mathrm{d}}Q_D F_D^{\mathrm{s}}g^{\mathrm{s}} \quad u = -t + \ell^{\mathrm{s}}\varepsilon_D^{\mathrm{d}}Q_A F_A^{\mathrm{s}}g^{\mathrm{s}} \quad v = \ell^{\mathrm{s}}\varepsilon_A^{\mathrm{d}}Q_A F_A^{\mathrm{s}}g^{\mathrm{s}}$$
$$x = \ell^{\mathrm{a}}\varepsilon_D^{\mathrm{a}}Q_D F_D^{\mathrm{a}}g^{\mathrm{a}} \quad y = -x + \ell^{\mathrm{a}}\varepsilon_D^{\mathrm{a}}Q_A F_A^{\mathrm{a}}g^{\mathrm{a}} \quad z = \ell^{\mathrm{a}}\varepsilon_A^{\mathrm{a}}Q_A F_A^{\mathrm{a}}g^{\mathrm{a}} \tag{7.A1a–7.A3a}$$

Based on the three basic images, **D**, **A**, and **S**, expressions can be derived for the intensity of donors, acceptors, and sensitized emission in their own channel (i.e., the leak-through- and FRET-corrected quantities I_D^{d}, I_A^{a}, and I_S^{s}, respectively). Subsequently, to obtain FRET efficiency, I_S^{s} will be scaled to I_D^{d} analogous to the treatment in the main text.

7.A.2. Sensitized emission

Below, we work out the situation for $x = y = 0$, since in almost all cases, these factors can be neglected. For image sets in which these factors cannot be neglected a corrected image **A*** must first be determined from **A** by subtracting xN_D and $y\mathrm{EN_S}$ (7.A.5). In this case, **A*** should be used in all equations below. If $x = y = 0$ then

$$A = zN_A = I_A^{\mathrm{a}} \tag{7.A5}$$

and

$$N_D = \frac{\mathbf{D}}{p} - \frac{\mathrm{EN}_s q}{p} - \frac{\mathbf{A}r}{zp} \tag{7.A6}$$

and Eqs. (7.A5) and (7.A6) are substituted into the equation for **S** (Eq. 7.A2a)), yielding,

$$u\mathrm{EN_s} = S - \left(\frac{\mathbf{D}}{p} - \frac{\mathrm{EN}_s q}{p} - \frac{\mathbf{A}r}{zp}\right)t - \mathbf{A}v/z$$

hence:

$$\mathrm{EN_s} = \frac{\mathbf{S} - \mathbf{D}t/p - \mathbf{A}(v/2 - rt/pz)}{u - qt/p}$$

or

$$\mathrm{EN_S} = \frac{S - D\frac{\ell^{\mathrm{s}}F_D^{\mathrm{s}}g^{\mathrm{s}}}{\ell^{\mathrm{d}}F_D^{\mathrm{d}}g^{\mathrm{d}}} - A\left(\frac{\ell^{\mathrm{s}}\varepsilon_A^{\mathrm{d}}F_A^{\mathrm{s}}g^{\mathrm{s}}}{\ell^{\mathrm{a}}\varepsilon_A^{\mathrm{a}}F_A^{\mathrm{a}}g^{\mathrm{a}}} - \frac{\ell^{\mathrm{d}}\varepsilon_A^{\mathrm{d}}F_A^{\mathrm{d}}g^{\mathrm{d}}}{\ell^{\mathrm{a}}\varepsilon_A^{\mathrm{a}}F_A^{\mathrm{a}}g^{\mathrm{a}}}\frac{\ell^{\mathrm{s}}F_D^{\mathrm{s}}g^{\mathrm{s}}}{\ell^{\mathrm{d}}F_D^{\mathrm{d}}g^{\mathrm{d}}}\right)}{\ell^{\mathrm{s}}\varepsilon_D^{\mathrm{d}}Q_AF_A^{\mathrm{s}}g^{\mathrm{s}}\left(1 - \frac{\ell^{\mathrm{s}}F_D^{\mathrm{s}}g^{\mathrm{s}}\ell^{\mathrm{d}}F_A^{\mathrm{d}}g^{\mathrm{d}}}{\ell^{\mathrm{d}}F_D^{\mathrm{d}}g^{\mathrm{d}}\ell^{\mathrm{s}}F_A^{\mathrm{s}}g^{\mathrm{s}}}\right)} \tag{7.A7}$$

Relating back to Eq. (7.8) from the main text, the sensitized emission gray scale image I_S^{s} is composed of the emission from $\mathrm{EN_S}$, which depends on the acceptor quantum yield Q_A, scaled by factors for sensitized emission channel gain (g^{s}), fraction of acceptor fluorescence in the sensitized emission channel F_A^{s}, and donor excitation efficiency $\ell^{\mathrm{s}}\varepsilon_D^{\mathrm{d}}$;

$$I_S^{\mathrm{s}} = \mathrm{EN_S}\ell^{\mathrm{s}}\varepsilon_D^{\mathrm{d}}Q_AF_A^{\mathrm{s}}g^{\mathrm{s}} = \frac{S - D\frac{\ell^{\mathrm{s}}F_D^{\mathrm{s}}g^{\mathrm{s}}}{\ell^{d}F_D^{d}g^{d}} - A\left(\frac{\ell^{\mathrm{s}}\varepsilon_A^{\mathrm{d}}F_A^{\mathrm{s}}g^{\mathrm{s}}}{\ell^{a}\varepsilon_A^{a}F_A^{a}g^{a}} - \frac{\ell^{\mathrm{d}}\varepsilon_A^{\mathrm{d}}F_A^{\mathrm{d}}g^{\mathrm{d}}}{\ell^{\mathrm{a}}\varepsilon_A^{\mathrm{a}}F_A^{\mathrm{a}}g^{\mathrm{a}}}\frac{\ell^{\mathrm{s}}F_D^{\mathrm{s}}g^{\mathrm{s}}}{\ell^{\mathrm{d}}F_D^{\mathrm{d}}g^{\mathrm{d}}}\right)}{\left(1 - \frac{\ell^{\mathrm{s}}F_D^{\mathrm{s}}g^{\mathrm{s}}}{\ell^{\mathrm{d}}F_D^{\mathrm{d}}g^{\mathrm{d}}}\frac{\ell^{\mathrm{d}}F_A^{\mathrm{d}}g^{\mathrm{d}}}{\ell^{\mathrm{s}}F_A^{\mathrm{s}}g^{\mathrm{s}}}\right)} \tag{7.A8}$$

In Eq. (7.A8), the constants α, β, γ, and δ (see main text and Table 7.A2) are identified as detailed in Eqs. (7.A9)–(7.A12). Values for α, γ, and δ can be deduced from imaging of a sample with only acceptor molecules:

$$\frac{{}^{\mathrm{Acc}}D}{{}^{\mathrm{Acc}}A} = \frac{r}{z} = \frac{N_A\ell^d\varepsilon_A^dQ_AF_A^dg^d}{N_A\ell^a\varepsilon_A^aQ_AF_A^ag^a} = \frac{\ell^d\varepsilon_a^dF_A^dg^d}{\ell^a\varepsilon_A^aF_A^ag^a} = \alpha \tag{7.A9}$$

$$\frac{{}^{\mathrm{Acc}}D}{{}^{\mathrm{Acc}}S} = \frac{r}{v} = \frac{N_A\ell^d\varepsilon_A^dQ_AF_A^dg^d}{N_A\ell^s\varepsilon_A^dQ_AF_A^sg^s} = \frac{\ell^dF_A^dg^d}{\ell^sF_A^sg^s} = \delta \tag{7.A10}$$

$$\frac{{}^{\mathrm{Acc}}S}{{}^{\mathrm{Acc}}A} = \frac{N_A\ell^s\varepsilon_A^dQ_AF_A^sg^s}{N_A\ell^a\varepsilon_A^aQ_AF_A^ag^a} = \frac{\ell^s\varepsilon_A^dF_A^sg^s}{\ell^s\varepsilon_A^aF_A^ag^a} = \gamma \tag{7.A11}$$

Where again (compare Textbox 2), $\alpha = \gamma\delta$. Similarly, β is calculated from a sample with only donor molecules:

$$\frac{{}^{\mathrm{Acc}}S}{{}^{\mathrm{Acc}}D} = \frac{t}{p} = \frac{N_D\ell^s\varepsilon_D^dQ_DF_D^sg^s}{N_D\ell^d\varepsilon_D^dQ_DF_D^dg^d} = \frac{\ell^sF_D^sg^s}{\ell^dF_D^dg^d} = \beta \tag{7.A12}$$

Note that when **S** and **D** are collected simultaneously (typically for confocal imaging) β and δ are independent of relative laser line intensities.

Analogous to Eq. (7.8) (text) we can thus rewrite Eq. (7.A8) as:

$$I_S^{\mathrm{s}} = \frac{S - \beta D - \gamma A(1 - \beta\delta)}{1 - \beta\delta} \tag{7.A13}$$

Eqs. (7.A8) and (7.A13) are valid not only in case there is a single FRET population N_S with characteristic FRET efficiency E, but also when different FRET populations each with different characteristic FRET efficiency E_i are present $(N_{S,i})N_{S,i}$. One can

simply verify this by substituting N_S by $\sum_i N_{S,i}$ and $N_S E$ by $\sum_i N_{S,i} E_i$ in Appendix Table 7.A1 and Eqs. (7.A1)–(7.A7).

7.A.3. The unquenched donor image and E_D

To derive an expression for I_D^d (the unquenched donor image), **D** is corrected for leak-through as well as for signal lost to FRET. For this latter correction, the factor ϕ that relates the lost signal I_S^d in **D**, that is $\left(\mathrm{EN}_S \ell^d \varepsilon_D^d Q_D F_D^d g^d\right)$, to the gain I_S^s in **S**, or $(\mathrm{EN}_S \ell^s \varepsilon_D^d Q_A F_A^s g^s$, Eq. (7.A13)) is:

$$\phi = -\frac{\mathrm{EN}_S \ell^d \varepsilon_D^d Q_D F_D^d g^d}{\mathrm{EN}_S \ell^s \varepsilon_D^d Q_A F_A^s g^s} = \frac{-p}{u+t} = -\frac{\ell^d Q_D F_D^d g^d}{\ell^s Q_A F_A^s g^s} \tag{7.A14}$$

or:

$$\mathrm{EN}_S \ell^d \varepsilon_D^d Q_D F_D^d g^d = -\phi \mathrm{EN}_S \ell^s \varepsilon_D^d Q_A F_A^s g^s \tag{7.A15}$$

In order to solve I_D^d, Eq. (7.A1) is rearranged with information from Eqs. (7.A5), (7.A9), (7.A10), and (7.A14):

$$I_D^d = N_D \ell^d \varepsilon_D^d Q_D F_D^d g^d = \mathbf{D} - (\delta + \phi)\mathrm{EN}_S \ell^s \varepsilon_D^d Q_A F_A^s g^s - \alpha \mathbf{A} \tag{7.A16}$$

Combined with Eqs. (7.A8) and (7.A13) this rearranges Eq. (7.A16), which is identical to Eq. (7.13) in the main text.

$$I_D^d = \mathbf{D} - (\delta + \phi) I_S^s - \alpha \mathbf{A} = \frac{\beta\phi + 1}{1 - \beta\delta}\mathbf{D} - \frac{\phi + \delta}{1 - \beta\delta}\mathbf{S} + \gamma\phi\mathbf{A} \tag{7.A17}$$

Also ζ (Eq. (7.14) in main text) can be redefined after substitution of Eqs. (7.A9)–(7.A12) according to Eq. (7.A18):

$$\zeta = \frac{\beta(\delta + \phi)}{(1 - \beta\delta)} = \frac{\frac{\mathrm{tr}}{pv} - \frac{t}{u+t}}{1 - \frac{\mathrm{tr}}{pv}} = \frac{\frac{F_D^s}{F_A^s}\left(\frac{F_A^d}{F_D^d} - \frac{Q_D}{Q_A}\right)}{1 - \frac{F_D^s}{F_A^s}\frac{F_A^d}{F_D^d}} \tag{7.A18}$$

From Eq. (7.A18) it is clear that ζ only depends on filter throughput and the ratio of quantum yields for donor and acceptor and hence is independent on laser or detector gain settings. For a given combination of confocal filter settings and fluorophores ζ is therefore a constant (for our confocal settings, using CFP and YFP, $\zeta = -0.248$). Therefore, using ζ is distinctly advantageous during confocal imaging where excitation intensities and channel sensitivities are varied independently, whereas G (see main text) varies with detector settings. Now, Eq. (7.A17) can be rewritten:

$$I_D^d = N_D \ell^d \varepsilon_D^d Q_D F_D^d g^d = (1 + \zeta)\mathbf{D} - \frac{\zeta}{\beta}\mathbf{S} - \gamma\left(\delta - \frac{\zeta}{\beta} + \delta\zeta\right)\mathbf{A} \tag{7.A19}$$

By definition the E_D is calculated from the loss in donor signal, which can be defined from the symbols in Appendix Table 7.A1, and from the experimental images **S**, **D,** and **A** using Eqs. (7.12), (7.15), and (7.A16):

$$E_D = \frac{N_S}{N_D}E \equiv 1 - \frac{I_{D-S}^d}{I_D^d} = \frac{\beta\phi\mathbf{D} - \phi\mathbf{S} + \gamma\phi(1 - \beta\delta)\mathbf{A}}{(\beta\phi + 1)\mathbf{D} - (\delta + \phi)\mathbf{S} + \gamma\phi(1 - \beta\delta)\mathbf{A}}$$

$$= 1 - \frac{\mathbf{D}}{(1 + \zeta)D - \frac{\zeta}{\beta}\mathbf{S} - \gamma\left(\delta - \frac{\zeta}{\beta} + \delta\zeta\right)\mathbf{A}} \tag{7.A20}$$

ζ can be reliably determined, for example by acquiring the **D**, **S,** and **A** images before and after complete acceptor photobleaching. Since postbleach **D** is equal to $N_D \ell^d \varepsilon_D^d Q_D F_D^d g^d \left(= I_D^d\right)$ (see Eqs. (7.A1) and (7.A19)), ζ is found from:

$$\zeta = \frac{{}^{postbleach}\mathbf{D} - {}^{postbleach}\mathbf{D} + {}^{postbleach}\mathbf{A}\alpha}{{}^{postbleach}\mathbf{D} - {}^{postbleach}\mathbf{S}\frac{1}{\beta} + {}^{postbleach}\mathbf{A}\left(\frac{\gamma}{\beta} - \alpha\right)} \tag{7.A21}$$

TABLE 7.A2
Definition of correction factors and constants

Factor	Equations	Factorization	Calculate from	Prep	Comments
α	(7.4), (7.A9)	$\frac{\ell^{d}\varepsilon_A^{d}F_A^{d}g^{d}}{\ell^{a}\varepsilon_A^{a}F_A^{a}g^{a}}$	$\frac{\mathbf{D}}{\mathbf{A}}$	acc.	Leak-through of cross-excited acc. into **D**
β	(7.5), (7.A12)	$\frac{\ell^{s}F_D^{s}g^{s}}{\ell^{d}F_D^{d}g^{d}}$	$\frac{\mathbf{S}}{\mathbf{D}}$	donor	Leak-through of donors into **S**
γ	(7.6), (7.A11)	$\frac{\ell^{s}\varepsilon_A^{d}F_A^{s}g^{s}}{\ell^{a}\varepsilon_A^{a}F_A^{a}g^{a}}$	$\frac{\mathbf{S}}{\mathbf{A}}$	acc.	Cross excitation of acceptors
δ	(7.7), (7.A10)	$\frac{\ell^{d}F_A^{d}g^{d}}{\ell^{s}F_A^{s}g^{s}}$	$\frac{\mathbf{D}}{\mathbf{S}}$	acc.	Leak-through of s.e. into **D**
ϕ	(7.12), (7.A14)	$-\frac{\ell^{d}Q_DF_D^{d}g^{d}}{\ell^{s}Q_AF_A^{s}g^{s}}$	$-\frac{1+\delta G}{\beta+G}$	sensor[1]	Relates the loss in **D** due to FRET $\left(I_S^{d}\right)$ to the gain in **S** due to FRET $\left(I_S^{s}\right)$; negative
ρ	(7.A36)	$\frac{\ell^{a}\varepsilon_D^{a}g^{a}}{\ell^{s}\varepsilon_D^{d}g^{s}}$	$\frac{\mathbf{A}}{\mathbf{S}}$	donor	Relates signal from cross-excited donors in **S** to that in **A** (provided that emission filters are identical)
σ	(7.A26)	$\frac{\varepsilon_D^{d}}{\varepsilon_A^{d}}$	$-1/\phi\upsilon$	zero-FRET construct	Relates extinction coefficient of donors at λ_{ex}^{d} to that of acceptors at λ_{ex}^{d}
υ	(7.A28), (7.A32)	$\frac{\ell^{s}\varepsilon_A^{d}Q_AF_A^{s}g^{s}}{\ell^{d}\varepsilon_D^{d}Q_DF_D^{d}g^{d}}$	$-1/\phi\sigma$ or $\frac{\beta\mathbf{D}_0-\mathbf{S}_0}{\delta\mathbf{S}_0-\mathbf{D}_0}$	zero-FRET construct	Relates the visibility of acceptors in the **S** channel to the visibility of the same number of donors in the **D** channel
ζ	(7.14), (7.22), (7.A18), (7.A21)	$\frac{\frac{F_D^{s}}{F_A^{s}}\left(\frac{F_A^{d}}{F_D^{d}}\frac{Q_D}{Q_A}\right)}{1-\frac{F_D^{s}F_A^{d}}{F_A^{s}F_D^{d}}}$	$\frac{\beta(\delta+\phi)}{(1-\beta\delta)}$ *or:* $-\beta/(\beta+G)$	sensor	Used to relate the loss in **D** due to FRET to the gain in **S** due to FRET; independent from excitation intensity and gain and therefore constant for given filters and fluorophores; negative
G	(7.19), (7.A24)	$\frac{\frac{Q_DF_D^{s}g^{s}}{Q_AF_A^{s}g^{s}}-1}{\frac{\ell^{d}F_A^{d}g^{d}}{\ell^{s}F_A^{s}g^{s}}-\frac{\ell^{d}Q_DF_D^{s}g^{d}}{\ell^{s}Q_AF_A^{s}g^{s}}}$	$-\frac{\Delta S}{\Delta D}$ or: $-\frac{\beta\phi+1}{\phi+\delta}$	sensor	Alternative constant that relates the loss in **D** due to FRET to the gain in **S** due to FRET used in literature; note that G depends on changes in β and δ; positive

[1]Sensor: any single-polypeptide construct (containing the fluorophores to be used in the experiment) that can be induced to change FRET significantly and homogeneously; e.g., Yellow Cameleon in combination with ionomycin.

Alternatively, ζ can be related to G (see main text, Eq. (7.22)):

$$\zeta = -\frac{\beta}{\beta+G} \tag{7.A22}$$

Or conversely, G can be expressed in terms of β, δ, and ϕ by combining Eqs. (7.A22) and (7.A18);

$$\zeta = -\frac{\beta}{\beta+G} = \frac{\beta(\delta+\phi)}{(1-\beta\delta)} \tag{7.A23}$$

The constant G is isolated:

$$G = -\frac{\beta\phi+1}{\phi+\delta} = -\frac{\frac{u}{u+t}}{-\frac{p}{u+t}+\frac{t}{v}} = \frac{\frac{Q_DF_D^{s}g^{s}}{Q_AF_A^{s}g^{s}}-1}{\frac{\ell^{d}F_A^{d}g^{d}}{\ell^{s}F_A^{s}g^{s}}-\frac{\ell^{d}Q_DF_D^{d}g^{d}}{\ell^{s}Q_AF_A^{s}g^{s}}} \tag{7.A24}$$

from which dependency of G on detector gain is evident.

7.A.4. Direct acceptor excitation and E_A estimation

Apart from the unquenched donor image providing a FRET estimate E_D, another FRET estimate can be deduced directly from the pure sensitized emission $\left(I_S^{s}\right)$ and direct acceptor excitation $\left(I_A^{a}\right)$ components. From Appendix Table 7.A1, the following ratio can be defined[10]:

$$E_A \equiv \frac{N_S}{N_A}E = E\frac{N_S\ell^{s}\varepsilon_D^{d}Q_AF_A^{s}g^{s}}{N_A\ell^{a}\varepsilon_A^{a}Q_AF_A^{a}g^{a}\gamma\sigma} = \frac{I_S^{s}}{I_A^{a}}\frac{1}{\gamma\sigma}\left(=\frac{I_S^{s}}{I_A^{s}}\frac{1}{\sigma}\right) \tag{7.A25}$$

where

$$\sigma = \frac{\varepsilon_D^{d}}{\varepsilon_A^{d}} \tag{7.A26}$$

[10]Note the similarity of equation A25 between brackets and Eq.equation (16) of Chap. 1.

Combining Eqs. (7.A25) with (7.A5) and (7.A13) yields

$$E_A = \frac{I_S^s}{\gamma\sigma A} = \frac{\mathbf{S} - \beta\mathbf{D} - \gamma\mathbf{A}(1-\beta\delta)}{\gamma\sigma(1-\beta\delta)\mathbf{A}} \tag{7.A27}$$

Hence the quantity of E_A can be simply calculated from the corrected sensitized emission image and the acceptor only image provided the ratio of the molar extinction coefficients of the donor and acceptor at the donor excitation wavelength is known (σ). This quantity can be determined from absorption spectra of purified labeled components or can be experimentally determined as follows. First, let us define a factor υ that relates the signal of N acceptors in the **S** channel to the signal of the same number of donors in the **D** channel:

$$\upsilon = \frac{v}{p} = \frac{N\ell^s\varepsilon_A^d Q_A F_A^s g^s}{N\ell^d\varepsilon_D^d Q_D F_D^d g^d} = \frac{1}{-\phi\sigma} \tag{7.A28}$$

One easy way to determine υ is by using a donor–acceptor fusion chimera that displays no detectable FRET. In this case, $N = N_D = N_A$ and $N_S = 0$, and Eqs. (7.A1a) and (7.A2a) simplify to:

$$\mathbf{D}_0 = pN + rN \tag{7.A29}$$

$$\mathbf{S}_0 = tN + vN \tag{7.A30}$$

Combining Eqs. (7.A29) and (7.A30) with (7.A28), (7.A10), and (7.A12) it follows that:

$$\frac{\mathbf{S}_0}{\mathbf{D}_0} = \frac{t+v}{p+r} = \frac{\frac{t}{p}+\frac{v}{p}}{1+\frac{r}{v}\frac{v}{p}} = \frac{\beta+\upsilon}{1+\delta\upsilon} \tag{7.A31}$$

Here υ can be isolated to yield:

$$\upsilon = \frac{\beta\mathbf{D}_0 - \mathbf{S}_0}{\delta\mathbf{S}_0 - \mathbf{D}_0} \tag{7.A32}$$

7.A.5. The corrected acceptor image

For the acceptor image $\left(I_A^a\right)$ it suffices in almost all cases to simply use the **A** image, because the donor excitation at acceptor wavelength is essentially zero. However, in special cases (e.g., when FRETting between spectrally similar FPs such as CFP and GFP) ε_D^a may be larger and it may become necessary to correct for the leak-through terms. To accommodate such cases, we here derive **A***, a leak-through-corrected version that than must replace **A** in all calculations.[11] First, copy the expressions for **A** and **S** (Eqs. (7.A2a), (7.A3a), using (7.A4)), substituting (see note 3)F_A^s by $F_A^{a'}$ and F_D^s by $F_D^{a'}$:

$$\begin{cases} \mathbf{S} = t'N_D + u'N_S E + vN_a \\ \mathbf{A} = xN_D + yN_S E + zN_a \end{cases} \tag{7.A33}$$

with

$$\begin{aligned} t' &= \ell^s\varepsilon_D^d Q_D F_D^a g^s, \\ u' &= -t' + \ell^s\varepsilon_D^d Q_A F_A^a g^s, \\ \rho &= \frac{x}{t'} = \frac{y}{u'} = \frac{\ell^a\varepsilon_D^a g^a}{\ell^s\varepsilon_D^d g^s} \end{aligned} \tag{7.A34}$$

From combining Eqs. (7.A10), (7.A33), and (7.A34) it can be shown that:

$$\mathbf{A}^* = zN_A = \frac{\mathbf{A} - \rho\mathbf{S}}{1-\rho\gamma} \tag{7.A35}$$

Note that this equals Eq. (7.8a) of [1].

[11] This is straightforward in case the **A** and **S** filters are identical (i.e., $F_A^a = F_A^s$ and $F_D^a = F_D^s$). With confocal FRET this is commonly the case; with CCD imaging, it requires matching the filters. Without this assumption, an analogous result can be obtained, although derivation is significantly more complicated.

ρ can be determined experimentally in cells labeled with only donor molecules since:

$$\rho = \frac{{}^{\text{Don}}\mathbf{D}}{{}^{\text{Don}}\mathbf{S}} = \frac{x}{t'} = \frac{N_D \ell^a \varepsilon_D^{\text{a}} F_D^{\text{a}} Q_D g^a}{N_D \ell^s \varepsilon_D^d F_D^{\text{a}} Q_D g^s} = \frac{\ell^a \varepsilon_D^a g^a}{\ell^s \varepsilon_D^d g^s} \tag{7.A36}$$

7.A.6. Imaging FRET in tethered constructs using two channels

In this appendix, FRET in tethered constructs (where thus donor: acceptor stoichiometry is exactly 1) is calculated from just two images. Provided that independent estimates of cross talk magnitude are available, and the excitation power in both images is the same, full correction of leak through is possible from images:

- **D**, excitation and emission at donor wavelength
- **S**, excitation at donor wavelength and emission at acceptor wavelength. Approach and terminology are as detailed above, except that $N_D = N_A = N_S = N$ and $\ell^{\text{d}} = \ell^{\text{s}} = \ell$

Hence Eqs. (7.A1a) and (7.A2a) can be rewritten as:

$$\begin{cases} \mathbf{D} = pN + q\text{NE} + rN \\ \mathbf{S} = tN + u\text{NE} + vN \end{cases} \tag{7.A37}$$

This set of equations can be solved for N and NE yielding:

$$\begin{cases} N = \dfrac{q\mathbf{S} - u\mathbf{D}}{(t+v)q - (p+r)u} \\ \text{NE} = \dfrac{(t+v)\mathbf{D} - (p+r)\mathbf{S}}{(t+v)q - (p+r)u} \end{cases} \tag{7.A38}$$

Hence:

$$E = E_D = E_A = \frac{\text{NE}}{N} = \frac{(t+v)\mathbf{D} - (p+r)\mathbf{S}}{q\mathbf{S} - u\mathbf{D}} = \frac{\left(\frac{t}{p} + \frac{v}{p}\right)\mathbf{D} - \left(1 + \frac{r}{p}\right)\mathbf{S}}{\frac{q}{p}S - \frac{u}{p}\mathbf{D}} \tag{7.A39}$$

From Eqs. (7.A1)–(7.3A), and (7.A26) it follows that:

$$q = -p + \frac{\varepsilon_D^{\text{d}}}{\varepsilon_A^{\text{d}}} r = -p + \sigma r \tag{7.A40}$$

$$u = -t + \frac{\varepsilon_D^{\text{s}}}{\varepsilon_A^{\text{s}}} v = -t + \sigma v \tag{7.A41}$$

By referring to Eqs. (7.A10), (7.A12), (7.A14), and (7.A28) it follows that:

$$\delta = \frac{r}{v}; \beta = \frac{t}{p}; \phi = \frac{-p}{u+t}; \upsilon = \frac{v}{p}; \text{and } \upsilon = \frac{-1}{\sigma\phi} \tag{7.A42}$$

Combining Eqs. (7.A40)–(7.A42) yields:

$$\frac{r}{p} = \frac{r}{v}\frac{v}{p} = \delta\upsilon \tag{7.A43}$$

$$\frac{q}{p} = -1 + \sigma\frac{r}{p} = -1 + \sigma\delta\upsilon \tag{7.A44}$$

$$\frac{u}{p} = -\frac{t}{p} + \sigma\frac{v}{p} = -\beta + \sigma\upsilon \tag{7.A45}$$

Substituting Eqs. (7.A42)–(7.A45) into Eq. (7.A39) yields:

$$E = \frac{(\beta+\upsilon)\mathbf{D} - (1+\delta\upsilon)\mathbf{S}}{(\delta\sigma\upsilon - 1)\mathbf{S} - (\sigma\upsilon - \beta)\mathbf{D}} = \phi\frac{(\beta+\upsilon)\mathbf{D} - (1+\delta\upsilon)\mathbf{S}}{(\delta+\phi)\mathbf{S} - (1+\beta\phi)\mathbf{D}} \tag{7.A46}$$

A calibration procedure (using only **D** and **S** images) to yield β, δ, ϕ, and υ has been described in Eqs. (7.A12), (7.A10), (7.19)–(7.20), and (7.A32), respectively.

Acknowledgments

We are indepted to Drs L.Oomen and L. Brocks for sharing unpublished data; to Drs L.Oomen, G. vd. Krogt and M. Langeslag for critical reading and comments and to Dr G. vd. Krogt, B. Ponsioen and W. Zwart for preparation

of samples. Financially supported by NWO, the Netherlands Cancer Society and by the Josephine Nefkens Stichting.

References

[1] Gordon, G. W., Berry, G., Liang, X. H., Levine, B. and Herman, B. (1998). Quantitative fluorescence resonance energy transfer measurements using fluorescence microscopy. Biophys. J. *74*, 2702–13.

[2] Hoppe, A., Christensen, K. and Swanson, J. A. (2002). Fluorescence resonance energy transfer-based stoichiometry in living cells. Biophys. J. *83*, 3652–64.

[3] van Rheenen, J., Langeslag, M. and Jalink, K. (2004). Correcting confocal acquisition to optimize imaging of fluorescence resonance energy transfer by sensitized emission. Biophys. J. *86*, 2517–29.

[4] Wlodarczyk, J., Woehler, A., Kobe, F., Ponimaskin, E., Zeug, A. and Neher, E. (2008). Analysis of FRET signals in the presence of free donors and acceptors. Biophys. J. *94*, 986–1000.

[5] Xia, Z. and Liu, Y. (2001). Reliable and global measurement of fluorescence resonance energy transfer using fluorescence microscopes. Biophys. J. *81*, 2395–402.

[6] Zal, T. and Gascoigne, N. R. (2004). Photobleaching-corrected FRET efficiency imaging of live cells. Biophys. J. *86*, 3923–39.

[7] Miyawaki, A., Llopis, J., Heim, R., McCaffery, J. M., Adams, J. A., Ikura, M. and Tsien, R. Y. (1997). Fluorescent indicators for Ca^{2+} based on green fluorescent proteins and calmodulin. Nature *388*, 882–7.

[8] Ponsioen, B., Zhao, J., Riedl, J., Zwartkruis, F., van der Krogt, G., Zaccolo, M., Moolenaar, W. H., Bos, J. L. and Jalink, K. (2004). Detecting cAMP-induced Epac activation by fluorescence resonance energy transfer: Epac as a novel cAMP indicator. EMBO Rep. *5*, 1176–80.

[9] van der Wal, J., Habets, R., Varnai, P., Balla, T. and Jalink, K. (2001). Monitoring agonist-induced phospholipase C activation in live cells by fluorescence resonance energy transfer. J. Biol. Chem. *276*, 15337–44.

[10] Nagy, P., Vamosi, G., Bodnar, A., Lockett, S. J. and Szollosi, J. (1998). Intensity-based energy transfer measurements in digital imaging microscopy. Eur. Biophys. J. *27*, 377–89.

[11] Tron, L., Szollosi, J., Damjanovich, S., Helliwell, S. H., Arndt-Jovin, D. J. and Jovin, T. M. (1984). Flow cytometric measurement of fluorescence resonance energy transfer on cell surfaces. Quantitative evaluation of the transfer efficiency on a cell-by-cell basis. Biophys. J. *45*, 939–46.

[12] Wouters, F. S., Verveer, P. J. and Bastiaens, P. I. (2001). Imaging biochemistry inside cells. Trends Cell Biol. *11*, 203–11.

[13] Tomazevic, D., Likar, B. and Pernus, F. (2002). Comparative evaluation of retrospective shading correction methods. J. Microsc. *208*, 212–23.

[14] Chen, H., , Puhl, H. L.III, Koushik, S. V., Vogel, S. S. and Ikeda, S. R. (2006). Measurement of FRET efficiency and ratio of donor to acceptor concentration in living cells. Biophys. J. *91*, L39–L41.

[15] van Rheenen, J., Achame, E. M., Janssen, H., Calafat, J. and Jalink, K. (2005). PIP2 signaling in lipid domains: A critical re-evaluation. EMBO J. *24*, 1664–73.

[16] Clegg, R. M. (1992). Fluorescence resonance energy transfer and nucleic acids. Methods Enzymol. *211*, 353–88.

[17] van der Krogt, G. N., Ogink, J., Ponsioen, B. and Jalink, K. (2008). A comparison of donor-acceptor pairs for genetically encoded FRET sensors: Application to the Epac cAMP sensor as an example. PLoS ONE. *3*, e1916.

[18] Zucker, R. M. and Price, O. (2001). Evaluation of confocal microscopy system performance. Cytometry *44*, 273–94.

[19] Cogswell, C. J. and Larkin, K. G. (1995). The specimen illumination path and its effect on image quality. In: "Handbook of Biological Confocal Microscopy"(Pawley, J. B., ed.). Plenum press, New York, pp. 127–37.

[20] van Royen, M. E., Cunha, S. M., Brink, M. C., Mattern, K. A., Nigg, A. L., Dubbink, H. J., Verschure, P. J., Trapman, J. and Houtsmuller, A. B. (2007). Compartmentalization of androgen receptor protein-protein interactions in living cells. J. Cell Biol. *177*, 63–72.

[21] Demarco, I. A., Periasamy, A., Booker, C. F. and Day, R. N. (2006). Monitoring dynamic protein interactions with photoquenching FRET. Nat. Methods *3*, 519–24.

[22] Elangovan, M., Wallrabe, H., Chen, Y., Day, R. N., Barroso, M. and Periasamy, A. (2003). Characterization of one- and two-photon excitation fluorescence resonance energy transfer microscopy. Methods *29*, 58–73.

Adriaan Houtsmuller, Wednesday June 13th 2012, 11.30

Histochem Cell Biol (2001) 115:13–21
DOI 10.1007/s004180000234

REVIEW

Adriaan B. Houtsmuller · Wim Vermeulen

Macromolecular dynamics in living cell nuclei revealed by fluorescence redistribution after photobleaching

Accepted: 20 November 2000 / Published online: 15 December 2000

Abstract Regulation and structural requirements of vital nuclear processes such as DNA replication, transcription, RNA processing and DNA repair inside the eukaryote nucleus are as yet poorly understood. Although a wealth of evidence exists pointing to a considerable degree of spatial organisation of chromatin and nuclear processes, there are still questions concerning the dynamics and interaction of nuclear proteins that remain unanswered. The cloning of the gene encoding the green fluorescent protein (GFP) has revolutionised the study of proteins in living cells. The expression of recombinant cDNA fusion plasmids of GFP and proteins of interest currently enables the investigation of those proteins in living cells. Time-lapse confocal microscopy as well as quantitative fluorescence methods such as fluorescence redistribution after photobleaching (FRAP) and fluorescence resonance energy transfer are widely applied to living cells expressing GFP fusion proteins. This review gives an overview of the current state of knowledge of nuclear structure and function. In particular, the different applications of FRAP technology to study the dynamics of GFP-tagged nuclear proteins will be summarised.

Keywords Nuclear protein dynamics · GFP · FRAP · FLIP

Introduction

The relationship between structure and function in the cell nucleus has been the subject of much dispute (see, for example, van Driel et al. 1995; Singer and Green 1997; Lamond and Earnshaw 1998). It has been hypothesised that the spatial organisation of chromatin and nuclear protein complexes is essential for the proper regulation of processes that take place in the nucleus. The nucleus, in this view, consists of a number of immobile protein complexes, often referred to as factories (Cardoso et al. 1999) in which transcription, replication, repair or RNA processing take place. Enzymes required for function are actively recruited to the factories, and DNA is reeled through the fixed structures as it is being processed (see, for example, Cook 1999). In sharp contrast to this concept of highly compartmentalised nuclear activity stands the view that the nucleus is far less organised in a structural sense, and that nuclear processes are regulated by freely diffusing proteins. Microscopically visible protein/DNA/RNA structures are formed, in this view, as a result of protein activity, and they do not represent prerequisites for proper function (Singer and Green 1997; Lewis and Tollervey 2000). The development of green fluorescent protein (GFP) technology and the combination with fluorescence redistribution after photobleaching (FRAP) methods has recently lead to reconsideration of how different processes in the cell nucleus are organised (Lewis and Tollervey 2000; Pederson 2000a; Shopland and Lawrence 2000). The debate, that focuses on concepts such as the nuclear matrix, nuclear factories and compartmentalisation of the nucleus, was triggered by findings in various fields of research, including protein degradation mechanisms (Reits et al. 1997), DNA repair (Houtsmuller et al. 1999), regulation of gene transcription (McNally et al. 2000) and RNA processing (Kruhlak et al. 2000; Phair and Misteli 2000). Using GFP-tagged proteins and photobleaching techniques, these authors report an unexpected high mobility of the investigated proteins in the nucleoplasm. Here we will review some of the data, mainly obtained with GFP technology and different bleaching methods, that challenge these models. In addition, we will discuss some techniques that are currently being used to measure protein dynamics using photobleaching.

A.B. Houtsmuller (✉)
Department of Pathology, Josephine Nefkens Institute,
Erasmus University Rotterdam, P.O. Box 1738,
3000 DR Rotterdam, The Netherlands
e-mail: houtsmuller@path.fgg.eur.nl
Tel.: +31-10-4088456, Fax: +31-10-4089487

W. Vermeulen
Department of Cell Biology and Genetics,
Centre for Biology and Genetics (CBG),
Erasmus University Rotterdam, P.O. Box 1738,
3000 DR Rotterdam, The Netherlands

The nucleus

More than a century of microscopic studies has resulted in a differentiated and detailed view on the interphase nucleus. Distinct nuclear bodies, chromosome territories, interchromatin compartments and a nuclear scaffold consisting of insoluble proteins have been described. These structures have been appreciated with waves of popularity. However, a plethora of studies that is still being continued has not resulted yet in a definitive structure–function model. Below, we will summarise the current knowledge on the structure of the cell nucleus.

Chromatin

Chromosomes stained with general DNA dyes are clearly visible as distinct structures during mitosis. In interphase, however, they cannot be readily distinguished from each other by just staining DNA. Nevertheless, chromatin is not homogeneously distributed in the nucleus. Based on their appearance in electron micrographs, two types of chromatin can be identified, relatively condense regions, representing late replicating heterochromatin, and relatively decondensed chromatin, representing early replicating euchromatin. Presumably due to its less-condensed state, euchromatin is actively transcribed. In Giemsa-stained metaphase chromosomes, the two chromatin types are stained differentially, resulting in a banded pattern. Interestingly, these alternating bands, called G-bands (late replicating) and R-bands (early replicating), appear to be in different locations in the interphase nucleus too. Pulse labelling with Br-dUTP of synchronised Chinese hamster cells during replication revealed that late replicating chromatin is mainly found in the periphery and near the nucleolus whereas early replicating chromatin is preferentially located in the interior of the nucleus (Ferreira et al. 1997).

In spite of the fact that individual chromosomes are dispersed through the nucleus in interphase, it has been postulated already in the earliest years of chromosome research that chromosomes occupy distinct territories (Rabl 1885). Experimental evidence that confirmed this early hypothesis was presented only in the 1980s. Local induction of unscheduled DNA synthesis in Chinese hamster nuclei by UV micro-irradiation, resulted in the incorporation of pulse-labelled H^3-thymine exclusively in small regions within single chromosomes (Zorn et al. 1979; Cremer et al. 1982). Later, the development of in situ hybridisation techniques to label individual chromosomes in interphase nuclei (Manuelidis 1985; Cremer et al. 1993) provided direct visual proof of the existence of these chromosome territories. Taking into account the banded pattern in single chromosomes and the fact that heterochromatin and euchromatin show different nuclear localisation, the chromatin fibre within a single territory must loop many times from exterior to interior of the nucleus.

Since the discovery of chromosome domains in interphase, research has focused on the properties of chromatin structure and its relation to the organisation of nuclear processes (reviewed by Lamond and Earnshaw 1998). It was reported from several studies that active genes have a strong tendency to localise in the periphery of chromosome territories. Comparative three-dimensional analysis of active and inactive X-chromosomes showed that although similar in volume, the active X-chromosome has a much larger surface area than its inactive counterpart (Eils et al. 1996). In addition, it was shown by confocal microscopy and image restoration techniques that transcription sites coincide with the surface of the active X-chromosome (Verschure et al. 1999). Interestingly, transcription factors are not found in the interior of chromosome territories (Cmarko et al. 1999), suggesting the existence of an interchromatin compartment. Confocal microscopy of HeLa cells expressing GFP-tagged histone H2B, revealed that nascent RNA was almost exclusively found in the interchromatin areas in chromosome territories and in between strongly GFP-labelled chromatin domains. Moreover, using caged fluorochrome technology, it was recently shown that poly(A) RNA diffuses freely through the interchromatin compartment (Politz et al. 1999).

Although the above indicates that at least some nuclear proteins find their way in the nucleus through the interchromatin compartment, the question remains unanswered if this is true for all nuclear proteins. It has been shown using FRAP, that dextrans up to a molecular weight of 500 kDa diffuse freely through the nucleus (Seksek et al. 1997). In addition, free GFP homogeneously stains the living nucleus. Moreover, nucleotide excision repair proteins diffuse with rates consistent with their molecular weight, and show a homogeneous distribution throughout the nucleus (Houtsmuller et al. 1999). It may be argued that those molecules travel through interchromatin space only, and that light microscopic resolution fails to reveal this because the interchromatin channels are too small. However, it seems unlikely that repair factors only have access to the interchromatin space while DNA damage is distributed randomly throughout the entire genome and also in the interior of condensed heterochromatin areas. It can be argued that DNA itself moves upon damage induction, bringing lesions to the surface of chromatin territories. However, it has been shown with FRAP that chromatin itself is quite immobile (Abney et al. 1997; Marshall et al. 1997), although occasional movement over long distances of centromeres labelled with GFP-tagged CENP-A has been reported (Shelby et al. 1997). The question how DNA repair and maintenance proteins, like centromeric and telomeric proteins, and histones find their way to their targets that are buried in condensed chromatin areas of the nucleus remains unanswered. Future FRAP-based studies are expected to shed light on these issues.

Nuclear matrix

Already in the 1940s, a meshwork of proteins remaining on glass coverslips after extraction of DNA and soluble

proteins from cell nuclei was first described and patented by Russian researchers (Zbarskii and Debov 1948; Pederson 2000b). In the 1970s this precipitate was brought to the attention of the scientific community again. The extracted protein substance was termed 'nuclear matrix' (Berezney and Coffey 1974), and it was suggested that it may represent a framework for the spatial organisation of DNA and nuclear processes. Similar extraction methods applied to metaphase chromosomes revealed a chromosome-shaped precipitate with large DNA loops attached to it (Laemmli et al. 1977). Interestingly, it was shown that this 'chromosome scaffold' was rich in topoisomerase II (Gasser et al. 1985; Earnshaw et al. 1985), an enzyme capable of removing knots from DNA by passing two stretches of dsDNA through each other. In addition, it was reported that the sites where DNA remained attached were rich in specific sequences that were termed scaffold attachment regions (Mirkovitch et al. 1984).

After the initiation of the matrix/scaffold concept, it was readily recognised by many researchers that such a structure would be a perfect analogue to the cytoplasmic cytoskeleton with its multiple functions both in protein transport and in maintenance of subcellular structures. Since then, virtually all aspects of nuclear function have been related to the nuclear matrix (van Driel et al. 1995). However, the tempting concept of the presence of a nuclear protein matrix is the subject of fierce discussion (reviewed in Peterson 2000a). In contrast to the high reproducibility of the various extraction methods, and the likely abundance of the extracted proteins in the living cell nucleus, it has been impossible to convincingly visualise a meshwork of insoluble proteins, both in fixed and in living cells. This discrepancy has been the cause of reasonable doubt among scientists whether the observed structures are the artefacts of extraction methods rather than a biologically relevant nuclear organiser framework, and a means of guided transport.

The sceptical view of what has kept researchers puzzled for many decades has currently found new soil in the results of investigating the dynamics of GFP-tagged enzymes involved in DNA repair, in gene transcription and most recently also in DNA splicing (Houtsmuller et al. 1999; Kruhlak et al. 2000; Phair and Misteli 2000). The authors reported a high mobility of the nuclear proteins they studied. Two nucleotide excision repair proteins (ERCC1, XPA) and a transcription factor (TFIIH) studied by GFP tagging and FRAP measurement in living cells, appeared to travel through the nucleus at rates that correspond to the molecular weights of the complexes they reside in (Houtsmuller et al. 1999). In similar experiments, Phair and Misteli showed that factors involved in RNA processing (ASF and fibrillarin) can diffuse freely through the nucleus. They elegantly showed that the observed protein kinetics are not due to any active transport mechanism by measuring diffusion at temperatures ranging from 23 to 37°C. In these experiments, no effect on diffusion of temperature was found, which is consistent with a model of diffusion. Remarkably, the diffusion coefficients reported for the splicing factors (ca 0.5 $\mu m^2/s$) were considerably lower than those reported for nucleotide excision repair proteins (ca 15 $\mu m^2/s$). However, the observed high mobility of these proteins suggests that if interactions with an immobile protein matrix occur at all, these are highly dynamic.

Nuclear bodies

In addition to chromatin and the nuclear matrix, a number of nuclear substructures have been observed. The most prominent one undoubtedly is the nucleolus. Because it is easily visualised by ordinary light microscopy, it was actually one of the first intracellular structures described. It occupies a considerable portion of the nucleus, but it varies greatly in size and number depending on cell type and cell cycle stage. After the discovery that the nucleolus contains RNA and proteins, the nucleolus has long been seen as a ribosome factory. More recently, additional functions have been reported (reviewed by Pederson 1998). Recent studies on eukaryotic cell cycle regulatory proteins suggest that the nucleolus may act as a shelter for cell cycle proteins, that keeps them inactive until needed elsewhere (Shou et al. 1999; Weber et al. 1999). Apparently, the nucleolus has acquired the function of a compartment for sequestering cell cycle proteins.

Other examples of subnuclear structures that are often described are interchromatin granule clusters (also termed spliceosomes), Cajal bodies or coiled bodies, and PML bodies. Although the composition of these nuclear substructures is known to some extent, their respective functions are as yet unclear. Spliceosomes are predominantly found in the vicinity of active genes. They may be storage sites that keep splicing factors at short distance to their targets, nascent RNA. A role of nuclear bodies in maturation of snRNPs has also been suggested. Introducing plasmids encoding for GFP- and YFP-tagged components of snRNPs (Sm-proteins) by microinjection, resulting in pulsed expression of the tagged proteins, it was shown that snRNPs occur in various nuclear bodies in a fixed order. After entering the nucleus, snRNP follow a distinct route, possibly a maturation pathway (Sleeman and Lamond 1999): first, snRNPs are predominantly present in coiled bodies and nucleoli, and only in a later stage in spliceosomes. In addition, it was shown that the exchange rate of GFP-tagged splicing factors between spliceosomes and the nucleoplasm is very rapid (Kruhlak et al. 2000). A similar high protein exchange was reported for steroid receptors with MMTV promoters in living cell nuclei. Gordon Hager and coworkers applied FRAP and fluorescence loss in photobleaching (FLIP; see below and Fig. 1g, h) to study the interaction of GFP-tagged glucocorticoid receptors (GR) with a long tandem array (>100 copies) of MMTV promoters which were stably integrated in the genome of the cell line used (McNally et al. 2000). Binding of GFP-tagged GR to this

structure resulted in a clearly visible spot in living nuclei. FRAP and FLIP measurements revealed a high exchange rate of GR with the spot (<1 min), arguing against a stable transcription initiation complex. Although the latter 'nuclear body' is an artificial one, the above findings point to a highly dynamic nucleus in which the composition of observed substructures is continuously changing. This of course does not exclude a model in which such structures are 'factories' or 'storage sites', but it contrasts with the results of FRAP on structural proteins like histones, nuclear lamins and fluorescently labelled chromatin, which appear relatively immobile (Marshall et al. 1997; Broers et al. 1999).

Fluorescence redistribution after photobleaching

In modern cell biology, various fluorescence-based techniques are utilised to visualise and quantitate localisation, translocation and kinetics of distinct processes in living cells. The recent technical developments in the field of fluorescence microscopy, digital image analysis, and molecular and cellular biology has set the prior conditions to perform quantitative microscopic investigations inside living cells. Cloning and ectopic expression of the living-cell marker GFP has contributed largely to development and appreciation of living cell studies in the field of cell biology. This increased interest has brought together distinct, previously remote, scientific and technological disciplines such as molecular biology, cell biology, digital microscopic imaging, biophysics and computer science. FRAP, for instance, is currently widely applied by researchers in many fields of biology to determine the dynamics and interaction of GFP-tagged proteins in living cells (White and Stelzer 1999). In addition, other frequently used fluorescence techniques are fluorescence resonance energy transfer (FRET), mainly to investigate protein–protein interactions, and fluorescence correlation spectroscopy (FCS), for the measurement of protein mobility. The highly multidisciplinary quality of this type of research is prone to lead to a Babylonian confusion of tongues and makes it difficult for the biologist to judge the validity of presented data from state of the art FRAP-based measurements on GFP-tagged cellular components. Here we summarise some of the methods that are currently applied.

In all FRAP variants, the property of fluorescent molecules to become non-fluorescent after exposure to excessive excitation light is exploited. This property, usually referred to as photobleaching, irreversibly alters the fluorescent molecule so that it is no longer fluorescent. Although this characteristic is in many cases unwanted, it can be put to use to reveal the mobility of molecules tagged with fluorescent dyes. When a small region within a larger volume containing fluorescent molecules is irradiated (usually with a focused laser) at relatively high intensity, these molecules will get photobleached. The subsequent redistribution of the bleached molecules and fluorescent molecules outside the region, can be monitored at relatively low light intensity. The characteristics of redistribution give information on diffusion, mobile fraction and duration of transient immobilisation of the molecule under investigation (discussed in more detail below).

FRAP was developed in the 1970s by Axelrod and coworkers (1976). It was initially utilised to study plasma membranes of living cells. Ever since, it has become

Fig. 1a–h Fluorescence recovery after photobleaching (FRAP) assays for quantitative FRAP in the cell nucleus. **a** Schematic drawing representing a nucleus with homogeneously distributed fluorescent molecules. A relatively short bleach pulse at relatively high laser intensity is given and the fluorescence intensity is subsequently monitored at a relatively low intensity as fluorescent molecules diffuse into the bleached region. **b** Relative fluorescence intensity (I_t/I_0) of the experiment is plotted against time. The *black line* represents a situation where molecules are freely mobile. (Note that the final intensity I_f will be lower than the initial intensity due to overall bleaching by the bleach pulse.) The *red line* represents a situation where a fraction of the same molecules, with the same diffusion coefficient are immobile. The *dotted line* represents a situation where the immobilisation is transient. In the depicted case, molecules are bound on average for 10 s. The *red line* represents a situation in which molecules are all mobile, but have a smaller diffusion coefficient. **c, d** Alternative method to determine immobile fraction (Houtsmuller et al. 1999). **c** A laser beam is focused in the centre of the nucleus and the region in the beam is bleached for a relatively long period at a relatively low intensity. If all molecules are immobile (*top row*), only those in the beam will get bleached, resulting in a dark hole in the nucleus when an image is taken. However, if all molecules are mobile, a significant part (depending on diffusion rate) will pass through the beam in this period, get bleached and diffuse through the nucleus (*bottom row*). If a period of redistribution is allowed after bleaching, this will result in a homogeneous decrease of fluorescence. In the intermediate situation, when some of the molecules are mobile, the resulting image will be an intermediate between the two extreme situations. **d** Ratio of mean fluorescence intensity of pre- and postbleach images (of the cases shown in **c**) plotted as a function of distance *d* to the laser spot. The corresponding situations are as indicated. **e, f** Method to determine transient immobilisation. **e** The fate of molecules that are transiently immobile at the time of bleaching (t=0) is monitored by recording postbleach images at increasing time intervals after bleaching. Molecules that are released during this time interval will diffuse through the nucleus and no longer contribute to the measured immobile fraction. **f** Theoretical curves of the decay of the measured immobile fraction after bleaching determined by computer simulation of diffusion in an ellipsoid volume. The *solid line* represents the theoretical decay of the measured immobile fraction when molecules are transiently immobile. The intersection with the time axis determines the average binding time, in this case approximately 5 min. The *dotted lines* represent the decay of the measured immobile fraction when a slowly diffusing fraction redistributes through the nucleus. **g** Fluorescence loss in photobleaching (FLIP) assays. A region distant from the subnuclear accumulation is bleached for a relatively long period of time. Subsequently, confocal images are taken at certain time intervals, monitoring the diffusion of bleached molecules and the exchange of fluorescence molecules between the accumulation and the surrounding nucleoplasm. The *top row* shows a FLIP assay where the laser is focused at a single spot and the *bottom row* an assay where a strip region is bleached (cf. **a**). **h** Relative fluorescence in several regions in the image plotted against time. The average residence time of individual molecules can be calculated by subtraction of the control curve from the curve sampled in the accumulation. A subsequent correction should be made for the diffusion time of the investigated protein from the bleach spot to the accumulation

FRAP

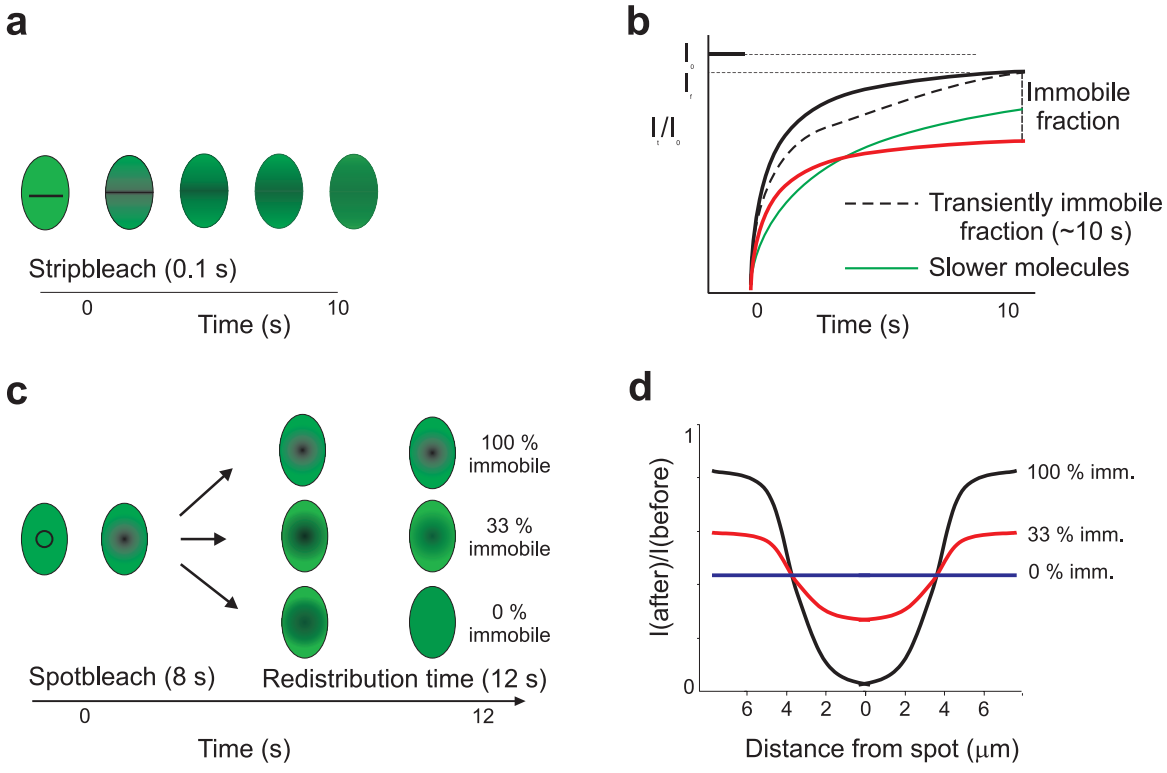
a
Stripbleach (0.1 s)
0
10
Time (s)
b
I/I
Immobile fraction
Transiently immobile fraction (~10 s)
Slower molecules
0
10
Time (s)
c
100 % immobile
33 % immobile
0 % immobile
Spotbleach (8 s)
Redistribution time (12 s)
0
12
Time (s)
d
I(after)/I(before)
1
0
100 % imm.
33 % imm.
0 % imm.
6 4 2 0 2 4 6
Distance from spot (μm)

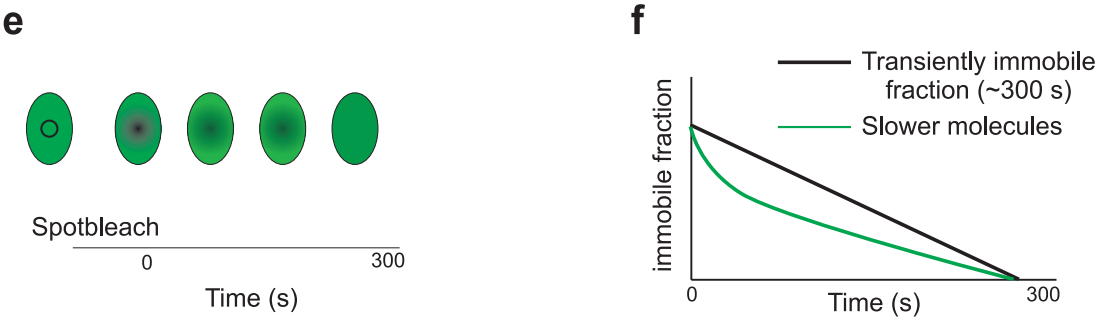
e
Spotbleach
0
300
Time (s)
f
Transiently immobile fraction (~300 s)
Slower molecules
immobile fraction
0
300
Time (s)

FLIP

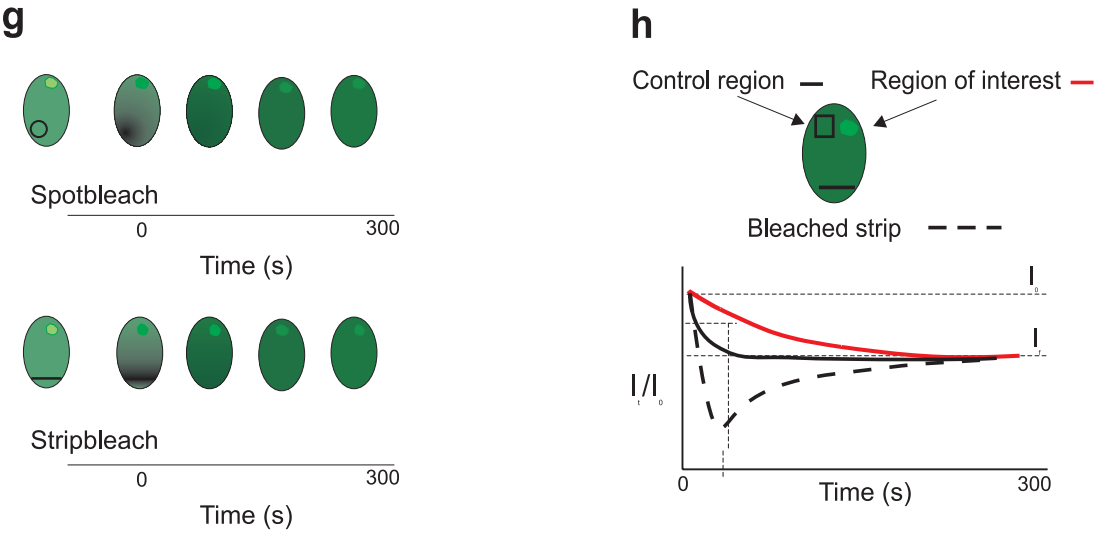
g
Spotbleach
0
300
Time (s)
Stripbleach
0
300
Time (s)
h
Control region
Region of interest
Bleached strip
I/I
0
300
Time (s)

a standard in membrane research to determine the mobility of membrane bound molecules, i.e. rate of diffusion and immobile fraction (reviewed in Edidin 1993). The introduction of confocal microscopy made it possible to extend the topics of research where FRAP can be applied to the inside of living cells (see, for example, Seksek et al. 1997; Lukacs et al. 2000). Eventually, the development of GFP tagging made it possible to study fluorescently tagged proteins that are either stably or transiently expressed in living cells, avoiding time-consuming invasive techniques like microinjection. Subsequently, improvements in GFP technology and fluorescence microscopy in recent years have developed simultaneously with the increasing speed and memory of personal computers to handle the large amounts of data that are generated by digital microscopy. Moreover, the GFP tag itself seems to have properties that make it well suited for its use in living cells. The fact that the fluorescent structure is encapsulated in a protein barrel appears to protect the cellular environment from photodamage that is often observed using synthetic fluorophores, such as fluorescein isothiocyanate. Although some concern still exists on the possible damage inferred to cells during (laser) microscopy, there are ample documented results showing that cells containing fluorescent molecules retain their viability after long periods of imaging or FRAP experiments (Wolf et al. 1980; Nakata et al. 1998; Houtsmuller et al. 1999; White and Stelzer 1999).

Several variants of FRAP are currently being used in nuclear research practice (Fig. 1). The most straight forward method is to bleach a small area (Fig. 1a) and subsequently collect the light intensity data from the previously bleached area (for instance with a photomultiplier tube; Fig. 1b). Another way of collecting the data is to digitally image the entire volume (nucleus in this case) and afterwards analyse the acquired images by digital image analysis techniques (Fig. 1c–h). When all molecules are freely mobile, for example free GFPs in a cell nucleus (Houtsmuller et al. 1999; Phair and Misteli 2000), fluorescent molecules will return into the bleached region and, eventually, the region will be fully fluorescent again (provided that the number of bleached molecules in the region is low compared to the total volume). The velocity at which fluorescence recovers in the bleached area is a measure for the rate of diffusion of the molecules (see below). When all molecules are immobile, no fluorescence recovery will be observed, and the bleached region will remain dark. In the intermediate situation, when some of the molecules are immobile, fluorescence in the bleached region will partly recover (Fig. 1c, d). The percentage of recovery is a measure for the fraction of molecules that is mobile (Fig. 1b, d). Apart from the parameters, diffusion coefficient and immobile fraction, a third quantitative parameter can be determined by FRAP: the duration of transient immobilisation of individual molecules (Fig. 1e, f). To determine this parameter the fluorescence in the bleached region is followed for a prolonged period of time, at least the time an average molecule stays immobile. The release and subsequent redistribution of temporarily trapped or bound molecules will result in a secondary, long-term fluorescence recovery in the bleached region (Fig. 1b, f; Houtsmuller et al. 1999).

FLIP, a variation of FRAP (Presley et al. 1997), can be utilised for several other measurements. It was initially used to determine whether subcellular compartments or substructures are in contact with each other (Lippincott-Schwarz and Zaal 2000). Molecules in one compartment are bleached, and the fluorescence in the presumably connected compartment is inspected. Usually, a few rounds of bleaching are applied to get an optimal effect. The loss or reduction of fluorescence in the other compartment, is indicative of a connection between the investigated compartments. The velocity at which redistribution occurs is a measure for the exchange of molecules between compartments. Measurements have to be corrected for the diffusion coefficient of the investigated molecule. Another powerful approach to use the FLIP method is to determine ‘residence time’ of molecules in specific accumulations such as nuclear bodies or long tandem repeats of protein recognition sequences (Fig. 1g, h; Kruhlak et al. 2000; McNally et al. 2000; Phair and Misteli 2000). In these type of experiments, the use of one relatively long bleach pulse at relatively low intensity (instead of the repeated bleaching usually applied in compartment studies) is expected to facilitate highly accurate measurement, since the amount of bleaching and the redistribution characteristics are more accurately controlled. Moreover, the development of mathematical models describing the entire process is more straight forward in this way.

Calculation of FRAP parameters

Diffusion coefficient

The described FRAP and FLIP approaches can be used for qualitative or semiquantitative investigations. However, as knowledge accumulates (about the dynamics of proteins in living cells) it may be required to apply more accurate quantitative assays in order to be able to compare different mechanisms under different conditions. An accurate ‘effective’ diffusion coefficient (D) can be calculated from the redistribution of fluorescence, when (relative) fluorescence intensity in the bleached region is plotted as a function of time (Fig. 1b). D can be derived by fitting experimentally obtained curves to a mathematical function describing diffusion. However, photobleaching theory, developed by Axelrod and others in the early years of FRAP, only provides methods for determining D from bleaching a small spot in the plasma membrane, which is essentially two dimensional (Axelrod et al. 1976). For the study of membrane trafficking of ER and Golgi proteins, Jeniffer Lippincott-Schwartz and coworkers (Presley et al. 1997) used strip bleaching (Fig. 1a, b) to determine diffusion in the two-dimensional membrane meshwork. For calculation of the effective diffusion coefficient, the data was fitted to a

mathematically derived curve describing one-dimensional diffusion into a plane (the strip). It was shown with the aid of computer simulation, that fitting the experimental data to the first part of the theoretical curve yields a good approximation of the effective diffusion constant. This method seems to be feasible for measurement of nuclear diffusion too (Houtsmuller et al. 1999). However, due to the irregular shape of nuclei, the actual diffusion coefficient might be different from that derived from imaging only the confocal image plane. To determine the effective diffusion coefficient as accurately as possible, theoretical models may have to be developed that take topology into account (Ellenberg et al. 1998). In addition, the use of computer simulation may be a powerful solution, avoiding the necessity to derive mathematical descriptions of each new application (Siggia et al. 2000). Eventually, it is expected that the computer simulation method will become more feasible as computers become faster and knowledge of how to model the living cell will increase.

Immobile fraction

To calculate the immobile fraction of a protein there are several methods that can be used. Immobile fraction is reflected by the percentage of recovery into the bleached area. In a relatively small volume, like the cell nucleus, a correction for a fraction bleached by the pulse is necessary. A disadvantage of this method is that the immobile fraction is determined only in the bleached area. In case the protein under investigation displays a heterogeneous binding pattern, this may lead to inaccurate or erroneous conclusions. To circumvent this problem it is possible to monitor the fluorescence distribution in the entire nucleus, instead of only the bleached region (Fig. 1c, d; Houtsmuller et al. 1999). In this method, the laser beam is focused in the centre of the nucleus. The region within the beam is subsequently bleached at relatively low laser intensity for a relatively long period of time, allowing a large percentage of mobile molecules to pass through the laser beam and get bleached. Subsequently, the mobile molecules are allowed to completely redistribute through the nucleus. The time this takes may differ for different molecules depending on their diffusion coefficient. The ratio of fluorescence intensity of confocal images taken before and after this procedure is then plotted against distance to the laser spot (Fig. 1d). To accurately calculate the immobile fraction from this plot one should obtain two reference curves, representing the situations in which all molecules are immobile and in which all molecules are mobile. The first can be obtained by performing the same experiments on fixed cells. The second may be more difficult to obtain. In the case of an inducible system, like nucleotide excision repair proteins, it is possible to use cells that have virtually no DNA damage, in which the repair proteins can freely diffuse (Houtsmuller et al. 1999). When it is not possible to obtain curves of fully mobile molecules, one may derive a theoretical curve, i.e. the horizontal line through the intersection of the reference curve and the experimentally derived curve (Fig. 1d).

Questions and models

Currently evidence is accumulating from FRAP and GFP methodology applied to living cells that point to a high mobility for nuclear proteins and a high exchange rate between nuclear structures and the nucleoplasm. This has culminated into models in which the spatial organisation of nuclear processes is highly dynamic (Lewis and Tollervey 2000; Pederson 2000a). However, the key questions, whether proteins find targets in the nucleus by diffusion or by active transport and whether the observed nuclear substructures are either required for or the result of functioning, still require further research before they can be unequivocally answered. This is illustrated by two contrasting models as shown in Fig. 2.

In model 1 (Fig. 2a), proteins are present in specific storage sites until they are needed. When required, the proteins are actively guided from the storage sites, through the interchromatin space, to their sites of activity. There they enter preassembled factories that keep in place DNA or RNA and form a template for the efficient activity of the recruited proteins. In this way, the spatial organisation of both chromatin and factories play an important role in regulation of nuclear processes.

In model 2 (Fig. 2b), all protein movement in the nucleus is based on diffusion. In that way proteins distribute throughout the entire nucleus including condensed chromatin. In the more condensed regions the concentration may be lower because of the high chromatin density. When a protein accidentally collides with an other molecule (either mobile or immobile) for which it has affinity (for instance another protein, a DNA or RNA sequence, or DNA damage) it will bind there, possibly change its structure and provide a binding site for yet another protein. Large molecular complexes might be formed that become visible as distinct bodies in light microscopy. These structures are the result of proteins functioning rather than a prerequisite (Singer and Green 1997). In this way diffusion, affinity and concentration of various proteins are the key to regulation of nuclear processes.

The choice between these opposing views cannot be made yet. Moreover, it is likely that a combination of the two extremes exists, dependent on the type of nuclear factors and/or process in which these activities participate. For example a diffusion type of model for DNA repair proteins is favourable since these activities have to find lesions at any time, anywhere in the genome. In contrast, to control for instance the temporal expression of genes during the cell cycle or to establish a tight connection between transcription and mRNA maturation a spatial organisation may be beneficial.

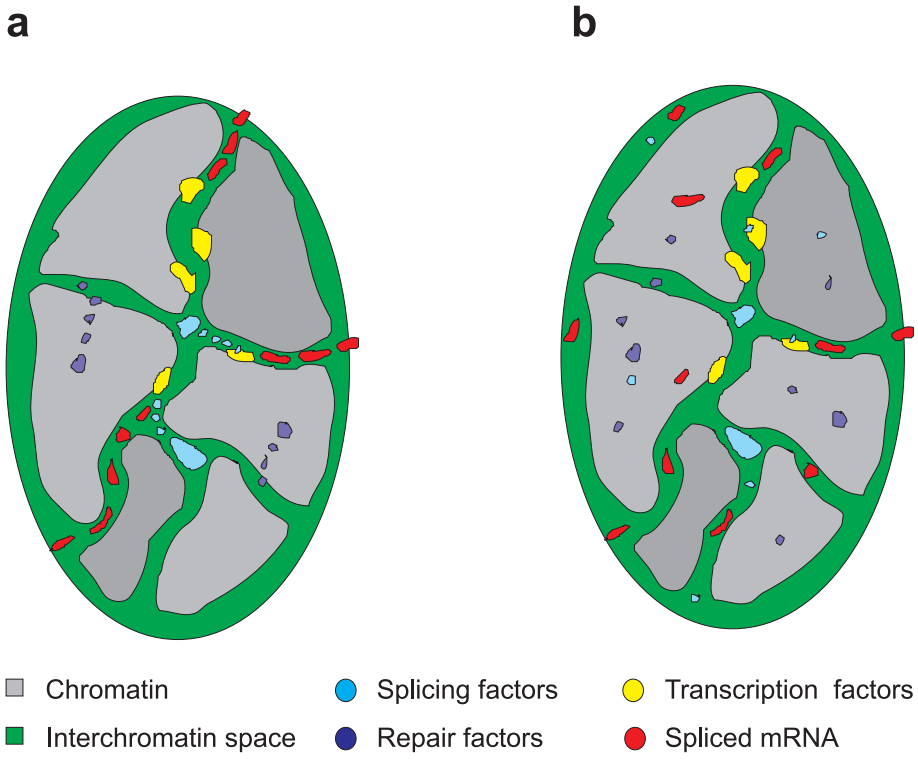

Fig. 2a, b Schematic drawings representing two extreme models for the organisation of processes in the nucleus. **a** Model in which a high spatial organisation governs processes going on in the nucleus. Transcription factors are actively transported to predefined places where transcription factories are located. Splicing factors march from the spliceosomes to the mRNA formed by the transcription factories. Subsequently spliced mRNAs move along predefined tracks to their own predefined nuclear pore. **b** Model in which proteins move about the nucleus by diffusion and find their targets at random: when they collide with another protein or DNA with which they have high affinity they will bind. In this way large functional protein complexes arise. The resulting products, such as mRNA, will diffuse through the nucleus and finally bind to the export machinery and get exported

In conclusion, it is expected that future experiments with living cells, using the GFP and other colour variants and quantitative fluorescence methodology, like FRAP, FRET and FCS will largely contribute to unravel the dynamic events taking place in the nucleus.

References

Abney JR, Cutler B, Fillbach ML, Axelrod D, Scalettar BA (1997) Chromatin dynamics in interphase nuclei and its implications for nuclear structure J Cell Biol 137:1459–1468

Axelrod D, Koppel DE, Schlessinger J, Elson E, Webb WW (1976) Mobility measurement by analysis of fluorescence photobleaching recovery kinetics. Biophys J 16:1055–1069

Berezney R, Coffey DS (1974) Identification of a nuclear protein matrix. Biochem Biophys Res Commun 60:1410–1417

Broers JL, Machiels BM, Eys GJ van, Kuijpers HJ, Manders EM, Driel R van, Ramaekers FC (1999) Dynamics of the nuclear lamina as monitored by GFP-tagged A-type lamins. J Cell Sci 112:3463–3475

Cardoso MC, Sporbert A, Leonhardt H (1999) Structure and function in the nucleus: subnuclear trafficking of DNA replication factors J Cell Biochem Suppl 32/33:15–23

Cmarko D, Verschure PJ, Martin TE, Dahmus ME, Krause S, Fu XD, Driel R van, Fakan S (1999) Ultrastructural analysis of transcription and splicing in the cell nucleus after bromo-UTP microinjection. Mol Biol Cell 1:211–223

Cook PR (1999) The organization of replication and transcription. Science 284:1790–1795

Cremer T, Cremer C, Schneider T, Baumann H, Hens L, Kirsch-Volders M (1982) Analysis of chromosome positions in the interphase nucleus of Chinese hamster cells by laser-UV-microirradiation experiments. Hum Genet 62:201–209

Cremer T, Kurz A, Zirbel R, Dietzel S, Rinke B, Schrock E, Speicher MR, Mathieu U, Jauch A, Emmerich P (1993) Role of chromosome territories in the functional compartmentalization of the cell nucleus. Cold Spring Harb Symp Quant Biol 58:777–792

Driel R van, Wansink DG, Steensel B van, Grande MA, Schul W, Jong L de (1995) Nuclear domains and the nuclear matrix. Int Rev Cytol 162A:151–189

Earnshaw WC, Halligan B, Cooke CA, Heck MM, Liu LF (1985) Topoisomerase II is a structural component of mitotic chromosome scaffolds. J Cell Biol 100:1706–1715

Edidin M (1993) Patches and fences: probing for plasma membrane domains. J Cell Sci Suppl 17:165–169

Eils R, Dietzel S, Bertin E, Schrock E, Speicher MR, Ried T, Robert-Nicoud M, Cremer C, Cremer T (1996) Three-dimensional reconstruction of painted human interphase chromosomes: active and inactive X chromosome territories have similar volumes but differ in and surface structure. J Cell Biol 135:1427–1440

Ellenberg J, Lippincott-Schwartz J, Presley JF (1998) Two-color green fluorescent protein time-lapse imaging. Biotechniques 25:838–846

Ferreira J, Paolella G, Ramos C, Lamond AI (1997) Spatial organization of large-scale chromatin domains in the nucleus: a magnified view of single chromosome territories. J Cell Biol 139:1597–1610

Gasser SM, Laroche T, Falquet J, Boy de la Tour E, Laemmli UK (1986) Metaphase chromosome structure. Involvement of topoisomerase II. J Mol Biol 188:613–629

Houtsmuller AB, Rademakers S, Nigg AL, Hoogstraten D, Hoeijmakers JH, Vermeulen W (1999) Action of DNA repair endonuclease ERCC1/XPF in living cells. Science 284:958–961

Kruhlak MJ, Lever MA, Fischle W, Verdin E, Bazett-Jones DP, Hendzel MJ (2000) Reduced mobility of the alternate splicing factor (ASF) through the nucleoplasm and steady state speckle compartments. J Cell Biol 150:41–51

Laemmli UK, Cheng SM, Adolph KW, Paulson JR, Brown JA, Baumbach WR (1977) Metaphase chromosome structure: the

role of nonhistone proteins. Cold Spring Harb Symp Quant Biol 42:351–360
Lamond AI, Earnshaw WC (1998) Structure and function in the nucleus. Science 280:547–553
Lewis JD, Tollervey D (2000) Like attracts like: getting RNA processing together in the nucleus. Science 288:1385–1389
Lippincott-Schwartz J, Zaal KJ (2000) Cell cycle maintenance and biogenesis of the Golgi complex. Histochem Cell Biol 114: 93–103
Lukacs GL, Haggie P, Seksek O, Lechardeur D, Freedman N, Verkman AS (2000) Size-dependent DNA mobility in cytoplasm and nucleus. J Biol Chem 275:1625–1629
Manuelidis L (1985) Individual interphase chromosome domains revealed by in situ hybridization. Hum Genet 71:288–293
Marshall WF, Straight A, Marko JF, Swedlow J, Dernburg A, Belmont A, Murray AW, Agard DA, Sedat JW (1997) Interphase chromosomes undergo constrained diffusional motion in living cells. Curr Biol 7:930–939
McNally JG, Muller WG, Walker D, Wolford R, Hager GL (2000) The glucocorticoid receptor: rapid exchange with regulatory sites in living cells. Science 287:1262–1265
Mirkovitch J, Mirault ME, Laemmli UK (1984) Organization of the higher-order chromatin loop: specific DNA attachment sites on nuclear scaffold. Cell 39:223–232
Nakata T, Terada S, Hirokawa N (1998) Visualization of the dynamics of synaptic vesicle and plasma membrane proteins in living axons. J Cell Biol 140:659–674
Pederson T (1998) The plurifunctional nucleolus. Nucleic Acids Res 26:3871–3876
Pederson T (2000a) Diffusional protein transport within the nucleus: a message in the medium. Nat Cell Biol 2:E73–E74
Pederson T (2000b) Half a century of “the nuclear matrix”. Mol Biol Cell 11:799–805
Phair RD, Misteli T (2000) High mobility of proteins in the mammalian cell nucleus. Nature 404:604–609
Politz JC, Tuft RA, Pederson T, Singer RH (1999) Movement of nuclear poly(A) RNA throughout the interchromatin space in living cells. Curr Biol 9:285–291
Presley JF, Cole NB, Schroer TA, Hirschberg K, Zaal KJ, Lippincott-Schwartz J (1997) ER-to-Golgi transport visualized in living cells. Nature 389:81–85
Rabl C (1885) Uber Zellteilung. Morphol Jahrb 10:214–230
Reits EAJ, Benham AM, Plougastel B, Neefjes J, Trowsdale J (1997) Dynamics of proteasome distribution in living cells. EMBO J 16:6087–6094
Seksek O, Biwersi J, Verkman AS (1997) Translational diffusion of macromolecule-sized solutes in cytoplasm and nucleus. J Cell Biol 138:131–142
Shelby RD, Vafa O, Sullivan KF (1997) Assembly of CENP-A into centromeric chromatin requires a cooperative array of nucleosomal DNA contact sites. J Cell Biol 136:501–513
Shopland LS, Lawrence JB (2000) Seeking common ground in nuclear complexity. J Cell Biol 150:F1–F4
Shou W, Seol JH, Shevchenko A, Baskerville C, Moazed D, Chen ZW, Jang J, Shevchenko A, Charbonneau H, Deshaies RJ (1999) Exit from mitosis is triggered by Tem1-dependent release of the protein phosphatase Cdc14 from nucleolar RENT complex. Cell 97:233–244
Siggia ED, Lippincott-Schwartz J, Bekiranov S (2000) Diffusion in inhomogeneous media: theory and simulations applied to whole cell photobleach recovery. Biophys J 79:1761–1770
Singer RH, Green MR (1997) Compartmentalization of eukaryotic gene expression: causes and effects. Cell 91:291–294
Sleeman JE, Lamond AI (1999) Newly assembled snRNPs associate with coiled bodies before speckles, suggesting a nuclear snRNP maturation pathway. Curr Biol 9:1065–1074
Verschure PJ, Kraan I van der, Manders EM, Driel R van (1999) Spatial relationship between transcription sites and chromosome territories. J Cell Biol 147:13–24
Weber JD, Taylor LJ, Roussel MF, Sherr CJ, Bar-Sagi D (1999) Nucleolar Arf sequesters Mdm2 and activates p53. Nat Cell Biol 1:20–26
White J, Stelzer E (1999) Photobleaching GFP reveals protein dynamics inside live cells. Trends Cell Biol 9:61–65
Wolf DE, Edidin M, Dragsten PR (1980) Effect of bleaching light on measurements of lateral diffusion in cell membranes by the fluorescence photobleaching recovery method. Proc Natl Acad Sci USA 77:2043–2045
Zbarskii IB, Debov SS (1948) On the proteins of the cell nucleus. Dokl Akad Nauk SSSR 63:795–798
Zorn C, Cremer C, Cremer T, Zimmer J (1979) Unscheduled DNA synthesis after partial UV irradiation of the cell nucleus. Distribution in interphase and metaphase. Exp Cell Res 124:111–119

Mark Hink, Thursday June 14th 2012, 9.00

Using fluorescence fluctuation spectroscopy techniques to study membrane-associated systems in living cells

One of the most intriguing challenges in life sciences is to understand how a complex mixture of molecular particles and structures can make up a living cell. Despite the immense number of studies still much is unknown about the molecular basis of numerous biological processes such as cell proliferation, differentiation, intra- and extra-cellular communication and apoptosis. To increase our understanding about the complexity of these processes in living cells, experimental data on the spatial-temporal organization is required. Fluorescence Fluctuation Spectroscopy (FFS) is a family of fluorescence techniques capable of detecting concentration, dynamics and interactions of fluorescent particles down to the single-molecule level. In FFS, a focussed laser beam illuminates a sub-femtoliter volume element. Fluorescently labeled particles present in this volume will generate a stream of fluorescence photons that contains information (f.e. brightness, mobility, blinking) about the particles. The data stream can be analysed via several statistical methods, each yielding different parameters.

In this talk I will illustrate the basic principles and discuss applications of some of these methods with emphasis on Fluorescence Correlation Spectroscopy (FCS), Photon Counting Histogram (PCH) and Number & brightness analysis (N&B). Special attention will be given to intracellular measurements, discussing the potential challenges and practical issues arising, when these techniques are being used in the living cell.

Biophys Rev (2009) 1:105–118
DOI 10.1007/s12551-009-0013-8

REVIEW

Fluorescence fluctuation spectroscopy: ushering in a new age of enlightenment for cellular dynamics

David M. Jameson · Justin A. Ross · Joseph P. Albanesi

Received: 4 June 2009 / Accepted: 7 July 2009 / Published online: 5 August 2009

Abstract Originally developed for applications in physics and physical chemistry, fluorescence fluctuation spectroscopy is becoming widely used in cell biology. This review traces the development of the method and describes some of the more important applications. Specifically, the methods discussed include fluorescence correlation spectroscopy (FCS), scanning FCS, dual color cross-correlation FCS, the photon counting histogram and fluorescence intensity distribution analysis approaches, the raster scanning image correlation spectroscopy method, and the Number and Brightness technique. The physical principles underlying these approaches will be delineated, and each of the methods will be illustrated using examples from the literature.

Keywords Fluorescence correlation spectroscopy · Fluorescence fluctuation spectroscopy · Number and brightness technique · Photon counting histogram · Raster scanning image correlation spectroscopy · Scanning FCS

Introduction

In fields as diverse as data transmission, stock market analysis and rock music, the saying "One man's noise is another man's signal" often comes to mind. This saying is particularly appropriate for the technique of fluorescence fluctuation spectroscopy (FFS). Serious interest in fluctuations dates to 1827 with the observations by Robert Brown (Brown 1828) that pollen grains from the American plant *Clarkia pulchella*, when suspended in water, demonstrated a continuous jittery movement. In his own words "While examining the form of these particles immersed in water, I observed many of them very evidently in motion; their motion consisting not only of a change of place in the fluid, manifested by alterations in their relative positions, but also not unfrequently of a change of form in the particle itself." And then: "These motions were such as to satisfy me, after frequently repeated observations, that they arose neither from currents in the fluid, nor from its gradual evaporation, but belonged to the particle itself." Jan Ingenhousz, famous for his discovery of photosynthesis, had made similar observations on coal dust on the surface of alcohol in 1785. Ingenhousz's work, however, did not appear to attract the same attention as did Brown's, which in fact created a lively debate about the cause and even the existence of such fluctuations. The phenomenon actively attracted the attention of physicists after the publications of Albert Einstein (Einstein 1905) and Marian Ritter von Smolan Smoluchowski (Smoluchowski 1906), respectively, which developed the theory underlying such fluctuations. In 1911, in an effort to verify the theory, Theodor H.E. Svedberg observed the fluctuations in the number of colloidal gold particles in a small volume observed under a microscope (Svedberg and Inouye 1911). These works, and a series of elegant studies by Jean Baptiste Perrin, eventually firmly established the existence of atoms and molecules. Interestingly, in his classic book, Les Atomes (Perrin 1913), Perrin stated: "I had hoped to perceive these fluctuations in dilute solutions of fluorescent substances. I have found, however, that such

D. M. Jameson (✉) · J. A. Ross
Department of Cell and Molecular Biology,
John A. Burns School of Medicine, University of Hawaii,
651 Ilalo St., BSB 222,
Honolulu, HI 96813, USA
e-mail: djameson@hawaii.edu

J. P. Albanesi
Department of Pharmacology, U.T. Southwestern Medical Center,
6001 Forest Park,
Dallas, TX 75390-9041, USA

bodies are destroyed by the light which makes them fluoresce." Thus Perrin almost anticipated fluorescence fluctuation studies.

As pointed out by Elliott Elson, in a marvelous overview of the historical development of FCS (Elson 2004), the theory and experimental realization of both relaxation kinetics and dynamic light scattering (DLS) attracted significant attention in the 1950s and 1960s. These relaxation methods typically used small perturbations of temperature or pressure to displace the system from its equilibrium position, and then the kinetics of the return to equilibrium was monitored. Dynamic light scattering, which had been used in the 1960s to study the diffusion rates of biological macromolecules, was also applied to studies of chemical kinetics in the hopes of observing systems in the absence of external perturbations, but technical difficulties hampered these efforts. Fluorescence offered solutions to these difficulties, and in the early 1970s Magde, Elson, and Webb published seminal papers on the theory and application of fluorescence fluctuation analysis, specifically fluorescence correlation spectroscopy (FCS) (Elson and Magde 1974; Magde et al. 1972, 1974). This technique, originally developed to study the kinetics of chemical reactions in the absence of external perturbations, and specifically to study the binding of ethidium bromide to DNA, eventually engendered a revolution in quantitative fluorescence microscopy which now provides unparalleled insights into the dynamics of cellular interiors. Wide-spread applications of FCS had to wait though until the 1990s when the advent of confocal and two-photon microscopy greatly reduced the observation volume and thus significantly improved the sensitivity of the method, even extending it to single-molecule levels (Denk et al. 1990; Eigen and Rigler 1994; Maiti et al. 1997; Qian and Elson 1991; Webb 2001). A number of commercial instruments are now available which can carry out different types of FFS measurements; these include instruments from ISS (www.ISS.com), Zeiss (www.zeiss.com/micro), Olympus (www.olympusamerica.com), Leica (www.leica-microsystems.com), and Sensor Technologies LLC (Lake Hiawatha, NJ). Once the province solely of physicists and physical chemists, the availability of commercial FFS instruments, coupled with the explosion in the use of recombinant fluorescent proteins, is bringing FFS into the mainstream of cell biology.

In this brief overview we shall define and describe some of the more popular FFS methods presently being applied to problems of cellular dynamics. The particular methods we shall focus on include (1) fluorescence correlation spectroscopy (FCS), (2) scanning FCS (sFCS), (3) fluorescence cross-correlation spectroscopy (FCCS), (4) photon counting histogram (PCH) and fluorescence intensity distribution analysis (FIDA), (5) raster scanning image correlation spectroscopy (RICS), and (6) Number and Brightness (N&B) analysis.

Before beginning this discussion, however, we should mention the various ways in which fluorescent molecules are introduced into living cells. In rare cases one may be interested in the natural autofluorescence of the cell, but since our understanding of the origins of autofluorescence—besides the more obvious sources, such as the pyridinic and flavin coenzymes, lipofuscin, porphyrins, elastin, and collagen—are incomplete, FFS studies on autofluorescence are rare (see, however, Brock et al. 1998). Perhaps the most popular method, and the method most researchers would first consider, is the attachment of a naturally fluorescent protein to the target protein via genetic techniques. As most readers will appreciate, the number of fluorescent proteins now available is large and ever increasing (see, for example, Nienhaus and Wiedenmann 2009). Another genetic method finding application is the use of the so-called FlAsH or ReAsH tags, wherein a tetracysteine motif (such as CCPGCC) is attached to the protein of interest using standard genetic techniques, and then a profluorescent compound is microinjected into the cell that attaches preferentially to the genetically introduced motif, becoming fluorescent upon the attachment (Gaietta et al. 2002; Griffin et al. 1998). More recently, the method of bimolecular fluorescence complementation was introduced in which the DNA coding for a fluorescent protein (such as YFP or CFP) is split into two parts after which one part is attached to the one target protein and the complementary part is attached to another target protein (Kerppola 2008). If the two target proteins form a complex in the cell, one may find that the fully fluorescent protein can develop and provide the signal. Alternatively, one may simply label the purified target protein in vitro and then microinject some into the cell (Paradise et al. 2007).

Fluorescence correlation spectroscopy (FCS)

In an FCS measurement, the sample—whether in vitro or a living cell—is illuminated by a light source focused to a very small volume, typically on the order of 1 femtoliter or less. The fluorescence originating from particles diffusing in and out of the detection volume, which usually does not correspond to the entire illumination volume, is recorded. This concept is illustrated in Fig. 1. While in the illumination volume, the fluorescent particles may be excited more than once and may also undergo chemical or photophysical processes which alter their fluorescence properties. Examples of such processes are the "blinking" demonstrated by green fluorescent protein (GFP; Dickson et al. 1997; Nirmal et al. 1995) and by quantum dots (Yao et al. 2005) and alterations in fluorophore quantum yields upon binding

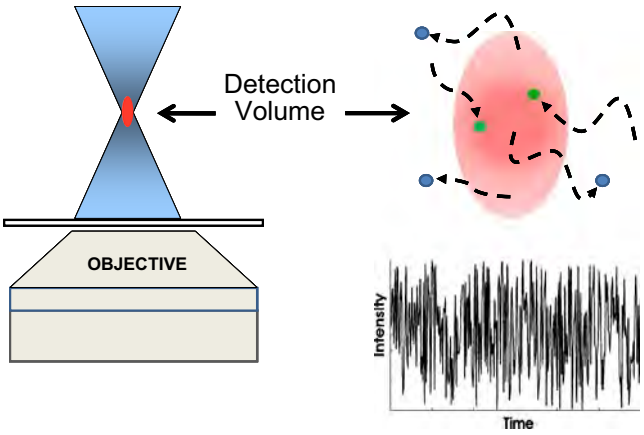

Fig. 1 A sketch illustrating excitation of a small sample volume and detection of emission from that volume. Also illustrated is the fluctuation in the fluorescence intensity to be expected as fluorophores diffuse into and out of the illumination/detection volume

to macromolecules (e.g., ethidium bromide binding to DNA). All of these considerations lead to fluctuations in the detected fluorescence signal. The data stream thus corresponds to the time course of the fluctuating fluorescence signal as depicted in Fig. 1.

Nowadays, FCS experiments are almost always conducted using a microscope. As in traditional confocal microscopy, the basic requirements for FCS microscopy are: a stable monochromatic excitation source, a high numerical aperture (NA) objective, dichroic and/or emission filters, and efficient photon detection [using either photomultiplier tubes (PMT) or avalanche photodiodes (APD)], combined with some additional electronics, such as autocorrelators, to process the data stream and appropriate software for data analysis. A stable excitation source is crucial because FCS experiments measure the time dependence of the signal fluctuation, and if there is a time-dependence inherent in the excitation intensity, that fluctuation will also be present in the recorded data. Technical aspects of the instrumentation, commercial and homebuilt, used to acquire FCS data have been reviewed many times and shall not be repeated here. Readers interested in such technical information are referred to more specialized discussions (such as those given in Berland et al. 1995; Borejdo 1979; Bulseco and Wolf 2007; Dertinger et al. 2008; Hess and Webb 2002; Lieto et al. 2003; Schwille et al. 1997a). For discussions of FCS applied to total internal reflection fluorescence (TIRF), the reader should see Lieto et al. (2003) and Ries et al. (2008). We should note that in order to extract diffusion rates from the FCS data, the precise shape of the detection volume, termed the point spread function (PSF), must be known (for an excellent discussion of point spread functions, the reader should view the lecture by Unruh and Colyer given at the 2006 Advanced Fluorescence Workshop and available on the website of the Laboratory for Fluorescence Dynamics at http://www.lfd.uci.edu/workshop/2006). Typically, FCS practitioners do not determine the PSF directly but, rather, a standard of known diffusional rate, such as fluorescein or rhodamine, is used to calibrate the system. In the literature one often sees a "standard" diffusion rate of 300 $\mu m^2 s^{-1}$ assigned to these fluorophores—yet this value appears to be anecdotal. Recent careful determinations of diffusional rates of various xanthene-based dyes (fluorescein, rhodamine, Alexa) suggests that a value near 430 $\mu m^2 s^{-1}$ would be more accurate (Müller et al. 2008; Petrasek and Schwille 2008).

One technical aspect that warrants consideration from the beginning is the use of either one- or two-photon excitation. In principle, FCS and the other fluorescence fluctuation techniques can be conducted using either excitation mode, but some practical considerations influence the use of one over the other. With one-photon excitation and confocal optics, all fluorophores exposed to the illumination beam are excited, but only the emission from those at the focal spot is detected. Out-of-focus fluorescence is eliminated by spatial filtering through a pinhole at a position which is confocal to the focal spot within the sample. In two-photon excitation, a very high local photon density [usually at near infra-red (IR) wavelengths] is achieved at the focal spot of the objective, and fluorophores can experience two-photon absorption, essentially the simultaneous absorption of two photons resulting in excitation of the fluorophore to the first excited singlet state, normally achieved via a one-photon process (for discussions of multiphoton methods and of two-photon cross-sections of various fluorophores, see Bestvater et al. 2002; Kim and Cho 2009; Pawlicki et al. 2009). As such, there is no need for a pinhole since fluorophores outside of the focal spot are not excited. Two-photon excitation is increasingly popular in FFS work on cells due to (1) its inherent optical sectioning, i.e., confocal aspect, (2) the fact that photo-toxicity of the out-of-focus near-IR illumination is generally much lower than that of one-photon excitation, and (3) the ability to eliminate Rayleigh or Raman scatter from the observed emission. Also, the illumination volume generated by two-photon excitation can be facilely placed almost anywhere within the cell. A typical PSF for two-photon excitation resembles an ellipsoid, being around 0.3 μm in the XY directions and 1.5 μm in the Z direction. Of course, there is one great advantage of one-photon excitation sources (such as laser diodes or small gas lasers) versus two-photon sources, namely cost. Two-photon sources have become smaller physically over the years, but they still remain very expensive.

An FCS data stream can be treated in different ways—but in this section we shall only consider the autocorrelation function, $G(\tau)$. The autocorrelation function is essentially the time-dependent decay of the fluorescence intensity

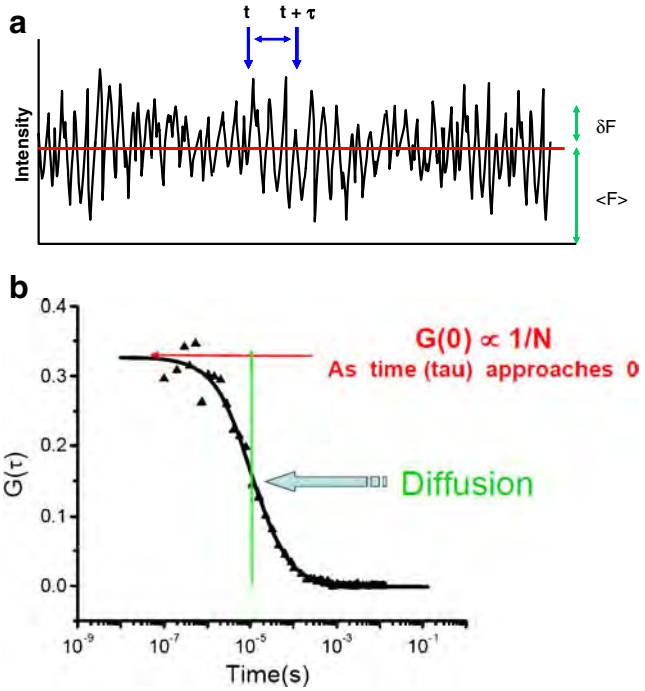

Fig. 2 **a** Fluorescence correlation spectroscopy (FCS) data intensity stream indicating the average intensity, <F(t)>, the deviation in intensity from the average at a particular time point, δF(t), and a time interval, t to t + τ. **b** Autocorrelation curve indicating the characteristic diffusion time of the curve and the value of the autocorrelation function extrapolated to τ=0, i.e. G(0), which is proportional to the reciprocal of the number of particles, N. (The authors acknowledge Enrico Gratton for sketch B, which is from his lecture in the 2007 Advanced Fluorescence Workshop presented by the Laboratory for Fluorescence Dynamics)

fluctuations. Consider the data stream depicted in Fig. 2. The average fluorescence intensity in the data stream is termed <F(t)>, while the variation of any point from the average is termed δF(t). To calculate the autocorrelation function, G(τ), one multiplies the intensity at some time, t, with the intensity at a later time, t + τ, as illustrated in Fig. 2. The average of the product of these two intensities is then divided by the square of the average fluorescence intensity for each value of τ.

$$G(\tau) = \frac{< \delta F(t).\delta F(t+\tau) >}{< F(t) >^2} \qquad (1)$$

As this calculation is made over many τ values, one eventually builds up an entire *autocorrelation curve*, as shown in Fig. 3. It is easy to understand why an autocorrelation curve has this general shape. Namely, when the signals at times close to one another are multiplied, they are likely to have nearly the same absolute magnitude, since it is likely that the fluorescent particle has not diffused far

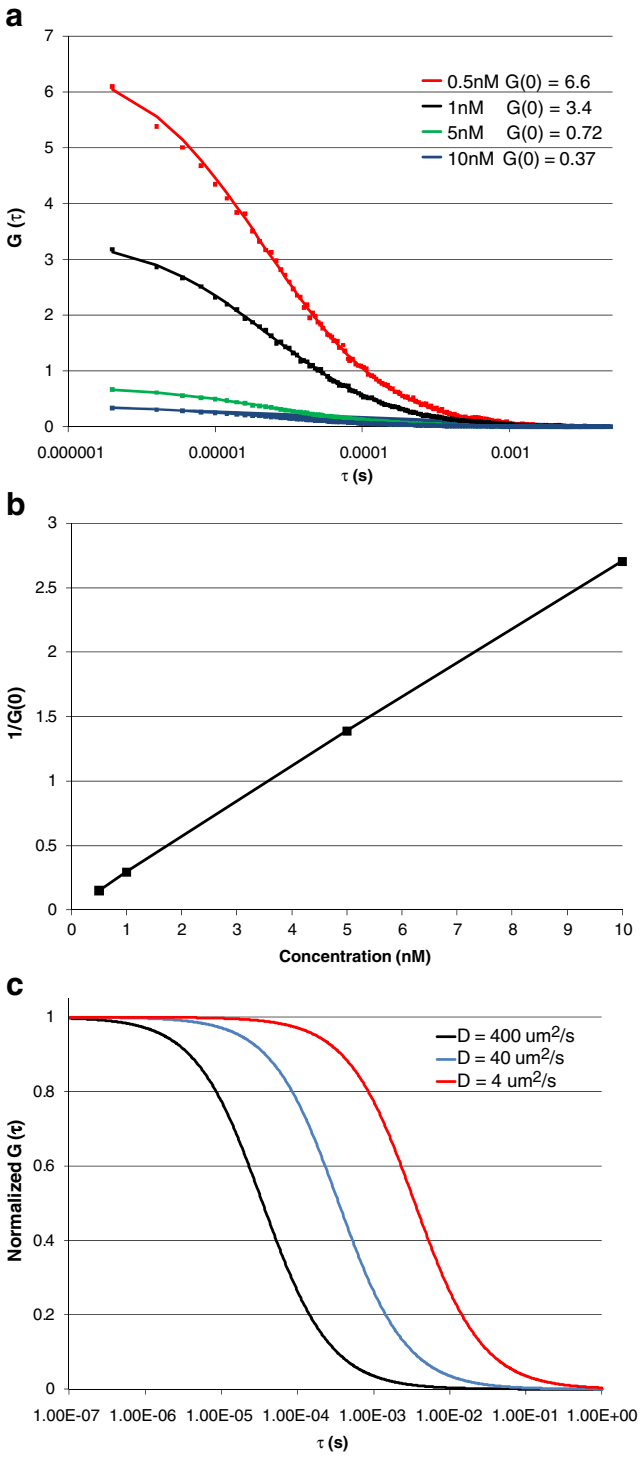

Fig. 3 **a** Autocorrelation curves obtained for aqueous solutions of rhodamine 110 (Rh 110) at 22°C. The concentrations used are indicated on the figure. *Squares* indicate experimental data while *solid lines* represent the fit of the data to a Gaussian–Lorentzian point spread function (PSF) with the diffusion constant of 430 $\mu m^2 s^{-1}$. Data were acquired on an ISS Alba FCS spectrometer (www.ISS.com) using 800 nm excitation from a Chameleon Ti:Sapphire laser (Coherent, Santa Clara, CA). **b** Plot of the reciprocal of G(0) (which is proportional to <N>) as a function of Rh 110 concentration. Note that the calculated 1/G(0) values vary in proportion to the fluorophore concentration, as expected. **c** Simulation of the autocorrelation function of molecules with different diffusion coefficients with the G(0) normalized to 1

between the two moments in time. Hence, the shorter the time intervals in which the signals are compared, i.e., t to t + τ, the more likely they are to be correlated. However, as the interval between these two points increases, it is less likely that the signals will correlate, which will result in a decrease in the autocorrelation function.

Alternatively, the autocorrelation function may be calculated using Fourier transforms. This approach has the advantage that it is much less computationally intensive, particularly for large data sets.

$$G(\tau) = \frac{f^{-1}\left[f(\delta F(t)).f^{*}(\delta F(t+\tau))\right]}{< F(t) >^2} \tag{2}$$

where f is the Fourier transform, f^{-1} is the inverse transform, and f^* is the complex conjugate. If the excitation volume and shape are known, one can relate G(τ) to the translational diffusion of the target molecule. For the case of a three-dimensional (3D) Gaussian excitation volume:

$$G(\tau) = \frac{\gamma}{< N >}\left(1+\frac{\tau}{\tau_D}\right)^{-1}\left(1+S^2\frac{\tau}{\tau_D}\right)^{-\frac{1}{2}} \tag{3}$$

where γ is a geometric scaling factor [$\gamma = 1/\sqrt{8}$ for one-photon 3D Gaussian or $\gamma = 3/(4\pi^2)$ for two-photon Gaussian–Lorentzian], <N> is the average particle number, τ_D is the characteristic diffusion time of the particle, also termed the residence time, and S = ω/z is the ratio of the axial/radial dimensions of the observation volume. Since the characteristic diffusion time, τ_D, is related to the diffusion coefficient, D, by $\tau_D = \omega^2/4D$, the autocorrelation function thus leads directly to the diffusion rate of the target molecule, which in turn provides information on the size of the molecule via the Stokes–Einstein–Sutherland equation:

$$D = \frac{kT}{6\pi\eta r} \tag{4}$$

where k is Boltzmann's constant, T is the absolute temperature, η is the viscosity of the solvent, and r is the Stokes radius of the particle.

We should note another very important feature of FCS data, namely that the method permits determination of the absolute concentration of the target fluorophore in the illumination/detection volume. Although this parameter may be obvious when dealing with homogeneous solutions of known concentration, it is extremely difficult to obtain when working with living cells and may be an important parameter in such studies.

For many years, diffusion rates were the main point of the experiment. Diffusion rates, for example, provided information on the interaction of the fluorophore with other molecules, as in the case of the original use of the method, ethidium bromide binding to DNA. As the method matured and as instrumentation became commercially available, an increasing number of in vitro studies appeared. Since this review is primarily concerned with applications of FFS to cells, we shall not give detailed descriptions of such in vitro applications. However, since many in vitro FCS studies illustrate the type of problems which can be studied with the method and may hold interest to some readers, we provide a brief, though obviously incomplete, list of such studies.

(1) The association and dissociation kinetics of the interaction of α-bungarotoxin with detergent solubilized nicotinic acetylcholine receptors (AChR) of *Torpedo californica* was studied by Rauer et al. (Rauer et al. 1996).
(2) The aggregation of α-synuclein, which plays a key role in Parkinson's disease, was studied by Gerard et al. (Gerard et al. 2006; Humpolickova et al. 2006) and the binding of α-synuclein to lipid vesicles was quantified by Rhoades et al. (Rhoades et al. 2006).
(3) Prion aggregation has been investigated by Riesner (2001) (Elson Rigler book).
(4) Aggregation of β-amyloid-peptide using FCS has been reported by several groups, including Tjernberg et al. (Tjernberg et al. 1999) and Garai et al. (Garai et al. 2007).
(5) Hazlett et al. (Hazlett et al. 2005) reviewed the use of FCS to quantify antigen–antibody interactions.
(6) Sanchez et al. (Sanchez et al. 2001) described the use of two-photon FCS to follow the interaction of a phospholipase with single-lipid and mixed-lipid giant unilamellar vesicles.
(7) The activation of fibrinogen by thrombin and the early stages of the aggregation of fibrin monomers into fibrin polymers was followed by Bark et al. (Bark et al. 1999).
(8) Orden and Jung (Orden and Jung 2008) reviewed the application of FFS methods to study nucleic acid hairpin conformations in aqueous solutions.
(9) Anomalous diffusion in highly concentrated random-coiled polymer and globular protein solutions, imitating the crowded cellular environment, was studied by Banks and Fradin (Banks and Fradin 2005).
(10) Sengupta et al. (Sengupta et al. 2003) carried out theoretical and experimental studies on errors in FCS measurements and, in particular, demonstrated a method for extracting information on distributions of diffusion rates for highly heterogeneous systems.
(11) Sanchez et al. (Sanchez et al. 2004) used FCS and brightness analysis (vide infra) to study the dimer–monomer dissociation of αβ tubulin induced by guanidinium hydrochloride.

(12) Sanchez and Gratton wrote an excellent review (Sanchez and Gratton 2005) of the application of two-photon FCS to study lipid–protein interactions in giant unilamellar vesicles.
(13) FCS methodologies are also now being implemented in high throughput screening—see, for example, Komura et al. (2005) and Sugiki et al. (2009)
(14) We also note a series of theoretical studies by Földes-Papp (Földes-Papp 2006, 2007a, b), which present thought-provoking discussions of "true" single molecule FCS approaches.

The use of the autocorrelation function for studies in living cells, however, is more limited. The technique is certainly useful for certain applications, such as the binding of ligands to receptors on the cell surface. An excellent review of this area has been written by Briddon and Hill (Briddon and Hill 2007) who describe many such studies, including binding to GABA(A) receptors on hippocampal neurons (Meissner and Haberlein 2003), binding of proinsulin C-peptide to intact and detergent solubilized human skin fibroblasts (Henriksson et al. 2001), and transferrin binding to human transferrin receptor (Schuler et al. 1999), to mention but a few. As more FCS studies on living cells began to appear, however, it became clear that the diffusional rates of many proteins in cellular interiors were much slower than expected. Studies in the 1980s and 1990s on the cellular interiors, using a variety of techniques, had suggested that the translational diffusion of proteins in the crowded milieu of the cytoplasmic environment was about threefold slower than that expected in water. As more sophisticated cell imaging methods became available, however, the existence of networks of diffusional barriers became more evident (reviewed by Luby-Phelps 1994). It now appears that—with few exceptions—the translational diffusions of proteins in the cell interior are significantly slower than one expects from a simple consideration of the molecular mass. An examination of thousands of proteins in yeast cells has shown that the translational diffusion rates, measured by FCS, are much slower than the theoretical values, both in the cytoplasm and in the nucleus (the recording of a lecture on Proteosome-Wide Fluctuation Analysis on *Saccharomyces cerevisiae* by Winfried Wiegraebe, presented at the 2008 Weber Symposium, can be viewed at http://www.lfd.uci.edu/weber/symposium/2008/). A recent study from the Berland lab (Wu et al. 2009b) bears on these issues. Namely, these researchers studied the intracellular dynamics of nuclear import receptors (karyopherins), both wild-type and mutants [expressed as enhanced (E)GFP constructs], in human embryonic kidney cells, using both classic autocorrelation functions and brightness analysis (described below). They observed that karyopherins had two- to fivefold lower diffusion coefficients in cells than calculated based on their molecular weights and on the diffusion coefficient of EGFP in cells. This reduction in the diffusional rates indicated that the karyopherins are associated with huge (mega-Dalton) complexes, and not just with their cargo. Brightness analysis showed that the karyopherins were monomeric at all observed concentrations—from 100 to 1000 nM—and thus the slow diffusion was not due to receptor aggregation. Using FCS, Paradise et al. (2007) also noted the reduced mobility of nuclear transport proteins, both in the cytoplasm and in the nucleus, and also used photobleaching methods to ascertain the contribution from an immobile fraction. Dross et al. (2009) studied the diffusion of EGFP in cell interiors and also present a useful discussion of the FCS-specific artifacts typically encountered in live cell studies as well as strategies for minimizing them.

Scanning FCS

A particular variant of FCS that deserves mention is scanning FCS (sFCS). By sFCS, we do not mean simple raster-type scanning of a laser to accumulate an image. Rather, we refer to the method of scanning the excitation in a particular pattern—usually circular, but sometimes a simple line scan—while obtaining FCS data at each point along the scan. Although the earliest implementations of the scanning approach to FFS utilized fixed illumination and a translating sample stage (Petersen et al. 1986; Weissman et al. 1976), present-day scanning is almost always accomplished by keeping the sample stationary while scanning the laser (see, for example, Berland et al. 1996; Ruan et al. 2004; Skinner et al. 2005). The sFCS method is particularly useful in cases wherein it is difficult to localize the excitation beam precisely in a target area—for example, a membrane. By scanning across the membrane, one is sure to have the beam traverse the target area, and if a circular scan is utilized, the beam will cross the membrane twice during each scan. The data stream can then be presented as a "carpet" that renders evident which data are associated with particular regions. An example of a circular scan and the associated carpet is shown in Fig. 4 (obtained from Garcia-Marcos et al. 2008). In this case, different ribosomal stalk proteins were linked with EGFP, and the image of the resulting yeast cell is shown in Fig. 4a along with a red circle depicting the scan. The "carpet" corresponding to the scan is shown in Fig. 4b with the *X*-coordinate displaying the number of the scan and the *Y*-coordinate displaying the time along a particular scan. For each line in the "carpet", PCH analysis (discussed below) was carried out to determine how many EGFP-labeled proteins were in each ribosome, which addressed the question of the distribution

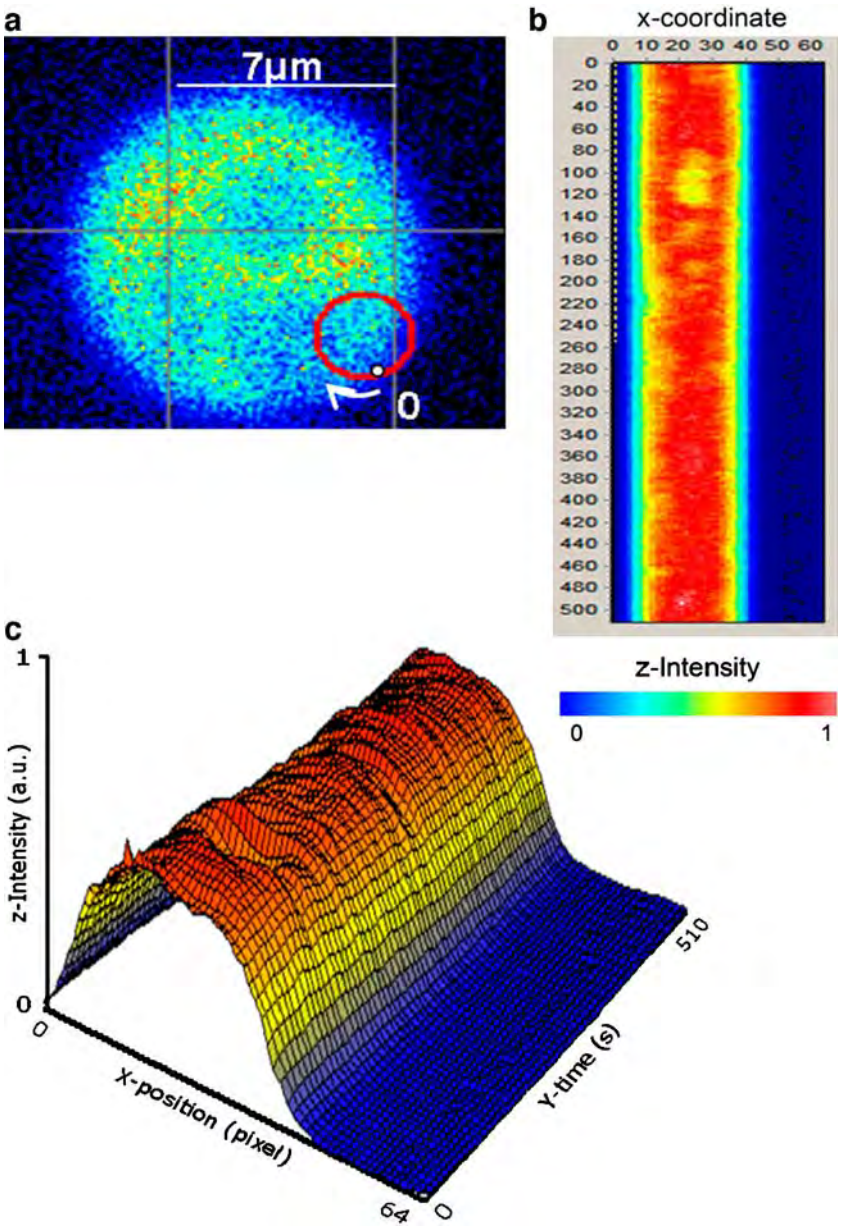

Fig. 4 **a** Intensity image of a yeast cell expressing enhanced green fluorescent protein (EGFP)-labeled ribosomal stalk proteins. The scanning orbit is depicted by the *red circle* (radius 1.52 µm). The point labeled *0* corresponds to the beginning of the scan (*point 0* in the *X*-position column in the "carpet") and the end of the scan (*point 63* in the *X*-position column in the "carpet"). **b** XY transformation of the raw scanning FCS. The *X*-position *columns* represent points along one circular scan, and the *Y*-position *rows* represent successive scans, with each scan taking 1 ms. The color scale indicates the relative intensities of the sections, with *orange* being the most intense and *blue* corresponding to intensities outside of the cell. Data were acquired at 64 kHz. **c** The time–intensity–position data of the "carpet" shown in **b** are replotted as a surface. The intensity–color scale is the same. (From Garcia-Marcos et al. 2008)

of different stalk proteins among the ribosome population in the living yeast cell. One should note that the diffusional rate of the target fluorophore should be slower than the orbital scanning rate to avoid biasing the recovered diffusion coefficient. Recently, Ries et al. (2009) used line-scan FCS (the data are collected along a single scan line) to obtain the diffusion coefficients and absolute concentrations of probes associated with biological membranes, while Petrasek et al. (2008) utilized scanning FCS to study the dynamics of the PAR-2 protein in the cytoplasm and on the cortex of *Caenorhabditis elegans* eggs before asymmetric cell division.

We note that an excellent source of information on RICS and other advanced FCS approaches, such as scanning FCS and N&B analysis (discussed below), can be found on the website for the Laboratory for Fluorescence Dynamics, and in particular on the sites presenting the lectures from the annual advanced workshops: http://www.lfd.uci.edu/workshop/.

Fluorescence cross-correlation spectroscopy

The suggestion that the signals from two different fluorophores, associated in some manner, could be followed by cross-correlation was first made by Rigler and Eigen (Eigen and Rigler 1994), and the first experimental realization of this approach was made by Schwille et al. (1997b). In the original manifestation of this method, two different laser beams, of two different wavelengths, were used in a one-photon mode to excite two different fluorophores. The

development and wide-spread utilization of two-photon lasers has greatly simplified the FCCS approach since typical fluorophores have sufficiently broad two-photon absorption cross sections, such that one excitation wavelength can effectively excite two different fluorophores. An example of this approach is given in Fig. 5. As indicated, the sample has two different fluorophores, indicated as red and green, whose emission can be separated by appropriate filters. The most common applications in cells utilize different fluorescent proteins, such as EGFP and mCherry. Each fluorophore will give rise to its own distinct autocorrelation curve, but it is also possible to cross-correlate the signals. In other words, the signal at one particular time

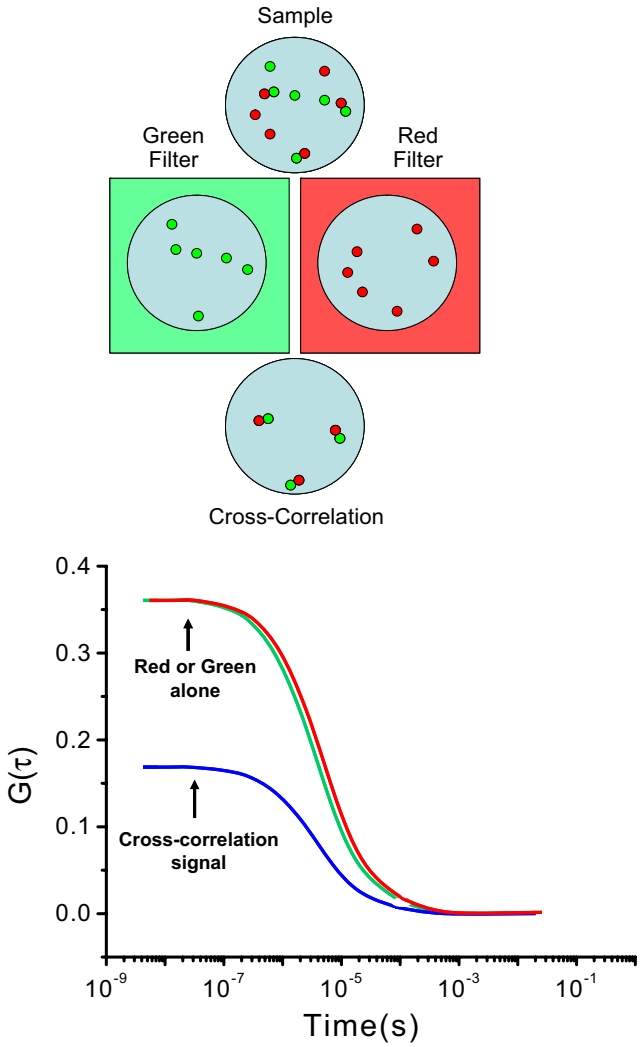

Fig. 5 Illustration depicting a dual color cross-correlation scenario. A sample containing both "*green*" and "*red*" proteins can be viewed through green or red filters that pass only one color. In this case, since the number of proteins and their diffusion rate are shown to be the same, the autocorrelation curves for data acquired through either green or red filters should look similar. When the green and red signals are cross-correlated, however, only the dimers containing both green and red proteins will contribute to the cross-correlated signal

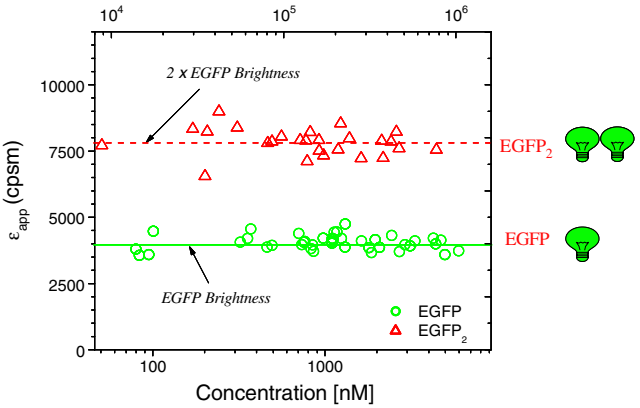

Fig. 6 Molecular brightness of EGFP and $EGFP_2$ as a function of average photon count rate and protein concentration. Note that the brightness levels are independent of concentration. Each *data point* represents the brightness measured in different cells expressing either EGFP or $EGFP_2$. (Adapted from Chen et al. 2003)

for fluorophore 1 can be correlated with the signal at a different time for fluorophore 2. If the two fluorophores are in some way linked, then the resulting cross-correlated signal will show correlation, as indicated in Fig. 5. (For examples and reviews of this approach, see Berland 2004; Bacia et al. 2002, 2006; Bacia and Schwille 2003; Hwang and Wohland 2007; Rarbach et al. 2001; Ruan and Tetin 2008; Weidtkamp-Peters et al. 2009.) The great advantage of this approach over fluorescence resonance energy transfer (FRET) methods commonly used to determine the proximity of fluorophores is that there is no requirement regarding the orientation or distance between the fluorophores. All that is required is that the movements of the two fluorophores are associated.

Photon counting histogram/fluorescence-intensity distribution analysis

Although the kinetics or temporal behavior of fluorescence fluctuations is best described by the autocorrelation function, the intensity of these fluctuations may also be analyzed in terms of a distribution. Initial approaches to this problem were presented by Palmer and Thompson (1987, 1989). Qian and Elson (1990a, b) then developed a technique based on the analysis of first and second moments of the photon counts. In 1999, two groups, from the USA and Germany independently extended this approach (Chen et al. 1999; Kask et al. 1999). The two groups named their methods photon counting histogram (PCH) (Chen et al.) and fluorescence-intensity distribution analysis (FIDA) (Kask et al.). In 2004, Müller developed the related fluorescence cumulant analysis (FCA) approach (Müller 2004). All of these methods rely on the determination of the inherent "brightness" of a fluorophore, i.e., the

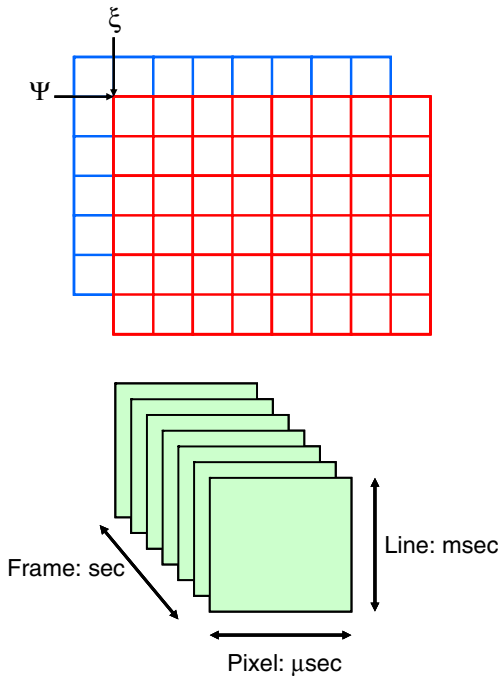

Fig. 7 Sketch illustrating the multiple-shifting operation carried out to calculate a spatial correlation function. The time scale associated with each aspect of an image is also shown. Typically, 50 to 100 frames are required for a raster scanning image correlation spectroscopy (RICS) analysis

actual counts per second per molecule (CPSM), which depends, of course, on the specific illumination and detection conditions of the particular experiment. The utility of the brightness approach to study protein complexes in living cells has been demonstrated by several groups (Chen et al. 2003; Chen and Müller 2007; Garcia-Marcos et al. 2008; Wu et al. 2009a, b). An illustration of the brightness principle is shown in Fig. 6 (taken from J. Müller; redrawn from Chen et al. 2003). In a recent tour de force of the application of brightness analysis, Chen et al. (2009) used the method to determine the stoichiometry of HIV-1 Gag proteins in viral-like particles (VLP) in COS-1 cells—finding values ranging from 750–2500, while the size of the VLPs remained relatively constant, as measured by the diffusion coefficients, which fit to a hydrodynamic diameter of 130 nm.

Raster scanning image correlation spectroscopy

Raster scanning image correlation spectroscopy (RICS) is one form of image correlation spectroscopy (ICS). The latter was originally developed by Nils Petersen (Petersen 1986; Petersen et al. 1986) as an image analog of traditional FCS. In ICS, spatial autocorrelations are calculated from

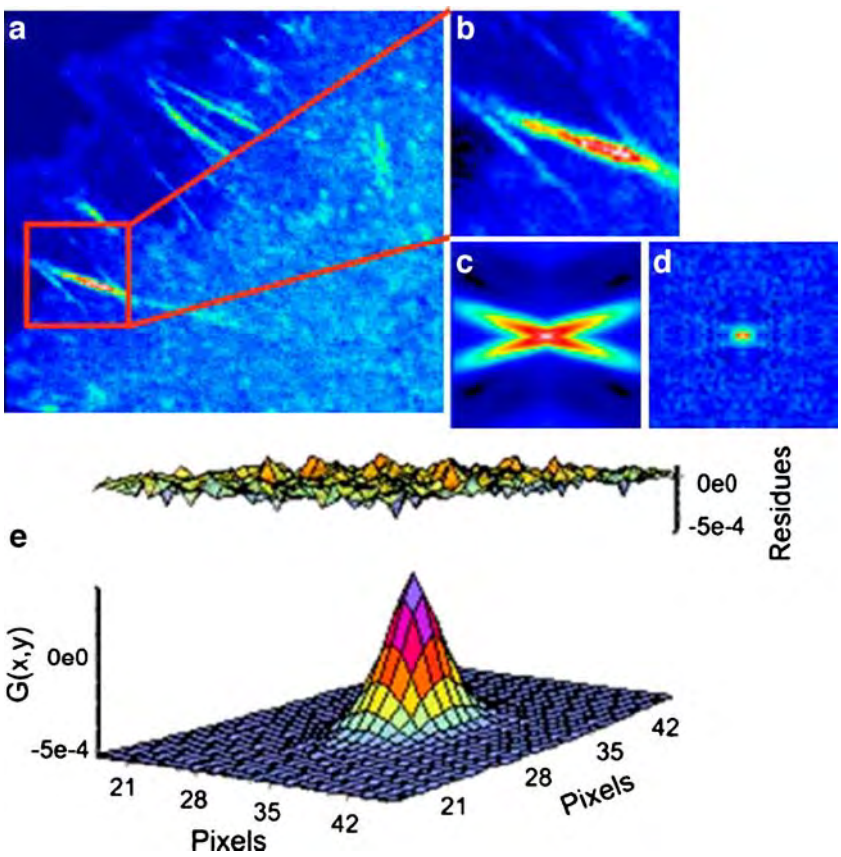

Fig. 8 **a** Image of a CHO-K1 cell expressing paxillin–EGFP. **b** 64×64 subframe in the cytosolic part of a focal adhesion structure. **c**, **d** Spatial autocorrelation before (**c**) and after (**d**) the subtraction of immobile structures. **e** Fit of the spatial correlation function in **d**. The diffusion coefficient in this cell region is 0.49 $\mu m^2 s^{-1}$. (From Digman et al. 2005a)

stacks of images obtained in a time-series. This method was extended in Enrico Gratton's lab (Digman et al. 2005a, b; Digman and Gratton 2009) to use a laser-scanning microscope to probe the time structure in images to spatially correlate pixels separated by microseconds (adjacent pixels in a line), milliseconds (pixels in successive lines), and seconds (pixels in different frames). Many other variants of the ICS method have appeared including TICS, ICCS, STICS, kICS, and PICS, and the bewildered reader should consult the excellent review by Kolen and Wiseman (Kolin and Wiseman 2007), which will guide him/her through this acronym jungle. The diffusion of a particle in a uniform medium can be described by the relation:

$$C(r,t) = \frac{1}{(4\pi Dt)^{3/2}} \exp\left(-\frac{r^2}{4Dt}\right) \quad (5)$$

where C(r, t) represents the concentration of the particle at position r and time t, and D is the diffusion coefficient. In a RICS experiment, we are concerned with the spatial aspect. In this method, the spatial autocorrelation is similar to the time-dependent autocorrelation function carried out in traditional FCS except that the correlation is carried out on different spatial points in the image, as illustrated in Fig. 7. In this case, the autocorrelation is defined as:

$$G(\xi,\psi) = \frac{< I(x,y).I(x+\xi,y+\psi) >}{< I(x,y) >^2} \quad (6)$$

where ξ and ψ represent the spatial increments in the x and y directions, respectively, which are correlated. Spatial correlation functions are illustrated in Fig. 8b–e. One must bear in mind that in a RICS experiment the scan rate must be compatible with the diffusion being examined, or for that matter with any process which affects this diffusion. Details on this consideration can be found in the initial publications by Digman et al. (2005a, b). An example of a RICS analysis is shown in Fig. 8 from Digman et al. (2008a). As shown, an important aspect of the RICS method is that it permits the subtraction of immobile components and hence allows one to better quantify dynamic aspects of the system. In the paxillin study, the authors were able to study the assembly and disassembly of paxillin aggregates at focal adhesions in various loci in the cell. A recent study by Gielen et al. (Gielen et al. 2009) used the RICS approach to measure the diffusion of lipid-like probes in artificial and natural membranes.

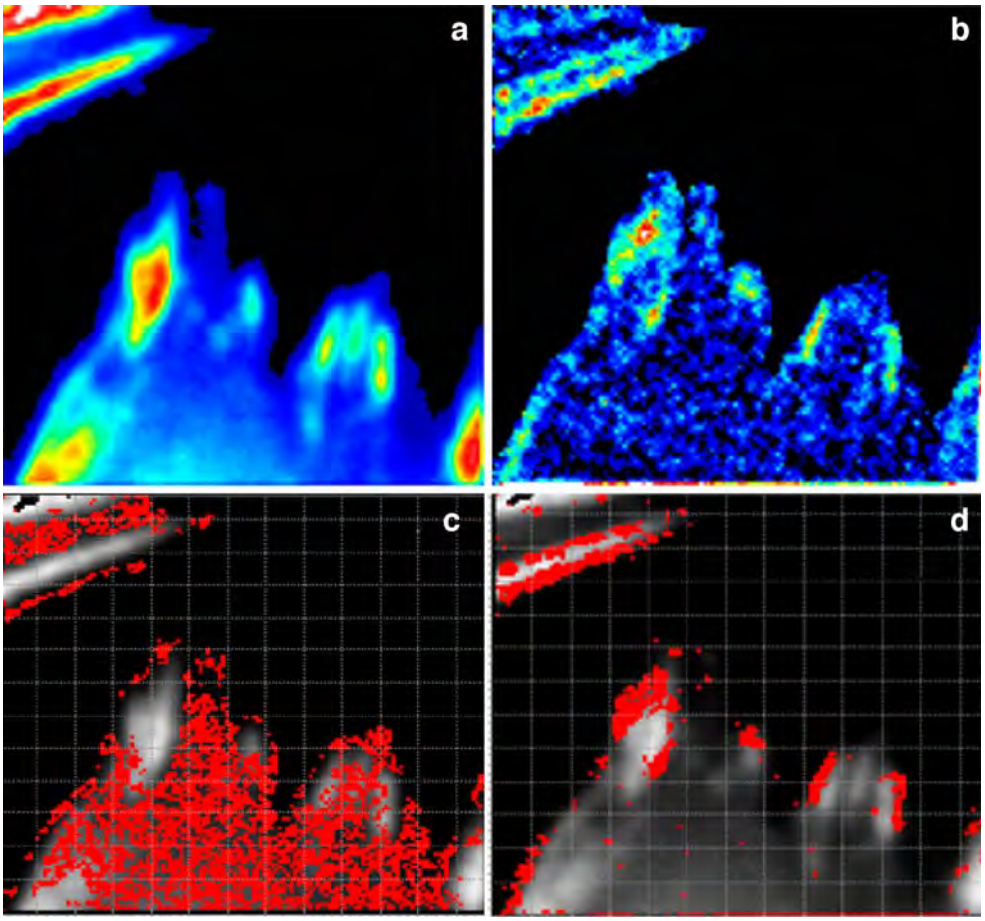

Fig. 9 An example of number and brightness (N&B) analysis from Digman et al. (2008b). Paxillin–EGFP was expressed in CHO-K1 cells. **a** Image intensity map showing paxillin accumulating at focal adhesions (image size 31×31 μm). **b** Brightness image showing that larger B values are at the borders of some adhesions. **c** All pixels having brightness values of 1150 counts/s/molecule (corresponding to EGFP monomers) are selected. Note that these points accumulate in the cytosol. **d** All pixels of 11,500 counts/s/molecule are selected. Note that these pixels are at the borders of the adhesions

Number and brightness

The number and brightness (N&B) approach to image analysis was recently introduced by Enrico Gratton's laboratory (Digman et al. 2008b, 2009). This technique can be applied to images acquired using confocal microscopy or TIRF (Unruh and Gratton 2008) as long as the pixel dwell time is less than the characteristic diffusion time of the particle. The N&B approach can be considered the imaging equivalent of the PCH method; however, N&B does not require a non-linear fit of the data, and the average particle number <N> and particle brightness B are extracted directly from the image intensity data.

$$B = \frac{\sigma^2}{< k >}; \qquad < N >= \frac{< k >^2}{\sigma^2} \tag{7}$$

where $<k> = \Sigma k_i/M$ is the average number of counts, k is the number of counts for each image i, M is the total number of images, $\sigma^2 = \Sigma(k_i - < k >)^2/M$ is the variance of the number of counts. This analysis is carried out for each pixel. However there is also a contribution to the variance of the signal due to the shot noise of the detector; thus, the true number of molecules, n, and brightness, ε, are given by:

$$n = \frac{< k >^2}{\sigma^2 - < k >}; \qquad \varepsilon = \frac{\sigma^2 - < k >}{< k >} \tag{8}$$

It should be noted that the PCH method requires acquisition of a large number of photons at each point for reasonable precision of the oligomeric state of the target molecule and as such does not readily lend itself to image analysis. The N&B approach, although not as precise at each pixel in the image as the PCH method, nonetheless allows for a rapid estimation of aggregate size. The general concept is illustrated in Fig. 9 (modified from Digman et al. 2008a). The N&B approach has thus far only been applied to relatively few biological systems. One of the more recent applications was by Sanabria et al. (2008) who used N&B and RICS to investigate the effect of calcium on eGFP–calmodulin and its interaction with other cellular proteins.

Closing remarks

The preceding discussion has briefly covered several of the FFS methods currently being applied to cell biology. These techniques are becoming ever more accessible to biologists as commercial instrumentation becomes less expensive and as specialized workshops and courses teaching the latest methodologies reach increasing numbers of students. Given these considerations, coupled with the continual appearance of new and exciting genetic and molecular biological manipulations, one can expect ever increasing applications of FFS in the life sciences. We hope this review will motivate some readers to learn more about this exciting area and to consider using FFS to shed light on their favorite biological mystery.

Acknowledgments The authors wish to thank Nicholas James for critically reading the manuscript. This work was supported by National Institutes of Health grant RO1GM076665 (DMJ) and a grant from Allergan, Inc.

References

Bacia K, Schwille P (2003) A dynamic view of cellular processes by in vivo fluorescence auto- and cross-correlation spectroscopy. Methods 29:74–85

Bacia K, Majoul IV, Schwille P (2002) Probing the endocytic pathway in live cells using dual-color fluorescence cross-correlation analysis. Biophys J 83:1184–1193

Bacia K, Kim SA, Schwille P (2006) Fluorescence cross-correlation spectroscopy in living cells. Nat Methods 3:83–89

Banks DS, Fradin C (2005) Anomalous diffusion of proteins due to molecular crowding. Biophys J 89:2960–2971

Bark N, Földes-Papp Z, Rigler R (1999) The incipient stage in thrombin-induced fibrin polymerization detected by FCS at the single molecule level. Biochem Biophys Res Commun 260:35–41

Berland KM (2004) Detection of specific DNA sequences using dual-color two-photon fluorescence correlation spectroscopy. J Biotechnol 108:127–136

Berland KM, So PT, Gratton E (1995) Two-photon fluorescence correlation spectroscopy: method and application to the intracellular environment. Biophys J 68:694–701

Berland KM, So PT, Chen Y, Mantulin WW, Gratton E (1996) Scanning two-photon fluctuation correlation spectroscopy: particle counting measurements for detection of molecular aggregation. Biophys J 71:410–420

Bestvater F, Spiess E, Stobrawa G, Hacker M, Feurer T, Porwol T, Berchner-Pfannschmidt U, Wotzlaw C, Acker H (2002) Two-photon fluorescence absorption and emission spectra of dyes relevant for cell imaging. J Microsc 208:108–115

Borejdo J (1979) Motion of myosin fragments during actin-activated ATPase: fluorescence correlation spectroscopy study. Biopolymers 18:2807–2820

Briddon SJ, Hill SJ (2007) Pharmacology under the microscope: the use of fluorescence correlation spectroscopy to determine the properties of ligand-receptor complexes. Trends Pharmacol Sci 28:637–645

Brock R, Hink MA, Jovin TM (1998) Fluorescence correlation microscopy of cells in the presence of autofluorescence. Biophys J 75:2547–2557

Brown R (1828) A brief account of microscopical observations made in the months of June, July and August 1827 on the particles contained in the pollen of plants; and on the general existence of active molecules in organic and inorganic bodies. Ray Society (1868), London

Bulseco DA, Wolf DE (2007) Fluorescence correlation spectroscopy: molecular complexing in solution and in living cells. Methods Cell Biol 81:525–559

Chen Y, Müller JD (2007) Determining the stoichiometry of protein heterocomplexes in living cells with fluorescence fluctuation spectroscopy. Proc Natl Acad Sci USA 104:3147–3152

Chen Y, Müller JD, Berland KM, Gratton E (1999) Fluorescence fluctuation spectroscopy. Methods 19:234–252

Chen Y, Wei LN, Müller JD (2003) Probing protein oligomerization in living cells with fluorescence fluctuation spectroscopy. Proc Natl Acad Sci USA 100:15492–15497

Chen Y, Wu B, Musier-Forsyth K, Mansky LM, Müller JD (2009) Fluorescence fluctuation spectroscopy on viral-like particles reveals variable gag stoichiometry. Biophys J 96:1961–1969

Denk W, Strickler JH, Webb WW (1990) Two-photon laser scanning fluorescence microscopy. Science 248:73–76

Dertinger T, Loman A, Ewers B, Müller CB, Kramer B, Enderlein J (2008) The optics and performance of dual-focus fluorescence correlation spectroscopy. Opt Express 16:14353–14368

Dickson RM, Cubitt AB, Tsien RY, Moerner WE (1997) On/off blinking and switching behaviour of single molecules of green fluorescent protein. Nature 388:355–358

Digman MA, Gratton E (2009) Analysis of diffusion and binding in cells using the RICS approach. Microsc Res Tech 72:323–332

Digman MA, Brown CM, Sengupta P, Wiseman PW, Horwitz AR, Gratton E (2005a) Measuring fast dynamics in solutions and cells with a laser scanning microscope. Biophys J 89:1317–1327

Digman MA, Sengupta P, Wiseman PW, Brown CM, Horwitz AR, Gratton E (2005b) Fluctuation correlation spectroscopy with a laser-scanning microscope: exploiting the hidden time structure. Biophys J 88:L33–L36

Digman MA, Dalal R, Horwitz AF, Gratton E (2008a) Mapping the number of molecules and brightness in the laser scanning microscope. Biophys J 94:2320–2332

Digman MA, Brown CM, Horwitz AR, Mantulin WW, Gratton E (2008b) Paxillin dynamics measured during adhesion assembly and disassembly by correlation spectroscopy. Biophys J 94: 2819–2831

Digman MA, Wiseman PW, Choi C, Horwitz AR, Gratton E (2009) Stoichiometry of molecular complexes at adhesions in living cells. Proc Natl Acad Sci USA 106:2170–2175

Dross N, Spriet C, Zwerger M, Müller G, Waldeck W, Langowski J (2009) Mapping eGFP oligomer mobility in living cell nuclei. PLoS ONE 4:e5041

Eigen M, Rigler R (1994) Sorting single molecules: application to diagnostics and evolutionary biotechnology. Proc Natl Acad Sci USA 91:5740–5747

Einstein A (1905) Über die von der molekularkinetischen Theorie der Wärme geforderte Bewegung von in ruhenden Flüssigkeiten suspendierten Teilchen. Ann Phys 322:549–560

Elson EL (2004) Quick tour of fluorescence correlation spectroscopy from its inception. J Biomed Opt 9:857–864

Elson EL, Magde D (1974). Fluorescence correlation spectroscopy. I. Conceptual basis and theory. Biopolymers 13(1):1–27

Földes-Papp Z (2006) What it means to measure a single molecule in a solution by fluorescence fluctuation spectroscopy. Exp Mol Pathol 80:209–218

Földes-Papp Z (2007a) Fluorescence fluctuation spectroscopic approaches to the study of a single molecule diffusing in solution and a live cell without systemic drift or convection: a theoretical study. Curr Pharm Biotechnol 8:261–273

Földes-Papp Z (2007b) 'True' single-molecule molecule observations by fluorescence correlation spectroscopy and two-color fluorescence cross-correlation spectroscopy. Exp Mol Pathol 82:147–155

Gaietta G, Deerinck TJ, Adams SR, Bouwer J, Tour O, Laird DW, Sosinsky GE, Tsien RY, Ellisman MH (2002) Multicolor and electron microscopic imaging of connexin trafficking. Science 296:503–507

Garai K, Sureka R, Maiti S (2007) Detecting amyloid-beta aggregation with fiber-based fluorescence correlation spectroscopy. Biophys J 92:L55–L57

Garcia-Marcos A, Sanchez SA, Parada P, Eid J, Jameson DM, Remacha M, Gratton E, Ballesta JP (2008) Yeast ribosomal stalk heterogeneity in vivo shown by two-photon FCS and molecular brightness analysis. Biophys J 94:2884–2890

Gerard M, Debyser Z, Desender L, Kahle PJ, Baert J, Baekelandt V, Engelborghs Y (2006) The aggregation of alpha-synuclein is stimulated by FK506 binding proteins as shown by fluorescence correlation spectroscopy. FASEB J 20:524–526

Gielen E, Smisdom N, vandeVen M, De Clercq B, Gratton E, Digman M, Rigo JM, Hofkens J, Engelborghs Y, Ameloot M (2009) Measuring diffusion of lipid-like probes in artificial and natural membranes by raster image correlation spectroscopy (RICS): use of a commercial laser-scanning microscope with analog detection. Langmuir 25:5209–5218

Griffin BA, Adams SR, Tsien RY (1998) Specific covalent labeling of recombinant protein molecules inside live cells. Science 281: 269–272

Hazlett TL, Ruan Q, Tetin SY (2005) Application of fluorescence correlation spectroscopy to hapten-antibody binding. Methods Mol Biol 305:415–438

Henriksson M, Pramanik A, Shafqat J, Zhong Z, Tally M, Ekberg K, Wahren J, Rigler R, Johansson J, Jornvall H (2001) Specific binding of proinsulin C-peptide to intact and to detergent-solubilized human skin fibroblasts. Biochem Biophys Res Commun 280:423–427

Hess ST, Webb WW (2002) Focal volume optics and experimental artifacts in confocal fluorescence correlation spectroscopy. Biophys J 83:2300–2317

Humpolickova J, Gielen E, Benda A, Fagulova V, Vercammen J, Vandeven M, Hof M, Ameloot M, Engelborghs Y (2006) Probing diffusion laws within cellular membranes by Z-scan fluorescence correlation spectroscopy. Biophys J 91:L23–L25

Hwang LC, Wohland T (2007) Recent advances in fluorescence cross-correlation spectroscopy. Cell Biochem Biophys 49:1–13

Kask P, Palo K, Ullmann D, Gall K (1999) Fluorescence-intensity distribution analysis and its application in biomolecular detection technology. Proc Natl Acad Sci USA 96:13756–13761

Kerppola TK (2008) Bimolecular fluorescence complementation (BiFC) analysis as a probe of protein interactions in living cells. Annu Rev Biophys 37:465–487

Kim HM, Cho BR (2009) Two-photon probes for intracellular free metal ions, acidic vesicles, and lipid rafts in live tissues. Acc Chem Res (in press)

Kolin DL, Wiseman PW (2007) Advances in image correlation spectroscopy: measuring number densities, aggregation states, and dynamics of fluorescently labeled macromolecules in cells. Cell Biochem Biophys 49:141–164

Komura H, Matsuda K, Shigemoto Y, Kawahara I, Ano R, Murayama Y, Moriwaki T, Yoshida NH (2005) High throughput screening of pharmacokinetics and metabolism in drug discovery (II)-investigation on in vitro and in vivo correlation in drug metabolism screening. Yakugaku Zasshi 125:131–139

Lieto AM, Cush RC, Thompson NL (2003) Ligand-receptor kinetics measured by total internal reflection with fluorescence correlation spectroscopy. Biophys J 85:3294–3302

Luby-Phelps K (1994) Physical properties of cytoplasm. Curr Opin Cell Biol 6:3–9

Madge DE, Elson EL, Webb WW (1972) Thermodynamics fluctuations in a reacting system: measurement by fluorescence correlation spectroscopy. Phys Rev Lett 29:705–708

Magde D, Elson EL, Webb WW (1974) Fluorescence correlation spectroscopy. II. An experimental realization. Biopolymers 13:29–61

Maiti S, Haupts U, Webb WW (1997) Fluorescence correlation spectroscopy: diagnostics for sparse molecules. Proc Natl Acad Sci USA 94:11753–11757

Meissner O, Haberlein H (2003) Lateral mobility and specific binding to GABA(A) receptors on hippocampal neurons monitored by fluorescence correlation spectroscopy. Biochemistry 42:1667–1672

Müller JD (2004) Cumulant analysis in fluorescence fluctuation spectroscopy. Biophys J 86:3981–3992

Müller CB, Loman A, Pacheco V, Koberling F, Willbold D, Richtering W, Enderlein J (2008) Precise measurement of diffusion by multi-color dual-focus fluorescence correlation spectroscopy. EPL 83:46001p1–46001p5

Nienhaus GU, Wiedenmann J (2009) Structure, dynamics and optical properties of fluorescent proteins: perspectives for marker development. ChemPhysChem 10(9-10):1369–1379

Nirmal M, Norris DJ, Kuno M, Bawendi MG, Efros AL, Rosen M (1995) Observation of the "Dark exciton" in CdSe quantum dots. Phys Rev Lett 75:3728–3731

Orden AV, Jung J (2008) Review fluorescence correlation spectroscopy for probing the kinetics and mechanisms of DNA hairpin formation. Biopolymers 89:1–16

Palmer AG 3rd, Thompson NL (1987) Molecular aggregation characterized by high order autocorrelation in fluorescence correlation spectroscopy. Biophys J 52:257–270

Palmer AG 3rd, Thompson NL (1989) High-order fluorescence fluctuation analysis of model protein clusters. Proc Natl Acad Sci USA 86:6148–6152

Paradise A, Levin MK, Korza G, Carson JH (2007) Significant proportions of nuclear transport proteins with reduced intracellular mobilities resolved by fluorescence correlation spectroscopy. J Mol Biol 365:50–65

Pawlicki M, Collins HA, Denning RG, Anderson HL (2009) Two-photon absorption and the design of two-photon dyes. Angew Chem Int Ed Engl 48:3244–3266

Perrin J (1913) Les Atomes. Librairie Felix Alcan, Paris

Petersen NO (1986) Scanning fluorescence correlation spectroscopy. I. Theory and simulation of aggregation measurements. Biophys J 49:809–815

Petersen NO, Johnson DC, Schlesinger MJ (1986) Scanning fluorescence correlation spectroscopy. II. Application to virus glycoprotein aggregation. Biophys J 49:817–820

Petrasek Z, Schwille P (2008) Precise measurement of diffusion coefficients using scanning fluorescence correlation spectroscopy. Biophys J 94:1437–1448

Petrasek Z, Hoege C, Mashaghi A, Ohrt T, Hyman AA, Schwille P (2008) Characterization of protein dynamics in asymmetric cell division by scanning fluorescence correlation spectroscopy. Biophys J 95:5476–5486

Qian H, Elson EL (1990a) Distribution of molecular aggregation by analysis of fluctuation moments. Proc Natl Acad Sci USA 87:5479–5483

Qian H, Elson EL (1990b) On the analysis of high order moments of fluorescence fluctuations. Biophys J 57:375–380

Qian H, Elson EL (1991) Analysis of confocal laser-microscope optics for 3-D fluorescence correlation spectroscopy. Appl Optics 30:1185–1195

Rarbach M, Kettling U, Koltermann A, Eigen M (2001) Dual-color fluorescence cross-correlation spectroscopy for monitoring the kinetics of enzyme-catalyzed reactions. Methods 24:104–116

Rauer B, Neumann E, Widengren J, Rigler R (1996) Fluorescence correlation spectrometry of the interaction kinetics of tetramethylrhodamin alpha-bungarotoxin with *Torpedo californica* acetylcholine receptor. Biophys Chem 58:3–12

Rhoades E, Ramlall TF, Webb WW, Eliezer D (2006) Quantification of alpha-synuclein binding to lipid vesicles using fluorescence correlation spectroscopy. Biophys J 90:4692–4700

Ries J, Petrov EP, Schwille P (2008) Total internal reflection fluorescence correlation spectroscopy: effects of lateral diffusion and surface-generated fluorescence. Biophys J 95:390–399

Ries J, Chiantia S, Schwille P (2009) Accurate determination of membrane dynamics with line-scan FCS. Biophys J 96:1999–2008

Riesner D (2001) In: Rigler R, Elson E (eds) Fluorescence correlation spectroscopy theory and applications, pp. 225–247

Ruan Q, Tetin SY (2008) Applications of dual-color fluorescence cross-correlation spectroscopy in antibody binding studies. Anal Biochem 374:182–195

Ruan Q, Cheng MA, Levi M, Gratton E, Mantulin WW (2004) Spatial-temporal studies of membrane dynamics: scanning fluorescence correlation spectroscopy (SFCS). Biophys J 87:1260–1267

Sanabria H, Digman MA, Gratton E, Waxham MN (2008) Spatial diffusivity and availability of intracellular calmodulin. Biophys J 95:6002–6015

Sanchez SA, Gratton E (2005) Lipid-protein interactions revealed by two-photon microscopy and fluorescence correlation spectroscopy. Acc Chem Res 38:469–477

Sanchez SA, Chen Y, Müller JD, Gratton E, Hazlett TL (2001) Solution and interface aggregation states of *Crotalus atrox* venom phospholipase A2 by two-photon excitation fluorescence correlation spectroscopy. Biochemistry 40:6903–6911

Sanchez SA, Brunet JE, Jameson DM, Lagos R, Monasterio O (2004) Tubulin equilibrium unfolding followed by time-resolved fluorescence and fluorescence correlation spectroscopy. Protein Sci 13:81–88

Schuler J, Frank J, Trier U, Schafer-Korting M, Saenger W (1999) Interaction kinetics of tetramethylrhodamine transferrin with human transferrin receptor studied by fluorescence correlation spectroscopy. Biochemistry 38:8402–8408

Schwille P, Bieschke J, Oehlenschlager F (1997a) Kinetic investigations by fluorescence correlation spectroscopy: the analytical and diagnostic potential of diffusion studies. Biophys Chem 66:211–228

Schwille P, Meyer-Almes FJ, Rigler R (1997b) Dual-color fluorescence cross-correlation spectroscopy for multicomponent diffusional analysis in solution. Biophys J 72:1878–1886

Sengupta P, Garai K, Balaji J, Periasamy N, Maiti S (2003) Measuring size distribution in highly heterogeneous systems with fluorescence correlation spectroscopy. Biophys J 84:1977–1984

Skinner JP, Chen Y, Müller JD (2005) Position-sensitive scanning fluorescence correlation spectroscopy. Biophys J 89:1288–1301

Smoluchowski M (1906) Zur kinetischen Theorie der Brownschen Molekularbewegung und der Suspensionen. Ann Phys 21:756–780

Sugiki T, Yoshiura C, Kofuku Y, Ueda T, Shimada I, Takahashi H (2009) High-throughput screening of optimal solution conditions for structural biological studies by fluorescence correlation spectroscopy. Protein Sci 18:1115–1120

Svedberg T, Inouye K (1911) Eine neue Methode zur Prüfung der Gültigkeit des Boyle-Gay-Lussacschen Gesetzes für Kolloide Lösungen. Zeit Phys Chem 77:145–191

Tjernberg LO, Pramanik A, Bjorling S, Thyberg P, Thyberg J, Nordstedt C, Berndt KD, Terenius L, Rigler R (1999) Amyloid beta-peptide polymerization studied using fluorescence correlation spectroscopy. Chem Biol 6:53–62

Unruh JR, Gratton E (2008) Analysis of molecular concentration and brightness from fluorescence fluctuation data with an electron multiplied CCD camera. Biophys J 95:5385–5398

Webb WW (2001) Fluorescence correlation spectroscopy: inception, biophysical experimentations, and prospectus. Appl Opt 40:3969–3983

Weidtkamp-Peters S, Felekyan S, Bleckmann A, Simon R, Becker W, Kuhnemuth R, Seidel CA (2009) Multiparameter fluorescence image spectroscopy to study molecular interactions. Photochem Photobiol Sci 8:470–480

Weissman M, Schindler H, Feher G (1976) Determination of molecular weights by fluctuation spectroscopy: application to DNA. Proc Natl Acad Sci USA 73:2776–2780

Wu B, Chen Y, Müller JD (2009a) Fluorescence fluctuation spectroscopy of mCherry in living cells. Biophys J 96:2391–2404

Wu J, Corbett AH, Berland KM (2009b) The intracellular mobility of nuclear import receptors and NLS cargoes. Biophys J 96:3840–3849

Yao J, Larson DR, Vishwasrao HD, Zipfel WR, Webb WW (2005) Blinking and nonradiant dark fraction of water-soluble quantum dots in aqueous solution. Proc Natl Acad Sci USA 102:14284–14289

Eric Reits, Thursday June 14th 2012, 10.00

From fixed to FRAP: measuring protein mobility and activity in living cells

Eric A.J. Reits and Jacques J. Neefjes*

Division of Tumor Biology, The Netherlands Cancer Institute, Plesmanlaan 121, 1066 CX Amsterdam, The Netherlands
**e-mail: jneefjes@nki.nl*

Experiments with fluorescence recovery after photobleaching (FRAP) started 30 years ago to visualize the lateral mobility and dynamics of fluorescent proteins in living cells. Its popularity increased when non-invasive fluorescent tagging became possible with the green fluorescent protein (GFP). Many researchers use GFP to study the localization of fusion proteins in fixed or living cells, but the same fluorescent proteins can also be used to study protein mobility in living cells. Here we review the potential of FRAP to study protein dynamics and activity within a single living cell. These measurements can be made with most standard confocal laser-scanning microscopes equipped with photobleaching protocols.

In FRAP experiments, fluorescent molecules are irreversibly photobleached in a small area of the cell by a high-powered focused laser beam. Subsequent diffusion of surrounding non-bleached fluorescent molecules into the bleached area leads to a recovery of fluorescence, which is recorded at low laser power. FRAP experiments started in the 1970s using lipophilic or hydrophilic fluorophores, like fluorescein, coupled to proteins and lipids[1,2]. The cloning of GFP from the jellyfish *Aequorea victoria* introduced a new fluorescent reporter protein to study the localization of chimaeric proteins in living cells. This development made it possible to perform FRAP on living cells without disruption by microinjection. In addition, GFP-tagged molecules can be targeted to various sites in the cell and can be observed for long periods because the GFP molecule is very photostable. The attachment of GFP rarely affects the function and localization of the fusion protein. These properties of GFP thus considerably enhanced the biological applications of photobleaching studies.

Quantitative photobleaching

FRAP experiments provide information about the mobility of a fluorescent molecule in a defined compartment. Two parameters can be deduced from FRAP: the mobile fraction of fluorescent molecules and the rate of mobility, which is related to the characteristic diffusion time, τ_D. Figure 1 shows a typical fluorescence recovery curve, allowing the determination of the two parameters. The mobile fraction can be determined by comparing the fluorescence in the bleached region after full recovery (F_∞) with the fluorescence before bleaching (F_i) and just after bleaching (F_0). The mobile fraction R is defined as

$$R = (F_\infty - F_0)/(F_i - F_0)$$

The mobile fraction can change in different circumstances, for example when the fluorescent protein interacts with other molecules or membranes. The mobile fraction can also be affected by membrane barriers and microdomains in the membrane. These discontinuities can prevent, or temporarily restrict, the free diffusion of membrane molecules.

When motion due to active transport or unidirectional flow can be discounted, protein mobility in a cell is due to brownian motion. The mobility is expressed as the diffusion coefficient D, which is related to the diffusion time τ_D. Most formulas describing this relationship are based on the two-dimensional diffusion equation described by Axelrod *et al.*[3]:

$$\tau_D = \omega^2\gamma/4D$$

where ω is defined as the radius of the focused circular laser beam at the e^{-2} intensity and γ is a correction factor for the amount of bleaching. This equation assumes unrestricted two-dimensional diffusion in a circular bleached area, with no recovery from above and below the focal plane. Because this is valid for diffusion in membranes and thin films of liquid only, other formulas have evolved as well[4,5]. It is beyond the scope of this review to discuss all mathematical models in detail, but we shall mention some biologically important parameters determining diffusion of soluble and membrane-bound molecules.

Unrestricted diffusion of a particle in a free-volume model is described by the Stokes–Einstein formula[6]:

$$D = kT/6\pi\eta R_h$$

which correlates the hydrodynamic behaviour of a sphere with the absolute temperature T, the viscosity of the solution η, the Boltzmann constant k and the hydrodynamic radius of the particle R_h. Because the local absolute temperature is hardly affected by bleaching[7], and the viscosity of water and cytosol are relatively constant under experimental conditions, D is determined mainly by R_h. When a molecule is assumed to be a sphere with a volume proportional to its molecular mass, the diffusion coefficient is proportional to the inverse of the cube root of molecular mass ($D \sim M^{-1/3}$). The relationship between D and the hydrodynamic radius was confirmed with a range of macromolecules *in vitro*[8,9]. There is no clear size limit for free diffusion *in vivo* because even large protein complexes such as the proteasome[10] can diffuse freely through the cytoplasm and the nucleus. In addition to temperature, viscosity and radius, other factors affect diffusion in living cells, including specific interactions but also hindrance by mobile and immobile obstacles. Collision with other proteins and barriers such as cytoskeletal filaments affects mobility, as shown by experiments with swollen and shrunken cells[11,12].

FRAP has also been used extensively to study the lateral diffusion of membrane-associated proteins. This diffusion is considerably slower than that of soluble proteins because membranes have a much higher viscosity. The aqueous phase of a transmembrane molecule hardly affects diffusion because the viscosity of the mem-

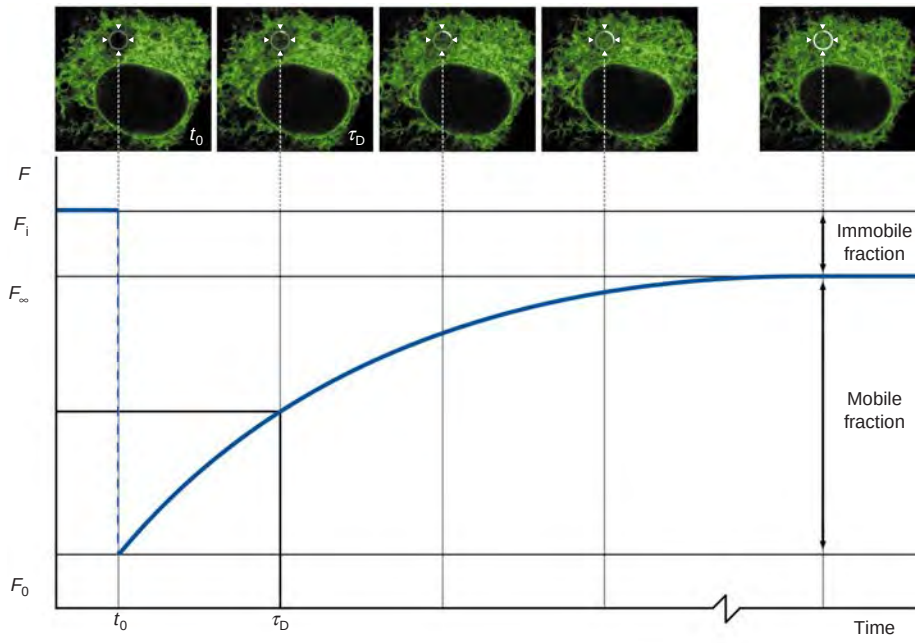

Figure 1 **Fluorescence recovery after photobleaching (FRAP).** When a region in the fluorescent area (here the endoplasmic reticulum) is bleached at time t_0 the fluorescence decreases from the initial fluorescence F_i to F_0. The fluorescence recovers over time by diffusion until it has fully recovered (F_∞). The characteristic diffusion time τ_D indicates the time at which half of the fluorescence has recovered. The mobile fraction can be calculated by comparing the fluorescence in the bleached region after full recovery (F_∞) with that before bleaching (F_i) and just after bleaching (F_0).

brane is much higher. For instance, large deletions in the cytoplasmic domain of the epidermal growth factor (EGF) receptor do not affect its lateral mobility[13]. Nevertheless, similar mathematics apply to the diffusion of membrane-associated molecules, although the main variable is now the radius of the protein segment located in the membrane phase. The Saffman–Delbrück equation[14] thus correlates the diffusion mainly with the radius of the transmembrane segment but again also with viscosity and the absolute temperature:

$$D = cT\ln[(k/ha) - 0.5772]$$

where D is the diffusion coefficient, c and k are constants incorporating the viscosity of the aqueous phase and the membrane bilayer thickness, T is the absolute temperature, η is the viscosity of the membrane and a is the radius of the transmembrane segment. When different large membrane proteins were compared, a dependence on radius and temperature was indeed observed[15].

The Saffman–Delbrück equation considers a theoretical protein with a cylindrical transmembrane segment without interactions with the surrounding lipid bilayer. However, most membrane molecules diffuse more slowly than expected for random brownian motion in a lipid layer. This might be due to interactions, tilted transmembrane segments, obstacles, and temporary binding sites in cell membranes[16]. The Saffman–Delbrück equation should therefore be considered an approximation from which the actual radius cannot be calculated. Few transmembrane proteins have a cylindrical transmembrane domain and most are subjected to conformational changes, aggregate formation and lipid interactions that can affect the mobility of the protein–lipid complex without changing the radius.

Applications of FRAP in living cells

FRAP can be used to address a number of questions about protein localization, dynamics and interactions with other components in living cells. The mobility of molecules within specific cell compartments has been visualized, as has membrane continuity. Experiments with GFP-tagged molecules targeted to specific organelles and compartments such as mitochondria[17] and the nucleus[18] show that most proteins can move freely within these compartments. Because their mobility is independent of ATP, diffusion is the primary means of movement. FRAP showed that protein immobilization is not responsible for the retention of either misfolded proteins in the endoplasmic reticulum (ER) membrane[19] or Golgi molecules[20], as these membrane molecules diffuse rapidly as well. Proteins in the ER lumen and membrane can diffuse with a high mobility through the ER and the perinuclear envelope, which forms a continuous membrane system. In comparison with organelles, some cell-surface proteins have a much lower mobility[21] and an altered mobile fraction. This is possibly due to interactions with cytoskeleton elements or the extracellular matrix.

Whereas these studies visualize the dynamics of proteins in a cell organelle, FRAP can also be used to follow events during cell division and signalling. For example, the nuclear envelope fuses with the ER during mitosis, as was observed using the GFP-tagged nuclear membrane molecule lamin-B receptor[22]. Although immobile in the nuclear envelope of interphase cells, the lamin-B receptor diffuses freely and rapidly when redistributed to the ER. Similarly, the disassembly and reassociation of nucleoli during mitosis was monitored with fibrillarin–GFP[23], showing a large mobile fraction of nucleolar components during reassembly. The import of fluorescent molecules can be followed by the bleaching of compartments in the cell. When the nuclear pool of proteasomes is bleached, a slow recovery of fluorescence is observed that is due to the unidirectional transport of cytosolic proteasomes into the nucleus[10].

FRAP can be used to measure protein interactions and conformational changes as well as protein dynamics. The association of fluorescent proteins with other molecules can be determined *in vivo* by lateral mobility, as shown for GFP-tagged MHC class I molecules in the ER[24]. Empty MHC class I molecules are bound to the TAP peptide transporter complex in the ER, decreasing its lateral mobility. The diffusion coefficient increases after peptide loading,

as the class I molecule is released from the antigen loading complex. By measuring mobility in living cells, protein activity can be studied at the single-cell level. The activities of GTPases such as ARF1–GFP[25] and K-ras[26] have been quantified by FRAP. Because the GDP-bound form resides in the cytosol and the GTP-bound form is membrane-associated, photobleaching the membrane pool reveals the kinetics of the GTP cycle *in vivo*. Finally, conformational changes associated with activity can be visualized by FRAP, as shown for GFP–TAP[27]. The lateral mobility of the peptide pump decreases during peptide translocation and increases when inactive. The diffusion rate can be used to show the relative quantities of cytosolic peptides present in living cells. These powerful observations demonstrate the value of FRAP in single-cell biology.

Considerations

Although diffusion coefficients can be deduced from FRAP experiments, one should be careful to compare diffusion coefficients and mobile fractions between different cell lines or compartments. Diffusion coefficients of the same molecule in different membranes vary not only because of specific interactions but also as a result of membrane topology and viscosity. For example, the ER forms a complex three-dimensional structure that differs from the plasma membrane in both architecture and membrane viscosity. Similarly, membrane factors such as cholesterol, phospholipids and proteins as well as cytoplasmic viscosity can result in cell-type-specific diffusion coefficients for the same molecule of interest.

Temperature affects the mobility of both soluble and membrane-associated molecules. Because viscosity is highly dependent on temperature, the effect of temperature on diffusion can be striking. FRAP experiments performed at 37 °C with soluble GFP targeted to the ER result in a 1.4-fold faster recovery rate than at 23 °C, owing to differences in viscosity[28]. The diffusion coefficient of TAP complexes in the ER doubles when the temperature is raised from 25 to 37 °C (E.A.J.R. and J.J.N., unpublished results). The diffusion of phospholipid probes in liposomes was also strongly dependent on temperature over the range 15–37 °C. The temperature effect was biphasic owing to a sharp phase transition in the membrane lipid, affecting lateral diffusion when solid-phase lipid regions turned into fluid-phase lipid regions[29]. This implies that FRAP experiments should be performed in a carefully controlled temperature stage, ideally at a physiological temperature.

Future roads and perspectives

FRAP is a powerful and continuously improving tool, available on most commercial confocal laser-scanning microscope systems, that can be used to address a number of questions regarding protein localization, activity, interactions and dynamics within a living cell. FRAP has been used to measure the continuity of membrane compartments and the behaviour of proteins during mitosis. However, the diffusion rate can also be interpreted in biochemical terms, being a readout for protein interactions and activity. FRAP will become a rapid and non-invasive technique to study biochemical processes not with isolated proteins but in the most complicated but relevant biological system: the living cell. □

1. Edidin, M., Zagyansky, Y. & Lardner, T. J. Measurement of membrane protein lateral diffusion in single cells. *Science* **191,** 466–468 (1976).
2. Axelrod, D. *et al.* Lateral motion of fluorescently labeled acetylcholine receptors in membranes of developing muscle fibers. *Proc. Natl Acad. Sci. USA* **73,** 4594–4598 (1976).
3. Axelrod, D., Koppel, D. E., Schlessinger, J., Elson, E. & Webb, W. W. Mobility measurement by analysis of fluorescence photobleaching recovery kinetics. *Biophys. J.* **16,** 1055–1069 (1976).
4. Salome, L., Cazeils, J. L., Lopez, A. & Tocanne, J. F. Characterization of membrane domains by FRAP experiments at variable observation areas. *Eur. Biophys. J.* **27,** 391–402 (1998).
5. Periasamy, N. & Verkman, A. S. Analysis of fluorophore diffusion by continuous distributions of diffusion coefficients: application to photobleaching measurements of multicomponent and anomalous diffusion. *Biophys. J.* **75,** 557–567 (1998).
6. Arrio-Dupont, M., Foucault, G., Vacher, M., Douhou, A. & Cribier, S. Mobility of creatine phosphokinase and β-enolase in cultured muscle cells. *Biophys. J.* **73,** 2667–2673 (1997).
7. Periasamy, N., Bicknese, S. & Verkman, A. S. Reversible photobleaching of fluorescein conjugates in air-saturated viscous solutions: singlet and triplet state quenching by tryptophan. *Photochem. Photobiol.* **63,** 265–271 (1996).
8. Gribbon, P. & Hardingham, T. E. Macromolecular diffusion of biological polymers measured by confocal fluorescence recovery after photobleaching. *Biophys. J.* **75,** 1032–1039 (1998).
9. Arrio-Dupont, M., Cribier, S., Foucault, G., Devaux, P. F. & d'Albis, A. Diffusion of fluorescently labeled macromolecules in cultured muscle cells. *Biophys. J.* **70,** 2327–2332 (1996).
10. Reits, E. A. J., Benham, A. M., Plougastel, B., Neefjes, J. & Trowsdale, J. Dynamics of proteasome distribution in living cells. *EMBO J.* **16,** 6087–6094 (1997).
11. Kao, H. P., Abney, J. R. & Verkman, A. S. Determinants of the translational mobility of a small solute in cell cytoplasm. *J. Cell Biol.* **120,** 175–184 (1993).
12. Swaminathan, R., Bicknese, S., Periasamy, N. & Verkman, A. S. Cytoplasmic viscosity near the cell plasma membrane: translational diffusion of a small fluorescent solute measured by total internal reflection-fluorescence photobleaching recovery. *Biophys. J.* **71,** 1140–1151 (1996).
13. Livneh, E. *et al.* Large deletions in the cytoplasmic kinase domain of the epidermal growth factor receptor do not affect its lateral mobility. *J. Cell Biol.* **103,** 327–331 (1986).
14. Saffman, P. G. & Delbruck, M. Brownian motion in biological membranes. *Proc. Natl Acad. Sci. USA* **72,** 3111–3113 (1975).
15. Vaz, W. L., Criado, M., Madeira, V. M., Schoellmann, G. & Jovin, T. M. Size dependence of the translational diffusion of large integral membrane proteins in liquid-crystalline phase lipid bilayers. A study using fluorescence recovery after photobleaching. *Biochemistry* **21,** 5608–5612 (1982).
16. Kucik, D. F., Elson, E. L. & Sheetz, M. P. Weak dependence of mobility of membrane protein aggregates on aggregate size supports a viscous model of retardation of diffusion. *Biophys. J.* **76,** 314–322 (1999).
17. Partikian, A., Olveczky, B., Swaminathan, R., Li, Y. & Verkman, A. S. Rapid diffusion of green fluorescent protein in the mitochondrial matrix. *J. Cell Biol.* **140,** 821–829 (1998).
18. Phair, R. D. & Misteli, T. High mobility of proteins in the mammalian cell nucleus. *Nature* **404,** 604–609 (2000).
19. Nehls, S. *et al.* Dynamics and retention of misfolded proteins in native ER membranes. *Nature Cell Biol.* **2,** 288–295 (2000).
20. Cole, N. B. *et al.* Diffusional mobility of Golgi proteins in membranes of living cells. *Science* **273,** 797–801 (1996).
21. Edidin, M., Zuniga, M. C. & Sheetz, M. P. Truncation mutants define and locate cytoplasmic barriers to lateral mobility of membrane glycoproteins. *Proc. Natl Acad. Sci. USA* **91,** 3378–3382 (1994).
22. Ellenberg, J. *et al.* Nuclear membrane dynamics and reassembly in living cells: targeting of an inner nuclear membrane protein in interphase and mitosis. *J. Cell Biol.* **138,** 1193–1206 (1997).
23. Dundr, M., Misteli, T. & Olson, M. O. The dynamics of postmitotic reassembly of the nucleolus. *J. Cell Biol.* **150,** 433–446 (2000).
24. Marguet, D. *et al.* Lateral diffusion of GFP-tagged H2Ld molecules and of GFP-TAP1 reports on the assembly and retention of these molecules in the endoplasmic reticulum. *Immunity* **11,** 231–240 (1999).
25. Vasudevan, C. *et al.* The distribution and translocation of the G protein ADP-ribosylation factor 1 in live cells is determined by its GTPase activity. *J. Cell Sci.* **111,** 1277–1285 (1998).
26. Yokoe, H. & Meyer, T. Spatial dynamics of GFP-tagged proteins investigated by local fluorescence enhancement. *Nature Biotechnol.* **14,** 1252–1256 (1996).
27. Reits, E. A., Vos, J. C., Gromme, M. & Neefjes, J. The major substrates for TAP *in vivo* are derived from newly synthesized proteins. *Nature* **404,** 774–778 (2000).
28. Dayel, M. J., Hom, E. F. & Verkman, A. S. Diffusion of green fluorescent protein in the aqueous-phase lumen of endoplasmic reticulum. *Biophys. J.* **76,** 2843–2851 (1999).
29. Alecio, M. R., Golan, D. E., Veatch, W. R. & Rando, R. R. Use of a fluorescent cholesterol derivative to measure lateral mobility of cholesterol in membranes. *Proc. Natl Acad. Sci. USA* **79,** 5171–5174 (1982).

ACKNOWLEDGEMENTS

We thank A. Griekspoor for the illustration, and A. Benham, K. Jalink and C. Vos for useful comments on the manuscript. Our work is supported by a Pioneer grant from NWO, The Netherlands.

Thomas Schmidt, Thursday June 14th 2012, 11.30

Probing Structure and Dynamics of the Cell Membrane with Single Fluorescent Proteins

Anna Pezzarossa, Susanne Fenz, and Thomas Schmidt

Abstract In recent years, our picture of the cell membrane has changed from a homogenous, fluid matrix to a highly dynamic and compartmentalized structure. This structuring influences the dynamical behavior of proteins embedded in the cell membrane. Since cell signaling is largely mediated through membrane-bound multi-protein complexes, there might be a direct link between membrane structure and signaling. In this chapter, we first review recent single molecule studies proving the existence of microdomains in the membrane of different cultured cell types and in a living organism by fluorescently labeling individual Ras proteins and studying their mobility. In the second part, we report on a study of the mobility of G protein-coupled receptors and G proteins in the model system *Dictyostelium discoideum*. The insights allowed building up a mechanistic model of the early steps of chemotaxis exemplifying the implication of membrane domains in cell signaling.

Keywords Chemotaxis · Diffusion · G protein-coupled receptor · Membrane domains · Ras protein · Single-molecule microscopy

Contents

A. Pezzarossa, S. Fenz, and T. Schmidt (✉)
Physics of Life Processes, Institute of Physics, Leiden University, Leiden, The Netherlands
e-mail: schmidt@physics.leidenuniv.nl

G. Jung (ed.), *Fluorescent Proteins II*, Springer Ser Fluoresc (2012) 12: 185–212,
DOI 10.1007/4243_2011_24 © Springer-Verlag Berlin Heidelberg 2011
Published online: 7 April 2011

1 Introduction

1.1 Membrane

Biological membranes form the outer layer of cells. They consist of an asymmetric lipid bilayer with phospholipids, cholesterol, and proteins as the main components. Glycosilated lipids and proteins built up a dense mesh protecting the cell against mechanical and chemical damage from outside. From the inside, the membrane is stabilized by the actin-rich cell cortex. The plasma membrane separates the contents (organelles, cytosol, cytoskeleton) and processes (e.g., protein synthesis, transport, and recycling) in the cell interior from the surrounding environment. At the same time, it plays a role in cell–cell communication, cell–cell recognition, and transport processes. The membrane represents the major regulatory platform for the initiation of early signaling events.

The role of lipids in membrane assembly and dynamics was the base for the Singer–Nicolson fluid mosaic model in the 1970s [1]. In this model, the bilayer is represented as a passive, neutral two-dimensional solvent in which active membrane proteins are homogeneously distributed and free to move. Some striking observations in epithelial cells proved this picture to be incorrect. Lipids were found to form functional microdomains insoluble in some detergents [2, 3]. Basic research on multicomponent lipid bilayers and vesicles containing two kinds of lipids with different phase transition temperatures and cholesterol revealed that even lipid mixtures exhibited complex phase separation behavior [4–7]. Based on these results, it was predicted that the spatial and temporal structure of the membrane might play an important regulatory role also in living cells. Although the observations on cells and biomimetic systems are still to be integrated into a global picture, it is accepted that lateral inhomogeneities are necessary for the function of biological membranes [8]. At present, the consensus is to describe the plasma membrane as a highly complex, organized structure at length scale in the order of tens of nanometers with a broad range of dynamic processes [8–10].

Genetic engineering of proteins made it possible to label membrane proteins with fluorescent proteins in living cells. In combination with single molecule fluorescence microscopy, it represents a powerful tool to study structure and dynamics of the cell membrane under physiological conditions.

1.2 Diffusion

The term diffusion refers to the Brownian motion of particles in a fluid medium, driven by thermal energy. We can picture the cell membrane as bilayer of lipids enriched in protein either embedded (integral proteins) or surface-adsorbed (peripheral proteins). Both proteins and lipids diffuse along the plane of the membrane (translational diffusion). A complete description of the motion in a membrane should also consider rotational diffusion, which accounts for the orientation of the molecules. In what follows, we will concentrate on translational diffusion only.

The lateral diffusion of a particle in a medium, characterized by a diffusion constant D, is described by Fick's second law:

$$\frac{\mathrm{d}}{\mathrm{d}t}p(\vec{x},t) = D \cdot \nabla^2 p(\vec{x},t), \tag{1}$$

where $\nabla^2 p(\vec{x},t)\mathrm{d}\vec{x}$ describes the probability of finding a particle, which started at $\vec{x}_0$ at time $t = 0$, within the volume $[\vec{x}, \vec{x} + \mathrm{d}\vec{x}]$ at time t. Solving in $\vec{x}$ yields:

$$p(\vec{x},t)\mathrm{d}\vec{x} = \left(\frac{1}{\sqrt{(4\pi Dt)^d}}\right)\exp\left(-\frac{(\vec{x}-\vec{x}_0)^2}{4Dt}\right)\mathrm{d}\vec{x}, \tag{2}$$

where d is the number of dimensions and $\vec{x}_0$ the starting position.

For analysis of actual data, it is advantageous to analyze cumulative distribution functions. Integration of $p(\vec{x},t)$ in (2) gives the cumulative probability distribution function $P_{\mathrm{cum}}(x^2, t)$, for particles that move up to the squared distance x^2 in time t [11, 12]. $P_{\mathrm{cum}}(x^2, t)$ reads for one, two, and three dimensions:

$$P_{\mathrm{cum}}^{d=1}(x^2,t) = \mathrm{erf}\left(\sqrt{\frac{x^2}{4Dt}}\right), \tag{3}$$

$$P_{\mathrm{cum}}^{d=2}(x^2,t) = 1 - \exp\left(-\frac{x^2}{4Dt}\right), \tag{4}$$

$$P_{\mathrm{cum}}^{d=3}(x^2,t) = \mathrm{erf}\left(\sqrt{\frac{x^2}{4Dt}}\right) - \sqrt{\frac{x^2}{\pi Dt}}\exp\left(-\frac{x^2}{4Dt}\right). \tag{5}$$

Those cumulative distribution functions are characterized by the typical area the molecule will cover during its diffusional path, the mean squared displacement (MSD):

$$\mathrm{MSD}\,(t) = \left\langle x^2(t)\right\rangle = \int (\vec{x}-\vec{x}_0)^2 p(\vec{x},t)\mathrm{d}\vec{x} = 2dDt. \tag{6}$$

The MSD increases linearly with time between observation for regular diffusion, the Brownian walk.

A biomolecule diffusing in a two-dimensional membrane will experience multiple forces and boundaries affecting its motion, causing a deviation from a free diffusion Brownian trajectory. Physical barriers such as other immobile membrane proteins or cytoskeletal fences can transiently or permanently restrict the lateral diffusion of proteins in the plasma membrane. In this scenario, the diffusional behavior of a molecule becomes more complex and it cannot be described by (6). It has been observed that deviations from the linear regime occur often in cell membranes. This motion is modeled according to anomalous or sub-diffusion:

$$\mathrm{MSD}\,(t) = \Gamma t^{1-\epsilon}; \epsilon \geq 0, \tag{7}$$

in which ε is the anomalous diffusion exponent [13]. In this model, the diffusion coefficient Γ appears to decrease with time. In case the molecules are restricted to diffuse within a square area with reflecting boundaries of side-length L, we speak of confined diffusion [14], described by:

$$\mathrm{MSD}\,(t) = \frac{L^2}{3}\left[1 - \exp\left(\frac{-12Dt}{L^2}\right)\right]. \tag{8}$$

In this scenario, we would observe free diffusion behavior on short time scales, when the particle cannot yet "feel" the barrier, but on longer time scales the mean square displacement levels off to an asymptotic value as illustrated in Fig. 1.

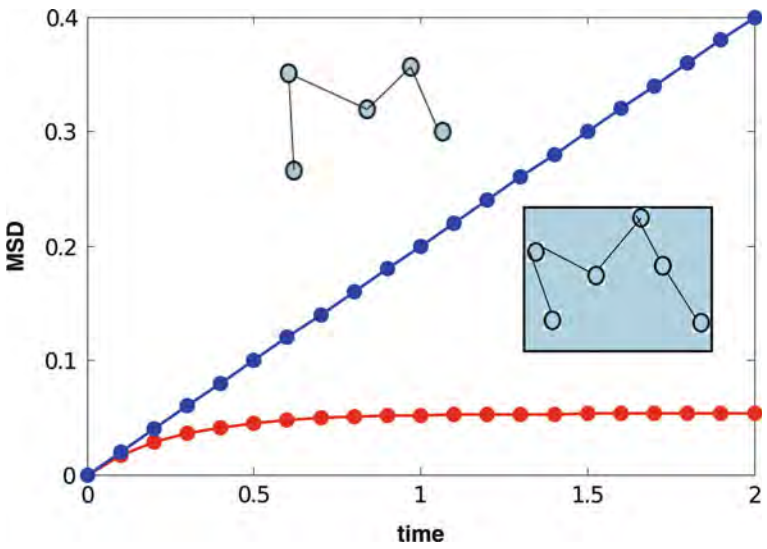

Fig. 1 Comparison between free (*blue curve*) and confined (*red curve*) diffusion. Graphs are created assuming identical diffusion coefficients

Many models have been proposed, which take into account all the possible situation a molecule can experience. It is worth to mention the hop diffusion model in which the molecules are temporarily trapped by a permeable barrier that restricts the available diffusion space to a few nanometers. There is a non-zero probability of barrier crossing and hopping to the adjacent domain [15]. This latter model, however, is not easily accessible experimentally, due to the time resolution limitation of current microscopy setups.

2 Single-Molecule Fluorescence Microscopy

Since its development, single-molecule fluorescence microscopy has been recognized as an ideal tool to observe dynamics in cells. Conventional microscopy is suitable to observe large objects, but to observe small biomolecules such as proteins, its resolution is not sufficient. At the beginning of the 1990s it became possible to detect single fluorophores and subsequently, thanks also to genetical engineering, to track objects in a living cells labeled with a fluorescent probe [16, 17, 93].

To understand how it is possible to visualize subwavelength structures, the main concepts of fluorophore localization will be given in what follows. The image of a fluorescent emitter is described by its diffraction pattern, known as the point spread function (PSF) given by an Airy disk of width $w = 0.61\ \lambda/\mathrm{NA}$, where λ is the imaging wavelength and NA the numerical aperture. In this scenario, the resolution limit is given by the Abbe limit or Rayleigh criterion, according to which two objects closer than the width of the Airy disk cannot be resolved. Using high NA oil objectives (NA = 1.4–1.5), in the visible region of light, this distance is typically 200 nm. Two emitters separated less than this distance would therefore be undistinguishable. An isolated fluorophore, on the other hand, can be localized with high precision. Its position is determined from the maximum of the PSF. Typically, this precision is in the order of tens of nanometers, depending on the signal-to-noise ratio. There are two ways to isolate the objects of interest: spatially [17] or spectrally [18]. Spatial isolation is achieved by dilution until there is only one fluorophore left within the Airy disk. The other option is to label the objects with spectrally well-separated fluorophores. In the latter case, multicolor imaging allows to distinguish between two objects closer than the width of their Airy disk.

The image of an arbitrary object is described as the sum of point light sources, localized at $\vec{s}_i$. For practical purposes, the PSF is approximated by a Gaussian, yielding the image $I(\vec{s})$:

$$I(\vec{s}) = \sum_i N_i \frac{1}{2\pi w^2} \exp\left(-\frac{(\vec{s}-\vec{s}_i)^2}{2w^2}\right), \tag{9}$$

where N_i is the number of emitted photons and w the width of the Gaussian. The Gaussian PSF predicts that the localization accuracy σ_i for an individual emitter is given by:

$$\sigma_i = w/\sqrt{N_i}. \tag{10}$$

Taking into consideration background noise b and pixelation (with pixel size a), σ_i is given by [19]:

$$\sigma_{si} = \sqrt{\left(\frac{w_i^2}{N_i} + \frac{a^2/12}{N_i} + \frac{8\pi w_i^4 b^2}{a^2 N_i^2}\right)}. \tag{11}$$

A more rigorous expression for σ_i that also takes into account the real PSF of a microscope and other noise sources has been derived by Ober et al. [20].

Prior to further data analysis, accurate image processing is needed to obtain the position of each single-molecule peak. The first step is to remove any static or slowly varying background. A reliable background image can be obtained by applying several different algorithms: high-order polynomial fitting, low-spatial-frequency filtering, mean-image calculation. The background-subtracted images are subsequently filtered by cross-correlation with the PSF of the microscope, approximated by a Gaussian. To reliably detect signals above the background, a threshold is set and only signals that are above the noise by a factor η, determined according to the experimental conditions, are further processed. Finally, each single-molecule peak is fitted to the PSF, and information about position, signal intensity, spatial width of the signal, and background signal are retrieved. In the following sections, we illustrate two widely used methods to obtain information on single-molecule dynamics from such position data.

2.1 Tracking

The single-molecule positions obtained from PSF fitting are the starting point for single-particle tracking. To generate trajectories, we need to correlate M mobile particles in an image to N mobile molecules in the subsequent image. A probabilistic algorithm is used to connect the positions of molecules in two frames, i and j, of a movie. The probability that a single particle k in image I_i with diffusion coefficient D is identical with particle l in image I_j is given by:

$$p(k,l) = \exp\left(-\frac{(\vec{s}_{k,i} - \vec{s}_{l,j})^2}{4D\Delta t}\right). \tag{12}$$

Δt is the time lag between the recording of the two images I_i and I_j.

A transitional matrix is built up out of (12) which includes the probabilities of all possible connections between all M molecules in I_i and N molecules in I_j. Trajectories are constructed by optimizing for the combination of all connections with the highest total probability, i.e., where $\sum_{k,j} \log\left(p(k,l)\right)$ is maximized. The algorithm implemented in our laboratory further includes corrections to deal with photobleaching and molecules that move into the field of view from outside. Starting from the trajectories, we construct the experimental cumulative probability to find the MSD.

Generating trajectories for all particles constitutes a NP-complete, or "traveling salesman" problem. Exact solutions can be calculated only for problems with a limited amount of particles (<20). However, there are approximative solutions that are close to the optimal. To calculate the approximate solution, we use Vogel's algorithm from operations research. The order in which the connectivity between subsequent images is drawn is determined by the maximal probability difference in connectivity for each molecule k in image i, $\{p(k, l)\}_l$. This simple sort-draw algorithm significantly reduces the computational costs of the analysis.

Single-particle tracking allows to directly visualize the diffusion behavior of single molecules drawn from a potentially inhomogeneous ensemble such as proteins diffusing in an inhomogeneous cell membrane. However, it suffers from fluorophore photobleaching that results in short trajectories [21]. This limitation can be overcome using quantum dots or gold nanoparticles, which permit longer observation times. Another drawback of this technique is that some prior knowledge on the dynamic of the system, i.e., its diffusion constant D, is needed to cope with the probabilistic nature of the tracking problem described in (12) [16]. This is particularly significant at high concentration of molecules when trajectories can be accidentally mixed.

2.2 *Particle Image Correlation Spectroscopy*

An alternative method to determine the P_{cum} without prior trajectory analysis was recently developed in our laboratory. This method does not require to assign individual traces and is consequently able to deal with high numbers of molecule as long as the Rayleigh criterium is fulfilled and individual molecules can be identified [22]. This algorithm is based on a correlation function, similarly as in spatiotemporal image correlation spectroscopy (STICS) [23].

In an isotropic medium, the cumulative correlation function of pairwise distances, C_{cum}, depends on two parameters: distance x and a time lag Δt. Thus, considering M molecules in image I_i and N molecules in image I_j, C_{cum} is given by:

$$C_{\mathrm{cum}}(x^2, \Delta t) = \frac{\sum_{k=1}^{M} \left\langle n(\vec{s}_{k,i}, x^2)\right\rangle_{\Delta t}}{M}, \tag{13}$$

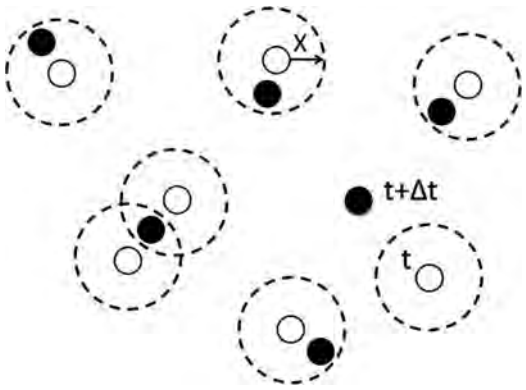

Fig. 2 PICS algorithm. For each molecule in image I_i (*white circles*), the number of molecules in image I_j (*black circles*) closer than x^2 is counted, 5 in this example. The peak on the left which lies within the overlap of two circles will be counted twice. Hence, the contribution due to diffusion is 4, whereas 1 count is due to random spatial proximity of the molecules

where $\vec{s}_{k,i}$ is the position of molecule k in image I_i and $n(\vec{s}_{k,i}, x^2)$ the number of particles in image I_j that lie in a circle of radius x around $\vec{s}_{k,i}$. The algorithm is illustrated in Fig. 2.

For each molecule in image I_i, the number of molecules in image I_j closer than x^2 is counted. Subsequently, the contributions from all molecules in I_i are summed and averaged over all image pairs. C_{cum} contains both temporal (e.g., diffusion) and spatial correlations (e.g., random proximity of the molecules).

The first contribution contains the information on the diffusion dynamics of the molecule and is equal to P_{cum} to find a diffusion step with size smaller than x^2 in the time lag Δt. In a two-dimensional case, for Brownian diffusion, with diffusion coefficient D, P_{cum} (x^2,Δt) is given by (4). For the second contribution, a correction term that accounts for random proximity needs to be calculated to correct for spatial correlation. Assuming that the particles are distributed uniformly and independently with a density c, the probability to find N molecules in a circle with radius x is given by a Poisson distribution with mean and variance equal to $c\pi x^2$. Combining the two contribution, P_{cum} is calculated from the experimental C_{cum} distribution:

$$P_{\text{cum}}(x^2, \Delta t) = C_{\text{cum}}(x^2, \Delta t) - c \cdot \pi x^2. \tag{14}$$

2.3 Fitting the Probability Distribution Function

In both the methods outlined above, the dynamic information is contained in the cumulative probability distribution function. In the scenario of a single diffusing species, P_{cum} is given by (4). However, this model is often not adequate to describe the dynamics of biomolecules in living cells. In many biologically relevant processes, it is often necessary to include more than one diffusing population. In case

of two mobile components, characterized by diffusion coefficients D_1 and D_2 respectively, P_{cum} assumes a double exponential form

$$P_{\text{cum}}(x^2, \Delta t) = 1 - \left[\alpha \exp\left(-\frac{x^2}{4D_1\Delta t}\right) + (1-\alpha)\exp\left(-\frac{x^2}{4D_2\Delta t}\right)\right], \qquad (15)$$

where α denotes the population size. In single-molecule experiments, the probability distributions are constructed either from the trajectories or by particle image correlation spectroscopy (PICS) as described above. This model has been applied successfully to describe protein dynamics in living cells [24].

2.4 *Fluorescent Proteins for Life Cell Imaging*

Single-molecule fluorescence microscopy is a powerful tool to address many biologically challenging questions both in vivo and in vitro. For its application though, the object under investigation (protein, DNA) must be specifically labeled by an appropriate fluorescent probe. Several fluorophore classes have emerged recently to label protein and intracellular structures, including (but not limited to) genetically encoded fluorescent proteins (FP), quantum dots (QD), and synthetic dyes.

An optimal probe for single-molecule tracking should meet several requirements: it should be expressed without toxicity in the system under investigation, it should be brighter than the cell's autofluorescence or have a different wavelength to be unequivocally detected, and should have sufficient photostability to be imaged for long time. The method that offers the least interference with a cell biological functions and allows the observation of dynamics in living cells is still fusion with a FP. In order to choose the best FP for a designed experiment, several photophysical parameters have to be taken into account: the saturation intensity (I_s), photobleaching time (τ_{bl}), and maximal photon emission rate (k_∞).

These parameters will be briefly described in this section and experimental results for the most common FP [eYFP (yellow), eGFP (green), eCFP (cyan), and DsRed (red)] will be given (see Table 1).

Following a standard two-level energy level diagram of a fluorophore, the dependence of τ_{bl} on the excitation intensity I is given by $\tau_{bl} = \tau_{bl}^{\infty}(1 + I_s/I)$,

Table 1 Photophysical properties of autofluorescent proteins, measured in a page gel compared to flavin-di-nucleotide, which was measured at high concentrations (>100 nM) [25]

Fluorophore	λ_{exc} (nm)	I_s (kW/cm^2)	k^∞ (photons/ms)	τ_{bl}^{∞} (ms)	ϕ_{bl} ($\times 10^{-5}$)
eCFP	458	48 ± 12	6,000 ± 3000	<1	>19
eGFP	488	13 ± 6	2,900 ± 200	2.8 ± 0.2	6.9 ± 0.5
eYFP	514	6 ± 1	3,100 ± 100	3.5 ± 0.5	5.5 ± 0.5
DsRed	532	50 ± 10	18,000 ± 2,000	0.4 ± 0.1	15 ± 3
flavin	514	35 ± 10	500 ± 100		

where τ_{bl}^{∞} is the photobleaching time limit. The detected signal (S_{det}) one can expect for a given experimental arrangement depends on the detector efficiency (η_{det}), on the integration time (t), the excitation intensity and wavelength, the chemical environment, and last on the photobleaching yield. Taking these parameters into account, we obtain the following expression for S_{det}:

$$S_{det} = \eta_{det} k_{\infty} \tau_{bl}^{\infty} \left[1 - \exp\left(\frac{-t}{\tau_{bl}^{\infty}(1 + I_s/I)} \right) \right]. \tag{16}$$

When photobleaching is negligible ($\tau_{bl} \gg t$), the equation converts into the simpler form:

$$S_{det} = \frac{\eta_{det} k_{\infty} t}{1 + I_s/I}. \tag{17}$$

Typical values for individual FPs when excited for 5 ms at an intensity of 1 kW/cm^2 are 100–200 counts detected on a back-illuminated CCD camera.

In a living cell, the main source of autofluorescence is given by flavinoids, which is located in the yellow-green spectral region. A spectral comparison between flavinoids and FPs shows an almost complete overlap of the flavine emission with eCFP, eGFP, and eYFP, where the excitation overlap with eCFP and eGFP is high, that with eYFP is low (see Fig. 3).

Taking into account the high concentration of flavinoids in a cell (10^7 molecules/cell), even excitation in the tail of their spectrum will cause a large autofluorescence background; therefore, FP with a red-shifted spectra are to be preferred.

From the above considerations, it appears that the suitability for single molecule microscopy is given by: eYFP > eGFP » eCFP (see Table 1). DsRed is not considered here due to its photobleaching rate, which is tenfold higher than the other FPs, which overwhelms the advantages given by the spectral separation from flavins. Many new variants of GFP have been created using genetic engineering, which cover almost the whole light spectrum [26, 27]. Most of those, however, are dimeric or even tetrameric, which is potentially toxic. Functional monomers can be engineered, but this results in a loss of brightness or photostability. Dimmer proteins require either higher laser power or longer exposure time to be imaged, which is limiting for fast in vivo experiments. For single molecule experiments though eYFP is still the preferred choice [26].

To overcome the limitations of autofluorescent protein, several alternative labeling techniques have been proposed [28]. Most of these rely on the possibility of specifically coupling a synthetic fluorophore to the biomolecule of interest through a chemical reaction. One widely used strategy is to create genetically modified proteins carrying a target domain (peptide tag) which is selectively posttranslationally labeled with a small complementary functionalized fluorophore. An important class of these peptide tags is represented by peptidyl carrier protein (PCP) and acyl carrier protein (ACP) domains [29, 30]. Those domains are modified by

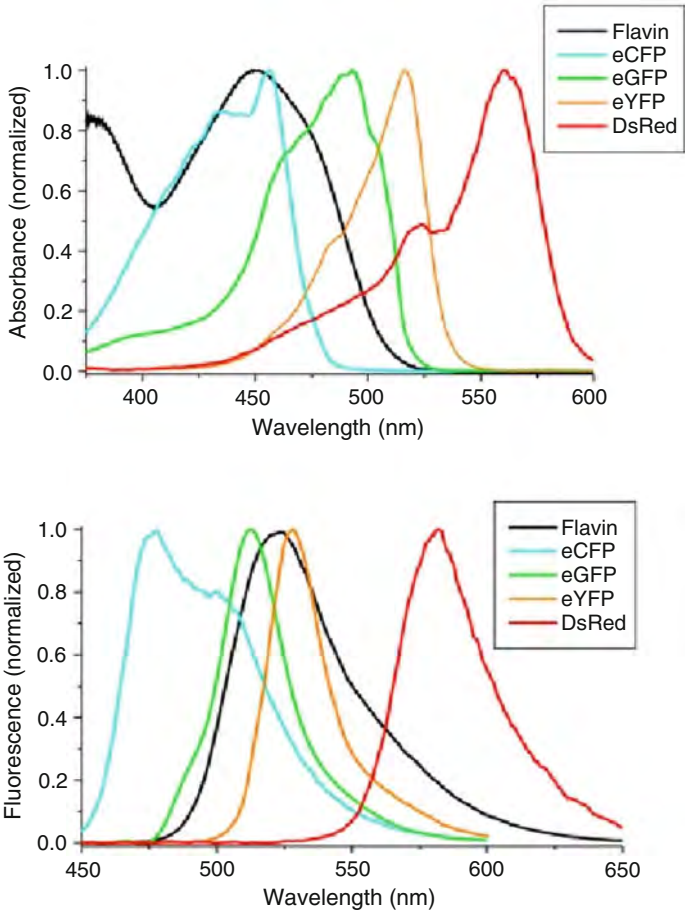

Fig. 3 Spectral comparison of flavin-di-nucleotide to fluorescent proteins. *Top*: Normalized absorption spectra. *Bottom*: Normalized emission spectra [25]

phosphopantetheinyl transferases (PPTases) of bacterial origin, such as the 4′-phosphopantetheinyl transferase (SFP) and the ACP synthase. The labeling reaction requires a fluorophore functionalized with a phosphopantetheinyl (Ppant) prosthetic group, derived from coenzyme A. In the reaction, the prosthetic group is covalently attached to a specific residue in the peptide tag by the enzyme (see Fig. 4).

Another commonly used peptide tag, HaLo, is based on an bacterial enzyme haloalkane dehalogenas. The enzymatic reaction relies on the formation of an ester bond between the fusion protein and a HaLo linker bound to a fluorescent reporter [31].

A different approach is based on the ability of particular sequences, rich in histidine residues, to bind transition metal complexes. One of those, the hexahistidine tag (His6), has been largely studied; however, this technique suffers from high

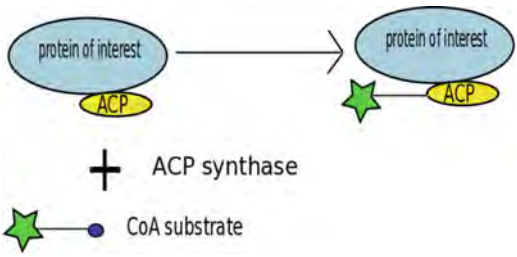

Fig. 4 ACP labeling reaction

dissociation constant (>300 nM), which makes it difficult to use for fluorescence experiments [32].

New opportunities arise from with the introduction of unnatural amino acid in the protein of interest, which allows direct or indirect introduction of fluorophores [33, 34]. The advantage of these techniques is that they allow for a wider choice of fluorophores, making it possible to reach a better spectral separation from cellular autofluorescence. Moreover, they are usually more photostable than FPs. On the other hand, most of these techniques suffer from nonspecific labeling and blinking (as in the case of QDots or nanocrystals), thus limiting their applicability. Moreover, they require specifically functionalized fluorophores, whose synthesis is quite laborious and which are potentially toxic for cells.

3 H-Ras Mobility in Membranes: From Cultured Cells to the Living Vertebrate

3.1 The Ras Family

Ras GTPases are small (~20 kDa), lipid-anchored membrane proteins involved in signal transduction. They play a major role in regulating cell growth, proliferation, and differentiation. Mutations in the Ras proteins are related to oncogenesis and cancer. Three different isoforms are expressed in all mammalian cells: H-Ras, K-Ras, and N-Ras. They are localized mainly in the inner leaflet of the plasma membrane, but they are found as well in the endoplasmic reticulum and in the Golgi apparatus [35–38]. Ras proteins effectively work as molecular switches, cycling between two possible states: a GTP-bound "on" state and a GDP bound "off" state which promotes association and activation of effector proteins. For signaling, they all interact with the same set of effectors, yet generating different output.

Ras proteins share 90% sequence homology, characterized by a highly conserved region in the N-terminus and showing a significant divergence in the C-terminus, which is referred to as hypervariable region, encoding for the membrane-anchoring domain [39]. Based on these structural observations, it was proposed that functional differences may result, at least partially, from a differential

membrane compartmentalization of the isoforms. Several biochemical evidences were obtained which support this model: first, cholesterol depletion in the plasma membrane hyperactivates downstream Ras signaling in an isoform-specific manner, inhibiting H-Ras but not K-Ras [40]. Second, cell fractioning experiments showed that the isoforms target different membrane domains [41, 42]. Biochemical and electron microscopy (EM) studies suggested that H-Ras, but not K-Ras, was associated with cholesterol and phospholipids-enriched domains, forming nanoclusters of proteins with diameter in the range of 6–11 nm [41, 43, 44]. Another hypothesis was that membrane anchor domain orientation plays a role in isoform diversity. But the orientation alone cannot explain the functional differences observed [45].

It had also been shown that H-Ras partitioning is regulated by its GTP-bound state, suggesting a complex model in which H-Ras segregation is activation dependent. However, biochemical studies were not able to provide an insight on domain distribution and dynamics, and EM studies are limited to thin sample sheets and cannot be performed on living cells. Ideally, direct visualization of those objects *in vivo* is needed to fully understand inner leaflet plasma membrane organization.

3.2 Mobility Studies of Membrane-Anchored Proteins Reveal Membrane Domains in Cultured Cells

The plasma membrane of mammalian cells is heterogenous in structure and contains different types of domains, varying in size from a few to several hundreds of nanometers. Most of these domains have been extensively studied in the exoplasmatic membrane of cells, because of its easier accessibility (for reviews, see [46, 47]). Only more recent work has been done on the cytoplasmic leaflet. The proteins of the Ras family and their membrane anchor motif (CAAX) are ideal to study the partitioning and dynamics property of the inner leaflet.

To investigate the presence of membrane domains *in vivo*, and to obtain dynamic information, single-molecule fluorescence microscopy was used in our group to track the membrane targeting domain of two Ras isoforms (H-Ras and K-Ras) fused with eYFP. These results were compared to those obtained for the membrane anchor of a member of the family of Src-kinase, Lck [24, 48].

The H-Ras targeting sequence consists of ten amino acids and contains three cysteines to which one S-prenyl and two S-acyl groups are attached posttranslationally [35, 38]. Biochemical studies showed its presence in the detergent-resistant membrane (DRM) fraction. Instead, the K-Ras membrane anchor, consisting of a farnesyl moiety in conjunction with a polybasic domain, does not co-precipitate with DRM [43]. On the other hand, Lck is anchored via two cysteine-linked S-acyl groups and one glycine-linked myristoyl group at the N-terminus of the protein, which confers a high affinity for cholesterol-rich membrane, analogous to H-Ras. The idea was to compare the mobility of these different anchors and retrieve from it information on inner leaflet membrane structure and the possible implication of domains in Ras signaling. Surprisingly, all those proteins showed similarity in their diffusional behavior.

The eYFP fusion constructs were tracked as described in the previous section, and from the traces analysis information on their dynamics in the membrane and confinement in domains was obtained.

All the anchors exhibited a biphasic behavior, represented by two distinct fractions, a fast moving one which included the majority of molecules [between 60% (H-Ras) and 84% (K-Ras)], and a slow diffusing one. Mean square displacement vs. time curves showed a linear increase with time, indicating free diffusion of the fast fraction for all the different anchors with slightly different diffusion coefficients: $D_{\mathrm{HRas}} = 1.13\ \mu m^2/s$, $D_{\mathrm{KRas}} = 1.00\ \mu m^2/s$, and $D_{\mathrm{Lck}} = 1.30\ \mu m^2/s$. The remaining fraction of molecules showed instead in all different experiments confined behavior to domains of ~200 nm in diameter with an initial diffusion coefficient of $D_{\mathrm{slow}} \sim 0.2\ \mu m^2/s$.

These results proved that if nanoclusters are present, anchors with high affinity (H-Ras and Lck) were not significantly slowed down when compared to K-Ras. These results did not exclude the presence of cholesterol-dependent Ras nanoclusters in the inner leaflets. Due to their supposedly very small size (<70 nm), it was not possible to visualize them. However, if they are present, their effects would be negligible in terms of protein mobility. Other studies using fluorescence recovery after photobleaching (FRAP) [41] and electron microscopy (EM) [44] confirmed a two state model in which 30% of H-Ras is present in 20 nm cholesterol-dependent domains. Although these domains are much smaller than what can be detected with SPT, the two observations are closely related. One possible explanation could be that these 20 nm domains are temporally trapped to the actin cytoskeleton and to scaffolding proteins, leading to observed 200 nm domains. To conclude, trapping in 200 nm domains was observable with SPT, but no isoform-specific effect on mobility was observable on the 10–60 ms time scale of the measurement.

A further study was conducted on full-length H-Ras protein to explore the relationship between Ras mobility and activation. Evidences on activation-dependent mobility were suggested by the results obtained by FRAP experiments [41]. A constitutive active mutant GFP-H-Ras(V12) showed an increase in its lateral mobility with the expression level in a saturable manner, suggesting association with saturable domains. To further investigate this relationship, we performed single-molecule tracking experiments on H-Ras and on two mutants, one constitutive active, eYFP-H-Ras(V12), and one inactive, eYFP-H-Ras(N17) *in vivo* [49]. We observed two mobile fractions for both mutants, a fast one showing free diffusion and a slow population that showed free diffusion for the inactive mutant and confinement to ~200 nm domains for the active one. Similarly, the eYFP-H-Ras (wt) slow fraction showed a mobility change upon insulin stimulation. Before activation, the H-Ras (wt) slow fraction appeared to diffuse freely, but after 5 min of insulin treatment a confinement of ~200 nm was observed (see Fig. 5).

Most likely the actin cytoskeleton plays a role in H-Ras trapping, as it is known that insulin induces rearrangements of the cytoskeleton [50–53]. The SPT results largely agreed with results from single molecule fluorescence resonance energy transfer (FRET) [54], which showed the involvement of actin in immobilization of active H-Ras.

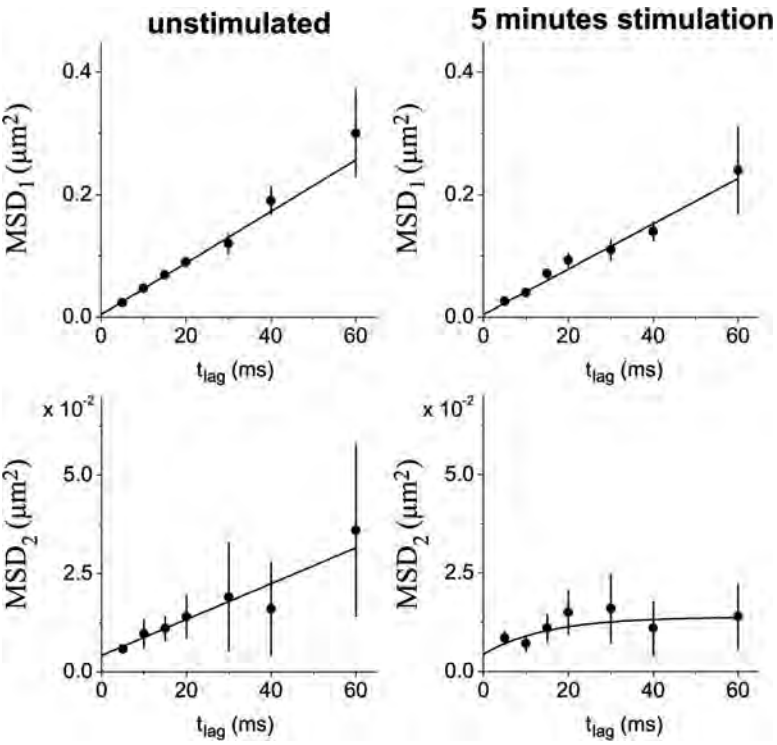

Fig. 5 Diffusion characteristics of eYFP-H-Ras(wt) before stimulation (*left*) and 5 min after stimulation with insulin (*right*). *Top*: Mean square displacement of the fast-diffusing fraction, MSD vs. timelag. *Bottom*: Mean square displacement of the slow diffusing fraction, MSD vs. timelag [49]

Those results proved a major role for the plasma membrane as a platform for Ras signaling. A mechanistic model for Ras microlocalization and activation had been suggested by Rotblat et al. [55], in which the interactions that regulate H-Ras membrane affinity also regulates its segregation in nanodomains. Recently, an increasing amount of evidence has proved a role for the growth factor receptor Gal-1 in H-Ras nanocluster formation [56]. These latter studies confirm the importance of microlocalization in signal transduction and identify new fundamental players that drive cluster formation.

3.3 H-Ras Studies in Zebrafish Embryos Prove Membrane Structuring in Living Organisms

A significant amount of experimental work has been done on cultured cells to study membrane structuring and its effects on cellular processes. Only recently, this approach has been extended to the living vertebrate organism, zebrafish [57–60].

Zebrafish was chosen because their embryos are small, transparent, and easy to manipulate, making it the ideal model system to study [61–63]. In our group, the membrane anchor of H-Ras was genetically fused to a YFP, YFP-C10H-Ras, and was used to demonstrate the possibility of measuring protein mobility in living organism [64].

In this study, results from *in vitro* measurements, performed on a cultured zebrafish cell line (ZF4), were compared to those obtained *ex vivo* on primary

Table 2 Comparison of the obtained diffusion characteristic for the different experimental conditions. α fast fraction size, D_{fast}, D_{slow} diffusion coefficient fast and slow fraction, respectively, L_1 and L_2 domain size fast and slow fraction, respectively

	α (%)	D_{fast} ($\mu m^2/s$)	L_1 (μm)	D_{slow} ($\mu m^2/s$)	L_2 (μm)
In vitro	70	0.67	0.79	0.06	0.16
Ex vivo	67	0.72	0.55	0.05	0.21
In vivo	75	0.51	Free	0.04	0.12

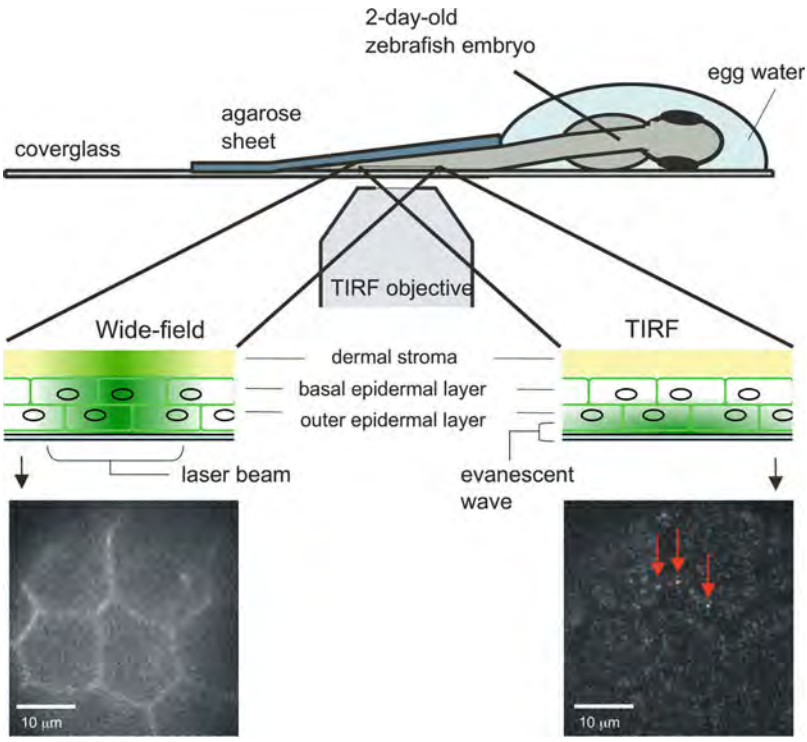

Fig. 6 Single molecule microscopy *in vivo*. The zebrafish embryo is placed on a coverslip and the tail region is covered with a sheet of agarose 0.75 mm thick. The sample was mounted on a microscopy setup suitable for wide field and TIRF microscopy. *Left*: Wide field picture, displaying membrane localization of the fluorescent signal. *Right*: TIRF image of the same region. *Arrows* indicate three examples of the YFP-H-Ras fluorescent peaks which can be attributed to single YFP molecules

embryonic stem cells and *in vivo* in 2 days old zebrafish embryo. In all the experiments, two populations in protein mobility were observed. Both *in vitro* and *ex vivo* the fast population appeared confined, but remarkably, *in vivo* data could be fitted according to a free diffusion model. The slow fraction instead showed a more stable behavior through all the different experiments, being always confined in small domains with comparable diffusion coefficients (see Table 2).

In vitro and *ex vivo* experiments were performed using epifluorescence microscopy, while *in vivo* experiments needed a different experimental setup because of the high level of out-of-focus fluorescence. A total internal reflection fluorescence (TIRF) microscopy approach was used, in which an evanescent light field excites the molecules within 100 nm from the coverglass (see Fig. 6).

Using this approach, it was possible, for the first time, to record individual molecules in a living organism. To summarize, the existence of two kinds of domains was observed, a smaller one with a diameter between 120 and 210 nm, present in all the experiments, and a bigger one, 550–790 nm found only in *in vitro* and *ex vivo* experiments [64].

This study showed that the two populations model of protein diffusion and their confinement in domains applies to living organisms as well as to cultured cells, and could play a physiological role in cell signaling. However, it also showed that large differences exist between cultured cells and living organism. Thus, to make physiologically relevant considerations on a system, studies in living organism are required.

4 Receptor and G Protein Mobility in *Dictyostelium discoideum*

The soil-living amoeba *Dictyostelium discoideum* is a widespread model organism for chemotaxis. Its completely sequenced 34 Mb-genome [65] contains many genes that are homologous to those in higher vertebrate species, thus representing an ideal model organism. Gene engineering and GFP technology provide a versatile toolbox to study vital processes such as cell motility, chemotaxis, or signal transduction in *D. discoideum*. This section highlights recent studies that yielded insight into the role of G protein-coupled receptor (GPCR) and G protein mobility in chemotaxis by combining fluorescent protein technology and high resolution microscopy.

4.1 Chemotaxis in D. discoideum

Nature developed fascinating strategies to ensure survival of a species. One example is the amoeba *D. discoideum*. Under optimal conditions, *D. discoideum* lives as an individual cell, but it has the ability to aggregate into a multicellular structure containing ~10^5 amoeba when the environmental conditions deteriorate. The resulting aggregate undergoes cell differentiation and morphogenesis leading to a so-called pseudoplasmodium or slug that has the ability to sense temperature and light.

These capabilities allow the pseudoplasmodium to find its way to the soil surface where it undergoes a final transformation into a fruiting body emitting robust spores. Taken away by the wind or animals, these spores bear the potential to germinate into a new protozoa under propitious environmental conditions. For an illustration of the complete cycle, see Fig. 7.

Chemotaxis, the directed cell movement in a chemical gradient, is at the basis of this complex process. An amoeba that experiences unfavorable conditions, e.g., starvation, secretes the chemoattractant cAMP. Neighboring amoeba detect cAMP, change their shape building up a leading and a trailing edge, migrate with the help of pseudopodia toward the source, and in turn also secret cAMP. Thereby, streamlines of amoeba are built up as a first level of organization.

On a molecular level, chemotaxis is triggered by the interaction of the chemoattractant with a GPCR embedded in the membrane of the chemotaxing cell. A crucial GPCR in *D. discoideum* chemotaxis is the cAMP receptor1 (cAR1). It is not only the first receptor expressed as a consequence of disadvantageous conditions but also the most sensitive to cAMP. For this reason, the function of cAR1 was studied extensively [66–69]. As implied by the name GPCR, these transmembrane receptors are associated with G proteins on their cytosolic side. G proteins are heterotrimers consisting of a G_α, and a heterodimeric $G_{\beta\gamma}$ subunit. The common view of G protein signaling implies that upon ligand binding to the receptor, the associated G proteins exchange guanine di-phosphate for guanine tri-phosphate in the G_α subunit. This leads to destabilization of the complex and the dissociation of the G protein in its G_α and $G_{\beta\gamma}$ subunit. In *D. discoideum* chemotaxis, both G_α and $G_{\beta\gamma}$ subsequently

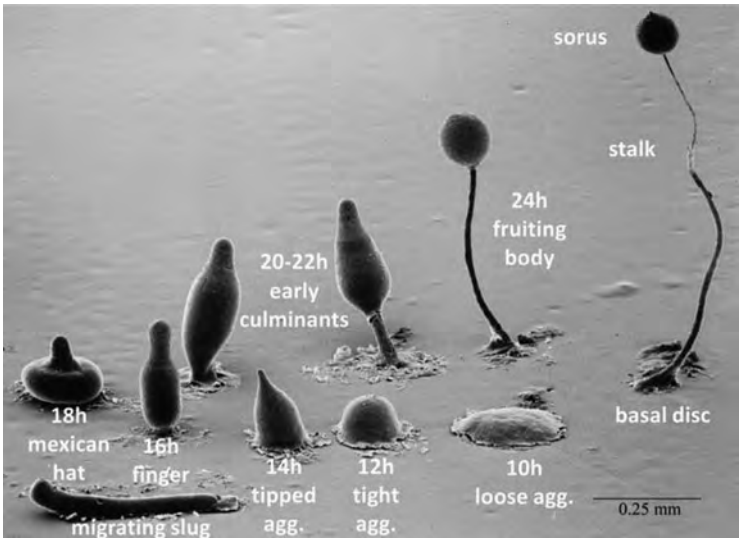

Fig. 7 Scanning electron micrograph of the developmental stages of the amoeba *D. discoideum*. Image copyright M. J. Grimson and R. L. Blanton, Biological Sciences Electron Microscopy Laboratory, Texas Tech University

activate different intracellular pathways that finally lead to cell polarization and directed migration toward the cAMP gradient.

Chemotaxis is triggered over a wide range of chemoattractant gradients and mean concentrations down to remarkably shallow gradients of 2% across the cell body. Thus, it is highly interesting to identify the ubiquitous molecular mechanisms that translate various extracellular gradients steadily in a highly polarized cellular phenotype exhibiting biased migration toward the source of the gradient. Several models were proposed for the early chemotaxis stages of gradient sensing followed by cell polarization: the pilot pseudopodia model [70, 71], the first hit model [72], several positive feedback loop models [73–75], the local excitation, global inhibition model [76, 77], and the balanced inactivation model [78]. Recently, increasing experimental evidence was found that questions the concept that signaling guides the generation of well-placed pseudopods [79–81]. *D. discoideum* cells move by default and constantly generate pseudopods in a probabilistic manner. Moreover, new pseudopods protrude preferentially from existing ones, but can be retracted after review. These new insights demand a reevaluation of the molecules important to chemotaxis with respect to their influence on pseudopod generation frequency, persistency, or the probabilistic distribution of their placement. To conclude, more quantitative information about the localization, mobility, and reaction rates of major players like cAR1 and the G protein subunits are required to elucidate their interaction with, e.g., the actin cytoskeleton that pushes the pseudopodia forward. These findings will allow to achieve a more realistic picture of chemotaxis.

4.2 GPCR and G Protein Exist as a Precoupled Complex

G proteins are important signal transducing molecules in cells. They not only are involved in chemotaxis, but also regulate many vital processes such as transcription and secretion in mammalian cells. Extensive research has been pursued since their discovery in the 1960s yielding the identification of more than 1,000 mammalian GPCRs and the atomic structure of three of them [82–84]. Nevertheless, it is not yet known how ligand-induced conformational changes of the GPCR activate the G protein. Another open question is whether GPCR association with the G protein before receptor stimulation is required or even stable. In 2005, Nobles et al. could prove the existence of a precoupled pentamer consisting of a GPCR dimer of either α2A adrenergic or muscarinic M4 receptor and the trimeric G protein in living HEK cells applying FRET [85]. More recently, we used single-molecule widefield microscopy (SMM) to deduce information about the GPCR/G protein complex from the diffusion behavior of cAR1 and the G protein subunits in *D. discoideum* [67]. Despite its low axial resolution of ~1 μm, SMM is ideally suited to study processes that are confined to two dimensions, like diffusion of transmembrane or membrane-bound proteins, with high spatial (~40 nm) and temporal (~50 ms) resolution. For this purpose, *D. discoideum* cells were stably transformed with

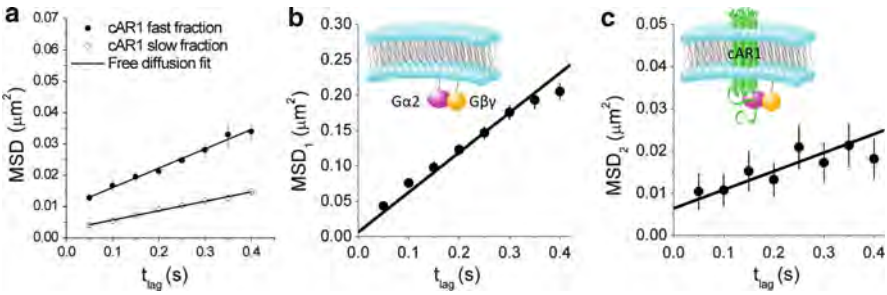

Fig. 8 Mobility of cAR1-YFP and G_{β}-YFP. (**a**) cAR1 exists in two populations exhibiting free diffusion. (**b**) Mean square displacement vs. time plot for the fast fraction of G_{β}-YFP. (**c**) Mean square displacement vs. time plot for the slow fraction of G_{β}-YFP [67]

Table 3 Results of cAR1 and G protein diffusion as measured in unstimulated *D. discoideum* cells. D_{FF} and D_{SF}, diffusion constants of the fast and slow fraction respectively. α, fast fraction

	D_{FF} ($\mu m^2/s$)	D_{SF} ($\mu m^2/s$)	α (%)	Diffusion type
cAR1	0.015 ± 0.002	0.007 ± 0.001	45 ± 6	Free
$G_{\alpha 2}$	0.14 ± 0.01	0.015 ± 0.001	68 ± 4	Free
$G_{\beta\gamma}$	0.15 ± 0.01	0.011 ± 0.001	68 ± 3	Free

cAR1-YFP, $G_{\alpha 2}$-YFP, or $G_{\beta\gamma}$-YFP constructs. Particle image correlation analysis [22] of the single molecule data allowed for the calculation of the cumulative probability of diffusion steps on different time lags. The results are summarized in Fig. 8 and Table 3. Neither cAR1 nor the G protein subunits were found to diffuse homogenously. Their P_{cum}s could be best fitted by a diffusion model taking two diffusing species into account (see Sect. 2.3). A global fit of all P_{cum}s at different time lags provided the MSDs of the fast and the slow fraction, as well as the fast fraction size α. Both cAR1 and the G protein subunits showed free diffusion on all observed timescales (50–400 ms; see Fig. 8a). The high similarity of the diffusion behavior of $G_{\alpha 2}$ and $G_{\beta\gamma}$ suggested that all membrane-bound G proteins were $G_{\alpha 2\beta\gamma}$ heterotrimers. Moreover, comparison of the diffusion constants of the slow moving fractions of $G_{\alpha 2}$ and $G_{\beta\gamma}$ with the fast moving fraction of cAR1 provided a strong argument that ~30% of the G proteins exist in a precoupled complex with cAR1 and therefore move at the same speed. This hypothesis could be further supported by alternative biochemical assays [67].

4.3 Polarized Mobility of GPCR and G Protein upon Agonist Stimulation

The same study [67] monitored the effect of global and gradient stimulation with cAMP on *D. discoideum* cells expressing either $G_{\alpha 2}$-YFP or $G_{\beta\gamma}$-YFP to identify the

Table 4 Results of G protein diffusion as measured in globally stimulated *D. discoideum* cells. D_{FF} and D_{SF}, diffusion constants of the fast and slow fraction respectively. α, fast fraction [67]

	D_{FF} ($\mu m^2/s$)	Diffusion type	D_{SF} ($\mu m^2/s$)	α (%)	Diffusion type
$G_{\alpha 2}$	0.19 ± 0.02	Confined	0.015 ± 0.001	68 ± 4	Free
$G_{\beta\gamma}$	0.16 ± 0.02	Confined	<0.001	59 ± 3	Immob.

molecular mechanism leading to cell polarization. It had been shown previously that the cAR1 receptors and the G proteins are homogenously distributed in the membrane of *D. discoideum*. Moreover, this homogeneous configuration was not affected by stimulation with cAMP [66, 69, 86, 87]. Thus, a simple picture, in which cell polarization is caused by asymmetric receptor or G protein distribution in the cell membrane, is not applicable.

The scenario described in Sect. 4.2 changed dramatically upon global stimulation with 10 µM cAMP (see Table 4). The diffusion behavior of the fast fraction of both the $G_{\alpha 2}$ and the $G_{\beta\gamma}$ subunit changed from free diffusion to confined diffusion within domains of ~600 nm diameter. Moreover, the slow fraction of the $G_{\beta\gamma}$ subunit increased from 32% to 41% and was immobilized ($D < 0.001$ $\mu m^2/s$). Both effects were shown to be F actin dependent by disrupting the actin cytoskeleton by adding latrunculin A. These observations led to the conclusion that the observed domains are imposed by the actin cytoskeleton, and that $G_{\beta\gamma}$ interacts either directly or indirectly with the F actin meshwork.

When exposed to a gradient of cAMP (~0.4 nM/µm), the diffusion behavior of the G protein subunits became polarized. The proteins at the trailing edge diffused like in the unstimulated situation (see Sect. 4.2). Both the fast and the slow fraction showed free diffusion. The proteins at the leading edge, on the other hand, exhibited the same diffusion characteristics as in the case of global stimulation: confined fast fractions of $G_{\alpha 2}$ and $G_{\beta\gamma}$ and immobilized as well as increased slow fraction of $G_{\beta\gamma}$. These results support the hypothesis that F actin plays an important regulatory role in maintaining cell polarity during chemotaxis.

Earlier single molecule studies investigated the cAMP/cAR1 dissociation rate in chemotaxing cells and found polarized behavior in the receptor off-rate [69]. cAMP/receptor complexes at the leading edge dissociated faster that those at the trailing edge. Since the steady-state amount of cAMP binding was measured to be almost equal at both locations, the association rates at the leading edge had to be increased, too. As a result, cAMP binding and unbinding and thus receptor and G protein activation are cycled faster at the leading edge of the cell. A possible explanation that why G protein reactivation is facilitated at the leading edge was provided by de Keijzer et al., who showed that the mobility of cAR1 is increased at the leading edge in comparison to the trailing edge [66]. Thus, activated cAR1 receptors that dissociated from the receptor/G protein complex are able to activate many more G proteins than at the trailing edge. Such a local amplification step leads to a final fivefold linear amplification of the external cAMP gradient to an intracellular gradient in active G proteins constituting the first step in diffusion-controlled asymmetric signaling.

4.4 Mechanistic Model of Early Chemotactic Signaling in D. discoideum

Combining existing knowledge about *D. discoideum* chemotaxis with new insights from single molecule fluorescence microscopy, we suggested a mechanistic model of early chemotaxis events [67]. In the resting state of the cell, the membrane is populated by cAR1 and complexed cAR1-$G_{\alpha 2\beta\gamma}$. The complexed G protein diffuses one order of magnitude slower than the free G protein [67, 68]. The cytosol provides a pool of $G_{\beta\gamma}$ [68, 78] and heterotrimeric G proteins. Upon cAMP binding to cAR1, the equilibrium between the $G_{\alpha 2\beta\gamma}$ heterotrimer and the complexed cAR1-$G_{\alpha 2\beta\gamma}$ gets disrupted by the formation of an activated cAR1-$G_{\alpha 2\beta\gamma}$ complex. This complex

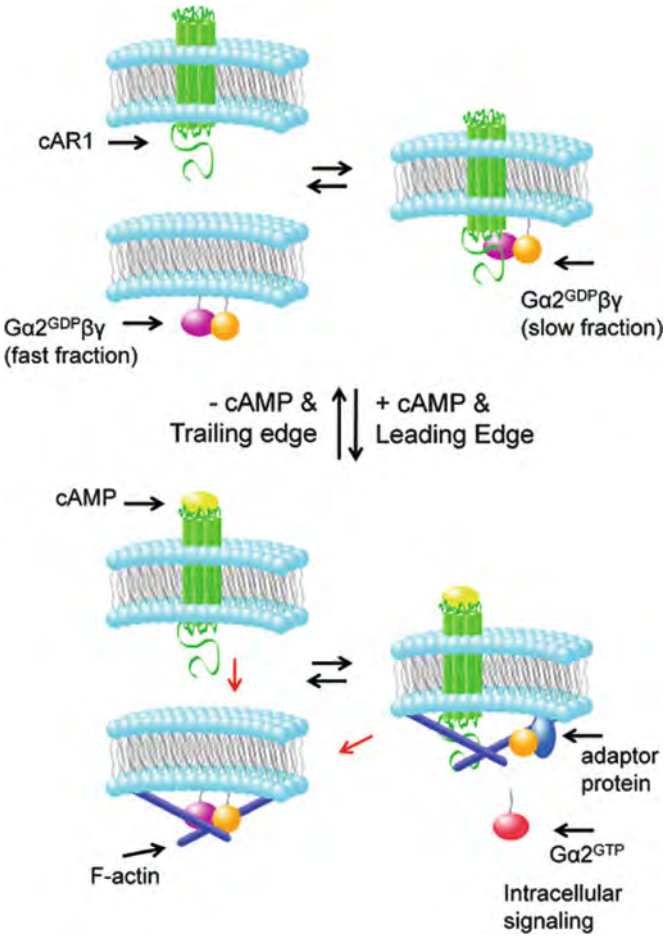

Fig. 9 Model describing the dynamic cAR1/G protein interaction at the leading and trailing edge [67]. For details, see text

subsequently dissociates into the activated receptor, and the free $G_{\alpha 2}$ and $G_{\beta\gamma}$ subunits. The stimulation-dependent dissociation of the G protein in its subunits was observed by Janetopoulos et al. with the help of FRET [88]. It takes approximately 0.4–1 s^{-1} until cAMP dissociates from cAR1 [89]. During that time, the activated receptor can activate more G proteins. Since the receptors at the leading edge diffuse considerably faster than at the trailing edge, an intracellular gradient in active G proteins is generated that is significantly larger than the external chemoattractant gradient [66]. G protein activation initiates multiple intracellular signaling cascades leading to actin cytoskeleton reorganization [90]. The tightening of the membrane-associated F actin is reflected in the diffusion properties of the G protein subunits. The fast fraction of both subunits becomes confined in actin-dependent 600 nm domains. This process is conceptually similar to the diffusion barriers at the leading edge of moving fish epidermal keratocytes [91]. Simultaneously, the slow fraction of $G_{\beta\gamma}$ gets immobilized by binding to F actin at the leading edge; at the trailing edge, $G_{\beta\gamma}$ diffuses into the cytosol. This allows for two scenarios: F actin either functions as a scaffold of $G_{\beta\gamma}$ signaling or impairs the discussed inhibitory function of $G_{\beta\gamma}$ [78].

$G_{\beta\gamma}$ immobilization might be another example for the widely used clustering of signaling components in a larger protein complex, a so-called signalosome. The cytoskeleton together with anchoring and scaffolding proteins was found to play a crucial role in the maintenance of these signaling complexes [92]. Figure 9 illustrates the dynamic cAR1/G protein interactions at the leading and the trailing edge.

5 Conclusion

In this chapter, we first reviewed the basic concepts of diffusion and single molecule microscopy. It was shown how combining fluorescent protein technology and high resolution microscopy lead to new insights into relevant biological processes. Two applications were introduced in detail. First, extensive work on the model proteins of the Ras family elucidated the role of membrane partitioning in protein dynamics and its influence on signaling. Moreover, we showed how this technique was extended to study protein dynamics in living organism. Second, single molecule fluorescence microscopy allowed to characterize the mobility of the GPCR cAR1 and its associated G protein in *D. discoideum*. On the basis of these data, a mechanistic model was developed to shed light on the molecular basis of cAR1-cAMP mediated chemotaxis in *D. discoideum*.

References

1. Singer SJ, Nicolson GL (1972) The fluid mosaic model of the structure of cell membranes. Science 175:720–731
2. Simons K, Ikonen E (1997) Functional rafts in cell membranes. Nature 387:569–572
3. Simons K, van Meer G (1998) Lipid sorting in epithelial cells. Biochemistry 27:6197–6202

4. Brown D, London E (2000) Structure and function of sphingolipid- and cholesterol-rich membrane rafts. J Biol Chem 275:17221–17224
5. Dietrich C, Volovyk Z, Levi M, Thompson N, Jacobson K (2001) Partitioning of thy-1, gm1, and cross-linked phospholipid analogs into lipid rafts reconstituted in supported model membrane monolayers. Proc Natl Acad Sci USA 98:10642–10647
6. Dietrich C, Bagatolli L, Volovyk Z, Thompson N, Levi M, Jacobson K, Gratton E (2001) Lipid rafts reconstituted in model membranes. Biophys J 80:1417–1428
7. Korlach J, Schwille P, Webb W, Feigenson G (1999) Characterization of lipid bilayer phases by confocal microscopy and fluorescence correlation spectroscopy. Proc Natl Acad Sci USA 96:8461–8466
8. Jacobson K, Mouritsen OG, Anderson RGW (2007) Lipid rafts: at a crossroad between cell biology and physics. Nat Cell Biol 9:7–14
9. Engelman DM (2005) Membranes are more mosaic than fluid. Nature 438:578–580
10. Kusumi A, Suzuki K (2005) Toward understanding the dynamics of membraneraft- based molecular interactions. Biochim Biophys Acta 1746:234–251
11. Almeida PFF, Vaz WLC (1995) Lateral diffusion in membranes. In: Lipowsky R, Sackmann E (eds) Handbook of biological physics, vol 1. Elsevier/North Holland, Amsterdam, pp 305–357
12. Anderson CM, Georgiou GN, Morrison IEG, Stevenson GVW, Cherry RJ (1992) Tracking of cell surface receptors by fluorescence digital imaging microscopy using a charge-coupled device camera. J Cell Sci 101:415–425
13. Feder TJ, Brust-Mascher I, Slattery JP, Baird B, Webb WWW (1996) Constrained diffusion or immobile fraction on cell surfaces: a new interpretation. Biophys J 70:2767–2773
14. Kusumi A, Sako J, Yamamoto M (1993) Confined lateral diffusion of membrane receptors as studied by single particle tracking (nanovid microscopy). Effects of calcium-induced differentiation in cultured epithelial cells. Biophys J 65:2021–2040
15. Wieser S, Moertelmaier M, Fuertbauer E, Stockinger H, Schutz GJ (2007) (Un)confined diffusion of CD59 in the plasma membrane determined by high-resolution single-molecule microscopy. Biophys J 92:3719–3728
16. Schmidt T, Schutz GJ, Gruber HJ, Schindler H (1995) Characterization of photophysics and mobility of single molecules in a fluid lipid membrane. J Phys Chem 99:17662–17668
17. Schmidt T, Schutz GJ, Baumgartner W, Gruber HJ, Schindler H (1996) Imaging of single molecule diffusion. Proc Natl Acad Sci USA 93:2926–2929
18. Funatsu T, Harada Y, Tokunaga M, Saito K, Yanagida T (1995) Imaging of single fluorescent molecules and individual ATP turnovers by single myosin molecules in aquous solution. Nature 374:555–559
19. Thompson RE, Larson DR, Webb WW (2002) Precise nanometer localization analysis for individual fluorescent probes. Biophys J 82:2775–2783
20. Abraham AV, Ram S, Chao J, Ward ES, Ober RJ (2009) Quantitative study of single molecule location estimation techniques. Opt Exp 17:23352–23373
21. Qian H, Sheetz MP, Elson EL (1991) Single particle tracking. Analysis of diffusion and flow in two-dimensional system. Biophys J 60:910–921
22. Semrau S, Schmidt T (2007) Particle image correlation spectroscopy (PICS): retrieving nanometer-scale correlations from high-density single molecule position data. Biophys J 92:613–621
23. Hebert B, Costantino S, Wiseman PW (2005) Spatiotemporal image correlation spectroscopy (STICS) theory, verification, and application to protein velocity mapping in living CHO cells. Biophys J 88:3601–3614
24. Lommerse PHM, Blab GA, Cognet L, Harms GS, Snaar-Jagalska EB, Spaink HP, Schmidt T (2004) Single-molecule imaging of lipid-anchored proteins reveals domains in the cytoplasmic leaflet of the cell membrane. Biophys J 86:609–616
25. Harms GS, Cognet L, Lommerse PHM, Blab GA, Schmidt T (2001) Autofluorescent proteins in single-molecule research: applications to live cell imaging microscopy. Biophys J 80:2396–2408

26. Shaner NC, Steinbach PA, Tsien RY (2005) A guide to choosing fluorescent proteins. Nat Methods 2:905–909
27. Zhang J, Campbell R, Ting AY, Tsien RY (2002) Creating new fluorescent probes for cell biology. Nat Rev Cell Biol 3:906–918
28. Kapanidis AN, Weiss S (2002) Fluorescent probes and bioconjugation chemistries for single molecule fluorescence analysis of biomolecule. J Chem Phys 117:10953–10964
29. Yin J, Lin AJ, Golan DE, Walsh CT (2006) Site-specific protein labeling by Sfp phosphopantetheinyl transferase. Nat Protoc 1:280–285
30. Zhou Z, Cironi P, Lin AJ, Xu Y, Hrvatin S, Golan DE, Silver PA, Walsh CT, Yin J (2007) Genetically encoded short peptide tags for orthogonal protein labeling by Sfp and AcpS phosphopantetheinyl transferases. ACS Chem Biol 2:337–346
31. Los G, Anson B, Zimprich C, Karassina N, January C, Buleit, RF (2004) The HaloTag: a novel technology for protein labeling in living cells: effect of the HaloTagTM system on hERG channel activity. FENS Forum 2004, Federation of European Neuroscience Societies (FENS), Berlin, 196
32. Kapanidis AN, Ebright YW, Ebright RH (2001) Site-specific incorporation of fluorescent probes into protein: hexahistidine-tag-mediated fluorescent labeling using (Ni2+:Nitrilotriacetic acid)n-fluorochrome conjugates. J Am Chem Soc 123:12123–12125
33. Cornish VW, Hahn KM, Schultz PG (1996) Site-specific protein modification using a ketone handle. J Am Chem Soc 118:8150–8151
34. Wang L, Magliery TJ, Liu DR, Schultz PG (2000) A new functional suppressor tRNA/Aminoacyl-tRNA synthetase pair for the in vivo incorporation of unnatural amino acids into proteins. J Am Chem Soc 122:5010–5011
35. Hancock JF, Paterson H, Marshall CJ (1990) A polybasic domain or palmitoylation is required in addition to the CAAX motif to localize p21ras to the plasma membrane. Cell 63:133–139
36. Hancock JF, Cadwallader K, Paterson H, Marshall CJ (1991) A CAAX or a CAAL motif and a second signal are sufficient for plasma membrane targeting of ras proteins. EMBO J 10:4033–4039
37. Choy E, Chiu VK, Silletti J, Feoktistov M, Morimoto T, Michaelson D, Ivanov IE, Philips MR (1999) Endomembrane trafficking of ras: the CAAX motif targets proteins to the ER and Golgi. Cell 98:69–80
38. Apolloni A, Prior IA, Lindsay M, Parton RG, Hancock JF (2000) H-ras but not K-ras traffics to the plasma membrane through the exocytic pathway. Mol Cell Biol 20:2475–2487
39. Alberts B, Johnson A, Lewis J, Raff M, Roberts K, Walter P (2007) Molecular biology of the cell. Garland Science, New York
40. Roy S, Luetterforst R, Harding A, Apolloni A, Etheridge M, Stang E, Rolls B, Hancock JF, Parton RG (1999) Dominant-negative caveolin inhibits H-ras function by disrupting cholesterol-rich plasma membrane domains. Nat Cell Biol 1:98–105
41. Niv H, Gutman O, Kloog Y, Henis YI (2002) Activated K-Ras and H-Ras display different interactions with saturable nonraft sites at the surface of live cells. J Cell Biol 157:865–872
42. Parmryd I, Adler J, Patel R, Magee AI (2003) Imaging metabolism of phosphatidylinositol 4,5-bisphosphate in T-cell GM1- enriched domains containing Ras proteins. Exp Cell Res 285:27–38
43. Prior IA, Harding A, Yan J, Sluimer J, Parton RG, Hancock JF (2001) GTP-dependent segregation of H-ras from lipid rafts is required for biological activity. Nat Cell Biol 3:368–375
44. Prior IA, Muncke C, Parton RG, Hancock JF (2003) Direct visualization of Ras proteins in spatially distinct cell surface microdomains. J Cell Biol 160:165–170
45. Abankwa D, Gorfe AA, Inder K, Hancock JF (2010) Ras membrane orientation and nanodomain localization generate isoform diversity. Proc Natl Acad Sci USA 107:1130–1135
46. Lommerse PHM, Spaink HP, Schmidt T (2004) In vivo plasma membrane organization: results of biophysical approaches. Biochem et Biophys Acta 1664:119–131

47. Kusumi A, Suzuki K (2005) Toward understanding the dynamics of membrane-raft-based molecular interactions. Biochem et Biophys Acta 1746:234–251
48. Lommerse PH, Vastenhoud K, Pirinen NJ, Magee AI, Spaink HP, Schmidt T (2006) Single-molecule diffusion reveals similar mobility for the Lck, H-ras, and K-ras membrane anchors. Biophys J 91:1090–1097
49. Lommerse PHM, Snaar-Jagalska EB, Spaink HP, Schmidt T (2005) Single-molecule diffusion measurements of H-Ras at the plasma membrane of live cells reveal microdomain localization upon activation. J Cell Sci 118:1799–1809
50. Li SL, Miyata Y, Yahara I, Fujita-Yamaguchi Y (1993) Insulin- induced circular membrane ruffling on rat 1 cells expressing a high number of human insulin receptors: circular ruffles caused by rapid actin reorganization exhibit high density of insulin receptors and phosphotyrosines. Exp Cell Res 205:353–360
51. Tsakiridis T, Bergman A, Somwar R, Taha C, Aktories K, Cruz TF, Klip A, Downey GP (1998) Actin filaments facilitate insulin activation of the src and collagen homologous/mitogen-activated protein kinase pathway leading to DNA synthesis and c-fos expression. J Biol Chem 273:28322–28331
52. Khayat ZA, Tong P, Yaworsky K, Bloch RJ, Klip A (2000) Insulin-induced actin filament remodeling colocalizes actin with phosphatidylinositol 3-kinase and GLUT4 in L6 myotubes. J Cell Sci 113:279–290
53. Dadke S, Chernoff J (2003) Protein-tyrosine phosphatase 1B mediates the effects of insulin on the actin cytoskeleton in immortalized fibroblasts. J Biol Chem 278:40607–40611
54. Murakoshi H, Iino R, Kobayashi T, Fujiwara T, Ohshima C, Yoshimura A, Kusumi A (2004) Single-molecule imaging analysis of Ras activation in living cells. Proc Natl Acad Sci USA 101:7317–7322
55. Rotblat B, Prior IA, Muncke C, Parton RG, Kloog Y, Henis YI, Hancock JF (2004) Three separable domains regulate GTP-dependent association of H-ras with the plasma membrane. Mol Cell Biol 24:6799–6810
56. Belanis L, Plowman SJ, Rotblat B, Hancock JF, Kloog Y (2008) Galectin-1 is a novel structural component and a major regulator of HRas nanoclusters. Mol Biol Cell 19:1404–1414
57. Ries J, Yu SR, Burkhardt M, Brand M, Schwille P (2009) Modular scanning FCS quantifies receptor-ligand interactions in living multicellular organisms. Nat Methods 6:643–645
58. Shi X, Foo YH, Sudhaharan T, Chong SW, Korzh V, Ahmed S, Wohland T (2009) Determination of dissociation constants in living zebrafish embryos with single wavelength fluorescence cross-correlation spectroscopy. Biophys J 97:678–686
59. Shi X, Teo LS, Pan X, Chong SW, Kraut R, Korzh V, Wohland T (2009) Probing events with single molecule sensitivity in zebrafish and Drosophila embryos by fluorescence correlation spectroscopy. Dev Dyn 238:3156–3167
60. Friedrich M, Nozadze R, Gan Q, Zelman-Femiak M, Ermolayev V, Wagner TU, Harms GS (2009) Detection of single quantum dots in model organisms with sheet illumination microscopy. Biochem Biophys Res Commun 390:722–727
61. Lieschke GJ, Currie PD (2007) Animal models of human disease: zebrafish swim into view. Nat Rev Genet 8:353–367
62. Hsu CH, Wen ZH, Lin CS, Chakraborty C (2007) The zebrafish model: use in studying cellular mechanisms for a spectrum of clinical disease entities. Curr Neurovasc Res 4:111–120
63. Trede NS, Langenau DM, Traver D, Look AT, Zon LI (2004) The use of zebrafish to understand immunity. Immunity 20:367–379
64. Schaaf MJM, Koopmans WJA, Meckel T, van Noort J, Snaar-Jagalska EB, Schmidt T, Spaink HP (2009) Single-molecule microscopy reveals membrane microdomain organization of cells in a living vertebrate. Biophys J 97:1206–1214
65. Eichinger L et al (2005) The genome of the social amoeba *Dictyostelium disciodeum*. Nature 435:43–57

66. de Keijzer S, Sergé A, van Hemert F, Lommerse PHM, Lamers GEM, Spaink HP, Schmidt T, Snaar-Jagalska E (2008) A spatially restricted increase in receptor mobility is involved in directional sensing during *Dictyostelium disciodeum* chemotaxis. J Cell Sci 121:1750–1757
67. van Hemert F, Lazova MD, Snaar-Jagalska E, Schmidt T (2010) Mobility of G proteins is heterogenous and polarized during chemotaxis. J Cell Sci 123:2922–2930
68. Elzie CA, Colby J, Sammons MA, Janetopoulos C (2009) Dynamic localization of G proteins in *Dictyostelium disciodeum*. J Cell Sci 122:2597–2603
69. Ueda M, Sako Y, Tanaka T, Devreotes P, Yanagida T (2001) Single molecule analysis of chemotactic signaling in *Dictyostelium* cells. Science 294:864–867
70. Caterina MJ, Devreotes PN (1991) Molecular insights into eukaryotic chmotaxis. Faseb J 5:3078–3085
71. Devreotes P, Janetopoulos C (2003) Eukryotic chemotaxis: distinctions between directional sensing and polarization. J Biol Chem 278:20445–20448
72. Rappel WJ, Thomas PJ, Levine H, Loomis WF (2002) Establishing direction during chemotaxis in eukaryotic cells. Biophys J 83:1361–1367
73. Meinhardt H (1999) Orientation of chemotactic cells and growth cones: models and mechanisms. J Cell Sci 112:2867–2874
74. Narang A, Subramaniam KK, Lauffenburger DA (2001) A mathematical model for chemoattractant gradient sensing based on receptor-regulated membrane phospholipid signaling dynamics. Ann Biomed Eng 29:677–691
75. Potsma M, van Haastert PJM (2001) A diffusion-translocation model for gradient sensing by chemotacic cells. Biophys J 81:1314–1323
76. Ma L, Janetopoulos C, Yang L, Devreotes PN, Iglesias PA (2004) Two complementary, local excitation, global inhibition mechanisms acting in parallel can explain the chemoattractant-induced regulation of PI(3,4,5)P-3 response in *Dictyostelium* cells. Biophys J 87:3764–3774
77. Gamba A, de Candia A, Talia S, Coniglio A, Bussolino F, Serini G (2005) Diffusion-limited phase separation in eukaryotic chemotaxis. Proc Natl Acad Sci USA 103:16927–16932
78. Levine H, Kessler DA, Rappel WJ (2006) Directional sensing in eukaryotic chemotaxis: a balanced inactivation model. Proc Natl Acad Sci USA 103:9761–9766
79. Andrew N, Insall RH (2007) Chemotaxis in shallow gradients is mediated independently of PtdIns 3-kinase by biased choices between random protrusion. Nat Cell Biol 9:193–200
80. Bosgraaf L, Haastert PJV (2009) Navigation of chemotactic cells by parallel signalling to pseudopod persistance and orientation. PLoS One 4:e6842
81. Sasaki AT, Janetopoulos C, Lee S, Charest PG, Takeda K, Sundgeimer LW, Meili R, Devreotes PN, Firtel RA (2007) G protein-independent Ras/PI3K/F-actin circuit regulates basic cell motility. J Cell Biol 178:185–191
82. Palczewski K et al (2000) Crystal structure of Rhodopsin: a G-protein coupled receptor. Science 289:739–745
83. Rasmussen SGF et al (2007) Crystal structure of the human [bgr]2 adrenergic G-protein-coupled receptor. Nature 450:383–387
84. Jaakola VP et al (2008) The 2.6 Angstrom crystal structure of a human A2A adenosine receptor bound to an antagonist. Science 322:1211–1217
85. Nobles M, Benians A, Tinker A (2005) Heterotrimeric G proteins precouple with G protein-coupled receptors in living cells. Proc Natl Acad Sci USA 102:18706–18711
86. Parent CA, Devreotes PN (1999) A cell's sense of direction. Science 284:765–770
87. Jin T, Zhang N, Long Y, Parent CA, Devreotes PN (2000) Localization of the G protein$\beta\gamma$ complex in living cells during chemotaxis. Science 287:1034–1036
88. Janetopoulos C, Jin T, Devreotes P (2001) Receptor-mediated activation of heterotrimeric G-proteins in living cells. Science 291:2408–2411
89. Janssens PM, van Haastert PJ (1987) Molecular basis of transmembrane signal transduction in *Dictyostelium Disciodeum*. Microbiol Rev 51:396–418

90. Franca-Koh J, Kamimura Y, Devreotes P (2006) Navigating signaling networks: chemotaxis in *Dictyostelium Disciodeum*. Curr Opin Genet Dev 16:333–338
91. Weisswange I, Bretschneider T, Anderson KI (2005) The leading egde is a lipid diffusion barrier. J Cell Sci 118:4375–4380
92. Pawson T, Scott JD (1997) Signaling through scaffold, anchoring, and adaptor proteins. Science 278:2075–2080
93. Schutz GJ, Schindler H, Schmidt T (1997) Single molecule microscopy on model membranes reveals anomalous diffusion. Biophys J 73:1073–1080

Section 3: Practical sessions

Confocal microscopy

Instructors: Erik Manders & Ronald Breedijk

Goal:

The goal of this practical is to get acquainted with the principles of a confocal fluorescence microscope. By imaging a couple of example specimen, the potential - and possible limitations - of this instrument will be demonstrated. We will measure the spatial resolution of the confocal microscope and compare with the wide-field microscope. At the end of this practical we will demonstrate our new Structured Illumination Microscope and measure the improvement of spatial resolution.

Introduction:

Fluorescence microscopy is of great importance to biological research in general and cell biology in particular. It combines great sensitivity with the possibility to label species of interest with unprecedented specificity through the range of available biochemical techniques. A normal fluorescence microscope in principle is a 2D imaging device; the third dimension - i.e. in the axial direction - can be resolved only in a limited way. Confocal fluorescence microscopy enables true three-dimensional imaging by suppressing all contributions from out-of-focus planes using a detection pinhole. The specimen can thus be "optically sliced" and a 3D image can be re-constructed from a series of 2D images taken at different focal planes.

In confocal fluorescence microscopy, true 3D resolution is accomplished by actively suppressing any signal coming from out-of-focus planes. This is achieved by using a pinhole in front of the detector as schematically depicted in figure 1. Light originating from an in-focus plane is imaged by the microscope objective such that it freely passes the pinhole, whereas light coming from out-of-focus planes is largely blocked by the pinhole. The size of the pinhole determines how much reduction of the background (i.e. of the out-of-focus contributions) can be realised.

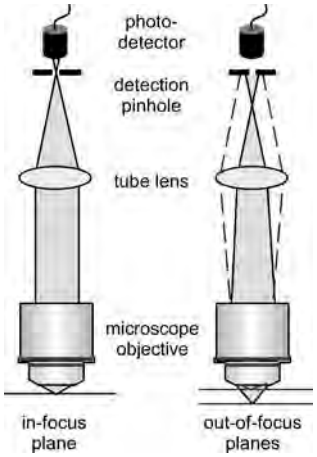

Figure 1. *The principle of confocal fluorescence microscopy. Light coming from out-of-focus planes is largely blocked by a pinhole in front of the detector.*

In a confocal fluorescence microscope (figure 2) the specimen is generally illuminated by a laser. The light coming from the laser passes through an (excitation) pinhole and is reflected by a dichroic mirror and focused by a microscope objective to a small spot in the specimen. The dichroic mirror has the property that it reflects light of a shorter wavelength (e.g. 488 nm from an

Argon-ion laser), while transmitting that of a longer wavelength (e.g. the fluorescence >510 nm from Fluorescein). Specific dichroic mirrors can be made for the relevant wavelength regions of excitation and fluorescence.
In the specimen the light is absorbed by the fluorophores - either intrinsically present or artificially added to label specific targets. After absorption, the fluorophores start to fluoresce, emitting light in a random direction and with a wavelength that is longer than that of the excitation. A fraction of the emitted fluorescence is collected by the microscope objective and imaged onto the detector.

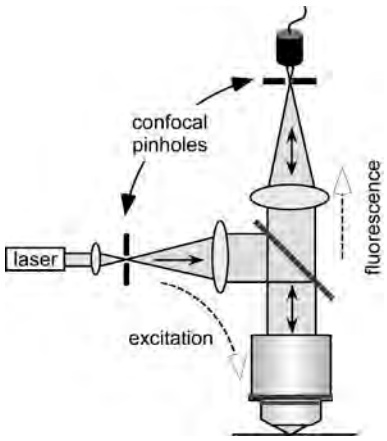

Figure 2 *Excitation of the specimen in confocal fluorescence microscopy by a laser. A fraction of the fluorescence emitted by the fluorophores in the specimen is collected by the microscope objective and imaged onto the detection pinhole in front of a photo-detector.*

For a specific setting of the microscope only a single point in the specimen is imaged at a time. In other words, confocal fluorescence microscopy is a serial rather than a parallel image acquisition system. To obtain a single optical section in a confocal fluorescence microscope, laser scanning is used. In laser scanning the specimen is kept stationary and the excitation spot is moved over the specimen.

Practical 1A (Zeiss, LSM-510)

First, the basic operation of the instrument will be demonstrated: the different components, the control software and how to make a stack and how to control the pinhole.

Make three dimensional images of two different specimen:

- **A.** an *acridine orange* labelled *Spathipyllum* pollen grain
- **B.** Fluorescent microbeads of 100 µm

Of each specimen you should make four 3D images with the following pinhole settings:

1. pinhole @ maximum
2. pinhole @ 1 * Airy
3. pinhole @ 0.25 * Airy

You should use the following objective: 63x/1.4-oil immersion

Q1. Based on the 3D-image of the micro-bead, measure the axial and lateral resolution for each pinhole setting.

Practical 1B (Nikon A1)

First, the basic operation of the instrument will be demonstrated: the different components, the control software and how to make multi-colour images and how to ise the spectral detector.

Make two dimensional images of Muntjac skin fibroblast cells with staining of the actin filaments (green), mitochondria (red) and DNA(DAPI) by using:

A. Multi-colour detection

B. Spectral detection and unmixing.

Q2. Try to unmix the spectral image. What gives the best colour-separation.

Practical 1C (Nikon N-SIM)

First, the basic operation of the instrument will be demonstrated: the different components, the control software and how to make a SIM-image.

Make wide-field and a SIM image of *:*

A**.** Fluorescent microbeads of 100 µm

Q3. Measure the lateral resolution and compare with the confocal data.

Practical notes

Total Internal Reflection Fluorescence Microscopy (TIRF) & Photo Activation Localization Microscopy (PALM)

Instructors: Kevin Crosby with assistance from Christiaan Zeelenberg & Dorus Gadella

Introduction:

Many critical biological processes occur at or near the plasma membrane of the cell. Total internal reflection fluorescence (TIRF) microscopy is a technique that is especially well suited to study events at the plasma membrane of adherent cells. The roots of total internal reflection, or evanescent wave microscopy date to its (non-fluorescence) use in the early sixties to study cell migration in fibroblasts (Ambrose, 1961) and fluorescence spectroscopy in the 1960s and 1970s (Hirschfeld, 1965). However, the method as we know it today really took shape in the seminal work of Daniel Axelrod and colleagues thirty years ago (Axelrod, 1981; Burghardt and Axelrod, 1981; Thompson et al., 1981). TIRF microscopy is now widely utilized to study a wide range of cellular processes such as endocytosis, exocytosis, cytoskeleton dynamics near the membrane, cell migration, and signaling. Additionally, a number of single-molecule techniques take advantage of the TIRF modality (see below). The evident limitation being, of course, that events that occur more than ~100 nm beyond the interface between the sample and the cover slip cannot be observed. The optical basis, implementation, and application of TIRF have already been introduced in the lecture. Additionally an advanced treatment of the theoretical aspects is contained in a recent review by Axelrod (Axelrod, 2008) and a more a more approachable guide written for cell biologist has been scribed by Mattheyses (Mattheyses et al., 2010).

Fluorescence light microscopy, while possessing many advantages for its use in the study of biological systems, has traditionally been limited in the degree of spatial resolution that can be achieved (Abbe, 1873). The so called Abbe, or diffraction, limit, which is theoretically set at ~200 nm in lateral space and ~500 nm axially, has been circumvented in the last few years by a plethora of super-resolution techniques. These include methods that rely upon stochastic processes that allow for the localization of individual fluorescent molecules, which are sequentially switched between a non-detectable and a detectable state. Such methodologies include (F)PALM ,STORM, and GSDIM (refs). (Betzig et al., 2006; Fölling et al., 2008; Hess et al., 2006; Rust et al., 2006). While the type of fluorescent molecules used and the photophysics of the switching process vary among these modalities, they all rely upon a computation localization analysis performed on a large series of images, each containing a sparse distribution of fluorescent molecules, whose individual position can be determined to a resolution of 20 to 50nms. The positions of all the images in the series can then be summed into a final super-resolution image.

Practical:

The instrument we will be using for this practical session is built around an inverted Nikon Eclipse Ti microscopy. The objective is a specialized 60x ApoTIRF 1.49NA, designed for the thru the objective TIRF configuration that this instrument utilizes. We have two lasers for excitation, a 1W Coherent OPSL 561 and a 50mW Coherent OBIS 488. We will also be using a 50mW Coherent CUBE 405 as the activating laser in our photoactivated localization microscopy (PALM) experiments . Our primary dichroic is a quad-pass 405/488/561/640. Emission filters are a long-pass 572 (Chroma), a band-pass 525-50 (Chroma), or a Razor-Edge long-pass 561 (Semrock).

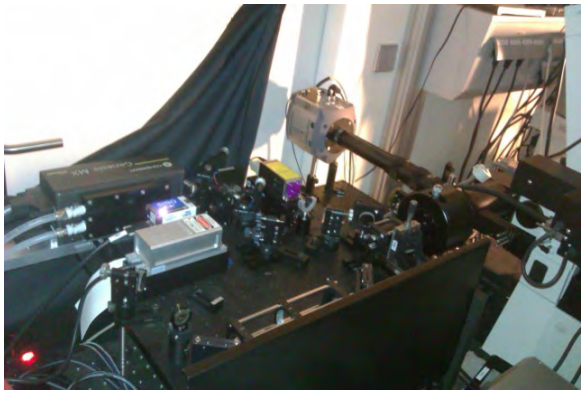

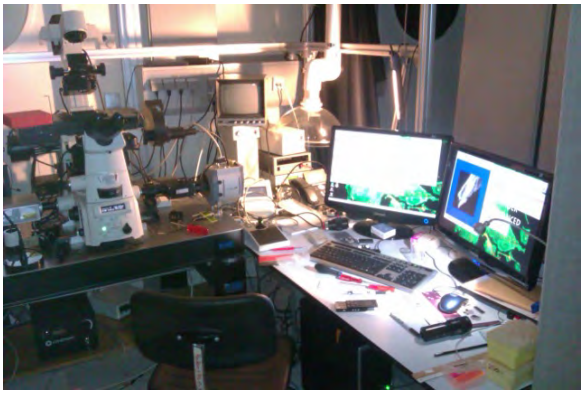

An outline of the experiments and samples will be presented on the day of the practical. Two review articles are also included in your packet.

References:

Abbe, E. 1873. Beiträge zur Theorie des Mikroskops und der mikroskopischen Wahrnehmung I. Die Construction von Mikroskopen auf Grund der Theorie. *Archiv für Mikroskopische Anatomie*. 9:413-418.

Ambrose, E.J. 1961. The movements of fibrocytes. *Exp Cell Res*. Suppl 8:54-73.

Axelrod, D. 1981. Cell-substrate contacts illuminated by total internal reflection fluorescence. *J Cell Biol*. 89:141-145.

Axelrod, D. 2008. Chapter 7: Total internal reflection fluorescence microscopy. *Methods in Cell Biology*. 89:169-221.

Betzig, E., G.H. Patterson, R. Sougrat, O.W. Lindwasser, S. Olenych, J.S. Bonifacino, M.W. Davidson, J. Lippincott-Schwartz, and H.F. Hess. 2006. Imaging intracellular fluorescent proteins at nanometer resolution. *Science*. 313:1642-1645.

Burghardt, T.P., and D. Axelrod. 1981. Total internal reflection/fluorescence photobleaching recovery study of serum albumin adsorption dynamics. *Biophys J*. 33:455-467.

Fölling, J., M. Bossi, H. Bock, R. Medda, C. Wurm, B. Hein, S. Jakobs, C. Eggeling, and S. Hell. 2008. Fluorescence nanoscopy by ground-state depletion and single-molecule return. *Nature Methods*. 5:943-945.

Hess, S., T.P. Girirajan, and M.D. Mason. 2006. Ultra-high resolution imaging by fluorescence photoactivation localization microscopy. *Biophysical Journal*. 91:4258-4272.

Hirschfeld, T. 1965. Total reflection fluorescence. *Canadian Spectroscopy*. 10:128.

Mattheyses, A.L., S.M. Simon, and J.Z. Rappoport. 2010. Imaging with total internal reflection fluorescence microscopy for the cell biologist. *Journal of Cell Science*. 123:3621-3628.

Rust, M., M. Bates, and X. Zhuang. 2006. Sub-diffraction-limit imaging by stochastic optical reconstruction microscopy (STORM). *Nature Methods*. 3:793-795.

Thompson, N.L., T.P. Burghardt, and D. Axelrod. 1981. Measuring surface dynamics of biomolecules by total internal reflection fluorescence with photobleaching recovery or correlation spectroscopy. *Biophys J*. 33:435-454.

Practical notes

Available online at www.sciencedirect.com

SciVerse ScienceDirect

Current Opinion in Chemical Biology

A starter kit for point-localization super-resolution imaging

Suliana Manley, Julia Gunzenhäuser and Nicolas Olivier

Super-resolution fluorescence imaging can be achieved through the localization of single molecules. By using suitable dyes, optical configurations, and software, it is possible to study a wide variety of biological systems. Here, we summarize the different approaches to labeling proteins. We review proven imaging modalities, and the features of freely available software. Finally, we give an overview of some biological applications. We conclude by synthesizing these different technical aspects into recommendations for standards that the field might apply to ensure quality of images and comparability of algorithms and dyes.

Address
Laboratory of Experimental Biophysics, École Polytechnique Fédérale de Lausanne, CH-1015 Lausanne, Switzerland

Corresponding author: Manley, Suliana (suliana.manley@epfl.ch)

Current Opinion in Chemical Biology 2011, **15**:813–821

This review comes from a themed issue on
Molecular Imaging
Edited by Alanna Schepartz and Ruben L Gonzalez, Jr.

Available online 24th November 2011

1367-5931/$ – see front matter

DOI 10.1016/j.cbpa.2011.10.009

Introduction

Super-resolution fluorescence imaging (SR) is enabling the visualization of the organization and dynamics of biological systems at unprecedented scales. This review focuses on SR derived from the point localization of individual molecules, an inherently single-molecule measurement. Advances in SR are rapidly occurring in the areas of algorithm development for rapid and maximal localization, the implementation of flexible labeling schemes and the diversification of usable fluorescent dyes, and meaningful biological applications. In this short review, we aim to create a 'starter kit' (Figure 1) with the basic information needed to navigate the dyes and software packages for image reconstruction, as well as a concise overview of imaging modalities and select biological applications. For more information, several in-depth reviews have recently been published [1,2], and detailed protocols provide a practical guide [3•,4,5].

The light from a point source, whether it is a star or a molecule, is invariably blurred by diffraction when it is imaged through a finite aperture. The form of this image, first derived by astronomer Sir George Biddell Airy [6], can be used to define the diffraction-limited resolving power of an imaging system. In the case of fluorescence microscopy of a structure densely labeled with dye molecules, diffraction limits the resolution to of order half the wavelength of visible light, or several hundred nanometers. However, with low background noise and efficient photon collection, molecular locations can be determined with high precision [7]. This is because the center of a molecular image or point spread function (PSF) can be localized, typically by fitting to a Gaussian function, even down to the nanometer scale [8]. Thus, by combining point localization with the stochastic switching of thousands of single molecules, resolving molecular distributions at the nanoscale is possible. Developed nearly in parallel by several groups, this method was alternately named photoactivated localization microscopy (PALM) [9••], fluorescence photoactivated localization microscopy (FPALM) [10], and stochastic optical reconstruction microscopy (STORM) [11]. Point-localization SR relies on the control of molecular fluorescence such that less than one molecule per diffraction-limited area emits at a time. Additionally, to achieve SR the density of localized molecules must satisfy the Nyquist criteria: in this context, the intermolecular spacing should not exceed twice the desired resolution [12].

Although a variety of properties can be used to isolate single molecules, such as spectrum [13], lifetime [14], and binding/dissociation [15] among others, photoswitching remains the most flexible strategy. While there is no substantive difference between PALM and FPALM, as implemented they differ from STORM in the mechanism of fluorophore photoswitching. (F)PALM imaging exploits photo-activatable fluorescent proteins (reviewed in Ref. [16]) as well as photoswitching YFP and GFP [17,18], while STORM imaging was demonstrated using pairs of switchable synthetic fluorophores. More recently direct STORM (dSTORM) [19] and ground state depletion microscopy followed by individual molecule return (GSDIM) [20] expanded the variety of synthetic fluorophores compatible with SR (reviewed in Ref. [2,21]). In summary, (F)PALM is compatible with genetically encoded labeling and live-cell imaging while (d)STORM has been realized primarily using antibody labeling and was thus limited to imaging in fixed cells. More recently, the use of self-labeling proteins [22,23] has brought some of the advantages of (F)PALM to (d)STORM, allowing more specific targeting of synthetic fluorophores [24] and live-cell imaging [25•]. In addition, extensive characterization of imaging and buffer conditions required to make standard dyes blink by transitioning into a reversible dark state or shifting spectrum [18,26]

Figure 1

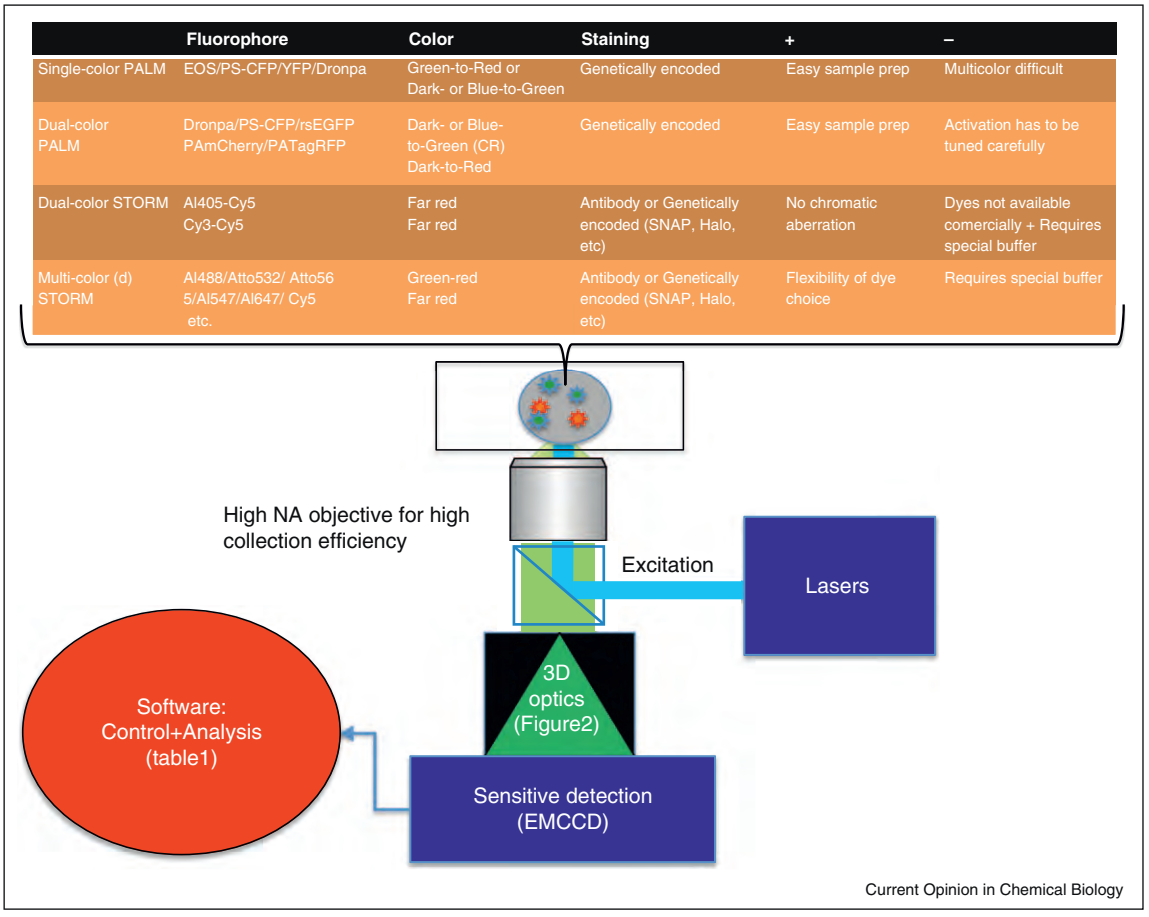

A super-resolution starter kit. SR requires a broad combination of competences; we present here several combinations of hardware, software, and sample preparation. On the hardware side, the requirements are: a sensitive and efficient detector, which implies using a high numerical aperture objective, an EMCCD camera, and ~10–100 mW lasers for excitation. A control software synchronizing the lasers with the camera can also be helpful [46,63]. For 3D imaging, several optical setups are possible and are described in Figure 2. For sample preparation, several options are presented since the requirements can be quite different depending on the application. We have noted here just a few of the most commonly used dye combinations, since there are many possibilities with new dyes being published frequently. For software, a good point-fitting algorithm is necessary, and several options are freely available, described in Table 1.

has broadened the palette of dyes compatible with SR imaging. However, a challenge remaining for these strategies is to control the transition rates between dark and bright states to meet the isolation criteria required for point localization while maintaining a high enough density of molecules to satisfy the Nyquist criteria for SR.

Technological advances

The publications introducing (F)PALM and STORM demonstrated single color 2D SR imaging either in fixed cell samples [9••], *in vitro* DNA loops [11] or on glass and sapphire surfaces [10]. This was due to significant limitations imposed by both hardware and sample preparation. On the hardware side, TIRF illumination was used to excite a 2D section, so as to increase the signal to noise ratio and eliminate signal from out-of-focus molecules. Samples were therefore limited to thin sections (suitable for correlative electron) and membranes microscopy [9••], or *in vitro* objects adhered to a coverslip [10,11]. Moreover, due to long integration times to maximize signal, acquisition times were far too long to allow imaging of living cells, a limitation that has been proven unnecessary for select applications [12,17,27]. Since then, technical developments have enabled multicolor [28••,29–31] and three-dimensional [32••,33–35] imaging and the combination of both in fixed [36,37] and more recently living cells [38]. In Figure 2, we provide a guide to the most readily implemented technologies used for 3D SR imaging. Additional technological advances enable the extraction of information about polarization [39], thick sample imaging [40,41•] and super-resolved high density single particle tracking [42••].

Figure 2

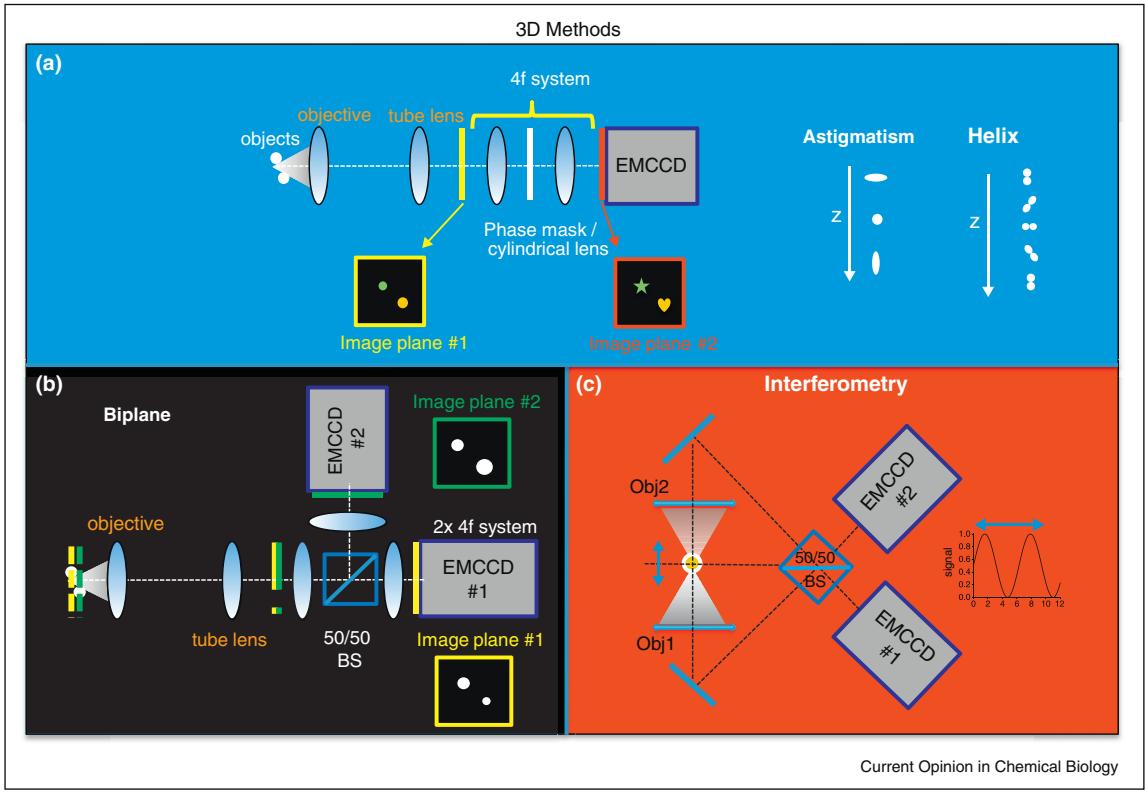

There are three main methods to extract the *z* position of a particle. **(a)** The first family of methods relies on deforming the point spread function (PSF) so that its shape depends on the z position of the particle. In Ref. [32••], astigmatism was induced by a cylindrical lens as a shaping method, which resulted in a PSF whose ellipticity depended on axial position. Different refinements of this method have been proposed using more controllable shaping methods resulting in a spiral [64] or helical [35] PSF, which aim at increasing the range over which molecules can be localized and the isotropy of the localization precision. **(b)** The second method [33] relies on simultaneously imaging two different planes, and extracting the z position from the relative form of the PSF in the two planes. **(c)** The third method, called iPALM [34] relies on interferometry: two opposing lenses are used to make single photons interfere on three different cameras, and the intensity ratio of the images provides a measure of the z-position of the particle. For simplicity, two-way interferometry is shown here. This method provides the highest resolution with the *z* localization, even exceeding the *x*–*y* localization.

Guide to dyes for multicolor imaging

One area of significant interest is multicolor imaging, which presents unique challenges. The photoswitching mechanisms of dyes available for (F)PALM and STORM necessitate a compromise between control over blinking rates and spectral overlap between the different fluorophores. That overlap can be in the switching wavelength, or in the imaging wavelength, or even in the initial fluorescent state in the case of photoconvertible proteins. For example, a green-to-red protein such as Eos is difficult to combine with another dye since it occupies most of the visible spectrum: it is activated by UV or blue light, fluoresces initially in the green, and photoconverts into a red form. A few of the most common labeling schemes are outlined in Figure 1.

The initial demonstrations of multicolor imaging relied in the case of STORM [28••] on two donor–acceptor pairs, Al405–Cy5 and Cy2–Cy5, where two different wavelengths were used sequentially for activation before bleaching both dyes with a single laser, yielding the additional advantage of removing the effects of chromatic aberration. In the case of PALM [30], a combination of irreversible green to red (tdEos) and reversible dark to green (Dronpa) proteins was used. The irreversibly switching tdEos was imaged first, and once completely bleached in both its green and red states allowed the imaging of Dronpa. However, even with the development of new red photoactivable proteins [29], which made multicolor imaging using two irreversibly switching proteins possible, issues associated with the use of different wavelengths exist, with potential unwanted activation and bleaching of fluorescent proteins yielding an effectively reduced labeling density.

A promising development for multicolor imaging is dSTORM/GSDIM [19] where common dyes based on rhodamine and cyanine are used, and blinking is obtained

Figure 3

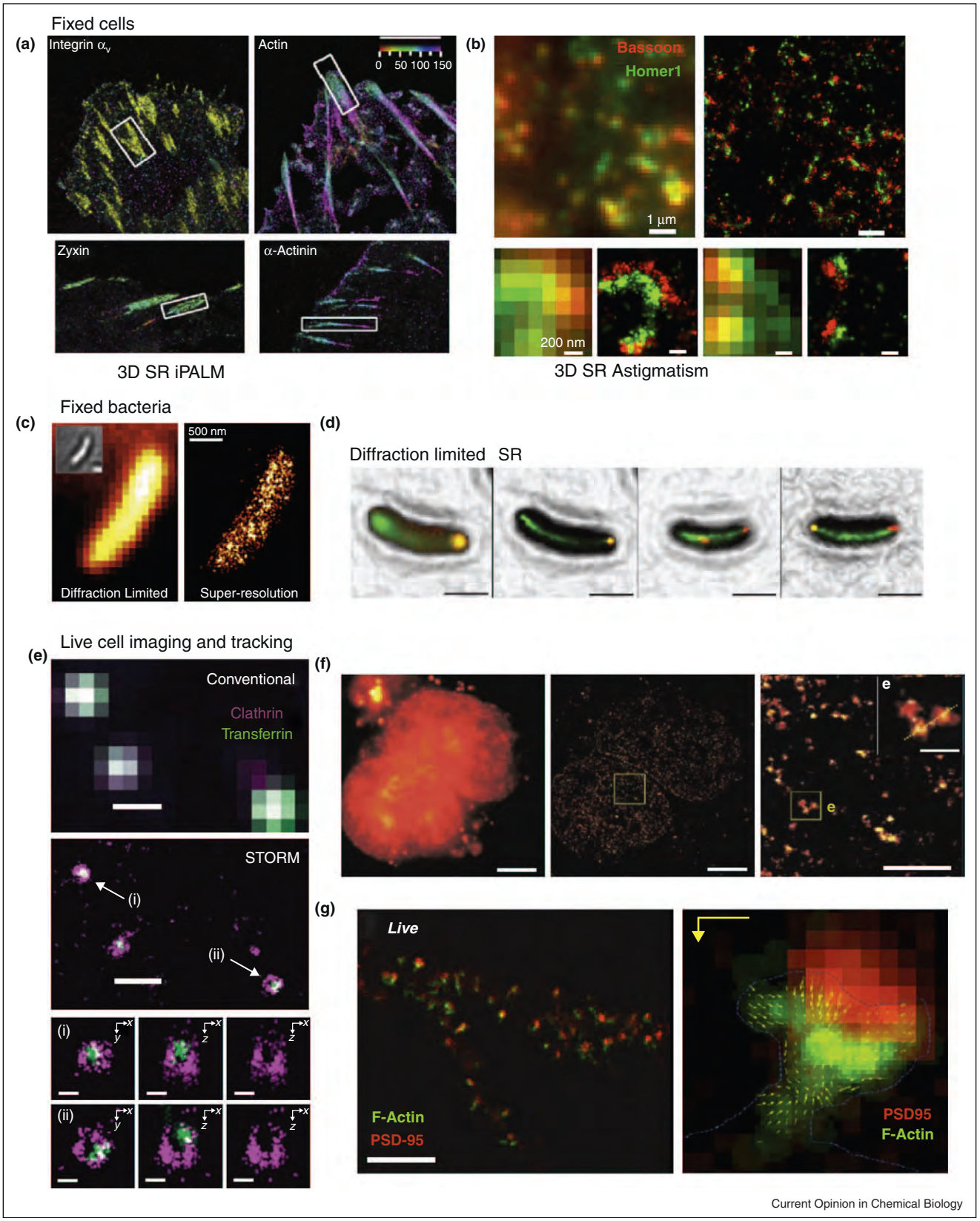
Fixed cells
(a)
Integrin α_v
Actin
0 50 100 150
Zyxin
α-Actinin
3D SR iPALM
(b)
Bassoon
Homer1
1 μm
200 nm
3D SR Astigmatism
Fixed bacteria
(c)
500 nm
Diffraction Limited
Super-resolution
(d)
Diffraction limited SR
Live cell imaging and tracking
(e)
Conventional
Clathrin
Transferrin
STORM
(i)
(ii)
(f)
e
e
(g)
Live
F-Actin
PSD-95
PSD95
F-Actin
Current Opinion in Chemical Biology

Table 1

The choice of an adapted software to convert the sparse and noisy raw data into a SR image is crucial, since it requires an efficient yet rapid way of localizing multiple peaks in each frame. We present here only open source software, since codes often have to be adapted for different dyes/applications and executable only software is therefore inconvenient or unusable.

Name	Language	Ref	Use friendly	3D	Misc
QuickPALM	(Java)	[49]	++ (ImageJ)	Astigmatism	Can be batch processed using ImageJ
PALM3D	(Python)	[41]	–	Astigmatism	3D imaging of thick samples
Rapid2STORM	(Java)	[51]	++	Astigmatism + biplane	Posttreatment + tracking
Octane	(Java)	[50]	++ (ImageJ)	2D only	Tracking

through reversible transitions into a dark state. This technique is therefore doubly multicolor friendly: not only do a large number of compatible dyes already exist (including Atto-dyes and Alexa-dyes), but since only one laser is used for both switching and excitation unwanted overlap is reduced. The downside comes from the need for 'blinking buffers', as the chemical environment has to be controlled to maintain reversible dark states, and different fluorophores often have different blinking rates in a given buffer. Moreover, even a small overlap in excitation and emission spectra can render pairs of dyes incompatible for simultaneous imaging, either through increased noise, STED-like de-excitation, or promoting different triplet state pathways leading to increased photobleaching. Nevertheless, this approach has enabled imaging with up to six different colors [21] although not simultaneously, and combined with spectral unmixing up to four dyes have been imaged simultaneously [43•]. Several reviews and articles are helpful in this quite complex field [26,44–47]. We draw your attention to [48•], where the blinking properties for a large number of dyes in several different buffers are compiled and the results are used to perform 4-color imaging.

Guide to software packages

The raw data for point-localization SR consist of a stack of images containing a few molecules in each frame. Thus, software for point localization and image reconstruction from molecular locations is indispensable. A number of open source software packages are now available [41•,49–51], so it is no longer necessary to write one's own analysis package. We present a summary of open source software that will as a minimum requirement process raw data and render SR images in Table 1. Although several freeware packages are also available, they are rife with limitations in terms of both their adaptability for new applications and their compatibility with new platform versions.

Biological applications

Most biological applications of point-localization SR use cellular systems as their subject of study. Cells are very crowded environments, with a mean spacing between proteins of ~10 nm, far below the diffraction limit. Previously, information on protein organization *in vivo* at the nanoscale could only be extracted for highly dilute proteins, or the spatial resolution for denser structures could be improved by deconvolving the obtained images, but without single molecule information. Extracting single molecule locations and dynamics with nanoscale accuracy in dense structures is now possible with point-localization SR. In this section we present select proof-of-principle measurements, but focus on examples where biologically significant information was obtained from nanoscale protein organization.

Fixed cell SR: from 2D, one color to 3D and multicolor

In fixed cells, the correlative single molecule information obtained with 2D multicolor PALM and dSTORM allowed the imaging of the nanoscale colocalization pattern of transferrin receptors and clathrin light chain (CLC) [29] and revealed heterogeneities in the distribution of kinases at the plasma membrane [52]. The high spatial resolution of 2D multicolor PALM also allowed the nanoscale structure of adhesion complexes to be resolved, revealing the relationship between different pairs of focal adhesion proteins [30]. Several pairs of these proteins that seem to colocalize in conventional images were found to form spatially distinct nanoscale structures.

(Figure 3 Legend) Biological applications of point-localization SR. **(a)** 3D iPALM image of integrin αV-tdEos, actin-mEos2, zyxin-mEos2, and α-actinin-mEos2 forming focal adhesions. The super-resolved 3D structural information obtained from these images and four other focal adhesion proteins allowed building a schematic model of focal adhesion molecular architecture [53••]. **(b)** 3D STORM imaging based on astigmatism of the presynaptic protein Bassoon and the postsynaptic protein Homer1. Proteins were labeled by immunohistochemistry using Cy3–A647 and A405–A647 conjugated antibodies, respectively. Left hand side images correspond to the diffraction limited images. The lower panels show individual synapses [54•]. **(c)** PALM imaging of the nucleoid-associated protein HU2-eYFP in fixed *C. crescentus* [58]. **(d)** Diffraction-limited and PALM images of ATPase ParA and centromere-binding protein ParB in *C. crescentus* tagged with eYFP and mCherry, respectively. A spindle-like structure involved in bacterial chromosome segregation could be resolved [57•]. **(e)** Diffraction-limited and 3D multicolor STORM image based on astigmatism of CCPs labeled with Alexa647 via a SNAP tag (magenta) and transferrin labeled directly with Alexa 568 (green) in live cells. Lower panels show the 3D view of individual CCPs [38]. **(f)** Diffraction-limited and dSTORM image of H2B labeled with ATTO655 via an eDHFR tag in living cells [25•]. **(g)** (Left side) Local density of actin-mEos2 molecules (green) with overlaid diffraction limited image of the postsynaptic density marker PSD-95-cerulean (red) in live neurons. (Right side) Local actin density and averaged molecular movement of actin within a spine as obtained by sptPALM [62••].

These results were recently extended to 3D using a composite of multiple one-color iPALM images (Figure 3a), providing the basis for a structural model of adhesion complexes at the molecular level [53••].

In neurons, 3D multicolor STORM imaging of immunostained fixed mouse neurons allowed the nanostructure of scaffolding proteins and receptors (Figure 3b) in chemical subdiffraction sized synapses to be resolved [54•]. Here, the three-dimensional super-resolved images show the postsynaptic and presynaptic protein distributions of single spines as well separated, and also resolve their correlation from side and top views. This information is the basis for creating a 3D model of synaptic protein distribution dynamics and could not have been obtained with conventional imaging.

In a cell-free membrane system, multicolor 3D STORM allowed the resolution and quantification of the subdiffraction axial elevation of clathrin-coated pits from the basal membrane before budding and fission [55].

The biological applications described here are essentially limited to thin structures near the cell surface, but the recent demonstration of confined activation for whole-cell PALM presents a promising way to resolve ultrastructure in mitochondria, the ER, or the nucleus [41•].

Imaging bacteria: small size, big challenge

Studying bacterial architecture is challenging due to their small size and high density of proteins. In this respect, SR provides a promising tool to resolve functional structures involving protein organization in bacteria. In *Escherichia coli*, PALM imaging of the chemotaxis network revealed that signaling proteins form clusters via stochastic self-assembly with no need for active transport [56•]. In *Caulobacter crescentus*, PALM imaging contributed to work that identified an unexpected chromosome partitioning apparatus similar to eukaryotic spindles [57•] (Figure 3d) and has been presented as a promising tool to study the structural organization of nucleoid-associated proteins [58] (Figure 3c). Most recently, nucleoid-associating proteins have been imaged in live bacteria using PALM [59] which identified the global transcriptional silencer H-NS as a key player in bacterial chromosomal organization.

Live-cell imaging and high density tracking: resolving dynamics

A tremendous step in the improvement of SR, toward making it more flexible for biological investigations, was its implementation in live-cell imaging. Although the acquisition time of localization-based SR techniques is still long relative to conventional wide-field imaging, it is now comparable to typical point-scanning microscopies (~10 s/frame). This has permitted the SR study of biological processes that take place on the time scale of minutes.

Live-cell dSTORM imaging enabled the study of the mobility of histone H2B proteins in the nucleus [25•] (Figure 3f), as well as the dynamic 3D colocalization of transferrin and CLC at the plasma membrane [38] (Figure 3e). In combination with the structural information obtained from fixed cells, this dynamic view may allow more light to be shed on signaling processes involving clathrin-coated pits and receptors. In neurons, live-cell PALM was used to study the long-term dynamics of the spine cytoskeleton and allowed the resolution of morphological changes in response to synaptic activity [60].

In live samples, the combination of PALM and single particle tracking (sptPALM) [42••] opened a new area of possible biological applications, by enabling the study of single molecule dynamics in highly dense structures at nanoscale resolution. This method has been demonstrated by tracking HIV Gag and VSVG proteins at the membrane [42••], and was used to study the actin dynamics in neuronal spines as well as the dynamics of prokaryotic cytoskeletal proteins [50,61,62••] (Figure 3g).

Conclusions and outlook

With point-localization SR, a wide array of imaging methods are possible, and have now been applied to address fundamental biological questions. It now remains for researchers to choose an imaging setup, fluorescent dye(s), and software to match their specific needs. This broad set of competences from molecular biology to chemistry to physics and computer science can be difficult for individual groups to achieve, but as the field of SR advances, more resources become available for users of the technology. Further innovations in multicolor and multimode imaging, probe design, and flexible, user-friendly analysis packages will result in even more widespread use of SR in the future. New fluorescent probes with better quantum yield (fluorescent proteins), better cell permeability (synthetic dyes), and optimized control for photoswitching and blinking will further open the possibilities for combining live-cell and multicolor imaging. Growth in this area will also depend on distribution and commercialization of new dyes.

An important challenge for the field is to agree upon quality and disclosure standards for dyes, software, and biological images. For fluorescent proteins, a histogram of single-molecule photon yields is already standard, and should become standard for synthetic dyes. Dyes for (d)STORM should be characterized for their photon yield during their 'on' periods, as well as their ability to recover which can be shown by plotting the number of localizations per raw image over the acquisition period, or the equivalent. An excellent example of quantitative characterization for (d)STORM is found in Ref. [48]. Better benchmarking of software, through open-source access and shared standard data sets will help to allow clear

comparisons between different analysis approaches. We have made available one biological and one synthetic data set, http://bigwww.epfl.ch/palm/, for such a purpose. Similarly, standards should be enforced for resolution as determined by localization accuracy and molecular density; this should be integrated into software to help users better understand their data quality. Specifically, it should be verified that published images contain points localized with high enough precision, and at sufficient densities (as determined by Nyquist) to match the resolutions claimed. Related to this, the number of raw images and localized molecules that go into creating each PALM image should be specified. These standards are exemplified well in Ref. [12]. Finally, the algorithms used for rendering molecules to create an image should be specified or described. The default rendering should be as similar as possible to what one would expect from a 'normal' image: the summed intensity of molecules individually considered as Gaussian point sources, whose width reflects the uncertainty in their position. Other choices for rendering should be explained and described, as would be required for altered or manipulated 'normal' images.

References and recommended reading

Papers of particular interest, published within the period of review, have been highlighted as:

- • of special interest
- •• of outstanding interest

1. Huang B, Babcock H, Zhuang X: **Breaking the diffraction barrier: super-resolution imaging of cells**. *Cell* 2010, **143**:1047-1058.

2. Fernandez-Suarez M, Ting AY: **Fluorescent probes for super-resolution imaging in living cells**. *Nat Rev Mol Cell Biol* 2008, **9**:929-943.

3. • Shroff H, White H, Betzig E: **Photoactivated localization microscopy (PALM) of adhesion complexes**. *Curr Protoc Cell Biol* 2008, **41(Suppl.)** 4.21.1–4.21.27.

Focal adhesion complexes in living cells are imaged using PALM, showing the diversity of dynamics present. This also presents a good overview of the considerations for creating SR images, based on density and motion of localized molecules.

4. Gould TJ, Verkhusha VV, Hess ST: **Imaging biological structures with fluorescence photoactivation localization microscopy**. *Nat Protoc* 2009, **4**:291-308.

5. Manley S, Gillette JM, Lippincott-Schwartz J: **Single-particle tracking photoactivated localization microscopy for mapping single-molecule dynamics**. *Methods Enzymol* 2010, **475**:109-120.

6. Airy GB: **On the diffraction of an object-glass with circular aperture**. *Trans Camb Philos Soc* 1834, **5**:283.

7. Thompson RE, Larson DR, Webb WW: **Precise nanometer localization analysis for individual fluorescent probes**. *Biophys J* 2002, **82**:2775-2783.

8. Yildiz A, Forkey JN, McKinney SA, Ha T, Goldman YE, Selvin PR: **Myosin V walks hand-over-hand: single fluorophore imaging with 1.5-nm localization**. *Science* 2003, **300**:2061-2065.

9. •• Betzig E, Patterson GH, Sougrat R, Lindwasser OW, Olenych S, Bonifacino JS, Davidson MW, Lippincott-Schwartz J, Hess HF: **Imaging intracellular fluorescent proteins at nanometer resolution**. *Science* 2006, **313**:1642-1645.

Demonstrates PALM imaging of photoswitchable fusion proteins in cells. Images are constructed of a number of diverse structures in cells, from the cytoskeleton to membrane proteins. Included correlative electron microscopy.

10. Hess ST, Girirajan TPK, Mason MD: **Ultra-high resolution imaging by fluorescence photoactivation localization microscopy**. *Biophys J* 2006, **91**:4258-4272.

11. Rust MJ, Bates M, Zhuang X: **Sub-diffraction-limit imaging by stochastic optical reconstruction microscopy (STORM)**. *Nat Methods* 2006, **3**:793-795.

12. Shroff H, Galbraith CG, Galbraith JA, Betzig E: **Live-cell photoactivated localization microscopy of nanoscale adhesion dynamics**. *Nat Methods* 2008, **5**:417-423.

13. Van Oijen AM, Koehler J, Schmidt J, Mueller M, Brakenhoff GJ: **Far-field fluorescence microscopy beyond the diffraction limit**. *J Opt Soc Am A: Opt Image Sci Vis* 1999, **16**:909-915.

14. Heilemann M, Herten DP, Heintzmann R, Cremer C, Mueller C, Tinnefeld P, Weston KD, Wolfrum J, Sauer M: **High-resolution colocalization of single dye molecules by fluorescence lifetime imaging microscopy**. *Anal Chem* 2002, **74**:3511-3517.

15. Sharonov A, Hochstrasser RM: **Wide-field subdiffraction imaging by accumulated binding of diffusing probes**. *Proc Natl Acad Sci U S A* 2006, **103**:18911-18916.

16. Patterson G, Davidson M, Manley S, Lippincott-Schwartz J: **Superresolution imaging using single-molecule localization**. *Annu Rev Phys Chem* 2010, **61**:345-367.

17. Biteen JS, Thompson MA, Tselentis NK, Bowman GR, Shapiro L, Moerner WE: **Super-resolution imaging in live *Caulobacter crescentus* cells using photoswitchable EYFP**. *Nat Methods* 2008, **5**:947-949.

18. Matsuda A, Shao L, Boulanger J, Kervrann C, Carlton PM, Kner P, Agard D, Sedat JW: **Condensed mitotic chromosome structure at nanometer resolution using PALM and EGFP-histones**. *PLoS ONE* 2010, **5**:1-12.

19. Heilemann M, Van De Linde S, Schöttpelz M, Kasper R, Seefeldt B, Mukherjee A, Tinnefeld P, Sauer M: **Subdiffraction-resolution fluorescence imaging with conventional fluorescent probes**. *Angew Chem — Int Ed* 2008, **47**:6172-6176.

20. Foelling J, Bossi M, Bock H, Medda R, Wurm CA, Hein B, Jakobs S, Eggeling C, Hell SW: **Fluorescence nanoscopy by ground-state depletion and single-molecule return**. *Nat Methods* 2008, **5**:943-945.

21. Heilemann M, Van De Linde S, Mukherjee A, Sauer M: **Super-resolution imaging with small organic fluorophores**. *Angew Chem — Int Ed* 2009, **48**:6903-6908.

22. Hinner MJ, Johnsson K: **How to obtain labeled proteins and what to do with them**. *Curr Opin Biotechnol* 2010, **21**:766-776.

23. Miller LW, Cornish VW: **Selective chemical labeling of proteins in living cells**. *Curr Opin Chem Biol* 2005, **9**:56-61.

24. Dellagiacoma C, Lukinavičius G, Bocchio N, Banala S, Geissbühler S, Märki I, Johnsson K, Lasser T: **Targeted photoswitchable probe for nanoscopy of biological structures**. *ChemBioChem* 2010, **11**:1361-1363.

25. • Wombacher R, Heidbreder M, Van De Linde S, Sheetz MP, Heilemann M, Cornish VW, Sauer M: **Live-cell super-resolution imaging with trimethoprim conjugates**. *Nat Methods* 2010, **7**:717-719.

Uses chemical tag to target organic fluorophores for dSTORM in living cells. The nuclear histone marker H2B is imaged.

26. Vogelsang J, Steinhauer C, Forthmann C, Stein IH, Person-Skegro B, Cordes T, Tinnefeld P: **Make them blink: probes for super-resolution microscopy**. *ChemPhysChem* 2010, **11**:2475-2490.

27. Hess ST, Gould TJ, Gudheti MV, Maas SA, Mills KD, Zimmerberg J: **Dynamic clustered distribution of hemagglutinin resolved at 40 nm in living cell membranes discriminates between raft theories**. *Proc Natl Acad Sci U S A* 2007, **104**:17370-17375.

28. •• Bates M, Huang B, Dempsey GT, Zhuang X: **Multicolor super-resolution imaging with photo-switchable fluorescent probes**. *Science* 2007, **317**:1749-1753.

Introduces labels for imaging up to three colors, and performs simultaneous multicolor STORM imaging of two different structures (clathrin-coated pits and microtubules) in cells.

29. Subach FV, Patterson GH, Manley S, Gillette JM, Lippincott-Schwartz J, Verkhusha VV: **Photoactivatable mCherry for high-resolution two-color fluorescence microscopy**. *Nat Methods* 2009, **6**:153-159.

30. Shroff H, Galbraith CG, Galbraith JA, White H, Gillette JM, Olenych S, Davidson MW, Betzig E: **Dual-color superresolution imaging of genetically expressed probes within individual adhesion complexes**. *Proc Natl Acad Sci U S A* 2007, **104**:20308-20313.

31. Bock H, Geisler C, Wurm CA, Von Middendorff C, Jakobs S, Schoenle A, Egner A, Hell SW, Eggeling C: **Two-color far-field fluorescence nanoscopy based on photoswitchable emitters**. *Appl Phys B* 2007, **88**:161-165.

32. •• Huang B, Wang W, Bates M, Zhuang X: **Three-dimensional super-resolution imaging by stochastic optical reconstruction microscopy**. *Science* 2008, **319**:810-813.
Demonstrates three-dimensional STORM of structures in cells (clathrin-coated pits and microtubules) using optical astigmatism to encode axial position.

33. Juette MF, Gould TJ, Lessard MD, Mlodzianoski MJ, Nagpure BS, Bennett BT, Hess ST, Bewersdorf J: **Three-dimensional sub-100 nm resolution fluorescence microscopy of thick samples**. *Nat Methods* 2008, **5**:527-529.

34. Shtengel G, Galbraith JA, Galbraith CG, Lippincott-Schwartz J, Gillette JM, Manley S, Sougrat R, Waterman CM, Kanchanawong P, Davidson MW *et al.*: **Interferometric fluorescent super-resolution microscopy resolves 3D cellular ultrastructure**. *Proc Natl Acad Sci U S A* 2009, **106**:3125-3130.

35. Pavani SRP, Thompson MA, Biteen JS, Lord SJ, Liu N, Twieg RJ, Piestun R, Moerner WE: **Three-dimensional, single-molecule fluorescence imaging beyond the diffraction limit by using a double-helix point spread function**. *Proc Natl Acad Sci U S A* 2009, **106**:2995-2999.

36. Huang B, Jones SA, Brandenburg B, Zhuang X: **Whole-cell 3D STORM reveals interactions between cellular structures with nanometer-scale resolution**. *Nat Methods* 2008, **5**:1047-1052.

37. Aquino D, Schonle A, Geisler C, Middendorff Cv, Wurm CA, Okamura Y, Lang T, Hell SW, Egner A: **Two-color nanoscopy of three-dimensional volumes by 4Pi detection of stochastically switched fluorophores**. *Nat Methods* 2011, **8**:353-359.

38. Jones SA, Shim SH, He J, Zhuang X: **Fast, three-dimensional super-resolution imaging of live cells**. *Nat Methods* 2011, **8**:499-505.

39. Gould TJ, Gunewardene MS, Gudheti MV, Verkhusha VV, Yin S-R, Gosse JA, Hess ST: **Nanoscale imaging of molecular positions and anisotropies**. *Nat Methods* 2008, **5**:1027-1030.

40. Vaziri A, Tang J, Shroff H, Shank CV: **Multilayer three-dimensional super resolution imaging of thick biological samples**. *Proc Natl Acad Sci U S A* 2008, **105**:20221-20226.

41. • York AG, Ghitani A, Vaziri A, Davidson MW, Shroff H: **Confined activation and subdiffractive localization enables whole-cell PALM with genetically expressed probes**. *Nat Methods* 2011, **8**:327-333.
Combines nonlinear activation and astigmatic detection to provide a way to make 3D super-resolved images of thick samples. Software is included.

42. •• Manley S, Gillette JM, Patterson GH, Shroff H, Hess HF, Betzig E, Lippincott-Schwartz J: **High-density mapping of single-molecule trajectories with photoactivated localization microscopy**. *Nat Methods* 2008, **5**:155-157.
A new method combines single molecule tracking with PALM to create high-density maps of protein motions in living cells. Membrane and membrane-binding proteins in living cells are imaged and tracked, and analyzed for their diffusive properties.

43. • Testa I, Wurm CA, Medda R, Rothermel E, Von Middendorf C, Foelling J, Jakobs S, Schoenle A, Hell SW, Eggeling C: **Multicolor fluorescence nanoscopy in fixed and living cells by exciting conventional fluorophores with a single wavelength**. *Biophys J* 2011, **99**:2686-2694.
Combines dSTORM of common dyes and proteins with spectral unmixing to demonstrate up to 4-color simultaneous imaging.

44. Dempsey GT, Bates M, Kowtoniuk WE, Liu DR, Tsien RY, Zhuang X: **Photoswitching mechanism of cyanine dyes**. *J Am Chem Soc* 2009, **131**:18192-18193.

45. Van De Linde S, Krstic I, Prisner T, Doose S, Heilemann M, Sauer M: **Photoinduced formation of reversible dye radicals and their impact on super-resolution imaging**. *Photochem Photobiol Sci* 2011, **10**:499-506.

46. Henriques R, Griffiths C, Rego EH, Mhlanga MM: **PALM and STORM: unlocking live-cell super-resolution**. *Biopolymers* 2011, **95**:322-331.

47. Rasnik I, McKinney SA, Ha T: **Nonblinking and long-lasting single-molecule fluorescence imaging**. *Nat Methods* 2006, **3**:891-893.

48. • Dempsey GT, Vaughan JC, Chen KH, Zhuang X: **Evaluation of fluorophores for optimal performance in localization based super-resolution imaging**. *Nat Methods*, 2011, advance online publication 10.1038/nmeth.1768.
The authors evaluate the blinking characteristics of 26 different dyes with spectra ranging from green to IR in 4 buffer conditions, and identify a combination of dyes and buffers that can be used for 4-color imaging.

49. Henriques R, Lelek M, Fornasiero EF, Valtorta F, Zimmer C, Mhlanga MM: **QuickPALM: 3D real-time photoactivation nanoscopy image processing in ImageJ**. *Nat Methods* 2010, **7**:339-340.

50. Niu L, Yu J: **Investigating intracellular dynamics of FtsZ cytoskeleton with photoactivation single-molecule tracking**. *Biophys J* 2008, **95**:2009-2016.

51. Wolter S, Schuettpelz M, Tscherepanow M, Van De Linde S, Heilemann M, Sauer M: **Real-time computation of subdiffraction-resolution fluorescence images**. *J Microsc* 2010, **237**:12-22.

52. Owen DM, Rentero C, Rossy J, Magenau A, Williamson D, Rodriguez M, Gaus K: **PALM imaging and cluster analysis of protein heterogeneity at the cell surface**. *J Biophotonics* 2010, **3**:446-454.

53. •• Kanchanawong P, Shtengel G, Pasapera AM, Ramko EB, Davidson MW, Hess HF, Waterman CM: **Nanoscale architecture of integrin-based cell adhesions**. *Nature* 2010, **468**:580-584.
The authors use iPALM to resolve the 3D nanoscale structure of focal adhesions in fixed cells. The 3D localizations of 9 different focal adhesion forming proteins are used to propose a model of the molecular structure.

54. • Dani A, Huang B, Bergan J, Dulac C, Zhuang X: **Superresolution imaging of chemical synapses in the brain**. *Neuron* 2010, **68**:843-856.
This publication presents the first application of multicolor 3D STORM to study the molecular architecture of synapses. The authors analyze the nanoscale distribution of scaffolding proteins and receptors.

55. Wu M, Huang B, Graham M, Raimondi A, Heuser JE, Zhuang X, De Camilli P: **Coupling between clathrin-dependent endocytic budding and F-BAR-dependent tubulation in a cell-free system**. *Nat Cell Biol* 2010, **12**:902-908.

56. • Greenfield D, McEvoy AL, Shroff H, Crooks GE, Wingreen NS, Betzig E, Liphardt J: **Self-organization of the *Escherichia coli* chemotaxis network imaged with super-resolution light microscopy**. *PLoS Biol* 2009, **7**: Article number e1000137.
The authors use PALM to resolve the spatial distribution of central bacterial chemotaxis proteins in *E. coli* and show that the observed pattern can be explained by stochastic self-assembly.

57. • Ptacin JL, Lee SF, Garner EC, Toro E, Eckart M, Comolli LR, Moerner WE, Shapiro L: **A spindle-like apparatus guides bacterial chromosome segregation**. *Nat Cell Biol* 2010, **12**:791-798.
Using PALM, the authors could identify and resolve the structure of a partitioning apparatus for chromosomes in *Caulobacter crescentus*.

58. Lee SF, Thompson MA, Schwartz MA, Shapiro L, Moerner WE: **Super-resolution imaging of the nucleoid-associated protein HU in *Caulobacter crescentus***. *Biophys J* 2011, **100**:L31-L33.

59. Wang W, Li GW, Chen C, Xie XS, Zhuang X: **Chromosome organization by a nucleoid-associated protein in live bacteria**. *Science* 2011, **333**:1445-1449.

60. Izeddin I, Specht CG, Lelek M, Darzacq X, Triller A, Zimmer C, Dahan M: **Super-resolution dynamic imaging of dendritic spines using a low-affinity photoconvertible actin probe**. *PLoS ONE* 2011, **6**: Article number e15611.

61. Tatavarty V, Kim EJ, Rodionov V, Yu J: **Investigating sub-spine actin dynamics in rat hippocampal neurons with super-resolution optical imaging**. *PLoS ONE* 2009, **4**: Article number e7724.

62. •• Frost NA, Shroff H, Kong H, Betzig E, Blanpied TA: **Single-molecule discrimination of discrete perisynaptic and distributed sites of actin filament assembly within dendritic spines**. *Neuron* 2010, **67**:86-99.

Actin-tdEos is tracked within dendritic spines, extracting velocities and filament polymerization rates in different spine compartments, identified by multicolor imaging. The authors show that actin dynamics are highly heterogenous within the spine.

63. Edelstein A, Amodaj N, Hoover K, Vale R, Stuurman N: **Computer control of microscopes using manager**. *Curr Protoc Mol Biol* 2011, **92(Suppl.)** 14.20.1–14.20.17.

64. Lew MD, Lee SF, Badieirostami M, Moerner WE: **Corkscrew point spread function for far-field three-dimensional nanoscale localization of pointlike objects**. *Opt Lett* 2011, **36**:202-204.

Fluorescence fluctuation spectroscopy techniques to monitor membrane-associated systems

Instructor: Mark Hink

***Goal*:**
In this practical various FFS approaches to quantify protein or lipid dynamics in or near the membrane will be demonstrated, using point-FCS, FCCS & N&B analysis. Using different biological systems we will discuss practical issues, challenges and limitations.

***Introduction*:**
Fluorescence Fluctuation Spectroscopy (FFS) is a family of techniques that analyses the (spatio-) temporal fluctuations of the detected fluorescence and links these to physical parameters. It was developed as a correlation technique (FCS) in the early nineteen seventies to monitor chemical kinetics and motional properties of fluorescent molecules. Since the development of sensitive detection devices and the introduction of the confocal microscope, in late nineteen eighties, there has been a large increase in the number of FCS-applications.

Also the number of techniques increased over the years with applications for multiple colors (FCCS), brightness analysis (PCH, FIDA) or fluctuation analysis of whole images (ICS, STICS, RICS, N&B). In addition, fluctuation analysis could be combined with other parameters like fluorescence lifetime or polarization.

The confocal microscope used in FFS does not only improve the signal-to-noise ratio compared to wide-field detection, but could also be used to perform *in vivo* measurements at selected sub-cellular locations (f.e. at the membrane, in the nucleus etc.). These measurements, performed in a non-invasive manner, can provide a wealth of information about protein concentrations, diffusion rates, their aggregation state, their interaction with other cellular moieties or the intracellular environment. Problems, which may arise, are high background intensity (auto-fluorescence), the reduction in detected intensity due to scattering and dye-depletion due to photo-bleaching. Therefore a proper selection of cell-type, dye, excitation wavelength and intensity is required.

Practical:
FCS is a powerful technique to measure f.e. the concentration and diffusion rate of a molecule. This can give information how mobile molecules in the cell are and if they are reduced in their movement, due to f.e. their size or interaction with other molecules.

Perform a FCS-experiment measuring a small fluorescent dye, Alexa488, in buffer.

Q1. Estimate from the FCS-curve the diffusion time and the concentration of the dye if the confocal detection volume is 0.4 femtoliter in size. Check your estimations by fitting the curve to a standard triplet-state model.

Q2. What happens to the amplitude and shape of the FCS-curve if the Alexa488 sample is diluted 4 times? Perform this measurement.

Q3. What kind of FCS-curve would you expect if purified eGFP is measured in buffer? Perform this experiment.

As outlined above one could use FCS to measure molecules in living cells as well. However not all transfected cells are suitable for FFS measurements, like the ones having a high expression level.

Q4. Why are these high expressing cells not suitable, since the cell will have a very high fluorescence-to-noise-ratio, almost ideal for fluorescence imaging?

Q5. Measure and fit the curve of the HeLa cells expressing EGFR-eGFP. What will happen to the curve if all measured EGFR-eGFP would be monomeric and start to dimerize?

Interactions between molecules could be measured by using two different color tags.

Q6. Setup the microscope filters for detecting two cytoplasmic signalling proteins p85-sGFP2 and p110-mCherry and perform the measurement.

Q7. What kind of controls do we need to include if we want to get quantitative binding information from this measurement (f.e. we want to estimate the p85-p110 dissociation constant *in vivo*)?

Q8. Measure and fit the curve of the cytoplasmic annexin A-IV-sGFP2 fusion protein (60 kDa) in HeLa cells. Why is the diffusion time almost the same to the value of free eGFP, since this fusion protein is almost twice the size of free eGFP?

Q9. Stimulate the cells with ionomycin (increases intracellular calcium levels), wait for a few minutes and try to measure the diffusion of the membrane-bound protein. What is your conclusion about this experiment?

Q10. Repeat the two measurements (7 & 8) but now using the number and brightness approach (N&B) and give an estimate of the oligomerisation state of annexin A-IV-sGFP2 relative to the given brightness of the free sGFP2 before and after stimulation.

References:

Schwille, P. and E. Haustein. Fluorescence Correlation Spectroscopy: An introduction to its concepts and applications, link

Bacia, K and P. Schwille. A dynamic view of cellular processes by in vivo fluorescence auto- and cross-correlation spectroscopy. *Methods* 29, 74 (2003).

Maeder et al. Spatial regulation of Fus3 MAP kinase activity through a reaction-diffusion mechanism in yeast pheromone signalling Nat. Cell Biol. 9, 1319 (2007).

Practical notes:

FLIM: Fluorescence lifetime imaging microscopy

Instructors: Joachim Goedhart, Marcel Raspe & Dorus Gadella

Goal:
In this practical you will learn about fluorescence lifetime imaging. Both technical and practical aspects will be highlighted. The use of FLIM will be illustrated by experiments on single living cells

Introduction:
Fluorescence lifetime imaging microscopy measures the excited state lifetime of fluorophores. Since it is an imaging technique, the image will show of a spatial distribution of fluorescence lifetimes. The lifetime is usually very short, i.e. in the nanosecond time-range (excited state lifetimes of GFP and its variants are between 1-4 ns), which requires dedicated equipment. One of its key advantages is that the lifetime is a kinetic parameter and hence, it is independent of intensity, cell-thickness and local concentration of fluorophores.
A primary application is its use for measuring FRET. Since the lifetime of a donor depends directly on proximity of FRET acceptors, FLIM is a robust way of determining FRET

Practical:
During the hands-on session, the components of the FLIM will be explained and a variety of samples will be measured. We will measure CFP lifetimes, and use CFP variants with different lifetimes to show lifetime-based contrast within cells.
If time allows, FLIM will be used to measure FRET in a fusion protein, a FRET-based biosensors for cAMP and a rapamycin-based translocation system.

References:

Goedhart, J., von Steten, D., Noirclerc-Savoye, M., Lelimousin, M., Joosen, L., Hink, M.A., van Weeren, L., Gadella, T.W., Jr., Royant, A. (2012) Structure-guided evolution of cyan fluorescent proteins towards a quantum yield of 93%. Nat. Communications 3, 751.

Klarenbeek, J.B., Goedhart, J., Hink, M.A., Gadella, T.W.J. & Jalink, K. (2011). A mTurquoise-based cAMP sensor for both FLIM and ratiometric read-out has improved dynamic range. PLoS One, 6(4), e19170.

T.W.J. Gadella (Ed.), FRET and FLIM Techniques (2009). Laboratory techniques in biochemistry and molecular biology 33, Elsevier Science, Amsterdam.

Practical notes:

Detecting FRET by measuring Sensitized Emission intensity: Ratio-FRET and FilterFRET

Instructor: Kees Jalink

Goal:

In this practical, students will use the fluorescence microscope to dynamically follow FRET changes by recording Donor- and Acceptor emission intensities. We will study the dynamics of signal transduction events semi-quantitatively with high temporal resolution by ratio-FRET and quantitatively by applying the "filterFRET" approach on sets of intensity images obtained with the confocal microscope.

Introduction:

Förster Resonance Energy Transfer (FRET) may be detected in various ways. One of the most intuitive, convenient and sensitive ways is to detect the acceptor emission upon excitation of the donor moiety. This so-called 'sensitized emission' (SE) can be readily detected by simple fluorescence microscopy using a proper combination of excitation- and detection filters. However, it is obvious that quantitative FRET levels (or, often more relevant to the biologist, the fraction of molecules that interact) cannot be deduced unambiguously from sensitized emission images alone (for example, equal amounts of sensitized emission may be expected from *n* molecules that FRET for 20% and from 2*n* molecules that FRET for 10%). In this pratical, we will explore what controls and measurements are necessary to extract meaningfull biological data from intensity-based FRET recordings. We will see that on some occasions, it suffices to simply record the ratio of donor- to sensitized emission to draw powerful conclusions on the dynamic behaviour of second messengers in living cells, whereas on other occasions a more complete set of measurements and corrections (filterFRET) must be carried out to be able to interpret the data.

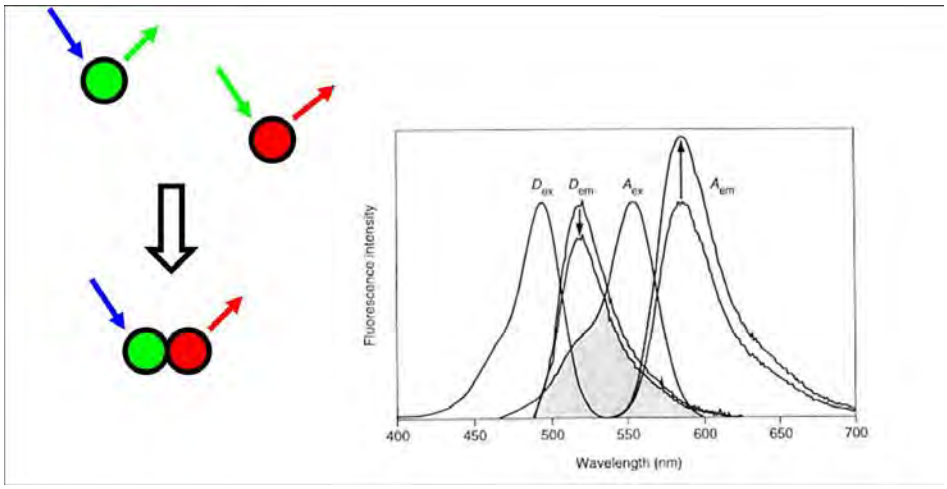

Sensitized emission: FRET increases acceptor emission
SE is the amount of acceptor emission gained from FRET (0 - ∞), while FRET efficiency is the fraction of excited donors that loose their energy through energy transfer (0-1).

We will set up the confocal microscope to do a time-lapse series of images from cells coexpressing CFP-PH(PLCδ_1) + YFP-PH(PLCδ_1), our PIP_2 FRET sensor (van der Wal et al, 2000). We will study spatial distribution of PIP_2 along the membrane, and agonist-induced changes therein, and explore the controls necessary to make those recordings quantitative. Time permitting, we will also demonstrate sub-second time-resolved PIP_2 recording using a dual-photometer system.

Practical:

Mount a coverslip with living cells in a suitable culture medium on the microscope and set up conditions for imaging CFP and sensitized emission.
Q1. What are the requirements for the microscopy medium?
Q2. Based on the spectra of CFP and YFP, what are the excitation- and emission filter settings you choose for recording the ratio?
Q3. If you want to detect fluorescence from these cells for >30 min, how would you set laser power and image quality?
Q4. The FRET sensor is expected to yield a *drop* in FRET when PIP_2 is broken down. What does this mean for your PMT settings?
Q5. What is the expected time course of the response? How often will you image? Explain what trade-off you made.

Start the time-lapse and record a baseline for a few minutes. Set up the software to quantify the ratio on-the-fly. Then, add agonist from a concentrated stock solution, making sure you stirr the solution well without hitting (displacing) the preparation. After a while, calibrate the recording by adding ionomycin + extra Ca2+ (5 mM) sequentially from the stock solutions.
Q6. Why is this calibration necessary?

Time permitting, repeat the experiment with fresh cells and a different agonist / different settings. Save all your recordings and the quantitation data on memory stick.

B. Now, we will determine sensitized emission quantitatively by 'filterFRET'. We will use cells expressing the PIP_2 FRET sensor pair CFP-PH + YFP-PH, co-expressed in the same cells. For calibration, we also need cells with either cytosolic CFP or nuclear YFP alone. A preparation with a mixture of these cell types in a single well has been made.

Mount the coverslip on the microscope. Hunt for a nice (group of) FRET cells that are accompanied in the same image field by at least one CFP and one YFP reference cell. Focus and zoom in as needed to reveal as much cellular detail as possible. Acquire 3 images: **D** (donor excitation, donor emission channel), **S** (acceptor emission when excited at donor), and **A** (acceptor excitation, acceptor detection channel).
Q7. What is bleedthrough? What determines the magnitude of bleedthrough?
Identify clear parts with leakthrough in the image. Is leakthrough also present in the FRET cells?
Q8. What is cross-excitation? What factors determine its magnitude? Identify clear parts with cross-excitation in the image. Is cross-excitation also present in the FRET cells?

THEORY

From the lecture, you remember that:

We have composite images ***D***, ***S*** and ***A*** that consist of unknown components *donor*, *acceptor* and *SE as:*

$$\boldsymbol{D} = (donor - SE) + \alpha.\ acceptor + \delta.\ SE \qquad (1)$$

$$\boldsymbol{S} = SE + \beta.\ (donor - SE) + \gamma.\ acceptor \qquad (2)$$

$$\boldsymbol{A} = acceptor \qquad (3)$$

here, β is the leakthrough coefficient and γ is the cross-excitation coefficient. α and δ are minor components of acceptor signal that may be detectable in the donor channel when there is much more A or S signal than D.

Further, we can extract the real distribution of sensitized emission *SE*.by combining (1) and (3):

$$(donor\text{-}SE) = \boldsymbol{D} - \alpha.\boldsymbol{A} - \delta.\ SE \qquad (4)$$

rearrange (2), using (3):

$$SE = \boldsymbol{S} - \beta.\ (donor - SE) - \gamma.\ \boldsymbol{A} \qquad (5)$$

substitute (4) in (5):

$$SE = \boldsymbol{S} - \beta.\ (\boldsymbol{D} - \alpha.\boldsymbol{A} - \delta.\ SE\ ) - \gamma.\ \boldsymbol{A} \qquad (6)$$

which rearranges to

$$SE = (\boldsymbol{S} - \beta\boldsymbol{D} - (\gamma - \alpha\beta)\boldsymbol{A}) / (1 - \beta\delta) \qquad (7)$$

Q9. α and δ are often very small. From the shape of the CFP- and YFP emission and excitation spectra, explain why that is.

Let's therefore ignore the small contributions of.α and δ

Q10. How does that change (7)? Explain in your own words what this new equation means.

Q11. How can we determine β from the image set? Draw suitable ROIs in the images to measure the necessary intensities and calculate β. What is de minimum value β could ever take? What the maximum?

Q12. How can we determine γ from the image set? Draw suitable ROIs in the images to measure the necessary intensities and calculate γ. What is de minimum value γ could ever take? What the maximum?

Q13. Using the confocal software or ImageJ, calculate SE according to the equation you derived in Q10. NOTE: make sure floating point arithmatic is used or bias will be introduced in the results. Discuss with your practicum leader why!

This concludes the simplified procedure to determine SE. Note that the obtained image quantifies the amount of energy transfer (SE) per pixel, and ***not*** FRET efficiency.

Q14. Can you think of situations where part of a cell shows *more* SE but *less* FRET efficiency? Can you think of a remedy for that? Apply that to your SE image.

Time permitting: full correction including calculation of α and δ is not in the scope of this practical, but you may try it if you feel brave.

Practical notes:

FRAP, fluorescent pulse-chase experiments and photo-oxidation in membranes

Instructors: Eric Reits, Henk van Veen & Joachim Goedhart

Goal:
In this practical you will learn about various FRAP approaches to visualize protein dynamics in the membrane, use FlAsH/ReAsH to study membrane dynamics and correlate confocal images to electron microscopy, hands-on.

Introduction:
The development of fluorophores like GFP allowed researchers to study the intracellular distribution of proteins in living cells instead of using fixed cells for immuno-histochemistry. In addition, protocols like photo-bleaching can be used to study the dynamics of membrane-localized proteins in time. Hands-on training in various photo-bleaching related techniques will be performed to visualise these dynamics, using FRAP to measure diffusion speed and FLIP to detect exchange of proteins between different membrane regions.

Genetically encoded reporters derived from fluorescent proteins (FPs) have proved to be extremely useful for localization and interaction studies in living cells. However, the large size and spectral properties of FP impose certain limitations for their use. The recently developed Fluorescein Arsenical Hairpin (FlAsH/tetracysteine) binder technology emerged as a promising alternative to FP for protein labeling and cellular localization studies. The combination of a small genetically encoded peptide tag with a small molecule detection reagent makes this technology particularly suitable for the investigation of biochemical changes in living cells that are difficult to approach with fluorescent proteins as molecular tags. We will demonstrate the usage of these and other techniques, mostly by hands-on, and also show how labeled cells can be processed for correlative electron microscopy to relate fluorescent distribution to high-magnification EM.

Practical (roughly):

- examples of FRAP and FLIP experiments using GFP-tagged membrane molecules
- labeling of cells expressing different tetracysteine-tagged proteins with ReAsH
- presentation on FlAsH/tetracysteine and correlative EM
- labeling of same cells with FlAsH (pulse-chase experiment)
  or fixation of cells followed by fluorescence imaging and photo-oxidation

Protocol:

I. FlAsH/ReAsH labeling

- Pre-incubate 10 min. 1 mM ReAsH in 100 mM EDT in DMSO
- Wash cells with OptiMEM/PBS
- Add 1 mL label (1 µM ReAsH in 100 µM EDT in OptiMEM)
- 45 min @ 37^{o} , protect from light
- Wash 30 min with 1-5 mM EDT in OptiMEM with 10% FCS, replace 5x
- Wash 1 à 2x with complete medium
- Add complete medium

reagents

Stock FlAsH: 2.5 mM in DMSO

Stock ReAsH: 2.5 mM in DMSO (0.00234 gr into 1.716 mL DMSO)

EDT: 1,2-Ethanedithiol (MW = 94.20; density = 1.123 g/mL -> 11.92 M)

BAL: 2,3-Dimercapto-1-propanol (MW=124.22; density= 1.24 g/cm^3 ->10M)

II. Photoconversion of ReAsH-stained cells

Staining:

Wash 3x DMEM 0/0

Standard 1.0 uM ReAsH Batch 4 / 10 uM EDT 1hr in DMEM 0/0

Wash 3x 10' with 0.25 mM BAL (1:40 DMSO -1:1000) in DMEM 10/0

Everything cold - EM

- Fix in 2% glutaraldehyde (RT 5'); 15' on ice
- Wash 5x in cacodylate buffer; Block for 30' on ice; Wash 1x in blocking buffer
- Stage at 4'C, install oxygen tent, find target area, make picture
- Add DAB solution to plate, Illuminate target area, Go to next area

- Wash 5x in cacodylate buffer, Fix in osmium tetroxide (30' ice); Wash 3x 1' H2O
- O/n in filtered 2% UA in H2O (4'C).
- 2x H_2O, dehydrate: 20-50-70-90-100-100% cold EtOH
- Durcupan: A:B:C:D=10:10:0.3:0.1 g
- Plastic T-beker, Mix, transfer to vial, remaining add equal part EtOH, Mix, add to dish, 30', pour out,
- add 1/3 of the vial, 1hr, remove with Pasteur (back),
- add new resin, 1hr, scrape out
- add new resin, 48 hrs oven.

Fix (2% Glutaraldehyde in 0.1 M Cacodylate buffer pH7.4)			**12 ml**
7	3.5	ml H2O	
4	2.0	ml 0.3 M cacodylate stock pH7.4	
1	0.5	ml fresh 25% glutaaraldehyde	

Wash 0.1 M Cacodylate pH7.4		**60 ml**
40	ml H20	
20	ml 0.3 M cacodylate stock pH7.4	

Block (50 mM Glycine and 5 mM KCN in cacodylate buffer)		**60 ml**
30.6	ml H20	
20	ml 0.3 M cacodylate stock pH 7.4	
6	ml 0.5 M Glycine	
0.6	ml 0.5 M KCN	
2.4	ml 0.5 M aminotrizole (20 mM final)	
0.2	ml 0.3% H2O2 (1:100 diluted stock)	

Reaction (6 mM DAB)			**20 ml**
18	9	ml block buffer	
2	1	ml DAB filtered into block buffer	

Fix 1% osmium tetra-oxide			**10 ml**
4.2	1.7	ml H2O	
3.3	1.3	ml 0.3 M cacodylate stock	
2.5	1.0	ml 4% osmium tetra-oxide	

Practical notes:

Section 4: Course contacts

Lecturers:

Tamas Balla
Section Molecular & Signal Transduction
National Institute of Cell Health & Human Development
49 Convent Dr Room 5A52, MSC 4510
Bethesda Md 20892-4510
U.S.A.
Tel: 01-435-5637
E-mail: ballat@mail.nih.gov

Carsten Schultz
EMBL Heidelberg
Meyerhofstraße 1
69117 Heidelberg
Germany
Tel: +49-6221-387 8210
E-mail: Schultz@embl.de

Ulrike Engel
Bioquant / Institute of Zoology
University of Heidelberg
D-69120 Heidelberg
Germany
Tel: +49-6221-54 5652
E-mail: ulrike.engel@bioquant.uni-heidelberg.de

Dorus Gadella Jr.
van Leeuwenhoek Centre Adv. Microscopy
Molecular Cytology, Swammerdam Institute for Life Sciences
University of Amsterdam
Science Park 904
1098 XH Amsterdam
The Netherlands
Tel: +31-20-525 6259
Email: Th.W.J.Gadella@uva.nl

Mark Hink
van Leeuwenhoek Centre Adv. Microscopy
Molecular Cytology, Swammerdam Institute for Life Sciences
University of Amsterdam
Sciencepark 904
1098 XH Amsterdam
Tel: +31-20-525 6211
E-mail: M.A.Hink@uva.nl

Adriaan Houtsmuller
Microscopy and Image Analysis Unit
Josephine Nefkens Institute
Dept. Pathology
Erasmus University Rotterdam
3000 DR Rotterdam
The Netherlands
Tel: +31-10-4088456
Email: a.houtsmuller@erasmusmc.nl

Kees Jalink
van Leeuwenhoek Centre Adv. Microscopy
Cellular Biophysics, Dept. Cell Biology
The Netherlands Cancer Institute
Plesmanlaan 121
1066 CX Amsterdam
The Netherlands
Tel: +31-20-512 6242
E-mail: K.Jalink@nki.nl

Erik Manders
van Leeuwenhoek Centre Adv. Microscopy
Molecular Cytology, Swammerdam Institute for Life Sciences
University of Amsterdam
Sciencepark 904
1098 XH Amsterdam
Tel: +31-20-525 6225
E-mail: Manders@uva.nl

Eric Reits
van Leeuwenhoek Centre Adv. Microscopy
Dept. Cell Biology and Histology
Academic Medical Center, University of Amsterdam
Meibergdreef 15
1105 AZ Amsterdam
The Netherlands
Tel: +31+20-566 6259
Email: E.A.Reits@amc.uva.nl

Thomas Schmidt
Physics of Life Processes
Leiden Institute of Physics
Leiden University
Niels Bohrweg 2
2333 CA Leiden
The Netherlands
Tel: +31-71-527 5982
E-mail: Schmidt@physics.leidenuniv.nl

Vladislav Verkhusha
Dept. Anatomy and Structural Biology
Albert Einstein College of Medicine
1300 Morris Park Avenue
Bronx, NY 10461
U.S.A.
Tel: 718.430.8591
E-mail: Vladislav.Verkhusha@einstein.yu.edu

Paul Wiseman
McGill University
Ernest Rutherford Physics Building
Department of Physics
3600 University St.
Montreal, PQ H3A 2T8
Canada
Tel: 514-398-6524
E-mail: Paul.Wiseman@mcgill.ca

Instructors:

Ronald Breedijk
Van Leeuwenhoek Centre Adv. Microscopy
Molecular Cytology, Swammerdam Institute for Life Sciences
University of Amsterdam
Science Park 904
1098 XH Amsterdam
The Netherlands
Tel: +31-20-525 7860
E-mail: R.M.P.Breedijk@uva.nl

Kevin Crosby
Molecular Cytology, Swammerdam Institute for Life Sciences
University of Amsterdam
Science Park 904
1098 XH Amsterdam
The Netherlands
Tel: +31-20-525 8366
E-mail: K.C.Crosby@uva.nl

Joachim Goedhart
Molecular Cytology, Swammerdam Institute for Life Sciences
University of Amsterdam
Science Park 904
1098 XH Amsterdam
The Netherlands
Tel: +31-20-525 7774
E-mail: J.Goedhart@uva.nl

Marcel Raspe
Cellular Biophysics, Dept. Cell Biology
The Netherlands Cancer Institute
Plesmanlaan 121
1066 CX Amsterdam
The Netherlands
Tel: +31-20-512 1931
E-mail: M.Raspe@nki.nl

Henk van Veen
Dept. Cell Biology and Histology
Academic Medical Center, University of Amsterdam
Meibergdreef 15
1105 AZ Amsterdam
The Netherlands
Tel: +31+20-566 4703
Email: H.A.vanVeen@amc.uva.nl

Participants:

Name	**Valentina Bettio**
Address	Translational medicine University of Piemonte Orientale "Amedeo Avogadro" via Solaroli n°17 28100, Novara, Italy
Email	Valentina.Bettio@med.unipmn.it
ESF-researcher	-
Research interest	I've been studying the role of Diacylglycerol kinase alpha (Dgka) in different biological pathways. Dgka is an enzyme that phosphorylates diacylglycerol (DAG), with formation of phosphatidic acid (PA), acting as regulator of DAG- and PA-mediated signalling. In particular, I've been studying the role of the lipid kinase in MDCK epithelial cells during cell migration and polarization, analyzing its role in ruffle formation, Golgi polarization in wound healing assays (2D system) and cyst organization (3D system), which is my major interest. When cultured in 3D extracellular matrix, epithelial cells organize in spherical, polarized, hollowed cysts, mirroring the polarized organization they feature in vivo. I demonstrated that Dgka is necessary for the formation of a single central lumen in MDCK cyst by regulating vesicular trafficking on one side and, on the other hand, by controlling the mitotic spindle orientation during cell mitosis. Furthermore, I started working with MDA MB-231 breast cancer cell line, studying the role of Dgka in migration, adhesion and integrin-mediated spreading of this cells.

Name	**Jenny Brinkmann**
Address	MESA+, Molecular Nanofabrication University of Twente Hallenweg 15 7522 NB, Enschede, The Netherlands
Email	J.Brinkmann@utwente.nl
ESF-researcher	-
Research interest	Coronary artery blockage is most frequently treated by placement of a stent to re-open the vessel. However, re-narrowing, or restenosis, occurs after stent placement. The importance of rapid re-endothelialization of stent surfaces to prevent such complications has become well acknowledged in recent years. Creating an artificial environment on surfaces encoding endothelial cell (EC) "triggering" extracellular matrix (ECM) cues, i.e. endothelial cell adhesion and migration promoting peptides or proteins, could provide new insights into EC migration. Dynamical switching of such cues allows additional tuning of the ECM environment. Our aim is to investigate reversible stimuli-responsive semi-synthetic proteins and peptides that will be immobilized on the material surface by supramolecular inter-actions such as host-guest chemistry and thereby create complex patterns of signaling molecules that will direct the adhesion and migration of ECs on stent materials.

Name	**Nadezda Chakrova**
Address	Imaging Science and Technology Delft University of Technology Weteringkade 91 2515 AM, Den Haag, The Netherlands
Email	N.Chakrova@tudelft.nl
ESF-researcher	-
Research interest	In contemporary patterned illumination microscopy techniques resolution is increased by the cost of the high illumination dose. Hence, living cells suffer from photo-bleaching and photo-toxicity in super-resolution fluorescence microscopy with patterned illumination. In order to reduce the illumination and ensure the survival of the living cells a new technique—combination of the structured illumination microscopy (SIM) with the controlled light exposure microscopy (CLEM/PAM)—will be investigated in the first part of my PhD project. The second part is directed to implement patterned illumination techniques to fluorescence lifetime imaging microscopy (SIM-FLIM). Using the modulated electron multiplying (MEM) camera as a detector in a SIM-FLIM microscope, we expect to double the resolution and to provide optical sectioning of the images.

Name	**Anna Daniel**
Address	Sanquin Research, Molecular Cell Biology department University of Amsterdam Saenredamstraat 39 rd 2021 ZM, Haarlem, The Netherlands
Email	A.Daniel@sanquin.nl
ESF-researcher	-
Research interest	The subject of my PhD is the dynamic behaviour of vascular endothelial (VE) cadherin during leukocyte transmigration. Leukocyte transmigration is the process of leukocytes moving from the blood stream across the vessel wall to underlying tissues and sites of inflammation. Transmigration is a multi-step process that involves attachment to the vessel wall, rolling, firm adhesion, and extravasation. I am mainly interested in the last process, also called transendothelial migration (TEM). During TEM leukocytes breach the endothelial cell barrier and squeeze between endothelial cells in order to get to underlying tissues. The main molecular obstacle that leukocytes encounter is VE-cadherin, a cell adhesion molecule that confers endothelial monolayer integrity and prevents the movement of cells and solutes out of the blood stream. To allow leukocytes to cross VE-cadherin needs to be moved out of the way by mechanisms that are in essence still poorly understood. I am using high resolution microscopy techniques to get a clearer idea about what happens with VE-cadherin during TEM. Later on during my PhD I will study signalling pathways involving small GTPases by means of FRET and biochemical assays to answer the question of how they regulate the endothelial junction during TEM.

Name	**Giulia de Luca**
Address	Molecular Cytology, Swammerdam Institute for Life Sciences University of Amsterdam Science Park 904 1098 XH, Amsterdam,The Netherlands
Email	G.deLuca@uva.nl
ESF-researcher	-
Research interest	I am a PhD student at University of Asterdam. The aim of my work is to study how to achieve an improvement in spatial resolution in confocal microscopy. I will study a fast and sensitive detector capable to acquire as much information as possible and I will focus on the illumination technique. After that, I will develop algorithms to reconstruct a confocal image with improved resolution.

Name	**Lindsay Haarbosch**
Address	Molecular Cytology, Swammerdam Institute for Life Sciences University of Amsterdam Science Park 904 1098 XH, Amsterdam,The Netherlands
Email	L.Haarbosch@uva.nl
ESF-researcher	-
Research interest	Engineering Improved Fluorescent Proteins. Since the discovery that the green fluorescent protein (GFP) isolated from the jellyfish Aequorea victoria can be used as a molecular tool (i.e. labeling of proteins and detect their locations), many research was performed to optimize FPs. Modifications were introduced to, for example, increase the quantum yield (i.e. ratio of amount of emitted fluorescent photon to amount of photons that are absorbed), increase the photostability and obtain faster maturation (i.e. autocatalytic formation of the chromophore within the beta barrel). Besides these modifications, also color mutants were obtained: GFP can be converted into blue (BFP), cyan (CFP) and yellow (YFP) fluorescent proteins by changing only one or two amino acids. In my research I make use of the above knowledge to optimize fluorescent proteins (FPs) by site-directed and random mutagenesis. First I want to obtain the optimal (red) FP that has a fast maturation, high quantum yield, low phototoxicity and other desired features. And later during the project this improved fluorescent protein and other FPs will be changed into photoswitchable fluorescent proteins (psFPs), so they can be used for super resolution microscopy: by switching on just one individual fluorescent protein, the exact location of a molecule can be determined with an accuracy that is well below the optical diffraction limit.

Name	**Niels Heemskerk**
Address	Molecular Cell Biology Sanquin Waldeck Pyrmontstraat 5a 2123 PA, Leiden, The Netherlands
Email	N.Heemskerk@sanquin.nl
ESF-researcher	-
Research interest	During leukocyte extravasation, leukocytes use the endothelial adhesion molecule ICAM-1 to stably adhere to the endothelium. Integrin-mediated adhesion of neutrophils to the endothelium results in local clustering of the integrin-ligand ICAM-1. Subsequently, this clustering induces intracellular signals into the endothelium that result in F-actin-rich membrane protrusions at the endothelial apical surface, actively supporting leukocyte extravasation. The small GTPases Rac1 and RhoA are activated downstream ICAM-1 signalling and are important for leukocyte extravasation though the endothelium. However, the spatial-temporal activation of Rac and Rho inside the endothelium during leukocyte extravasation is still unknown. Using small GTPase biosensors we try to unravel the localization and the timing of GTPase activation during leukocyte extravasation.

Name	**Angelika Holm**
Address	Medical Microbiology Linköping University Faculty of Health Science 581 85, Linköping, Sweden
Email	Angelika.Holm@liu.se
ESF-researcher	TRAPPS
Research interest	The aquaglyceroporin AQP9 has been suggested to play a pivotal role in inflammatory cell migration, differentiation and metabolism. Thus, we want to investigate the role and regulation of AQP9 infection and inflammation, focusing on cell volume regulation, motility and metabolism. We are currently looking at the AQP9 expression in response to different inflammatory stimuli at mRNA and protein levels using molecular and imaging techniques.

Name	**Marko Kamp**
Address	Resonant Nanonphotonics FOM Insitute AMOLF Sciencepark 104 1098 XG, Amsterdam, The Netherlands
Email	Kamp@amolf.nl
ESF-researcher	-
Research interest	As the Microscopy Technician I work for several groups. Within these groups I am responsible for building and purchasing new setups as well as implementing new techniques to current setups. The setups are being used in a wide range of research projects. Some projects I am involved in are used for the investigation of: -Strength and stretching properties of DNA bonds between microspheres, surfaces and vesicles -Optical properties (spectral and intensity) of scattering nano particles and single molecules, spatial and angular. -folding mechanisms of proteins -Mechanical properties of actin networks Some of the setups used are original commercial setups, but other setups are built from scratch.

Name	**Rene Platzer**
Address	Center of Pathophysiology, Infectiology, Immunology Medical University of Vienna Mittelgasse 6/2/13 1060, Vienna, Austria
Email	Rene.Platzer@meduniwien.ac.at
ESF-researcher	Lipidprod
Research interest	Imaging the Immunological Synapse and T-Cell Antigen Recognition T cell antigen recognition is indispensable for most adaptive immune responses. This process is driven by specific T-cell antigen receptors (TCRs) binding to peptide-major histocompatibility complex (pMHC) molecules on specialized antigen presenting cells (APCs). Successful interactions promote the formation of a highly organized cellular interface, termed the immunological synapse, which consists in addition to TCRs and pMHCs a plethora of accessory proteins including (among many others) co-receptors, adhesion molecules and co-stimulatory molecules. Antigenic pMHCs are often rare and TCR-pMHC are typically in low affinity (mM range). Nonetheless, T cells can sense the presence of a single antigenic pMHC among many non-stimulatory, yet structurally similar pMHCs present on the APC surface . The basis underlying this remarkable phenomenon is currently unknown. Two recent studies have shown that the molecular dynamics of synaptic TCR-pMHC binding is drastically accelerated. However, the synapse-specific factors promoting binding and antigen recognition are not clear. Identifying

	and characterizing these factors is the aim of our research. For this we will apply advanced imaging approaches including super-resolution microscopy to resolve the local distribution of synaptic key players, as well as single molecule and Förster Resonance Energy Transfer (FRET) microscopy to measure TCR-pMHC interaction kinetics in situ. To this end we are currently engineering suitable imaging probes, which include mono- and divalent site-specifically labeled streptavidin, photo-switchable fluorescent proteins as well as monovalent functionalized single chain antibody fragments. We expect that our studies will help explain at least in part the molecular foundation of antigenic tolerance and autoimmunity, as the composition of the immune synapse, and thus the conditions for T cell antigen recognition, are subject to regulation in T cell development and APC maturation.

Name	**Dion Richardson**
Address	Molecular Cell Biology Sanquin Engelenburg 160 2036 RV, Haarlem, The Netherlands
Email	D.Richardson@sanquin.nl
ESF-researcher	-
Research interest	Prions are infectious agents that cause neurodegenerative diseases and comprise a conformational variant (PrPSc) of the host protein PrPC. Upon infection, PrPSc accumulates in lymphoid organs (i.e. spleen), where it replicates before reaching the brain via the peripheral nervous system. Prion infectivity in blood is associated with plasma and PBMCs, but the source of prions in plasma and the mechanism of prion acquisition by blood cells are unknown. Endothelial cells (ECs) express PrPC and may support the transfer of prion from infected tissues to blood and vice versa, e.g. following blood transfusion. We found that ECs shed endogenous PrP into the medium as soluble and microvesicle-associated protein. PrP shedding requires metalloprotease activity and is increased by stimulation of endothelial cells with pro-inflammatory cytokines. We also found endothelial cell-to-cell transfer of prions through connecting nanotubes, a route that is also used by pathogens such as HIV. These findings support the notion that the vascular endothelium actively promotes prion dissemination, a function that can be enhanced upon inflammation. The endothelium is the largest organ in the human body and its contribution to the infectious process is likely not trivial. Future studies in our group will therefore focus on the molecular and mechanistic basis of prion transfer via the vascular endothelium.

Name	**Kayode Salami**
Address	Microbiology OLABISI ONABANJO University 234037, AGOIWOYE, AGO-IWOYE Nigeria
Email	Masterhealth07@gmail.com
ESF-researcher	-
Research interest	-

Name	**Kay Oliver Schink**
Address	Biochemistry The Norwegian Radium Hospital Stensgata 18 358, Oslo, Norway
Email	Kay.Oliver.Schink@rr-research.no
ESF-researcher	TRAPPS
Research interest	We are investigating the intracellular dynamics and localisation of the phosphoinositide PtdIns(3)P. PtdIns(3)P is predominantly found on early endosomal vesicles, but has also been found in autophagosomes and at the plasma membrane. The main role of PtdIns(3)P is in endosomal sorting and autophagy, but recently, an additional role for PtdIns(3)P-binding proteins during cell division was found. We are following the distribution of this lipid duing endosomal sorting, autophagy and cytokinesis using fluorescently tagged lipid-binding FYVE and PX domains. In order to elucidate the role of PtdIns(3)P during cell division, we have analysed the distribution of PtdIns(3)P and its effector proteins in dividing cells. Time lapse imaging revealed that PtdIns(3)P-positive structures undergo rapid reorganization during cell division. During cytokinesis, PtdIns(3)P-positive structures accumulate at the cleavage furrow and adjacent to the intercellular bridge between the two dividing cells, possibly providing membrane material necessary for the physical separation of the two cells. Furthermore, PtdIns(3)P accumulates next to the midbody of dividing cells directly prior to abscission, suggesting that PtdIns(3)P-binding proteins are recruited here to ensure correct cell division. We found that this accumulation coincides with the localization of Rab family GTPases, which might locally regulate the synthesis of PtdIns(3)P. Currently, we are trying to elucidate the role of PtdIns(3)P during cell division by acute perturbation of this lipid and by disrupting the regulation of PtdIns(3)P synthesis by Rab family GTPases. Apart form the role of PtdIns(3)P during cytokinesis, we are currently looking into the role of PtdIns(3)P during the formation of autophagosomes at the ER using similar PtdIns(3)P-binding protiens and perturbation approaches.

Name	**Gülis Zengin**
Address	Chalmers University of Technology, Applied Physics, Bionanophotonics 412 96, Gothenburg, Sweden
Email	Gulis@chalmers.se
ESF-researcher	Plasmon-Bionanosense
Research interest	FRET is a long distance transfer of electronic excitation energy between fluorophores and one of very few methods able to probe the interaction between proteins in vivo. Appropriate donor and acceptor fluorophores (in particular genetically expressed fluorescent fusion proteins) tag selected protein pairs and an interaction is studied through a change in e.g. donor lifetime or acceptor intensity. The problem with FRET is that the interaction distances for which it is useful (characterized by the so-called Förster distance) is very small, typically only ~5 nm. This limits the use of FRET method for large protein interactions. However, it is now known that FRET effects can be greatly modified by the local photon density of states (PDOS) of the material in the immediate vicinity of the donor-acceptor pair. It was for example shown that FRET occurs across a Ag film as thick as 120 nm, i.e. an order of magnitude higher than the conventional 10 nm "limit". The donor-acceptor coupling is in this case mediated by the plasmons of the film, which strongly modifies the PDOS and extend the range of donor-to-acceptor energy transfer. Still, the best improvement of FRET rates probably lies in using localized antenna modes to further strengthen the near-field coupling between the molecules. In my project, we will attempt to construct dense plasmonic 2D antenna arrays specifically designed for enhancing interactions between fluorescent proteins in cell membranes. We are particularly interested in membrane localized FRET systems since to enhance the FRET process, plasmonic structures should be placed at a certain distance to donor and acceptor fluorescent proteins. The idea is to use these plasmonic substrates as a platform where cells can grow on and FRET process can be enhanced at the same time. Increasing Förster distance of the most popular donor-acceptor pair in biology, cyan-yellow variant fluorescent proteins, from the "natural value" of ~ 4.8 - 5.7 nm up to 10 nm would for example have tremendous impact on our possibility to study membrane protein interactions.

Name	**Dimitra Touli**
Address	Molecular Cytology, Swammerdam Institute for Life Sciences University of Amsterdam Science Park 904 1098 XH, Amsterdam,The Netherlands
Email	D.Touli@uva.nl
ESF-researcher	-
Research interest	-

Name	**Alexander Zwirzitz**
Address	Molecular Immunology Institute for Hygiene and Applied Immunology Center for Pathophysiology Infectiology and Applied Immunology Medical University of Vienna Ayrenhoffgasse 8/14 1090, Vienna, Austria
Email	Alexander.Zwirzitz@meduniwien.ac.at
ESF-researcher	Lipidprod
Research interest	As a PhD student involved in the LIPIDPROD project, I aim to unravel how proteins are directed into specific membrane microdomains and decipher the molecular determinants responsible for lipid raft association. Since GPI-anchored proteins are generally said to be 'raftophilic' but not all of them to a comparable extent, my current emphasis lies on the generation of GPI-anchor swap mutants (of e.g. CD48, CD55, CD59, CD87), which will be used to examine whether the protein domain itself or the respective GPI-anchor accounts for lipid raft association. In addition, I am investigating the raft partitioning behavior of the Src family tyrosine kinase Lck.